Molecular simulations on leaf anchor peptides and microgel carriers suitable for advanced/sustainable nutrient and herbicide delivery

Inaugural-Dissertation

zur Erlangung des Doktorgrades

der Mathematisch-Naturwissenschaftlichen Fakultät

der Heinrich-Heine-Universität Düsseldorf

vorgelegt von

Jonas Dittrich

aus Duisburg

Düsseldorf, November 2022

aus dem Institut für Pharmazeutische und Medizinische Chemie
der Heinrich-Heine-Universität Düsseldorf

Gedruckt mit der Genehmigung der
Mathematisch-Naturwissenschaftlichen Fakultät der
Heinrich-Heine-Universität Düsseldorf

Berichterstatter:
1. Prof. Dr. Holger Gohlke
2. Prof. Dr. Georg Groth

Tag der mündlichen Prüfung: 12.04.2023

Eidesstattliche Erklärung

Ich, Jonas Dittrich, versichere an Eides Statt, dass die Dissertation von mir selbständig und ohne unzulässige fremde Hilfe unter Beachtung der „Grundsätze zur Sicherung guter wissenschaftlicher Praxis an der Heinrich-Heine-Universität Düsseldorf“ erstellt worden ist.

Diese Dissertation wurde in der vorgelegten oder einer ähnlichen Form noch bei keiner anderen Institution eingereicht, und es wurden bisher keine erfolglosen Promotionsversuche von mir unternommen.

Düsseldorf, November 2022

to my wife Sarah and my family

„Ich bin nicht auf der Welt, um alles richtig zu machen.“

-Marco Tschirpke

Table of Contents

List of Figures x
List of Publications xvii
Abbreviations xviii
Abstract xx
Zusammenfassung xxi
1. Introduction 1
2. Background 5
2.1. Plant Protection 5
2.1.1. Anchor Peptides for Surface Functionalization 6
2.1.2. Stimuli-responsive Polymers as Carrier 10
2.1.3. Herbicides in Modern Agriculture 13
2.2. Computational Chemistry and Molecular Modeling 18
2.2.1. Modeling Peptides and Proteins 20
2.2.2. Exploring Polymer Dynamics *in silico* 22
2.2.3. Investigating Biological Interfaces 23
3. Scope of the Thesis 25
4. Publications 29
4.1. Publication I 29
4.2. Publication II 37
4.3. Publication III 43
5. Summary and Perspectives 51
6. Acknowledgments 53
7. Reprint Permissions 55
8. Publication I 57
Rational Design Yields Molecular Insights on Leaf-Binding of Anchor Peptides 57
9. Publication II 91
Temperature-Induced Coil-to-Globule Transition of Poly(*N*-vinylcaprolactam) 91
10. Publication III 149
PNVCL Microgels as Stimuli-Responsive Carrier for Okanin 149
11. Curriculum Vitae 255
12. Bibliography 259

List of Figures

Figure 1. Estimations and probabilistic projections of the total world population. Estimations are based on the probabilistic projections of total fertility and life expectancy at birth using a Bayesian Hierarchical Model**.** The probabilistic median is depicted as red solid line, the 80 % prediction and the 95 % prediction intervals of the probabilistic population projection are depicted as dashed and dotted red lines, respectively. Figure adapted from ref. 1. 1

Figure 2. Concept of the *GreenRelease* technology for foliar delivery of nutrients. Microgels (blue) loaded with nutrients (yellow) and decorated with anchor peptides (red) show adhesion to the surface of a leaf. The ingredients are not only limited to nutrients, but may also be insecticides, fungicides, or herbicides. Reprinted from Meurer *et al.*[24] with permission.....5

Figure 3. Examples of anchor peptides used for surface functionalization. LCI (**A**, PDB ID: 2B9K[47], UniProt ID: P82243) consists mainly of anti-parallel beta strands (yellow), whereas Macaque Histatin (**B**, homology model generated with TopModel[52], UniProt ID: P34084) displays an α-helical (red) structure. Loop regions are colored green and the protein surface is shown in translucent grey. 7

Figure 4. Amphipathic character of the APs Macaque Histatin (**A,** UniProt ID: P34084) character of Plantaricin A (**B,** PDB ID: 1YTR, UniProt ID: P80214). The Macaque Histatin contains a considerable fraction of basic polar residues (red), mainly histidine, whereas the Plantaricin A consists of mainly nonpolar (blue) or uncharged polar (yellow) residues. The respective helical wheels show the location of the different AAs on the helix. Although structurally different in terms of hydrophobicity, both APs show good adhesion towards epicuticular waxes. 9

Figure 5. Representation of the volume phase transition (VPT) of PNVCL MGs (**A**) and the coil-to-globule transition of oligomeric PNVCL upon reaching the lower critical solution temperature (LCST) (**B**). The core of the core-shell structure of the PNVCL MG is depicted schematically as a transparent grey circle. Driving forces causing the coil-to-globule transition of a

thermoresponsive (linear) polymer observed at LCST are closely connected to the observed changes in the morphology of the corresponding microgel 11

Figure 6. Difference in the photosynthetic reactions and carbon fixation in C_3 (left) and C_4 plants (right). In both cases, CO_2 is absorbed through the leaf stomata. For C_3 plants, RuBisCo uses the CO_2 for the carboxylation of RuBP yielding PGA, which is then transformed into starch and sugars under ATP and NADPH consumption (Calvin cycle). In C_4 plants, the CO_2 is hydrated and then used for the carboxylation of PEP by PEPC yielding oxaloacetate, which is potentially reduced or transaminated further. Within the bundle sheath cell, the C4 compound is then decarboxylated by PCK (in the case of oxaloacetate) yielding pyruvate and CO_2, which is fixed by RuBisCo within the Calvin cycle. Figure adapted from Yamori and Hikosaka[107]. 16

Figure 7. PEPC plays an essential role in carbon fixation in C_4 plants. **A** Homology model of the PEPC tetramer of *A. retroflexus* generated from sequence using SWISS-MODEL[113]. **B** Potential binding pose obtained by docking of okanin in the binding pocket of PEPC from *A. retroflexus* obtained via homology modeling [unpublished results]. **C** Chemical structure of the C_4 plant selective herbicide okanin (2′,3′,4′,3,4-pentahydroxy-chalcone). 17

Figure 8. Number of sequence entries in the UniProtKB and structures in the PDB (**A**) and the taxonomic distribution of the sequences within the complete UniProtKB dataset (**B**) and the Eukaryote subset (**C**). Decreasing entry numbers for the UniProtKB database are caused by merging similar entries to reduce redundancy. The graph contains data up to April 2021 and August 2021 for the UniProtKB and the PDB, respectively. 20

Figure 9. Crystal structure of the AP LCI (PDB ID: 2B9K, red) in comparison to a model obtained from ten 20 µs long folding simulations (blue) following the approach of Nguyen *et al.*[150]. The C_α-atoms show a root-mean-square deviation (RMSD) of 3.6 Å [unpublished results]. 21

Figure 10. Exemplary structure of the cutin matrix as proposed by Fich *et al.*[194]. The polyester matrix is formed by ω-hydroxy fatty acids of different chain lengths, while C_{16} and C_{18} fatty acids account for the majority of fatty acids within the cutin matrix. Midchain hydroxyl groups allow for a dendritic/crosslinked structure. 24

Figure 11. Stepwise creation of an atomistic leaf surface model. **A)** Three-layered crystalline Iβ cellulose. **B)** Loosely packed polyester matrix of crosslinked 10,18-dihydroxyoctadecanoic acid located above the cellulose sheet. **C)** Compacted cutin layer atop the cellulose sheet after 25 ns of NVT MD simulations. **D)** Randomly placed wax components above the compact cutin layer. **E)** Solvated system. **F)** Snapshot obtained after 100 ns of MD simulations of the complete model. Figure and figure caption taken from Publication I, see page 60.....31

Figure 12. **A)** Residue-wise relative contacts of MacHis with the wax molecules during 10 x 250 ns of MD simulations of AP adsorption. The secondary structure, as determined by DSSP,[199] is indicated on the top. The color code relates to that shown in panel B. Error bars denote the SEM. **B)** Homology model of MacHis colored according to the relative number of contacts a residue forms within 7 Å with the wax molecules; sidechains of residues with a relative contact > 0.04 are depicted as sticks and spheres. Figure and figure caption taken from Publication I, see page 64. 32

Figure 13. Adaptive steered MD of the desorption process of MacHis (cyan) from the leaf surface model. The potential of mean force (PMF, black solid line) of desorption determined as the average of the work of each stage (blue transparent lines) is depicted as inlay. The starting structure (stage 1) of MacHis as well as a structure selected from stage 12 of the steered MD are shown translucent, the completely detached AP is shown opaque (stage 17); corresponding stages are highlighted in the PMF profile. Figure and figure caption taken from Publication I, see page 66. 33

Figure 14. **A)** Potential of mean force (PMF) profiles for the desorption of MacHis (blue), Plantaricin A (green), LCI (orange), Pleurocidin (red), and Magainin (purple) as determined by adaptive steered MDs. The work of the 25 individual replicas per stage is depicted as transparent, and the PMF is shown opaque. **B)** Force profile as difference quotient ΔPMF/1 Å, where the denominator relates to the distance difference with respect to the leaf surface. **C)** Bar plot depicting the maxima of the forces shown in panel **B**. Figure and figure caption taken from Publication I, see page 67.....34

Figure 15. Radius of gyration (R_G) during five·MD simulations of 1 µs length of an atactic PNVCL 40mer (**A**, **C**) and during five MD simulations of 500 ns

length of an atactic PVP 40mer (**B**, **D**) at 293 K (**A**, **B**) and 313 K (**C**, **D**). Corresponding frequency distributions are shown next to the time series in matching color, a frequency distribution of all data is shown as dashed black line. Sample structures taken from each simulation setup are depicted next to the corresponding simulation. Figure and figure caption taken from Publication II, see page 97 39

Figure 16. HMMs for an atactic PNVCL 40mer at 293 K (A) and 313 K (B) projected on the same IC space. The probabilities π_i obtained from the stationary distributions π are shown for each state; the size of the arrows between states is scaled by the corresponding transition probability for each HMM, which is given as label for the lag time of 0.5 ns. For each macrostate, the ten most probable representative structures are shown. The structure with the highest probability in each set is shown in non-transparent representation. Figure and figure caption taken from Publication II, see page 98. 40

Figure 17. Bar plot showing energetic differences for the coil-to-globule transition of an atactic PNVCL 40mer at 293 K and 313 K. ΔG_{eff} is decomposed into the difference in gas-phase energy ΔE_{MM} and solvation free energy ΔG_{solv}. Configurational entropies of the polymer are estimated by NMA. The error bars depict the standard error of the mean. Differences in energy components between both temperatures, as well as corresponding errors determined according to the laws of error propagation, are depicted below and above the respective horizontal lines. Figure and figure caption taken from Publication II, see page 99.....41

Figure 18. Decomposition of a microgel into atomistic models for the shell and core section. Simulations of linear oligomers mimic the loosely crosslinked shell of the microgel (left); the *N,N′*-methylenebisacrylamide crosslinked cubic PNVCL models mimic the highly crosslinked core (right). Figure and figure caption adapted from Publication III, see page 159. 44

Figure 19. Influence of the loading of okanin on the hydrodynamic radius R_H, the thermo-responsiveness, and the morphology of PNVCL microgels. **A** Loading of okanin into pure PNVCL microgels determined by UV/Vis for varying molar ratios $n_{\mathrm{okanin}}/n_{\mathrm{CU}}$. **B** R_{H} of PNVCL loaded with okanin as determined by DLS at 20 °C and 50 °C for varying $n_{\mathrm{okanin}}/n_{\mathrm{CU}}$ ratios. **C**

Exemplary STEM images of a PNVCL microgel for varying n_{okanin}/n_{CU} ratios. Figure and figure caption taken from Publication III, see page 166. 45

Figure 20. Two-dimensional histograms of the binding free energy of okanin to the linear PNVCL 50mer and its components (changes in the gas phase energy and solvation free energy ($\Delta E_{MM} + \Delta G_{solvation}$, **A**) and changes in the configurational entropy of the solutes ($T\Delta S$, **B**)) in relation to the number of formed contacts. The binding free energy ($\Delta G^0_{binding}$, **C**) of okanin to the PNVCL polymer shows an inverse linear correlation (regression line shown solid, 95% prediction interval shown dotted, Pearson correlation coefficient and linear equation are depicted in the corresponding legend) with the number of formed contacts. Exemplary binding poses are shown for adsorbed okanin (**I**, < 475 contacts, $\Delta G^0_{binding} > 0$) and bound okanin (**II**, > 475 contacts, $\Delta G^0_{binding} < 0$). The MM-PBSA analysis was performed for trajectories of the linear PNVCL 50mer, in which a collapse of the chain was observed; only frames where okanin formed contacts to PNVCL were considered. Figure and figure caption taken from Publication III, see page 169. 46

Figure 21. Quantification of different okanin species and interactions. Okanin stacks in solution (**A** two molecules, **B** three molecules), on adsorbed okanin (**C**), and within a bound state (**D**) at high molar ratio ($n_{okanin}/n_{CU} = 1.11$). E Quantification of okanin species. Okanin species fractions are given in relation to the overall number of okanin molecules within the respective system. With increasing okanin concentration, the fraction of okanin molecules in a stacking configuration in solution increases linearly for molar ratios above 0.28 (purple), while the overall fraction including stacking to bound/adsorbed okanin (blue) increases linearly for all molar ratios. The fraction of adsorbed (yellow), bound (green), and okanin stacked within the microgel (red) decreases with increasing okanin concentration. **F** Comparison of experimentally determined bound okanin per constitutional unit ($n_{okanin,bound}/n_{CU}$) with okanin considered bound and/or stacked within the microgel (> 475 contacts to PNVCL or > 475 contacts and at least 250 contacts formed with PNVCL) in MD simulations. The grey shaded area

depicts the uncertainty related to a change of the cutoff of ± 25 contacts (i.e., 450 and 500 contacts for the upper and lower bound, respectively), which corresponds to a change of the computed binding free energy of approximately ±1 kcal mol^{-1}. Figure and figure caption taken from Publication III, see page 172. 48

List of Publications

This thesis is based on the following publications:

I **Dittrich, J. (30 %)**[#], Brethauer, C.[#], Goncharenko, L., Bührmann, J., Zeisler-Diehl, V., Pariyar, S., Jakob, F., Kurkina, T., Schreiber, L., Schwaneberg, U., Gohlke, H.
"Rational Design Yields Molecular Insights on Leaf-Binding of Anchor Peptides"
DOI: 10.1021/acsami.2c00648
ACS Applied Materials & Interfaces, **2022**, 14, 28412-28426.
Journal Impact Factor 2021: 10.383

II **Dittrich, J. (70 %)**, Kather, M., Holzberger, A., Pich, A., Gohlke, H.
"Cumulative Submillisecond All-Atom Simulations of the Temperature-Induced Coil-to-Globule Transition of Poly(N-vinylcaprolactam) in Aqueous Solution"
Macromolecules, **2020**, *53*, 9793−9810.
Journal Impact Factor 2020: 5.985

III **Dittrich, J. (35 %)**[#], Kolodzy, F.[#], Töpel, A., Pich, A., Gohlke, H.
"Loading and Co-Solvent-Triggered Release of Okanin, a C_4 Plant Key Enzyme Inhibitor, into/from Functional Microgels"
DOI: 10.26434/chemrxiv-2022-sgbx9-v2 (ChemRxiv, 13.10.2022)

[#]these authors contributed equally.

Abbreviations

AA	amino acid
AI	artificial intelligence
AMBER	Assisted Model Building with Energy Refinement
AMP	antimicrobial peptide
AP	anchor peptide
ASMD	adaptive steered molecular dynamics
ATP	adenosine triphosphate
CA	carbonic anhydrase
CAM	Crassulacean acid metabolism
CG	coarse-grained
CHARMM	Chemistry at HARvard Macromolecular Mechanics
CU	constitutional unit
DL	deep learning
DLS	dynamic light scattering
DoE	design of experiments
eGFP	enhanced green fluorescent protein
FF	force field
FID	flame ionization detection
GAFF	general AMBER force field
GC	gas chromatography
GMA	glycidyl methacrylate
HM	homology modeling
IARC	International Agency for Research on Cancer
k	Boltzmann constant
KnowVolution	knowledge-gaining directed evolution
LCST	lower critical solution temperature
MacHis	Macaque Histatin
MD	molecular dynamics
MG	microgel
ML	machine learning
MM-PBSA	molecular mechanics Poisson-Boltzmann surface area

MS	mass spectrometry
$NADP^+$	nicotinamide adenine dinucleotide phosphate
NG	nanogel
NMR	nuclear magnetic resonance
PCK	phosphoenolpyruvate carboxykinase
PDB	Protein Data Bank
PEP	phosphoenolpyruvate
PEPC	phosphoenolpyruvate carboxylase
PET	polyethylene terephthalate
PGA	3-phosphoglyceric acid
PMF	potential of mean force
PNIPAM	poly(*N*-isopropylacrylamide)
PNVCL	poly(*N*-vinylcaprolactam)
PP	polypropylene
PPDK	pyruvate phosphate dikinase
PS	polystyrene
PVP	poly(*N*-vinylpyrrolidone)
R_G	radius of gyration
RMSD	root-mean-square deviation
RuBisCo	ribulose-1,5-bisphosphate carboxylase-oxygenase
RuBP	ribulose-1,5-bisphosphate
SDM	site-directed mutagenesis
SSM	site-saturation mutagenesis
STEM	scanning transmission electron microscopy
T	temperature (in K)
UniProt	Universal Protein Resource
UniProtKB	UniProt Knowledgebase
VPT	volume phase transition
VPTT	volume phase transition temperature

Abstract

The constant growth in world population is accompanied by a steadily increasing demand for food. This challenge has to be addressed in several ways. One option is increasing the efficiency of food production, as modern agriculture struggles with pests, especially weeds, reducing the yield significantly. The excessive use of agrochemicals to reduce pests, however, leads to the accumulation of agrochemicals within the ecosystem. Thus, the overall amount of used agrochemicals has to be reduced in the future, to reduce burdens on the ecosystem while simultaneously providing the same or even enhanced crop protection. Within the *GreenRelease* project, microgels anchored to crops or weeds using specialized peptides are being developed for a controlled release of agrochemicals while minimizing the amount applied. To improve this novel technology, understanding the mechanisms at an atomistic level at every stage is key. In an interdisciplinary approach, in which I used molecular dynamics simulations in combination with experiments done by the working groups of Prof. Dr. Schwaneberg and Prof. Dr. Pich, key mechanisms of the *GreenRelease* technology were elucidated.

First, I investigated the adsorption of different anchor peptides to the epicuticular wax of apple leaves using molecular dynamics simulations and identified residues of major importance for the binding to the leaf wax, which were subsequently validated experimentally. Moreover, my constructed model of a leaf surface can successfully distinguish anchor peptides of different binding affinities as determined in experiments, establishing a platform for the rational peptide design.

Second, in an extensive simulation study on the temperature-induced coil-to-globule transition of poly-(*N*-vinylcaprolactam) oligomers in a multi-parameter approach, we established a platform for analyzing microgels as potential carriers. The transition was elaborated on in detail using various methods of free energy estimation and by constructing Hidden Markov Models. Here, I could show that the collapse of the oligomers may be caused by a delicate enthalpy-entropy compensation at elevated temperatures.

Third, I used linear as well as crosslinked poly-(*N*-vinylcaprolactam) models in simulations with varying concentrations of the C_4 plant key enzyme inhibitor okanin to investigate the uptake and release into/from the microgel used as a carrier. The simulations revealed a fraction of permanently bound molecules, providing a sensible explanation of the experimentally observed loading and establishing the basis for further tailoring and improvement of the microgel.

Zusammenfassung

Die stetig wachsende Weltbevölkerung führt unweigerlich zu einem global steigenden Bedarf an Lebensmittel. Um diesen Bedarf zu decken, ist es nötig, mehreren Strategien zu folgen, von der eine die Effizienzsteigerung der Lebensmittelproduktion ist. In der modernen Agrarwirtschaft sorgen Schädlinge, besonders Unkraut, für hohe Ertragseinbußen. Der übermäßige Gebrauch von Agrochemikalien zur Schädlingsbekämpfung führt jedoch zu einer Akkumulierung dieser Stoffe im Ökosystem. Um dies zu verhindern, muss die Menge der verwendeten Chemikalien bei mindestens gleichbleibender Effizienz vermindert werden. Innerhalb des Projekts *GreenRelease*, werden Mikrogele, welche mit Ankerpeptiden versehen sind, entwickelt, um eine kontrollierte Freisetzung von Wirkstoffen zu erzielen und somit die benötigte Menge der genutzten Ressourcen zu reduzieren. Um diese neue Technologie optimieren zu können, ist es wesentlich, alle involvierten Mechanismen auf atomarer Ebene zu verstehen. In einem interdisziplinären Ansatz aus Simulationen und Laborexperimenten in den Gruppen von Prof. Dr. Schwaneberg und Prof. Dr. Pich wurden die wesentlichen Prozesse dieser Technologie auf atomarer Ebene untersucht.

Zuerst habe ich die Adsorption der Ankerpeptide auf epikutikulärem Blattwachs mittels molekulardynamischer Simulationen untersucht und für die Adsorption wichtige Aminosäuren identifiziert, welche anschließend experimentell validiert wurden. Das Model der Blattoberfläche ermöglicht es, die Bindestärken verschiedener Ankerpeptide zu differenzieren und schafft somit die Grundlage das rationale Design der Ankerpeptide.

Zweitens haben wir die thermoreaktiven Eigenschaften des Knäuel-Globuli-Übergangs von oligomeren Poly-(*N*-Vinylcaprolactam) in einer Multiparameteranalyse untersucht, um eine Grundlage für die Erforschung der Mikrogele als Wirkstoffträger zu schaffen. Der Übergang wurde mittels Berechnung der freien Energie und der Erstellung von Markov Modellen näher betrachtet. Ich konnte eine Enthalpie-Entropie Kompensation als Ursache für den Übergang identifizieren.

Drittens habe ich die Be- und Entladung von linearem und vernetztem Poly-(*N*-Vinylcaprolactam) mit Okanin, einem Inhibitor des Schülsselenzyms von C_4-Pflanzen, untersucht. In den Simulationen wurde die Adsorption des Okanin untersucht und eine Fraktion an permanent gebundenem Okanin beobachtet, welches die experimentell beobachtete Beladung erklärt. Diese Arbeit schafft ermöglicht die weitere Optimierung des Mikrogels als potenzielles Trägermaterial in agrochemischen Anwendungen.

1. Introduction

With a steadily growing world population estimated to reach ten billion[1] by the end of the year 2060 (Figure 1), innovative and sustainable resource management is more urgent than ever. Naturally, the growth in world population is accompanied by a growing demand for food[2], notwithstanding the continuous struggle with the unsolved problem of world hunger[3].

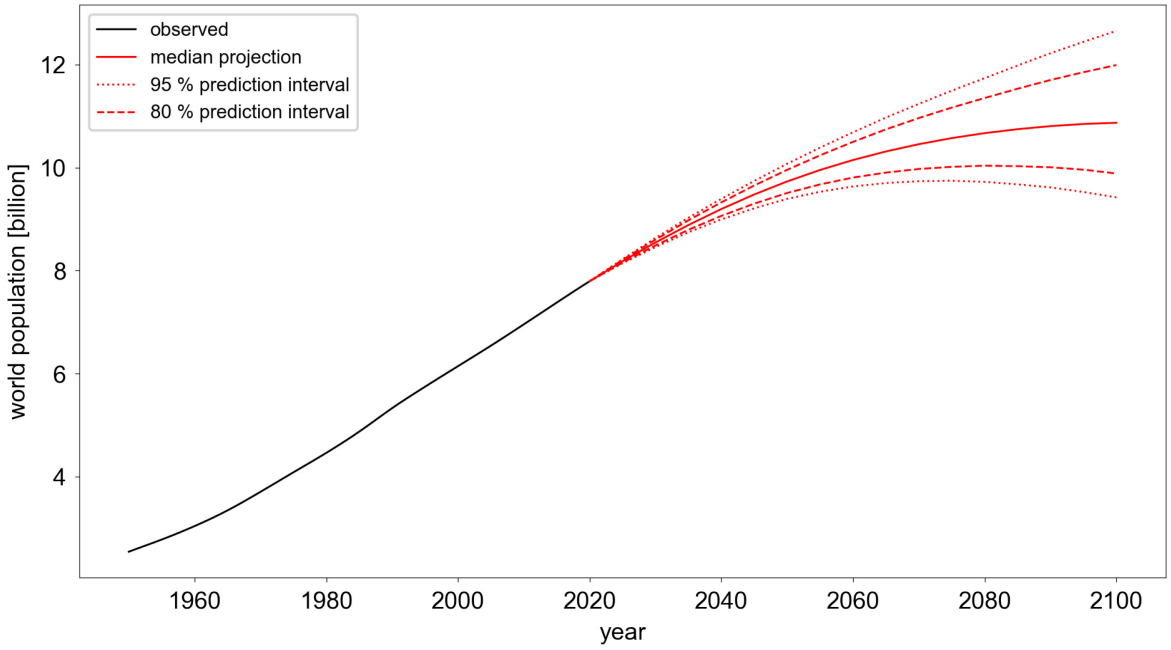

Figure 1. Estimations and probabilistic projections of the total world population. Estimations are based on the probabilistic projections of total fertility and life expectancy at birth using a Bayesian Hierarchical Model**.** The probabilistic median is depicted as red solid line, the 80 % prediction and the 95 % prediction intervals of the probabilistic population projection are depicted as dashed and dotted red lines, respectively. Figure adapted from ref. 1.

This challenge presented by the continuously growing demand for food has to be addressed at many different levels simultaneously, e.g., by reducing food waste and overconsumption[3] on the one hand and by increasing sustainable food production[4] on the other hand. The latter can be achieved by either increasing the overall production quantity or by improving its efficiency. However, meeting the higher demand for food quantity will only be possible for a limited time, as the available area of arable land will eventually become scarce for numerous reasons, e.g., the demand for living space, environmental pollution, erosion, and soil degradation as well as other harm caused by climate change, and many more[5]. Moreover, modern agriculture is constantly at risk due to pests, including weeds, pathogens, and animals[6-7]. Exemplarily, the global loss due to pests varies from

~50 % in wheat production to more than 80 % in cotton production.[6] Overall, with more than 30 %, weeds alone cause the highest loss among all pests. The losses combined with the costs for weed control and management pose a major part of farmers' costs[6]. Despite lots of effort to overcome the weed challenge on global food production, there is a constant need in overcoming rapidly evolving resistances against herbicides among many weed species. Over the last century, many synthetic[8] and natural compounds[9-12] have been developed and investigated as potential herbicides. In recent years, a clear research trend towards natural and "greener", i.e., biodegradable and/or bio-based, compounds is noticeable, as they are regarded as sustainable in contrast to purely synthetic herbicides[13-14].

Despite the increasing use of sustainable agrochemicals, the high amount of pest control agents used during application inevitably leads to an accumulation of the compounds not only in the soil but also in the groundwater eventually[15-17]. Consequent concerns about the potential long-term health effects led to a change of thinking. The idea of a controlled release of agrochemicals to counter bioaccumulation has been proposed early, together with the recommendation to work on new, environmentally friendly herbicides[18]. Recently, carriers and active agents from the fields of nano-[19-22] and microtechnology[23-24] found their way into modern agriculture as potential candidates for pest control management. Often, these increase the rain fastness of pest control agents and formulations, which is of major importance not only for performance but also for sustainability. A decreased amount of applied chemicals is of economic benefit and eventually results in conservation of arable land increasing overall crop yields. Furthermore, the development of selective herbicides can decrease the amount of deployed herbicides, easier usage, and reduce the resistance development among weeds.

Meurer *et al.* described a novel technology for the foliar delivery of nutrients using microgel (MG) containers as carriers, which are decorated with anchor peptides (APs) to promote adhesion to leaf surfaces[24]. Within the interdisciplinary *GreenRelease* project, this concept is used as the basis for further technological optimization and the development of a fundamental understanding of the involved mechanisms. Although the concept has been proven experimentally, detailed knowledge about the processes, at an atomistic level, has remained elusive so far. To further optimize the technology and tailor the application, it is essential, to understand the adsorption process to the plant and the interactions of the agrochemical with the carrier MG.

In this thesis, the investigation of the driving forces at an atomistic level for the most important steps within the *GreenRelease* technology is presented. By using computational means, such as molecular dynamics (MD) simulations and free energy estimations in combination with laboratory experiments provided by the working groups of Prof. Dr. Schwaneberg and Prof. Dr. Pich, it is possible to elucidate key interactions of this novel technology at an atomistic level.

So far, the interface/interacting residues between the APs and a complex biological surface such as a plant leaf is/are unknown, yet vital for the rational design of better-performing peptides. The knowledge about the interactions at atomistic level can be exploited to increase their adhesion or tailor the APs with switchable and/or targeted adhesion.

Therefore, in **Publication I**, the adhesion of APs to apple leaf wax is elucidated in an integrated manner. To this end, all-atom models of an apple leaf surface including a cellulose layer, a cutin layer, and epicuticular wax were generated. The adsorption of AP was simulated to determine residues of importance for binding to the wax layer. Experiments performed in the working group of Prof. Dr. Schwaneberg confirmed the importance of the identified residues in an alanine scan using a novel fluorescence-based microtiter assay. By using steered simulations, I quantified the adsorption strength of different APs, which matches the experimentally determined binding strengths.

Understanding the dynamics of the polymer used as a carrier allows for modifying the microgel's uptake and releasing properties to yield optimal long-term release and/or targeted release. Stimuli-responsive carriers can be potentially exploited for a triggered release of agrochemicals. Based on the thermo-responsiveness and the favorable toxicological properties of poly(*N*-vinylcaprolactam) (PNVCL) MGs, they depict an excellent choice as potential carrier for agrochemicals. However, compared to the computational studies on other thermo-responsive polymers, simulation data on the coil-to-globule transition of PNVCL was comparatively rare.

Thus, in **Publication II**, the hitherto most comprehensive investigation of the temperature-induced coil-to-globule transition of linear oligomeric PNVCL using MD simulation is presented. MD simulations in combination with free energy calculations and the generation of Markov State Models provide insights into the driving forces of the temperature-induced coil-to-globule transition. Experimental data on the thermo-

responsiveness of oligomeric PNVCL generated within the working group of Prof. Dr. Pich were in agreement with the computational studies. The work presented establishes a platform for the in-depth investigation of PNVCL MGs and the loading and release of substances into/from the MGs.

Within the *GreenRelease* project, PNVCL MGs were used for the delivery of the C_4 plant key enzyme inhibitor okanin. However, the interactions between okanin and PNVCL MGs have not been investigated at this point, neither experimentally nor in simulation experiments. Building upon knowledge gained in **Publication II**, in **Publication III**, the ad- and desorption of okanin on/from the PNVCL microgel is investigated *in silico* as well as experimentally. For this, atomistic models of sections of an MG with a densely crosslinked core and loosely crosslinked shell, as often found in PNVCL microgels[25], were generated. Consecutively, the atomistic models were used in MD simulations to probe the interaction of okanin with PNVCL and elucidate the adsorption process as well as desorption in different solvents. Complementary, the loading and solvent-triggered release of okanin into/from PNVCL MGs were investigated experimentally within the working group of Prof. Dr. Pich. Simulations and free energy calculations yielded valuable insights into the ad- and desorption processes and provided potential explanations for the experimentally observed changes in the MGs morphology upon okanin loading.

2. Background

2.1. Plant Protection

In times of a constantly growing world population and increasing demand for food, sustainable agriculture is key. Within the interdisciplinary BioSC *GreenRelease* project, MGs decorated with adhesion promoting peptides are anchored to crops and used for a controlled release of fungicides, herbicides, or nutrients (Figure 2), while minimizing applied resources. Initial studies on the general mechanism of ingredient loading and release as well as the superior rain fastness of the decorated microgel containers have been reported[24].

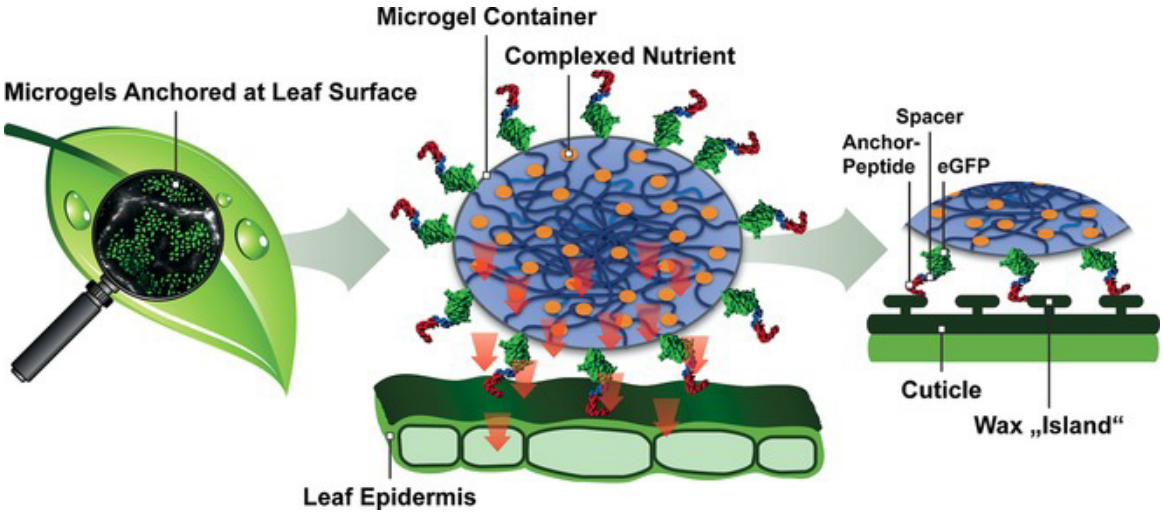

Figure 2. Concept of the *GreenRelease* technology for foliar delivery of nutrients. Microgels (blue) loaded with nutrients (yellow) and decorated with anchor peptides (red) show adhesion to the surface of a leaf. The ingredients are not only limited to nutrients, but may also be insecticides, fungicides, or herbicides. Reprinted from Meurer *et al.*[24] with permission.

The majority of investigated APs are antimicrobial peptides that provide a green and versatile method for surface functionalization[26-29]. The rain fastness of pest control agents and formulations is of major importance not only for performance but also with regard to their economy and sustainability. Here, the APs promote the adhesion to the plant's leaf or fruit, enabling the long-term release of the herbicide, fungicide, or insecticide. The MG serves as a carrier and reservoir for the agrochemical. The physicochemical properties of the MGs potentially allow a targeted release of the compounds, as some MGs are stimuli-responsive[30-32], i.e., they undergo conformational changes, such as collapsing or swelling, upon a change in temperature[33-36] or pH[37-38]. In the following chapters, each component of the *GreenRelease* technology will be described in more detail.

2.1.1. Anchor Peptides for Surface Functionalization

APs are a class of peptides used for surface functionalization, e.g., they promote adhesion to synthetic surfaces such as polypropylene (PP)[29, 39], polystyrene (PS)[28], polyethylene terephthalate (PET)[26], and other polymers[40-41], as well as complex biological surfaces such as plant leaves or fruits[24]. The immobilization of proteins and peptides with APs can be used in a variety of biomaterial surface modifications, e.g., in biocatalysis[42] and biosensors[43], for the generation of antimicrobial surfaces[44], drug delivery[45] and the foliar application of nutrients[24]. APs are often used in environmentally friendly and mild conditions, i.e., under moderate/ambient temperatures and often in aqueous solutions[24, 40, 46]. In plant protection applications, APs provide an environmentally-friendly way to increase the rain fastness and thus the efficiency.

Commonly used APs are small peptides typically ~20 to ~60 amino acids (AAs) long and often show antimicrobial activity. One of the well-investigated APs so far is LCI (PDB ID: 2B9K, UniProt ID: P82243), a 47 AA long antimicrobial peptide (AMP) isolated from *Bacillus subtilis*[47]. LCI forms antiparallel beta-strands (Figure 3A) compared to the secondary structure of the majority of identified anchor peptides, which predominantly form α-helices, such as Macaque Histatin (Figure 3B and Figure 4A) and Plantaricin (Figure 4B). AMPs were found to be often suitable adhesion promoters and thus can be used as potential APs[29]. Moreover, AMPs cover a broad structural spectrum with regard to secondary structure elements, as already shown, and a diverse AA composition[48]. Attempts to deduce the AMP's natural mode of action, e.g., membrane destabilization or permeabilization and pore formation, from its structure were presented in literature[48-49]. However, the knowledge on the structure-function relationship for the adhesion of the AMP towards other surfaces is comparatively sparse. The adhesion to synthetic surfaces such as PP, PS, and PET has been suggested to be caused by π-π interactions, where applicable, hydrophobic interactions, or hydrogen bonds[41, 50-51]. The results of the investigations are limited to small tetrameric and 7-mer peptides in one case[50-51] and a 12-mer in the other case[41]. However, the potential number of AA combinations increases exponentially with every additional AA in the sequence. Moreover, the small peptides investigated barely form helical structures and the formation of more complex structures, e.g., anti-parallel beta-sheets, is not possible at all. Even though artificial polymeric surfaces are less complex than biological ones in many cases, there is still a considerable amount of structural deviations, as the polymer's composition, its crosslinking density, and the amount of linear

and branched elements determine its overall morphology. Despite the fact that initial investigations yield first insights into the different binding types of APs, only a section of the possible combinations of APs and (artificial) interfaces has been explored yet.

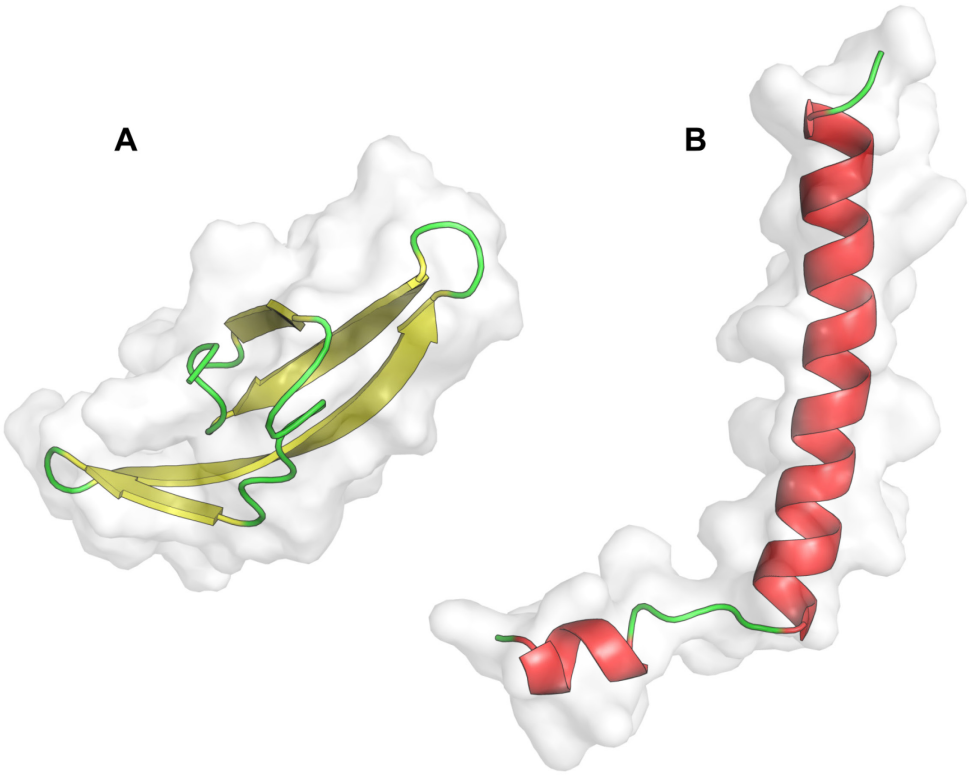

Figure 3. Examples of anchor peptides used for surface functionalization. LCI (**A**, PDB ID: 2B9K[47], UniProt ID: P82243) consists mainly of anti-parallel beta strands (yellow), whereas Macaque Histatin (**B**, homology model generated with TopModel[52], UniProt ID: P34084) displays an α-helical (red) structure. Loop regions are colored green and the protein surface is shown in translucent grey.

These initial investigations on the driving forces for the adhesion of small peptides on polymeric surfaces provide a basis for the further investigation of the adhesion of APs with a considerably higher number of AAs. For more complex APs, however, rational protein design using an adequate design of experiments (DoE) is necessary to fully understand the complex interactions with different surfaces. For LCI, the adhesion towards PP was improved using a knowledge-gaining directed evolution (KnowVolution) approach[39]. Rübsam *et al.* were able to identify 11 beneficial residues to be replaced for an increased adhesion towards PP within the first phase of the KnowVolution. During the second phase, site-saturation mutagenesis (SSM) was performed on the identified residues yielding 8 positions with significantly increased binding properties. In the third phase, computational analysis was used to elucidate potential cooperative effects. Finally, in the fourth phase of the KnowVolution, site-directed mutagenesis (SDM) was performed for the

two residues identified by the computational analysis, yielding an LCI variant with a 5-fold increased adhesion towards PP. The KnowVolution approach depicts a DoE for a rational design of APs. However, the first phase of the KnowVolution approach is dependent on a sufficiently large variant library. Moreover, the experimental effort is considerable, not only for the generation of the variant library but also for the SSM and SDM, if more residues are subject to further investigation in phases two and three of the KnowVolution.

An expansion of the DoE of the KnowVolution has to be considered when it is applied for optimization of AP adhesion towards more complex surfaces, such as plant leaves and fruits. It has been shown, that selected APs can promote the adhesion towards these complex biological surfaces[24]. For the adsorption to cucumber plants leaves, Plantaricin A (PDB ID: 1YTR, UniProt ID: P80214) was one of the most promising APs. Plantaricin A is a 26 AA long peptide that originates from *Lactobacillus plantarum*, and it shows a partial α-helical structure with largely unstructured N-terminal part[53] (Figure 4B). However, LCI and Macaque Histatin (MacHis, UniProt ID: P34084), which consists of 38 AAs and also displays supposedly a predominantly helical structure, were found to be suitable APs to increase adhesion towards cucumber plant leaves, too (see SI of ref [24]). As all three structurally different APs show adhesion to the same surface, the mode of action for the adhesion, i.e., the driving forces at the atomistic level, might differ for each AP. In terms of secondary structure, LCI differs from the majority of APs, as it displays anti-parallel beta-sheets instead of a helical structure common for AMPs. Plantaricin A and MacHis on the other hand, predominantly form an α-helical structure (Figure 4). Despite their similar secondary structure, these two APs very distinctly show different hydrophobic and electrostatic properties. On the one hand, the Macaque Histatin shows a high fraction of basic, polar AAs (Histidine, Arginine, and Lysine) and a fraction of unpolar AAs (Glycine, Tyrosine, Leucine, and Phenylalanine) on the opposite side of the α-helix, giving the AP an amphipathic character (Figure 4A) with a higher polar fraction. This is similar to many C-termini of GPCRs, which act as membrane anchors and thus serve a similar purpose[54]. On the other hand, the majority of the AAs of Plantaricin A is nonpolar except for a few polar, but uncharged AAs (Serine, Glutamine) and six Lysine residues, giving the AP an amphipathic character as well, but with a comparatively higher nonpolar fraction (Figure 4B).

Because of the complex nature of biological surfaces, such as in plants or fruits, it is not possible to infer adhesion properties directly from the AP's structure, as key

interactions at the atomistic level presumably differ for each case. As depicted above, experiments[24] have shown that the structurally different APs presented here display increased adhesion to the surface of cucumber leaves.

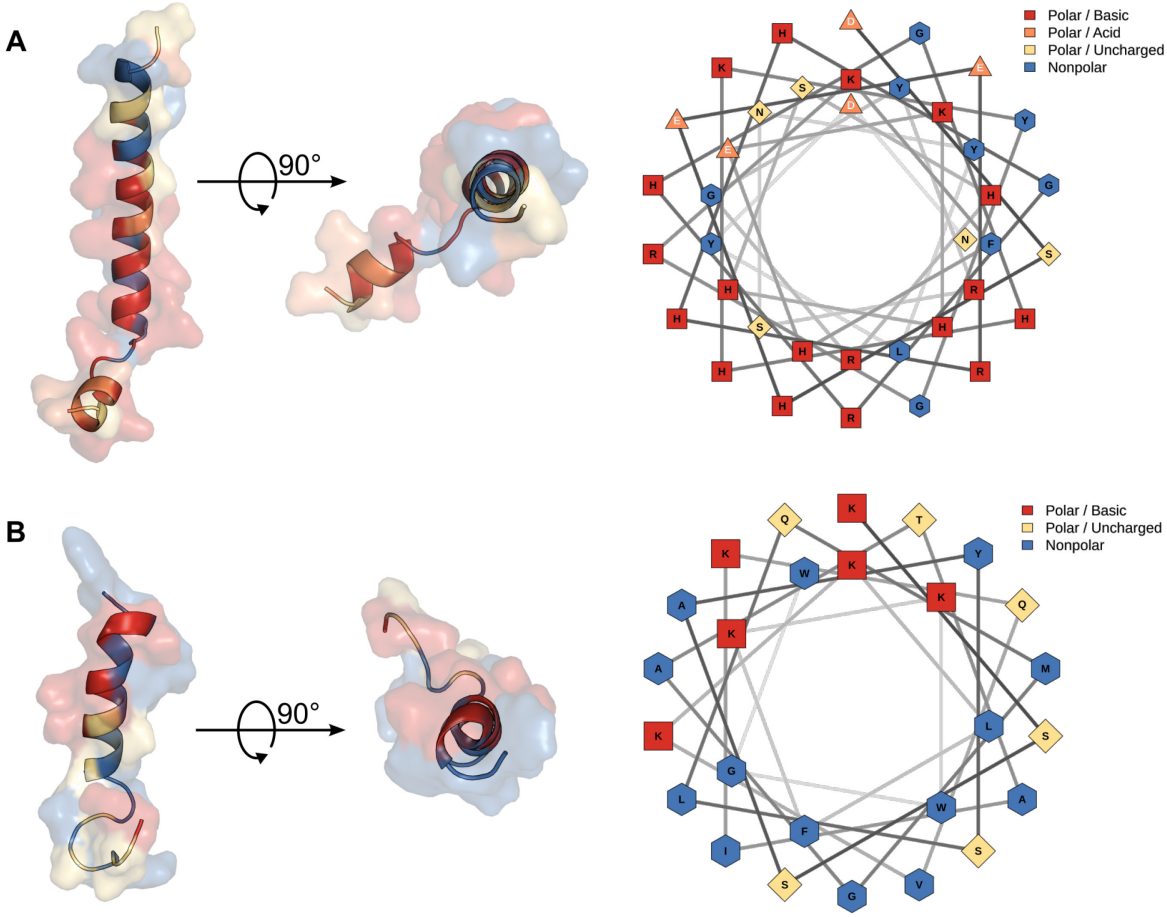

Figure 4. Amphipathic character of the APs Macaque Histatin (**A,** UniProt ID: P34084) character of Plantaricin A (**B,** PDB ID: 1YTR, UniProt ID: P80214). The Macaque Histatin contains a considerable fraction of basic polar residues (red), mainly histidine, whereas the Plantaricin A consists of mainly nonpolar (blue) or uncharged polar (yellow) residues. The respective helical wheels show the location of the different AAs on the helix. Although structurally different in terms of hydrophobicity, both APs show good adhesion towards epicuticular waxes.

In conclusion, gaining insights into the interactions of APs to complex synthetic as well as biological surfaces is key for the further development of the adsorption properties of APs. Tackling this challenge purely experimentally is exceedingly demanding in resources. However, in an integrated approach using computational means, it is possible to elucidate key interactions at an atomistic level allowing performing targeted experiments, saving time and costs in laboratory experiments. Moreover, computational methods allow tackling the problem of exponentially increasing complexity by better covering the structural space spanned by all possible AP variants using rationally chosen representatives.

2.1.2. Stimuli-responsive Polymers as Carrier

However, being able to attach peptides to plant surfaces is only one of the challenges we face within the *GreenRelease* technology. Another challenge is finding a suitable carrier for the loading and controlled release of agrochemicals. Stimuli-responsive polymers are versatile and offer the possibility of achieving this. Stimuli-responsive polymers react to changes in their environment such as pH shifts[37-38, 55-56], changes in osmolyte concentration[55, 57-59], temperature[35-36, 60-62], radiation[63-65], or combinations thereof[55, 66-68], either irreversibly or reversibly. The terms microgel and nanogel (NG) are commonly based on the sizes of the polymers, i.e., the sizes of the molecules are within the µm and nm range, respectively, irrespective of their molecular structure, stimuli-responsiveness, preparation, or application.[69] MGs and NGs often can be customized and tailored as to stimuli-responsiveness, size, and uptake properties. MGs and NGs are versatile and, thus, can be used in numerous applications[70-71], e.g., as carriers in drug delivery[31-32, 61, 66-67, 72-74], in crop protection[24, 75], and for surface modification[30, 76-77]. For the use in crop and plant protection and the triggered release of nutrients, herbicides, fungicides, and insecticides numerous important aspects have to be considered. E.g., the used MGs have to be environmentally friendly, nontoxic, and preferably biodegradable. Moreover, the trigger mechanism for substance release has to be environmentally friendly as well as practically sensible. For this matter, thermo-responsive MGs are predestined for this use case, as no additional application of chemicals is needed. The most popular and potentially best investigated thermo-responsive polymer is poly(*N*-isopropylacrylamide) (PNIPAM)[78-82]. However, PNIPAM more toxic than poly(*N*-vinylcaprolactam) (PNVCL)[83]. The thermo-responsiveness and the favorable toxicological properties made PNVCL popular, especially in bio(medical) applications[35].

Around 30 °C to 40 °C, a volume phase transition (VPT) is observed for PNVCL and PNIPAM, while the collapse of PNIPAM occurs in a narrower temperature interval compared to PNVCL[84]. The VPT is characterized by a sudden discontinuous change in the degrees of swelling (Figure 5A) and the potential coexistence of two gel phases with different degrees of swelling at a characteristic temperature (volume phase transition temperature (VPTT)[85]. The VPT can be exploited for a controlled release of active ingredients previously loaded into the MG. The VPT of an MG is closely related to the thermo-responsiveness of the oligomer of the same type. The lower critical solution temperature (LCST), at which the oligomer becomes insoluble and precipitates, is typically

around the VPTT of the corresponding MG. For PNVCL and PNIPAM, a so-called coil-to-globule transition (Figure 5B) is observed at LCST, i.e., linear coils of the oligomer collapse, form a globule, and potentially agglomerate leading to the precipitation of the oligomer[78, 80, 84, 86-87]. Therefore, the driving forces causing the coil-to-globule transition of a thermoresponsive (linear) polymer observed at LCST are closely connected to the observed changes in the morphology of the corresponding microgel.

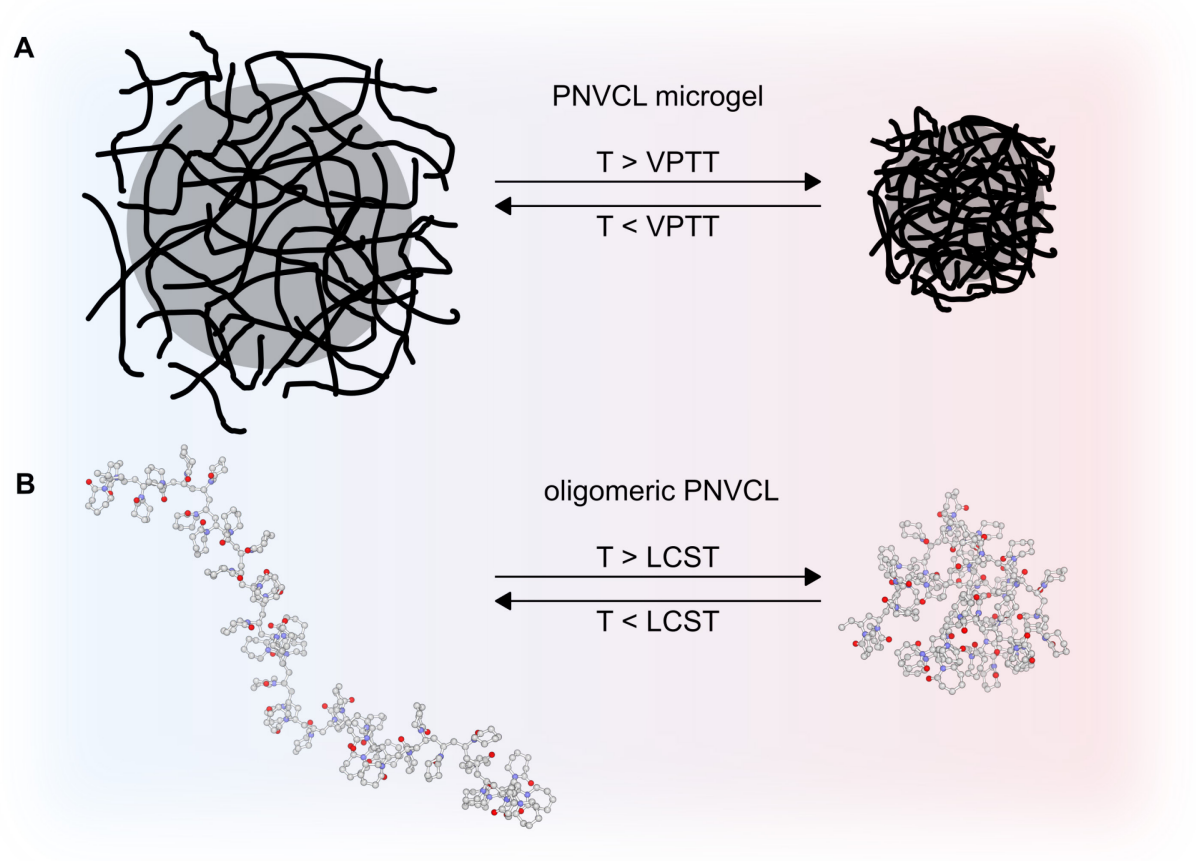

Figure 5. Representation of the volume phase transition (VPT) of PNVCL MGs (**A**) and the coil-to-globule transition of oligomeric PNVCL upon reaching the lower critical solution temperature (LCST) (**B**). The core of the core-shell structure of the PNVCL MG is depicted schematically as a transparent grey circle. Driving forces causing the coil-to-globule transition of a thermoresponsive (linear) polymer observed at LCST are closely connected to the observed changes in the morphology of the corresponding microgel

Depending on the preparation technique[25], PNVCL MGs display a core-shell structure, i.e., the center of the MG shows a higher crosslinking density and thus a decreased chain length between crosslinks, while the shell part shows a lower crosslinking density and an increased amount of unbranched PNVCL. Although a variety of (co)polymers show stimuli-responsiveness and thermo-responsiveness in particular, the driving forces at the atomistic level are strictly dependent on the polymer type and often cannot be transferred to other polymers. MD simulations have been proven to be a viable

tool to investigate the driving forces for the stimuli-responsiveness at the atomistic level[86, 88-91].

For the knowledge-based tailoring of the MG for an optimal use in plant protection applications, two mechanisms have to be understood thoroughly. First, the thermo-responsiveness of oligomeric PNVCL and, closely related, the VPT of PNVCL MGs and, second, the interactions with substrates, their uptake and release kinetics, which are intertwined. The VPT and the corresponding changes in morphology of the MG are vital for the loading and release of substances into/from the carrier. Moreover, the carrier used for the delivery of agrochemicals have to be tailored to the respective compound. PNVCL-based MGs are especially suited for the delivery of small organic compounds rather than metal ions. Chalcone derivatives, especially the C_4 plant selective herbicide okanin, depict promising candidates to be used with a PNVCL carrier.

2.1.3. Herbicides in Modern Agriculture

Modern agriculture makes high demands on agrochemicals, including pesticides such as fungicides, insecticides, and herbicides, which have to meet several criteria to ensure sustainability. Among all pests, weeds cause the highest loss, up to ~30 %, and thus add more to farmers' production costs, as the use of herbicides is inevitable.[6] For all agrochemicals, biodegradability is key to avoid accumulation and contamination of soil and eventually ground water[15-16, 18]. In addition to the demands on sustainability, increasing herbicide resistances among weeds has become an increasing concern[8, 92-94].

For example, in 2006 already over 300 biotypes of weeds were known to have developed resistances towards at least one and potentially more commonly used types of herbicide, including glyphosate (*N*-(phosphonomethyl) glycine), one of the most widely used herbicides globally[95] and considered to be a "once-in-a-century"[96] herbicide. Recent investigations on the use of glyphosate as herbicide, however, raise serious concerns[97-99] about bioaccumulation of glyphosate and its decomposition products, leading to chronic low dose effects on animals and humans[98], changes in the microbiome, and the development of resistances among weeds.

In 2015, the International Agency for Research on Cancer (IARC) of the World Health Organization reclassified glyphosate as probably carcinogenic to humans[100-101]. Notably, the U.S. Environmental Protection Agency came to the opposite conclusion as the IARC by classifying the substances as "not likely to be carcinogenic to humans"[102]. Although more research on the potential hazards of glyphosate is needed, this case serves as a good example of the importance of an in-depth risk assessment of a potential herbicide including potential health hazards, biodegradability, accumulation potential, as well as effects on the microbiome.

In contrast, natural herbicides became an appealing alternative to synthetic ones in recent years[9, 12-13]. Natural compounds cover a considerable amount of the chemical space, as they include compounds such as phenols of varying complexity, derivatives of coumarin (2*H*-chromen-2-one), lignans, flavonoids, tannins, amino acids, and many more[11]. These compounds provide promising lead structures for a targeted design of herbicides with potentially fewer hazards and risks. Developing a pallet of potent herbicides with different modes of action, rather than broad-spectrum herbicides, can contribute to a reduced risk for the development of herbicide-resistant weeds[103].

Furthermore, selective herbicides can decrease the amount of deployed herbicides, increase the ease of use, and help to avoid resistance development among weeds. Many weeds of agricultural importance are distinct from crops in the way they photosynthesize and fixate inorganic carbon, mainly CO_2. This can be exploited to tailor and create selective herbicides.

The temperature dependence of the photosynthetic efficiency led to the development of different carbon fixation pathways among plants. There are three different pathways for carbon fixation in plants, i.e., Crassulacean acid metabolism[104] (CAM), C_3[105], and C_4[106] carbon fixation. Independent of the pathway, the Calvin cycle[105], which describes a series of redox reactions, is essential for carbon fixation. Within this cycle, CO_2 is used for the carboxylation of ribulose-1,5-bisphosphate (RuBP) to 3-phosphoglyceric acid (PGA) by the ribulose-1,5-bisphosphate carboxylase-oxygenase (RuBisCo). Adenosine triphosphate (ATP) and NADPH, the reduced form of nicotinamide adenine dinucleotide phosphate ($NADP^+$), which are produced in the light-dependent reactions of photosynthesis, are used for the conversion to sugars and starch as well as the regeneration of RuBP from PGA[107].

For C_3 plants, open stomata are needed to adsorb CO_2 used in the Calvin cycle. This way of CO_2 absorption, however, displays a major disadvantage at elevated temperatures, as opened stomata inevitably lead to the loss of moisture. Thus, the stomata are (partly) closed at elevated temperatures to avoid dehydration. Thus, the photosynthetic efficiency of C_3 plants is decreased at elevated temperatures.

Therefore, plants growing under harsher conditions, such as elevated temperatures, high light intensities, and/or arid conditions, developed mechanisms to avoid dehydration by separating the initial carbon fixation either temporally or spatially from the carbon fixation in the Calvin cycle. In C_4 plants, the initial fixation of absorbed CO_2 takes place in the mesophyll cell. Within the mesophyll cell, the CO_2 is hydrated by carbonic anhydrase (CA) to bicarbonate, which is consecutively used in the carboxylation of phosphoenolpyruvate (PEP) by the phosphoenolpyruvate carboxylase (PEPC) yielding oxaloacetate. The PEP needed in this reaction is produced by the pyruvate phosphate dikinase (PPDK) using pyruvate, inorganic phosphate, and ATP. Depending on the subtype of the C_4 species, the oxaloacetate can be either reduced to malate or transaminated by the aspartate aminotransferase to aspartate in a reaction with alanine. Within the bundle sheath cell, where the RuBisCo is present, the respective C_4 compound (oxaloacetate/malate/aspartate) is then decarboxylated either by NADP-malic enzyme

(NADP-ME), in the case of malate, or by phosphoenolpyruvate carboxykinase (PCK), in the case of oxaloacetate, yielding pyruvate and CO_2 in both cases. The former is then regenerated to PEP by PPDK, the latter is fixed by RuBisCo within the Calvin cycle. This CO_2 concentrating mechanism leads to a 10-100 fold increase in the CO_2 concentration at the RuBisCo in the bundle sheath cell compared to CO_2 concentration in mesophyll cells of C_3 plants[108-109]. Because of the increased efficiency of CO_2 fixation, fewer CO_2 intake is necessary resulting in a lower need to open the stomata and thus a lower risk of dehydration.

A comparison of both carbon fixation pathways, C_3 and C_4, is depicted in Figure 6. Similar to C_4 plants, CAM plants are growing in arid conditions[110]. However, CAM plants differ from C_4 plants as the carbon fixation happens in temporal rather than special separation. In CAM plants, CO_2 is fixated at night as a 4-carbon intermediate (malic acids). During the daytime, this intermediate is then transformed into CO_2 again for the further reaction in the Calvin cycle.

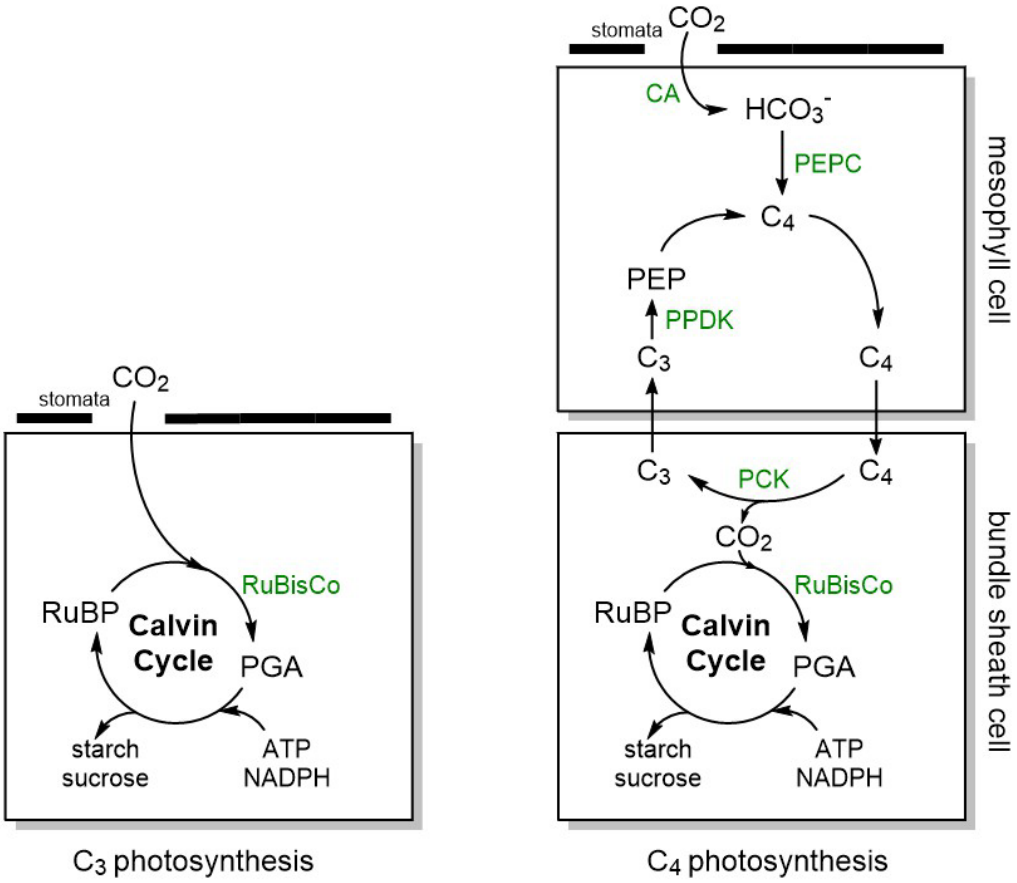

Figure 6. Difference in the photosynthetic reactions and carbon fixation in C_3 (left) and C_4 plants (right). In both cases, CO_2 is absorbed through the leaf stomata. For C_3 plants, RuBisCo uses the CO_2 for the carboxylation of RuBP yielding PGA, which is then transformed into starch and sugars under ATP and NADPH consumption (Calvin cycle). In C_4 plants, the CO_2 is hydrated and then used for the carboxylation of PEP by PEPC yielding oxaloacetate, which is potentially reduced or transaminated further. Within the bundle sheath cell, the C4 compound is then decarboxylated by PCK (in the case of oxaloacetate) yielding pyruvate and CO_2, which is fixed by RuBisCo within the Calvin cycle. Figure adapted from Yamori and Hikosaka[107].

As the majority of all plants, the majority of crops, such as rice, wheat, barley, rye, soybean, and potato, are C_3 plants, whereas a considerable amount of weeds are C_4 plants, such as *Amaranthus retroflexus*. Hence, enzymes playing an important role in the C_4 and not the C_3 pathway, such as the PEPC (Figure 7A), represent attractive targets for potential inhibition leading to decreased or even no carbon fixation and eventually withering of the weed. The use of (*trans*)-chalcones as potential herbicides was first reported[111] in 2014. However, neither a potential molecular target nor the mode of action was elucidated in these studies. To elucidate the binding of chalcones to the different PEPC, molecular docking has been performed[10] using the available crystal structures of PEPC from *F. trinervia* (PDB ID 3ZGE[112]) and C_3 PEPC from *F. pringlei* (PDB ID 3ZGB[112]). The work of Nguyen *et al.* on this topic showed that chalcone derivatives act on PEPC, rendering

them potential C_4 plant selective herbicides[10]. Especially okanin (2′,3′,4′,3,4-pentahydroxy-chalcone), was shown to be a 45-times stronger inhibitor of PEPC of C_4 plants (IC_{50} = 0.6 ± 0.1 µM, PEPC from *Flanervia trinervia*) than of the PEPC from C_3 plants (IC_{50} = 26.8 ± 3.5 µM, PEPC from *Flanervia pringlei*)[10]. Moreover, okanin did not show any influence on bacterial growth on complex and minimal media, while showing a significant effect on plant growth[10].

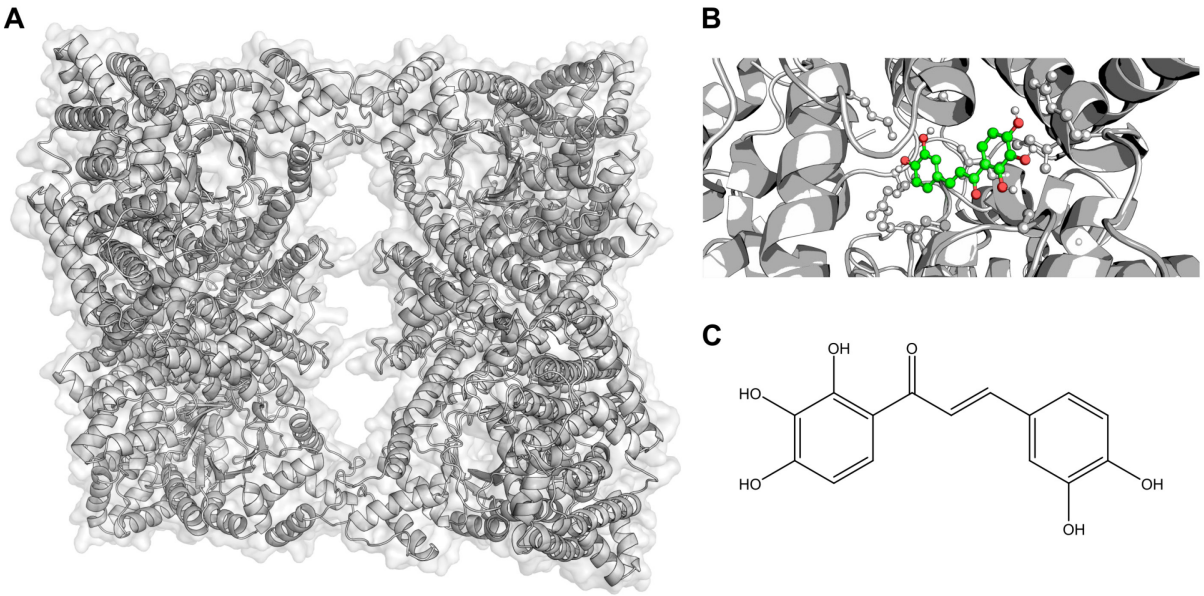

Figure 7. PEPC plays an essential role in carbon fixation in C_4 plants. **A** Homology model of the PEPC tetramer of *A. retroflexus* generated from sequence using SWISS-MODEL[113]. **B** Potential binding pose obtained by docking of okanin in the binding pocket of PEPC from *A. retroflexus* obtained via homology modeling [unpublished results]. **C** Chemical structure of the C_4 plant selective herbicide okanin (2′,3′,4′,3,4-pentahydroxy-chalcone).

The binding pockets of both PEPC variants are nearly identical except for residue 884, being a glycine in the C_4 PEPC and an arginine in the C_3 PEPC, which was identified to be the selectivity-determining residue. However, plant experiments were carried out for *A. retroflexus* and *Brassica napus* (rapeseed), as these plants depict a real-world scenario. Recent investigations on the transcriptomes of 1000 plants[114] revealed, that the sequence of PEPC from *A. retroflexus* differs from the binding site of PEPC from *F. trinervia.* Sequence information in combination with homology modeling (see chapter 2.2.1) allowed the prediction of the protein structure of PEPC from *A. retroflexus* (Figure 7A). The structural model can be used in molecular docking to identify potential binding poses of okanin within the binding site of the protein (Figure 7B). Obtained binding poses for okanin (Figure 7C) were found to be similar to the ones identified by Nguyen *et al.*, strengthening the hypothesis that okanin binds as a competitive inhibitor to PEPC [unpublished results].

2.2. Computational Chemistry and Molecular Modeling

Computer-aided design, simulations, and modeling play an important role in today's pharmaceutical and medicinal chemistry as well as in material sciences in both academic and industrial research[115-117]. The employed methods are extremely diverse, ranging from simulations at different scales, over docking of ligands into proteins to protein structure prediction using homology modeling (HM) and artificial intelligence (AI) based protein structure prediction. In HM, known structures of proteins are used as templates to predict the structure of a protein, for which, e.g., only sequence information is available. HM became an essential tool, where available experimental data is sparse, incomplete, or accompanied by high experimental burden and/or costs. The structures of the majority of the investigated APs in **Publication I**, for example, were determined using nuclear magnetic resonance (NMR) spectrometry, however, for the Macaque Histatin, the protein structure had to be modeled based on its sequence by using templates with TopModel[52]. Using HM, a structural model of Macaque Histatin was generated and investigated in MD simulations.

Lately, novel approaches within the field of computational (bio)chemistry successfully employ AI. Interestingly, the idea of AI is comparatively old, starting in the 1950s. The conference at Dartmouth College in July 1956 is often regarded as the starting point, as the phrase artificial intelligence was coined there[118]. Back then, potential applications for AI were limited. In the last decades, however, machine learning (ML) and in particular deep learning (DL) approaches have become popular for many applications, such as speech and image recognition, but also within computational (bio)chemistry[119]. Recently, DL algorithms have been successfully employed to predict complex protein structures with precision either close to or within the range of experimental errors[120-121]. With the current increase in available experimental data, ML approaches, especially DL, which are heavily dependent on big data sets, have become more precise and diverse, to the point where e.g. conventional HM approaches are superseded by DL-based approaches.

Besides structural modeling, many other applications within the field of computational (bio)chemistry benefit considerably from the availability of big data sets as well as the increase in computational performance. Similar to the beginning of AI, the origin of MD simulations date back as far as the 1950s[122]. The constant development in computing performance, algorithms, and parametrizations throughout the years rendered this method an essential tool in modern (bio)chemistry. Today, it is one of the most widely

used techniques in scientific computing[123], with a vast pool of MD simulation software available, delivering insight into molecular interactions on an atomistic scale[124]. Among these software, there are some notable programs and software suites such as AMBER[125-126] ("Assisted Model Building with Energy Refinement"), CHARMM[127-128] ("Chemistry at HARvard Macromolecular Mechanics"), and GROMACS[129-130], which find vast application in academic as well as industrial research. Atomistic simulations benefit from the increased computational performance, in particular, allowing simulations in the microsecond timescale[131-132].

In MD simulations, Newton's equations of motion are solved numerically for all particles of the system at any given time during the simulation. Interactions between the particles as well as their potential energy are calculated with the help of so-called force fields (FFs). The FFs may be derived from *ab initio* quantum chemical methods, can be empirical, or a combination of both. To adequately reflect thermodynamic, dielectric, structural, and dynamic properties obtained from experimental data, FFs are often tailored for certain types of molecules, such as water and ions[133-134], peptides and proteins[135-137], DNA[138] and RNA[139], carbohydrates[140], lipids[141], or small organic molecules[142]. For the latter, the general AMBER force field (GAFF2) is used. Although general FFs might be less refined compared to specifically designed FFs, they are capable of representing purely synthetic macroscopic structures, such as artificial polymers, as well as microscopic structures, such as drugs and inhibitors. In all of the presented publications, MD simulations were used to elucidate key interactions at the atomistic level. In **Publication I**, the adhesion of APs towards an atomistic model of an apple leaf surface was investigated (chapter 2.1.1). The simulations on the APs adhesion process revealed which residues of the APs are crucial for binding to the waxy leaf surface and thus established a platform for the rational design of APs with tailored leaf binding properties. In **Publication II**, MD simulations were employed to elucidate the thermo-responsiveness of PNVCL (chapters 2.1.2 and 2.2.2). The computational study revealed a delicate enthalpy-entropy compensation during the coil-to-globe transition of oligomeric PNVCL. Finally, in **Publication III**, the uptake and release of the C_4 plant key enzyme inhibitor okanin (chapter 2.1.3) into/from an oligomeric and crosslinked PNVCL were probed in MD simulations. Obtained insights on the adsorption of okanin to the microgel were used to generate a copolymer microgel with increased loading capacity.

2.2.1. Modeling Peptides and Proteins

In recent years, the available number of sequences and structural information for peptides and proteins have drastically increased (Figure 8). The structures deposited in the Protein Data Bank (PDB)[143-144] are determined using modern high-resolution techniques such as X-ray crystallography, NMR, and cryogenic electron microscopy (cryo-EM). While X-ray crystallography and cryo-EM resolve static structures, NMR is capable of resolving structural dynamics of proteins, often rendering it a complemental method in structural proteomics[145-146]. High-resolution models of proteins deposited in the PDB establish a valuable platform for investigations of protein interactions at an atomistic level using computational means. However, solving the tertiary structure of proteins experimentally is often time-consuming and expensive. The determination of only protein sequences, however, is comparably cheap and time-inexpensive, yielding a more than 1000-fold larger database for protein sequences. The Universal Protein Resource (UniProt) database[147-148] comprises more than 214 million entries to date compared to the approximately 180 thousand structures deposited in the PDB (Figure 8A).

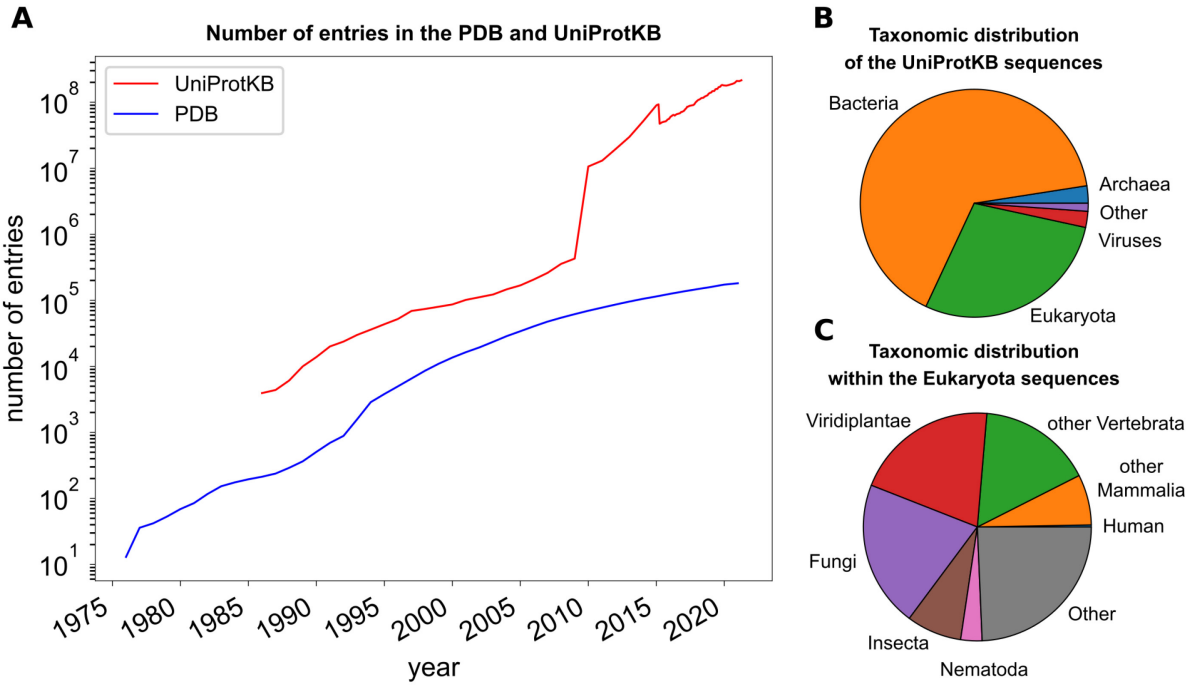

Figure 8. Number of sequence entries in the UniProtKB and structures in the PDB (**A**) and the taxonomic distribution of the sequences within the complete UniProtKB dataset (**B**) and the Eukaryote subset (**C**). Decreasing entry numbers for the UniProtKB database are caused by merging similar entries to reduce redundancy. The graph contains data up to April 2021 and August 2021 for the UniProtKB and the PDB, respectively.

The majority of the sequences within the UniProt Knowledgebase (UniProtKB) database are sequences of proteins found in bacteria (Figure 8B), directly followed by sequences of eukaryotic proteins. Within the subset of sequences from Eukaryotes, not even 1 % of the available sequences has a human origin, despite the fact that this subset corresponds to more than 175 thousand sequences (Figure 8B). The knowledge about sequences thus surpasses the knowledge about protein structures by far. Yet, knowledge about the structure is essential to understand the function of the protein. Modern algorithms for predicting proteins structures exploit the considerable increase in the size of both sequences and structure-based data sets. TopModel[52] and SwissModel[113] are notable representatives of HM software that use structural information derived from experiments to predict the structure of potentially similar proteins. Recent approaches, such as AlphaFold[120] and RoseTTAFold[121], exploit DL to predict a protein's structure. DL algorithms can be trained on a variety of (structural) descriptors, such as information from multiple sequence alignment, geometric features such as angles and distances between atoms, contacts between residues of the protein, and potentially many more.

In addition to HM, it has been shown in multiple studies that atomistic MD simulations can be used for *in silico* protein folding[149-153]. Although this approach is computationally often far more demanding compared to HM, it demonstrates the accuracy of modern FFs and their capability of accurately reproducing biologically relevant processes at an atomistic level. Exemplarily, Figure 9 shows the result of a 20 µs long folding simulation of the AP LCI. Starting from an unfolded structure, within the course of the simulation, LCI formed its characteristic secondary structure, matching structural data derived from NMR experiments (PDB ID: 2B9K). However, this approach is only practically feasible for smaller proteins.

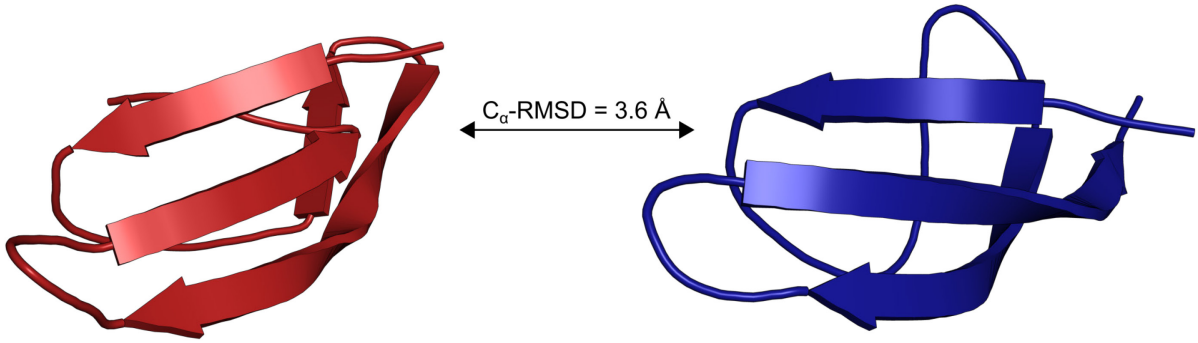

Figure 9. Crystal structure of the AP LCI (PDB ID: 2B9K, red) in comparison to a model obtained from ten 20 µs long folding simulations (blue) following the approach of Nguyen *et al.*[150]. The C_α-atoms show a root-mean-square deviation (RMSD) of 3.6 Å [unpublished results].

2.2.2. Exploring Polymer Dynamics *in silico*

Simulations are a versatile tool for the investigation of not only proteins and peptides but have also proven to be a valuable tool for the investigation of synthetically synthesized polymers[154-155]. Besides atomistic MD simulations, especially coarse-grained (CG) simulations are a suitable tool to investigate larger systems that otherwise would be limited by particle number[156-157]. In CG simulations, one or several groups of atoms, (repeating) units, or even bigger structural elements are condensed into single beads or sticks, thus significantly reducing the overall number of particles[158-159]. Consequently, polymer structure and dynamics can be scrutinized on a multiscale[160-161]. Atomistic and CG simulations are used to investigate material characteristics and dynamics, e.g., physicochemical[86, 162] as well as mechanical[156, 163-164] properties and processes such as polymer chain folding[165-166]. However, for the investigation of stimuli-responsive polymers, knowledge of the mechanism at an atomistic level is required. The potentially best-investigated thermo-responsive polymer is PNIPAM, which has been excessively investigated experimentally[73, 81, 167-169] as well as in simulations[80, 90-91, 170-173]. However, due to its toxicological properties, i.e., it is decomposed into small, potentially carcinogenic amide derivatives upon hydrolysis[83], PNIPAM is unsuitable for an application as a carrier for agrochemicals. In contrast to PNIPAM, PNVCL shows favorable toxicological and ecological properties, making it a viable option for the use as carrier for agrochemicals. Studies on the thermo-responsiveness of PNVCL and the effect of the salt concentration and types on the LCST using simulations have been reported previously[57, 88, 162, 174-176]. These studies comprise simulations at the coarse-grained[176], united-atom[88], and atomistic level[57, 174]. Interestingly, the majority of the published simulation data[86, 88-89, 91, 174] on thermo-responsive polymers describes the collapse at the LCST as a seemingly irreversible process, as no transition from globule back to coil is observed during the simulations. This, however, is in contradiction to experimental observations[84, 177]. Notable exceptions[162] showing simulations of a reversible process exist.

As for all simulation studies, it is of vital importance to estimate the model's accuracy and reliability. For this, it is inevitable to evaluate the impact of the known parameters on the model, i.e., in a DoE, the impact of the polymer's size, tacticity, and concentration on the phase transition have to be scrutinized prior to any other experiment using the generated atomistic models.

2.2.3. Investigating Biological Interfaces

Many biological systems are exceptionally complex and multifarious in their nature and composition[178]. Starting at the genetic level, over the cellular and system level, to a complete ecosystem, this complexity is observed at every stage. Plant leaves are no exception to this rule[179]. To describe complex systems, one might refer to the concept of thermodynamics, i.e., describing systems by their energetic traits, such as the free energy[180] or the entropy[181], often as Shannon entropy[182], of the system. This, however, often provides only a coarse-grained model of the system of interest. Despite the challenges complex biological systems pose, there has been an early and striving effort to generate computational (multiscale) models for various kinds of systems[183-186]. Understandably, these models are not able to fully represent and describe the complexity of the system. However, the generated models often provide valuable information and help to interpret and understand results obtained in experiments. For example, molecular dynamics simulations always include a certain level of approximation, uncertainty, and compromise[117]. However, as elucidated in chapters 2.2.1 and 2.2.2, computational models have come a long way and deliver extremely useful insights at an atomistic level. Although the main focus of computational biochemistry and structural modeling is the investigation of proteins and their interactions with substrates[187-188], many other fields have been explored using *in silico* methods in recent years[119, 189-191].

In this work, the biological interface of interest is the surface of a plant leaf. The generation of an atomistic model of the leaf surface may lead to novel insights of interactions of various substrates with the epicuticular wax layer and is potentially useful for a variety of foliar applications. A simplified atomistic model of a leaf should contain the main structural elements of a leaf, i.e., cellulose, a cutin matrix, and finally a layer of cuticular waxes. Within the plant cell wall, cellulose is the most prominent polysaccharide.

Cellulose fibers are linear polymers of hundreds of β(1→4)-linked D-glucopyranose moieties. The polymer chains aggregate into bundles, so-called (micro)fibrils[192]. These fibrils are embedded in a matrix of other polysaccharides forming a rigid cell wall. Atop of the polysaccharide cell wall, a cuticular polyester matrix of inter-esterified ω-hydroxy acids is located[193]. The fatty acids are interlinked via ester bonds, forming a polyester of indeterminate size.

An example of a section of the cutin matrix is depicted in Figure 10. The composition of the cutin layer may vary strongly depending on the plant[194].

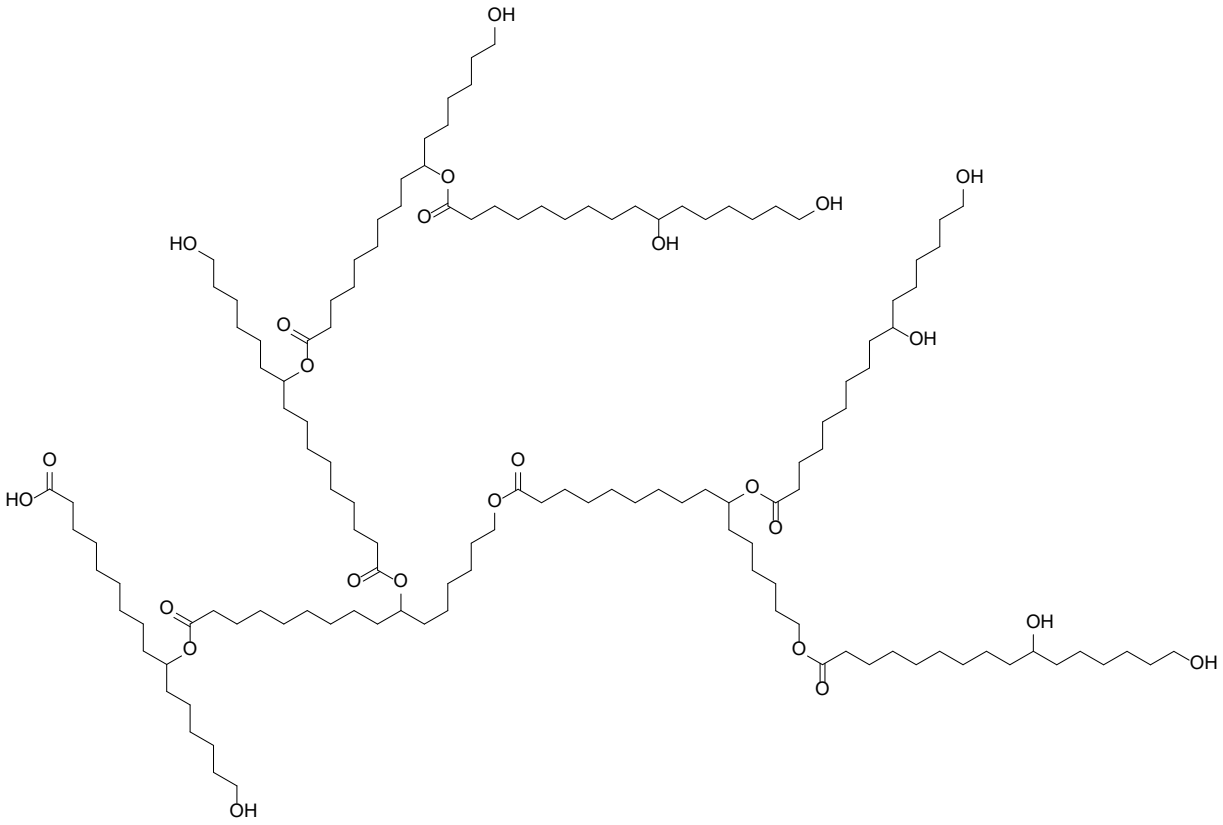

Figure 10. Exemplary structure of the cutin matrix as proposed by Fich *et al.*[194]. The polyester matrix is formed by ω-hydroxy fatty acids of different chain lengths, while C_{16} and C_{18} fatty acids account for the majority of fatty acids within the cutin matrix. Midchain hydroxyl groups allow for a dendritic/crosslinked structure.

Cutin is impregnated and covered with cuticular and epicuticular waxes, respectively[195]. These waxes often comprise molecules of numerous structural classes, like long aliphatic molecules, sterols, and terpenoids. The composition and diversity of the epicuticular wax are also strongly dependent on the plant. Thus, it is mandatory to determine the exact composition beforehand, using modern analytical methods to generate an atomistic model.

3. Scope of the Thesis

The increasing world population poses a variety of challenges. One of the most important questions humankind has to answer is how to overcome the increasing demand for food, while simultaneously limiting the exploitation of natural resources. As shown in the introduction of this thesis, the world population is estimated to reach ten billion people by the year 2050. Sustainable agriculture is of vital importance to ensure sufficient nutrition for the global population and future generations. Undisputedly, an overall reduction of the applied pest control leads to a decrease in environmental pollution and consequently to higher crop yields[196]. The amount of applied agrochemicals, such as pesticides and herbicides, can be decreased by developing target-specific agents. Moreover, the effectiveness of the application can be increased by reducing the number of treatments needed, e.g., by improving the formulation's rain fastness. Chapter 2.1 depicts the novel *GreenRelease* technology, which follows the motto "achieve more with less". Within the *GreenRelease* technology, anchor peptides (APs, described in chapter 2.1.1) are used to enhance the rain fastness of microgel carriers (MGs, described in chapter 2.1.2) for a smart delivery and release of agrochemicals. MGs can be used to deliver nutrients, pesticides, fungicides, and herbicides. Okanin, a small organic compound that could be delivered by such MGs, belongs to the structural class of chalcones and shows great potential as a C_4 plant key enzyme inhibitor (chapter 2.1.3). While experiments in which MGs decorated with APs were used for foliar delivery of micronutrients (e.g. Fe^{3+}) showed promising results[24], many of the involved interactions remained elusive. Therefore, to fully unlock the potential of this novel plant protection technology, gaining deeper knowledge, especially at the atomistic level, is required.

This thesis aims at understanding the involved mechanisms of the *GreenRelease* technology at every crucial step. This comprises the interaction of the APs with biological interfaces such as plant leaves (**Publication I**), the generation of structural models of the MGs (**Publication II**) and the potential understanding of their defining characteristics, and finally, the loading and release processes of okanin into/from the microgel carrier (**Publication III**). The obtained knowledge is essential for the optimization of the technology.

First, the adsorption of APs to synthetic surfaces, such as polymers, has been well investigated experimentally, however, the adsorption to biological interfaces (chapters 2.1.1 and 2.2.3), such as plant leaves has been hardly investigated, and there has not been

any investigation on the interactions at the atomistic level so far. In **Publication I**, an interdisciplinary approach to overcome this challenge is described. Here, the composition of the wax of an apple leaf was determined experimentally.* Based on the experimental findings, I generated a novel three-layered atomistic model of the apple leaf surface and used it in unbiased and steered MD simulations to obtain knowledge about the adsorption of APs at an atomistic level. Using unbiased MD simulations, I was able to identify residues within the AP that are of major importance for binding. The steered MD simulations were used to predict leaf binding performance of structurally different APs. A novel fluorescence-based assay was developed† to quantify the leaf wax binding properties of different APs and AP variants. Based on the atomistic insights I gained from the simulations, I proposed several AP variants to test experimentally to validate the simulation experiments. In conclusion, I generated a novel atomistic model of a leaf surface used it in MD simulations to identify residues of high importance for binding of the APs. The obtained knowledge about the interaction between the AP and the leaf wax at an atomistic level is helpful for the rational design of APs with increased adhesion properties.

Second, for the investigation of the microgel container as a carrier for agrochemicals, it is of vital importance to generate atomistic models that correctly reflect the polymer's physicochemical properties. Poly(*N*-vinylcaprolactam) (PNVCL) is a biodegradable, stimuli-responsive polymer. Upon reaching the volume phase transition temperature, PNVCL microgels transition from a swollen conformation to a collapsed one. Not only polymeric PNVCL shows a thermo-responsiveness but also oligomeric PNVCL shows a lower critical solution temperature upon which the oligomers undergo a conformational change known as coil-to-globule transition (chapters 2.1.2 and 2.2.2). In **Publication II**, I investigated the thermo-responsiveness of short-chain PNVCL oligomers in depth using exhaustive MD simulations in combination with experimental validation‡. For the first time, the impact of several parameters, such as the polymer concentration, its size, and the chosen water model and thermodynamic ensemble on the observed coil-to-globule transition, was studied systematically. Moreover, I investigated the transition using

* The leaf samples were provided by Dr. Shyam Pariyar at the Department of Horticultural Sciences, University of Bonn; the wax composition was analyzed by Dr. Viktoria Zeisler-Diehl and Prof. Dr. Lukas Schreiber at the Department of Ecophysiology, University of Bonn.
† The experimental work was performed by Christin Brethauer under the supervision of Dr. Felix Jakob and Prof. Dr. Ulrich Schwaneberg at the Institute of Biotechnology, RWTH Aachen University.
‡ The experimental work was performed by Michael Kather and Anna Holzberger under the supervision of Prof. Dr. Andrij Pich at the DWI-Leibniz-Institute for Interactive Materials, RWTH Aachen University.

end-point free energy methods and Markov State modeling. At the time of publication, this study was presumably the most comprehensive computational study on the temperature-induced coil-to-globule transition of oligomeric PNVCL.

Third, based on the knowledge gained from the simulations of the oligomeric PNVCL, the interactions of agrochemicals with the PNVCL carrier can be investigated *in silico* (chapters 2.1.2 and 2.2.2). Initial experiments revealed that upon uptake of the C_4 plant key enzyme inhibitor okanin (chapter 2.1.3), PNVCL microgels show a distinct structural change. To elucidate interactions at the atomistic level and understand structural changes of the microgel, an integrated approach is necessary. In **Publication III**, the uptake of okanin into PNVCL-based microgels is studied experimentally[§] and computationally. Upon loading, the microgel's collapse was traced by dynamic light scattering (DLS). The change in the particle's morphology was investigated using scanning transmission electron microscopy (STEM) and atomic force microscopy (AFM). I decomposed the complex and structural inhomogeneous microgel into two sections to elucidate the loading and release of the okanin in MD simulations: a linear PNVCL oligomer represents the loosely crosslinked shell/corona of the microgel including single linear polymer chains often referred to as dangling ends. A crosslinked cubic model of the PNVCL, on the other hand, represents the core of the microgel. I simulated the adsorption of okanin in various concentrations to the linear and crosslinked PNVCL. To determine the energetics of this process, I used end-point free energy estimations and discovered two different binding modes. The simulations explain the structural change of the microgel upon loading of okanin and match the results for the co-solvent triggered release. Insights gained from the atomistic study were used to generate a co-polymer with increased loading capacity and can be used for future tailoring of the microgel and optimizing the loading and release of different agrochemicals.

[§] The experimental work was performed by Fabian Kolodzy and Dr. Alexander Töpel under the supervision of Prof. Dr. Andrij Pich at the DWI-Leibniz-Institute for Interactive Materials, RWTH Aachen University.

4. Publications

4.1. Publication I

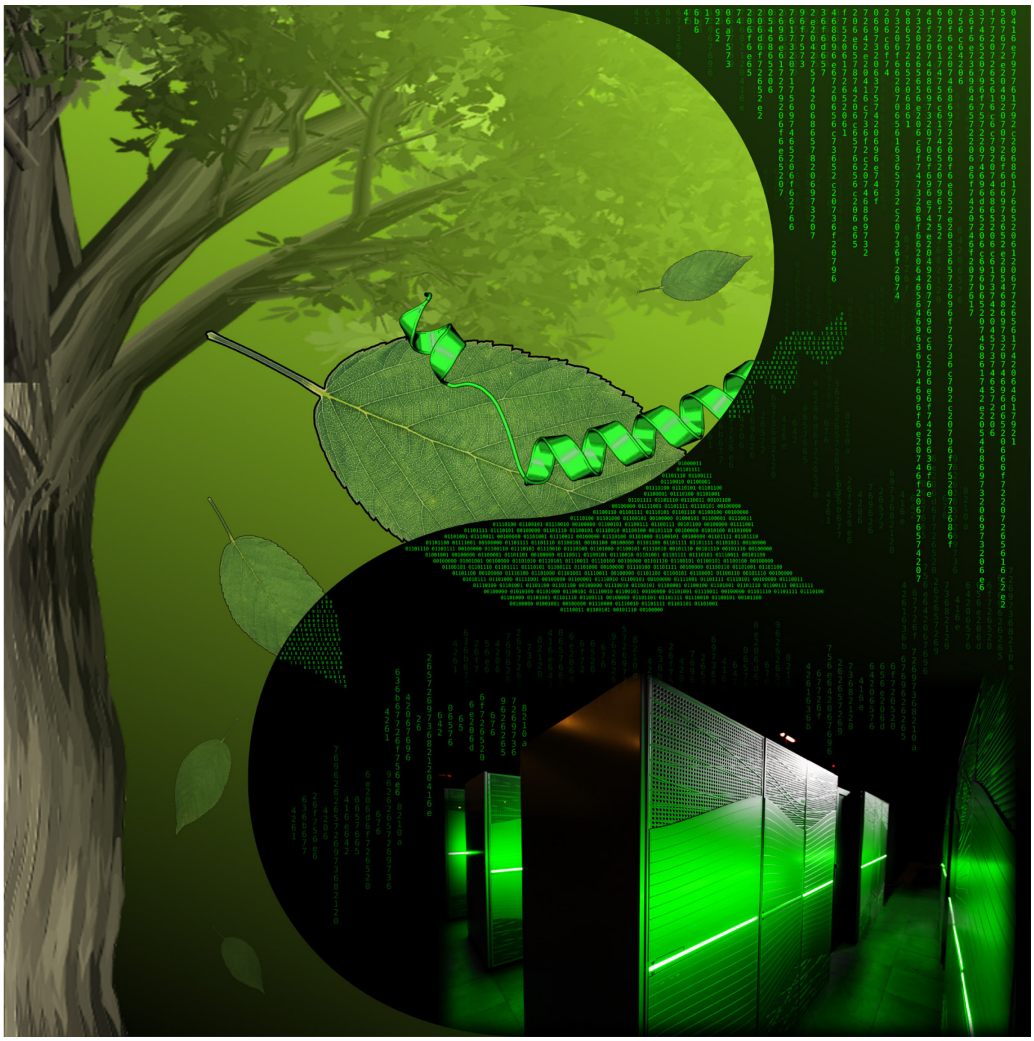

Rational Design Yields Molecular Insights on Leaf-Binding of Anchor Peptides

Jonas Dittrich[#], Christin Brethauer[#], Liudmyla Goncharenko, Jens Bührmann, Viktoria Zeisler-Diehl, Shyam Pariyar, Felix Jakob, Tetiana Kurkina, Lukas Schreiber, Ulrich Schwaneberg, and Holger Gohlke

[#]these authors contributed equally.

ACS Applied Materials & Interfaces, **2022**, 14, 28412-28426.

DOI: 10.1021/acsami.2c00648

For the original publication, see pages 58-90.

The content in this chapter was taken and modified from Publication I.

Background

With the constantly growing world population and increasing demand for food, sustainable agriculture is necessary to insure sufficient nutrition. Increased rain fastness of agrochemical formulations is of vital importance to avoid severe environmental pollution due to the wash-off of active agents, such as nutrients, herbicides, fungicides, or pesticides. To date, polymeric adjuvants are added to the agrochemicals to increase the rain fastness of the formulation. However, some adjuvants will be classified as microplastics in the future; thus, a sustainable alternative is needed. Anchor Peptides (APs) are biobased and biodegradable adhesion promoters and represent a sustainable alternative. While the adsorption of several APs towards artificial surfaces, such as polymers, was already investigated in theory and experimentally, mechanisms at the atomistic level for the adhesion to complex biological surfaces remained elusive so far. Due to the complex nature of biological interfaces, such as the surface of a plant leaf, the generation of an accurate model is complicated. In this publication, I set up an integrated approach to generate an atomistic model of an apple leaf, taking into account the experimentally determined composition of leaf wax. The MD-based predictions obtained for AP variants and different APs were validated using a novel quantitative assay. For the AP Macaque Histatin, aromatic and positively charged amino acids were identified to be essential for binding to the waxy apple leaf surface.

Generating a three-layered atomistic model of the apple leaf surface

The surface of a leaf often consists of a cuticular polyester matrix of inter-esterified ω-hydroxy acids, impregnated with cuticular waxes, covered with epicuticular waxes[195], and located atop of a polysaccharide cell wall[193]. To reflect the complex structure, a three-layered model was generated stepwise using MD simulations for every addition of a new layer (Figure 11). For the generation of the first layer, the Cellulose-Builder[197] was used to generate a crystalline sheet of Iβ cellulose (Figure 11A). Next, 10,18-dihydroxyoctadecanoic acid was chosen as a representative fatty acid for the generation of the cutin matrix. Several linear and branched structures with up to 17 fatty acid moieties were generated and packed atop the sheet of Iβ cellulose using PACKMOL[198] (Figure 11B). A short MD simulation of 25 ns length yields a compact structure of the cutin layer (Figure 11C).

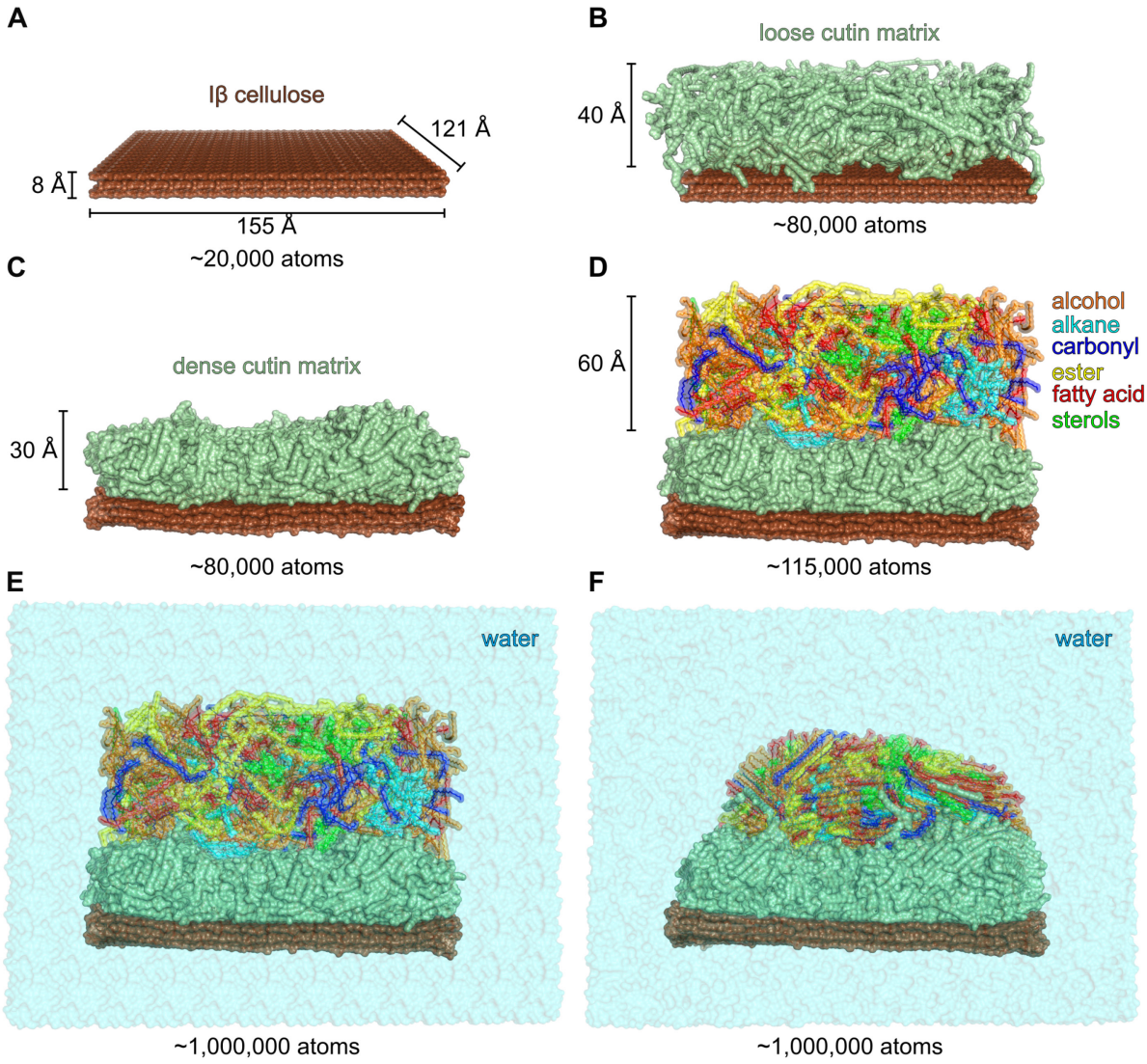

Figure 11. Stepwise creation of an atomistic leaf surface model. **A)** Three-layered crystalline Iβ cellulose. **B)** Loosely packed polyester matrix of crosslinked 10,18-dihydroxyoctadecanoic acid located above the cellulose sheet. **C)** Compacted cutin layer atop the cellulose sheet after 25 ns of NVT MD simulations. **D)** Randomly placed wax components above the compact cutin layer. **E)** Solvated system. **F)** Snapshot obtained after 100 ns of MD simulations of the complete model. Figure and figure caption taken from Publication I, see page 60.

Consecutively, a wax layer was added using PACKMOL (Figure 11D) and the system was solvated in a water box (Figure 11E). A short simulation yielded compaction of the wax layer (Figure 11F), resulting in a system suitable to investigate the interaction of various APs with the cuticular wax. The composition of the cuticular wax was determined experimentally by my collaborators using gas chromatography equipped with flame ionization detection and mass spectrometry (GC-FID/GC-MS).

MD simulations reveal residues within Macaque Histatin (MacHis) that are important for leaf wax binding

In the next step, the adoption of APs to the novel atomistic model of the leaf surface was simulated. It was possible to identify the residues of the proteins that form the majority of contacts to the waxy surface. Presumably, the number of contacts formed by each residue correlates to the contribution of the individual residue to the overall adsorption of the AP. Therefore, from unbiased MD simulation I identified residues with a high number of contacts to the leaf wax. Exemplarily, the adsorption of the AP MacHis to the waxy layer was investigated and the number of relative contacts was determined. The relative contact per residue is depicted in Figure 12A. In Figure 12B, the findings are mapped onto the structure, colored according to the observed contacts.

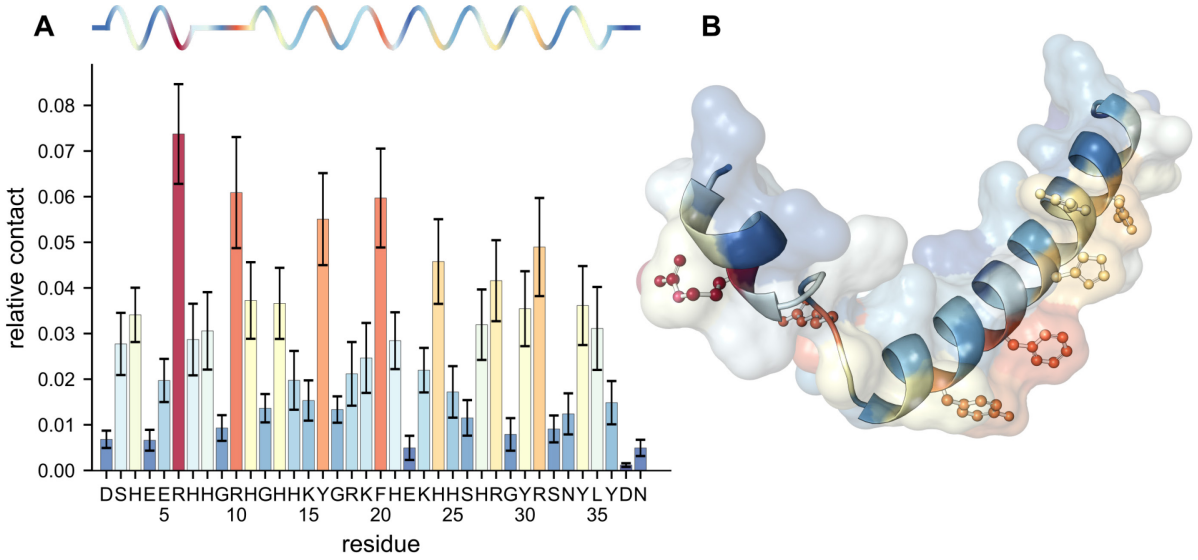

Figure 12. **A)** Residue-wise relative contacts of MacHis with the wax molecules during 10 x 250 ns of MD simulations of AP adsorption. The secondary structure, as determined by DSSP,[199] is indicated on the top. The color code relates to that shown in panel B. Error bars denote the SEM. **B)** Homology model of MacHis colored according to the relative number of contacts a residue forms within 7 Å with the wax molecules; sidechains of residues with a relative contact > 0.04 are depicted as sticks and spheres. Figure and figure caption taken from Publication I, see page 64.

The MD simulations for the adsorption of MacHis showed that one side of the α-helix is favored for binding to the wax layer. Moreover, the simulations reveal that aromatic and positively charged amino acids are essential for binding to the waxy apple leaf surface.

The leaf wax binding strength of structurally different APs can be predicted using adaptive steered MD simulations

The desorption of the APs from the leaf surface was investigated using adaptive steered molecular dynamics (ASMD) simulations. In ASMD simulations, the reaction coordinate along which the pulling force is applied is segmented into so-called stages. For each stage, several replicas were simulated. The non-equilibrium work was determined using Jarzynski's equality[200]. The replica with the work closest to the determined average was used as starting point for all replicas of the subsequent stage. This way, the desorption of different APs and the non-equilibrium work, as well as the corresponding potential of mean force (PMF) were determined. Figure 13 depicts the steered desorption exemplarily for the AP MacHis.

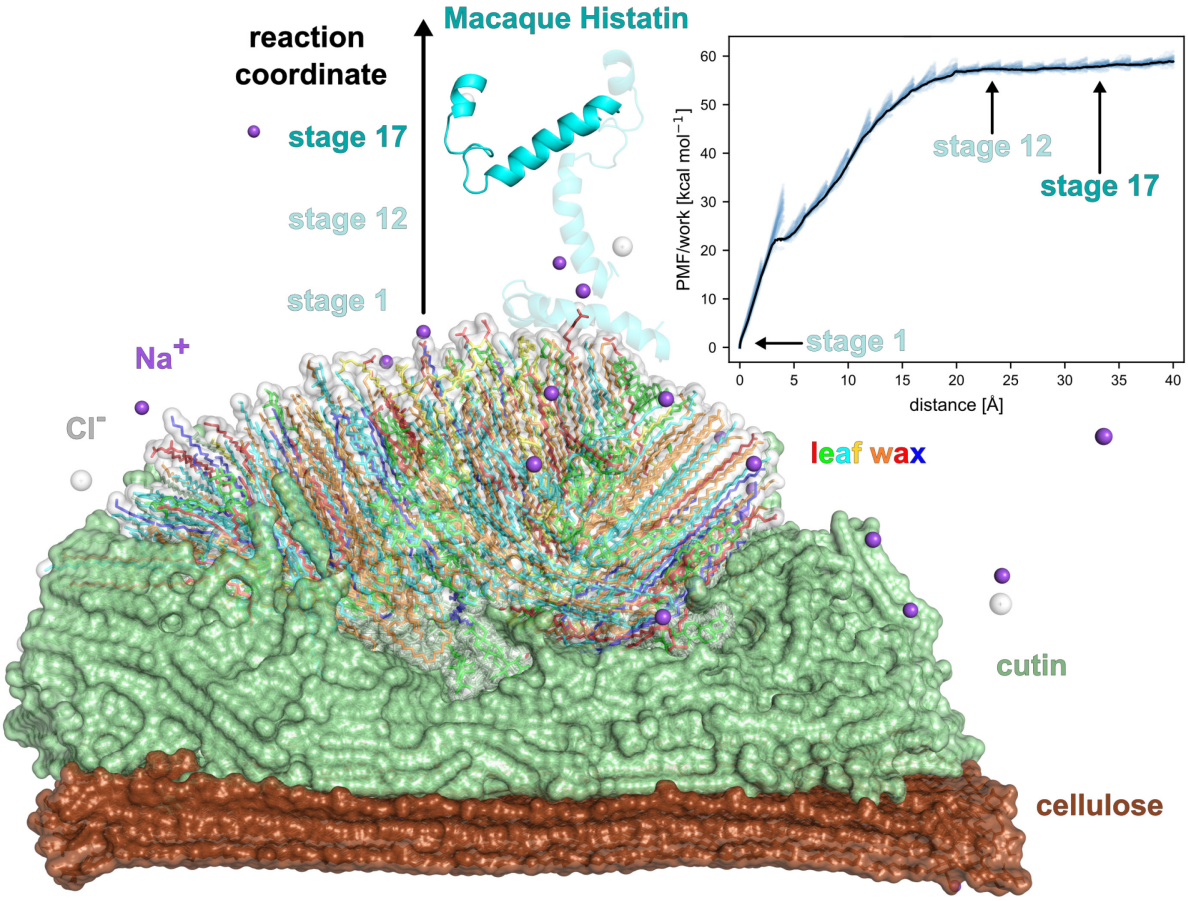

Figure 13. Adaptive steered MD of the desorption process of MacHis (cyan) from the leaf surface model. The potential of mean force (PMF, black solid line) of desorption determined as the average of the work of each stage (blue transparent lines) is depicted as inlay. The starting structure (stage 1) of MacHis as well as a structure selected from stage 12 of the steered MD are shown translucent, the completely detached AP is shown opaque (stage 17); corresponding stages are highlighted in the PMF profile. Figure and figure caption taken from Publication I, see page 66.

In this study, I used ASMD simulations to investigate the binding strength of structurally different APs, such as MacHis, Plantaricin, LCI, Pleurocidin, and Magainin. The investigated APs showed distinct differences in binding to the surface of apple leaves in a qualitative fluorescence-based assay using whole leaves. The needed work and PMF determined from the ASMD simulations for each AP are depicted in Figure 14A. The derivative of the work is indicative of the force applied during that stage (Figure 14B), i.e., the steeper the PMF, the higher the force applied during that step. Next to the overall PMF, and thus the amount of work needed for the desorption, the maximum amount of force needed (Figure 14C) potentially depicts thresholds for the AP to bind to the waxy surface.

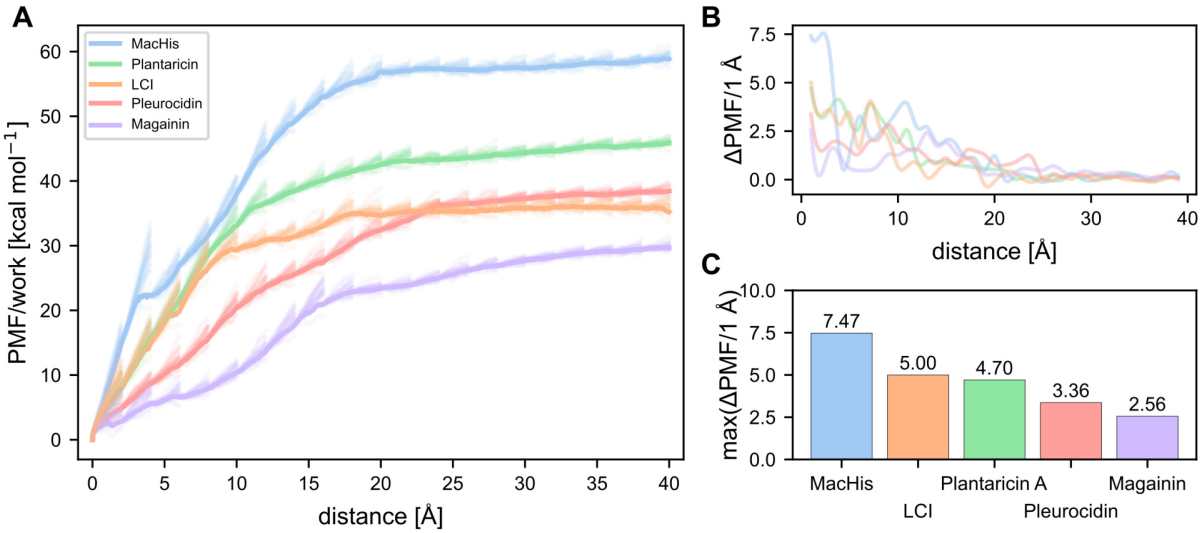

Figure 14. **A)** Potential of mean force (PMF) profiles for the desorption of MacHis (blue), Plantaricin A (green), LCI (orange), Pleurocidin (red), and Magainin (purple) as determined by adaptive steered MDs. The work of the 25 individual replicas per stage is depicted as transparent, and the PMF is shown opaque. **B)** Force profile as difference quotient ΔPMF/1 Å, where the denominator relates to the distance difference with respect to the leaf surface. **C)** Bar plot depicting the maxima of the forces shown in panel **B**. Figure and figure caption taken from Publication I, see page 67.

The results of the ASMD simulations identified MacHis as the best binding AP, while LCI and Plantaricin A still showed considerable binding, and Pleurocidin as well as Magainin, showed potentially the least binding. Experiments suggested that LCI is the best binding AP, followed by MacHis. Plantaricin A still shows considerable binding, Pleurocidin is indistinguishable from the pure fluorescence reporter (enhanced green fluorescent protein (eGFP)), and Magainin is potentially worse than pure eGFP. Overall, the ranking of the APs with regard to their wax binding potential determined by ASMD simulations matches the experimentally determined ranking well.

Conclusions and significance

In this work, I established a multidisciplinary workflow for selecting suitable APs and rational improvement of their binding properties towards specific plant leaves. Therefore, I generated a multi-layered atomistic model of an apple leaf surface. The model was used to elucidate the interaction of APs with the waxy surface. In parallel, a quantitative fluorescence-based assay was developed by my collaborators to evaluate the leaf binding strengths of different APs and AP variants. Overall, predictions for the modification of the AP MacHis matched experimental observations, yielding molecular insights into the binding mechanism of MacHis. The prediction of the binding strength of structurally different APs matched results from the novel experimental assay and observations from experiments using the whole leaf.

The main results of this study are:

- The generation of a three-layer atomistic model of an apple leaf surface that can be used in MD simulations to investigate various kinds of foliar applications.
- Unbiased MD simulations of the AP Macaque Histatin revealed residues of vital importance for binding to the waxy surface of a leaf. My collaborators validated the MD-based predictions by generating of Macaque Histatin variants and testing their binding properties using the novel binding assay.
- ASMD simulations were used to investigate the desorption of the AP and the binding strength. The non-equilibrium work determined was used to calculate a PMF for desorption of structurally different APs. Predictions based on the calculated PMFs matched results from the novel binding assay and observations using whole apple tree leaves.

4.2. Publication II

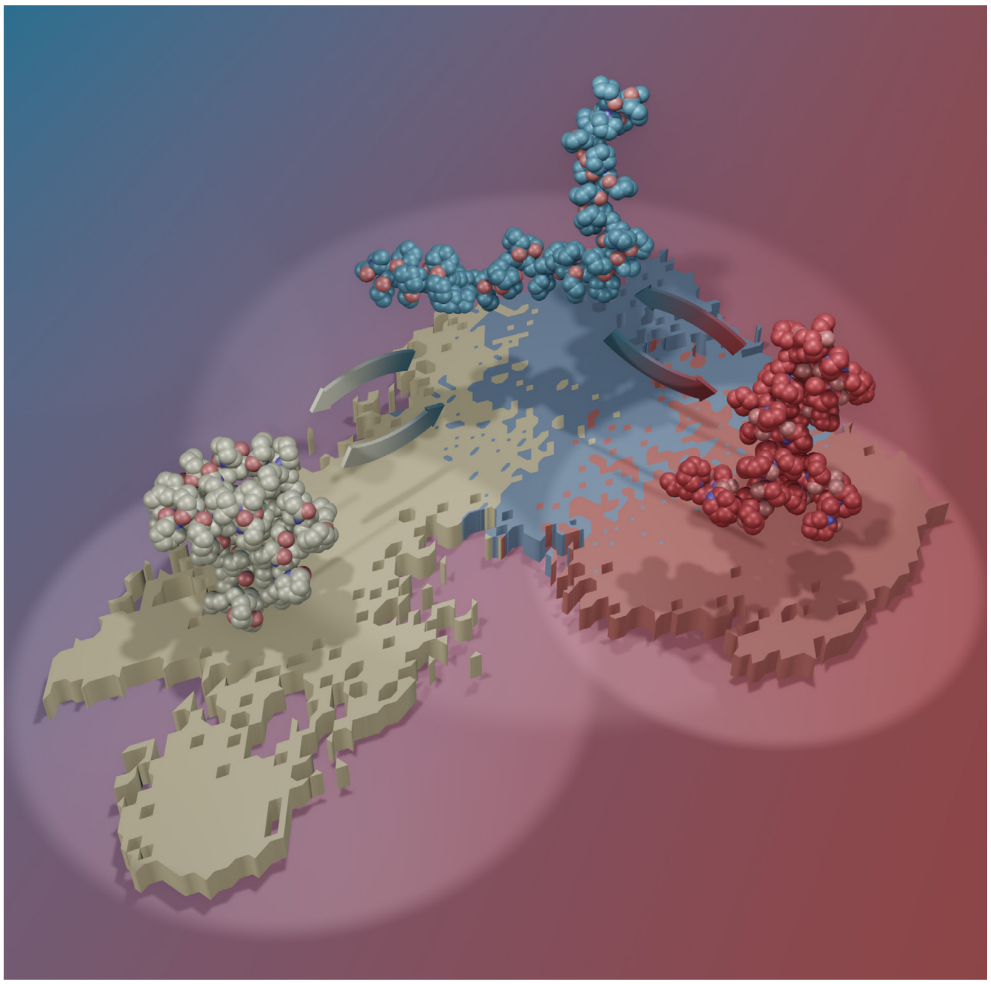

Cumulative Submillisecond All-Atom Simulations of the Temperature-Induced Coil-to-Globule Transition of Poly(*N*-vinylcaprolactam) in Aqueous Solution

Jonas Dittrich, Michael Kather, Anna Holzberger, Andrij Pich, and Holger Gohlke

Macromolecules, **2020**, 53, 9793−9810

DOI: 10.1021/acs.macromol.0c01896

For the original publication, see pages 92-147.

The content in this chapter was taken and modified from Publication II.

Background

PNVCL is polymer whose water solubility is dependent on temperature. Upon exceeding the LCST of ~32-37 °C, the polymer becomes insoluble in water and undergoes a conformational change from a coil to a globule[87, 201]. The LCST of PNVCL depends on multiple parameters such as polymer length and concentration[60, 202-203], types and concentrations of ions[204], detergents[205], and other osmolytes[57]. Stimuli-responsive polymers play a vital role in health, biomedicine, environment, and agriculture/plant sciences. Understanding the thermo-responsiveness at the atomistic level allows the tailoring of the polymers.

In this work, I aimed at elucidating the driving forces of the PNVCL coil-to-globule transition at the LCST by computational structural and energetic analyses. The coil-to-globule transition was investigated while paying particular attention to the impact of polymer characteristics and validating the simulation results against experiments. The systematic assessment of the influence of polymer length, tacticity, and concentration on the coil-to-globule transition is particularly noteworthy as these analyses were novel for PNVCL. Moreover, energetic determinants of the transition have only been computed for interactions between two isolated VCL monomers so far, rather than for oligomeric structures.

MD simulations are sensitive enough to capture the coil-to-globule transition of oligomeric PNVCL

Simulations of not only PNVCL of varying sizes but also atactic poly(*N*-vinylpyrrolidone) (PVP) 40mers were performed at 293 K and 313 K to probe if MD simulations can discriminate between polymers showing LCST or not. PVP generally does not show LCST behavior in water. Therefore, PVP oligomers provide a valuable negative control, as they are structurally similar to PNVCL oligomers but do not show the characteristic thermo-responsiveness.

As the coil-to-globule transition describes a substantial change in the conformation of the polymer chain, it is well described by changes in geometric parameters such as the radius of gyration (R_G), as it is a measure for the structural compactness of the polymer.

For PNVCL, the R_G frequently fluctuated between 12 and 25 Å at lower temperatures (Figure 15A). Therefore, multiple collapses and extensions of the polymer are sampled during the simulation time of 1000 ns. At elevated temperatures, however, extended conformations are less frequently sampled, and the likelihood of observing such states decreases with increasing simulation time (Figure 15C). At 313 K, polymer conformations with $R_G < 15$ Å dominate the frequency distribution, i.e., globular conformations are predominant at temperatures above LCST.

For PVP, at both temperatures, fluctuations of R_G between 10 and 24 Å were observed (Figure 15B, D). However, extended periods of simulation time showing low R_G were not found, yielding highly similar frequency distributions between 292 K and 313 K. These findings indicate the absence of a coil-to-globule transition in a PVP 40mer.

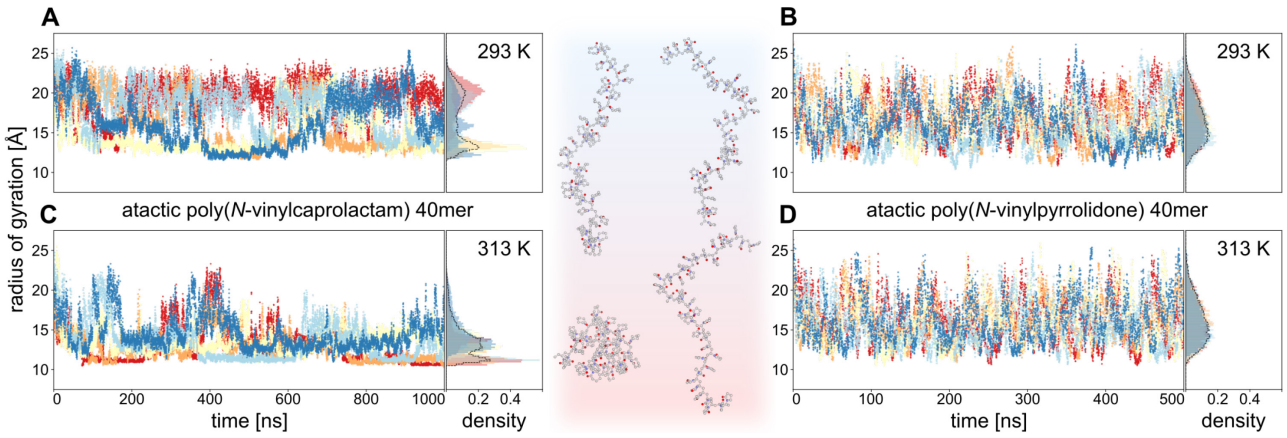

Figure 15. Radius of gyration (R_G) during five·MD simulations of 1 µs length of an atactic PNVCL 40mer (**A**, **C**) and during five MD simulations of 500 ns length of an atactic PVP 40mer (**B**, **D**) at 293 K (**A**, **B**) and 313 K (**C**, **D**). Corresponding frequency distributions are shown next to the time series in matching color, a frequency distribution of all data is shown as dashed black line. Sample structures taken from each simulation setup are depicted next to the corresponding simulation. Figure and figure caption taken from Publication II, see page 97

In essence, atomistic MD simulations are seemingly capable to discriminate between the LCST behavior of the PNVCL 40mer and the absence of thermo-responsiveness of the structurally similar PVP 40mer.

Hidden Markov Models reveal an additional compact state for PNVCL at elevated temperatures as well as the inversion of state distribution and transition rates

For the atactic PNVCL 40mer, two similar, coarse-grained hidden states, comprising PNVCL in coil and globular conformations, at 293 K and 313 K were identified in the HMM. However, the ratio of stationary distributions (π) for the two states inverted upon increasing the temperature. The predominant state ($\pi = 0.68$ at 293 K and $\pi = 0.25$ at 313 K) comprised elongated polymer chains in coil conformation. The second state ($\pi = 0.32$ at 293 K and $\pi = 0.42$ at 313 K) comprised PNVCL oligomers in a hairpin conformation. The HMM constructed from the simulations at elevated temperature also unveils a new, compact state, which was not observed at lower temperatures. The third state comprised oligomers in a dense globular conformation ($\pi = 0.33$ at 313 K).

Concerning the free energy differences of the coil-to-globule transition, the HMMs revealed that the free energy difference at 313 K versus 293 K is slightly larger than kT, where k is the Boltzmann constant and T the absolute temperature.

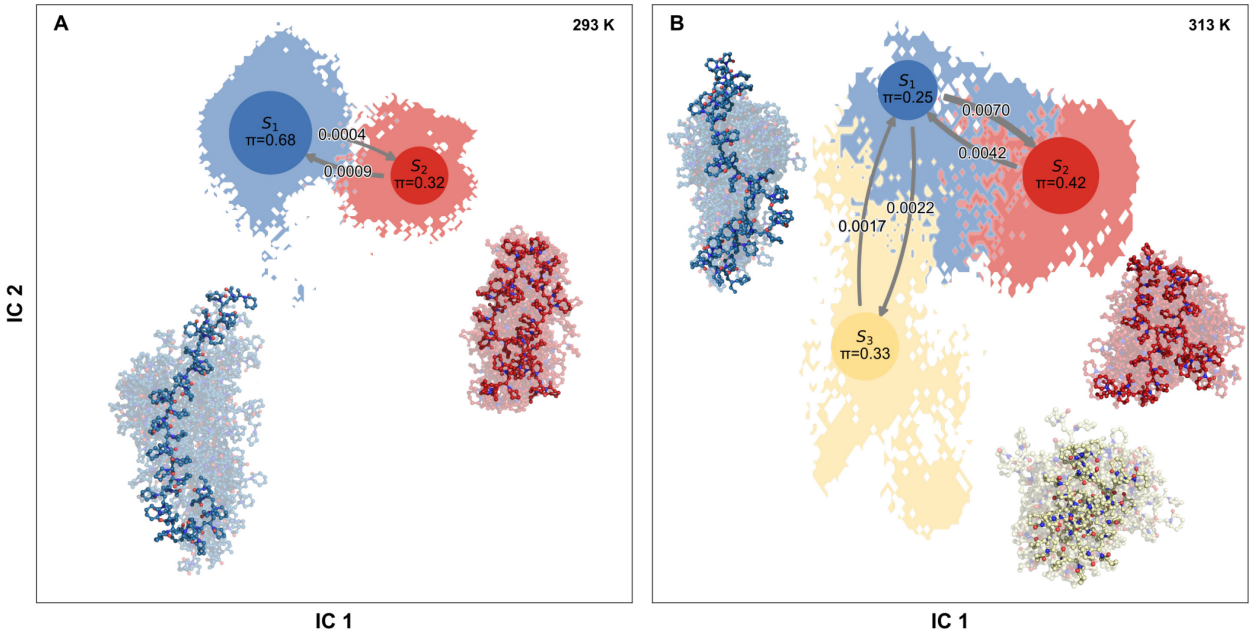

Figure 16. HMMs for an atactic PNVCL 40mer at 293 K (A) and 313 K (B) projected on the same IC space. The probabilities π_i obtained from the stationary distributions π are shown for each state; the size of the arrows between states is scaled by the corresponding transition probability for each HMM, which is given as label for the lag time of 0.5 ns. For each macrostate, the ten most probable representative structures are shown. The structure with the highest probability in each set is shown in non-transparent representation. Figure and figure caption taken from Publication II, see page 98.

A delicate enthalpy-entropy compensation is revealed by end-point free energy decomposition for the coil-to-globule transition of PNVCL

To validate transition free energies obtained from the constructed HMMs, end-point free energy computations were performed following the molecular mechanics Poisson-Boltzmann surface area (MM-PBSA) approach[206-207]. In this approach, effective energies, comprising molecular mechanics energies, solvation free energies, and configurational entropies, were computed on the structural ensembles extracted from the MD simulation (Figure 17). In this study, I determined differences in these energies for the coil-to-globule transition at 293 K and 313 K, respectively.

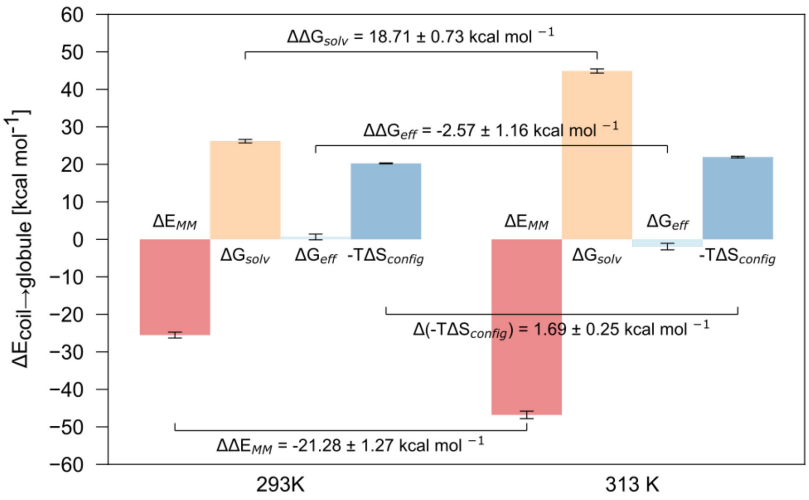

Figure 17. Bar plot showing energetic differences for the coil-to-globule transition of an atactic PNVCL 40mer at 293 K and 313 K. ΔG_{eff} is decomposed into the difference in gas-phase energy ΔE_{MM} and solvation free energy ΔG_{solv}. Configurational entropies of the polymer are estimated by NMA. The error bars depict the standard error of the mean. Differences in energy components between both temperatures, as well as corresponding errors determined according to the laws of error propagation, are depicted below and above the respective horizontal lines. Figure and figure caption taken from Publication II, see page 99.

The difference in free energy for the coil-to-globule transition at 313 K versus 293 K agreed with $\Delta\Delta G$ computed from the stationary distribution of the HMMs. The energy decomposition revealed that at a higher temperature, favorable van der Waals and intramolecular electrostatic interactions outbalance the loss in solvation free energy and configurational entropy supporting the coil-to-globule transition.

Conclusions and significance

The presented study is the most comprehensive computational study on the thermo-responsiveness of PNVCL at the time of publication. For the first time, the influence of polymer length, tacticity, polymer concentration, and the chosen MD parameters, such as the water model and the used thermodynamic ensemble, on the thermo-responsiveness of PNVCL were systematically investigated. The study is the first to use end-point free energy estimation methods such as MM-PBSA and the construction of Markov States to unravel the coil-to-globule transition of PNVCL.

The main results of this study are:

- All-atom MD simulations are sensitive enough to describe the coil-to-globule transition of PNVCL while correctly depicting the structural dynamics of PVP, which is not thermo-responsive although structurally very similar to PNVCL.
- HMMs revealed that upon temperature increase, the stationary distributions of the polymer in coil and hairpin conformation inverse, as do the transitions between the states. Moreover, a compact globular conformation of the PNVCL oligomer was observed at elevated temperatures.
- Simulations and experiments suggest that increasing intramolecular interactions between C_3 and C_4 of the caprolactam ring and more favorable cavity formation energies outweigh the loss in polar and hydrophobic solvation and the loss of configurational entropy in the coil-to-globule transition. Therefore, these interactions particularly can be considered the driving forces of the polymer's collapse at LCST.
- MD simulations and (free) energy computations were validated experimentally internally by collaborators and against published experimental data.

4.3. Publication III

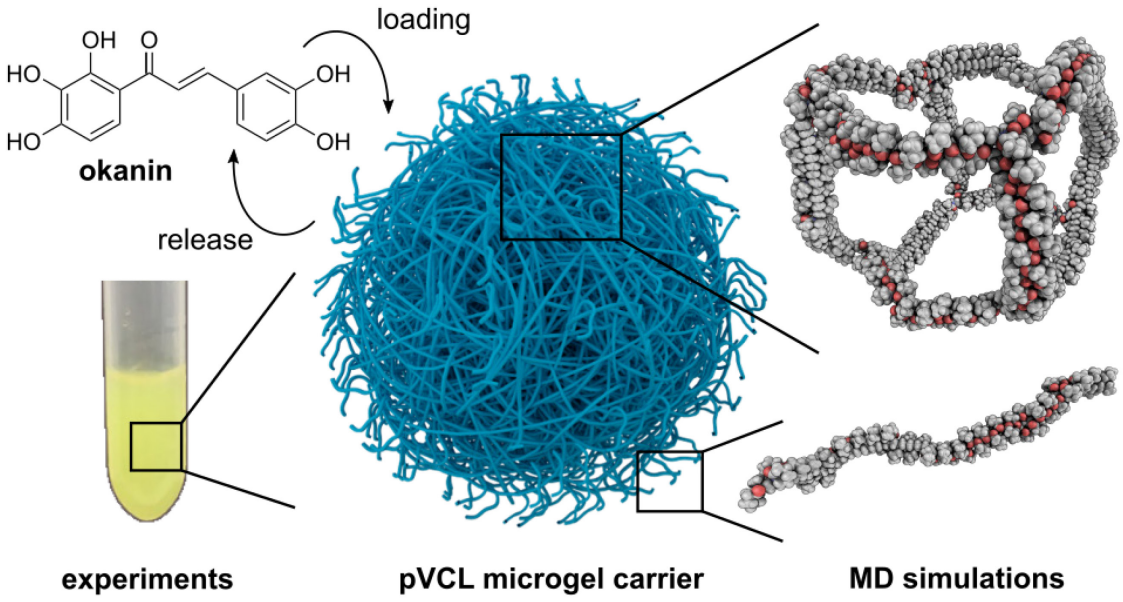

Loading and Co-Solvent-Triggered Release of Okanin, a C_4 Plant Key Enzyme Inhibitor, into/from Functional Microgels

Jonas Dittrich[#], Fabian Kolodzy[#], Alexander Töpel, Andrij Pich, and Holger Gohlke

[#]these authors contributed equally.

DOI: 10.26434/chemrxiv-2022-sgbx9-v2 (ChemRxiv, 13.10.2022)

For the original manuscript, see pages 150-254.

The content in this chapter was taken and modified from Publication III.

Background

Sustainable agriculture is of major importance for the constantly growing world population. Using fertilizers and pesticides can enhance crop productivity significantly[10, 208-209]. Among pests, weeds pose a major threat to global food production by rapidly developing resistance against commonly used herbicides. Rain, however, leads to losses of up to 80 % of the applied agrochemicals due to wash-off[24]. As a result, chemicals accumulate in the soil and groundwater, posing serious health risks for humans and animals. Reducing the amount of chemicals leaching into the environment is one of modern agriculture's most important challenges. This challenge can be addressed in several ways, one of which is increasing the formulation's rain fastness utilizing a long-term release or release-on-demand mechanism[210-211]. Such release mechanisms can be achieved by using novel carriers such as PNVCL-based MGs. In this study, the interactions between the selective herbicide okanin and PNVCL-based MGs were investigated in an integrated manner, using experiments as well as MD simulations of structural elements of a PNVCL (pVCL) microgel (Figure 18).

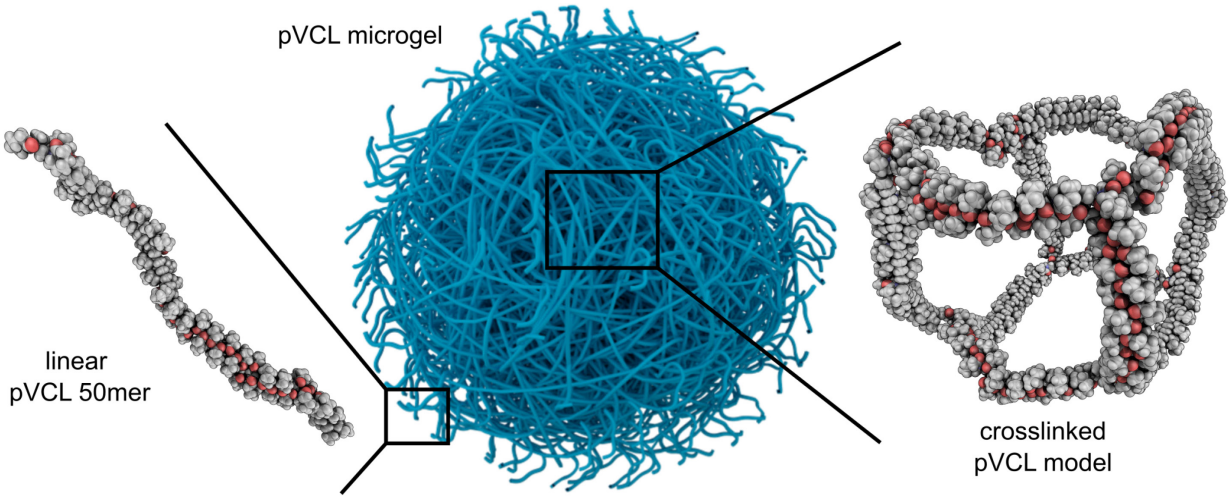

Figure 18. Decomposition of a microgel into atomistic models for the shell and core section. Simulations of linear oligomers mimic the loosely crosslinked shell of the microgel (left); the *N,N′*-methylenebisacrylamide crosslinked cubic PNVCL models mimic the highly crosslinked core (right). Figure and figure caption adapted from Publication III, see page 159.

Experiments reveal the collapse and rigidification of the PNVCL microgel.

DLS measurements showed the collapse of the particle with an increasing amount of okanin in solution and thus with an increasing amount of okanin (given as the molar ratio between okanin and the constitutional units (CUs) of the MG) taken up by the MG (Figure 19A,B). Scanning transmission electron microscopy (STEM) reveals, that upon loading of okanin into PNVCL, the diffuse structure of the PNVCL MG becomes more rigid and spherical (Figure 19C).

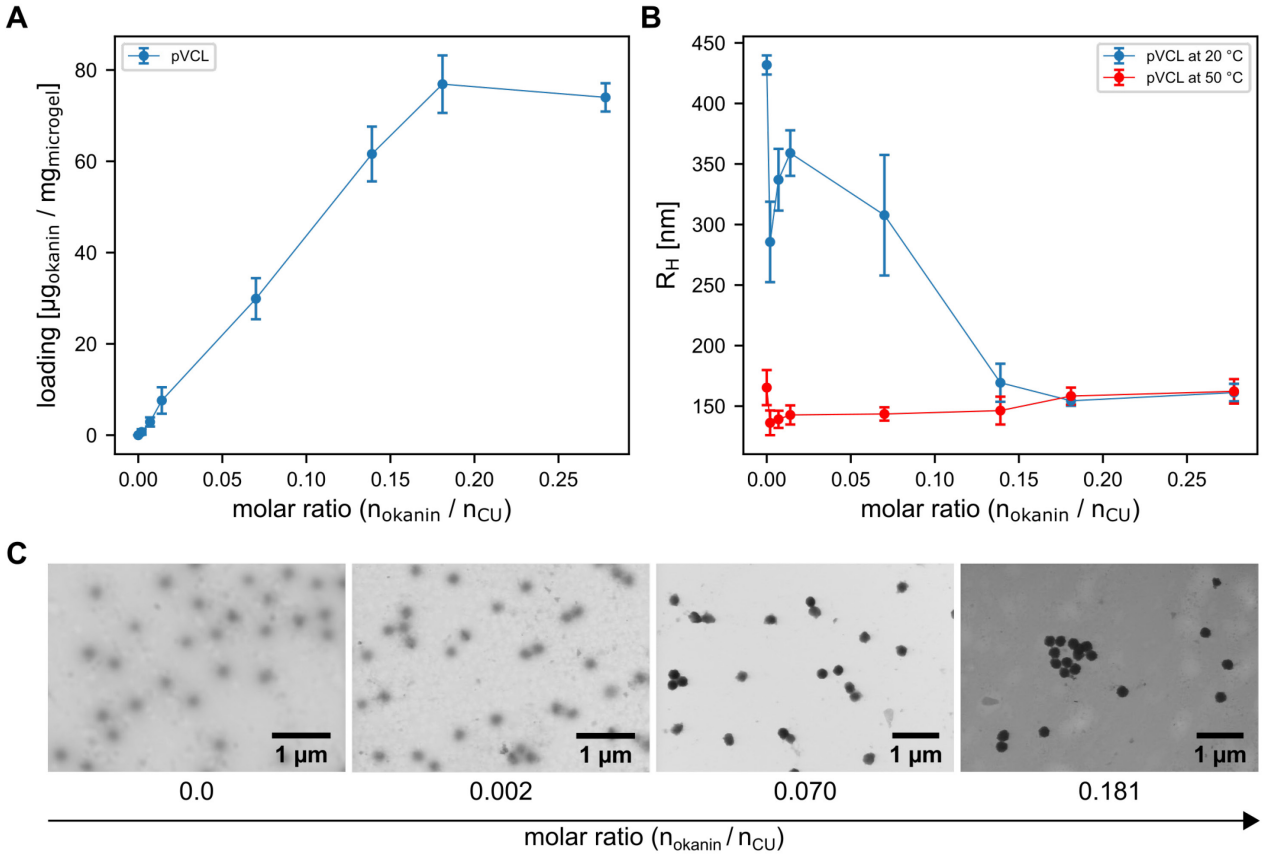

Figure 19. Influence of the loading of okanin on the hydrodynamic radius R_H, the thermo-responsiveness, and the morphology of PNVCL microgels. **A** Loading of okanin into pure PNVCL microgels determined by UV/Vis for varying molar ratios n_{okanin}/n_{CU}. **B** R_H of PNVCL loaded with okanin as determined by DLS at 20 °C and 50 °C for varying n_{okanin}/n_{CU} ratios. **C** Exemplary STEM images of a PNVCL microgel for varying n_{okanin}/n_{CU} ratios. Figure and figure caption taken from Publication III, see page 166.

The experimentally observed changes in the MG's morphology and structures was investigated in-depth using MD simulations. Next to adsorption of okanin to the surface of the MG, simulations revealed inter-chain crosslinks between the PNVCL mediated by (stacking) okanin molecules.

To elucidate the okanin-MG interaction, MM-PBSA calculations were performed to estimate the binding free energy for the adsorption process (Figure 20). Favorable binding energies were found for binding poses in which okanin formed at least 475 contacts to the MG, e.g., as found in an MG-okanin-MG configuration. These findings support the idea of okanin-mediated inter-chain crosslink leading to the MG compaction.

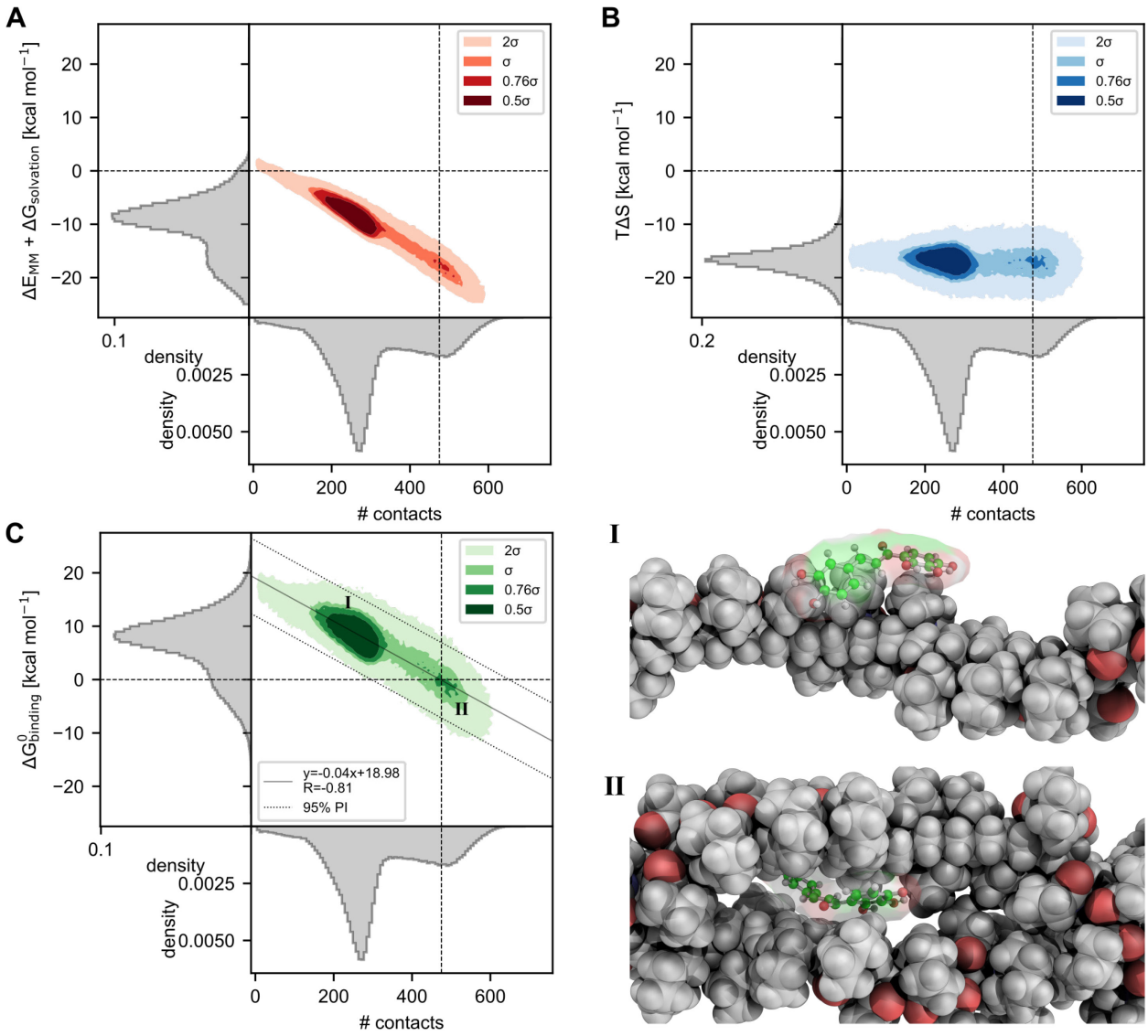

Figure 20. Two-dimensional histograms of the binding free energy of okanin to the linear PNVCL 50mer and its components (changes in the gas phase energy and solvation free energy ($\Delta E_{MM} + \Delta G_{solvation}$, **A**) and changes in the configurational entropy of the solutes ($T\Delta S$, **B**)) in relation to the number of formed contacts. The binding free energy ($\Delta G^0_{binding}$, **C**) of okanin to the PNVCL polymer shows an inverse linear correlation (regression line shown solid, 95% prediction interval shown dotted, Pearson correlation coefficient and linear equation are depicted in the corresponding legend) with the number of formed contacts. Exemplary binding poses are shown for adsorbed okanin (**I**, < 475 contacts, $\Delta G^0_{binding} > 0$) and bound okanin (**II**, > 475 contacts, $\Delta G^0_{binding} < 0$). The MM-PBSA analysis was performed for trajectories of the linear PNVCL 50mer, in which a collapse of the chain was observed; only frames where okanin formed contacts to PNVCL were considered. Figure and figure caption taken from Publication III, see page 169.

Thus, okanin molecules with a high number of contacts to the MG were considered bound, whereas okanin molecules with a lower number of contacts were considered adsorbed. While bound okanin remains within the MG, the okanin molecules adsorbed to the surface are in a constant exchange with okanin in solution. However, with increasing okanin concentration, it is not possible to experimentally determine the amount of okanin taken up by the polymer, as particles in the solution begin to precipitate. Simulations with high okanin concentrations were performed to unravel the reasons for this observation. With increasing okanin concentration, the number of okanin-okanin interactions increased, including okanin in solution (Figure 21A,B) and already bound/adsorbed okanin (Figure 21C,D). Stacking interactions involving okanin already interacting with the polymer are preferred over stacking in solution (Figure 21E). Considering that at higher okanin concentration within the system, okanin stacking interactions become more frequent, it is mandatory to consider new configurations, i.e. okanin-okanin-MG and MG-okanin-okanin-MG, when determining the fraction of bound okanin. When including inter-okanin contacts in the estimation of bound okanin, the amount of loaded okanin observed in MD simulation is similar to the experimentally determined amount of loaded okanin (Figure 21F).

The energy decomposition of the free energy calculations revealed that mainly polar interactions between the okanin and the MG drive the adsorption and binding of the herbicide. Therefore, glycidyl methacrylate (GMA) was incorporated into the MG to increase its loading capacity potentially. GMA moieties increase potential polar interactions while providing an opportunity for further surface functionalization of the MG, e.g., the attachment of APs. Experimentally, the GMA copolymers showed an overall increased loading capacity compared to the PNVCL MG, supporting the findings of the free energy calculations.

Finally, the co-solvent triggered release of okanin from the MG was investigated experimentally and *in silico*. Only green solvents[212-213], which are environmentally compatible and authorized as additives in agricultural applications, were considered for release. Overall, for the release triggered by water and ethyl acetate, the observation in MD simulations agrees with the experimentally observed amount of released okanin, lending mutual support to either result.

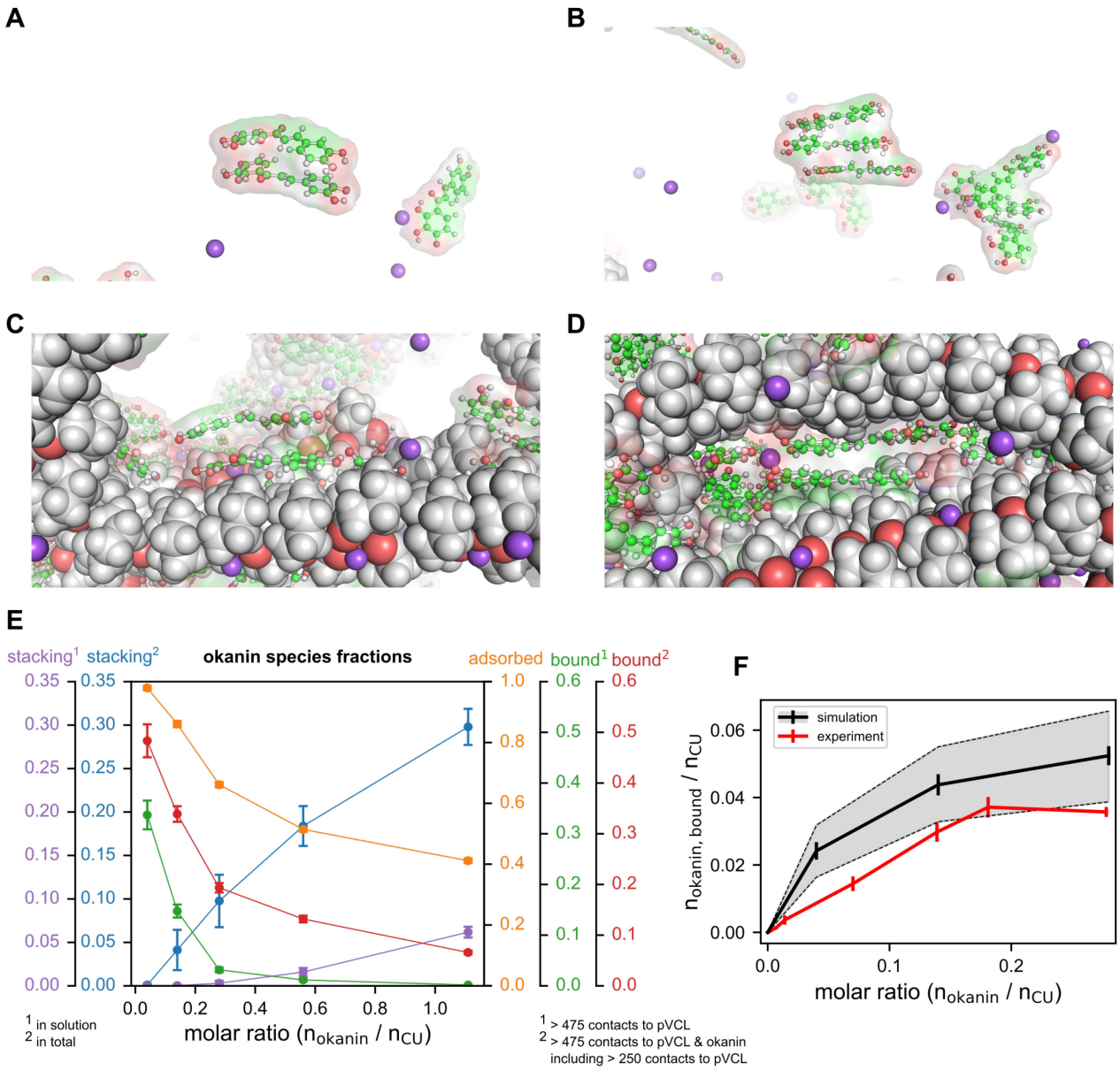

Figure 21. Quantification of different okanin species and interactions. Okanin stacks in solution (**A** two molecules, **B** three molecules), on adsorbed okanin (**C**), and within a bound state (**D**) at high molar ratio (n_{okanin}/n_{CU} = 1.11). E Quantification of okanin species. Okanin species fractions are given in relation to the overall number of okanin molecules within the respective system. With increasing okanin concentration, the fraction of okanin molecules in a stacking configuration in solution increases linearly for molar ratios above 0.28 (purple), while the overall fraction including stacking to bound/adsorbed okanin (blue) increases linearly for all molar ratios. The fraction of adsorbed (yellow), bound (green), and okanin stacked within the microgel (red) decreases with increasing okanin concentration. **F** Comparison of experimentally determined bound okanin per constitutional unit ($n_{okanin,bound}/n_{CU}$) with okanin considered bound and/or stacked within the microgel (> 475 contacts to PNVCL or > 475 contacts and at least 250 contacts formed with PNVCL) in MD simulations. The grey shaded area depicts the uncertainty related to a change of the cutoff of ± 25 contacts (i.e., 450 and 500 contacts for the upper and lower bound, respectively), which corresponds to a change of the computed binding free energy of approximately ±1 kcal mol^{-1}. Figure and figure caption taken from Publication III, see page 172.

Conclusions and significance

The integrated study elucidates the interactions between the herbicide okanin and stimuli-responsive PNVCL-based MGs. Experimental work and simulations yielded insights into the interaction of the chalcone with the MG carrier. Collaborators experimentally determined the okanin loading capacity of the PNVCL MG, while I investigated interactions of okanin with the polymer at an atomistic level by employing MD simulations. Using simulations, it is possible to distinguish between permanently bound okanin and adsorbed okanin, which is in constant exchange with solvated okanin. I used robust free energy calculations to investigate the energetics of the adsorption/binding process. Moreover, the importance of okanin stacking for high okanin concentration during loading of the MG was revealed in my simulations. Finally, the solvent-triggered release of okanin from the MG was investigated both experimentally and *in silico*. Overall, experiments and simulations agreed with each other for the loading and release of okanin into/from the MG, establishing a platform for using PNVCL-based (co)polymers as a potential carrier for agrochemicals.

The main results of this study are:

- The generation of a linear and crosslinked PNVCL was used in MD simulation to investigate the interaction with the chalcone okanin.
- Free energy calculation yielded insights into the nature of interactions between the okanin and the MG and revealed that polar interactions are the driving factor for okanin binding. Thus, the okanin-mediated inter-chain crosslink causing the MG to collapse is comparable to the physical crosslinking of PNVCL through tannic acid.
- Green solvents, such as ethyl acetate may be used to trigger the release of okanin from the PNVCL-based carrier. Simulations of the solvent-triggered release agrees with the okanin release observed in experiments.

5. Summary and Perspectives

GreenRelease is a novel plant protection technology, in which agrochemicals are loaded into MG carriers decorated with APs for increased rain fastness. This thesis aimed at understanding the atomistic mechanisms of each step of the *GreenRelease* technology. For this, the interaction of the APs with apple tree leaves was investigated experimentally and the adsorption mechanism was elucidated at an atomistic level using MD simulations (**Publication I**). To understand the loading and release processes of herbicides into/from the MG, an accurate model of the polymer had to be generated and validated first. Therefore, exhaustive simulations of oligomeric PNVCL were performed and validated using experimental data to establish a platform for all consecutive analyses (**Publication II**). Finally, using the obtained knowledge, the loading and release processes of the herbicide okanin into/from the microgel carrier were investigated (**Publication III**). Overall, molecular models of all components, i.e., APs, microgels, and the herbicide okanin were generated. Using the generated models in combination with atomistic MD simulations allowed fundamental insights into involved mechanisms and crucial interactions within the *GreenRelease* technology.

In **Publication I**, the leaf binding of the AP MacHis was investigated in an integrated manner. A novel atomistic model of the leaf surface is used in unbiased as well as steered MD simulations to identify residues within the AP of major importance for the adsorption to the leaf surface and to estimate the binding strength. The identified residues were subjected to an alanine scanning, revealing that a single substitution might lead to a decrease in binding strength of up to 80 %. Using adaptive steered MDs, the binding strength of five different APs was determined *in silico*. The ranking based on binding strength matches the experimentally determined one. For further investigations on the experimental side, site-saturation mutagenesis is necessary to have a full picture. The same applies to the *in silico* studies on the adsorption, i.e., the explicit simulation of the adsorption of the different AP variants identified experimentally can potentially lead to new insights. The generated models also establish a platform for the generation of CG models, potentially enabling an *in silico* screening of AP variants or potentially novel APs. Besides the further rational improvement of APs, the generated model can be used for a multitude of other foliar applications.

In **Publication II**, exhaustive MD simulations yielded valuable insights into the thermo-responsiveness of PNVCL at an atomistic level. Although the work was the most

comprehensive computational study on the coil-to-globule transition of PNVCL at the time of publication with 660 µs of cumulative simulation time, it revealed that potentially further sampling in simulations is needed to fully capture the temperature-induced transition of PNVCL. For the first time, methods such as end-point free energy estimation using MM-PBSA and the construction of Markov State Models were used to elucidate the energetics of the coil-to-globule transition of PNVCL. However, the applied methods are limited by fundamental and, depending on the approach, technical reasons. For example, decomposing the solvation free energy into an enthalpic and entropic part using MM-PBSA is not straightforward. It is not possible to tell whether a major proportion of the solvation free energy is determined by the losses in translational and rotational entropy of water molecules when forming solvent cages. To elucidate the energetics further, novel computational methods have to be developed. Experimental validation of the determined energetics is mandatory, and thus, calorimetric experiments of the transition for oligomeric PNVCL are necessary. The presented study contributed significantly to the *in silico* investigation of thermo-responsive oligomers, promoting the unconventional use of computational methods and enhanced sampling to capture the polymer's structural dynamics.

In **Publication III**, the uptake and co-solvent triggered release of the herbicide okanin into/from a PNVCL microgel was investigated in an integrated approach. Experimentally, the uptake and release of okanin as well as changes in the morphology of the particles were assessed. The complex structure of an MG was decomposed into atomistic models of linear and crosslinked PNVCL to investigate the influence of the MG's structure upon the uptake of okanin. The loading capacity and co-solvent triggered release observed in the MD simulations match experiments. Moreover, the determined binding modes explain the structural and morphological changes of the MG upon loading. Incorporating GMA of the PNVCL MG showed an increase in the okanin loading capacity of the MG. However, VCL-GMA copolymers have not been investigated *in silico*, yet. Moreover, there is a multitude of potential monomers that can be used instead of GMA to further increase the loading capacity or alter loading and release characteristics. The established procedures can be easily adapted to investigate the interaction of small organic molecules such as okanin with different PNVCL-based copolymers. Finally, the atomistic models can be used to generate a coarse-grained model of the full MG, to investigate diffusion processes within the carrier.

6. Acknowledgments

I want to express my sincere gratitude to my supervisor Prof. Dr. Holger Gohlke for giving me the opportunity to work in his team and to earn my PhD at the Heinrich-Heine University. He gave me the chance to work on an interesting and likewise challenging project. Prof. Dr. Gohlke provided guidance when needed and the freedom to pursue my ideas and interests.

Within the BioSC project, I met and worked with many fantastic people who deserve recognition. First, I want to thank Prof. Dr. Georg Groth for being my second supervisor and together with Dr. Alexander Hofmann for their collaboration during the work with okanin and PEPC. Second, I want to thank Prof. Dr. Ulrich Schwaneberg, Dr. Felix Jakob, Liudmyla Goncharenko, and Christin Brethauer for their collaboration on the anchor peptides. Third, I want to thank Dr. Shyam Pariyar, Dr. Viktoria Zeisler-Diehl, and Prof. Dr. Lukas Schreiber for their collaboration and for providing valuable insights on the structure of leaves. Finally, I want to express my gratitude to Prof. Dr. Andrij Pich, Michael Kather, Anna Holzberger, Dr. Alexander Töpel, and Fabian Kolodzy for their collaboration on the microgels.

Of course, a lot of credit goes to all current and former members of the CPClab, as throughout the years we not only had serious (“scientific”) discussions but also lots of fun. Therefore, I want to thank (in alphabetical order) Annika, Bastian, Benoit, Benedikt, Birte, Christina, Christoph, Christopher, Daniel B., Daniel C., Daniel M., David, Denis, Fathoni, Filip, Jesko, Karel, Korana, Lisa, Lucas, Michele, Mohan, Mykola, Neha, Nicola, Pablo, Pegah, Peter, Rocco, Sabah, Steffi, Susanne, Till, and Yu Lin. Thank you very much for the nice work environment, good discussions, and valuable insights. In particular, I want to thank Denis for helping me make the first steps into the world of computational chemistry and bioinformatics. Bastian, Christoph, Christopher, Daniel B., Denis, Neha, and Stephan, thank you for the amazing time we had and the good friendships that developed during the years.

Thanks to Christoph, Stephan, Christopher, and Sarah for corrections and feedback on this thesis.

Last, but not least, I want to thank my wife Sarah and my family. Without them, certainly, none of this would have been possible. I want to thank them for their constant love and unconditional support.

7. Reprint Permissions

Publication I

"*Rational Design Yields Molecular Insights on Leaf-Binding of Anchor Peptides*"

Jonas Dittrich, Christin Brethauer, Liudmyla Goncharenko, Jens Bührmann, Viktoria Zeisler-Diehl, Shyam Pariyar, Felix Jakob, Tetiana Kurkina, Lukas Schreiber, Ulrich Schwaneberg, and Holger Gohlke

ACS Applied Materials & Interfaces, **2022**, 14, 28412-28426.

DOI: 10.1021/acsami.2c00648

Publication II

"*Cumulative Submillisecond All-Atom Simulations of the Temperature-Induced Coil-to-Globule Transition of Poly(N-vinylcaprolactam) in Aqueous Solution*"

Jonas Dittrich, Michael Kather, Anna Holzberger, Andrij Pich, and Holger Gohlke

Macromolecules, **2020**, 53, 9793−9810.

DOI: 10.1021/acs.macromol.0c01896

Publication III

"Loading and Co-Solvent-Triggered Release of Okanin, a C_4 Plant Key Enzyme Inhibitor, into/from Functional Microgels"

Jonas Dittrich, Fabian Kolodzy, Alexander Töpel, Andrij Pich, Holger Gohlke

DOI: 10.26434/chemrxiv-2022-sgbx9-v2 (ChemRxiv, 13.10.2022)

8. Publication I

Rational Design Yields Molecular Insights on Leaf-Binding of Anchor Peptides

Rational Design Yields Molecular Insights on Leaf-Binding of Anchor Peptides

Jonas Dittrich[#], Christin Brethauer[#], Liudmyla Goncharenko, Jens Bührmann, Viktoria Zeisler-Diehl, Shyam Pariyar, Felix Jakob, Tetiana Kurkina, Lukas Schreiber, Ulrich Schwaneberg, and Holger Gohlke

[#]these authors contributed equally.

ACS Applied Materials & Interfaces, **2022**, 14, 28412-28426.

DOI: 10.1021/acsami.2c00648 (ACS Applied Materials & Interfaces)

ACS APPLIED MATERIALS & INTERFACES

www.acsami.org Research Article

Rational Design Yields Molecular Insights on Leaf-Binding of Anchor Peptides

Jonas Dittrich,[†] Christin Brethauer,[†] Liudmyla Goncharenko, Jens Bührmann, Viktoria Zeisler-Diehl, Shyam Pariyar, Felix Jakob, Tetiana Kurkina, Lukas Schreiber, Ulrich Schwaneberg, and Holger Gohlke*

Cite This: *ACS Appl. Mater. Interfaces* 2022, 14, 28412−28426 Read Online

ACCESS | Metrics & More | Article Recommendations | Supporting Information

ABSTRACT: In times of a constantly growing world population and increasing demand for food, sustainable agriculture is crucial. The rainfastness of plant protection agents is of pivotal importance to reduce the amount of applied nutrients, herbicides, and fungicides. As a result of protective agent wash-off, plant protection is lost, and soils and groundwater are severely polluted. To date, rainfastness of plant protection products has been achieved by adding polymeric adjuvants to the agrochemicals. However, polymeric adjuvants will be regarded as microplastics in the future, and environmentally friendly alternatives are needed. Anchor peptides (APs) are promising biobased and biodegradable adhesion promoters. Although the adhesion of anchor peptides to artificial surfaces, such as polymers, has already been investigated in theory and experimentally, exploiting the adhesion to biological surfaces remains challenging. The complex nature and composition of biological surfaces such as plant leaves and fruit surfaces complicate the generation of accurate models. Here, we present the first detailed three-layered atomistic model of the surface of apple leaves and use it to compute free energy profiles of the adhesion and desorption of APs to and from that surface. Our model is validated by a novel fluorescence-based microtiter plate (MTP) assay that mimics these complex processes and allows for quantifying them. For the AP Macaque Histatin, we demonstrate that aromatic and positively charged amino acids are essential for binding to the waxy apple leaf surface. The established protocols should generally be applicable for tailoring the binding properties of APs to biological interfaces.

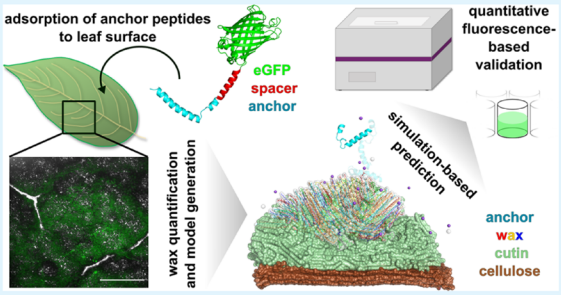

KEYWORDS: *adaptive-steered MD, potential of mean force, atomistic leaf surface model, cutin, leaf wax, all-atom, MTP assay, fluorescence*

1. INTRODUCTION

With the increasing demand for food worldwide, sustainable and innovative plant nutrition and protection methods have become progressively crucial for agricultural production.[1] An ecologically friendly and tailored application of plant nutrients and protectants may help to reduce the amount of applied substances significantly by improving resistance against rainfall and sunlight and, thus, minimizing the ecological footprint. In particular, the rainfastness of foliar applications has been proven to play a major role in its long-term effectiveness and often becomes the limiting factor for the timespan after which reapplication is necessary. Thus, investigating and improving the rainfastness of agrochemicals has been of high interest for a long time.[2−6] Increased rainfastness is guaranteed by adding adjuvants to the agrochemicals. These adjuvants greatly vary in their chemical nature. Commonly used polymeric adjuvants, however, will be regarded as microplastics in the future.[2,7,8] According to the European Chemical Agency, the use of intentionally added microplastics to plant health products will be prohibited within the next five years. Therefore, it is of pivotal importance to identify biodegradable alternatives to ensure future food production.

Anchor peptides (APs) are short amphiphilic peptides with sizes ranging from 20 to 100 amino acids that bind from aqueous solutions to natural[9,10] and synthetic surfaces[11−14] including metals.[15,16] Tailor-made APs are thus applicable in many fields, including biotechnology,[17] catalysis,[18] nanoparticles,[19] medicine,[20] and agriculture.[9]

APs were reported to bind microgel containers to the plant surface. Such containers can be applied for the long-term controlled release of nutrients, herbicides, and fungicides. APs increase the rainfastness and, hence, reduce the overall amount of chemicals needed for effective plant protection and

Received: January 11, 2022
Accepted: April 29, 2022
Published: May 23, 2022

https://doi.org/10.1021/acsami.2c00648
ACS Appl. Mater. Interfaces 2022, 14, 28412−28426

fertilization.[9] In another study,[10] APs were fused to an antifungal peptide and successfully protected soybean plants against its most severe disease, Asian soybean rust (*Phakopsora pachyrhizi*). Therefore, APs are promising candidates for microplastic-free adhesion-promoting adjuvants to increase the rainfastness of agrochemicals.

The antimicrobial AP LCI[21] shows significant binding to poly(propylene);[13] the subsequent rational improvement of the binding characteristics to this synthetic material was reported.[11,12] However, the rational improvement of AP adhesion to biological surfaces remained challenging because of the complex nature and composition of biological surfaces and the diversity of the forces involved.

Here, we developed and validated a workflow for the rational improvement of AP adhesion to specific plant leaves based on a multidisciplinary approach, comprising molecular dynamics (MD) simulations and a tailored fluorescence-based screening experiment. To obtain insights at the atomistic level into the adhesion properties of APs on apple leaves, we generated the, to our knowledge, first three-layered atomistic model of an apple leaf surface consisting of Iβ cellulose, a cutin matrix, and a leaf wax layer and probed AP adhesion to it by MD simulations. The predictive power of the model was validated by a novel fluorescence-based quantitative assay designed to probe the adhesion of APs toward the leaf surfaces of plants. The generated atomistic models allow investigating not only the binding of APs, but can also aid in scrutinizing the adsorption, penetration, and accumulation[22] of nutrients, herbicides, pesticides, or fungicides on/through the outer surface of plant leaves. The fluorescence-based assay allows for rapidly identifying new potential APs and selecting variants with improved binding properties.

2. MATERIALS AND METHODS

Chemicals and Materials. All chemicals used in this study were purchased from Carl Roth GmbH (Karlsruhe, Germany), Sigma-Aldrich Corp. (St. Louis, MO and Deisenhofen, Germany), Fluka, (Ulm, Germany), Macherey-Nagel (Düren, Germany), or AppliChem GmbH (Darmstadt, Germany) and had at least analytical-reagent grade purity unless specified. Synthetic genes were obtained from GenScript (Nanjing, China), and oligonucleotides were acquired from Eurofins Scientific SE (Ebersberg, Germany) in salt-free form. Enzymes were obtained from New England Biolabs GmbH (Frankfurt am Main, Germany). Plasmid extraction and polymerase chain reaction (PCR) purification kits were ordered from Macherey-Nagel GmbH & Co. KG (Düren, Germany) and Qiagen GmbH (Hilden, Germany). Black polypropylene microtiter plates (MTPs) were obtained from Greiner Bio-One GmbH (Frickenhausen, Germany). The plasmid pET28a(+) (Novagen, Darmstadt, Germany) was used as the expression vector. The *Escherichia coli* strains DH5α and BL21-Gold (DE3) were purchased from Agilent Technologies (Santa Clara, CA). *E. coli* DH5α was used as cloning host and *E. coli* BL21-Gold (DE3) was used for protein expression.

Data Acquisition, Model Generation, Assay Development, and Model Validation. In the following, we first describe the plant growth conditions and the cuticular wax analysis. Next, this data is used for the in silico model generation and molecular simulations for the prediction of binding residues within APs and the binding strength of APs. Finally, the predictions are investigated and validated using a novel quantitative fluorescence-based screening.

Plant Growth Condition and Leaf Sampling. Stratified apple (*Malus domestica*, cultivar "Bittenfelder") seeds were sown on wet sands for germination. After germination (2−3 leaves stage), seedlings were transplanted in soil pots (1 plant per pot). Seedlings were grown under semicontrolled conditions in the greenhouse to the 12-leaves stage. Then, they were transferred to the field. These apple plants were grown under an ambient field environment at the Research Station of Campus Endenich, University of Bonn (50° 73.09′ north latitude, 7° 7.34′ east longitude), and northwest of the city of Bonn. Only one plant per pot was allowed to grow after germination to avoid nutrition, soil moisture, and light competition. The plants were grown in well-watered (soil moisture content above 60%) and nourished soil media (pot with basal-diameter 11 cm, soil mixture: TKS [Brill Typ 5 + sand + perlite, mixing ratio 1:1.2:0.3], water holding capacity: 1.29 kg water kg^{-1} dry mass). Climate data such as global radiation, UVA, rainfall, and photoactive radiation in ambient outdoor conditions were continuously recorded every minute at the meteorological station (MWS 9−5 Microprocessor Weather Station, Rheinhardt System- und Messelectronic GmbH, Diessen-Oebermuel-hausen, Germany) in the field, whereas plant canopy level temperature plus relative humidity was continuously recorded every 10 min by Tinytag data loggers (Tinytag, Gemini Data Loggers, Chichester, UK). During the growth period (18.05−10.07.2017), the global radiation, photoactive radiation, and ultraviolet radiation A in the field were 328 ± 14 W m^{-2} (mean ± standard error (SEM)), 554 ± 20 μmol m^{-2} s^{-1}, and 5.0 ± 0.2 W m^{-2}, respectively. There were 29 rainfall days with daily cumulative rainfall ranging from 0.11 mm (23.06.2017) to 15.28 mm (10.07.2017), yielding a mean value of 3.5 ± 0.8 mm (SEM) and a median of 1.5 mm rainfall. The canopy level temperature was 23.7 ± 0.5 °C (mean ± SEM), and relative humidity was 61.4 ± 1.4 (mean ± SEM). Fifteen-day-old apple leaf (15 days exposed to the field environment) samples were taken for wax analysis from 17th-position leaves from the base on June 13, 2017, each from five biological replications. The freshly harvested leaves were placed in humid polybags and brought to the lab for wax extraction.

Quantification of Apple Leaf Wax Components via GC/FID and GC/MS. Surface waxes were extracted from the adaxial leaf side of apple leaves. Waxes were extracted by gently pressing a glass vial containing 5 mL of chloroform on the adaxial leaf side for 10 s. Immediately after extraction, samples were spiked with an internal standard (50 μL tetracosane of a chloroform solution of 10 mg in 50 mL; Fluka, Ulm, Germany), enabling the quantification of the individual wax compounds. The chloroform volume was reduced under a gentle stream of nitrogen at 60 °C to an end-volume of 200 μL. Hydroxylic and carboxyl groups of alcohols and acids were transformed into the corresponding trimethylsilyl ethers and -esters by derivatization. Derivatization was done using 20 μL of *N,O*-bis(trimethylsilyl)-trifluoroacetamid (BSTFA; Macherey-Nagel, Düren, Germany) and 20 μL of pyridine (Sigma-Aldrich Corp., Deisenhofen, Germany) for 45 min at 70 °C. One microliter of each sample was analyzed by on-column injection and a gas chromatograph equipped with flame ionization detection (GC-FID; CG-Hewlett-Packard 5890 series H, Hewlett-Packard, Palo Alto, CA, USA, column-type: 30 m DB-1 i.d. 0.32 mm, film 0.1 μm; J&W Scientific, Folsom, CA, USA). For identification of the individual wax components (i.e., fatty acids, alcohols), again 1 μL of the samples was analyzed by GC-MS (gas chromatography equipped with a mass spectrometer, quadrupole mass selective detector HP 5971, Hewlett-Packard, Palo Alto, CA, USA). All wax molecules, including the fatty acids, were quantified based on the amount of internal standard via GC-FID analysis. Identification of the single compounds was made using a homemade wax database and by comparing the obtained fragmentation pattern with known substances. Calculations were performed for every single component individually. The raw data are provided in Table S1.

Computational Methods. To rationally improve the adhesion of the tested APs to the surface of an apple leaf, we generated an atomistic model of an apple leaf surface and performed (steered) molecular dynamics simulations of the ad- and desorption of the tested APs to/from this model.

Generation of an All-Atom Model of a Leaf Surface. The outer part of the leaf surface consists of a cuticular polyester matrix of interesterified ω-hydroxy acids, impregnated with cuticular waxes, covered with cuticular waxes,[23] and located atop a polysaccharide cell wall.[24] We used the Cellulose-Builder[25] to generate a crystalline sheet of Iβ cellulose, consisting of three layers of 15 chains each with 15

https://doi.org/10.1021/acsami.2c00648
ACS Appl. Mater. Interfaces 2022, 14, 28412−28426

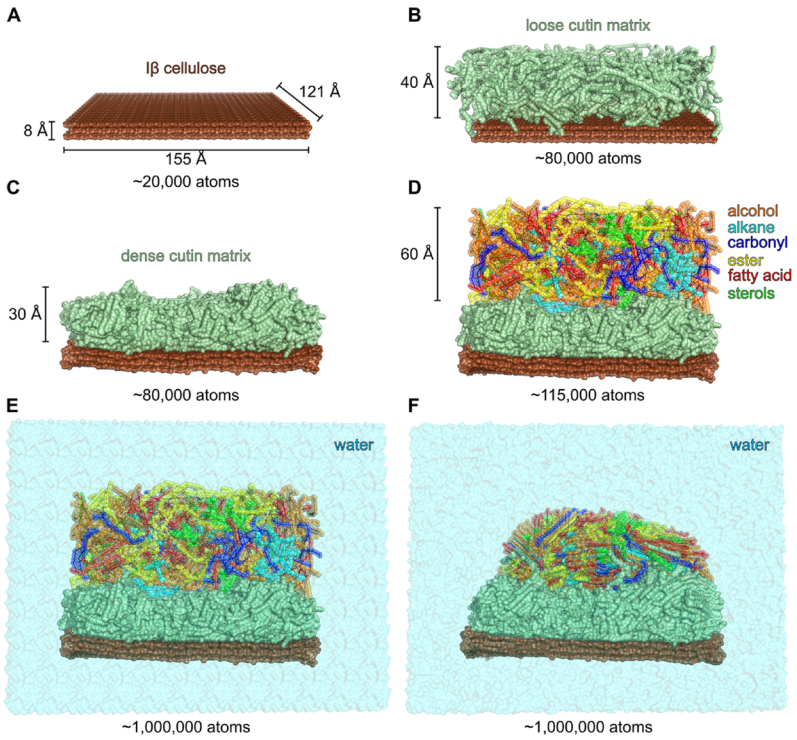

Figure 1. Stepwise creation of an atomistic leaf surface model. (A) Three-layered crystalline Iβ cellulose. (B) Loosely packed polyester matrix of cross-linked 10,18-dihydroxyoctadecanoic acid located above the cellulose sheet. (C) Compacted cutin layer atop the cellulose sheet after 25 ns of NVT MD simulations. (D) Randomly placed wax components above the compact cutin layer. (E) Solvated system. (F) Snapshot obtained after 100 ns of NVT MD simulations of the complete model.

$\beta(1 \rightarrow 4)$-linked D-glucopyranose moieties per chain, yielding a sheet of 155 Å × 121 Å × 8 Å size (Figure 1A) that serves as a rigid surface for our cutin model. Force field parameters for the $\beta(1 \rightarrow 4)$-linked D-glucopyranose units and the terminal hydroxyl groups were taken from *GLYCAM06*.[26]

Cutin is a waxy polymer composed of ω-hydroxy acids (mostly long-chain (16- or 18-carbon) fatty acids) and their derivatives, which are interlinked via ester bonds, forming a polyester polymer of indeterminate size. Its composition varies depending on the plant.[27] As a representative fatty acid, we chose 10,18-dihydroxyoctadecanoic acid. To generate building blocks for all possible ester cross-links, all possible 2^3 structures differentially methylated at all hydroxyl groups were generated in Schrödinger's *MAESTRO* software suite.[28] In subsequent preparation steps, methyl caps were removed, connection records were added instead, and the structures were saved in an *Amber* library file (.lib), allowing one to generate custom polyester matrixes. We generated several linear polyesters, ranging from dimers to hexamers, and branched structures with up to 17 residues. The polyesters were packed into a rectangular box (160 Å × 120 Å × 80 Å) atop the cellulose using *PACKMOL*,[29] thereby keeping a minimal distance of at least 2 Å between all structures. This loosely packed cutin matrix (Figure 1B) was solvated using TIP3P water[30] and energy-minimized and thermalized. MD simulations of 25 ns length under NVT conditions (see the next section for details) were then performed to compact the matrix (Figure 1C). The water from the resulting cellulose/cutin model was stripped, and the system was used as a starting structure for all consecutive MD simulations performed to generate the complete atomistic model of the leaf wax on a cutin surface. Note that the thickness of the cutin layer may vary considerably in nature.[23] However, as we are focusing on interactions of the peptides with the leaf surface, our polyester layer merely serves to mimic the outer part of the cutin layer to adequately model interactions between the leaf surface and the wax components.

The composition of the wax was based on experimental data obtained by GC/FID and GC/MS of an apple leaf wax/chloroform extract (see Quantification of Apple Leaf Wax Components via GC/FID and GC/MS). To keep our computations tractable, we used 1/45 of the experimentally determined amount of wax components per surface area of the cellulose/cutin system. *PACKMOL*[29] was used to pack the wax components into a rectangular box atop the cellulose/cutin system (Figure 1D). Ten initial starting structures were created by selecting different random seeds for the packing process of the wax components. The resulting systems were again solvated (Figure 1E) with TIP3P[30] water such that the distance between the boundary of the box and the closest solute atom was at least 20 Å. MD simulations of 100 ns length in the NVT ensemble were then performed (Figure 1F), as described in the following section after minimization and thermalization. Atomic charges of cutin and wax components were determined using the AM1-BCC method[31,32] as implemented in antechamber.[33] Force field parameters were taken from the GAFF2 force field.[34] Na^+ counterions were used to balance the charges of the deprotonated fatty acids. The solvated system comprises more than 1 000 000 atoms. At the time the model was constructed, *Amber* did not have the option to handle covalent bonds across periodic boundaries. Therefore, we were limited to a finite sheet of cellulose which has to be restrained during simulations (see Molecular Dynamics Simulations) and the padding of the system with solvent molecules.

The coordinates of the ten generated leaf surface models are provided in PDB format, and *Amber* library files are provided for the cutin and wax components in the Supporting Information.

AP/Leaf Systems. Peptide structures were taken from the Protein Data Bank (PDB)[35] when available (name, PDB ID: LCI, 2B9K;

https://doi.org/10.1021/acsami.2c00648
ACS Appl. Mater. Interfaces 2022, 14, 28412−28426

Magainin, 2MAG; Plantaricin A, 1YTR; Pleurocidin, 1Z64). If a PDB entry contained an ensemble of structures, the first structure was taken, and if the protein was present as a multimer, the first subunit was used. We employed *TopModel*,[36] a meta-method for protein structure prediction using top-down consensus and deep neural networks, to generate a structural model for Macaque Histatin (MacHis). Ten systems for the simulation of the adhesion for each peptide were created by placing three APs randomly above the ten different leaf wax replicas using *PACKMOL* while keeping a minimum distance of at least 5 Å between the APs as well as to the wax surface. Na^+/Cl^- counterions were added to neutralize the charges. Thus, for all peptides, ten independent MD simulations of 250 ns length each were performed, using differently packed leaf wax models for each system. To probe the influence of the initial conformation of the leaf wax surface on the simulation, we simulated ten replicas of LCI for each of the ten initial leaf wax models for 250 ns, thus, in total 100 runs.

Molecular Dynamics Simulations. MD simulations were carried out with the *Amber18* suite of programs[37,38] using the GPU-accelerated CUDA version of PMEMD.[39,40] We applied the ff14SB[41] (for the peptides), GLYCAM06[26] (for Iβ cellulose), and GAFF2 (for cutin and wax components) force fields[34] in all simulations. The structures were solvated in a box of TIP3P[30] water such that the distance between the boundary of the box and the closest solute atom was at least 20 Å. Periodic boundary conditions were applied using the particle mesh Ewald (PME) method[42] to treat long-range electrostatic interactions. Bond lengths involving bonds to hydrogen atoms were constrained by the SHAKE[43] algorithm. The time step for all MD simulations was 2 fs, and a direct-space nonbonded cutoff of 8 Å was applied. First, the solvent was minimized for 250 steps by using the steepest descent method followed by conjugate gradient minimization of 50 steps. Subsequently, the same approach was used to minimize the entire system. Afterward, the system was heated from 0 to 100 K using canonical ensemble (NVT) MD simulations, and from 100 to 293 K using isobaric MD simulations. The solvent density was adjusted to 0.97 g cm^{-3} using isothermal−isobaric ensemble (NPT) MD simulations. Positional restraints applied during thermalization were reduced in a stepwise manner over 50 ps, followed by 50 ps of unrestrained canonical ensemble (NVT) MD simulations at 293 K with a time constant of 2 ps for heat bath coupling with the Berendsen thermostat.[44] Production MD simulations for the leaf model only and the system comprising the APs were run for 100 and 250 ns length, respectively, using 10 ps for heat bath coupling.[44] Coordinates were saved at 100 ps intervals. To prevent twisting of the cellulose layer, positional restraints with a force constant of 1 kcal mol^{-1} $Å^{-2}$ were applied to the glucopyranose moieties throughout the production simulations.

Estimation of the Potential of Mean Force for AP Desorption by Adaptive Steered Molecular Dynamics Simulations. To estimate the work needed to release the AP from the wax surface, we performed adaptive-steered molecular dynamics (ASMD) simulations.[45,46] Using Jarzynski's equality,[47] the nonequilibrium work $W_{A\to B}$ performed on the system in a steered MD simulation can be related to the free energy difference $\Delta F = F_B - F_A$ between state A and B[48] as depicted in eq 1 and eq 2 (T: absolute temperature; k_B: Boltzmann constant):

$$F_B - F_A = -k_B T \ln(\langle e^{-W_{A\to B}/k_B T}\rangle) \quad (1)$$

$$e^{-\Delta F/k_B T} = \langle e^{-W_{A\to B}/k_B T}\rangle \quad (2)$$

In steered MD simulations (SMDs), a steering force is applied along the desired reaction coordinate $\xi(r)$ at a constant velocity v to explore the system.[45,48] The system's original Hamiltonian $H(r, p)$ is extended by a guiding potential $h_\lambda(r)$, with the spring constant k and the time-dependent perturbation $\lambda = \lambda(t)$ (eq 3), yielding the total Hamiltonian $\tilde{H}_\lambda(r, p)$ (eq 4):[48]

$$h_\lambda(r) = \frac{k}{2}[\xi(r) - \lambda]^2$$

with

$$\lambda(t) = \lambda(0) + vt; \quad v = \text{const} \quad (3)$$

$$\tilde{H}_\lambda(r, p) = H(r, p) + h_\lambda(r) \quad (4)$$

When applying Jarzyski's equality to the $\tilde{H}$ system, we obtain eq 5:

$$F_{\lambda(\tau)} - F_{\lambda(0)} = -k_B T \ln(\langle e^{-W(\tau)/k_B T}\rangle)$$

with

$$W(\tau) = \int_0^\tau \mathrm{d}t \left[\frac{\partial}{\partial t}\tilde{H}_{\lambda(t)}(r, p)\right]_{(r,p)=(r(t),p(t))} \quad (5)$$

where F_λ is the Helmholtz free energy of the $\tilde{H}$ system and $W(\tau)$ is the work done during the time interval $[0, \tau]$ calculated for each trajectory $(r(t), p(t))$.

$e^{-F_\lambda/k_B T}$ can be expressed in terms of the Helmholtz free energy profile (potential of mean force) PMF(ξ) along ξ, with the highest contribution of the integral coming from the region around $\xi = \lambda$ for large k, known as stiff-spring approximation.[48] Taking the Taylor series of $e^{-\mathrm{PMF}(\xi)/k_B T}$ about λ, then, allows for calculating the potential of mean force (PMF) from the leading order, yielding $\mathrm{PMF}(\lambda) = F_\lambda$.[48] The latter can be calculated from eq 5, resulting in PMF as a function of the distance d from the leaf surface plus a constant const = $F_{\lambda(0)}$ according to eq 6:

$$\mathrm{PMF}(\lambda = d) = -k_B T \ln(\langle e^{-W(\tau)/k_B T}\rangle) + \text{const} \quad (6)$$

In general, a high number of simulations must be performed to converge the average over all realizations of an external process that takes the system from the equilibrium state A to a new, generally nonequilibrium state B and, thus, obtain a converged PMF.[48] ASMD tackles this problem by dividing the reaction path into smaller segments called stages.[49] Within these stages, the trajectory closest to the Jarzynski average is determined, and the final state of this trajectory is used as starting point for the consecutive stage.[50] Thus, trajectories contributing little to the overall PMF are disregarded in the next stage, that way reducing the total number of simulations to be performed.

Here, we performed ASMD simulations with a pulling velocity of v = 1 Å ns^{-1} along the surface normal of the leaf model, and only the work applied along this axis is determined. We employed a uniform force constant of k = 100 kcal mol^{-1} $Å^{-2}$. For each stage, 25 replicas are simulated for 2 ns each, resulting in an increase of 2 Å in the distance between the center of mass of the AP and the leaf surface per stage. As the amount of required simulation time is considerable for a system comprising more than 1 000 000 atoms (∼6−8 h on state-of-the-art GPUs for 1 ns of simulation time), we limited the tested APs to MacHis, LCI, Plantaricin A, Magainin, and Pleurocidin. These peptides cover the range from strong adhesion (MacHis, LCI) over medium adhesion (Plantaricin A) to weak/no significant adhesion (Magainin, Pleurocidin) as determined from qualitative experiments on the apple. For each AP, one system out of the ten replicas is chosen for ASMD simulations, where one of the three APs present in the system is adsorbed approximately at the center of the wax surface and does not interfere with the remaining APs.

Identification of Residues Contributing to Binding. To identify residues important for the adhesion of the AP to the leaf surface, we calculated all contacts of the peptides to the wax components within a distance cutoff of 7 Å for each replica. On the basis of the identified interactions, MacHis variants were generated by substituting the residues showing the highest number of contacts with alanine. As a negative control, alanine variants of residues showing less frequent contacts were generated (see Generation of eGFP-MacHis Variants and Characterization of eGFP-AP Binding Strength to Apple Leaf Wax). The geometric analyses of the trajectories were performed with *CPPTRAJ*.[51]

https://doi.org/10.1021/acsami.2c00648
ACS Appl. Mater. Interfaces 2022, 14, 28412−28426

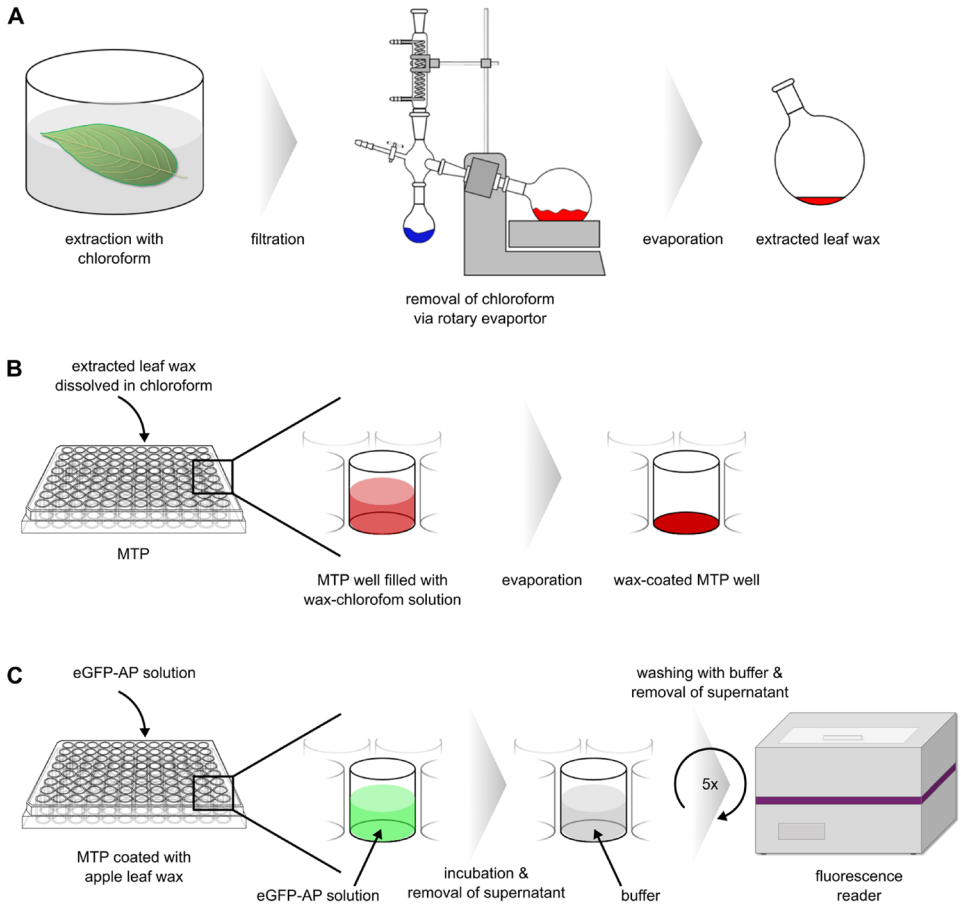

Figure 2. Generation of an MTP-based assay for evaluating the adsorption of APs toward surface wax. (A) Surface wax extraction of an apple leaf using chloroform. The extracted wax can be stored and (re)dissolved for coating. (B) Wax coating of an MTP well. (C) Procedure of the binding assay describing the application of the eGFP-AP solution and consecutive washing steps. The remaining fluorescence is detected using a fluorescence reader.

Assay Development and Model Validation. To quantify the AP's binding strength to the cuticular wax and validate the computational predictions, we developed a fluorescence-based MTP assay to screen the APs and AP variants rapidly. The basis for the development was the reliable and robust ABBA assay successfully applied for the characterization of anchor peptide-binding strength.[11,12] In the following, we describe the developed assay and the generation of the AP fusion constructs.

Wax Extraction and Coating of MTPs. For cuticular wax extraction, apple leaves (*Malus domestica*, cultivar "Pinova", 200 leaves) were immersed in pure chloroform for 10 s. The remaining cuticular wax−chloroform mixture was filtered (cellulose folded filter paper; 4−12 μm pore size, M&N 615 1, Ø 185 mm, Macherey-Nagel GmbH & Co. KG), and chloroform was evaporated (rotary evaporator; 500 mbar to 250 mbar, 49−50 °C water bath, IKA-Werke GmbH & CO. KG) (Figure 2A). For the MTP wax coating, the wax−chloroform mixture was added to each well (50 μg/cm^2 apple wax; 50 μL per well), and the chloroform was evaporated completely (RT, 16 h) (Figure 2B). Wax-coated MTPs were subsequently used for the characterization of AP binding strength.

Generation of eGFP-AP Fusion Constructs. The synthetic genes of LCI (UniProt ID: P82243), MacHis (UniProt ID: P34084), Magainin (UniProt ID: P11006), Plantaricin A (UniProt ID: P80214), and Pleurocidin (UniProt ID: P81941) were codon-optimized for *E. coli* and synthesized by GenScript (Nanjing, China) (Table S2). All synthetic genes contained a stiff spacer helix (17 amino acids; AEAAAKEAAAKEAAAKA)[52] followed downstream by a TEV cleavage site (7 amino acids: ENLYFQG)[53] at the 5′-end of the AP gene. APs were cloned in the pET28a(+)::eGFP (enhanced green fluorescent protein) backbone applying "sequence-independent phosphorothioate-based ligase-independent gene cloning" (PLICing)[54] as previously described.[13] For the performed binding study, the TEV cleavage site was removed. Primers were designed (Table S3), and a two-step PCR amplification was performed under the following conditions: pre-PCR for single-primer extension ((98 °C, 2 min; one cycle), (98 °C, 15 s/55 °C, 15 s/72 °C, 4 min; 6 cycles)) followed by a final elongation step (72 °C, 10 min; one cycle) and a PCR for efficient recombination ((98 °C, 2 min; one cycle), (98 °C, 15 s/55 °C, 15 s/72 °C, 4 min; 15 cycles)) followed by a final elongation step (72 °C, 10 min; one cycle). All generated constructs were digested (20 U *Dpn1*; 2 h, 37 °C) and purified using a PCR cleanup kit (Macherey-Nagel). As eGFP-control, the construct pET28a-(+)::eGFP-17xHelix was generated. All generated constructs were transformed in electrocompetent *E. coli* DH5α and BL21-Gold (DE3) cells. Successful cloning was confirmed by sequencing (Eurofins Genomics GmbH, Ebersberg, Germany).

Generation of eGFP-MacHis Variants. Amino acid substitutions were introduced into the eGFP-MacHis system by side-directed mutagenesis using the pET28a::eGFP-17xHelix-TEV-MacHis template and the primer pairs shown in Tables S1 and S2 using a two-step

https://doi.org/10.1021/acsami.2c00648
ACS Appl. Mater. Interfaces 2022, 14, 28412−28426

ACS Applied Materials & Interfaces www.acsami.org Research Article

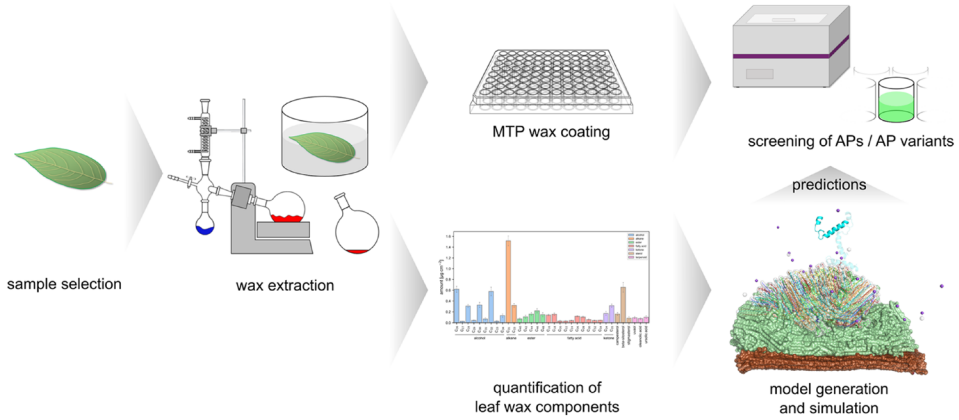

Figure 3. Multidisciplinary workflow for the rational improvement of the binding strength of APs toward apple leaves.

PCR. The PCR conditions were pre-PCR for single-primer extension ((98 °C, 2 min; one cycle), (98 °C, 15 s/55 °C, 15 s/72 °C, 4 min; 6 cycles)) followed by a final elongation step (72 °C, 10 min; one cycle) and a protocol for efficient introduction of point mutations ((98 °C, 2 min; one cycle), (98 °C, 15 s/55 °C, 15 s/72 °C, 4 min; 15 cycles)) followed by a final elongation step (72 °C, 10 min; one cycle). All generated constructs were digested (20 U *Dpn1*; 2 h, 37 °C), purified using a PCR cleanup kit (Macherey-Nagel), and transformed in electrocompetent *E. coli* DH5α and BL21-Gold (DE3) cells. Successful construction and cloning were confirmed by sequencing (Eurofins Genomics GmbH, Ebersberg, Germany).

Production of eGFP-AP Fusion Constructs. eGFP-control, eGFP-LCI, eGFP-MacHis, eGFP-Magainin, eGFP-Plantaricin A, eGFP-Pleurocidin, and eGFP-MacHis variants were expressed in *E. coli* BL21-Gold (DE3) cells and produced in Erlenmeyer flasks as published previously.[13] Cultivation was performed for 24 h (20 °C, 900 rpm, 70% humidity; Multitron Pro; Infors AG). Cells were harvested by centrifugation (3200 g, 40 min, 4 °C; Eppendorf centrifuge 5810 R, Eppendorf AG, Hamburg, Germany), and the cell pellets were stored (−20 °C). The obtained cell pellets were suspended in tris(hydroxymethyl)-aminomethane (Tris/HCl) buffer (10 mL; pH 8.0, 50 mM) and disrupted by sonication on ice (2 × 3 min, interval 30 s, 70% amplitude). By centrifugation (3200 g, 30 min, 4 °C; Eppendorf centrifuge 5810 R), soluble proteins were separated from cell fragments and insoluble proteins. The supernatant was filtered through a 0.45 mm cellulose-acetate filter (GE Healthcare, Little Chalfont, UK) and subsequently used for further purification.

Purification of eGFP-AP Fusion Constructs. The eGFP-AP fusion proteins and the eGFP-control were purified using the N-terminal His_6-Tag and fast protein liquid chromatography (ÄKTAprime, GE Healthcare) with a prepacked ion affinity chromatography column (Ni-Sepharose 6 Fast Flow, 5 mL, GE Healthcare). Samples were eluted with imidazole, desalted by dialysis against Tris/HCl buffer (50 mM, pH 8.0; used membrane: Spectra/Por4, Spectrum Inc., Breda, The Netherlands), and concentrated using ultrafiltration (Amicon Ultra 15 mL Centrifugal Filters, Merck KGaA). Protein concentrations were determined with the BCA protein assay kit (Novagen, Merck KGaA), and protein homogeneity was analyzed by sodium dodecyl sulfate-polyacrylamide gel electrophoresis (SDS-PAGE; 5% stacking gel, 12% separation gel).

Characterization of eGFP-AP Binding Strength to Apple Leaf Wax. To analyze the binding strength of the different eGFP-APs and eGFP-MacHis variants toward apple leaf wax, we established a 96-well MTP-based assay (Figure 2). In the immobilization step, eGFP-APs (4 μM and 10 μM for eGFP-APs and eGFP-MacHis variants, respectively; supplemented to PBS buffer pH 7.4, 100 μL per well) were transferred to a black wax-coated MTP (PP, flat bottom, wax coating described above) and incubated (10 min, RT, 600 rpm, MTP shaker, TiMix5, Edmund Bühler GmbH, Hechingen, Germany). In five subsequent washing steps, the MTP wells were washed with PBS buffer (100 μL/well; 5 min, RT, 600 rpm) to remove nonspecific as well as weak binding peptides and select strong binding eGFP-APs. After removal of the liquid and desorbed peptides, the fluorescence of the bound eGFP-APs was measured directly on the wax-coated MTP surface with the 96-well MTP reader FLUOstar Omega (BMG LABTECH GmbH, Ortenberg, Germany; excitation (exc.) 485 nm, emission (em.) 520 nm, gain 1000, 35 reads/well). The obtained fluorescence was normalized by the fluorescence of the respective "dry" well after the initial treatment and removal of the supernatant to account for varying concentrations. Finally, a baseline correction was performed to account for the fluorescence of the pure eGFP.

Immobilization of eGFP-APs to Apple Leaves. Apple leaves were cleaned with water and cell-free extracts containing eGFP-APs (50 μL) were added to the apple leaves and incubated at room temperature. All nonspecific or weak binding peptides were removed in a subsequent washing step (50 mM Tris-HCl buffer pH 8.0, 1 mL, 3 min incubation). Immobilization of the APs on apple leaves was confirmed by detection of the fluorescent fusion partner eGFP and visualized by confocal microscopy (Leica Microsystems GmbH, Ex: 335 nm, Em: 454 nm, 405 diode laser).

3. RESULTS AND DISCUSSION

Here, we present our multidisciplinary workflow (Figure 3), ranging from apple leaf sample selection in the field over surface wax extraction, analysis, and MTP assay preparation on the laboratory scale to molecular modeling and simulations and back to the laboratory scale for the screening of the identified APs and AP variants. Thus, in the following, we will first present our findings with regard to the adaxial surface wax composition. Second, we will show the results of unbiased MD simulations involving the atomistic apple leaf surface model to identify residues of MacHis essential for binding to that surface and the experimental validation. Third, we show that our model can qualitatively predict the binding strength of structurally different APs, as the results match the ones obtained from the fluorescence assay.

Apple Leaf Wax Composition. Analytical investigations of the adaxial leaf side of *Malus domestica*, cultivar "Bittenfelder" using GC/FID and GC/MS indicate that the C_{31} alkane is the most prominent compound. Besides alkanes, primary alcohols (chain length C_{26} to C_{34}), esters (chain length C_{40} to C_{48}), primary acids (chain length C_{16} to C_{34}), and ketones were the dominating linear long-chain aliphatic wax compounds. In addition, triterpenoids representing typical wax compounds for species of the plant family *Rosaceae* were found

https://doi.org/10.1021/acsami.2c00648
ACS Appl. Mater. Interfaces 2022, 14, 28412−28426

ACS Applied Materials & Interfaces www.acsami.org Research Article

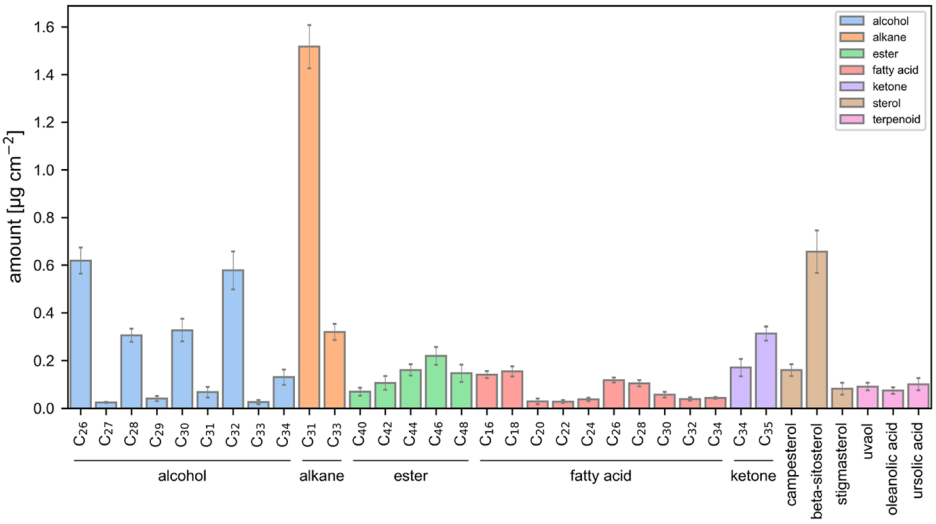

Figure 4. Composition of apple (*Malus domestica*, cultivar "Bittenfelder") adaxial leaf wax obtained via GC/FID and GC/MS. The bars depict the mean (n = 5) amount of the respective wax component, and the error bars depict the standard error of the mean.

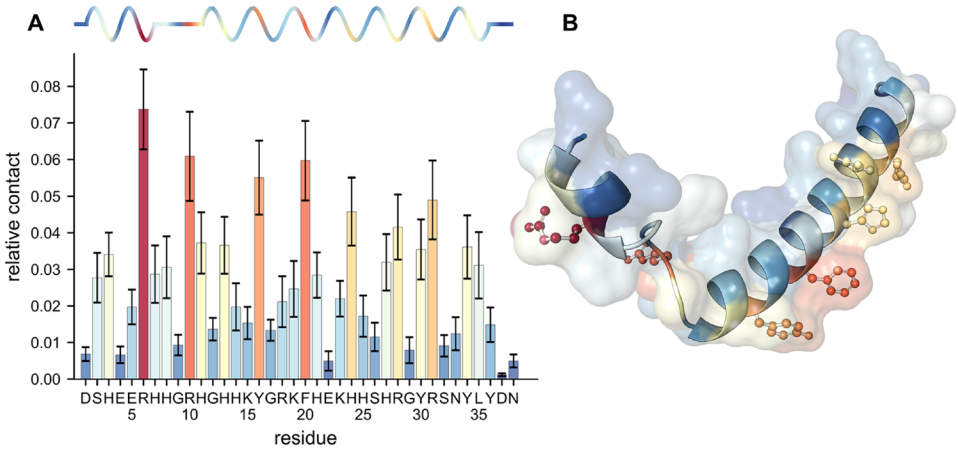

Figure 5. (A) Residue-wise relative contacts of MacHis with the wax molecules during 10 × 250 ns of MD simulations of AP adsorption. The secondary structure, as determined by DSSP,[61] is indicated on the top. The color code relates to that shown in panel B. Error bars denote the SEM. (B) Homology model of MacHis colored according to the relative number of contacts a residue forms with the wax molecules within 7 Å; side chains of residues with a relative contact >0.04 are depicted as sticks and spheres.

(Figure 4 and Table S3). Sterols were also identified in the wax extracts, however, since they are typical cell membrane components, it cannot be excluded that they partially also originated from the leaf interior. Our findings are in line with published data[55] on the adaxial apple leaf wax composition, where alkanes, alcohols, esters, and acids of similar size and triterpenoids were described as prominent wax compounds, whereas steroids were missing in this study. The complex composition of the leaf wax does not allow for drawing conclusions about the precise physicochemical properties of the wax layer and potential interactions with the APs, requiring MD simulations for further investigations. Our workflow for the extraction of surface wax from different kinds of leaves, e.g., different species, different growing conditions, and different positions on the plant, allows a standardized determination of the wax composition, and the resulting knowledge about the composition can be used to adapt our atomistic model to reflect the complex variety of surface waxes.

Generating an Atomistic Model of an Apple Leaf Surface. Using the determined composition of the apple leaf surface waxes, we tailored the wax layer of our three-layer leaf surface model to represent an apple leaf's outer surface adequately. As the generation of the model is a multistep process (Figure 1), a high number of alternative and independent conformations of the system results. Here, we used one template of the cellulose-cutin model (Figure 1C) for the generation of ten systems exhibiting differently packed wax layers to promote the versatility of the cuticular wax layer and account for natural changes within it. In principle, the composition of the wax layer can be adjusted to experimental data to reflect different kinds of plant leaves and growing conditions. We note that within the model the interfaces

https://doi.org/10.1021/acsami.2c00648
ACS Appl. Mater. Interfaces 2022, 14, 28412−28426

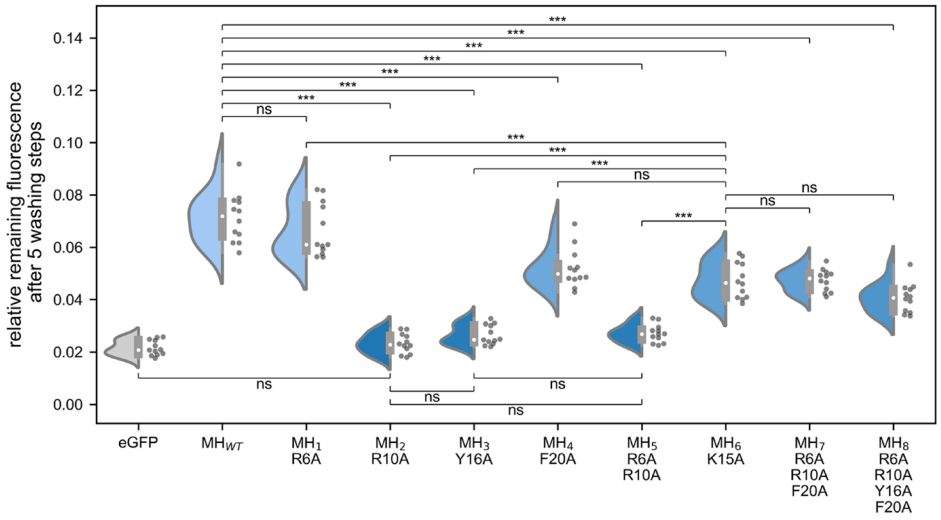

Figure 6. Binding of eGFP, eGFP-MacHis wild-type (MH_{WT}), and eGFP-MacHis variants (MH_{1-8}) to extracted cuticular wax from apple leaves. Binding was quantified by measuring the remaining fluorescence of the fusion partner eGFP after five washing steps on apple leaf cuticular wax in 96-well MTPs (four wells, three replicates). The similarity of the obtained distributions is evaluated using a two-sided Kolmogorov−Smirnov test; corresponding p-values are provided above/below the horizontal lines (ns: "not significant", ***: $p \leq 0.001$).

between the different layers are defined by noncovalent interactions. As we focus on the interaction between the AP and the leaf wax, we did not investigate these interfaces between the layers in detail in this study. The model, however, may be used for this in future work and can be altered to also account for the possible formation of covalent bonds connecting the interfaces. Besides allowing to identify key interactions of APs (see below), the model should be applicable to investigate deposition and penetration processes of agrochemicals through the different layers, potentially leading to accumulation in plants.[56−58] The generated atomistic model provides a detailed description of the outer leaf surface and is a platform for further coarse-graining[59,60] to speed up computational evaluation in the future when a simplified topology is sufficient. Here, we note that the generated models show a noticeable accumulation of the leaf wax components. Because of the solvation (at least 20 Å between the boundary of the box and the closest solute atom) during the preparation of the three-layered model (see Generation of an All-Atom Model of a Leaf Surface), the wax components accumulate in the center of the cutin plain to minimize the hydrophobic area exposed to the solvent. For future investigations, the atomistic model can be further optimized to tackle the aforementioned accumulation of wax components and speed up the simulation time. By packing our system similar to membrane systems where the solvent is located above and below the model, it is possible to exploit the periodic boundary conditions for a more accurate representation of a leaf section. To reduce the computational costs, the wax layer could be extracted once the locations of its components converged to investigate the interactions of APs with wax solely in consecutive simulations.

Identification of Preferred Leaf Wax-Binding Residues within MacHis. We identified the preferred binding residues of MacHis from the ten unbiased MD simulations of 250 ns length, each containing a leaf model and three AP moieties. We evaluated all contacts of the MacHis to the wax components within a distance of 7 Å and considered residues to preferentially bind to the leaf wax if they form >5% of all interactions (Figure 5A). The secondary structure of MacHis was predicted[36] to be predominantly an α-helix with a small loop region between residues 7 and 11. The MD simulations revealed that MacHis preferentially binds to the cuticular wax with one side of the α-helix (Figure 5B). Residues located at positions 6, 10, 16, and 20 showed the highest number of contacts (Figure 5A). These positions were selected for alanine scanning in combination with the high-throughput MTP assay to determine the importance of these residues for binding to the cuticular wax. The contact analysis for the remaining four investigated APs is shown in Figure S1.

To probe the dependency from the sample size, i.e., the number of observed AP−wax interactions, on the identification of preferred binding residues, we performed bootstrapping analyses on the MacHis (Figure S2) and LCI (Figure S3) simulation data. When using a sample size of 15 APs, i.e., approximately half of the MacHis set, in 71% (17%) of all cases, it is possible to identify two (three) out of the three residues identified using the complete data set. When considering the five best binding residues, in more than half of the cases (53%), it is still possible to identify four out of the five residues (in 13% of all cases, all five residues are identified), using half of the data set. In comparison, the bootstrapping analysis of the exhaustive simulations using LCI reveals that, with our setup (10 replicas à 3 APs), one can identify at least two out of the top three (three out of the top five) residues identified using a ten times larger data set in ∼80% (∼90%) of the cases, suggesting that the chosen setup (10 replicas à 3 APs) provides a reasonable balance between accuracy and computational demand.

Finally, a simulation time of 250 ns for adsorption proved to be sufficient, as upon binding to the wax layer, which is observed within less than 100 ns for the majority of all MacHis moieties, the binding pose of MacHis is stable for the remaining simulation time as indicated by only minor changes

https://doi.org/10.1021/acsami.2c00648
ACS Appl. Mater. Interfaces 2022, 14, 28412−28426

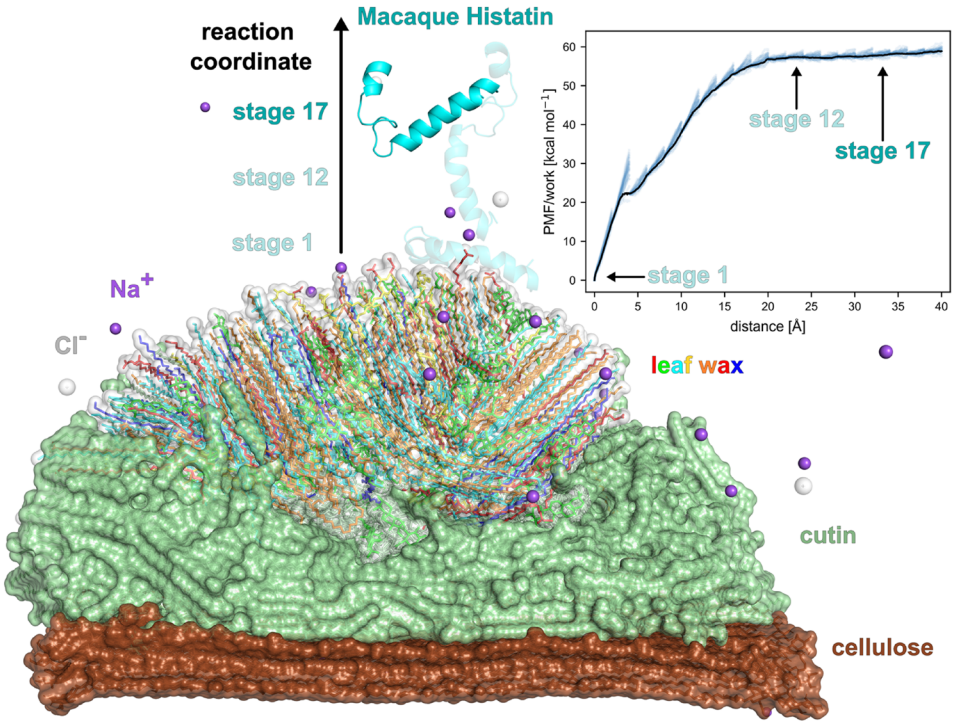

Figure 7. Adaptive steered MD of the desorption process of MacHis (cyan) from the leaf surface model. The potential of mean force (PMF, black solid line) of desorption determined as the average of the work of each stage (blue transparent lines) is depicted in the inset. The starting structure (stage 1) of MacHis as well as a structure selected from stage 12 of the steered MD are shown as translucent, the completely detached AP is shown as opaque (stage 17); corresponding stages are highlighted in the PMF profile.

compared to the previous frame ($\langle RMSD_{previous,100-250\ ns} \rangle$ = 2.16 ± 0.04 Å, Figure S4).

Alanine Scanning of the Identified Residues of MacHis Reveals their Importance for Binding to the Surface Wax. As a general trend, positively charged and aromatic amino acids (R6, R10, Y16, F20) were identified as preferred binding residues interacting with the wax layer. Amino acids at the four binding residues with the highest relative contact were exchanged for alanine (Figure 5); the generated variants are MH_1 (R6A), MH_2 (R10A), MH_3 (Y16A), MH_4 (F20A), MH_5 (R6A/R10A), MH_7 (R6A/R10A/F20A), and MH_8 (R6A/R10A/Y16A/F20A). In addition, one eGFP-MacHis variant, MH_6 (K15A), with an amino acid substitution at a residue with few relative contacts to the apple leaf wax was generated as a negative control. Overall, seven eGFP-MacHis variants were generated by site-directed mutagenesis.

The APs' binding strength to apple leave wax was quantified using the eGFP fluorescence. Through washing steps, peptides and proteins with weak interactions to the cuticular wax are removed, whereas peptides with higher affinity remain on the surface. Therefore, the binding strength of eGFP, eGFP-MacHis wild-type (MH_{WT}), and the eGFP-MacHis variants (MH_{1-8}) correlates with the determined fluorescence after washing. The remaining fluorescence of eGFP, MH_{WT}, and MacHis variants after five washing steps is depicted in Figure 6 (raw data are provided in Tables S4−S6, the remaining fluorescence after two washing steps is depicted in Figure S5).

Significant differences in binding strength with regard to the wild-type and the negative control MH_6 were observed for variants MH_2, MH_3, and MH_5. These variants showed the overall lowest binding strength with a decrease of 97%, 90%, and 89% in relative fluorescence compared to the wild-type, respectively, making them indistinguishable from pure eGFP. The variant MH_4 as well as the negative control MH_6 and the variants with multiple substitutions (MH_7 and MH_8) show a significant decrease in binding compared to the wild-type, however, to a lower extent than variants MH_2, MH_3, and MH_5. No significant difference in wax binding compared to the wild-type, however, was observed for variant MH_1.

Although single substitutions can lead to up to >90% decrease in binding, substitutions of several residues, including the single most impactful substitutions on positions 10 and 16, led to a decrease of at most 61% ($MH_{7,8}$) except for MH_5 (decrease of 89%) compared to the wild-type. However, MH_7 and MH_8 do not show a significant difference in comparison to the negative control MH_6. For MH_5, the mutation R6A hardly influences the loss in binding strength caused by the mutation R10A, as expected from the behavior of MH_1, leading to a significant decrease in binding compared to both the wild-type and the negative control. By contrast, in variants MH_7 and MH_8, the additional substitutions unexpectedly counterbalance the decrease in binding strength caused by the single substitutions at positions 10 and 16.

Out of the predicted preferred residues, identified from formed contacts, the two in the center (R10, Y16) show a significant effect on the binding strength, but the two on the

https://doi.org/10.1021/acsami.2c00648
ACS Appl. Mater. Interfaces 2022, 14, 28412−28426

ACS Applied Materials & Interfaces www.acsami.org Research Article

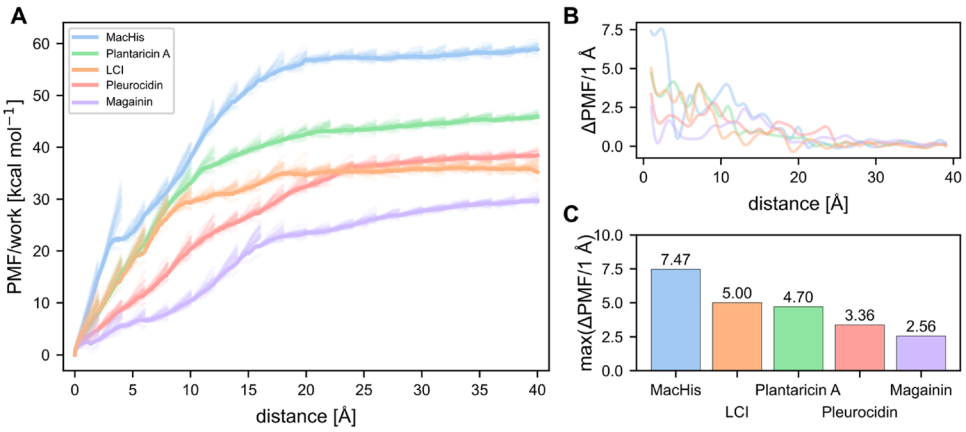

Figure 8. (A) Potential of mean force (PMF) profiles for the desorption of MacHis (blue), Plantaricin A (green), LCI (orange), Pleurocidin (red), and Magainin (purple) as determined by adaptive steered MDs. The work of the 25 individual replicas per stage is depicted as transparent, and the PMF is shown as opaque. (B) Force profile as the difference quotient ΔPMF/1 Å, where the denominator relates to the distance difference with respect to the leaf surface. (C) Bar plot depicting the maxima of the forces shown in panel B.

sides (R6, F20) do not. This suggests that the contacts formed by the latter originate as a secondary effect from the contacts formed by R10 and Y16 and the rigid secondary structure of the α-helix. The finding is reminiscent of the O-ring hypothesis in protein−protein interfaces[62] and indicates that more detailed energetic evaluations of residue contributions to binding[63] may be necessary to evaluate AP-wax binding. Still, the computational prediction of binding-relevant residues provides a 117 times more likely identification of the two key residues (R10 and Y16) out of four possible suggestions than a random drawing, considering that the chance for finding the identified two key residues (assuming these are the only residues of major importance for binding) by randomly choosing four out of 38 possible mutation sides amounts to $h(2|38;2;4) = 0.85\%$ based on the hypergeometric distribution. The two key residues are found in 53.8% of the time when randomly generating 28 variants ($h(2|38;2;28) = 53.8\%$) and, therefore, the prediction using the computational models reduces the experimental burden by a factor of ∼7 (28 random variants/4 predicted variants) on average. As to the unexpectedly small effects found for MH_7 and MH_8, we can only speculate that the multiple substitutions may lead to conformational changes of the AP and a differential binding mode, which was not captured in the MD simulations of the wild-type AP, suggesting that MD simulations of the variant APs are needed in such cases. In addition, in MH_1, the mutation is close to the end connected to the stiff helical spacer, which in turn is connected to the eGFP, potentially restricting the N-terminal end of MacHis to form contacts with the cuticular wax.

Binding Strengths Estimated via Adaptive Steered MD Match the Experimentally Determined Binding Strengths of APs. To estimate the individual binding properties of the APs, we performed adaptive-steered MD simulations. By applying a pseudoforce, we simulated the desorption of the AP from the leaf wax (Figure 7). The nonequilibrium work performed on the system can be related to the free energy difference between the bound and free states using Jarzynski's equality (eq 1, Figure 7 (inset, blue transparent lines), Figure 8A). From the work calculated for each trajectory within each stage, we can deduce the PMF(d) for each stage as a function of the distance d of the AP's geometric center from the surface of the leaf model (eq 6, Figure 7 (inset, black solid line), Figure 8A).

The higher the work needed to transfer the AP from the wax surface into the solution, the better the adhesion of the AP to the leaf surface. By determining the derivative of the applied work with respect to the distance, we obtained the force profile of the desorption process (Figure 8B), which could be used to determine a potential force threshold needed to release the AP from the leaf wax (Figure 8C). We performed the adaptive steered MDs for five APs, covering the range from weak to strong binding (Magainin, Pleurocidin, Plantaricin A, MacHis, and LCI).

The ASMD simulations reveal distinct differences in the PMFs for releasing the APs from the wax surface. The forced desorption of MacHis requires the most work (∼60 kcal mol^{-1}), followed by Plantaricin A (∼40 kcal mol^{-1}), LCI and Pleurocidin (∼35 kcal mol^{-1} each), and Magainin (∼30 kcal mol^{-1} each) (Figure 8A). As to the maximal force required during desorption (Figure 8B), MacHis and Magainin show the largest and smallest values, in line with the required work. The order of the other three APs is LCI > Plantaricin A > Pleurocidin, with the first two showing very similar values. The force needed to move the AP from the leaf surface is indicative of the steepness of the potential energy barriers along the reaction coordinate.

To assess our model's capability to predict and rank binding affinities for structurally different APs qualitatively, we analyzed all five APs for their binding performance in the MTP-based binding assay. For a more stable production of all contigs in *E. coli*, the TEV cleavage site was excised using noncontinuous (loop-out) primers during a PCR. As done in the alanine scanning, the APs' binding strength was characterized by quantifying eGFP fluorescence in apple leaf wax precoated 96-well-PP-MTPs using the assay described above. The binding of only eGFP and eGFP-APs corresponds to the determined relative fluorescence in each well (four wells, three replicas) in relation to the applied amount of AP. The results of the MTP assay of all eGFP-APs are depicted in Figure 9A (raw data are provided in Tables S7−S9).

https://doi.org/10.1021/acsami.2c00648
ACS Appl. Mater. Interfaces 2022, 14, 28412−28426

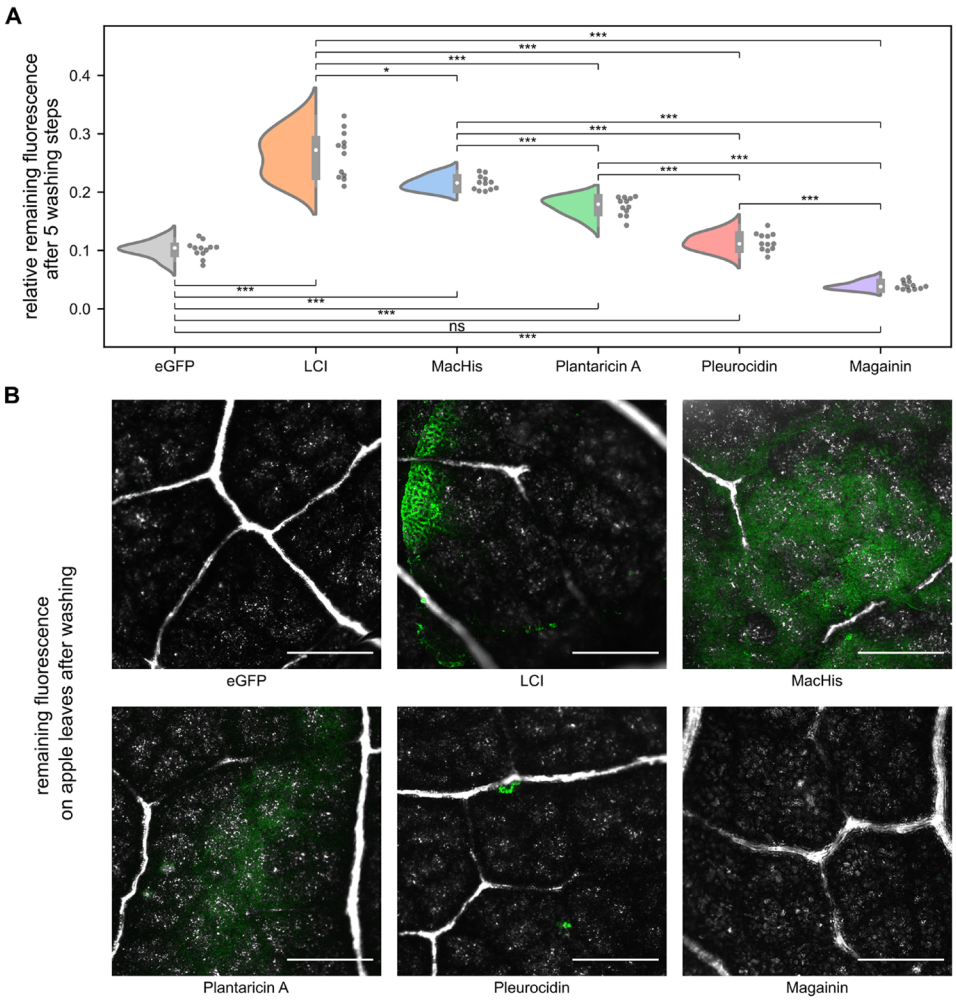

Figure 9. (A) Binding of eGFP-APs to extracted cuticular wax from apple leaves. AP binding was quantified by measuring the remaining fluorescence of the reporter protein eGFP after five washing steps on apple leaf cuticular wax in 96-well MTPs (four wells, three replicates). The similarity of the obtained distributions is evaluated using a two-sided Kolmogorov−Smirnov test; corresponding *p*-values are provided above/below the corresponding horizontal lines (ns: "not significant", *: $p \leq 0.05$, ***: $p \leq 0.001$). (B) Qualitative assessment of eGFP-AP binding on apple leaves after washing using confocal microscopy. Immobilization of eGFP-control and eGFP-APs to the surface of apple leaves was investigated by incubation (50 μL, 5 min, ambient temperature) followed by one washing step (1 mL, 50 mM Tris-HCl buffer pH 8.0). Scale bars represent 500 μm in all images.

After five washing steps, LCI and MacHis show the highest binding strength to surface apple leaf wax according to the relative remaining fluorescence, followed by Plantaricin A, Pleurocidin, and Magainin (Figure 9A); the relative remaining fluorescence of Pleurocidin is not significantly different from that of the pure eGFP, and that of Magainin is significantly worse (results after two washing steps are depicted in Figure S6). These results compare very favorably to the computed maximal forces required during desorption in that the same order of binding strength is obtained except for LCI and MacHis (Figure 8C).

During the production of eGFP-Plantaricin A and eGFP-Magainin in *E. coli*, a degradation band was observed in the SDS-PAGE at a size corresponding to eGFP. The eGFP-AP concentration was normalized based on the concentration quantified by SDS-PAGE using *ImageJ*/FiJi (Figure S7). Despite the normalized eGFP-AP concentration, the different peptide samples contained a varying amount of eGFP (eGFP-Magainin, ∼75%; eGFP-Plantaricin A, ∼10%). eGFP could interfere with the binding of Magainin and Plantaricin A, leading to a possibly lower binding strength.

The quantitative results from the MTP assay correspond well with qualitative results obtained from fluorescence microscopy of apple leaves first treated with the eGFP-AP solutions and subsequently washed (Figure 9B), supporting that the wax-coated MTPs adequately mimic the waxy surface of an apple leaf.

Overall, the results from the MTP assay largely match the computational predictions and the qualitative observations on entire apple leaves. The good agreement with the (AS)MD simulations supports the validity of our atomistic leaf model and the computational approach. To further increase the

https://doi.org/10.1021/acsami.2c00648
ACS Appl. Mater. Interfaces 2022, 14, 28412−28426

precision of the PMFs obtained from the ASMD simulations, ideally, several PMFs obtained from different starting conformations using different pulling directions should be calculated. However, ASMD simulations are computationally costly for systems comprising more than 1 000 000 atoms.

4. CONCLUSION

In this work, we present a workflow for the selection of suitable APs and rational improvement of their binding properties toward specific plant leaves using a multidisciplinary approach. For this, we created, to the best of our knowledge, the first multilayered model of an apple leaf surface, which can be used to investigate interactions of agrochemicals or nutrients with leaf surfaces at an atomistic level. The model consists of three layers: cellulose, cutin, and a surface wax layer. All layers can be modified and adjusted to reflect the properties of different plant leaves. With the leaf wax composition of apple leaves determined with GC/FID and GC/MS, we could tailor our atomistic model toward that specific leaf type, enabling the realistic modeling of adsorption properties.

To validate our model, we focused on investigating the adhesion of APs to the cuticular wax layer of the model. APs are versatile and well-studied adhesion promoters that can be applied in a variety of fields, including novel plant protection technologies.[9] For complex biological surfaces such as a leaf surface, however, the mechanisms of adsorption at the atomistic level have remained elusive. To elucidate the adsorption, we first used our atomistic leaf surface model to identify key residues of the AP MacHis that preferentially interact with the wax layer in MD simulations. The identified residues were further investigated experimentally using alanine scanning in combination with a newly developed MTP assay to rapidly quantify the surface wax binding properties of different APs or AP variants. With the obtained knowledge and the identified key binding residues of MacHis, we can tune the binding strength to improve the rainfastness to match application demands. For MacHis, we found that aromatic and positively charged amino acids on one side of the helix majorly contribute to the binding toward the surface wax of apple leaves. Therefore, engineered anchor peptides might become promising alternatives for polymeric adhesion promoters and will pave the way to developing microplastic-free and biodegradable plant protection products.

Second, we probed our workflow for use in AP screening. For this, we performed ASMD simulations to determine the PMF of desorption of five different APs from the leaf surface, ranging from weak to strong binding APs. The results were validated with the novel MTP assay. The quantitative experimental results match well with the computational predictions as well as with qualitative results obtained from experiments using entire leaves.

The established workflow opens up avenues for further experimental and computational studies revolving around foliar applications, such as optimizing APs and investigating the adsorption, incorporation, or diffusion of herbicides, fungicides, or nutrients on, into, or through the surface wax, cutin, or cellulose. Finally, the generated atomistic models and the MTP assay can be adapted to accommodate different plant types and growing conditions.

■ ASSOCIATED CONTENT

Supporting Information

The Supporting Information is available free of charge at https://pubs.acs.org/doi/10.1021/acsami.2c00648.

Additional information on the surface wax composition, nucleotide and primer sequences, SDS-PAGE data, contacts of the investigated APs with the leaf, bootstrapping analyses on the identified binding promoting residues, stability of the MacHis binding positions during MDs, and the remaining fluorescence of the eGFP-AP constructs after two washing steps (PDF)

Coordinates of the ten generated leaf surface models are provided in PDB format, and *Amber* library files are provided for the cutin and wax components (TAR)

■ AUTHOR INFORMATION

Corresponding Author

Holger Gohlke − *Bioeconomy Science Center (BioSC), Forschungszentrum Jülich, Jülich 52425, Germany; Institute for Pharmaceutical and Medicinal Chemistry, Heinrich Heine University Dusseldorf, Dusseldorf 40225, Germany; John von Neumann Institute for Computing (NIC), Jülich Supercomputing Centre (JSC), Institute of Biological Information Processing (IBI-7: Structural Biochemistry), and Institute of Bio- and Geosciences (IBG-4: Bioinformatics), Forschungszentrum Jülich GmbH, Jülich 52425, Germany;* orcid.org/0000-0001-8613-1447; Phone: (+49) 211 81 13662; Email: gohlke@uni-duesseldorf.de; Fax: (+49) 211 81 13847

Authors

Jonas Dittrich − *Bioeconomy Science Center (BioSC), Forschungszentrum Jülich, Jülich 52425, Germany; Institute for Pharmaceutical and Medicinal Chemistry, Heinrich Heine University Dusseldorf, Dusseldorf 40225, Germany;* orcid.org/0000-0003-2377-2268

Christin Brethauer − *Bioeconomy Science Center (BioSC), Forschungszentrum Jülich, Jülich 52425, Germany; Institute of Biotechnology, RWTH Aachen University, Aachen 52074, German; DWI - Leibniz-Institute for Interactive Materials, Aachen 52074, Germany;* orcid.org/0000-0003-4794-0203

Liudmyla Goncharenko − *Bioeconomy Science Center (BioSC), Forschungszentrum Jülich, Jülich 52425, Germany; Institute of Biotechnology, RWTH Aachen University, Aachen 52074, German; DWI - Leibniz-Institute for Interactive Materials, Aachen 52074, Germany*

Jens Bührmann − *Institute of Biotechnology, RWTH Aachen University, Aachen 52074, German*

Viktoria Zeisler-Diehl − *Department of Ecophysiology, University of Bonn, Bonn 53115, Germany*

Shyam Pariyar − *Bioeconomy Science Center (BioSC), Forschungszentrum Jülich, Jülich 52425, Germany; Institute of Crop Science and Resource Conservation, University of Bonn, Bonn 53115, Germany*

Felix Jakob − *Bioeconomy Science Center (BioSC), Forschungszentrum Jülich, Jülich 52425, Germany; Institute of Biotechnology, RWTH Aachen University, Aachen 52074, German; DWI - Leibniz-Institute for Interactive Materials, Aachen 52074, Germany*

Tetiana Kurkina − *Institute of Biotechnology, RWTH Aachen University, Aachen 52074, German*

https://doi.org/10.1021/acsami.2c00648
ACS Appl. Mater. Interfaces 2022, 14, 28412−28426

Lukas Schreiber − *Department of Ecophysiology, University of Bonn, Bonn 53115, Germany*

Ulrich Schwaneberg − *Bioeconomy Science Center (BioSC), Forschungszentrum Jülich, Jülich 52425, Germany; Institute of Biotechnology, RWTH Aachen University, Aachen 52074, German; DWI - Leibniz-Institute for Interactive Materials, Aachen 52074, Germany;* orcid.org/0000-0003-4026-701X

Complete contact information is available at: https://pubs.acs.org/10.1021/acsami.2c00648

Author Contributions

†J.D. and C.B. contributed equally. J.D. generated the atomistic models, performed the computational studies, analyzed results, and wrote the manuscript; C.B. generated and produced the anchor peptides and performed binding experiments, analyzed results, and wrote the manuscript; L.G. performed the immobilization of eGFP-APs on apple leaves; J.B. performed the wax extraction; S.P. provided leaf samples and wrote part of the manuscript; V.Z. and L.S. performed the wax analysis and wrote part of the manuscript; F.J. supervised the experimental work, analyzed the results, and wrote parts of the manuscript; T.K. supervised the experimental work and analyzed the results; U.S. supervised the experimental work, analyzed results, and wrote parts of the manuscript; H.G. conceived the study, supervised and managed the project, and wrote the manuscript. All authors have approved the final version of the manuscript

Funding

This research is part of the scientific activities of the Bioeconomy Science Center, which were financially supported by the Ministry of Innovation, Science and Research of the German Federal State of North Rhine-Westphalia (MIWF) within the framework of the NRW Strategy Project BioSC (313/323-400-00213) (funds to F.J., U.S., and H.G. within the FocusLab greenRelease) and innovation lab ProtLab funded by the BMBF (FKZ: 031B0918E) in the Sofortprogramm of the model region bioeconomy.

Notes

The authors declare no competing financial interest.

■ ACKNOWLEDGMENTS

We gratefully acknowledge the computational support provided by the "Center for Information and Media Technology" (ZIM) at the Heinrich Heine University Düsseldorf and the computing time provided by the John von Neumann Institute for Computing (NIC) on the supercomputer JUWELS at Jülich Supercomputing Centre (JSC) (user IDs: HKF7, project "microgels").

■ REFERENCES

(1) Cakmak, I. Enrichment of Cereal Grains with Zinc: Agronomic or Genetic Biofortification? *Plant Soil* **2008**, *302* (1), 1−17.

(2) Roggenbuck, F. C.; Rowe, L.; Penner, D.; Petroff, L.; Burow, R. Increasing Postemergence Herbicide Efficacy and Rainfastness with Silicone Adjuvants. *Weed Technol.* **1990**, *4* (3), 576−580.

(3) Hunsche, M.; Bringe, K.; Schmitz-Eiberger, M.; Noga, G. Leaf Surface Characteristics of Apple Seedlings, Bean Seedlings and Kohlrabi Plants and Their Impact on the Retention and Rainfastness of Mancozeb. *Pest Manage. Sci.* **2006**, *62* (9), 839−847.

(4) Vicent, A.; Armengol, J.; García-Jiménez, J. Rain Fastness and Persistence of Fungicides for Control of Alternaria Brown Spot of Citrus. *Plant Dis* **2007**, *91* (4), 393−399.

(5) Symonds, B. L.; Thomson, N. R.; Lindsay, C. I.; Khutoryanskiy, V. V. Rainfastness of Poly(Vinyl Alcohol) Deposits on Vicia Faba Leaf Surfaces: From Laboratory-Scale Washing to Simulated Rain. *ACS Appl. Mater. Interfaces* **2016**, *8* (22), 14220−14230.

(6) Gao, Y.; Li, X.; He, L.; Li, B.; Mu, W.; Liu, F. Role of Adjuvants in the Management of Anthracnose—Change in the Crystal Morphology and Wetting Properties of Fungicides. *J. Agric. Food Chem.* **2019**, *67* (33), 9232−9240.

(7) Reddy, K. N.; Singh, M. Organosilicone Adjuvant Effects on Glyphosate Efficacy and Rainfastness. *Weed Technol.* **1992**, *6* (2), 361−365.

(8) Symonds, B. L.; Lindsay, C. I.; Thomson, N. R.; Khutoryanskiy, V. V. Chitosan as a Rainfastness Adjuvant for Agrochemicals. *RSC Adv.* **2016**, *6* (104), 102206−102213.

(9) Meurer, R. A.; Kemper, S.; Knopp, S.; Eichert, T.; Jakob, F.; Goldbach, H. E.; Schwaneberg, U.; Pich, A. Biofunctional Microgel-Based Fertilizers for Controlled Foliar Delivery of Nutrients to Plants. *Angew. Chem., Int. Ed.* **2017**, *56* (26), 7380−7386.

(10) Schwinges, P.; Pariyar, S.; Jakob, F.; Rahimi, M.; Apitius, L.; Hunsche, M.; Schmitt, L.; Noga, G.; Langenbach, C.; Schwaneberg, U.; Conrath, U. A Bifunctional Dermaseptin−Thanatin Dipeptide Functionalizes the Crop Surface for Sustainable Pest Management. *Green Chem.* **2019**, *21* (9), 2316−2325.

(11) Rübsam, K.; Weber, L.; Jakob, F.; Schwaneberg, U. Directed Evolution of Polypropylene and Polystyrene Binding Peptides. *Biotechnol. Bioeng.* **2018**, *115* (2), 321−330.

(12) Rübsam, K.; Davari, M. D.; Jakob, F.; Schwaneberg, U. Knowvolution of the Polymer-Binding Peptide Lci for Improved Polypropylene Binding. *Polymers* **2018**, *10* (4), 423.

(13) Rübsam, K.; Stomps, B.; Böker, A.; Jakob, F.; Schwaneberg, U. Anchor Peptides: A Green and Versatile Method for Polypropylene Functionalization. *Polymer* **2017**, *116*, 124−132.

(14) Nöth, M.; Hussmann, L.; Belthle, T.; El-Awaad, I.; Davari, M. D.; Jakob, F.; Pich, A.; Schwaneberg, U. Microgelzymes: Ph-Independent Immobilization of Cytochrome P450 Bm3 in Microgels. *Biomacromolecules* **2020**, *21* (12), 5128−5138.

(15) Dedisch, S.; Wiens, A.; Davari, M. D.; Söder, D.; Rodriguez-Emmenegger, C.; Jakob, F.; Schwaneberg, U. Matter-Tag: A Universal Immobilization Platform for Enzymes on Polymers, Metals, and Silicon-Based Materials. *Biotechnol. Bioeng.* **2020**, *117* (1), 49−61.

(16) Apitius, L.; Buschmann, S.; Bergs, C.; Schönauer, D.; Jakob, F.; Pich, A.; Schwaneberg, U. Biadhesive Peptides for Assembling Stainless Steel and Compound Loaded Micro-Containers. *Macromol. Biosci.* **2019**, *19* (9), 1900125.

(17) Büscher, N.; Sayoga, G. V.; Rübsam, K.; Jakob, F.; Schwaneberg, U.; Kara, S.; Liese, A. Biocatalyst Immobilization by Anchor Peptides on an Additively Manufacturable Material. *Org. Process Res. Dev.* **2019**, *23* (9), 1852−1859.

(18) Grimm, A. R.; Sauer, D. F.; Mirzaei Garakani, T.; Rübsam, K.; Polen, T.; Davari, M. D.; Jakob, F.; Schiffels, J.; Okuda, J.; Schwaneberg, U. Anchor Peptide-Mediated Surface Immobilization of a Grubbs-Hoveyda-Type Catalyst for Ring-Opening Metathesis Polymerization. *Bioconj. Chem.* **2019**, *30* (3), 714−720.

(19) Schwemmer, T.; Baumgartner, J.; Faivre, D.; Börner, H. G. Peptide-Mediated Nanoengineering of Inorganic Particle Surfaces: A General Route toward Surface Functionalization Via Peptide Adhesion Domains. *J. Am. Chem. Soc.* **2012**, *134* (4), 2385−2391.

(20) Gao, X.; Ran, N.; Dong, X.; Zuo, B.; Yang, R.; Zhou, Q.; Moulton, H. M.; Seow, Y.; Yin, H. Anchor Peptide Captures, Targets, and Loads Exosomes of Diverse Origins for Diagnostics and Therapy. *Sci. Transl. Med.* **2018**, *10* (444), No. eaat0195.

(21) Gong, W.; Wang, J.; Chen, Z.; Xia, B.; Lu, G. Solution Structure of Lci, a Novel Antimicrobial Peptide from Bacillus Subtilis. *Biochemistry* **2011**, *50* (18), 3621−3627.

(22) Hess, F. D.; Falk, R. H. Herbicide Deposition on Leaf Surfaces. *Weed Sci.* **1990**, *38* (3), 280−288.

(23) Kolattukudy, P. E. Biopolyester Membranes of Plants: Cutin and Suberin. *Science* **1980**, *208* (4447), 990−1000.

(24) Bakan, B.; Marion, D. Assembly of the Cutin Polyester: From Cells to Extracellular Cell Walls. *Plants* **2017**, *6* (4), 57.
(25) Gomes, T. C. F.; Skaf, M. S. Cellulose-Builder: A Toolkit for Building Crystalline Structures of Cellulose. *J. Comput. Chem.* **2012**, *33* (14), 1338−1346.
(26) Kirschner, K. N.; Yongye, A. B.; Tschampel, S. M.; González-Outeiriño, J.; Daniels, C. R.; Foley, B. L.; Woods, R. J. Glycam06: A Generalizable Biomolecular Force Field. Carbohydrates. *J. Comput. Chem.* **2008**, *29* (4), 622−655.
(27) Fich, E. A.; Segerson, N. A.; Rose, J. K. C. The Plant Polyester Cutin: Biosynthesis, Structure, and Biological Roles. *Annu. Rev. Plant Biol.* **2016**, *67* (1), 207−233.
(28) *Maestro*; Schrödinger: New York, 2019.
(29) Martínez, L.; Andrade, R.; Birgin, E. G.; Martínez, J. M. Packmol: A Package for Building Initial Configurations for Molecular Dynamics Simulations. *J. Comput. Chem.* **2009**, *30* (13), 2157−2164.
(30) Jorgensen, W. L.; Chandrasekhar, J.; Madura, J. D.; Impey, R. W.; Klein, M. L. Comparison of Simple Potential Functions for Simulating Liquid Water. *J. Chem. Phys.* **1983**, *79* (2), 926−935.
(31) Jakalian, A.; Bush, B. L.; Jack, D. B.; Bayly, C. I. Fast, Efficient Generation of High-Quality Atomic Charges. Am1-Bcc Model: I. Method. *J. Comput. Chem.* **2000**, *21* (2), 132−146.
(32) Jakalian, A.; Jack, D. B.; Bayly, C. I. Fast, Efficient Generation of High-Quality Atomic Charges. Am1-Bcc Model: Ii. Parameterization and Validation. *J. Comput. Chem.* **2002**, *23* (16), 1623−1641.
(33) Wang, J.; Wang, W.; Kollman, P. A.; Case, D. A. Automatic Atom Type and Bond Type Perception in Molecular Mechanical Calculations. *J. Mol. Graph. Model.* **2006**, *25* (2), 247−260.
(34) Wang, J.; Wolf, R. M.; Caldwell, J. W.; Kollman, P. A.; Case, D. A. Development and Testing of a General Amber Force Field. *J. Comput. Chem.* **2004**, *25* (9), 1157−1174.
(35) Berman, H. M.; Westbrook, J.; Feng, Z.; Gilliland, G.; Bhat, T. N.; Weissig, H.; Shindyalov, I. N.; Bourne, P. E. The Protein Data Bank. *Nucleic Acids Res.* **2000**, *28* (1), 235−242.
(36) Mulnaes, D.; Porta, N.; Clemens, R.; Apanasenko, I.; Reiners, J.; Gremer, L.; Neudecker, P.; Smits, S. H. J.; Gohlke, H. Topmodel: Template-Based Protein Structure Prediction at Low Sequence Identity Using Top-Down Consensus and Deep Neural Networks. *J. Chem. Theory Comput.* **2020**, *16* (3), 1953−1967.
(37) Case, D. A.; Cheatham, T. E., III; Darden, T.; Gohlke, H.; Luo, R.; Merz, K. M., Jr.; Onufriev, A.; Simmerling, C.; Wang, B.; Woods, R. J. The Amber Biomolecular Simulation Programs. *J. Comput. Chem.* **2005**, *26* (16), 1668−1688.
(38) Case, D. A.; Ben-Shalom, I. Y.; Brozell, S. R.; Cerutti, D. S.; Cheatham, T. E., III; Cruzeiro, V. W. D.; Darden, T. A.; Duke, R. E.; Ghoreishi, D.; Gilson, M. K.; Gohlke, H.; Goetz, A. W.; Greene, D.; Harris, R.; Homeyer, N.; Izadi, S.; Kovalenko, A.; Kurtzman, T.; Lee, T. S.; LeGrand, S.; Li, P.; Lin, C.; Liu, J.; Luchko, T.; Luo, R.; Mermelstein, D. J.; Merz, K. M.; Miao, Y.; Monard, G.; Nguyen, C.; Nguyen, H.; Omelyan, I.; Onufriev, A.; Pan, F.; Qi, R.; Roe, D. R.; Roitberg, A.; Sagui, C.; Schott-Verdugo, S.; Shen, J.; Simmerling, C. L.; Smith, J.; Salomon-Ferrer, R.; Swails, J.; Walker, R. C.; Wang, J.; Wei, H.; Wolf, R. M.; Wu, X.; Xiao, L.; York, D. M.; Kollman, P. A. *Amber*; University of California: San Francisco, 2021.
(39) Salomon-Ferrer, R.; Götz, A. W.; Poole, D.; Le Grand, S.; Walker, R. C. Routine Microsecond Molecular Dynamics Simulations with Amber on Gpus. 2. Explicit Solvent Particle Mesh Ewald. *J. Chem. Theory Comput.* **2013**, *9* (9), 3878−3888.
(40) Le Grand, S.; Götz, A. W.; Walker, R. C. Spfp: Speed without Compromise—a Mixed Precision Model for Gpu Accelerated Molecular Dynamics Simulations. *Comput. Phys. Commun.* **2013**, *184* (2), 374−380.
(41) Maier, J. A.; Martinez, C.; Kasavajhala, K.; Wickstrom, L.; Hauser, K. E.; Simmerling, C. Ff14sb: Improving the Accuracy of Protein Side Chain and Backbone Parameters from Ff99sb. *J. Chem. Theory Comput.* **2015**, *11* (8), 3696−3713.
(42) Darden, T.; York, D.; Pedersen, L. Particle Mesh Ewald: An N·Log(N) Method for Ewald Sums in Large Systems. *J. Chem. Phys.* **1993**, *98* (12), 10089−10092.
(43) Ryckaert, J.-P.; Ciccotti, G.; Berendsen, H. J. C. Numerical Integration of the Cartesian Equations of Motion of a System with Constraints: Molecular Dynamics of N-Alkanes. *J. Comput. Phys.* **1977**, *23* (3), 327−341.
(44) Berendsen, H. J. C.; Postma, J. P. M.; van Gunsteren, W. F.; DiNola, A.; Haak, J. R. Molecular Dynamics with Coupling to an External Bath. *J. Chem. Phys.* **1984**, *81* (8), 3684−3690.
(45) Ozer, G.; Valeev, E. F.; Quirk, S.; Hernandez, R. Adaptive Steered Molecular Dynamics of the Long-Distance Unfolding of Neuropeptide Y. *J. Chem. Theory Comput.* **2010**, *6* (10), 3026−3038.
(46) Ozer, G.; Quirk, S.; Hernandez, R. Adaptive Steered Molecular Dynamics: Validation of the Selection Criterion and Benchmarking Energetics in Vacuum. *J. Chem. Phys.* **2012**, *136* (21), 215104.
(47) Jarzynski, C. Nonequilibrium Equality for Free Energy Differences. *Phys. Rev. Lett.* **1997**, *78* (14), 2690.
(48) Park, S.; Schulten, K. Calculating Potentials of Mean Force from Steered Molecular Dynamics Simulations. *J. Chem. Phys.* **2004**, *120* (13), 5946−5961.
(49) Ozer, G.; Quirk, S.; Hernandez, R. Thermodynamics of Decaalanine Stretching in Water Obtained by Adaptive Steered Molecular Dynamics Simulations. *J. Chem. Theory Comput.* **2012**, *8* (11), 4837−4844.
(50) Ahmad, S.; Strunk, C. H.; Schott-Verdugo, S. N.; Jaeger, K.-E.; Kovacic, F.; Gohlke, H. Substrate Access Mechanism in a Novel Membrane-Bound Phospholipase a of Pseudomonas Aeruginosa Concordant with Specificity and Regioselectivity. *J. Chem. Inf. Model.* **2021**, *61* (11), 5626−5643.
(51) Roe, D. R.; Cheatham, T. E. Ptraj and Cpptraj: Software for Processing and Analysis of Molecular Dynamics Trajectory Data. *J. Chem. Theory Comput.* **2013**, *9* (7), 3084−3095.
(52) Arai, R.; Ueda, H.; Kitayama, A.; Kamiya, N.; Nagamune, T. Design of the Linkers Which Effectively Separate Domains of a Bifunctional Fusion Protein. *Protein Engineering, Design and Selection* **2001**, *14* (8), 529−532.
(53) Kapust, R. B.; Tözsér, J.; Fox, J. D.; Anderson, D. E.; Cherry, S.; Copeland, T. D.; Waugh, D. S. Tobacco Etch Virus Protease: Mechanism of Autolysis and Rational Design of Stable Mutants with Wild-Type Catalytic Proficiency. *Protein Engineering, Design and Selection* **2001**, *14* (12), 993−1000.
(54) Blanusa, M.; Schenk, A.; Sadeghi, H.; Marienhagen, J.; Schwaneberg, U. Phosphorothioate-Based Ligase-Independent Gene Cloning (Plicing): An Enzyme-Free and Sequence-Independent Cloning Method. *Anal. Biochem.* **2010**, *406* (2), 141−146.
(55) Bringe, K.; Schumacher, C. F. A.; Schmitz-Eiberger, M.; Steiner, U.; Oerke, E.-C. Ontogenetic Variation in Chemical and Physical Characteristics of Adaxial Apple Leaf Surfaces. *Phytochemistry* **2006**, *67* (2), 161−170.
(56) Sterling, T. M. Mechanisms of Herbicide Absorption across Plant Membranes and Accumulation in Plant Cells. *Weed Sci.* **1994**, *42* (2), 263−276.
(57) Mishra, V. K.; Upadhyay, A. R.; Tripathi, B. D. Bioaccumulation of Heavy Metals and Two Organochlorine Pesticides (Ddt and Bhc) in Crops Irrigated with Secondary Treated Waste Water. *Environ. Monit. Assess.* **2009**, *156* (1), 99−107.
(58) Liu, Q.; Liu, Y.; Dong, F.; Sallach, J. B.; Wu, X.; Liu, X.; Xu, J.; Zheng, Y.; Li, Y. Uptake Kinetics and Accumulation of Pesticides in Wheat (Triticum Aestivum L.): Impact of Chemical and Plant Properties. *Environ. Pollut.* **2021**, *275*, 116637.
(59) Izvekov, S.; Voth, G. A. A Multiscale Coarse-Graining Method for Biomolecular Systems. *J. Phys. Chem. B* **2005**, *109* (7), 2469−2473.
(60) Saunders, M. G.; Voth, G. A. Coarse-Graining Methods for Computational Biology. *Annual Review of Biophysics* **2013**, *42* (1), 73−93.
(61) Kabsch, W.; Sander, C. Dictionary of Protein Secondary Structure: Pattern Recognition of Hydrogen-Bonded and Geometrical Features. *Biopolymers* **1983**, *22* (12), 2577−2637.
(62) Li, Y.; Huang, Y.; Swaminathan, C. P.; Smith-Gill, S. J.; Mariuzza, R. A. Magnitude of the Hydrophobic Effect at Central

https://doi.org/10.1021/acsami.2c00648
ACS Appl. Mater. Interfaces 2022, 14, 28412−28426

Versus Peripheral Sites in Protein-Protein Interfaces. *Structure* **2005**, *13* (2), 297−307.
(63) Gohlke, H.; Kiel, C.; Case, D. A. Insights into Protein−Protein Binding by Binding Free Energy Calculation and Free Energy Decomposition for the Ras−Raf and Ras−Ralgds Complexes. *J. Mol. Biol.* **2003**, *330* (4), 891−913.

https://doi.org/10.1021/acsami.2c00648
ACS Appl. Mater. Interfaces 2022, 14, 28412−28426

SUPPORTING INFORMATION

Rational Design yields Molecular Insights on Leaf-Binding of Anchor Peptides

Jonas Dittrich[1,2,†], Christin Brethauer[1,3,4,†], Liudmyla Goncharenko[1,3,4], Jens Bührmann[3], Viktoria Zeisler-Diehl[5], Shyam Pariyar[1,6], Felix Jakob[1,3,4], Tetiana Kurkina[3], Lukas Schreiber[5], Ulrich Schwaneberg[1,3,4], Holger Gohlke*[,1,2,7]

[†]These authors contributed equally.

[1]Bioeconomy Science Center (BioSC), Forschungszentrum Jülich, 52425 Jülich, Germany

[2]Institute for Pharmaceutical and Medicinal Chemistry, Heinrich Heine University Düsseldorf, 40225 Düsseldorf, Germany

[3]Institute of Biotechnology, RWTH Aachen University, 52074 Aachen, German

[4]DWI-Leibniz-Institute for Interactive Materials, 52074 Aachen, Germany

[5]Department of Ecophysiology, University of Bonn, Bonn 53115, Germany

[6]Department of Horticultural Sciences, University of Bonn, Bonn 53121, Germany

[7]John von Neumann Institute for Computing (NIC), Jülich Supercomputing Centre (JSC), Institute of Biological Information Processing (IBI-7: Structural Biochemistry), and Institute of Bio- and Geosciences (IBG-4: Bioinformatics), Forschungszentrum Jülich GmbH, 52425 Jülich, Germany.

Author ORCID
Jonas Dittrich: 0000-0003-2377-2268
Christin Brethauer: 0000-0003-4794-0203
Viktoria Zeisler-Diehl: 0000-0001-7050-9716
Shyam Pariyar: 0000-0002-3643-1553
Felix Jakob: 0000-0002-9815-2066
Tetiana Kurkina: 0000-0002-9300-3731
Lukas Schreiber: 0000-0001-7003-9929
Ulrich Schwaneberg: 0000-0003-4026-701X
Holger Gohlke: 0000-0001-8613-1447

*Corresponding Author: Holger Gohlke

Address: Universitätsstr. 1, 40225 Düsseldorf, Germany.

Phone: (+49) 211 81 13662; Fax: (+49) 211 81 13847

E-mail: gohlke@uni-duesseldorf.de

Table of Contents

Supplementary Tables 5

Table S1. Composition of apple (*Malus domestica*; cultivar 'Bittenfelder') cuticular wax obtained via GC/FID and GC/MS. 5

Table S2. Nucleotide sequences of ordered synthetic genes of LCI (UniProt ID: P82243), Macaque Histatin (MacHis; UniProt ID: P34084), Magainin 2 (UniProt ID: P11006), Plantaricin A (PlnA; UniProt ID: P80214), and Pleurocidin (UniProt ID: P81941). Underlined sequence encodes for the 17 Helix spacer, grey nucleotides encodes for the TEV protease cleavage site, bold nucleotides represent the peptide sequences. The genes were codon-optimized for *E. coli* and synthesized by GeneScript (Nanjing, China). 6

Table S3. Primer sequences for TEV site remove in a PCR and amino acid substitution into MacHis..... 7

Table S4. Remaining fluorescence (in relative fluorescence units [RFU]) of the cuticular wax-coated MTP plate treated with buffer only ("buffer"), pure eGFP ("eGFP"), and the eGFP-MacHis constructs (wild-type MH_{WT} and the variants MH_{1-8}) after initial treatment with buffer/eGFP/AP solution and removal of the supernatant (4 wells per system/variant for each of the 3 MTPs)..... 8

Table S5. Remaining fluorescence (in relative fluorescence units [RFU]) of the cuticular wax-coated MTP plate treated with buffer only ("buffer"), pure eGFP ("eGFP"), and the eGFP-MacHis constructs (wild-type MH_{WT} and the variants MH_{1-8}) after two washing steps (4 wells per system/variant for each of the 3 MTPs). 8

Table S6. Remaining fluorescence (in relative fluorescence units [RFU]) of the cuticular wax-coated MTP plate treated with buffer only ("buffer"), pure eGFP ("eGFP"), and the eGFP-MacHis constructs (wild-type MH_{WT} and the variants MH_{1-8}) after five washing steps (4 wells per system/variant for each of the 3 MTPs). 9

Table S7. Remaining fluorescence (in relative fluorescence units [RFU]) of the cuticular wax-coated MTP plate treated with buffer only ("buffer"), pure eGFP ("eGFP"), and the eGFP-APs (LCI, MacHis, Plantaricin, Pleurocidin, Magainin) after initial treatment with buffer/eGFP/eGFP-AP solution and removal of the supernatant (4 wells per system/variant for each of the 3 MTPs). 9

Table S8. Remaining fluorescence (in relative fluorescence units [RFU]) of the cuticular wax-coated MTP plate treated with buffer only ("buffer"), pure eGFP ("eGFP"),

and the eGFP-APs (LCI, MacHis, Plantaricin, Pleurocidin, Magainin) after two washing steps (4 wells per system/variant for each of the 3 MTPs). 10

Table S9. Remaining fluorescence (in relative fluorescence units [RFU]) of the cuticular wax-coated MTP plate treated with buffer only (“buffer”), pure eGFP (“eGFP”), and the eGFP-APs (LCI, MacHis, Plantaricin, Pleurocidin, Magainin) after five washing steps (4 wells per system/variant for each of the 3 MTPs). 10

Supplementary Figures **11**

Figure S1. Residue-wise relative contacts of (A) LCI, (B) Macaque Histatin, (C) Magainin, (D) Pleurocidin, and (E) Plantaricin with the wax molecules within 10 x 250 ns long MD simulations of anchor peptide adsorption. Error bars denote the SEM. Geometrical analyses of the MD simulations were performed using cpptraj.[1] On top of the plots, the secondary structure of the APs is indicated (wavy line: α-helix, arrow: β-strand) as determined by DSSP[2] analysis of the protein structures. 11

Figure S2. Bootstrapping analysis for identifying residues important for cuticular wax binding of MacHis in dependence of the sample size. Samples of different sizes (5, 10, 15, 20, 25, 29) were drawn 10,000 times with replacement from the original set containing 29 samples. For each sample set size, the overlap with the top three (**A**, **B**) and top five (**C**, **D**) identified residues using the original set is calculated. The probability of identifying exactly X residues out of the three/five is given in **A** and **C**, the probability of identifying at least X residues out of the three/five is given in **B** and **D** for each sample size. 12

Figure S3. Bootstrapping analysis for identifying residues important for cuticular wax binding of LCI in dependence of the sample size. Samples of different sizes (5, 15, 25, 50, 100, 200, 281) were drawn 10,000 times with replacement from the original set containing 281 samples. For each sample set size, the overlap with the top three (**A**, **B**) and top five (**C**, **D**) identified residues using the original set is calculated. The probability of identifying exactly X residues out of the three/five is given in **A** and **C**, the probability of identifying at least X residues out of the three/five is given in **B** and **D** for each sample size. 13

Figure S4. RMSD (in Å) for all three MacHis peptides to their states 1 ns before, respectively, depicted for all ten simulated replicas. One peptide (MacHis 1, replica 8) is excluded, as it did not adsorb to the wax layer. Upon adsorption, observed within < 100 ns for the majority of the cases, the RMSD fluctuation of the peptide is decreased to 2.16 ± 0.04 Å (mean ± SEM for 100-250 ns)..... 14

Figure S5. Binding of eGFP-MacHis wild-type (MH_{WT}) and eGFP-MacHis variants (MH_{1-8}) to extracted cuticular wax from apple leaves. Binding was quantified by measuring the remaining fluorescence of the fusion partner eGFP after five washing steps on apple leaf cuticular wax in 96-well-MTPs (4 wells, 3 replicates)..... 15

Figure S6. Binding of different eGFP-APs to extracted cuticular wax from apple leaves. Binding was quantified by measuring the remaining fluorescence of the fusion partner eGFP after two washing steps on apple leaf cuticular wax in 96-well-MTPs (4 wells, 3 replicates). 15

Figure S7. Sodium dodecyl sulfate polyacrylamide gel electrophoresis (SDS-PAGE) image of eGFP and eGFP-APs for determination of purity with ImageJ[3] (version 1.53e). 16

Supplementary References 17

Supplementary Tables

Table S1. Composition of apple (*Malus domestica*; cultivar 'Bittenfelder') cuticular wax obtained via GC/FID and GC/MS.

component		amount[a] replica					mean[a]	SEM[a,b]
		1	2	3	4	5		
fatty acid	C_{16}	0.120	0.130	0.108	0.187	0.161	0.141	0.014
	C_{18}	0.132	0.131	0.108	0.226	0.180	0.155	0.021
	C_{20}	0.016	0.016	0.018	0.021	0.074	0.029	0.011
	C_{22}	0.012	0.028	0.023	0.029	0.050	0.028	0.006
	C_{24}	0.023	0.040	0.064	0.026	0.035	0.037	0.007
	C_{26}	0.095	0.129	0.152	0.105	0.110	0.118	0.010
	C_{28}	0.083	0.153	0.102	0.103	0.081	0.105	0.013
	C_{30}	0.095	0.068	0.038	0.031	0.053	0.057	0.011
	C_{32}	0.015	0.042	0.048	0.060	0.031	0.039	0.008
	C_{34}	0.029	0.055	0.044	0.044	0.044	0.043	0.004
alcohol	C_{26}	0.574	0.510	0.812	0.534	0.664	0.619	0.055
	C_{27}	0.018	0.023	0.033	0.024	0.024	0.024	0.002
	C_{28}	0.281	0.248	0.390	0.260	0.352	0.306	0.028
	C_{29}	0.028	0.006	0.056	0.065	0.046	0.040	0.010
	C_{30}	0.245	0.238	0.481	0.282	0.392	0.327	0.047
	C_{31}	0.021	0.129	0.067	0.104	0.016	0.067	0.022
	C_{32}	0.338	0.517	0.823	0.559	0.652	0.578	0.080
	C_{33}	0.004	0.057	0.029	0.026	0.015	0.026	0.009
	C_{34}	0.073	0.109	0.255	0.110	0.108	0.131	0.032
alkane	C_{31}	1.677	1.522	1.749	1.374	1.265	1.517	0.090
	C_{33}	0.406	0.361	0.340	0.282	0.213	0.320	0.033
sterol	campesterol	0.227	0.160	0.104	0.203	0.108	0.161	0.025
	beta-sitosterol	0.643	0.341	0.872	0.769	0.657	0.656	0.089
	stigmasterol	0.093	0.005	0.102	0.157	0.055	0.083	0.025
terpenoid	uvaol	0.056	0.133	0.104	0.112	0.052	0.091	0.016
	oleanolic acid	0.034	0.116	0.066	0.085	0.071	0.074	0.013
	ursolic acid	0.069	0.063	0.198	0.068	0.107	0.101	0.026
ketone	C_{34}	0.153	0.082	0.281	0.115	0.224	0.171	0.036
	C_{35}	0.421	0.324	0.261	0.282	0.280	0.314	0.029
ester	C_{40}	0.027	0.058	0.128	0.063	0.070	0.069	0.017
	C_{42}	0.052	0.118	0.215	0.073	0.075	0.107	0.029
	C_{44}	0.136	0.152	0.254	0.122	0.141	0.161	0.024
	C_{46}	0.196	0.181	0.363	0.142	0.217	0.220	0.038
	C_{48}	0.133	0.097	0.288	0.082	0.133	0.147	0.037

[a] In µg cm^{-2}.

[b] Standard error of the mean.

Table S2. Nucleotide sequences of ordered synthetic genes of LCI (UniProt ID: P82243), Macaque Histatin (MacHis; UniProt ID: P34084), Magainin 2 (UniProt ID: P11006), Plantaricin A (PlnA; UniProt ID: P80214), and Pleurocidin (UniProt ID: P81941). The underlined sequence encodes for the 17 Helix spacer, grey nucleotides encode for the TEV protease cleavage site, bold nucleotides represent the peptide sequences. The genes were codon-optimized for *E. coli* and synthesized by GeneScript (Nanjing, China).

LCI 5'- GCAGAAGCAGCAGCAAAAGAAGCCGCTGCCAAAGAAGCGGCAGCGAAAGCAGAAAATCTGTAT TTTCAGGGT**GCCATTAAACTGGTTCAGAGCCCGAATGGTAATTTTGCAGCAAGCTTTGTTCT** **GGATGGCACCAAATGGATCTTCAAAAGCAAATACTATGACAGCAGCAAAGGTTATTGGGTG** **GGTATTTATGAAGTGTGGGATCGCAAA**TAATAA-3'
Macaque Histatin 5'- GCAGAAGCAGCTGCCAAAGAAGCGGCAGCGAAAGAAGCGGCGGCCAAAGCCGAGAATCTGTAC TTTCAGGGC**GATTCTCACGAAGAACGCCATCATGGTCGTCATGGTCACCACAAGTATGGCC** **GCAAATTCCACGAGAAACATCACAGTCATCGTGGCTATCGCTCGAACTATCTGTACGACAA** **C**TGATAA-3'
Plantaricin A 5'- GCAGAAGCAGCAGCCAAAGAAGCTGCGGCGAAAGAAGCGGCAGCCAAAGCGGAGAACCTGTA CTTTCAAGGC**AAAAGCAGTGCGTATTCCTTGCAAATGGGTGCCACCGCCATTAAACAGGTT** **AAGAAACTGTTCAAGAAATGGGGCTGG**TAA-3'
Pleurocidin 5'- GCAGAAGCAGCGGCAAAAGAGGCTGCTGCGAAAGAAGCTGCGGCCAAAGCGGAGAACCTGTAC TTTCAGGGT**GGATGGGGCTCGTTCTTTAAGAAGGCTGCACATGTGGGCAAACACGTTGGGA** **AAGCCGCCTTAACGCACTATCTG**TGATAA-3'
Magainin 5'- GCAGAAGCAGCGGCCAAAGAAGCGGCAGCGAAAGAGGCTGCAGCGAAAGCCGAAAACCTGTAT TTTCAGGGT**GGTATTGGGAAATTCCTGCATTCCGCGAAGAAATTCGGCAAAGCCTTTGTTG** **GCGAGATCATGAACTCG**TGATAA-3'

Table S3. Primer sequences for TEV site removal in a PCR and amino acid substitution into MacHis.

Name	**Sequence 5'-3'**
LCI-TEV-fw	GCCAAAGAAGCGGCAGCGAAAGCAGCCATTAAACTGGTTCAGAGCCCG
LCI-TEV-rv	TGCTTTCGCTGCCGCTTCTTTGGC
MacHis-TEV-fw	GCGGCGGCCAAAGCCGATTCTCACGAAGAACGCC
MacHis-TEV-rv	GGCGTTCTTCGTGAGAATCGGCTTTGGCCGCCGC
Plantaricin-TEV-fw	GCGAAAGAAGCGGCGGCCAAAGCCAAAAGCAGTGCGTATTCCTTGC
Plantaricin-TEV-rv	GGCTTTGGCCGCCGCTTCTTTCGC
Pleurocidin-TEV-fw	GCGAAAGAAGCGGCGGCCAAAGCCGGATGGGGCTCGTTCTTTAAGAAGGC
Pleurocidin-TEV-rv	GGCTTTGGCCGCCGCTTCTTTCGC
Magainin-TEV-fw	GCGAAAGAAGCGGCGGCCAAAGCCGGTATTGGGAAATTCCTGCATTCC
Magainin-TEV-rv	GGCTTTCGCTGCAGCCTCTTTCGC
MacHis-R6A-fw	TCTCACGAAGAAGCCCATCATGGTCGTC
MacHis-R6A-rv	GACGACCATGATGGGCTTCTTCGTGAG
MacHis-R10A-fw	CGCCATCATGGTGCCCATGGTCACCAC
MacHis-R10A-rv	GTGGTGACCATGGGCACCATGATGGCG
MacHis-Y16A-fw	GGTCACCACAAGGCCGGCCGCAAATTC
MacHis-Y16A-rv	GAATTTGCGGCCGGCCTTGTGGTGACC
MacHis-F20A-fw	GGCCGCAAAGCCCACGAGAAACATCACAGTCATCGTGGC
MacHis-F20A-rv	GCCACGATGACTGTGATGTTTCTCGTGGGCTTTGCGGCC
MacHis-R6A/R10A-fw	GAAGAAGCCCATCATGGTGCCCATGGTCACC
MacHis-R6A/R10A-rv	GGTGACCATGGGCACCATGATGGGCTTCTTC
MacHis-K15A-fw	GGTCACCACGCGTATGGCCGCAAATTCC
MacHis-K15A-rv	GGAATTTGCGGCCATACGCGTGGTGACC

Table S4. Remaining fluorescence (in relative fluorescence units [RFU]) of the cuticular wax-coated MTP plate treated with buffer only ("buffer"), pure eGFP ("eGFP"), and the eGFP-MacHis constructs (wild-type MH_{WT} and the variants MH_{1-8}) after initial treatment with buffer/eGFP/AP solution and removal of the supernatant (4 wells per system/variant for each of the 3 MTPs).

MTP	well	buffer	eGFP	MH_{WT}	MH_1	MH_2	MH_3	MH_4	MH_5	MH_6	MH_7	MH_8
1	1	47	7638	11242	10738	10392	11404	10373	20489	12450	13595	11813
	2	45	7733	11423	11700	11118	11520	11808	20697	11630	13068	15629
	3	45	7563	11669	11406	10859	12756	12554	22576	11972	12097	11867
	4	52	8006	10183	10664	10831	11843	13303	25630	12752	14065	11351
2	1	47	10024	12834	12319	11387	11827	13513	23069	13557	12080	12380
	2	52	9322	14242	14231	11705	14132	14339	24713	13403	12843	12573
	3	48	9996	15348	14117	12400	15057	14269	24571	15493	13404	13072
	4	47	10547	14623	14638	12184	13802	15847	25559	15232	13884	13329
3	1	49	8556	11734	13707	12125	13055	14518	26681	13774	14949	14223
	2	50	9311	13282	13648	12538	13933	15496	26410	14627	14933	14625
	3	48	9092	13072	13222	11228	13560	14326	27762	15131	14908	16038
	4	47	9395	11716	12972	10934	13095	14302	25753	16248	16000	14197

Table S5. Remaining fluorescence (in relative fluorescence units [RFU]) of the cuticular wax-coated MTP plate treated with buffer only ("buffer"), pure eGFP ("eGFP"), and the eGFP-MacHis constructs (wild-type MH_{WT} and the variants MH_{1-8}) after two washing steps (4 wells per system/variant for each of the 3 MTPs).

MTP	well	buffer	eGFP	MH_{WT}	MH_1	MH_2	MH_3	MH_4	MH_5	MH_6	MH_7	MH_8
1	1	51	214	968	968	325	400	777	718	717	702	601
	2	51	212	976	962	305	435	782	752	714	713	598
	3	49	214	943	969	394	437	776	727	740	721	584
	4	51	225	1055	951	368	440	771	808	739	787	687
2	1	46	219	984	928	319	411	761	685	722	683	594
	2	50	210	969	877	400	389	745	753	685	674	591
	3	46	205	979	892	268	391	798	704	698	683	590
	4	47	211	997	901	314	398	761	764	725	734	615
3	1	45	202	998	899	265	350	746	666	671	703	542
	2	52	198	931	872	260	345	733	662	641	661	568
	3	43	197	939	868	264	352	742	692	648	709	589
	4	48	212	943	868	291	367	750	704	708	740	588

Table S6. Remaining fluorescence (in relative fluorescence units [RFU]) of the cuticular wax-coated MTP plate treated with buffer only ("buffer"), pure eGFP ("eGFP"), and the eGFP-MacHis constructs (wild-type MH_{WT} and the variants MH_{1-8}) after five washing steps (4 wells per system/variant for each of the 3 MTPs).

MTP	well	buffer	eGFP	MH_{WT}	MH_1	MH_2	MH_3	MH_4	MH_5	MH_6	MH_7	MH_8
1	1	50	190	886	877	270	350	715	665	675	632	530
	2	49	189	890	882	265	377	733	680	658	650	533
	3	46	195	869	885	312	352	716	663	690	662	520
	4	53	205	935	875	290	367	692	719	683	710	606
2	1	46	190	898	852	255	355	707	618	665	622	550
	2	51	195	878	802	338	339	693	697	627	632	528
	3	47	186	888	811	229	337	731	636	631	631	537
	4	49	186	901	823	274	344	678	689	658	680	536
3	1	48	192	906	836	230	318	704	619	633	634	497
	2	50	181	863	808	225	307	685	609	598	613	522
	3	49	185	861	799	239	314	684	626	582	656	540
	4	51	195	865	792	253	323	688	655	650	676	559

Table S7. Remaining fluorescence (in relative fluorescence units [RFU]) of the cuticular wax-coated MTP plate treated with buffer only ("buffer"), pure eGFP ("eGFP"), and the eGFP-APs (LCI, MacHis, Plantaricin, Pleurocidin, Magainin) after initial treatment with buffer/eGFP/eGFP-AP solution and removal of the supernatant (4 wells per system/variant for each of the 3 MTPs).

MTP	well	buffer	eGFP	LCI	MacHis	Plantaricin	Pleurocidin	Magainin
1	1	56	4766	4773	4445	6089	2965	28740
	2	56	4587	4798	4547	6498	2894	29813
	3	65	4768	4716	4503	6943	3067	31290
	4	57	5302	4835	4679	7382	3513	32198
2	1	59	4769	5787	4695	6853	3914	36062
	2	59	5240	6516	4602	7112	4083	39839
	3	72	5835	6115	5141	7109	4750	40479
	4	55	7709	6200	5067	8221	5016	41232
3	1	52	4058	4144	4733	5883	3006	25294
	2	53	4466	4617	4781	6506	3438	28197
	3	51	4728	5117	4954	7390	3572	29008
	4	53	5299	5916	4858	7051	3957	31875

Table S8. Remaining fluorescence (in relative fluorescence units [RFU]) of the cuticular wax-coated MTP plate treated with buffer only ("buffer"), pure eGFP ("eGFP"), and the eGFP-APs (LCI, MacHis, Plantaricin, Pleurocidin, Magainin) after two washing steps (4 wells per system/variant for each of the 3 MTPs).

MTP	well	buffer	eGFP	LCI	MacHis	Plantaricin	Pleurocidin	Magainin
1	1	56	573	1505	1120	1439	500	1171
	2	57	553	1345	1086	1488	431	1344
	3	59	568	1366	1174	1543	465	1298
	4	55	589	1354	1110	1680	494	1339
2	1	55	581	1385	1045	1379	465	1398
	2	61	560	1375	1182	1541	471	1455
	3	70	554	1382	1137	1391	555	1482
	4	55	640	1382	1242	1565	532	1436
3	1	54	549	1361	1074	1134	429	1515
	2	54	516	1383	1117	1460	429	1505
	3	49	509	1356	1092	1450	449	1439
	4	51	728	1356	1089	1160	501	1472

Table S9. Remaining fluorescence (in relative fluorescence units [RFU]) of the cuticular wax-coated MTP plate treated with buffer only ("buffer"), pure eGFP ("eGFP"), and the eGFP-APs (LCI, MacHis, Plantaricin, Pleurocidin, Magainin) after five washing steps (4 wells per system/variant for each of the 3 MTPs).

MTP	well	buffer	eGFP	LCI	MacHis	Plantaricin	Pleurocidin	Magainin
1	1	58	503	1494	1006	1166	424	1031
	2	59	484	1333	987	1197	372	1189
	3	60	498	1344	1063	1327	384	1182
	4	56	509	1354	1014	1396	437	1236
2	1	55	516	1358	966	1186	401	1262
	2	60	499	1369	1078	1309	407	1331
	3	64	482	1379	1035	1194	492	1353
	4	56	574	1378	1128	1435	445	1298
3	1	56	507	1370	968	940	383	1359
	2	53	465	1388	1028	1253	380	1399
	3	50	476	1363	1001	1175	398	1349
	4	55	636	1354	1006	1009	441	1377

Supplementary Figures

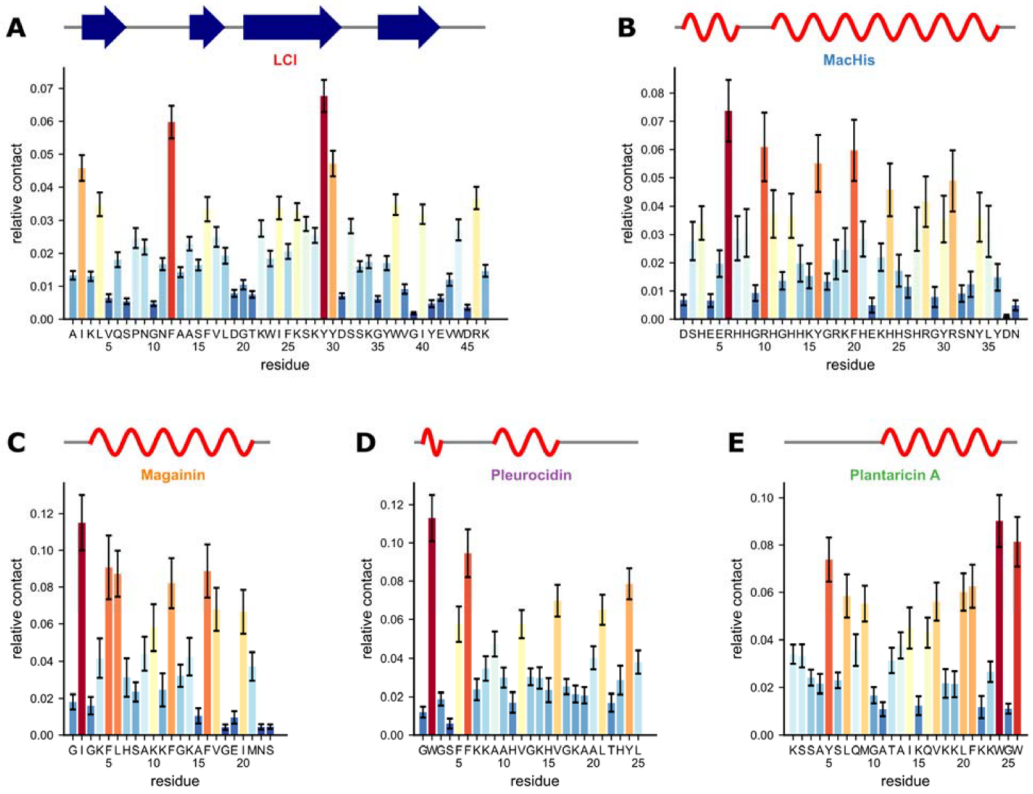

Figure S1. Residue-wise relative contacts of (A) LCI, (B) Macaque Histatin, (C) Magainin, (D) Pleurocidin, and (E) Plantaricin with the wax molecules within 10 x 250 ns long MD simulations of anchor peptide adsorption. Error bars denote the SEM. Geometrical analyses of the MD simulations were performed using cpptraj.[1] On top of the plots, the secondary structure of the APs is indicated (wavy line: α-helix, arrow: β-strand) as determined by DSSP[2] analysis of the protein structures.

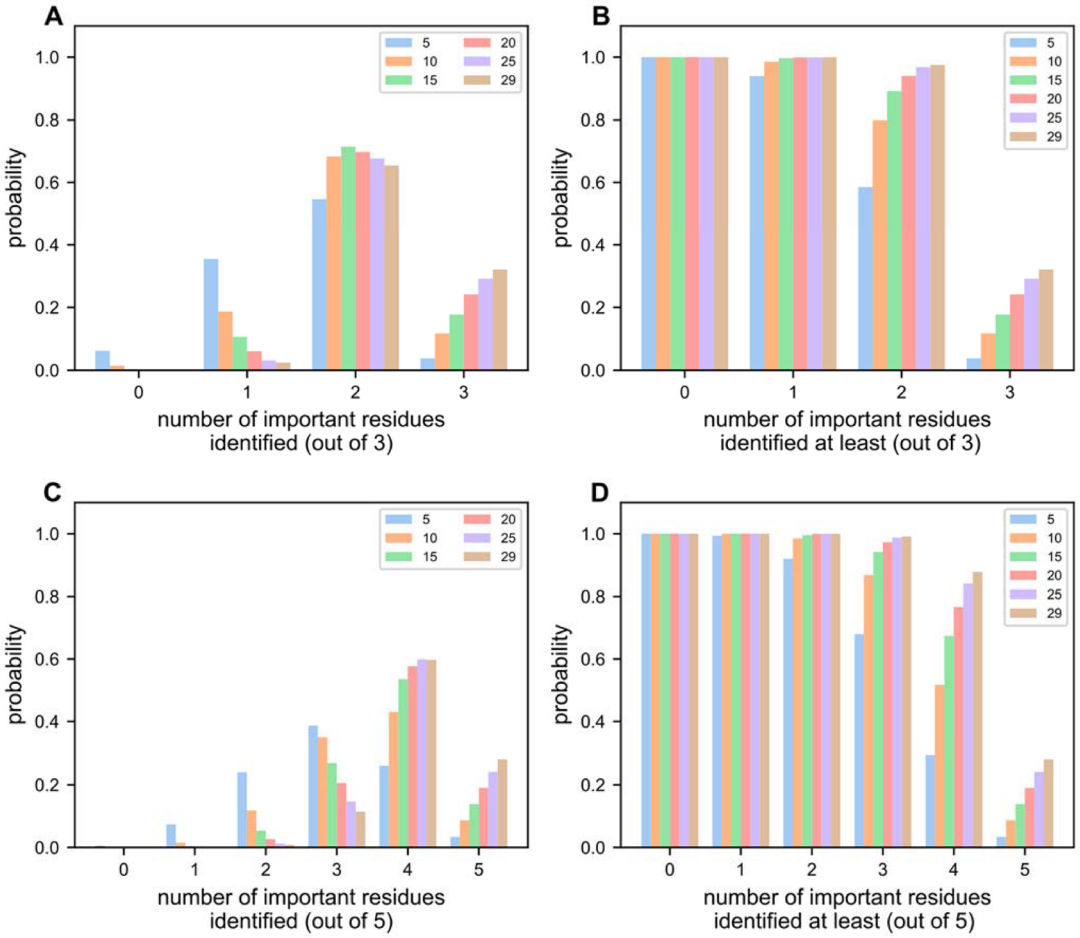

Figure S2. Bootstrapping analysis for identifying residues important for cuticular wax binding of MacHis in dependence of the sample size. Samples of different sizes (5, 10, 15, 20, 25, 29) were drawn 10,000 times with replacement from the original set containing 29 samples. For each sample set size, the overlap with the top three (**A**, **B**) and top five (**C**, **D**) identified residues using the original set is calculated. The probability of identifying exactly X residues out of the three/five is given in **A** and **C**, the probability of identifying at least X residues out of the three/five is given in **B** and **D** for each sample size.

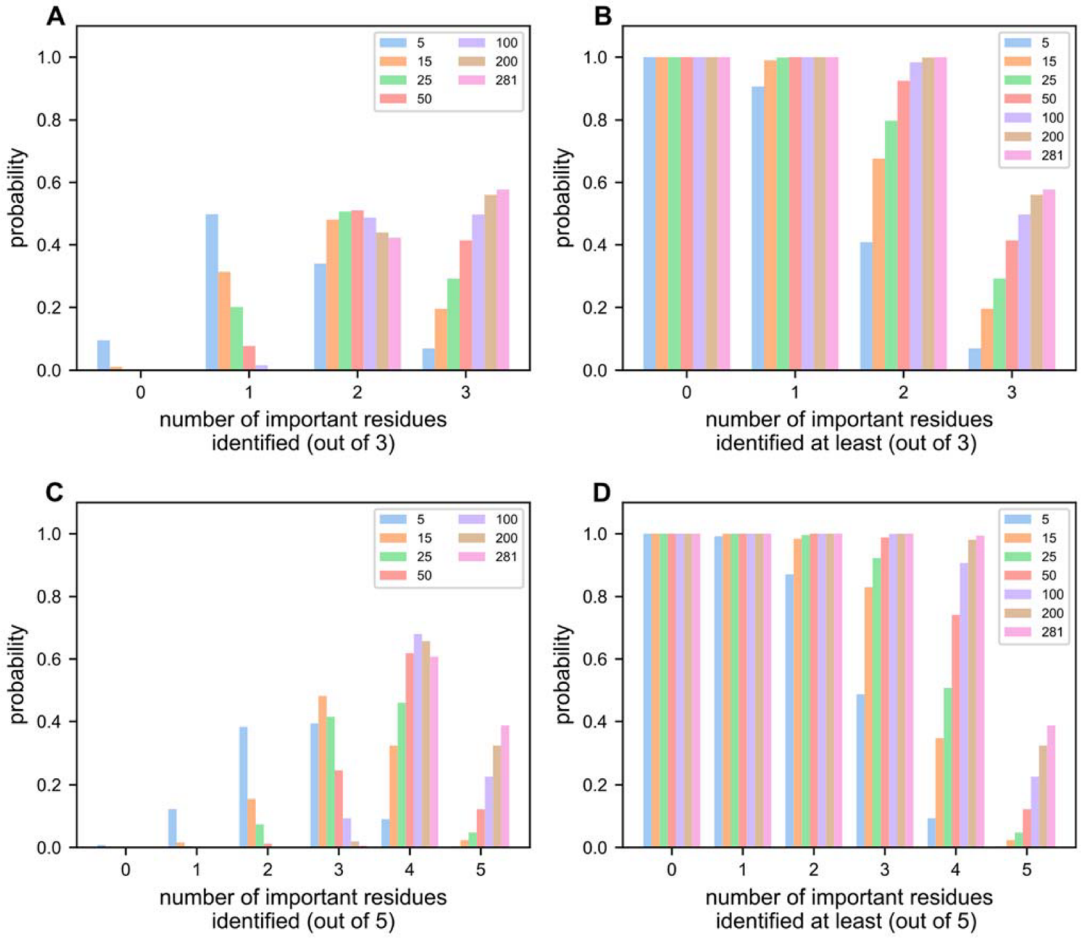

Figure S3. Bootstrapping analysis for identifying residues important for cuticular wax binding of LCI in dependence of the sample size. Samples of different sizes (5, 15, 25, 50, 100, 200, 281) were drawn 10,000 times with replacement from the original set containing 281 samples. For each sample set size, the overlap with the top three (**A**, **B**) and top five (**C**, **D**) identified residues using the original set is calculated. The probability of identifying exactly X residues out of the three/five is given in **A** and **C**, the probability of identifying at least X residues out of the three/five is given in **B** and **D** for each sample size.

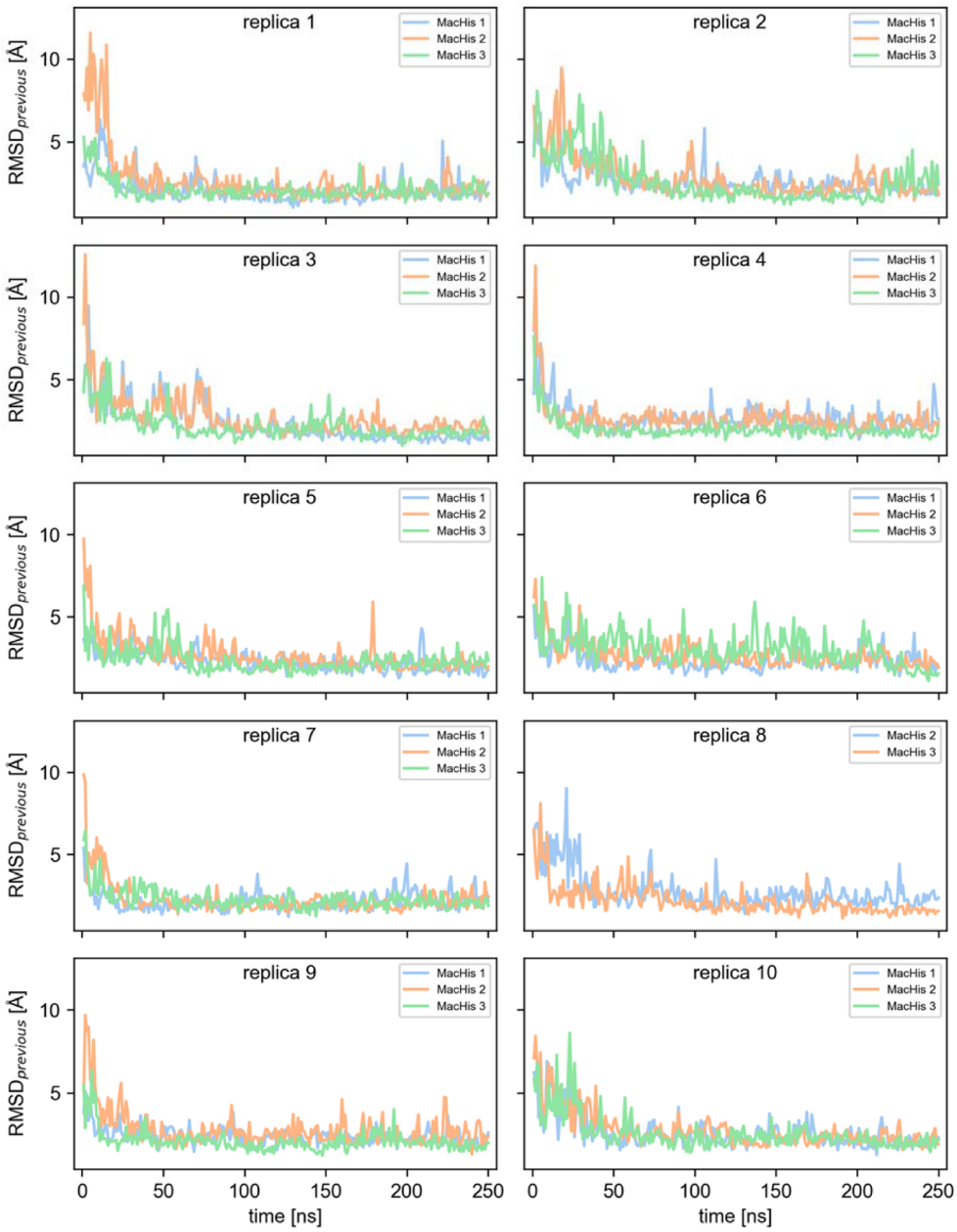

Figure S4. RMSD for all three MacHis peptides to their states 1 ns before, respectively, depicted for all ten simulated replicas. One peptide (MacHis 1, replica 8) is excluded, as it did not adsorb to the wax layer. Upon adsorption, observed within < 100 ns for the majority of the cases, the RMSD fluctuation of the peptide is decreased to 2.16 ± 0.04 Å (mean ± SEM for 100-250 ns)

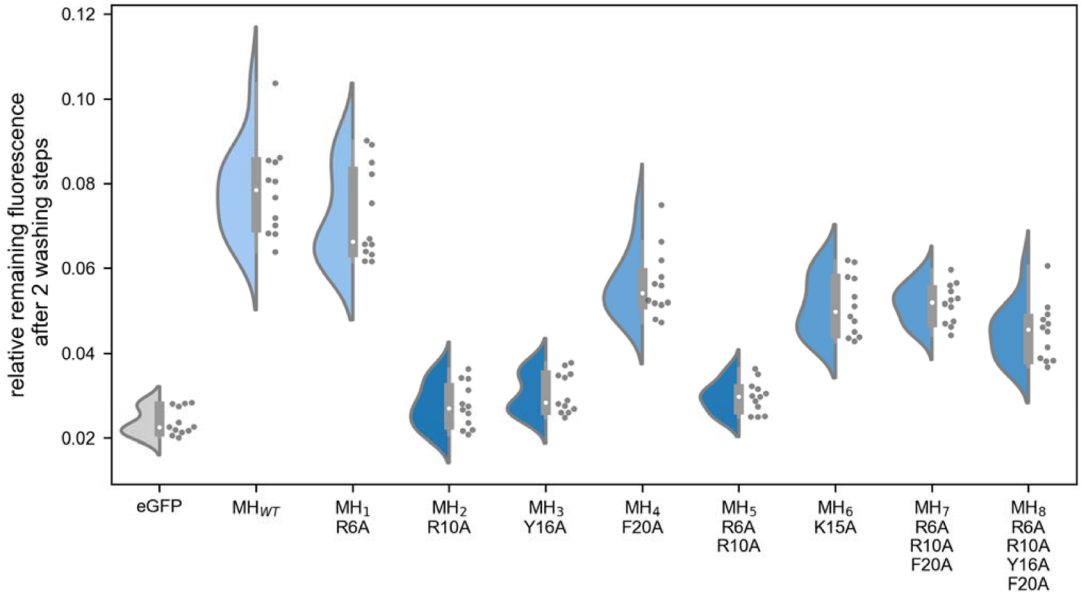

Figure S5. Binding of eGFP-MacHis wild-type (MH_{WT}) and eGFP-MacHis variants (MH_{1-8}) to extracted cuticular wax from apple leaves. Binding was quantified by measuring the remaining fluorescence of the fusion partner eGFP after two washing steps on apple leaf cuticular wax in 96-well-MTPs (4 wells, 3 replicates).

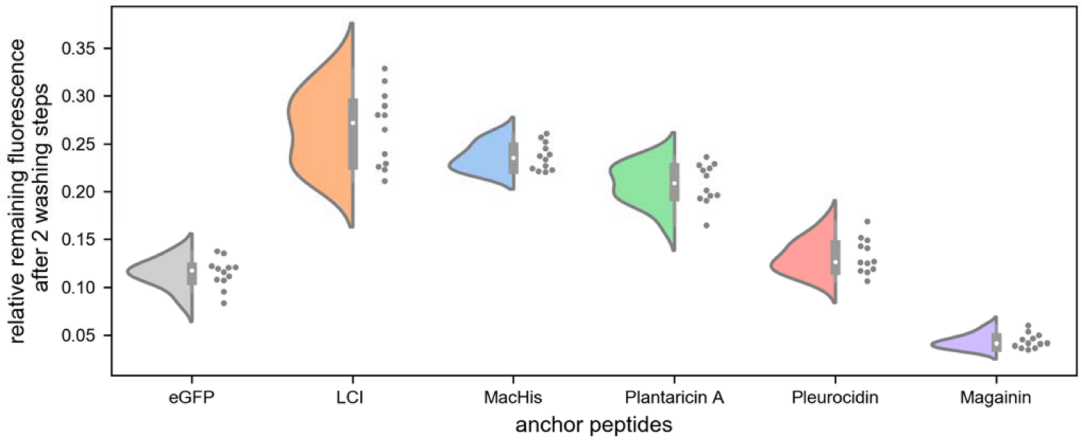

Figure S6. Binding of different eGFP-APs to extracted cuticular wax from apple leaves. Binding was quantified by measuring the remaining fluorescence of the fusion partner eGFP after two washing steps on apple leaf cuticular wax in 96-well-MTPs (4 wells, 3 replicates).

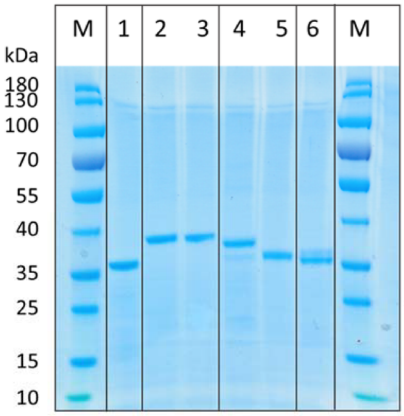

1	eGFP 1 µg	31.5 kDa
2	LCI no TEV 1 µg	36.5 kDa
3	MacHis no TEV 1 µg	35.4 kDa
4	Plantaricin A no TEV 1 µg	33.6 kDa
5	Pleurocidin no TEV 1 µg	33.4 kDa
6	Magainin 2 no TEV 1 µg	33.1 kDa

Figure S7. Sodium dodecyl sulfate-polyacrylamide gel electrophoresis (SDS-PAGE) image of eGFP and eGFP-APs for determination of purity with ImageJ[3] (version 1.53e).

Supplementary References

(1) Roe, D. R.; Cheatham, T. E., PTRAJ and CPPTRAJ: Software for Processing and Analysis of Molecular Dynamics Trajectory Data. *J. Chem. Theory Comput.* **2013,** *9* (7), 3084-3095.

(2) Kabsch, W.; Sander, C., Dictionary of protein secondary structure: Pattern recognition of hydrogen-bonded and geometrical features. *Biopolymers* **1983,** *22* (12), 2577-2637.

(3) Rasband, W., ImageJ: Image processing and analysis in Java. *Astrophysics Source Code Library* **2012**, ascl: 1206.013.

9. Publication II

Temperature-Induced Coil-to-Globule Transition of Poly(*N*-vinylcaprolactam)

Cumulative Submillisecond All-Atom Simulations of the Temperature-Induced Coil-to-Globule Transition of Poly(*N*-vinylcaprolactam) in Aqueous Solution

Jonas Dittrich, Michael Kather, Anna Holzberger, Andrij Pich, and Holger Gohlke

Macromolecules, 2020, 53, 9793−9810.

DOI: 10.1021/acs.macromol.0c01896

Macromolecules

pubs.acs.org/Macromolecules Article

Cumulative Submillisecond All-Atom Simulations of the Temperature-Induced Coil-to-Globule Transition of Poly(*N*-vinylcaprolactam) in Aqueous Solution

Jonas Dittrich, Michael Kather, Anna Holzberger, Andrij Pich, and Holger Gohlke*

Cite This: *Macromolecules* 2020, 53, 9793−9810 Read Online

ACCESS | Metrics & More | Article Recommendations | Supporting Information

ABSTRACT: Poly(*N*-vinylcaprolactam) (PNVCL) polymers are stimuli-responsive and change their conformation in aqueous solutions upon changes in salt concentration, concentration of organic solvents, or temperature, making these molecules highly interesting for tailored release of drugs or fabrication of sensors or actuators. At lower critical solution temperature (LCST), PNVCL chains undergo a transition from a coil to a globule and become insoluble. In contrast to other polymers, however, PNVCL has received much less attention as to elucidating driving forces of its coil-to-globule transition at an atomistic level. Here, we show by a combined computational and experimental study that upon temperature increase, PNVCL chains dissolved in water experience an increase of intramolecular interactions between C_3 and C_4 of the caprolactam ring. Therefore, more favorable cavity formation energies and the increase of intramolecular interactions outweigh the loss in polar and hydrophobic solvation, and the loss of configurational entropy in the coil-to-globule transition and, thus, may be considered driving forces of the polymer's collapse at LCST. These results are based on molecular dynamics simulations of in total 600 μs length and transition (free) energy computations that have been validated internally and against experimental data. We systematically tested the influence of the polymer's length, concentration, tacticity, of the thermodynamic ensemble, and of the water model. Tacticity was found to be most influential, with atactic polymers showing the strongest tendency to collapse. The presented approach should be applicable to scrutinize at the atomistic level the impact of, for example, ion and polymer dispersity on the coil-to-globule transition of PNVCL, and the LCST behavior of other polymers.

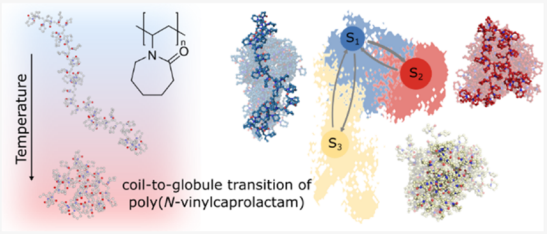

INTRODUCTION

Poly(*N*-vinylcaprolactam) (PNVCL) is a thermoresponsive polymer whose water solubility is temperature-dependent. When exceeding the lower critical solution temperature (LCST) of ∼32−37 °C, the polymer becomes insoluble in water and undergoes a conformational change from a coil to a globule.[1,2] Note that the exact LCST depends on parameters such as polymer length and concentration[3−5] as well as types and concentrations of ions,[6] detergents,[7] and other osmolytes.[8] The coil-to-globule transition is visible to the naked eye, that is, an initially clear solution becomes turbid upon polymer precipitation when reaching a defined temperature, also referred to as cloud point temperature. This phenomenon is of particular interest, as thermoresponsive polymers play a vital role in applications in health, biomedicine, environment, and agriculture/plant sciences. There, the polymers can be used as carriers and allow a controlled release of a variety of substances, such as drugs, fertilizers, herbicides, or nanoparticles.[9−17] Besides the main application as a carrier, thermoresponsive gels (partially) based on PNVCL are also applied in (bio)analytics,[18,19] catalysis,[20,21] and in a synergetic use with nanoparticles.[10,11,22] The thermoresponsiveness even allows mimicking a biopolymer/protein-like behavior.[23] Compared to other thermoresponsive polymers, for example, the well-studied poly(*N*-isopropylacrylamide) (PNIPAM),[1,24−28] PNVCL shows favorable toxicological and ecological properties because it is not decomposed into small, potentially carcinogenic amide derivatives upon hydrolysis,[29] making it a viable option especially for medical applications.

Interestingly, not only long-chain PNVCL polymers but also short PNVCL oligomers of ∼20−25 repeating units show a distinct LCST behavior at a temperature of ∼50 °C. However, experimental data for uniform short-chain PNVCL (molecular weight < 7000 g mol^{-1}, <50 repeating units) are rare, as the synthesis of uniform PNVCL oligomers remains challenging. These data, however, are crucial to evaluate and validate

Received: August 15, 2020
Revised: October 17, 2020
Published: November 4, 2020

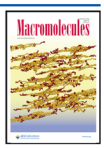

https://dx.doi.org/10.1021/acs.macromol.0c01896
Macromolecules 2020, 53, 9793−9810

Macromolecules pubs.acs.org/Macromolecules Article

Scheme 1. Synthesis of Linear PNVCL Using RAFT Polymerization

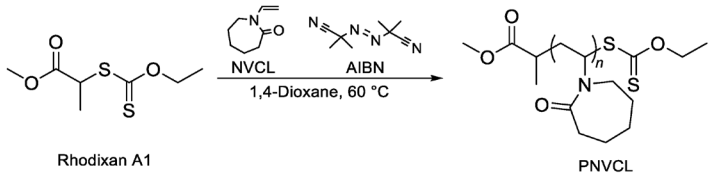

computational approaches, such as molecular dynamics (MD) simulations and free energy computations, which, inversely, provide insights at the atomistic level as to the molecular origin of the transition that complement experimental analyses.[30−34] The knowledge gained from the simulations can be finally used to further tailor the polymers to one's needs.

First studies on the thermoresponsiveness of PNVCL and the effect of the salt concentration and types on the LCST using MD simulations have been reported recently.[8,35−39] These include MD simulations at the coarse-grained,[39] united-atom,[36] and atomistic levels.[8,35] While indicating that modern MD simulations are suitable to investigate the coil-to-globule transition in PNVCL at the LCST, the majority of the published simulation data[35,36,40−42] for thermoresponsive polymers describe the collapse at the LCST as a seemingly irreversible process because often no transition from the globule back to the coil is observed during the simulation time, which contradicts experimental observations;[34,43] notable exceptions exist.[38,44,45] Furthermore, a systematic assessment of the influence of polymer length, tacticity, and concentration on the thermoresponsiveness observed in MD simulations is rare. Finally, while most MD simulation studies evaluate structural parameters of the coil-to-globule transition, energetic determinants of the transition have only been computed for interactions between two isolated NVCL (*N*-vinylcaprolactam) monomers so far.[38]

Here, we aim at elucidating the driving forces of the PNVCL coil-to-globule transition at the LCST by computational structural and energetic analyses, in doing so paying particular attention to the impact of polymer characteristics and to validating our simulation results against experiment. We, therefore, performed extensive all-atom MD simulations with a cumulated simulation time of over 600 μs to investigate the influence of the polymer size, tacticity, concentration, and the chosen water model on the coil-to-globule transition observed at the LCST. We validated our simulation results by comparing computed structural descriptors, such as the radius of gyration, and transition enthalpies to experimental data.[33,34] Moreover, we constructed hidden Markov models (HMMs) to identify metastable states constituting PNVCL ensembles at temperatures below and above the LCST and performed free energy calculations, including a decomposition into energetic components, to elucidate driving forces of the PNVCL collapse. A series of PNVCL samples with variable molecular weights (1000−15,000 g mol^{-1}) and narrow dispersities were synthesized using macromolecular design by the interchange of xanthates and reversible addition−fragmentation chain transfer (MADIX/RAFT) polymerization and their cloud points in aqueous solutions were determined by UV−vis spectroscopy.

Our simulation results are in good agreement with experiments, both in terms of configurational and energetic aspects of the coil-to-globule transition, and provide unprecedentedly detailed insights into the LCST behavior of PNVCL at an atomistic level.

METHODOLOGY

Experimental Approach. In the following, we describe the synthesis of oligomeric PNVCL and its characterization.

Materials. NVCL (98%, Sigma-Aldrich) was purified by distillation under vacuum and recrystallized in hexane (99%, VWR). Methyl 2-bromopropionate (MEP) (97%, Alfa Aesar), potassium ethyl xanthogenate (PEX) (96%, Sigma-Aldrich), and azobisisobutyronitrile (AIBN) (98%, Sigma-Aldrich) were used as received.

Synthesis of *O*-Ethyl-*S*-(1-methoxycarbonyl)ethyl Dithiocarbonate (Rhodixan A1). A solution of 5 g of MEP (29.25 mmol), dissolved in ethanol (38 mL), is stirred at 0 °C. To this solution, 5.39 g PEX (33.6 mmol) is consecutively added over 45 min. Afterward, the ice bath is removed and the solution stirred for another 3 h. To purify the product, the formed potassium bromide is removed by filtration and the solution concentrated in vacuo. The remaining solution is dissolved in dichloromethane (DCM) (80 mL) and washed four times with water (15 mL). The organic phase is dried over Na_2SO_4 overnight and filtered. After removing of DCM and subsequent drying under vacuum, a bright yellow liquid is obtained (5.67 g, 27.2 mmol, 93%).

^{1}H NMR (400 MHz, $CDCl_3$): 4.60−4.45 (m, 2 H), 4.29 (q, J = 7.39 Hz, 1 H), 3.65 (s, 3 H), 1.47 (d, J = 7.41 Hz, 3 H), 1.32 (t, J = 7.13 Hz, 3 H) ppm.

^{13}C NMR (75 MHz, $CDCl_3$): 211.70, 171.60, 70.10, 52.55, 46.79, 16.71, 13.50 ppm.

Synthesis of Linear PNVCL Using MADIX/RAFT. In an example, for the synthesis of linear PNVCL with polymerization degree P_n = 106 via MADIX/RAFT,[46] a solution of 1 g NVCL (7.2 mmol), 15 mg Rhodixan A1 (0.072 mmol), and 3.55 mg AIBN (0.022 mmol) in dioxane (2 mL) is degassed by four freeze−pump−thaw cycles and then purged with argon. Afterward, the solution is added to a preheated oil bath at 60 °C, and the reaction is carried on for 21 h. After completion, the reaction is quenched in liquid nitrogen. The polymer is gained through precipitation in hexane and filtration as a colorless or slightly yellowish solid (Scheme 1).

The polymerization degree of PNVCL chains was controlled by the variation of the monomer (NVCL) to chain transfer agent (CTA) ratio. Increasing the amount of the CTA Rhodixan A1 in the polymerization mixture reduced the polymerization degree, while a decrease in the CTA concentration caused the opposite effect.

Determination of Molecular Weights by MALDI-TOF. Matrix-assisted laser desorption/ionization (MALDI) time-of-flight (TOF) mass spectrometry was performed on a Bruker UltrafleXtreme. Dithranol (Aldrich, 97%) was used as the matrix. Sodium trifluoroacetate was added for ion formation. Samples were prepared from the tetrahydrofuran solution by

https://dx.doi.org/10.1021/acs.macromol.0c01896
Macromolecules 2020, 53, 9793−9810

mixing the matrix (25 mg/mL), sample (10 mg/mL), and salt (10 mg/mL). About 1 μL of the resulting mixture was applied to a steel target to evaporate the solvent and create a thin matrix/analyte layer.[47] The number-average molecular weights, M_n, of the polymer samples were determined in linear mode for samples with high mass and in reflective mode for low molecular weight samples. Analysis of the spectra was performed using the Flex Analysis software (v. 3.3).

Determination of Cloud Points. For the determination of the cloud point, the change in turbidity was monitored using a Varian Cary 100 Bio UV-Visible Spectrometer. PNVCL samples were dissolved in double-distilled water, filled into a cuvette, and placed in the instrument. The absorption was measured while changing the temperature in intervals between 30 and 85 °C at a heating rate of 0.2 K/min for different wavelengths (400, 500, 600, 700, 800, and 900 nm). The cloud point was taken as the mean from all wavelengths (Figure S1).

Computational Approach. We tested the influence of a multitude of parameters on the PNVCL transition during the MD simulations of short-chain PNVCL polymers. The simulation systems each consisted of a single chain of an iso-, syndio-, or atactic PNVCL polymer with 5, 10, 15, 20, 25, 30, 40, or 50 repeating units each, resulting in 3 × 8 = 24 different system setups. Initial structures created by the LEaP program show a left-handed helical conformation with a full turn every 50 repeating units, which becomes a straight extended coil conformation during minimization and thermalization. To examine the polymers' thermoresponsiveness, these systems were simulated for 1 μs at 293, 313, and 343 K, using the TIP3P water model[48] and five replicas per setup, which resulted in, in total, 360 μs of cumulative simulation time. In order to probe for the influence of the used water model, we also performed simulations of iso-, syndio-, or atactic PNVCL polymers with 30, 40, or 50 repeating units at 293 and 313 K using the OPC water model,[49] resulting in additional 135 μs of cumulative simulation time. To probe the influence of the chosen MD ensemble, we simulated the iso-, syndio-, and atactic PNVCL 40mer in an isothermal−isobaric ensemble (NPT), yielding an additional 30 μs of the cumulative simulation time. Finally, we increased the TIP3P water box of the 50mer in two steps to investigate the influence of a decreasing polymer concentration at 293 and 313 K, thereby going from ∼1.0 to ∼0.8 and ∼0.6 wt % of the polymer, yielding another 60 μs of cumulative simulation time. See Table S1 for an overview of the performed simulations. These simulations provide the basis for geometric and energetic analyses as well as for constructing HMMs (see below).

MD simulations of poly(*N*-pyrrolidone) (PVP) oligomers serve as negative control, as PVP does not show the distinct thermoresponsiveness although being structurally similar to PNVCL.[6] Iso-, syndio-, or three different atactic PVP polymers with 30, 40, or 50 repeating units were created and simulated in TIP3P water at 293 and 313 K, yielding 75 μs of cumulative simulation time. See Table S2 for an overview of the performed simulations. See Table S3 for an overview of the number of atoms within each system.

MD Simulations. MD simulations were carried out with the Amber18 suite of programs[50,51] using the GPU-accelerated CUDA version of PMEMD[52,53] by following an established procedure.[54] We applied the GAFF2 force field[55] in all simulations. The structures were solvated in a truncated octahedron of TIP3P[48] (OPC[49]) water such that the distance between the boundary of the box and the closest solute atom was at least 12 Å (18, 24 Å for the PNVCL 50mer at reduced concentrations). Periodic boundary conditions were applied using the particle mesh Ewald method[56] to treat long-range electrostatic interactions. Bond lengths involving bonds to hydrogen atoms were constrained using the SHAKE[57] algorithm. The time step for all MD simulations was 2 fs, and a direct-space nonbonded cutoff of 8 Å was applied. First, the solvent was minimized for 250 steps by using the steepest descent method followed by conjugate gradient minimization of 50 steps. Subsequently, the same approach was used to minimize the entire system. Afterward, the system was heated from 0 to 100 K using canonical ensemble (NVT) MD simulations, and from 100 to 293 K (313, 343 K) using isothermal−isobaric (NPT) MD simulations, also adjusting the solvent density according to 1 bar. Positional restraints applied during thermalization were reduced in a stepwise manner over 50 ps, followed by 50 ps of unrestrained NVT MD simulations at 293 K (313, 343 K) with a time constant of 2 ps for heat bath coupling.[58] Each MD simulation of PNVCL was run for 1 μs using a time constant of 10 ps for heat bath coupling,[58] and coordinates were saved at 100 ps intervals. For the NPT simulations of the PNVCL 40mer, the temperature was maintained by using Langevin dynamics,[59] with a friction coefficient of 1 ps^{-1}, and the pressure was maintained using an isotropic Berendsen barostat.[58] Each NVT MD simulation of PVP was run for 500 ns using a time constant of 10 ps for heat bath coupling,[58] and coordinates were saved at 100 ps intervals. In all cases, five independent replicas were simulated, resulting in cumulative simulation times of 585 and 75 μs for PNVCL and PVP, respectively. Geometric analyses of the trajectories were performed with CPPTRAJ.[60]

Structure Preparation. For computing atomic charges following the restrained electrostatic potential (RESP) procedure,[61] NVCL and *N*-vinylpyrrolidone monomers were modified by terminating the vinyl moiety with methyl groups and changing the hybridization state of the involved carbon atoms to sp^3 in order to mimic the aliphatic polymer backbone. OpenEye's OMEGA[62,63] (v. 3.0.0.1) was then used to generate eight additional low-energy conformers of PNVCL to examine the robustness of the charges computed for the initial low-energy conformer. As *N*-vinylpyrrolidone shows a distinct envelope conformation, we only considered one low-energy conformation. The electrostatic potential (ESP) was calculated at the HF/6-31G* level using Gaussian09.[64] Afterward, the ESP was fitted using the RESP charge fitting procedure implemented in antechamber.[65] Intentionally, we did not refit any other force field parameters in order to examine the capability of the GAFF2 force field to describe the transition of PNVCL at LCST correctly. The parametrized repeating units were saved in an Amber library (.lib) file, facilitating the generation of polymers of different size and tacticity. The corresponding library files can be downloaded free of charge via the internet at http://pubs.acs.org. For atactic polymers, the configuration of each repeating unit was chosen randomly (for details, see Table S4). The generated polymer structures were methyl-terminated, although custom modifications can be applied in future simulations.

Hidden Markov Models. For further elucidating the collapse mechanism and kinetics, we constructed HMMs from the MD simulations of the atactic PNVCL 40mer below (293 K) and above (313 K) LCST using the PyEMMA[66] python library (v. 2.5.6). HMMs are a practically feasible approximation of projected Markov models, for which, in

https://dx.doi.org/10.1021/acs.macromol.0c01896
Macromolecules 2020, 53, 9793−9810

contrast to Markov state models (MSMs), it is not necessary to assume a Markov chain on a cluster discretization of the state space. Instead, it is assumed that the full phase-space MD is Markovian, and a projection of this full dynamics is observed on the discrete states.[67]

Initially, the conformational space of the polymers was discretized and the trajectory reduced to a sequence of transitions between discrete states, as good state space discretization is crucial to obtain a descriptive and predictive model.[68] We described the conformations of the polymer chain by the set of distances between every fifth carbon atom of the polymer backbone bound to a caprolactam ring to the polymers' ends, the mid-point, and the lower and upper quarter as well as the radius of gyration, resulting in $40/5 \times (2 + 1 + 2) + 1 = 41$ dimensions. In order to reduce the dimensionality, we performed a time-lagged independent component analysis (TICA),[69,70] reducing the 41 dimensions to two dimensions represented by independent components (ICs) IC1 and IC2. TICA finds coordinates of maximal autocorrelation at a given lag time, thus, it is useful to find the slow components in a dataset and provides an approximation to the eigenfunctions and eigenvalues of the underlying Markov operator.[71] To make the two HMMs comparable that were obtained from MD simulations at the respective temperatures, the TICA was performed on both sets of 41 dimensions, yielding that the feature sets were projected onto the same IC space. For further analysis, the trajectories of the different temperatures were treated separately again: *k*-means clustering was applied to identify 40 microstates within the reduced systems, generating a 40-state MSM for each temperature. Kinetically similar microstates of the granular MSM were then further assigned to metastable states by applying the PCCA+ algorithm,[72] yielding an HMM with two to three hidden states. As HMMs show a low sensibility to discretization errors compared to regular MSMs,[67] we could afford to estimate our HMM at a small lag time of 0.5 ns and, thus, resolve more processes than one can resolve with regular MSMs.[67] The implied timescale analysis, as well as the results of the Chapman–Kolmogorov test, are shown in Figures S2–S5.

Free Energy Computations. In order to determine the difference in free energy for the coil-to-globule transition of PNVCL, ΔG, we followed different approaches. First, we deduced ΔG for the transition at different temperatures from the HMMs. From the stationary distribution π, the molar free energy of state i relative to a state 0 is given by (eq 1).[67]

$$\Delta G = -RT \ln\left(\frac{\pi_i}{\pi_0}\right) \tag{1}$$

Second, we validated the obtained ΔG by an independent method, using the molecular mechanics Poisson–Boltzmann surface area (MM-PBSA) approach[73−76] to estimate the changes in the effective energy ($\Delta E_{MM} + \Delta G_{solvation}$) and normal mode analysis[77] (NMA) to approximate the changes in configurational entropy of the solute (ΔS_{config}) upon the coil-to-globule transition as implemented in MMPBSA.py.[78] ΔG is then given as (eqs 2a and 2b)

$$\Delta G_{coil \rightarrow globule} = G_{globule} - G_{coil} \tag{2a}$$

with

$$G_{\{globule,coil\}} = E_{MM,\{globule,coil\}} + G_{solv,\{globule,coil\}} - TS_{config,\{globule,coil\}} \tag{2b}$$

E_{MM} is the sum of bonded and nonbonded intramolecular energies of the polymer (eq 3)

$$E_{MM} = \sum_{bonds} E_{bond} + \sum_{angles} E_{angle} + \sum_{torsions} E_{torsion} + \sum_{i \neq j}^{atoms} E_{vdW} + \sum_{i \neq j}^{atoms} E_{electrostatic} \tag{3}$$

and G_{solv} denotes the solvation free energy of the polymer (eq 4).

$$G_{solv} = G_{pol} + G_{nonpol} \tag{4}$$

G_{pol} is computed by solving the linear Poisson–Boltzmann equation[79,80] using a dielectric constant of 1 for the solute and accounting for the temperature dependency of the dielectric constant of water,[81,82] which was set to 80 and 74 at 293 K and 313 K, respectively. G_{nonpol} is further decomposed into a repulsive cavitation solvation free energy term G_{cavity} and an attractive dispersion solvation free energy term $G_{dispersion}$, which are calculated using a term linearly proportional to the molecular volume enclosed by the solvent-accessible surface area (SASA) and a surface-based integration method, respectively.[83] Finally, for the NMA, we assume that the polymer chains obey a rigid-rotor model, such that vibrational frequencies of normal modes can be calculated at local minima of the potential energy surface, and translational as well as rotational entropies can be calculated using standard statistical mechanical equations.[84] For the NMA, we chose GB^{HCT}[85,86] as a water model, and each snapshot was minimized until the convergence criteria of a difference in minimized energy of <0.001 kcal mol^{-1} is satisfied. In the MM-PBSA approach, no cutoff is used for the calculation of the nonbonded energies in the E_{MM} part, and there are no cutoffs for long-range interactions in the Poisson–Boltzmann model either.

G values computed according to eq 2b were averaged over members of an ensemble. To do so, for each temperature (293 K and 313 K), ten times 100 different conformations with a relative radius of gyration (R_g is scaled by $R_{g,0}$, the radius of gyration of the first frame; the conformations of oligomers of the same length are similar after minimization and thermalization) $R_g/R_{g,0} > 0.9$, indicative of a coil-like conformation, and $R_g/R_{g,0} < 0.6$, indicative of a globule-like conformation, were randomly selected from the trajectories. Results of G across all ten sets (G_i, $n = 10$) were then averaged, yielding $\bar{G}$. The standard error of the mean (SEM) $\sigma_{\bar{G}}$ and the error of ΔG were determined according to the laws of error propagation (eqs 5 and 6).

$$\sigma_{\bar{G}} = \frac{\sigma}{\sqrt{n}}; \qquad \sigma = \sqrt{\frac{1}{n-1}\sum_{i=1}^{n}(G_i - \bar{G})^2} \tag{5}$$

$$\sigma_{\Delta \bar{G}_{coil \rightarrow globule}} = \sqrt{\sigma_{\bar{G}_{globule}}^2 + \sigma_{\bar{G}_{coil}}^2} \tag{6}$$

Although the decomposition of the free energy computed by MM-PBSA into energy components according to eqs 2a and 2b[87] provides useful insights into each energy component's contribution to the coil-to-globule transition, it is not immediately possible to entirely separate enthalpic and

https://dx.doi.org/10.1021/acs.macromol.0c01896
Macromolecules 2020, 53, 9793−9810

entropic components because G_{solv} contains both types.[88] Hence, it is not possible to compare the MM-PBSA energy components to results from coil-to-globule transition enthalpy measurements based on calorimetry[4,31,34] or NMR.[32]

We, therefore, adapted an approach by Fenley et al.[89] to relate potential energies obtained from MD simulations using explicit water with experimentally determined differences in the enthalpies for the phase transition. To do so, we computed average total potential energies of MD simulations of the PNVCL 40mer in the NPT ensemble, $\langle U_{P,H_2O}\rangle$, and subtracted the average potential energy of the same number of water molecules without the polymer, $\langle U_{H_2O}\rangle$, both at 293 and 313 K. These values can also be computed from MD simulations in the NVT ensemble if the simulation box volumes at equilibrium are known. For this, it is exploited that the system's potential energy is linearly proportional to the box volume within the ranges of box volumes sampled during the thermalization and pressure adjustment process; thus, the system's potential energy can be interpolated for a given box volume, ideally the equilibrium volume of the system.[89]

The enthalpy of the polymer in a solvent environment at a given temperature is the difference $\langle U_{P,H_2O}\rangle - \langle U_{H_2O}\rangle$. For error estimation, averages are computed for each replica trajectory and then processed similar to eq 5. The enthalpy difference for the coil-to-globule transition, ΔH_{trans}, is finally approximated from the MD simulations at 293 and 313 K (eq 7).

$$\begin{aligned}\Delta H_{trans} &= H_{P,313K} - H_{P,293K} \\ &= \langle U_{P,H_2O,313K}\rangle - \langle U_{H_2O,313K}\rangle \\ &\quad - (\langle U_{P,H_2O,293K}\rangle - \langle U_{H_2O,293K}\rangle)\end{aligned} \tag{7}$$

The error of ΔH_{trans} is calculated according to the laws of error propagation, similar to eq 6. The error of ΔH_{trans} per repeating unit is assumed to be equal on average for all repeating units and independent from each other and, thus, obtained as the square root of the squared error of ΔH_{trans} divided by the number of repeating units.

RESULTS

PNVCL samples synthesized by RAFT polymerization exhibit tunable molecular weights (M_n: 1000−15,000 g mol^{-1}) and variable polymerization degrees (P_n: 7−106) at narrow dispersities ($Đ$) (Table 1). The polymerization degree (P_n) was varied by adjusting the monomer to CTA ratio in the reaction mixture.

Table 1. Molecular Weight (M_n), Polymerization Degree (P_n), and Dispersity ($Đ$) of PNVCL Chains Determined by MALDI-TOF Mass Spectroscopy

M_n/g mol^{-1}	P_n/a.u.	$Đ$/a.u.
15,000	106	1.650
9670	68	1.409
5607	39	1.155
4265	29	1.078
2416	16	1.053
1854	12	1.053
1713	11	1.055
1140	7	1.207

The cloud points of synthesized PNVCL samples were investigated in aqueous solutions using UV−vis spectroscopy. Figure 1 shows the dependency of the experimentally

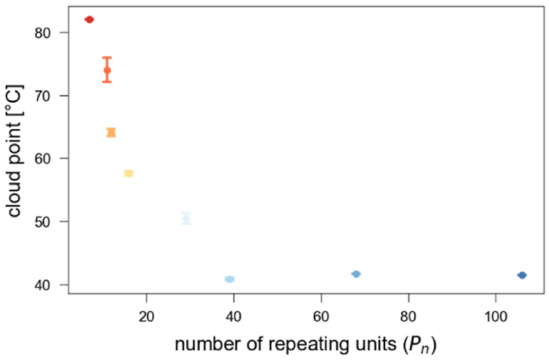

Figure 1. Influence of the polymerization degree (P_n) on the cloud point of PNVCL at a polymer concentration of 0.4 wt %. The error bars depict the standard deviation of the mean. The color scheme of the dots is as used in later figures to indicate the number of repeating units.

determined cloud points for PNVCL samples with different molecular weights. The increase in chain length leads to a strong decrease in cloud point temperature. This trend is in agreement with previous observations by Laukkanen and coworkers, who investigated phase transitions of PNVCL in aqueous solutions using both cloud point determination and differential scanning calorimetry (DSC).[31]

In addition, we investigated the influence of polymer concentration in aqueous solution on cloud point temperatures. Figure 2 shows the cloud points measured for five

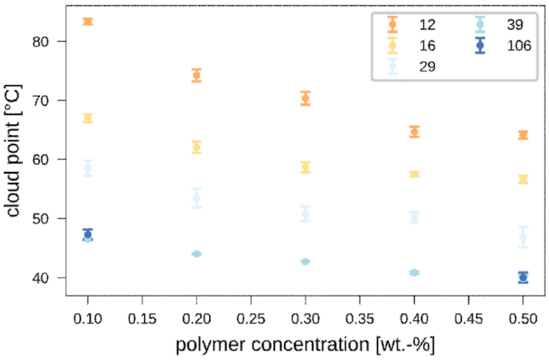

Figure 2. Cloud points of linear PNVCL 12mer, 16mer, 29mer, 39mer, and 106mer (indicated by color, yellow to dark blue) depending on the polymer concentration. The error bars depict the standard deviation of the mean.

PNVCL samples with P_n 12, 16, 29, 39, and 106. It is obvious that the increase of the polymer concentration decreases the cloud point temperature exponentially. This effect has been reported previously[90,91] and attributed to the enhanced probability of interchain interactions between hydrophobic segments.

https://dx.doi.org/10.1021/acs.macromol.0c01896
Macromolecules 2020, 53, 9793−9810

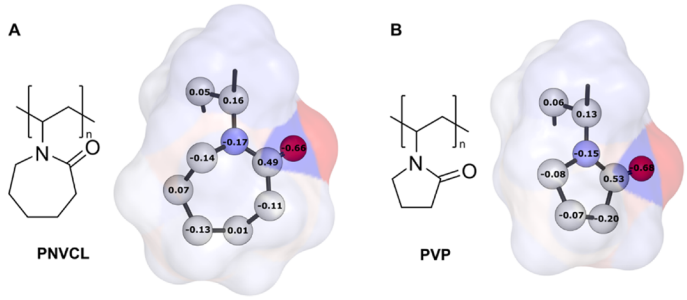

Figure 3. Atomic partial charges of the repeating units of (A) PNVCL (chair conformation) and (B) PVP (envelope conformation) as determined by the RESP procedure[61] are shown as labels and are projected onto the molecule surface (blue: positive partial charge and red: negative partial charge). Atoms are depicted as spheres colored by their respective element type (carbon, nitrogen, and oxygen atoms in gray, blue, and red, respectively). See Tables S5 and S6 for charges of the hydrogens. The repeating units possess two open valences/connect records each; their net charge is zero.

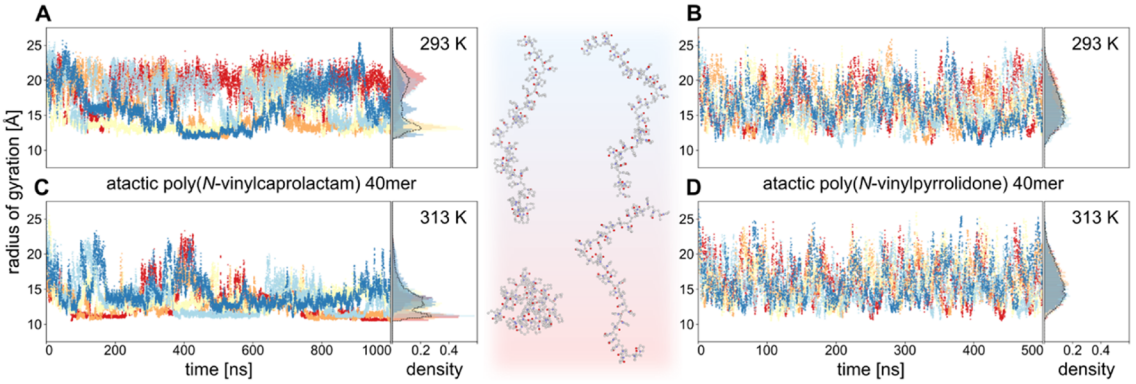

Figure 4. Radius of gyration (R_g) during five NVT·MD simulations of 1 μs length of an atactic PNVCL 40mer (A,C) and during five NVT MD simulations of 500 ns length of an atactic PVP 40mer (B,D) at 293 (A,B) and 313 K (C,D). Corresponding frequency distributions are shown next to the time series in matching color, a frequency distribution of all data is shown as the dashed black line. Sample structures taken from each simulation setup are depicted next to the corresponding simulation.

Parametrized Repeating Units of the Polymers. The modular parametrization of the repeating units of the polymers served to prepare polymers varying in size and tacticity. Doing so allowed us to investigate the influence of these characteristics on the LCST behavior of PVP and PNVCL; the former, although structurally very similar to PNVCL, does not show a distinct LCST behavior in water[6,92] without altering the polymer composition[93,94] or the presence of additives[6,95] and, thus, serves as a negative control. The computed atomic partial charges are similar between respective atoms of the repeating units of PVP and PNVCL (Figure 3). The geometry optimization at the ab initio-level yielded an envelope conformer of the pyrrolidine ring and a chair conformer of the azepane ring, which is in agreement with other quantum-mechanical calculations as well as experimental studies on vinylpyrrolidone derivatives, such as *N*-methylpyrrolidone[96] and vinylcaprolactam.[97,98] The SEM of the atomic partial charges across the set of eight low-energy conformers of PNVCL is small (<0.02*e* for 28 atoms (90%) and <0.04*e* for the remaining three atoms; Figure S6) and within the range of deviations found among other published parameterizations.[35,96] The largest SEM values are found for the backbone carbon atom connected to the nitrogen, the nitrogen itself, and the C_α atom. The partial charges and positions for all atoms of the PNVCL and PVP repeating units are listed in Tables S5 and S6, respectively.

PNVCL 40mer Shows Coil-To-Globule Transition at Elevated Temperature, but PVP 40mer Does Not. To probe whether atomistic MD simulations discriminate between polymers showing or not showing an LCST, we performed five MD simulations of 1 μs length each of an atactic PNVCL 40mer in an explicit solvent at 293 or 313 K, which shows LCST behavior in water at ~315 K (see the Experimental Approach part; as shown below, in the MD simulations, no further compaction arises at 343 K than at 313 K; hence, we restrict our analyses in the next three chapters on 293 and 313 K). Across all five simulations at lower temperature, the radius of gyration, R_G, a measure for the structural compactness of the polymer, frequently fluctuated between values of 12 and 25 Å (Figure 4A); the R_G of the fully extended polymer is 25 Å. This behavior is also shown by trajectories that reside at low R_G for an extended period of the simulation (see, e.g., the trajectory colored blue in Figure 4A). These findings indicate overall that during the simulation time, multiple collapses and extensions of the polymer are sampled. Still, differences between frequency distributions of each trajectory suggest that the simulations have not yet reached equilibrium.

https://dx.doi.org/10.1021/acs.macromol.0c01896
Macromolecules 2020, 53, 9793−9810

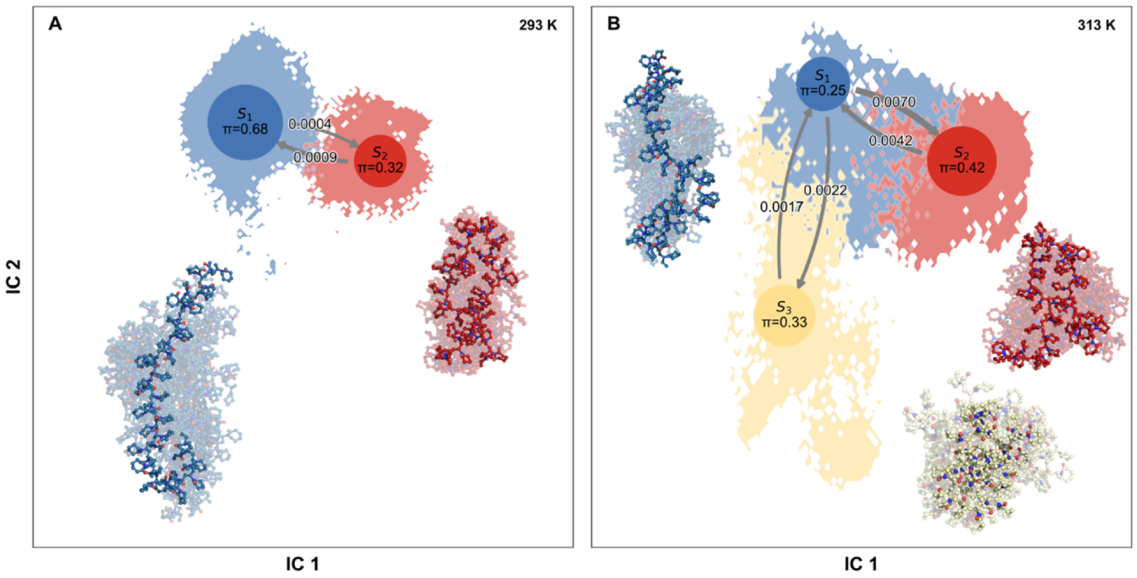

Figure 5. HMMs for an atactic PNVCL 40mer, obtained from NVT MD simulations at 293 (A) and 313 K (B) projected on the same IC space. The probabilities π_i obtained from the stationary distributions π are shown for each state; the size of the arrows between states is scaled by the corresponding transition probability for each HMM, which is given as the label for a lag time of 0.5 ns. For each macrostate, the ten most probable representative structures are shown. The structure with the highest probability in each set is shown in nontransparent representation.

A distinct picture emerges for the PNVCL 40mer at elevated temperature. Although also here fluctuations in R_G are observed (Figure 4B), large R_G values are less frequently sampled, and the likelihood to observe such states decreases with increasing simulation time. As a result, polymer conformations with R_G < 15 Å dominate the frequency distribution, overall indicating a preference for globular polymer states at 313 K.

As a negative control, we also performed MD simulations of atactic PVP 40mers at 293 K or 313 K. PVP does not show LCST behavior in water. At both temperatures, marked fluctuations of R_G between 10 and 24 Å are observed, and extended periods of simulation time with low R_G are not found. Accordingly, the frequency distributions between 292 and 313 K are highly similar. In total, these results indicate the absence of a coil-to-globule transition in PVP 40mer.

To conclude, atomistic MD simulations on the microsecond timescale discriminate between the LCST behavior of the PNVCL 40mer and the absence of thermoresponsiveness of the PVP 40mer.

HMMs Reveal an Additional Compact State for the PNVCL 40mer at the LCST Temperature. To shed light on mechanistic details of the coil-to-globule transition of PNVCL polymers, we constructed HMMs from in total 2 × 5 μs MD simulations of the PNVCL 40mer at 293 and 313 K.

We consider two/three hidden states, because an MSM timescale analysis (Figure S4) showed a timescale separation between the first and second (Figure S4B) and between the second and third (Figure S4D) relaxation timescale for 293 and 313 K, respectively. These findings suggest that for coarse-graining, the dynamics retaining one (293 K) and two (313 K) relaxation timescales and, therefore, two (293 K) and three (313 K) metastable states is a good choice. To obtain a cluster discretization, we first computed the slowest ICs with TICA.[67,69,70] The data were then projected onto the two slowest components, and we considered a cluster discretization into 40 clusters using *k*-means clustering. The number of needed clusters was determined using a variational approach for Markov processes.[99]

Note that we applied the TICA on both data sets at 293 and 313 K together, and each data set was subsequently projected onto the same IC space. Figure 5 shows the constructed HMMs, depicting representative clusters of structures for each hidden state at 293 and 313 K. As the identification of microstates is done on each data set individually, the respective microstates, in principle, could be part of different hidden states. Yet, the hidden states S_1 or S_2 overlap well between both projections, suggesting a similar assignment of similar microstates to the same hidden states at different temperatures.

At 293 K, states S_1 and S_2 comprise PNVCL conformations with R_g of 18.2 ± 0.4 Å (mean ± SEM, as calculated from 50 sample conformations, chosen by probability) and 13.4 ± 0.1 Å, respectively. At 313 K, states S_1 and S_2 have R_g of 14.8 ± 0.4 and 13.2 ± 0.3 Å, respectively. In addition, a further hidden, more compact state S_3 with R_g of 13.0 ± 0.2 Å is revealed. Compared to the rather extended state S_1, S_2 results from folding of the polymer in the middle region, leading to a hairpin shape. By contrast, state S_3 contains conformations where the termini of the polymer chain are located in the center of the globule.

Although hidden states S_1 and S_2 are present at both temperatures, the probabilities of observing a macrostate, π_i, are approximately inverted, going from a ratio of π_{S_1}/π_{S_2} = 68/32 ≈ 2.1 at 293 K to one of 25/42 ≈ 0.60 at 313 K. At 313 K, the probability of S_3, π_{S3}, is 0.33. Even at a temperature ∼15 K below the LCST, globular conformations are present already, such that the transition at the LCST occurs as a shift of existing populations rather than a distinct, abrupt conformational

https://dx.doi.org/10.1021/acs.macromol.0c01896
Macromolecules 2020, 53, 9793−9810

change, as conveyed by other studies.[34,43] The transition probabilities between the hidden states change accordingly. The probabilities shown in Figure 5 are given for a lag time of 0.5 ns. At 293 K, the transition from a globular state to a coil conformation is twice as likely as the coil-to-globule transition. At 313 K, the probabilities for the collapse and unfolding are inverted, similar to the stationary distributions. Moreover, the HMM reveals that the collapse into the new, very compact state S_3 from a coil conformation is approximately as likely as the unfolding process back to an extended conformation.

We used the logarithmic probabilities $\ln(\pi_i)$ obtained from the stationary distributions to compute relative free energies between states S_i (eq 1). Note that such free energy representations generally suffer from an overlap of states in the directions not resolved in this plot, and only serve to provide a qualitative impression.[67] At 293 K, the free energy associated with going from S_1 to S_2 is $\Delta G_{S_1 \rightarrow S_2}$ = 0.44 kcal mol^{-1}, indicating that the polymer collapse is endergonic at this temperature. In turn, at 313 K, $\Delta G_{S_1 \rightarrow S_2}$ = −0.32 kcal mol^{-1}, indicating an exergonic process. If S_3 is considered in addition, S_1 becomes unfavorable with respect to the two collapsed states by 0.63 kcal mol^{-1}. Together, this results in a free energy difference for the coil-to-globule transition at 313 K versus 293 K of $\Delta\Delta G$ = −0.76 kcal mol^{-1} if S_3 is not considered, and −1.07 kcal mol^{-1} if it is considered.

To conclude, the constructed HMMs for the atactic PNVCL 40mer identify two similar, coarse-grained hidden states, comprising PNVCL in coil and globular conformations, at 293 and 313 K, although the ratio of probabilities for the two states inverts between the two temperatures. Furthermore, the HMM for the elevated temperature also unveils another, compact state, which is not observed at lower temperatures. Finally, the HMMs reveal that the free energy difference for the coil-to-globule transition at 313 K versus 293 K is slightly larger than kT.

End-point free energy decomposition for the coil-to-globule transition of PNVCL reveals a delicate enthalpy-entropy compensation that drives the collapse at elevated temperatures. To validate the free energy differences between states S_i revealed by the stationary distribution of the HMMs, we performed end-point free energy computations following the MM-PBSA approach.[74,100] Here, effective energies, comprising molecular mechanics energies, solvation free energies, and configurational entropies, are computed (eqs 2b−4) on the structural ensembles of polymers extracted from the MD trajectories. We investigated the coil-to-globule transition, that is, we compared end-point free energies for polymers with $R_g/R_{g,0} > 0.9$, which are considered a coil, and polymers with $R_g/R_{g,0} < 0.6$, which are considered a globule. Note that the different temperatures pertaining to the respective MD simulations were accommodated in the MM-PBSA postprocessing step by adapting the dielectric constant of water in the PB computations and the temperature entering the statistical mechanics' equations for configurational entropies. The components of the end-point free energies are displayed in Figure 6 and compared component-wise between the two temperatures. This is done because MM-PBSA free energies may be influenced by system-specific features[101] such that a system-specific weighting of configurational entropies with respect to effective energies may be required to obtain accurate free energies.[102]

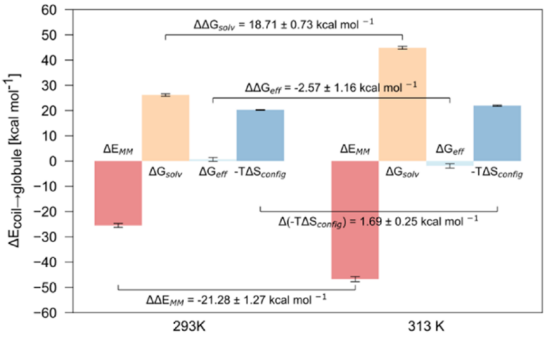

Figure 6. Bar plot showing energetic differences for the coil-to-globule transition of an atactic PNVCL 40mer observed in NVT MD simulations at 293 and 313 K. ΔG_{eff} is decomposed into the difference in gas-phase energy ΔE_{MM} and solvation free energy ΔG_{solv} (eq 2b). Configurational entropies of the polymer are estimated by NMA. The error bars depict the SEM. Differences in energy components between both temperatures, as well as corresponding errors determined according to the laws of error propagation, are depicted below and above the respective horizontal lines.

At both temperatures, $-T\Delta S_{config}$ is positive for the coil-to-globule transition, indicating the loss of configurational entropy in that transition, in agreement with expectations, as the confinement of a polymer into a smaller space is thermodynamically unfavorable because of the reduction of the number of conformational states.[103] The loss is higher by 1.69 ± 0.25 kcal mol^{-1} at 313 K, a result of both a higher number of configurational degrees of freedom of the coil state and the presence of the compact state S_3 at that temperature (Figure S7). In turn, the effective energy ΔG_{eff} becomes more favorable on going from 293 to 313 K by −2.57 ± 1.16 kcal mol^{-1}. This change results from a much more favorable molecular mechanics energy ΔE_{MM} at 313 K, which is partially compensated by a more disfavorable solvation contribution at the higher temperature, indicating that at this temperature the globular polymer state relative to the coil one is even less solvated than at the low temperature (see below for further corroboration). A further decomposition into polar and nonpolar contributions to the solvation free energy reveals that the free energy needed for the endergonic process of cavity formation in the solvent because of polymer insertion (ΔG_{cavity}) is smaller for the globule than the coil (Figure S8), as expected. In contrast, both favorable polar (ΔG_{pol}) and dispersion ($\Delta G_{dispersion}$) contributions to the polymer solvation are smaller for the globule than the coil, which becomes more pronounced at 313 K, outweighing the previously mentioned favorable $\Delta\Delta G_{cavity}$ in both cases (Figure S8). The overall—counterintuitively—too positive nonpolar solvation contribution to the globule formation has been observed likewise in the case of dimer formation of nucleobases.[83] On the other hand, the loss in solvation free energy when going from a coil to a globule is partially compensated by favorable van der Waals (ΔE_{vdW}) and electrostatic (ΔE_{el}) intramolecular interactions at 293 K and even more so at 313 K, that way promoting the globular conformation at a higher temperature (Figure S9). The favorable ΔE_{vdW} is mainly determined by intramolecular interactions of the lactam ring, especially of atoms C_3 and C_4, as revealed by the atomwise decomposition of ΔE_{vdW} (Figure S10), whereas the changes in electrostatic interactions

https://dx.doi.org/10.1021/acs.macromol.0c01896
Macromolecules 2020, 53, 9793−9810

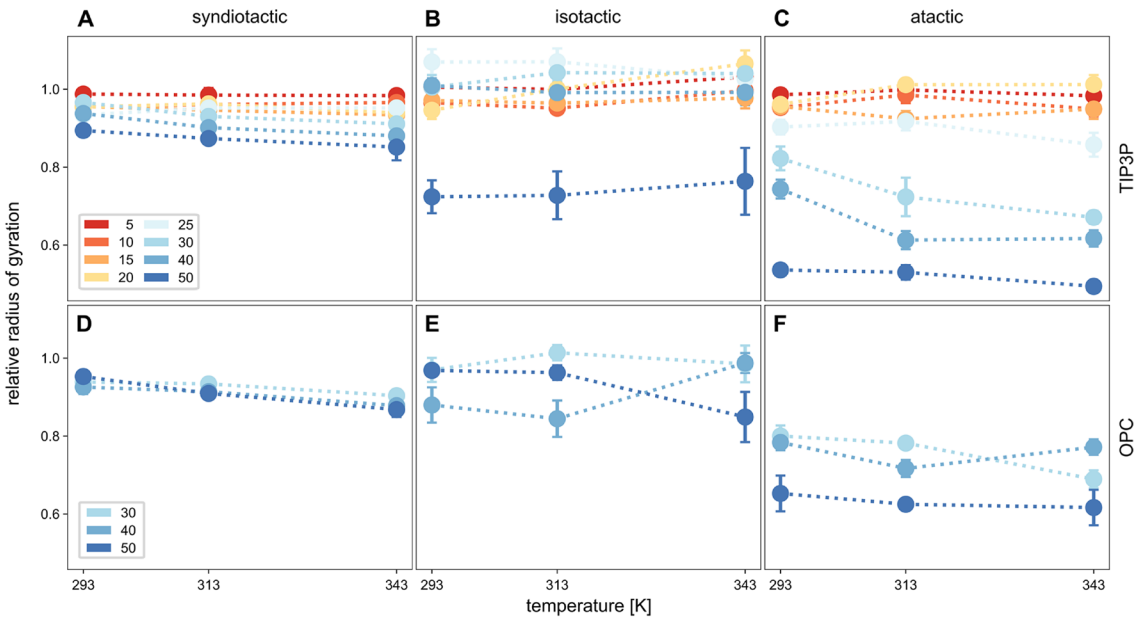

Figure 7. Dependence of the mean relative radius of gyration (R_g/R_{g0}) of PNVCL oligomers with different chain lengths (varying from 5 to 50 repeating units, colored accordingly from red to dark blue) on the temperature (x-axis), tacticity [(A,D) syndiotactic; (B,E) isotactic; and (C,F) atactic PNVCL] and water models [(A–C) TIP3P; (D–F) OPC]. Mean values are calculated from 5 × 1 μs of NVT MD simulations each, the corresponding standard errors of the mean are depicted as error bars.

at higher temperature are mainly caused by the carbonyl carbon and carbonyl oxygen atoms (Figure S11). The more favorable effective energy ($\Delta G_{effective}$) at 313 K compared to 293 K finally overcompensates the loss of configurational entropy (Figure 6). Together, these changes lead to a free energy difference for the coil-to-globule transition at 313 K versus 293 K of $\Delta\Delta G = (-2.57 \pm 1.16$ kcal mol$^{-1}) + (1.69 \pm 0.25$ kcal mol$^{-1}) = -0.88 \pm 1.19$ kcal mol^{-1}, following the laws of error propagation.

To conclude, the MM-PBSA results for the free energy difference for the coil-to-globule transition at 313 K versus 293 K, although having a high uncertainty, are in perfect agreement with $\Delta\Delta G$ computed from the stationary distribution of the HMMs above, lending mutual support to either result. As to the energy decomposition, the MM-PBSA analysis reveals that at a higher temperature, favorable van der Waals and intramolecular electrostatic interactions outbalance the loss in solvation free energy and configurational entropy and, thus, promote the coil-to-globule transition.

Transition Enthalpies Determined from Explicit Solvent MD Simulations. The decomposition of the MM-PBSA free energies allowed us to identify key energetic components of the coil-to-globule transition. However, the determined quantities are difficult to relate to the experimental calorimetric data, because it is not straightforward to further decompose the solvation free energy into enthalpic and entropic parts, overall preventing to separate enthalpic and entropic contributions accurately.[104]

Hence, we adapted a method used to relate potential energies from MD simulations to enthalpies determined by isothermal titration calorimetry (ITC) (eq 7).[89] We computed the coil-to-globule transition enthalpy ΔH_{trans} for a PNVCL 40mer and divided it by 40 to obtain an enthalpy per residue. Figures S12–S14 show that the cumulative running average of the respective potential energies stabilizes during the five NPT MD simulations of 1 μs length. This also applies for the NVT MD simulations (Figure S15), although the average values there depend on the box size of the simulation system (Figure S16). For the isotactic, atactic, and syndiotactic polymers, such ΔH_{trans} values determined from NPT simulations are 1.92 ± 0.56, 1.95 ± 0.51, and 2.17 ± 0.33 kcal mol^{-1}, respectively. The interpolated result considering the mean (equilibrium) volume obtained from the NPT simulations for the NVT simulation of the atactic PNVCL 40mer yields $\Delta H_{trans} = 1.98$ kcal mol^{-1} (Figure S16), agreeing well with the direct results from the NPT simulations.

To conclude, the computed transition enthalpies are within the range of enthalpies reported in the literature (see the Discussion section for a comparison).[34]

Influence of polymer length, tacticity, temperature, concentration, water model, and the chosen MD ensemble on the simulation of the PNVCL collapse. In order to probe the influence of parameters on the observed behavior of the PNVCL, we systematically varied the structures with regard to length and tacticity and tested the effect of temperature and water model used in the MD simulations. Figure 7 summarizes the influence of the tested parameters on the radius of gyration. R_g per se was shown above (Figure 4) to discriminate between the coil and globular conformations of the polymer; here, we divide R_g by R_g of the first frame of the production MD simulation (R_{g0}) as a proxy to normalize the results with respect to the molecular size of the polymers. We consider a polymer mainly collapsed if a relevant decrease ($\geq$0.1) in the mean relative radius of gyration (R_g/R_{g0}) is observed when going from a lower temperature to a higher temperature.

https://dx.doi.org/10.1021/acs.macromol.0c01896
Macromolecules 2020, 53, 9793–9810

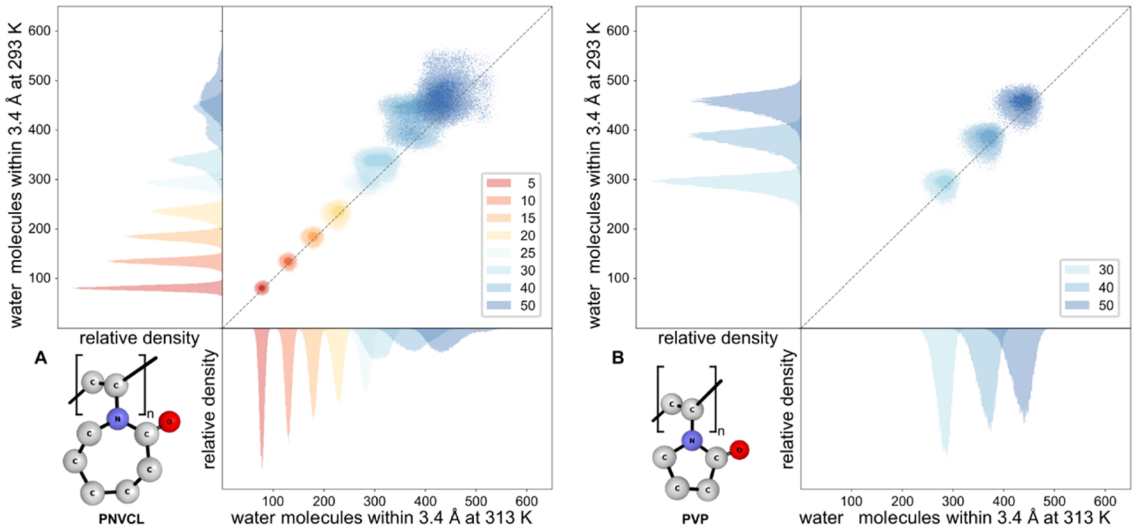

Figure 8. Two-dimensional histogram of the number of water atoms within the first solvation shell, i.e., within a distance of 3.4 Å of atactic PNVCL (A) and PVP (B), for varying polymer sizes (indicated by color) at 293 K (left histogram) and 313 K (bottom histogram) observed in NVT MD simulations.

In general, we do not see a coil-to-globule transition for PNVCL polymers with 5 to 20 repeating units at 313 K (Figure 7A−C), in agreement with experiments (Figure 1). As to MD simulations in TIP3P water, in the case of isotactic polymers, a transition is only observed for the largest polymer tested (50mer) (Figure 7A−C). By contrast, for atactic polymers, coil-to-globule transitions are found for 25, 30, 40, and 50mers, with a pronounced temperature dependence occurring in the case of 30 and 40mers. For the atactic PNVCL 25mer, we do not observe a coil-to-globule transition at 313 K, but at 343 K, which is in agreement with the experimentally observed, higher LCST of approximately 50 °C for small PNVCL oligomers of 2500 g·mol^{-1}. For the atactic PNVCL 50mer, however, we already see a collapse of the polymer at 293 K, which is even more pronounced than the decrease in R_g/R_{g0} observed for the isotactic PNVCL. Considering the structure of CTA Rhodixan A1 used to synthesize the PNVCL polymers and general polymerization mechanism, it can be assumed that synthesized polymers are atactic, as this CTA does not allow for steric control during the polymerization. The experimental results show better agreement with the simulation results of atactic polymers, further supporting this hypothesis. For the future, the synthesis of PNVCL polymers with defined tacticity would help support simulation results. However, to our knowledge, no successful synthesis routes to obtain the syndiotactic or isotactic PNVCL chains have been established yet.

To probe whether the transition of the 50mer at 293 K already is because of a too high polymer concentration in the simulation box, which would entropically disfavor the coil state, similar to what is known as crowding effect in protein folding,[105,106] we repeated the MD simulations with larger box sizes, that way decreasing the polymer concentration from 1 to 0.8 and 0.6 wt %. Note that the polymer concentrations chosen here are well within the ranges of those used to determine LCST behavior experimentally (see the Experimental Approach section). The decrease of polymer concentration showed varying effects on the PNVCL 50mer, depending on the polymer's tacticity. The syndiotactic PNVCL does not show relevant coil-to-globule transitions at any polymer concentration or temperature (Figures S17 and S18). The isotactic PNVCL clearly shifts to the coil with decreasing polymer concentrations at 293 K (Figure S19) and, to a lesser extent, at 313 K (Figure S20). Finally, the atactic PNVCL shows coil-to-globule transitions at all polymer concentrations or temperatures (Figures S21 and S22).

Less consistent results are found if the OPC water model is used instead of the TIP3P water model (Figure 7D−F). First, the OPC model tends to stabilize the coil state. Second, the polymer length dependence of the collapse is less pronounced, which is at variance with experiment.[107] Finally, the temperature dependence of the collapse is less pronounced (see atactic 40mer) or even inverted (see isotactic 40mer). The differences in the SASA of the polymers between MD simulations in TIP3P or OPC water are negligible for syndio- and isotactic polymers except for the isotactic PNVCL 50mer (Figures S23 and S24), concordant with that small changes in R_g do not necessarily change the SASA in the case of hairpin conformations. Only for atactic PNVCL do we observe a marked decrease in R_g/R_{g0} for MD simulations in TIP3P water compared to those in OPC water, which is accompanied by a likewise decrease in the SASA (Figure S25).

Finally, we investigated the influence of the chosen MD ensemble used in our simulations by simulating the iso-, syndio-, and atactic PNVCL 40mer in an NPT ensemble. The distributions of SASA (Figure S26) show nonuniform and overall small differences with respect to the NVT ensemble at both temperatures. Noticeable differences in the distribution of R_g (Figure S27A,B) are because of single trajectories of the corresponding set and, therefore, might indicate still insufficient sampling rather than differences because of the chosen MD ensemble. Upon removal of the respective trajectories, the distributions of R_g also show nonuniform

https://dx.doi.org/10.1021/acs.macromol.0c01896
Macromolecules 2020, 53, 9793−9810

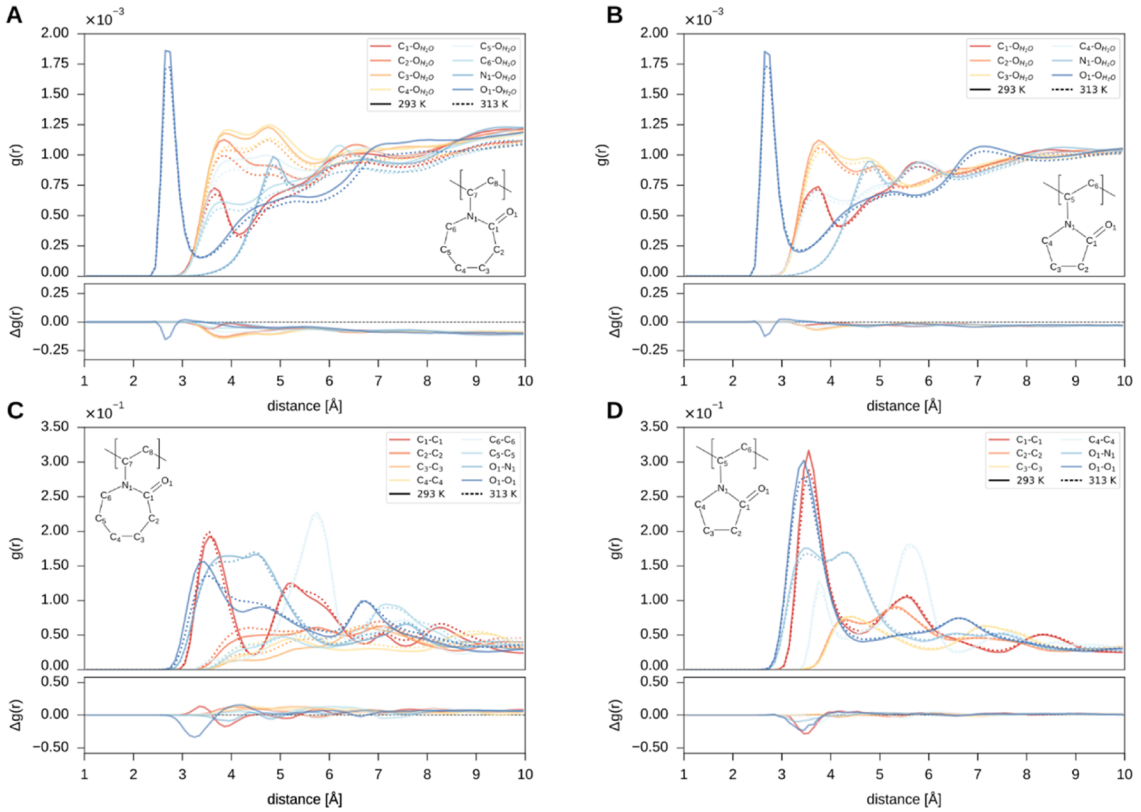

Figure 9. RDFs ($g(r)$) for pairs of ring atoms of PNVCL (A) and PVP (B) and the oxygen of the surrounding water molecules, as well as pairs of atoms between lactam rings of PNVCL (C) and PVP (D). The RDFs were calculated for the atactic PNVCL and PVP 40mers simulated in the NVT ensemble. Atom pairings are depicted in the respective colors, and RDFs calculated from trajectories at 293 and at 313 K are shown as a solid line and a dotted line, respectively. Differences in the RDFs, $\Delta g(r) = g(r)_{313} - g(r)_{293}$, are shown in the separate plots below.

and overall small differences at both temperatures (Figure S27C,D).

To conclude, with increasing temperature and increasing chain lengths, the probability that PNVCL undergoes a coil-to-globule transition increases. Atactic polymers show a much higher tendency to collapse into a globule, whereas for syndiotactic polymers, hardly any temperature effect is observed. As to the influence of the polymer's concentration, because of potential crowding effects, the coil conformation is favored for isotactic polymers with decreasing polymer concentration, whereas the syndiotactic polymer always remains in a coil conformation and the atactic polymer always shows a coil-to-globule transition regardless of the polymer concentration. To examine whether the latter points to an issue of the applied simulation methodology, further experimental validations are necessary; for example, the investigation of short oligomers with known tacticity using DLS. We also note that the concentration we refer to merely reflects the average amount of water surrounding the oligomer in an ideal mixture. This implies that interactions involving water should be adequately reflected; however, further MD simulations of systems comprising multiple oligomers need to be done to probe effects due to interactions between the oligomers. As to the chosen thermodynamic ensembles, the NVT simulations yield virtually identical results with regard to the polymer SASA and R_g as the NPT simulations. As to the chosen water model, the OPC model tends to stabilize the coil state irrespective of polymer length or temperature, which is particularly notable for atactic PNVCL.

Importance of the Lactam Ring Size for the Solvation of PNVCL and PVP at Different Temperatures. The MM-PBSA analysis of the coil-to-globule transition revealed that intramolecular van der Waals and, to a lesser extent, electrostatic interactions generally favor the globular conformation of PNVCL, and more so at 313 K than 293 K (Figure S9), whereas both polar and nonpolar solvation effects favor the coil conformation, again more so at 313 K than 293 K (Figure S8).

To understand this finding, we computed the number of water molecules in the first solvation layer within a distance of 3.4 Å to PNVCL and PVP polymers at 293 and 313 K (Figure 8). First, with increasing polymer size in the case of PNVCL, the first solvation shell becomes more diffuse (as measured by the variance of the marginal distribution: σ_{293K}^2 = 294.5, 819.5, and 1110.2 for 30, 40, and 50 repeating units, respectively); this effect is less pronounced in the case of PVP (σ_{293K}^2 = 199.2, 343.7, and 395.6 for 30, 40, and 50 repeating units, respectively). Second, at 313 K, PNVCL polymers with ≥30 residues are between 1.06- and 1.12-fold less solvated than at 293 K; this effect is less pronounced in the case of PVP

https://dx.doi.org/10.1021/acs.macromol.0c01896
Macromolecules 2020, 53, 9793−9810

(1.04- to 1.05-fold lower solvation). These findings mirror that larger PNCVL polymers at elevated temperature form a globule, thereby expelling water molecules from buried atoms. As the burial involves the polar amide groups, this may explain why polar contributions to the solvation free energy disfavor globule formation (Figure S8). The loss of water molecules in the first solvation shell also mirrors that dispersion interactions between polymer and solvent disfavor the coil-to-globule transition (Figure S8).

To further investigate the interaction of each atom in the polymer's side chain to other polymer atoms or solvent, we computed radial distribution functions (RDFs) of the respective atom pairs (Figure 9). As to interactions with water (Figure 9A,B), as expected, only the carbonyl O shows a pronounced peak at hydrogen bond distance, for both PNVCL and PVP. $\Delta g(r) = g(r)_{313} - g(r)_{293} < 0$ for that interaction indicates a partial desolvation of the carbonyl group at 313 K. Interactions involving the carbonyl C and the amide N are similar in both systems, and $\Delta g(r) \approx 0$ in both cases. A marked difference is seen for C_3 and C_4 of PNCVL versus the equivalent C_3 in PVP in that in the former case at 293 K ∼1.5-fold larger $g(r)$ values are found at ∼4.7 Å, indicating a more pronounced solvation of the hydrophobic PNVCL atoms in the coil conformation. At 313 K, particularly these atoms then lose interactions with waters when forming the globule, as indicated by $\Delta g(r) < 0$ in the range of ∼3.5−5.2 Å, whereas the loss for C_3 in PVP is marginal.

As to interactions between pairs of atoms of different lactam rings (Figure 9C,D), main differences between PNVCL and PVP are found for those of carbonyl Os and carbonyl Cs, respectively: these interactions are ∼1.5-fold more frequent at contact distances for PVP than PNVCL, suggesting more favorable interactions between carbonyl groups[108,109] in the case of PVP that may be a crucial factor in the stabilization of the coil conformation. The loss of such interactions on going from 293 to 313 K is similar for both systems, however. By contrast, interactions between C_3 and C_4, respectively, of PNVCL are more frequent at higher temperatures for PVNCL than between the equivalent C_3 in PVP.

The change of solvation of the polymer backbone within 6 Å plays a minor role in the coil-to-globule transition of PNVCL (Figure S28A), and hardly any role in PVP (Figure S28B). Because of the prevalence of compact forms at 313 K, where many PNVCL repeating units are buried within the globule, we also observe a decreased amount of water molecules within 6 to 10 Å, as the neighborhood of a unit is then occupied by other polymer units rather than water.

To conclude, the additional methylene units in the lactam ring of PNVCL are better accessible for water molecules than the carbon atoms close to the backbone in the coil, but are the ones that show the largest decrease in interactions with water upon globule formation at elevated temperature. By contrast, the change of solvation of the polymer backbone plays a minor role in the coil-to-globule transition. Thus, these carbon atoms do not only contribute a major part to the nonpolar solvation energy but also contribute to more frequent intramolecular interactions at higher temperatures, rendering them essential for the difference in LCST behavior compared to PVP. Inversely, favorable interactions between carbonyl groups are more prevalent in PVP, which may contribute to the stabilization of its coil.

DISCUSSION

We aimed at elucidating the driving forces of the PNVCL coil-to-globule transition at the LCST, in doing so, paying particular attention to the impact of polymer characteristics and to validating our simulation results against the experiment.

The experimental results presented in Figures 1 and 2, and Table 1 indicate that small linear PNVCL chains undergo temperature-induced phase separation, potentially because of the increased intermolecular interactions leading to aggregation and/or increased intramolecular interactions resulting in a coil-to-globule transition. The experimentally determined cloud points for the series of PNVCL samples strongly depend on the molecular weight and concentration of PNVCL. The cloud points decrease if the chain length and concentration of PNVCL increase.

The MD simulations strongly suggest that upon heating of PNVCL, increasing intramolecular interactions between C_3 and C_4 of the caprolactam ring and more favorable cavity formation energies outweigh the loss in polar and hydrophobic solvation, as well as the loss of configurational entropy in the coil-to-globule transition and, thus, may be considered the driving forces of the polymer's collapse at LCST.

Attempts to investigate the LCST behavior of PNVCL by all-atom MD simulations have been comparatively sparse,[35−38] and evaluations of the underlying thermodynamics, which is of great importance to fully understand the coil-to-globule transition, have been even rarer.[38] Moreover, to our knowledge, there is no study in which, in a comparative manner, the behavior of PVP was probed under identical simulation conditions. However, PVP is a valuable negative control, as it does not show distinct LCST behavior while being structurally similar to PNVCL (Figure 3). Here, we demonstrated that all-atom MD simulations with modern force fields are sensitive and specific enough to discriminate between the PNVCL and PVP behaviors (Figure 4). Inversely, the simulation results of the negative control provide additional information on structural determinants that drive the coil-to-globule transition of PNVCL or prevent it as to PVP.

The thermodynamics of the PNVCL coil-to-globule transition was investigated using three independent methods. First, we constructed two HMMs from MD trajectories of 5 μs length of the PNVCL 40mer to characterize conformational states and their transitions at 293 and 313 K (Figure 5). The HMMs support the existence of different intermediate conformations of PNVCL, with varying populations at different temperatures: We observed metastable states comprising extended, but also hairpin-like conformations in MD simulations below the LCST (Figure 5A), where the coil state is favored; above the LCST, a new, very compact third metastable state is present, which comprises conformations similar to the proposed (molten) globule. Overall, the observed shift from the coil via the hairpin-like conformation to the (molten) globule (Figure 5B) with increasing temperature is similar to the transition path Wu and Wang[1] proposed for PNIPAM. For the atactic 40mer, even in the pretransition region, a comparatively high number of repeating units was found to be partially inaccessible to water, because we observed a transition to a hairpin conformation at lower temperatures already, as indicated by DSC[34] and fluorescence[43] experiments. Interestingly, above the LCST, a polymer in a hairpin conformation has to first adopt an open, coil-like

https://dx.doi.org/10.1021/acs.macromol.0c01896
Macromolecules 2020, 53, 9793−9810

conformation to then form the compact globule. Wu et al. reported on the folding pathways of generic, semiflexible polymers, characterized by unspecific beats, proposing several pathways for the coil-to-globule transition of an 80mer, with the direct transition being the most prominent one with ∼40% of occurrence frequency.[110] However, one has to consider that differences in chain length and molecular properties of the building blocks may lead to differences in preferred folding pathways.

Second, to gain insights into the composition of the coil-to-globule transition free energy of PNVCL, we performed MM-PBSA computations for ensembles of coil and globule conformations extracted from MD simulations below and above the LCST (Figure 6). The resulting difference in free energies for the transitions at 293 and 313 K matched well with the difference in free energies calculated using the constructed HMMs, leading to mutual support of either method. The energetic decomposition of the free energy shows that van der Waals and intramolecular electrostatic interactions outbalance the loss in solvation free energy and configurational entropy and, thus, promote the coil-to-globule transition. These results are in line with structural analysis of both PNVCL and PVP in terms of RDFs, in that the additional methylene units in the lactam ring of PNVCL are better accessible for water molecules than the carbon atoms close to the backbone in the coil, but are the ones that show the largest decrease in interactions with water upon globule formation at elevated temperature (Figure 9). These carbon atoms also contribute to more frequent intramolecular interactions at higher temperatures, overall rendering them essential for the difference in LCST behavior compared to PVP. Inversely, favorable interactions between carbonyl groups are more prevalent in PVP, which may contribute to the stabilization of its coil.

Third, to relate the computed energies to experimentally accessible quantities such as transition enthalpies determined by DSC and NMR, we adapted a method used to correlate potential energies from MD simulations using explicit solvent with ITC experiments.[89] The computed transition enthalpy of ∼2 kcal mol^{-1} per repeating unit is similar to enthalpies reported by Dubovik et al.[34] Note, though, that the experimental data of transition enthalpies of PNVCL cover a broad range, that is, transition enthalpies determined by (HS)-DSC or NMR range from ∼0.5 kcal mol^{-1},[7] over ∼1 kcal mol^{-1}[14,31,32] and ∼1.5 kcal mol^{-1}[32] to ∼2.0 kcal mol^{-1} and ∼2.6 kcal mol^{-1}[34] per repeating unit for PNVCL polymers of likely varying molecular weights, concentrations, and tacticity. Interestingly, Lozinsky et al.[33] explained differences in transition enthalpies with differences in polymer−polymer interactions and proposed that mainly syndiotactic polymers show higher transition enthalpies than polymers with isotactic regions. This suggestion is confirmed by the trend of transition enthalpies found by us.

The exact estimation of (free) energies of the coil-to-globule transition using MD simulations remains challenging because of multiple factors, such as unknown, incomplete, or imprecisely determined properties of PNVCL, including the polymer's tacticity or molecular weight (distribution). Still, the presented methods performed on full-length PNVCL 40mer help to gain useful insights into the energetics of the coil-to-globule transition as well as complement and validate each other. To our knowledge, this is the first time that computations of (free) energies of the coil-to-globule transition of PNVCL have been performed. Previously, Mochizuki presented a detailed potential of the mean force study, albeit performed only on two isolated PNVCL monomers.[38] That way, the results cannot take into account potential influences because of the attachment of the sidechains to a backbone, and it is also not clear that the energetics of monomer interactions remains constant irrespective of whether monomers in the middle of the chain or at its ends interact. Unsurprisingly, our results differ somewhat from Mochizuki's results,[38] because we do observe a significant change in the solvation shell of PNVCL (Figure 8) upon heating, which is in agreement with absorption millimeter-wave measurements.[111] Furthermore, Mochizuki identified increased caprolactam−caprolactam interactions because of reduced water-mediated repulsion as the driving force for the collapse upon heating. By contrast, we identified a delicate balance of several factors as a driving force for the transition: favorable intramolecular polymer interactions overcompensate the disfavorable loss in solvation free energy and configurational entropy. While the latter term cannot be accounted for in Mochizuki's work, both our studies agree on that a favorable cavity formation free energy accompanies globule formation. Finally, note that in both Mochizuki's work and ours, the impact of other polymer chains on the energetics of the coil-to-globule transition is not taken into account.

Besides temperature, we systematically tested the influence of the polymer's length, concentration, and tacticity, of the thermodynamic ensemble, and of the water model on the coil-to-globule transition of PNVCL during MD simulations. For PNVCL, the influence of the tacticity on the coil-to-globule transition had not been assessed in MD simulations so far and has also been rarely considered in experimental studies.[33,112] Of all tested parameters, the tacticity was shown to be most important with respect to the conformational space explored by the polymer: we observed a collapse at elevated temperatures for atactic and, partially, for isotactic PNVCL, but not for syndiotactic PNVCL (Figure 7). By contrast, for PNIPAM, the influence of the tacticity on the collapse of the polymer during MD simulations was less pronounced.[113] Our MD simulations using TIP3P water reflected PNVCL's type I LCST behavior, that is, that the LCST decreases with an increasing molecular weight of the polymer[5] (Figure 7). By contrast, MD simulations of PNCVL polymers in OPC water did not show this trend, although OPC water is generally considered to better represent bulk water characteristics than TIP3P.[49] The OPC water model presumably overestimates polar interactions with the polymer, that way favoring the coil conformation and hampering the transition to the globular conformation. Additionally, all water models differ in their standard molar entropy,[114] which may also influence the delicate enthalpy−entropy compensation underlying the coil-to-globule transition. We also note that the potentially increasing influence of the polymer end-groups with decreasing polymer size may not be adequately reflected using methyl-capped PNVCL model structures. Notably, our MD simulations are apparently sensitive enough to detect an influence of polymer concentration on the transition behavior, particularly for isotactic PNVCL (Figure S19 and S20). Finally, we demonstrated that the thermodynamic ensemble had little, if at all, influence on the coil-to-globule transition (Figure S26 and S27), given a sufficiently long volume adjustment time prior to NVT production simulations.

While the present study, to our knowledge, provides the most detailed assessment of the coil-to-globule transition of

https://dx.doi.org/10.1021/acs.macromol.0c01896
Macromolecules 2020, 53, 9793−9810

PNVCL polymers at the atomistic level, further (computational) work is required to fully understand the underlying molecular processes. Methods used for energy decomposition are inherently limited by fundamental[115−117] and, depending on the approach, technical reasons. For example, a further decomposition of the solvation free energy into an enthalpic and entropic part using MM-PBSA is not straightforward, such that we cannot tell whether a major proportion of the solvation free energy is determined by the losses in translational and rotational entropy of water molecules when forming solvent cages, which is sometimes considered to be the major cause for the hydrophobic effect.[118−120] Furthermore, we investigated comparatively small and single PNVCL oligomers, while synthesized polymers often vary in their molecular size and dispersity. We also neglected the influence of ions here, although, in the case of applications where PNVCL is used as a carrier, ions may play an important role in the coil-to-globule transition. Finally, despite the extensive MD simulations presented here, the construction of more detailed HMMs and the resolution of more metastable states during the coil-to-globule transition may benefit from further increased sampling.

In summary, our combined MD simulations and experimental study strongly suggest that upon heating PNVCL, increasing intramolecular interactions between C_3 and C_4 of the caprolactam ring and more favorable cavity formation energies outweigh the loss in polar and hydrophobic solvation, as well as the loss of configurational entropy in the coil-to-globule transition and, thus, may be considered the driving forces of the polymer's collapse at LCST. We paid particular attention to validating our MD simulations and (free) energy computations internally as well as against the experimental data, and to probe the impact on polymer properties and simulation details on the outcome. Molecular simulations and free energy computations of such a type should be applicable in the future to scrutinize at the atomistic level the impact of ions and polymer dispersity on the coil-to-globule transition of PNVCL, and the LCST behavior of other polymers.

■ ASSOCIATED CONTENT

Supporting Information

The Supporting Information is available free of charge at https://pubs.acs.org/doi/10.1021/acs.macromol.0c01896.

Additional information on the simulation data, including the evaluation and assessment of the HMMs, R_g, and SASA results and detailed information on the energy decomposition of the MM-PBSA results. MD parameters of the PNVCL and PNVP repeating units are provided as Amber library files and geometries used for electronic structure calculations are provided as Gaussian input files including Cartesian coordinates. Example of the experimental determination of the cloud point of PNVCL via UV−vis spectroscopy (PDF)

Simulation details (ZIP)

■ AUTHOR INFORMATION

Corresponding Author

Holger Gohlke − *Institute for Pharmaceutical and Medicinal Chemistry, Heinrich Heine University Düsseldorf, 40225 Düsseldorf, Germany; Bioeconomy Science Center (BioSC), Forschungszentrum Jülich, 52425 Jülich, Germany; John von Neumann Institute for Computing (NIC), Jülich Supercomputing Centre (JSC), Institute of Biological Information Processing (IBI-7: Structural Biochemistry), Forschungszentrum Jülich GmbH, 52425 Jülich, Germany;* orcid.org/0000-0001-8613-1447; Phone: (+49) 211 81 13662; Email: gohlke@uni-duesseldorf.de; Fax: (+49) 211 81 13847

Authors

Jonas Dittrich − *Institute for Pharmaceutical and Medicinal Chemistry, Heinrich Heine University Düsseldorf, 40225 Düsseldorf, Germany; Bioeconomy Science Center (BioSC), Forschungszentrum Jülich, 52425 Jülich, Germany;* orcid.org/0000-0003-2377-2268

Michael Kather − *DWI-Leibniz-Institute for Interactive Materials and Institute of Technical and Macromolecular Chemistry, RWTH Aachen University, 52056 Aachen, Germany*

Anna Holzberger − *DWI-Leibniz-Institute for Interactive Materials and Institute of Technical and Macromolecular Chemistry, RWTH Aachen University, 52056 Aachen, Germany*

Andrij Pich − *Bioeconomy Science Center (BioSC), Forschungszentrum Jülich, 52425 Jülich, Germany; DWI-Leibniz-Institute for Interactive Materials and Institute of Technical and Macromolecular Chemistry, RWTH Aachen University, 52056 Aachen, Germany;* orcid.org/0000-0003-1825-7798

Complete contact information is available at: https://pubs.acs.org/10.1021/acs.macromol.0c01896

Author Contributions

J.D. performed and analyzed the computational studies and wrote the manuscript; M.K. performed the experiments, analyses, and wrote part of the manuscript; A.H. worked on the experimental project and wrote part of the manuscript; A.P. supervised the experimental project and wrote part of the manuscript; H.G. conceived the study, supervised and managed the project, and wrote the manuscript. All authors have given approval to the final version of the manuscript.

Funding

This research is part of scientific activities of the Bioeconomy Science Center, which were financially supported by the Ministry of Innovation, Science, and Research of the German Federal State of North Rhine-Westphalia (MIWF) within the framework of the NRW Strategy Project BioSC (no. 313/323-400-00213) (funds to HG and AP within the FocusLab greenRelease). The financial support of the Deutsche Forschungsgemeinschaft (DFG) within project B4 of the Collaborative Research Center SFB 985 "Functional Microgels and Microgel Systems" is gratefully acknowledged.

Notes

The authors declare no competing financial interest.

■ ACKNOWLEDGMENTS

We gratefully acknowledge the computational support provided by the "Center for Information and Media Technology" (ZIM) at the Heinrich Heine University Düsseldorf and the computing time provided by the John von Neumann Institute for Computing (NIC) on the supercomputer JUWELS at Jülich Supercomputing Centre (JSC) (user IDs: HKF7, project "microgels"). We are grateful to OpenEye for an academic license. We gratefully acknowledge insightful comments and discussions with Dr. Denis

https://dx.doi.org/10.1021/acs.macromol.0c01896
Macromolecules 2020, 53, 9793−9810

Schmidt. We thank Prof. Mathias Destarac for providing the synthesis procedure for Rhodixan A1. Furthermore, we gratefully acknowledge Jonathan Tellers and Hadi Rastegar for supporting the synthesis and characterization of the linear PNVCL polymers.

■ REFERENCES

(1) Wu, C.; Wang, X. Globule-to-Coil Transition of a Single Homopolymer Chain in Solution. *Phys. Rev. Lett.* **1998**, *80*, 4092−4094.
(2) Zhang, Q.; Weber, C.; Schubert, U. S.; Hoogenboom, R. Thermoresponsive polymers with lower critical solution temperature: from fundamental aspects and measuring techniques to recommended turbidimetry conditions. *Mater. Horiz.* **2017**, *4*, 109−116.
(3) Tager, A. A.; Safronov, A. P.; Sharina, S. V.; Galayev, I. Y. Thermodynamics of aqueous solutions of polyvinylcaprolactam. *Polym. Sci. USSR* **1990**, *32*, 469−474.
(4) Aseyev, V.; Hietala, S.; Laukkanen, A.; Nuopponen, M.; Confortini, O.; Du Prez, F. E.; Tenhu, H. Mesoglobules of thermoresponsive polymers in dilute aqueous solutions above the LCST. *Polymer* **2005**, *46*, 7118−7131.
(5) Meeussen, F.; Nies, E.; Berghmans, H.; Verbrugghe, S.; Goethals, E.; Du Prez, F. Phase behaviour of poly(N-vinyl caprolactam) in water. *Polymer* **2000**, *41*, 8597−8602.
(6) Maeda, Y.; Nakamura, T.; Ikeda, I. Hydration and Phase Behavior of Poly(N-vinylcaprolactam) and Poly(N-vinylpyrrolidone) in Water. *Macromolecules* **2002**, *35*, 217−222.
(7) Mikheeva, L. M.; Grinberg, N. V.; Mashkevich, A. Y.; Grinberg, V. Y.; Thanh, L. T. M.; Makhaeva, E. E.; Khokhlov, A. R. Microcalorimetric Study of Thermal Cooperative Transitions in Poly(N-vinylcaprolactam) Hydrogels. *Macromolecules* **1997**, *30*, 2693−2699.
(8) Narang, P.; de Oliveira, T. E.; Venkatesu, P.; Netz, P. A. The role of osmolytes in the temperature-triggered conformational transition of poly(N-vinylcaprolactam): an experimental and computational study. *Phys. Chem. Chem. Phys.* **2020**, *22*, 5301−5313.
(9) Meurer, R. A.; Kemper, S.; Knopp, S.; Eichert, T.; Jakob, F.; Goldbach, H. E.; Schwaneberg, U.; Pich, A. Biofunctional Microgel-Based Fertilizers for Controlled Foliar Delivery of Nutrients to Plants. *Angew. Chem., Int. Ed.* **2017**, *56*, 7380−7386.
(10) Zhang, J.; Xu, S.; Kumacheva, E. Polymer Microgels: Reactors for Semiconductor, Metal, and Magnetic Nanoparticles. *J. Am. Chem. Soc.* **2004**, *126*, 7908−7914.
(11) Agrawal, G.; Schürings, M. P.; van Rijn, P.; Pich, A. Formation of catalytically active gold−polymer microgel hybrids via a controlled in situ reductive process. *J. Mater. Chem. A* **2013**, *1*, 13244−13251.
(12) Prabaharan, M.; Grailer, J. J.; Steeber, D. A.; Gong, S. Stimuli-Responsive Chitosan-graft-Poly(N-vinylcaprolactam) as a Promising Material for Controlled Hydrophobic Drug Delivery. *Macromol. Biosci.* **2008**, *8*, 843−851.
(13) Indulekha, S.; Arunkumar, P.; Bahadur, D.; Srivastava, R. Thermoresponsive polymeric gel as an on-demand transdermal drug delivery system for pain management. *Mater. Sci. Eng., C* **2016**, *62*, 113−122.
(14) Sanoj Rejinold, N.; Muthunarayanan, M.; Divyarani, V. V.; Sreerekha, P. R.; Chennazhi, K. P.; Nair, S. V.; Tamura, H.; Jayakumar, R. Curcumin-loaded biocompatible thermoresponsive polymeric nanoparticles for cancer drug delivery. *J. Colloid Interface Sci.* **2011**, *360*, 39−51.
(15) Li, X.; Zhong, H.; Li, X.; Jia, F.; Cheng, Z.; Zhang, L.; Yin, J.; An, L.; Guo, L. Synthesis of attapulgite/N-isopropylacrylamide and its use in drug release. *Mater. Sci. Eng., C* **2014**, *45*, 170−175.
(16) Oh, J. K.; Drumright, R.; Siegwart, D. J.; Matyjaszewski, K. The development of microgels/nanogels for drug delivery applications. *Prog. Polym. Sci.* **2008**, *33*, 448−477.
(17) Wang, Y.; Nie, J.; Chang, B.; Sun, Y.; Yang, W. Poly(vinylcaprolactam)-Based Biodegradable Multiresponsive Microgels for Drug Delivery. *Biomacromolecules* **2013**, *14*, 3034−3046.
(18) Arvidsson, P.; Ivanov, A. E.; Galaev, I. Y.; Mattiasson, B. Polymer versus monomer as displacer in immobilized metal affinity chromatography. *J. Chromatogr. B* **2001**, *753*, 279−285.
(19) Huang, R.; Kostanski, L. K.; Filipe, C. D. M.; Ghosh, R. Environment-responsive hydrogel-based ultrafiltration membranes for protein bioseparation. *J. Membr. Sci.* **2009**, *336*, 42−49.
(20) Beletskaya, I. P.; Khokhlov, A. R.; Tarasenko, E. A.; Tyurin, V. S. Palladium supported on poly(N-vinylimidazole) or poly(N-vinylimidazole-co-N-vinylcaprolactam) as a new recyclable catalyst for the Mizoroki−Heck reaction. *J. Organomet. Chem.* **2007**, *692*, 4402−4406.
(21) Beletskaya, I. P.; Selivanova, A. V.; Tyurin, V. S.; Matveev, V. V.; Khokhlov, A. R. Palladium nanoparticles stabilized by a copolymer of N-vinylimidazole with N-vinylcaprolactam as efficient recyclable catalyst of aromatic cyanation. *Russ. J. Org. Chem.* **2010**, *46*, 157−161.
(22) Wong, J. E.; Krishnakumar Gaharwar, A.; Müller-Schulte, D.; Bahadur, D.; Richtering, W. Layer-by-layer assembly of a magnetic nanoparticle shell on a thermoresponsive microgel core. *J. Magn. Magn. Mater.* **2007**, *311*, 219−223.
(23) Lozinsky, V. I.; Simenel, I. A.; Kulakova, V. K.; Kurskaya, E. A.; Babushkina, T. A.; Klimova, T. P.; Burova, T. V.; Dubovik, A. S.; Galaev, I. Y.; Mattiasson, B.; Khokhlov, A. R. Synthesis and Studies of N-Vinylcaprolactam/N-Vinylimidazole Copolymers that Exhibit the "Proteinlike" Behavior in Aqueous Media. *Macromolecules* **2003**, *36*, 7308−7323.
(24) Wang, X.; Wu, C. Light-Scattering Study of Coil-to-Globule Transition of a Poly(N-isopropylacrylamide) Chain in Deuterated Water. *Macromolecules* **1999**, *32*, 4299−4301.
(25) Graziano, G. On the temperature-induced coil to globule transition of poly-N-isopropylacrylamide in dilute aqueous solutions. *Int. J. Biol. Macromol.* **2000**, *27*, 89−97.
(26) Tavagnacco, L.; Zaccarelli, E.; Chiessi, E. On the molecular origin of the cooperative coil-to-globule transition of poly(N-isopropylacrylamide) in water. *Phys. Chem. Chem. Phys.* **2018**, *20*, 9997−10010.
(27) Budkov, Y. A.; Kolesnikov, A. L. Statistical description of co-nonsolvency suppression at high pressures. *Soft Matter* **2017**, *13*, 8362−8367.
(28) Budkov, Y. A.; Kolesnikov, A. L. Models of the Conformational Behavior of Polymers in Mixed Solvents. *Polym. Sci., Ser. C* **2018**, *60*, 148−159.
(29) Vihola, H.; Laukkanen, A.; Valtola, L.; Tenhu, H.; Hirvonen, J. Cytotoxicity of thermosensitive polymers poly(N-isopropylacrylamide), poly(N-vinylcaprolactam) and amphiphilically modified poly(N-vinylcaprolactam). *Biomaterials* **2005**, *26*, 3055−3064.
(30) Sun, S.; Wu, P. Infrared Spectroscopic Insight into Hydration Behavior of Poly(N-vinylcaprolactam) in Water. *J. Phys. Chem. B* **2011**, *115*, 11609−11618.
(31) Laukkanen, A.; Valtola, L.; Winnik, F. M.; Tenhu, H. Formation of Colloidally Stable Phase Separated Poly(N-vinylcaprolactam) in Water: A Study by Dynamic Light Scattering, Microcalorimetry, and Pressure Perturbation Calorimetry. *Macromolecules* **2004**, *37*, 2268−2274.
(32) Spěváček, J.; Dybal, J.; Starovoytova, L.; Zhigunov, A.; Sedláková, Z. Temperature-induced phase separation and hydration in poly(N-vinylcaprolactam) aqueous solutions: a study by NMR and IR spectroscopy, SAXS, and quantum-chemical calculations. *Soft Matter* **2012**, *8*, 6110−6119.
(33) Lozinsky, V. I.; Simenel, I. A.; Kurskaya, E. A.; Kulakova, V. K.; Galaev, I. Y.; Mattiasson, B.; Grinberg, V. Y.; Grinberg, N. V.; Khokhlov, A. R. Synthesis of N-vinylcaprolactam polymers in water-containing media. *Polymer* **2000**, *41*, 6507−6518.
(34) Dubovik, A. S.; Makhaeva, E. E.; Grinberg, V. Y.; Khokhlov, A. R. Energetics of Cooperative Transitions of N-Vinylcaprolactam Polymers in Aqueous Solutions. *Macromol. Chem. Phys.* **2005**, *206*, 915−928.
(35) Sun, X.; Qian, X. Atomistic Molecular Dynamics Simulations of the Lower Critical Solution Temperature Transition of Poly(N-

https://dx.doi.org/10.1021/acs.macromol.0c01896
Macromolecules 2020, 53, 9793−9810

vinylcaprolactam) in Aqueous Solutions. *J. Phys. Chem. B* **2019**, *123*, 4986−4995.
(36) Zhelavskyi, O. S.; Kyrychenko, A. Atomistic molecular dynamics simulations of the LCST conformational transition in poly(N-vinylcaprolactam) in water. *J. Mol. Graphics Modell.* **2019**, *90*, 51−58.
(37) Camara, M.; Liao, H.; Xu, J.; Zhang, J.; Swai, R. Molecular dynamics study of the intercalation and conformational transition of poly (N-vinyl caprolactam), a thermosensitive polymer in hydrated Na-montmorillonite. *Polymer* **2019**, *179*, 121718.
(38) Mochizuki, K. Reduction of water-mediated repulsion drives poly(N-vinylcaprolactam) collapse upon heating. *Phys. Chem. Chem. Phys.* **2020**, *22*, 1053−1060.
(39) Condon, J. E.; Martin, T. B.; Jayaraman, A. Effect of conjugation on phase transitions in thermoresponsive polymers: an atomistic and coarse-grained simulation study. *Soft Matter* **2017**, *13*, 2907−2918.
(40) Zhang, C.; Peng, H.; Puttick, S.; Reid, J.; Bernardi, S.; Searles, D. J.; Whittaker, A. K. Conformation of Hydrophobically Modified Thermoresponsive Poly(OEGMA-co-TFEA) across the LCST Revealed by NMR and Molecular Dynamics Studies. *Macromolecules* **2015**, *48*, 3310−3317.
(41) de Oliveira, T. E.; Marques, C. M.; Netz, P. A. Molecular dynamics study of the LCST transition in aqueous poly(N-n-propylacrylamide). *Phys. Chem. Chem. Phys.* **2018**, *20*, 10100−10107.
(42) Koochaki, A.; Moghbeli, M. R.; Javan Nikkhah, S. Coil-to-globule transition of thermo-responsive γ-substituted poly (ε-caprolactone) in water: A molecular dynamics simulation study. *Curr. Appl. Phys.* **2018**, *18*, 1313−1319.
(43) Chee, C. K.; Rimmer, S.; Soutar, I.; Swanson, L. Fluorescence investigations of the conformational behaviour of Poly(N-vinylcaprolactam). *React. Funct. Polym.* **2006**, *66*, 1−11.
(44) Dalgicdir, C.; Rodríguez-Ropero, F.; van der Vegt, N. F. A. Computational Calorimetry of PNIPAM Cononsolvency in Water/Methanol Mixtures. *J. Phys. Chem. B* **2017**, *121*, 7741−7748.
(45) García, E. J.; Hasse, H. Studying equilibria of polymers in solution by direct molecular dynamics simulations: poly(N-isopropylacrylamide) in water as a test case. *Eur. Phys. J.: Spec. Top.* **2019**, *227*, 1547−1558.
(46) Beija, M.; Marty, J.-D.; Destarac, M. Thermoresponsive poly(N-vinyl caprolactam)-coated gold nanoparticles: sharp reversible response and easy tunability. *Chem. Commun.* **2011**, *47*, 2826−2828.
(47) Wan, D.; Zhou, Q.; Pu, H.; Yang, G. Controlled radical polymerization of N-vinylcaprolactam mediated by xanthate or dithiocarbamate. *J. Polym. Sci., Part A: Polym. Chem.* **2008**, *46*, 3756−3765.
(48) Jorgensen, W. L.; Chandrasekhar, J.; Madura, J. D.; Impey, R. W.; Klein, M. L. Comparison of simple potential functions for simulating liquid water. *J. Chem. Phys.* **1983**, *79*, 926−935.
(49) Izadi, S.; Anandakrishnan, R.; Onufriev, A. V. Building Water Models: A Different Approach. *J. Phys. Chem. Lett.* **2014**, *5*, 3863−3871.
(50) Case, D. A.; Cheatham, T. E., III; Darden, T.; Gohlke, H.; Luo, R.; Merz, K. M., Jr.; Onufriev, A.; Simmerling, C.; Wang, B.; Woods, R. J. The Amber biomolecular simulation programs. *J. Comput. Chem.* **2005**, *26*, 1668−1688.
(51) Case, D. A.; Ben-Shalom, I. Y.; Brozell, S. R.; Cerutti, D. S.; Cheatham, T. E., III; Cruzeiro, V. W. D.; Darden, T. A.; Duke, R. E.; Ghoreishi, D.; Gilson, M. K.; Gohlke, H.; Goetz, A. W.; Greene, D.; Harris, R.; Homeyer, N.; Izadi, S.; Kovalenko, A.; Kurtzman, T.; Lee, T. S.; LeGrand, S.; Li, P.; Lin, C.; Liu, J.; Luchko, T.; Luo, R.; Mermelstein, D. J.; Merz, K. M.; Miao, Y.; Monard, G.; Nguyen, C.; Nguyen, H.; Omelyan, I.; Onufriev, A.; Pan, F.; Qi, R.; Roe, D. R.; Roitberg, A.; Sagui, C.; Schott-Verdugo, S.; Shen, J.; Simmerling, C. L.; Smith, J.; Salomon-Ferrer, R.; Swails, J.; Walker, R. C.; Wang, J.; Wei, H.; Wolf, R. M.; Wu, X.; Xiao, L.; York, D. M.; Kollman, P. A. *AMBER 2018*; University of California: San Francisco, 2018.
(52) Salomon-Ferrer, R.; Götz, A. W.; Poole, D.; Le Grand, S.; Walker, R. C. Routine Microsecond Molecular Dynamics Simulations with AMBER on GPUs. 2. Explicit Solvent Particle Mesh Ewald. *J. Chem. Theory Comput.* **2013**, *9*, 3878−3888.
(53) Le Grand, S.; Götz, A. W.; Walker, R. C. SPFP: Speed without compromise—A mixed precision model for GPU accelerated molecular dynamics simulations. *Comput. Phys. Commun.* **2013**, *184*, 374−380.
(54) Pfleger, C.; Minges, A.; Boehm, M.; McClendon, C. L.; Torella, R.; Gohlke, H. Ensemble- and Rigidity Theory-Based Perturbation Approach To Analyze Dynamic Allostery. *J. Chem. Theory Comput.* **2017**, *13*, 6343−6357.
(55) Wang, J.; Wolf, R. M.; Caldwell, J. W.; Kollman, P. A.; Case, D. A. Development and testing of a general amber force field. *J. Comput. Chem.* **2004**, *25*, 1157−1174.
(56) Darden, T.; York, D.; Pedersen, L. Particle mesh Ewald: An N·log(N) method for Ewald sums in large systems. *J. Chem. Phys.* **1993**, *98*, 10089−10092.
(57) Ryckaert, J.-P.; Ciccotti, G.; Berendsen, H. J. C. Numerical integration of the cartesian equations of motion of a system with constraints: molecular dynamics of n-alkanes. *J. Comput. Phys.* **1977**, *23*, 327−341.
(58) Berendsen, H. J. C.; Postma, J. P. M.; van Gunsteren, W. F.; DiNola, A.; Haak, J. R. Molecular dynamics with coupling to an external bath. *J. Chem. Phys.* **1984**, *81*, 3684−3690.
(59) Quigley, D.; Probert, M. I. J. Langevin dynamics in constant pressure extended systems. *J. Chem. Phys.* **2004**, *120*, 11432−11441.
(60) Roe, D. R.; Cheatham, T. E. PTRAJ and CPPTRAJ: Software for Processing and Analysis of Molecular Dynamics Trajectory Data. *J. Chem. Theory Comput.* **2013**, *9*, 3084−3095.
(61) Bayly, C. I.; Cieplak, P.; Cornell, W.; Kollman, P. A. A well-behaved electrostatic potential based method using charge restraints for deriving atomic charges: the RESP model. *J. Phys. Chem.* **1993**, *97*, 10269−10280.
(62) Hawkins, P. C. D.; Skillman, A. G.; Warren, G. L.; Ellingson, B. A.; Stahl, M. T. Conformer Generation with OMEGA: Algorithm and Validation Using High Quality Structures from the Protein Databank and Cambridge Structural Database. *J. Chem. Inf. Model.* **2010**, *50*, 572−584.
(63) Hawkins, P. C. D.; Nicholls, A. Conformer Generation with OMEGA: Learning from the Data Set and the Analysis of Failures. *J. Chem. Inf. Model.* **2012**, *52*, 2919−2936.
(64) Frisch, M. J.; Trucks, G. W.; Schlegel, H. B.; Scuseria, G. E.; Robb, M. A.; Cheeseman, J. R.; Scalmani, G.; Barone, V.; Mennucci, B.; Petersson, G. A.; Nakatsuji, H.; Caricato, M.; Li, X.; Hratchian, H. P.; Izmaylov, A. F.; Bloino, J.; Zheng, G.; Sonnenberg, J. L.; Hada, M.; Ehara, M.; Toyota, K.; Fukuda, R.; Hasegawa, J.; Ishida, M.; Nakajima, T.; Honda, Y.; Kitao, O.; Nakai, H.; Vreven, T.; Montgomery, J. A., Jr.; Peralta, J. E.; Ogliaro, F.; Bearpark, M.; Heyd, J. J.; Brothers, E.; Kudin, K. N.; Staroverov, V. N.; Kobayashi, R.; Normand, J.; Raghavachari, K.; Rendell, A.; Burant, J. C.; Iyengar, S. S.; Tomasi, J.; Cossi, M.; Rega, N.; Millam, J. M.; Klene, M.; Knox, J. E.; Cross, J. B.; Bakken, V.; Adamo, C.; Jaramillo, J.; Gomperts, R.; Stratmann, R. E.; Yazyev, O.; Austin, A. J.; Cammi, R.; Pomelli, C.; Ochterski, J. W.; Martin, R. L.; Morokuma, K.; Zakrzewski, V. G.; Voth, G. A.; Salvador, P.; Dannenberg, J. J.; Dapprich, S.; Daniels, A. D.; Farkas, Ö.; Foresman, J. B.; Ortiz, J. V.; Cioslowski, J.; Fox, D. J. *Gaussian 09*, Revision A.02; Gaussian, Inc.: Wallingford CT, 2016.
(65) Wang, J.; Wang, W.; Kollman, P. A.; Case, D. A. Automatic atom type and bond type perception in molecular mechanical calculations. *J. Mol. Graphics Modell.* **2006**, *25*, 247−260.
(66) Scherer, M. K.; Trendelkamp-Schroer, B.; Paul, F.; Pérez-Hernández, G.; Hoffmann, M.; Plattner, N.; Wehmeyer, C.; Prinz, J.-H.; Noé, F. PyEMMA 2: A Software Package for Estimation, Validation, and Analysis of Markov Models. *J. Chem. Theory Comput.* **2015**, *11*, 5525−5542.
(67) Noé, F.; Wu, H.; Prinz, J.-H.; Plattner, N. Projected and hidden Markov models for calculating kinetics and metastable states of complex molecules. *J. Chem. Phys.* **2013**, *139*, 184114.
(68) Chodera, J. D.; Noé, F. Markov state models of biomolecular conformational dynamics. *Curr. Opin. Struct. Biol.* **2014**, *25*, 135−144.

https://dx.doi.org/10.1021/acs.macromol.0c01896
Macromolecules 2020, 53, 9793−9810

(69) Molgedey, L.; Schuster, H. G. Separation of a mixture of independent signals using time delayed correlations. *Phys. Rev. Lett.* **1994**, *72*, 3634−3637.
(70) Pérez-Hernández, G.; Paul, F.; Giorgino, T.; De Fabritiis, G.; Noé, F. Identification of slow molecular order parameters for Markov model construction. *J. Chem. Phys.* **2013**, *139*, 015102.
(71) Pérez-Hernández, G.; Noé, F. Hierarchical Time-Lagged Independent Component Analysis: Computing Slow Modes and Reaction Coordinates for Large Molecular Systems. *J. Chem. Theory Comput.* **2016**, *12*, 6118−6129.
(72) Röblitz, S.; Weber, M. Fuzzy spectral clustering by PCCA+: application to Markov state models and data classification. *Adv. Data Anal. Classif.* **2013**, *7*, 147−179.
(73) Srinivasan, J.; Cheatham, T. E.; Cieplak, P.; Kollman, P. A.; Case, D. A. Continuum Solvent Studies of the Stability of DNA, RNA, and Phosphoramidate−DNA Helices. *J. Am. Chem. Soc.* **1998**, *120*, 9401−9409.
(74) Kollman, P. A.; Massova, I.; Reyes, C.; Kuhn, B.; Huo, S.; Chong, L.; Lee, M.; Lee, T.; Duan, Y.; Wang, W.; Donini, O.; Cieplak, P.; Srinivasan, J.; Case, D. A.; Cheatham, T. E. Calculating Structures and Free Energies of Complex Molecules: Combining Molecular Mechanics and Continuum Models. *Acc. Chem. Res.* **2000**, *33*, 889−897.
(75) Massova, I.; Kollman, P. A. Combined molecular mechanical and continuum solvent approach (MM-PBSA/GBSA) to predict ligand binding. *Perspect. Drug Discovery Des.* **2000**, *18*, 113−135.
(76) Homeyer, N.; Gohlke, H. Free Energy Calculations by the Molecular Mechanics Poisson−Boltzmann Surface Area Method. *Mol. Inf.* **2012**, *31*, 114−122.
(77) Case, D. A. Normal mode analysis of protein dynamics. *Curr. Opin. Struct. Biol.* **1994**, *4*, 285−290.
(78) Miller, B. R.; McGee, T. D.; Swails, J. M.; Homeyer, N.; Gohlke, H.; Roitberg, A. E. MMPBSA.py: An Efficient Program for End-State Free Energy Calculations. *J. Chem. Theory Comput.* **2012**, *8*, 3314−3321.
(79) Honig, B.; Nicholls, A. Classical electrostatics in biology and chemistry. *Science* **1995**, *268*, 1144−1149.
(80) Gilson, M. K.; Sharp, K. A.; Honig, B. H. Calculating the electrostatic potential of molecules in solution: Method and error assessment. *J. Comput. Chem.* **1988**, *9*, 327−335.
(81) Uematsu, M.; Frank, E. U. Static Dielectric Constant of Water and Steam. *J. Phys. Chem. Ref. Data* **1980**, *9*, 1291−1306.
(82) Archer, D. G.; Wang, P. The Dielectric Constant of Water and Debye-Hückel Limiting Law Slopes. *J. Phys. Chem. Ref. Data* **1990**, *19*, 371−411.
(83) Tan, C.; Tan, Y.-H.; Luo, R. Implicit Nonpolar Solvent Models. *J. Phys. Chem. B* **2007**, *111*, 12263−12274.
(84) McQuarrie, D. A. *Statistical Mechanics*, 2nd ed.; University Science Books, 2000.
(85) Hawkins, G. D.; Cramer, C. J.; Truhlar, D. G. Pairwise solute descreening of solute charges from a dielectric medium. *Chem. Phys. Lett.* **1995**, *246*, 122−129.
(86) Hawkins, G. D.; Cramer, C. J.; Truhlar, D. G. Parametrized Models of Aqueous Free Energies of Solvation Based on Pairwise Descreening of Solute Atomic Charges from a Dielectric Medium. *J. Phys. Chem.* **1996**, *100*, 19824−19839.
(87) Gohlke, H.; Kiel, C.; Case, D. A. Insights into Protein−Protein Binding by Binding Free Energy Calculation and Free Energy Decomposition for the Ras−Raf and Ras−RalGDS Complexes. *J. Mol. Biol.* **2003**, *330*, 891−913.
(88) Krieger, V.; Hamacher, A.; Cao, F.; Stenzel, K.; Gertzen, C. G. W.; Schäker-Hübner, L.; Kurz, T.; Gohlke, H.; Dekker, F. J.; Kassack, M. U.; Hansen, F. K. Synthesis of Peptoid-Based Class I-Selective Histone Deacetylase Inhibitors with Chemosensitizing Properties. *J. Med. Chem.* **2019**, *62*, 11260−11279.
(89) Fenley, A. T.; Henriksen, N. M.; Muddana, H. S.; Gilson, M. K. Bridging Calorimetry and Simulation through Precise Calculations of Cucurbituril−Guest Binding Enthalpies. *J. Chem. Theory Comput.* **2014**, *10*, 4069−4078.
(90) Kirsh, Y. E.; Soos, T. A.; Karaputadze, T. M. Poly-N-vinylamides, complexation and conformational changes in aqueous solution. *Eur. Polym. J.* **1983**, *19*, 639−645.
(91) Tager, A. A.; Safronov, A. P.; Berezyuk, E. A.; Galaev, I. Y. Lower critical solution temperature and hydrophobic hydration in aqueous polymer solutions. *Colloid Polym. Sci.* **1994**, *272*, 1234−1239.
(92) Giliomee, J.; Pfukwa, R.; Gule, N. P.; Klumperman, B. Smart block copolymers of PVP and an alkylated PVP derivative: synthesis, characterization, thermoresponsive behaviour and self-assembly. *Polym. Chem.* **2016**, *7*, 1138−1146.
(93) Trellenkamp, T.; Ritter, H. 3-Ethylated N-Vinyl-2-pyrrolidone with LCST Properties in Water. *Macromol. Rapid Commun.* **2009**, *30*, 1736−1740.
(94) Maji, S.; Zhang, Z.; Voorhaar, L.; Pieters, S.; Stubbe, B.; Van Vlierberghe, S.; Dubruel, P.; De Geest, B. G.; Hoogenboom, R. Thermoresponsive polymer coated gold nanoparticles: from MADIX/RAFT copolymerization of N-vinylpyrrolidone and N-vinylcaprolactam to salt and temperature induced nanoparticle aggregation. *RSC Adv.* **2015**, *5*, 42388−42398.
(95) Salamova, U. U.; Rzaev, Z. M. O.; Altindal, Ş.; Masimov, A. A. Effect of inorganic salts on the main parameters of the dilute aqueous poly(vinylpyrrolidone) solutions. *Polymer* **1996**, *37*, 2415−2421.
(96) Usula, M.; Mocci, F.; Marincola, F. C.; Porcedda, S.; Gontrani, L.; Caminiti, R. The structural organization of N-methyl-2-pyrrolidone + water mixtures: A densitometry, x-ray diffraction, and molecular dynamics study. *J. Chem. Phys.* **2014**, *140*, 124503.
(97) Groenewald, F.; Dillen, J. Conformational analysis of caprolactam, cycloheptene and caprolactone. *Struct. Chem.* **2012**, *23*, 723−732.
(98) Gruber, T.; Thompson, A. L.; Odell, B.; Bombicz, P.; Schofield, C. J. Conformational studies on substituted ϵ-caprolactams by X-ray crystallography and NMR spectroscopy. *New J. Chem.* **2014**, *38*, 5905−5917.
(99) Wu, H.; Noé, F. Variational approach for learning Markov processes from time series data. **2017**, arXiv:1707.04659. arXiv preprint.
(100) Gohlke, H.; Case, D. A. Converging free energy estimates: MM-PB(GB)SA studies on the protein−protein complex Ras−Raf. *J. Comput. Chem.* **2004**, *25*, 238−250.
(101) Homeyer, N.; Stoll, F.; Hillisch, A.; Gohlke, H. Binding Free Energy Calculations for Lead Optimization: Assessment of Their Accuracy in an Industrial Drug Design Context. *J. Chem. Theory Comput.* **2014**, *10*, 3331−3344.
(102) Ben-Shalom, I. Y.; Pfeiffer-Marek, S.; Baringhaus, K.-H.; Gohlke, H. Efficient Approximation of Ligand Rotational and Translational Entropy Changes upon Binding for Use in MM-PBSA Calculations. *J. Chem. Inf. Model.* **2017**, *57*, 170−189.
(103) Smyda, M. R.; Harvey, S. C. The Entropic Cost of Polymer Confinement. *J. Phys. Chem. B* **2012**, *116*, 10928−10934.
(104) Homeyer, N.; Ioannidis, H.; Kolarov, F.; Gauglitz, G.; Zikos, C.; Kolocouris, A.; Gohlke, H. Interpreting Thermodynamic Profiles of Aminoadamantane Compounds Inhibiting the M2 Proton Channel of Influenza A by Free Energy Calculations. *J. Chem. Inf. Model.* **2016**, *56*, 110−126.
(105) van den Berg, B.; Ellis, R. J.; Dobson, C. M. Effects of macromolecular crowding on protein folding and aggregation. *EMBO J.* **1999**, *18*, 6927−6933.
(106) Ellis, R. J. Macromolecular crowding: obvious but underappreciated. *Trends Biochem. Sci.* **2001**, *26*, 597−604.
(107) Shao, L.; Hu, M.; Chen, L.; Xu, L.; Bi, Y. RAFT polymerization of N-vinylcaprolactam and effects of the end group on the thermal response of poly(N-vinylcaprolactam). *React. Funct. Polym.* **2012**, *72*, 407−413.
(108) Kamer, K. J.; Choudhary, A.; Raines, R. T. Intimate Interactions with Carbonyl Groups: Dipole−Dipole or n→π^*? *J. Org. Chem.* **2013**, *78*, 2099−2103.
(109) Fischer, F. R.; Wood, P. A.; Allen, F. H.; Diederich, F. Orthogonal dipolar interactions between amide carbonyl groups. *Proc. Natl. Acad. Sci. U.S.A.* **2008**, *105*, 17290−17294.

https://dx.doi.org/10.1021/acs.macromol.0c01896
Macromolecules 2020, 53, 9793−9810

(110) Wu, J.; Cheng, C.; Liu, G.; Zhang, P.; Chen, T. The folding pathways and thermodynamics of semiflexible polymers. *J. Chem. Phys.* **2018**, *148*, 184901.
(111) Vorob'ev, M. M.; Burova, T. V.; Grinberg, N. V.; Dubovik, A. S.; Faleev, N. G.; Lozinsky, V. I. Hydration characterization of N-vinylcaprolactam polymers by absorption millimeter-wave measurements. *Colloid Polym. Sci.* **2010**, *288*, 1457−1463.
(112) Kirsh, Y. E.; Yanul, N. A.; Kalninsh, K. K. Structural transformations and water associate interactions in poly-N-vinylcaprolactam-water system. *Eur. Polym. J.* **1999**, *35*, 305−316.
(113) de Oliveira, T. E.; Mukherji, D.; Kremer, K.; Netz, P. A. Effects of stereochemistry and copolymerization on the LCST of PNIPAm. *J. Chem. Phys.* **2017**, *146*, 034904.
(114) Pascal, T. A.; Schärf, D.; Jung, Y.; Kühne, T. D. On the absolute thermodynamics of water from computer simulations: A comparison of first-principles molecular dynamics, reactive and empirical force fields. *J. Chem. Phys.* **2012**, *137*, 244507.
(115) Mark, A. E.; van Gunsteren, W. F. Decomposition of the Free Energy of a System in Terms of Specific Interactions: Implications for Theoretical and Experimental Studies. *J. Mol. Biol.* **1994**, *240*, 167−176.
(116) Brady, G. P.; Sharp, K. A. Decomposition of Interaction Free Energies in Proteins and Other Complex Systems. *J. Mol. Biol.* **1995**, *254*, 77−85.
(117) Boresch, S.; Karplus, M. The Meaning of Component Analysis: Decomposition of the Free Energy in Terms of Specific Interactions. *J. Mol. Biol.* **1995**, *254*, 801−807.
(118) Frank, H. S.; Evans, M. W. Free Volume and Entropy in Condensed Systems III. Entropy in Binary Liquid Mixtures; Partial Molal Entropy in Dilute Solutions; Structure and Thermodynamics in Aqueous Electrolytes. *J. Chem. Phys.* **1945**, *13*, 507−532.
(119) Harano, Y.; Kinoshita, M. Translational-Entropy Gain of Solvent upon Protein Folding. *Biophys. J.* **2005**, *89*, 2701−2710.
(120) Kinoshita, M. Importance of Translational Entropy of Water in Biological Self-Assembly Processes like Protein Folding. *Int. J. Mol. Sci.* **2009**, *10*, 1064−1080.

https://dx.doi.org/10.1021/acs.macromol.0c01896
Macromolecules 2020, 53, 9793−9810

SUPPORTING INFORMATION

Cumulative sub-millisecond all-atom simulations of the temperature-induced coil-to-globule transition of poly(*N*-vinylcaprolactam) in aqueous solution

Jonas Dittrich[†,‡], Michael Kather[#,Δ], Anna Holzberger[#,Δ], Andrij Pich[‡,#,Δ], Holger Gohlke*[,†,‡,§]

[†]Institute for Pharmaceutical and Medicinal Chemistry, Heinrich Heine University Düsseldorf, 40225 Düsseldorf, Germany

[‡]Bioeconomy Science Center (BioSC), Forschungszentrum Jülich, 52425 Jülich, Germany

[#]DWI-Leibniz-Institute for Interactive Materials, RWTH Aachen University, 52056 Aachen, Germany

[Δ]Institute of Technical and Macromolecular Chemistry, RWTH Aachen University, 52074 Aachen, Germany

[§]John von Neumann Institute for Computing (NIC), Jülich Supercomputing Centre (JSC), Institute of Biological Information Processing (IBI-7: Structural Biochemistry), Forschungszentrum Jülich GmbH, 52425 Jülich, Germany.

Author ORCID

Jonas Dittrich: 0000-0003-2377-2268

Michael Kather: 0000-0001-6139-3483

Anna Holzberger: 0000-0002-9748-240X

Andrij Pich: 0000-0003-1825-7798

Holger Gohlke: 0000-0001-8613-1447

*Corresponding Author: Holger Gohlke

Address: Universitätsstr. 1, 40225 Düsseldorf, Germany.

Phone: (+49) 211 81 13662; Fax: (+49) 211 81 13847

E-mail: gohlke@uni-duesseldorf.de

Table of Contents

Supplementary Figures 5

Figure S1. Cloud points were determined by measuring the absorption of the linear polymer in dependence of the temperature at various wavelengths. The first derivative was determined from these measurements, and the mean value of these peaks yields the respective cloud point. This example shows the cloud point determination of the 39mer at a polymer concentration of 0.3 wt.-%. 5

Figure S2. Implied timescale plot for HMMs constructed for five assumed hidden states (indicated by color) at different lag times up to 2.5 ns. The constructed HMM describes the coil-to-globule transition of a PNVCL 40mer at 293 K. It is constructed from 5x1 µs MD simulation. Errors are calculated using Bayesian error estimation and are depicted as corresponding error area. The maximum likelihood result is depicted as solid lines, and the dashed lines show the ensemble mean based on a Bayesian sampling procedure Calculations were performed with the PyEMMA[1] python library (v. 2.5.6)..... 6

Figure S3. Implied timescale plot for HMMs constructed for five assumed hidden states (indicated by color) at different lag times up to 1 ns. The constructed HMM describes the coil-to-globule transition of a PNVCL 40mer at 313 K. The HMM is constructed from 5x1 µs MD simulation data. Errors are calculated using Bayesian error estimation and are depicted as corresponding error area. The maximum likelihood result is depicted as solid lines, and the dashed lines show the ensemble mean based on a Bayesian sampling procedure Calculations were performed with the PyEMMA[1] python library (v. 2.5.6).. 6

Figure S4: Implied timescales (**A**,**C**) and timescale separation (**B**,**D**) of MSMs constructed from 5x1 µs MD simulation of the coil-to-globule transition of a PNVCL 40mer at 293 K (**A**,**B**) and 313 K **(C,D)**. The MSMs were constructed with a lag time of 2.5 ns and 1 ns for 293 K and 313 K, respectively. We consider two/three hidden states as there are gaps between the first and second (**B**) and between the second and third (**D**) relaxation timescale for 293 K and 313 K, respectively. Calculations were performed with the PyEMMA[1] python library (v. 2.5.6)..... 7

Figure S5. Chapman-Kolmogorov test for the constructed HMM describing the coil-to-globule transition of a PNVCL 40mer at 293 K **(A)** and 313 K **(B)**. The HMMs are constructed from 5x1 µs MD simulation data each. Estimated state transition probabilities and corresponding errors (at a 95 % confidence level) are depicted as dotted blue lines and error areas, respectively. Calculations were performed with the PyEMMA[1] python library (v. 2.5.6). In panel (B), black and blue lines lie on top of each other..... 8

Figure S6. Multi-conformer single point charge fit for methyl-capped *N*-(vinylcaprolactam) monomeric units. The charges were calculated at the HF/6-31G* level using Gaussian09[2]. Charge fitting was done using the RESP charge fitting procedure implemented in antechamber.[3] The mean value is depicted as dotted horizontal line, and the standard error is shown by error bars. The inset depicts an *N*-(vinylcaprolactam) monomeric unit with partial charges mapped onto the molecular surface. 9

Figure S7. Energy components of $T\Delta S_{config}$ computed with MM-PBSA for the coil-to-globule transition of a PNVCL 40mer in water at 293 K (hatched) and at 313 K (solid). The bar depicts $TS_{\{rot, vib\},globule}$ - $TS_{\{rot, vib\},coil}$. The difference in entropy for the coil-to-globule transition is mainly dominated by the loss in vibrational entropy. It is a result of both a higher number of configurational degrees of freedom of the coil state and the presence of a compact state of PNVCL at 313 K. Mean values were computed from ten MM-PBSA calculations of 100 MD snapshots of PNVCL in either coil or globule conformation; the

error is calculated following the laws of error propagation using the respective standard error of the mean. Calculations were performed using MMPBSA.py[4]. 10

Figure S8. Energy components of ΔG_{solv} computed with MM-PBSA for the coil-to-globule transition of a PNVCL 40mer in water at 293 K (hatched) and at 313 K (solid). The bar depicts $G_{\{pol, cavity, dispersion\},globule} - G_{\{pol, cavity, dispersion\},coil}$. Mean values were computed from ten MM-PBSA calculations of 100 MD snapshots of PNVCL in either coil or globule conformation; the error is calculated following the laws of error propagation using the respective standard error of the mean. Calculations were performed using MMPBSA.py[4]. 11

Figure S9. Energy components of ΔE_{MM} computed with MM-PBSA for the coil-to-globule transition of a PNVCL 40mer in water at 293 K (hatched) and at 313 K (solid). The bar depicts $E_{\{bond, angle, dihedral, vdW, eel, 1-4 vdW, 1-4 eel\},globule} - E_{\{ bond, angle, dihedral, vdW, eel, 1-4 vdW, 1-4eel \},coil}$. Mean values were computed from ten MM-PBSA calculations of 100 MD snapshots of PNVCL in either coil or globule conformation; the error is calculated following the laws of error propagation using the respective standard error of the mean. Calculations were performed using MMPBSA.py [4]. 12

Figure S10. Atomwise energy decomposition of ΔE_{vdW} (see Figure S9) for the coil-to-globule transition of an atactic PNVCL 40mer simulated under NVT conditions at 293 K (blue) and 313 K (red). The carbon atoms of the caprolactam ring, especially C_3 and C_4, contribute to the favorable increase in ΔE_{vdW} to a large extent, fostering the coil-to-globule transition at 293 K and even more at 313 K. 13

Figure S11. Atomwise energy decomposition of ΔE_{eel} (see Figure S9) for the coil-to-globule transition of an atactic PNVCL 40mer simulated under NVT conditions at 293 K (blue) and 313 K (red). The unfavorable increase in the ΔE_{eel} term for the lactam carbonyl carbon is outbalanced by a favorable interaction of the carbonyl oxygen, leading to a favorable contribution to the coil-to-globule transition at 313 K. 13

Figure S12. Running cumulative average of the potential energy of the 5x1 µs NPT simulations (depicted by color) of the isotactic PNVCL 40mer at 293 K (**A**) and 313 K (**B**). The running cumulative averages of the potential energy of the pure water system (5x300 ns) are shown as black lines. The enthalpy of the polymer part of the polymer/water system is -161.9 ± 3.3 kcal mol^{-1} and -85.1 ± 1.4 kcal mol^{-1} at 293 K and 313 K, respectively. Therefore, the transition enthalpy ΔH = 76.9 ± 3.6 kcal mol^{-1} for the 40mer, which is equivalent to 1.92± 0.56 kcal mol^{-1} per repeating unit. 14

Figure S13. Running cumulative average of the potential energy of the 5x1 µs NPT simulations (depicted by color) of the atactic PNVCL 40mer at 293 K (**A**) and 313 K (**B**). The running cumulative averages of the potential energy of the pure water system (5x300 ns) are shown as black lines. The enthalpy of the polymer part of the polymer/water system is -179.7 ± 1.7 kcal mol^{-1} and -101.7 ± 2.6 kcal mol^{-1} at 293 K and 313 K, respectively. Therefore, the transition enthalpy ΔH = 78.0 ± 3.1 kcal mol^{-1} for the 40mer, which is equivalent to 1.95 ± 0.51 kcal mol^{-1} per repeating unit. 15

Figure S14. Running cumulative average of the potential energy of the 5x1 µs NPT simulations (depicted by color) of the syndiotactic PNVCL 40mer at 293 K (**A**) and 313 K (**B**). The running cumulative averages of the potential energy of the pure water system (5x300 ns) are shown as black lines. The enthalpy of the polymer part of the polymer/water system is -183.1 ± 1.9 kcal mol^{-1} and -96.4 ± 0.9 kcal mol^{-1} at 293 K and 313 K, respectively. Therefore, the transition enthalpy ΔH = 86.6 ± 2.1 kcal mol^{-1}for the 40mer, which is equivalent to 2.17 ± 0.33 kcal mol^{-1} per repeating unit. 16

Figure S 15. Running cumulative average of the potential energy of the 5x1 µs NVT simulations (depicted by color) of the atactic PNVCL 40mer at 293 K (**A**) and 313 K **(B**). The running cumulative averages of the potential energy of the pure water system (5x100 ns) are depicted as black lines. The potential energy of the system is linearly dependent on the system's volume, indicating that the volume was not completely adjusted to the equilibrium value in the NPT step during thermalization. 17

Figure S16. Mean potential energies of pure water systems (**A**,**B**) and the atactic PNVCL 40mer (**C**,**D**) in water systems for MD simulations in the NVT ensemble at 293 K (**A**,**C**) and 313 K(**B**,**D**) as a function of the simulation box size for five independent replicas (depicted by color for the PNVCL). Green stars depict the interpolated potential energy of the system using the linear regression based on the five mean potential energies of the NVT simulations (determined parameters and statistics for the regression are displayed in each panel) and the mean volumes of the corresponding NPT simulations. The transition enthalpy is calculated according to eq. (7) of the main text and yields $\Delta H = 1.98$ kcal mol^{-1} per repeating unit for the NVT ensemble. 18

Figure S17. Radius of gyration (R_g) during five·MD simulations of 1 µs length of a syndiotactic PNVCL 50mer at 293 K for polymer concentrations of 1 wt.-%, 0.8 wt.-%, and 0.6 wt.-% (top to bottom). Corresponding frequency distributions are shown next to the time series in matching color, a frequency distribution of all data is shown as dashed black line.. 19

Figure S18. Radius of gyration (R_g) during five·MD simulations of 1 µs length of a syndiotactic PNVCL 50mer at 313 K for polymer concentrations of 1 wt.-%, 0.8 wt.-%, and 0.6 wt.-% (top to bottom). Corresponding frequency distributions are shown next to the time series in matching color, a frequency distribution of all data is shown as dashed black line.. 20

Figure S19. Radius of gyration (R_g) during five·MD simulations of 1 µs length of an isotactic PNVCL 50mer at 293 K for polymer concentrations of 1 wt.-%, 0.8 wt.-%, and 0.6 wt.-% (top to bottom). Corresponding frequency distributions are shown next to the time series in matching color, a frequency distribution of all data is shown as dashed black line..... 21

Figure S20. Radius of gyration (R_g) during five·MD simulations of 1 µs length of an isotactic PNVCL 50mer at 313 K for polymer concentrations of 1 wt.-%, 0.8 wt.-%, and 0.6 wt.-% (top to bottom). Corresponding frequency distributions are shown next to the time series in matching color, a frequency distribution of all data is shown as dashed black line..... 22

Figure S21. Radius of gyration (R_g) during five·MD simulations of 1 µs length of an atactic PNVCL 50mer at 293 K for polymer concentrations of 1 wt.-%, 0.8 wt.-%, and 0.6 wt.-% (top to bottom). Corresponding frequency distributions are shown next to the time series in matching color, a frequency distribution of all data is shown as dashed black line..... 23

Figure S22. Radius of gyration (R_g) during five·MD simulations of 1 µs length of an atactic PNVCL 50mer at 313 K for polymer concentrations of 1 wt.-%, 0.8 wt.-%, and 0.6 wt.-% (top to bottom). Corresponding frequency distributions are shown next to the time series in matching color, a frequency distribution of all data is shown as dashed black line..... 24

Figure S23. Influence of different water models on the solvent-accessible surface area (SASA) of syndiotactic PNVCL oligomers. The histograms depict the SASA observed in five independent 1 µs MD simulations for systems of PNVCL oligomers of varying length (30, 40, and 50 repeating units, from left to right) at different temperatures (293 K, 313K, and 343 K, from top to bottom) using the TIP3P water model (black) or the OPC water model (red). 25

Figure S24. Influence of different water models on the solvent-accessible surface area (SASA) of isotactic PNVCL oligomers. The histograms depict the SASA observed in five

independent 1 μs MD simulations for systems of PNVCL oligomers of varying length (30, 40, and 50 repeating units, from left to right) at different temperatures (293 K, 313K, and 343 K, from top to bottom) using the TIP3P water model (black) or the OPC water model (red). 26

Figure S25. Influence of different water models on the solvent-accessible surface area (SASA) of atactic PNVCL oligomers. The histograms depict the SASA observed in five independent 1 μs MD simulations for systems of PNVCL oligomers of varying length (30, 40, and 50 repeating units, from left to right) at different temperatures (293 K, 313K, and 343 K, from top to bottom) using the TIP3P water model (black) or the OPC water model (red). 27

Figure S26. Influence of the MD ensemble (NVT / NPT) on the solvent-accessible surface area (SASA) of the iso-, syndio-, and atactic PNVCL 40mer. The histograms depict the SASA observed in five independent 1 μs MD simulations for each tacticity of PNVCL (from left to right) at different temperatures (293 K and 313K, from top to bottom) using the NVT (black) or NPT (red) ensemble. 28

Figure S27. Influence of the MD ensemble (NVT / NPT) on the radius of gyration (R_g) of the iso-, syndio-, and atactic PNVCL 40mer. (**A, B**)The histograms depict the R_g observed in five independent 1 μs MD simulations for each tacticity of PNVCL (from left to right) at different temperatures (293 K (A) and 313K (B), from top to bottom) using the NVT (black) or NPT (red) ensemble. (**C, D**) Histograms are obtained by removing one deviating trajectory from the five trajectories of the three systems showing notable deviations in panel A and B, respectively (atactic PNVCL (293 K, NPT), isotactic PNVCL (293 K, NPT), isotactic PNVCL (313 K, NVT)). 29

Figure S28. Radial distribution functions (RDFs) for the polymer backbone carbons atoms of PNVCL **(A)** and PVP **(B)** and the oxygen of the surrounding water molecules. Atom pairings are depicted in respective colors, and RDFs calculated from trajectories at 293 K, and 313 K are shown as solid and dotted lines, respectively. Differences in the RDFs, $\Delta g(r) = g(r)_{313} - g(r)_{293}$, are depicted in the plots below. Calculations were performed using CPPTRAJ[5]. 30

Supplementary Tables 31

Table S1. Overview of performed simulations on poly(*N*-vinylcaprolactam) (PNVCL). 31

Table S2. Overview of performed simulations on poly(*N*-vinylpyrrolidone) (PVP): 32

Table S3. Number of atoms within each investigated system. Polymer (PNVCL/PVP) and simulation conditions (NVT/NPT and TIP3P/OPC) are provided for each section, number of repeating units and tacticity are given per row. 33

Table S4. Residues containing cabon atoms with inverted chirality for atactic structures of PNVCL and PVP. 35

Table S5. Partial charges and coordinates of the atoms of the PNVCL repeating unit. The repeating unit possesses two open valences/connect records (C9 and C10), its net charge is zero. 36

Table S6. Partial charges and coordinates of the atoms of the PVP repeating unit. The repeating unit possesses two open valences/connect records (C4 and C5); its net charge is zero. 36

References 37

Supplementary Figures

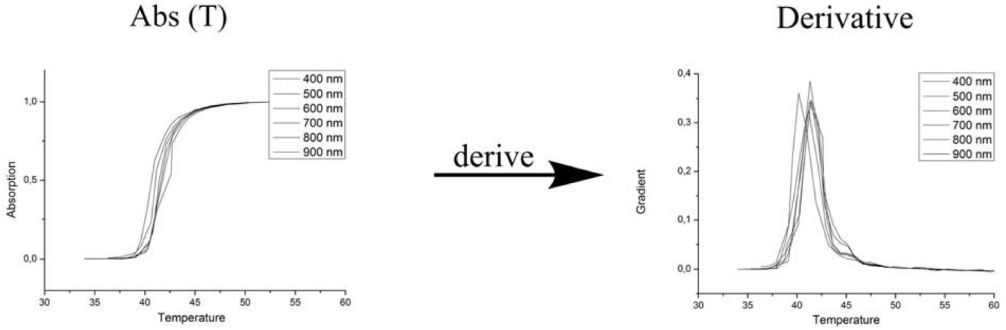

Figure S1. Cloud points were determined by measuring the absorption of the linear polymer in dependence of the temperature at various wavelengths. The first derivative was determined from these measurements, and the mean value of these peaks yields the respective cloud point. This example shows the cloud point determination of the 39mer at a polymer concentration of 0.3 wt.-%.

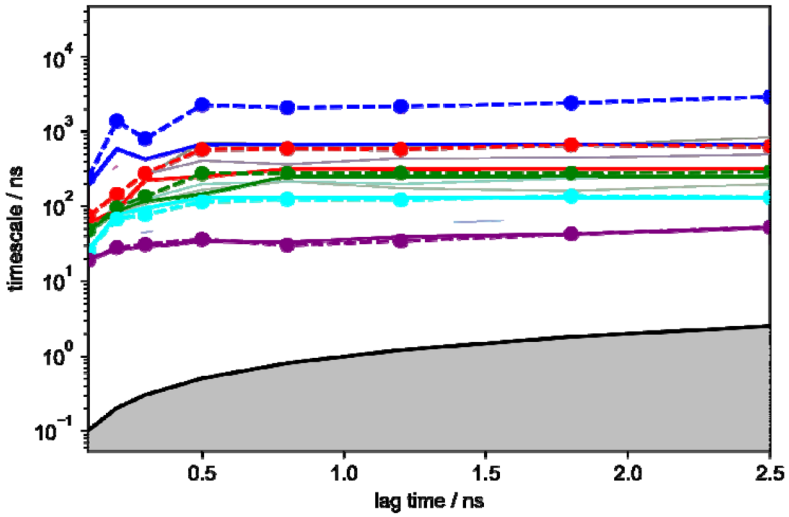

Figure S2. Implied timescale plot for HMMs constructed for five assumed hidden states (indicated by color) at different lag times up to 2.5 ns. The constructed HMM describes the coil-to-globule transition of a PNVCL 40mer at 293 K. It is constructed from 5x1 µs MD simulation. Errors are calculated using Bayesian error estimation and are depicted as corresponding error area. The maximum likelihood result is depicted as solid lines, and the dashed lines show the ensemble mean based on a Bayesian sampling procedure Calculations were performed with the PyEMMA[1] python library (v. 2.5.6).

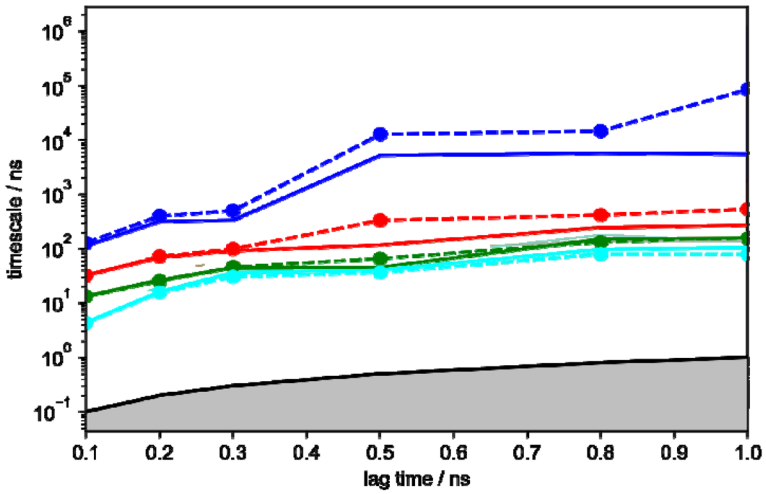

Figure S3. Implied timescale plot for HMMs constructed for five assumed hidden states (indicated by color) at different lag times up to 1 ns. The constructed HMM describes the coil-to-globule transition of a PNVCL 40mer at 313 K. The HMM is constructed from 5x1 µs MD simulation data. Errors are calculated using Bayesian error estimation and are depicted as corresponding error area. The maximum likelihood result is depicted as solid lines, and the dashed lines show the ensemble mean based on a Bayesian sampling procedure Calculations were performed with the PyEMMA[1] python library (v. 2.5.6).

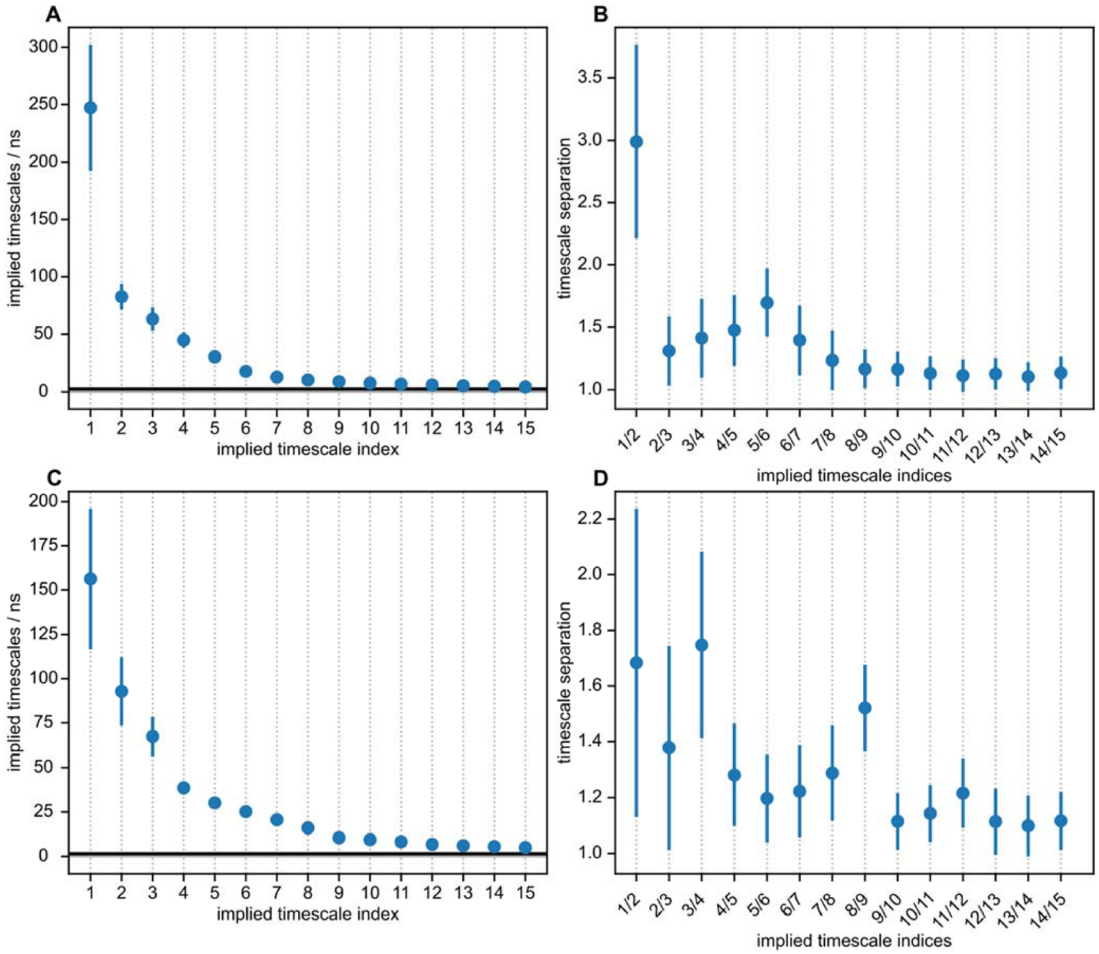

Figure S4: Implied timescales (**A**,**C**) and timescale separation (**B**,**D**) of MSMs constructed from 5x1 µs MD simulation of the coil-to-globule transition of a PNVCL 40mer at 293 K (**A**,**B**) and 313 K **(C,D)**. The MSMs were constructed with a lag time of 2.5 ns and 1 ns for 293 K and 313 K, respectively. We consider two/three hidden states as there are gaps between the first and second (**B**) and between the second and third (**D**) relaxation timescale for 293 K and 313 K, respectively. Calculations were performed with the PyEMMA[1] python library (v. 2.5.6).

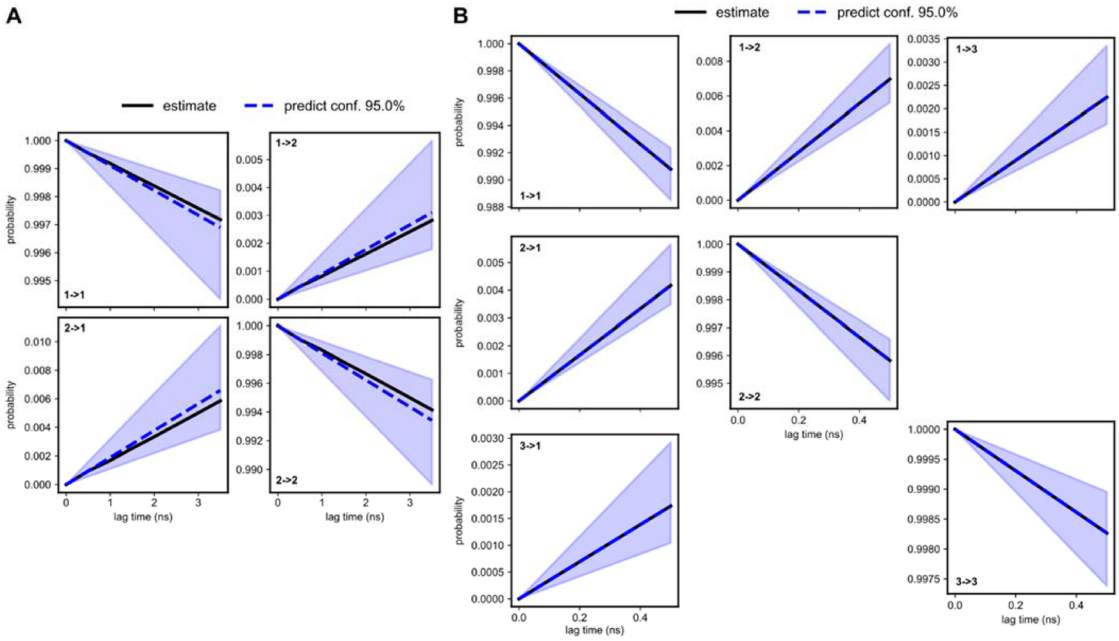

Figure S5. Chapman-Kolmogorov test for the constructed HMM describing the coil-to-globule transition of a PNVCL 40mer at 293 K **(A)** and 313 K **(B)**. The HMMs are constructed from 5x1 µs MD simulation data each. Estimated state transition probabilities and corresponding errors (at a 95 % confidence level) are depicted as dotted blue lines and error areas, respectively. Calculations were performed with the PyEMMA[1] python library (v. 2.5.6). In panel (B), black and blue lines lie on top of each other.

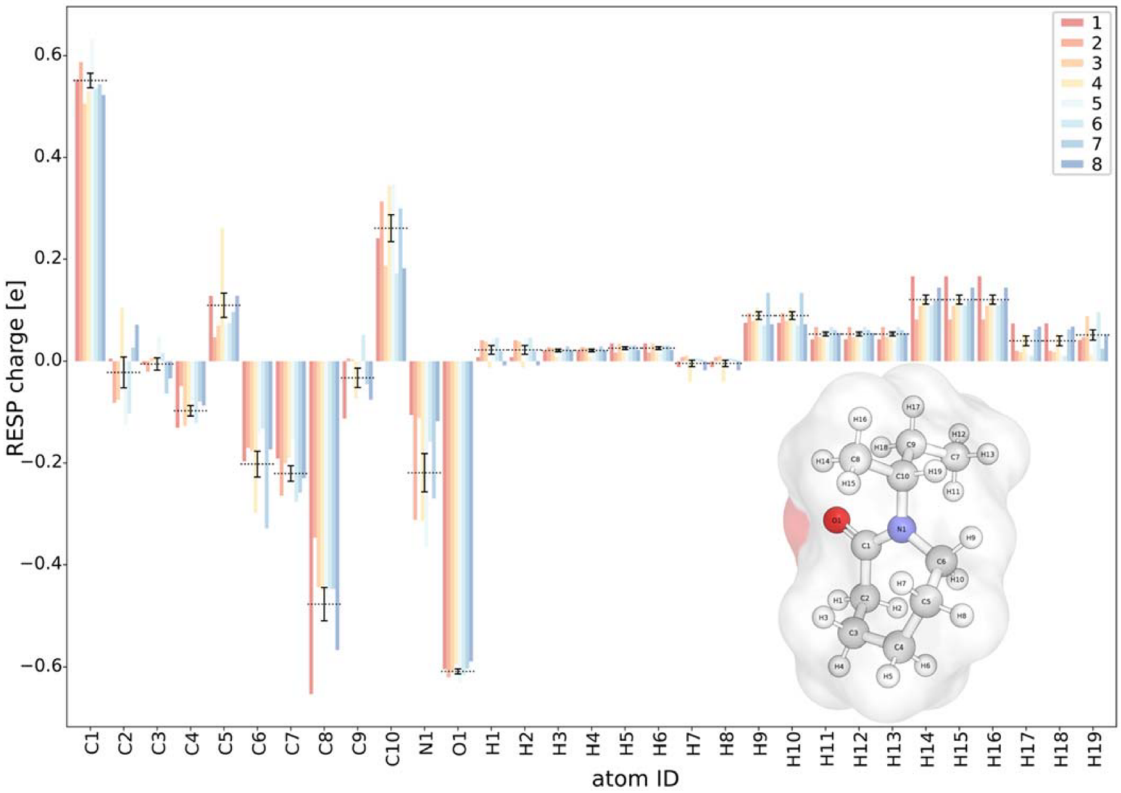

Figure S6. Multi-conformer single point charge fit for methyl-capped *N*-(vinylcaprolactam) monomeric units. The charges were calculated at the HF/6-31G* level using Gaussian09[2]. Charge fitting was done using the RESP charge fitting procedure implemented in antechamber.[3] The mean value is depicted as dotted horizontal line, and the standard error is shown by error bars. The inset depicts an *N*-(vinylcaprolactam) monomeric unit with partial charges mapped onto the molecular surface.

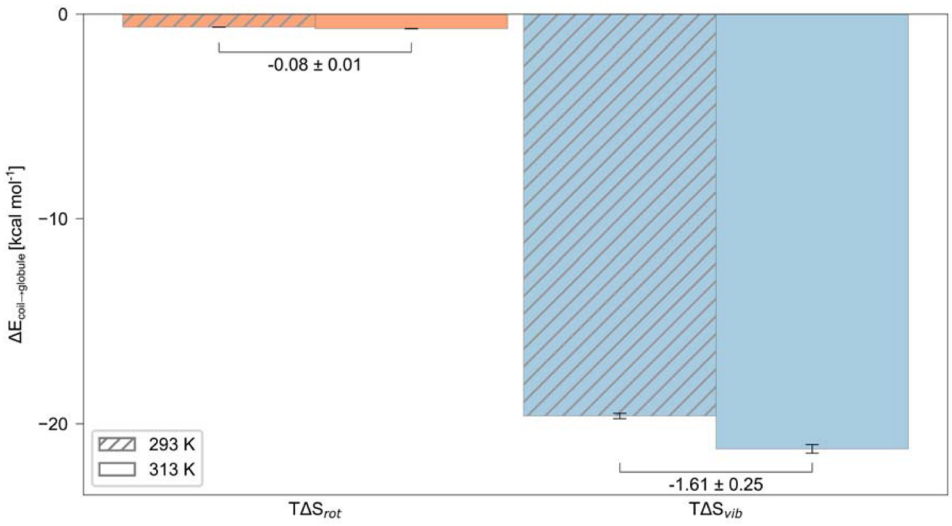

Figure S7. Energy components of $T\Delta S_{config}$ computed with MM-PBSA for the coil-to-globule transition of a PNVCL 40mer in water at 293 K (hatched) and at 313 K (solid). The bar depicts $TS_{\{rot,\ vib\},globule}$ - $TS_{\{rot,\ vib\},coil}$. The difference in entropy for the coil-to-globule transition is mainly dominated by the loss in vibrational entropy. It is a result of both a higher number of configurational degrees of freedom of the coil state and the presence of a compact state of PNVCL at 313 K. Mean values were computed from ten MM-PBSA calculations of 100 MD snapshots of PNVCL in either coil or globule conformation; the error is calculated following the laws of error propagation using the respective standard error of the mean. Calculations were performed using MMPBSA.py[4].

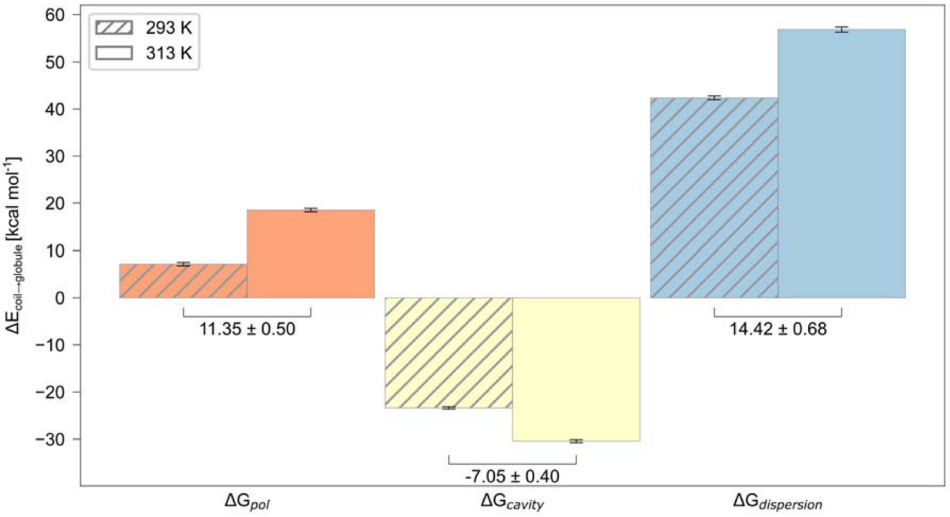

Figure S8. Energy components of ΔG_{solv} computed with MM-PBSA for the coil-to-globule transition of a PNVCL 40mer in water at 293 K (hatched) and at 313 K (solid). The bar depicts $G_{\{pol,\,cavity,\,dispersion\},globule} - G_{\{pol,\,cavity,\,dispersion\},coil}$. Mean values were computed from ten MM-PBSA calculations of 100 MD snapshots of PNVCL in either coil or globule conformation; the error is calculated following the laws of error propagation using the respective standard error of the mean. Calculations were performed using MMPBSA.py[4].

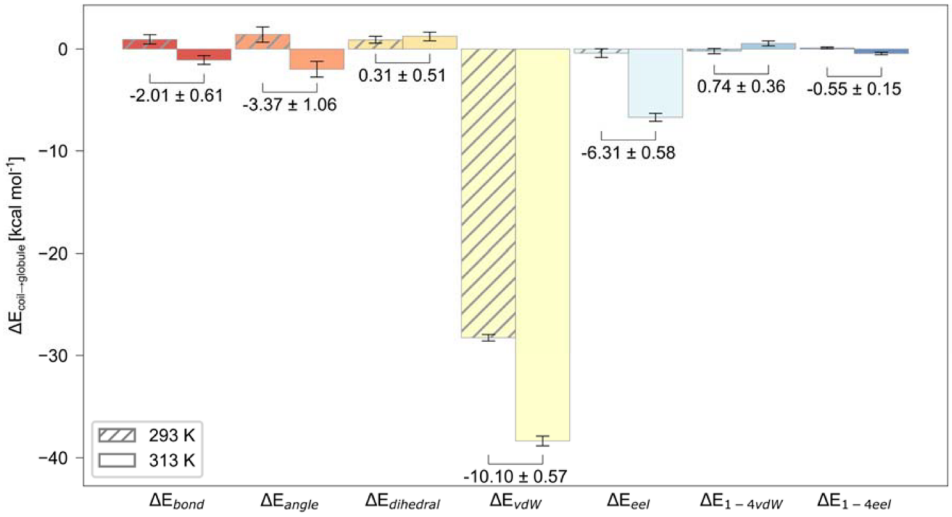

Figure S9. Energy components of ΔE_{MM} computed with MM-PBSA for the coil-to-globule transition of a PNVCL 40mer in water at 293 K (hatched) and at 313 K (solid). The bar depicts $E_{\{\text{bond, angle, dihedral, vdW, eel, 1-4 vdW, 1-4 eel}\},\text{globule}} - E_{\{\text{bond, angle, dihedral, vdW, eel, 1-4 vdW, 1-4eel}\},\text{coil}}$. Mean values were computed from ten MM-PBSA calculations of 100 MD snapshots of PNVCL in either coil or globule conformation; the error is calculated following the laws of error propagation using the respective standard error of the mean. Calculations were performed using MMPBSA.py [4].

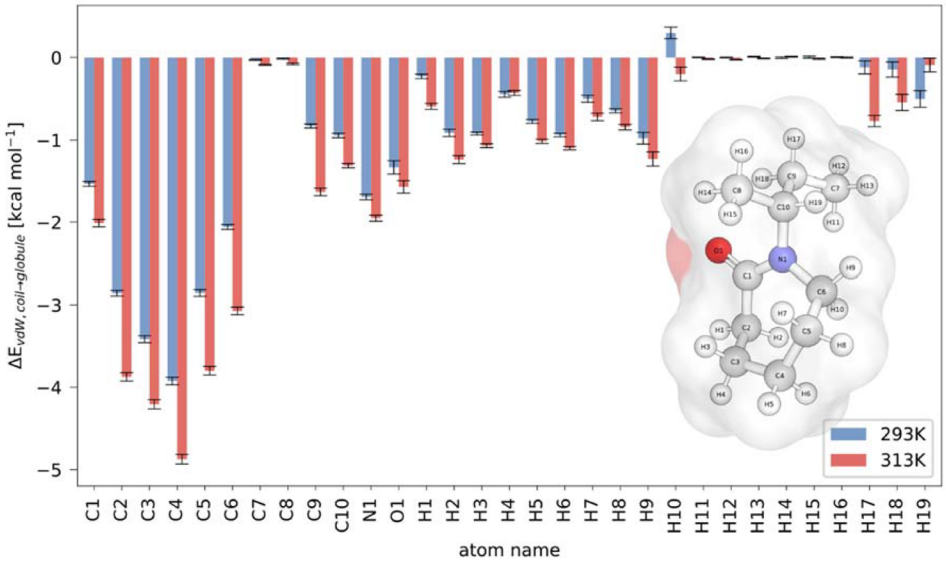

Figure S10. Atomwise energy decomposition of ΔE_{vdW} (see Figure S9) for the coil-to-globule transition of an atactic PNVCL 40mer simulated under NVT conditions at 293 K (blue) and 313 K (red). The carbon atoms of the caprolactam ring, especially C_3 and C_4, contribute to the favorable increase in ΔE_{vdW} to a large extent, fostering the coil-to-globule transition at 293 K and even more at 313 K.

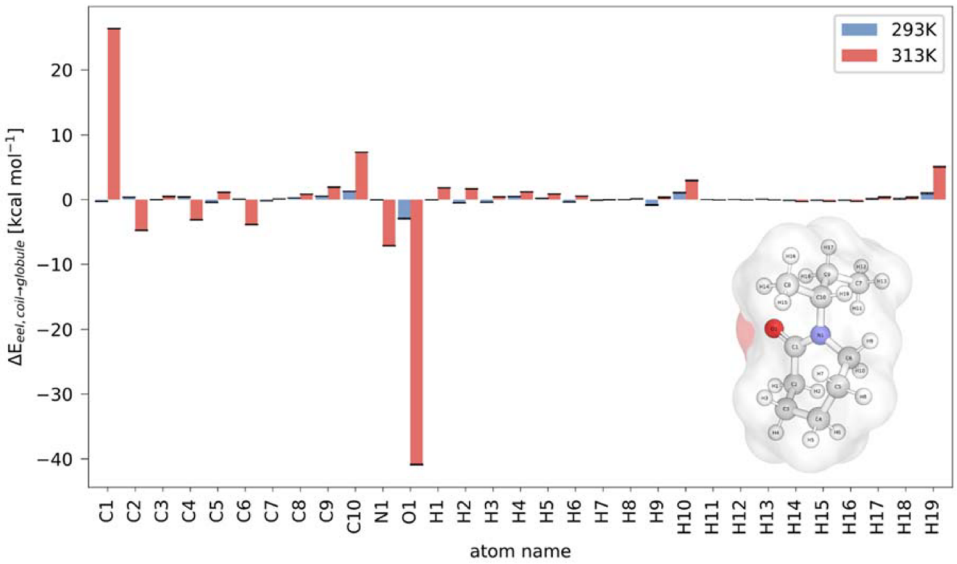

Figure S11. Atomwise energy decomposition of ΔE_{eel} (see Figure S9) for the coil-to-globule transition of an atactic PNVCL 40mer simulated under NVT conditions at 293 K (blue) and 313 K (red). The unfavorable increase in the ΔE_{eel} term for the lactam carbonyl carbon is outbalanced by a favorable interaction of the carbonyl oxygen, leading to a favorable contribution to the coil-to-globule transition at 313 K.

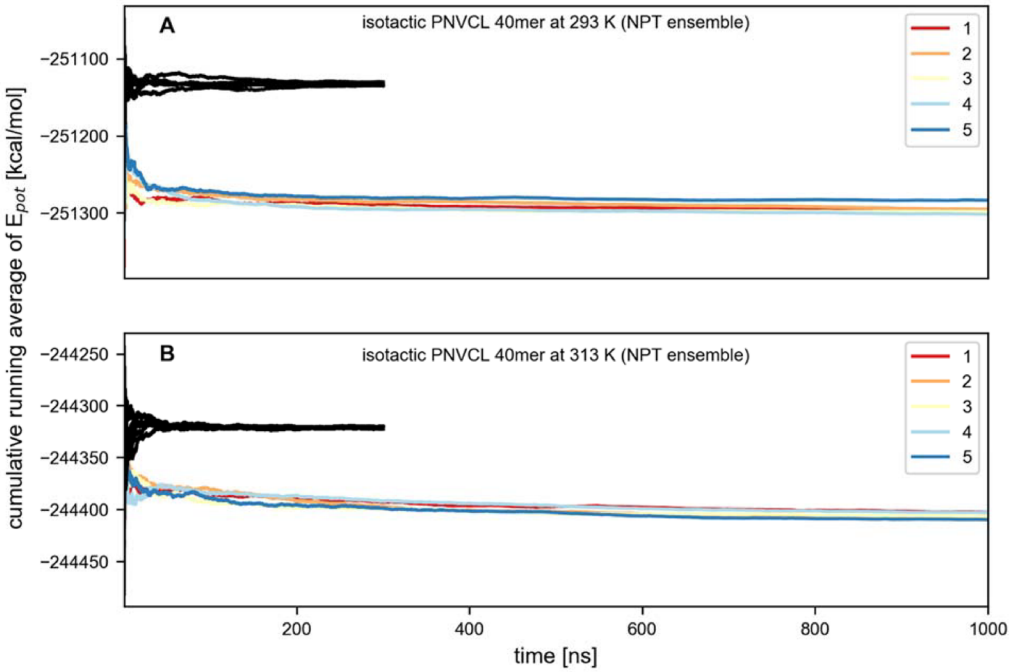

Figure S12. Running cumulative average of the potential energy of the 5x1 µs NPT simulations (depicted by color) of the isotactic PNVCL 40mer at 293 K (**A**) and 313 K (**B**). The running cumulative averages of the potential energy of the pure water system (5x300 ns) are shown as black lines. The enthalpy of the polymer part of the polymer/water system is -161.9 ± 3.3 kcal mol^{-1} and -85.1 ± 1.4 kcal mol^{-1} at 293 K and 313 K, respectively. Therefore, the transition enthalpy ΔH = 76.9 ± 3.6 kcal mol^{-1} for the 40mer, which is equivalent to 1.92± 0.56 kcal mol^{-1} per repeating unit.

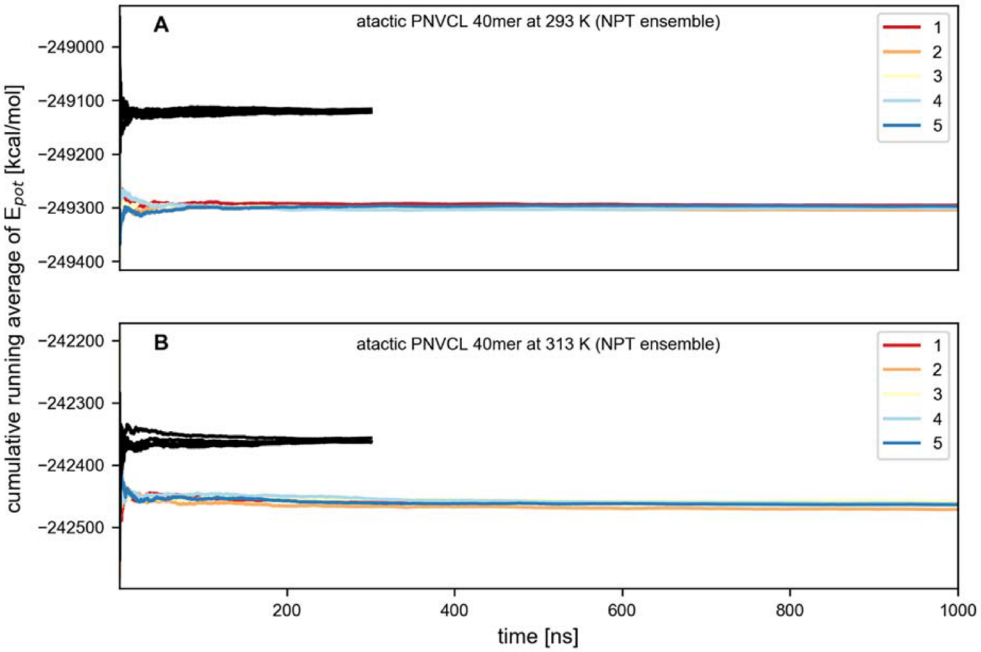

Figure S13. Running cumulative average of the potential energy of the 5x1 µs NPT simulations (depicted by color) of the atactic PNVCL 40mer at 293 K (**A**) and 313 K (**B**). The running cumulative averages of the potential energy of the pure water system (5x300 ns) are shown as black lines. The enthalpy of the polymer part of the polymer/water system is -179.7 ± 1.7 kcal mol^{-1} and -101.7 ± 2.6 kcal mol^{-1} at 293 K and 313 K, respectively. Therefore, the transition enthalpy ΔH = 78.0 ± 3.1 kcal mol^{-1} for the 40mer, which is equivalent to 1.95 ± 0.51 kcal mol^{-1} per repeating unit.

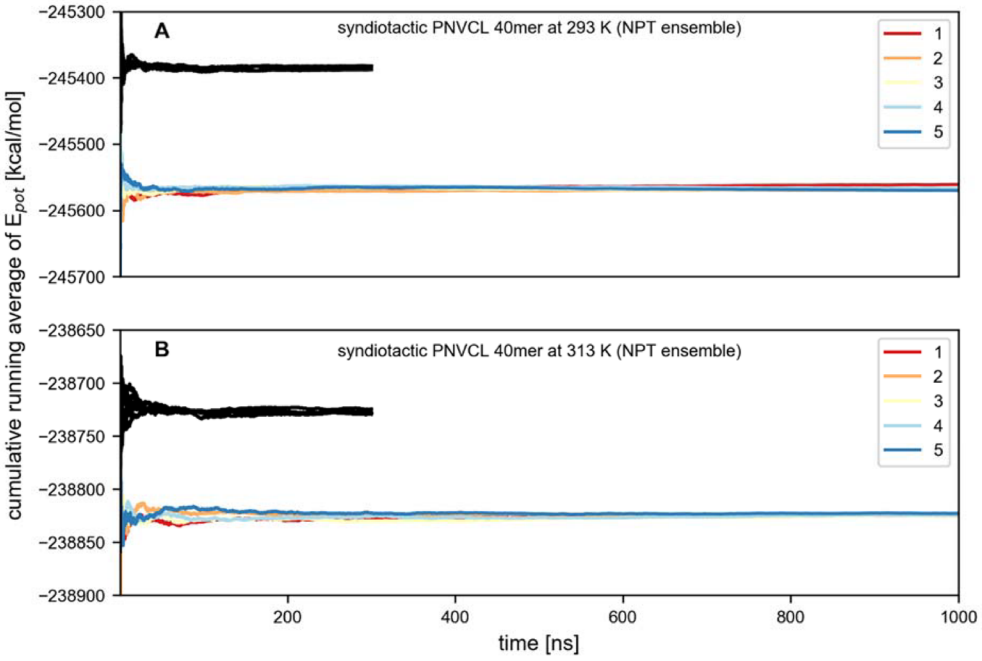

Figure S14. Running cumulative average of the potential energy of the 5x1 µs NPT simulations (depicted by color) of the syndiotactic PNVCL 40mer at 293 K (**A**) and 313 K (**B**). The running cumulative averages of the potential energy of the pure water system (5x300 ns) are shown as black lines. The enthalpy of the polymer part of the polymer/water system is -183.1 ± 1.9 kcal mol^{-1} and -96.4 ± 0.9 kcal mol^{-1} at 293 K and 313 K, respectively. Therefore, the transition enthalpy ΔH = 86.6 ± 2.1 kcal mol^{-1}for the 40mer, which is equivalent to 2.17 ± 0.33 kcal mol^{-1} per repeating unit.

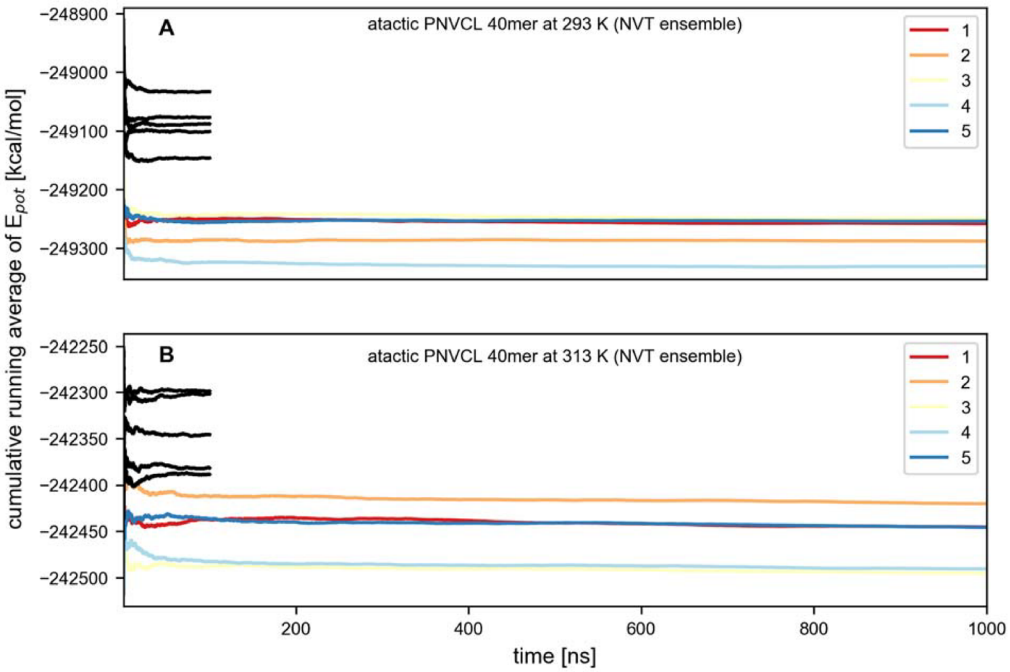

Figure S 15. Running cumulative average of the potential energy of the 5x1 µs NVT simulations (depicted by color) of the atactic PNVCL 40mer at 293 K (**A**) and 313 K (**B**). The running cumulative averages of the potential energy of the pure water system (5x100 ns) are depicted as black lines. The potential energy of the system is linearly dependent on the system's volume, indicating that the volume was not completely adjusted to the equilibrium value in the NPT step during thermalization.

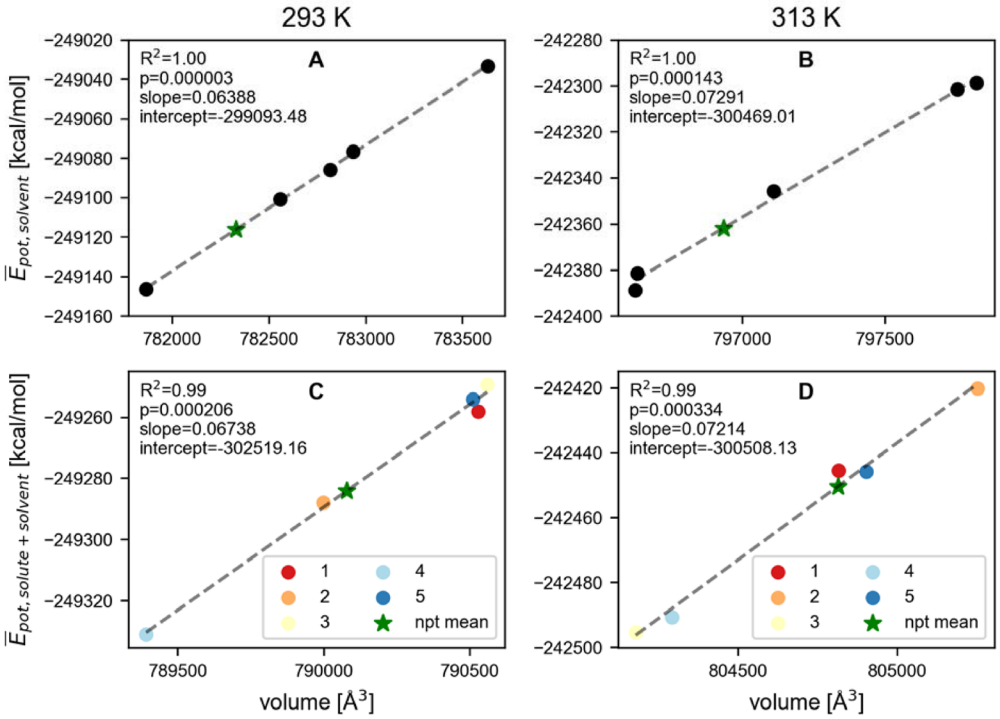

Figure S16. Mean potential energies of pure water systems (**A**,**B**) and the atactic PNVCL 40mer (**C**,**D**) in water systems for MD simulations in the NVT ensemble at 293 K (**A**,**C**) and 313 K(**B**,**D**) as a function of the simulation box size for five independent replicas (depicted by color for the PNVCL). Green stars depict the interpolated potential energy of the system using the linear regression based on the five mean potential energies of the NVT simulations (determined parameters and statistics for the regression are displayed in each panel) and the mean volumes of the corresponding NPT simulations. The transition enthalpy is calculated according to eq. (7) of the main text and yields $\Delta H = 1.98$ kcal mol^{-1} per repeating unit for the NVT ensemble.

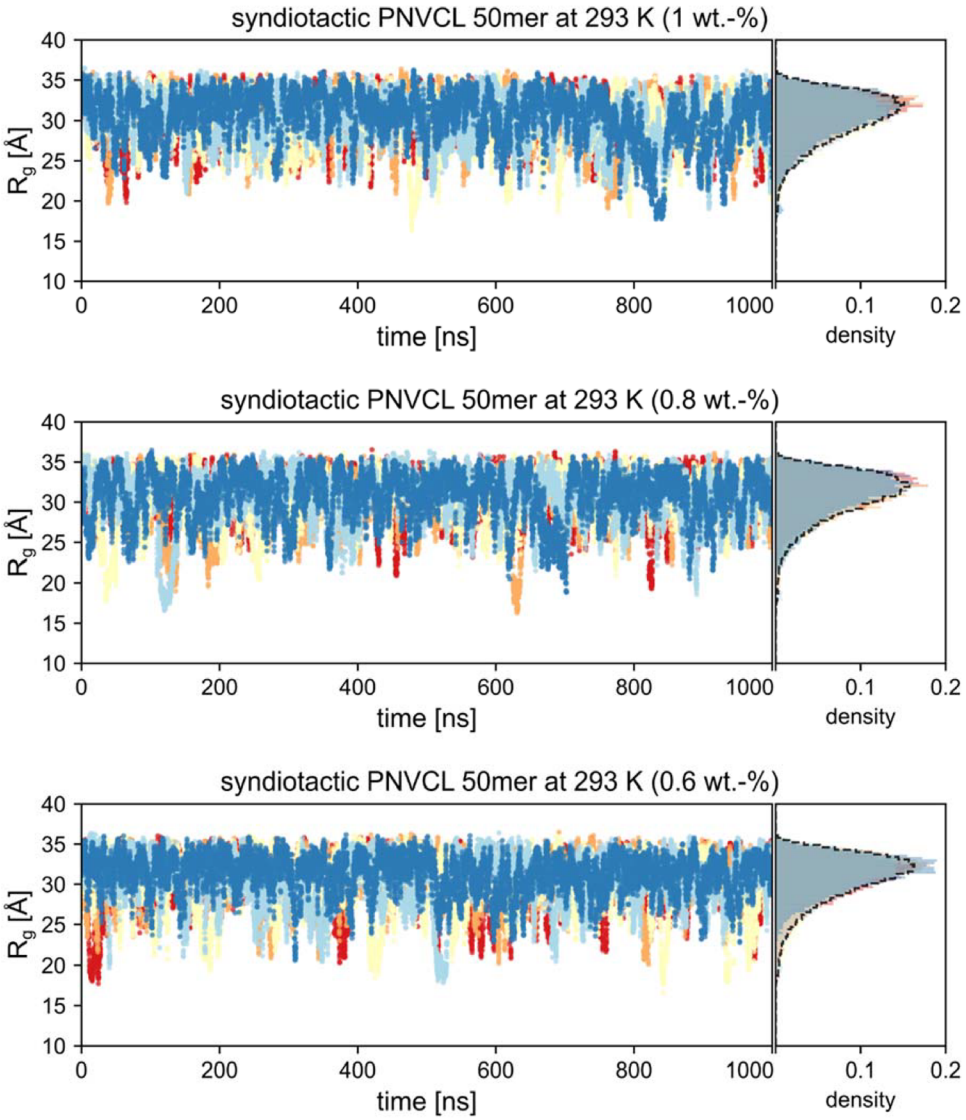

Figure S17. Radius of gyration (R_g) during five·MD simulations of 1 µs length of a syndiotactic PNVCL 50mer at 293 K for polymer concentrations of 1 wt.-%, 0.8 wt.-%, and 0.6 wt.-% (top to bottom). Corresponding frequency distributions are shown next to the time series in matching color, a frequency distribution of all data is shown as dashed black line.

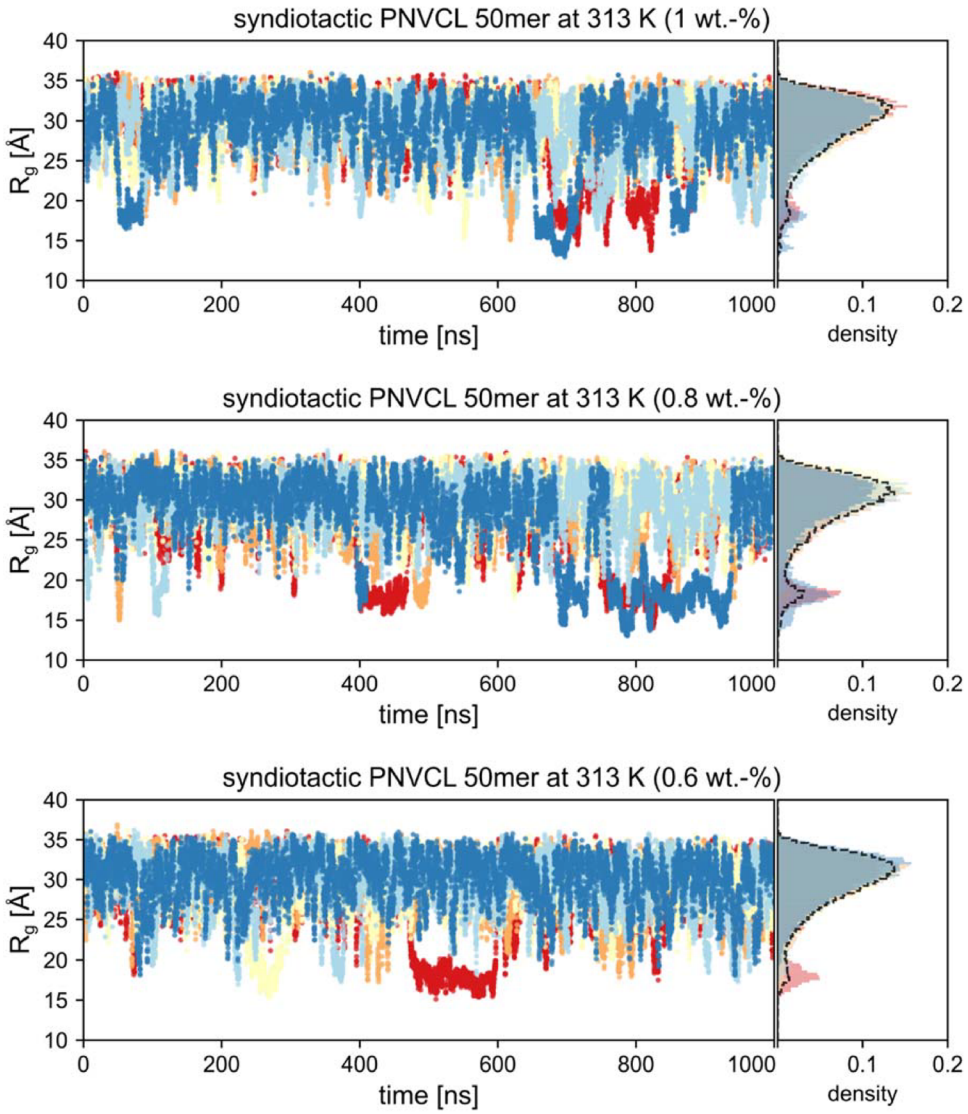

Figure S18. Radius of gyration (R_g) during five·MD simulations of 1 µs length of a syndiotactic PNVCL 50mer at 313 K for polymer concentrations of 1 wt.-%, 0.8 wt.-%, and 0.6 wt.-% (top to bottom). Corresponding frequency distributions are shown next to the time series in matching color, a frequency distribution of all data is shown as dashed black line.

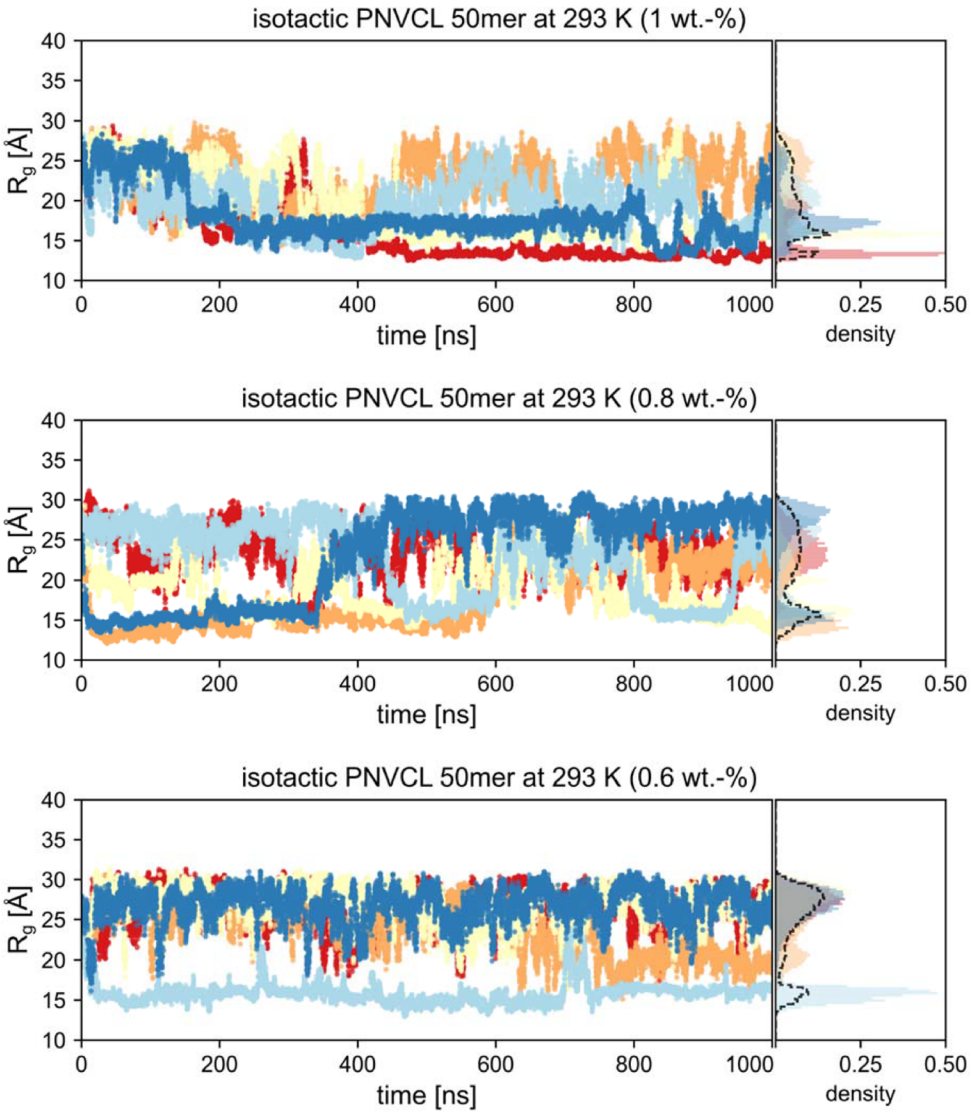

Figure S19. Radius of gyration (R_g) during five·MD simulations of 1 µs length of an isotactic PNVCL 50mer at 293 K for polymer concentrations of 1 wt.-%, 0.8 wt.-%, and 0.6 wt.-% (top to bottom). Corresponding frequency distributions are shown next to the time series in matching color, a frequency distribution of all data is shown as dashed black line.

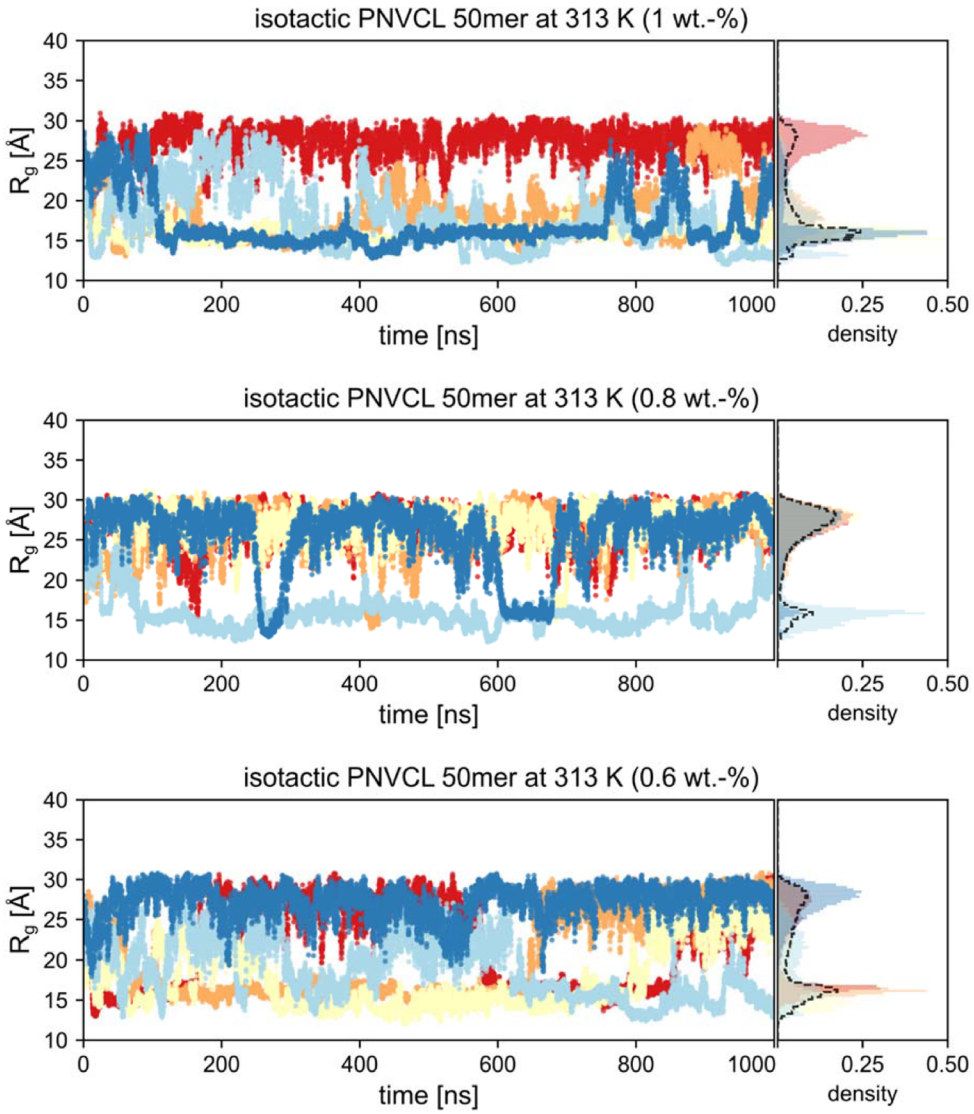

Figure S20. Radius of gyration (R_g) during five·MD simulations of 1 µs length of an isotactic PNVCL 50mer at 313 K for polymer concentrations of 1 wt.-%, 0.8 wt.-%, and 0.6 wt.-% (top to bottom). Corresponding frequency distributions are shown next to the time series in matching color, a frequency distribution of all data is shown as dashed black line.

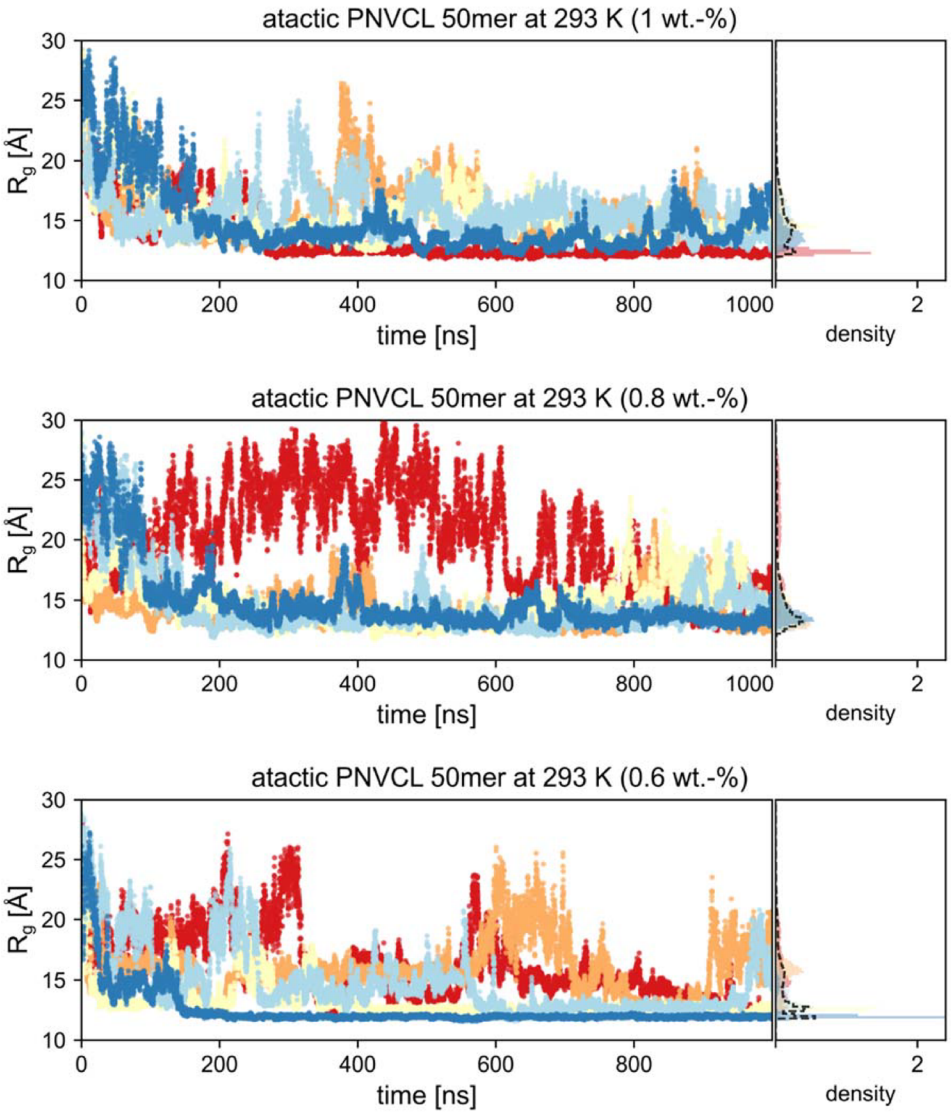

Figure S21. Radius of gyration (R_g) during five·MD simulations of 1 µs length of an atactic PNVCL 50mer at 293 K for polymer concentrations of 1 wt.-%, 0.8 wt.-%, and 0.6 wt.-% (top to bottom). Corresponding frequency distributions are shown next to the time series in matching color, a frequency distribution of all data is shown as dashed black line.

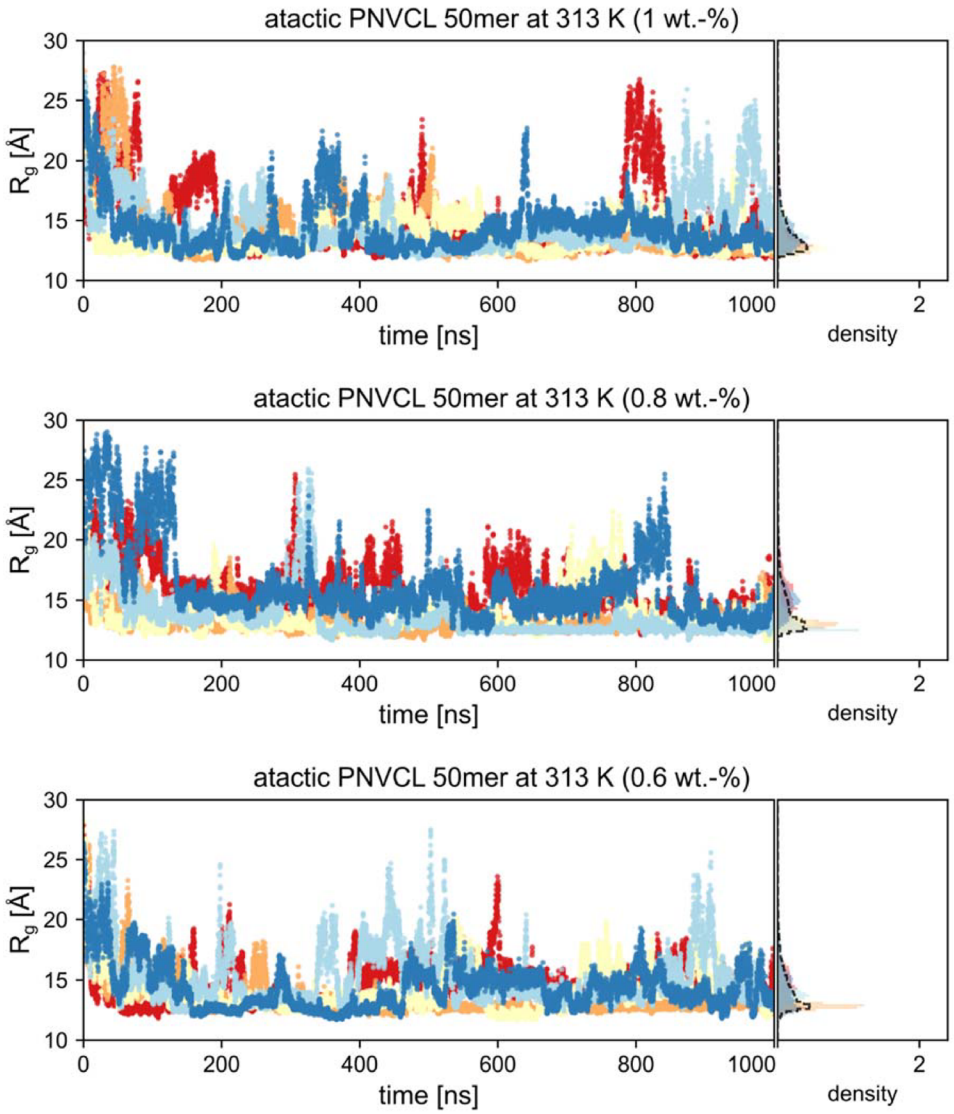

Figure S22. Radius of gyration (R_g) during five·MD simulations of 1 µs length of an atactic PNVCL 50mer at 313 K for polymer concentrations of 1 wt.-%, 0.8 wt.-%, and 0.6 wt.-% (top to bottom). Corresponding frequency distributions are shown next to the time series in matching color, a frequency distribution of all data is shown as dashed black line.

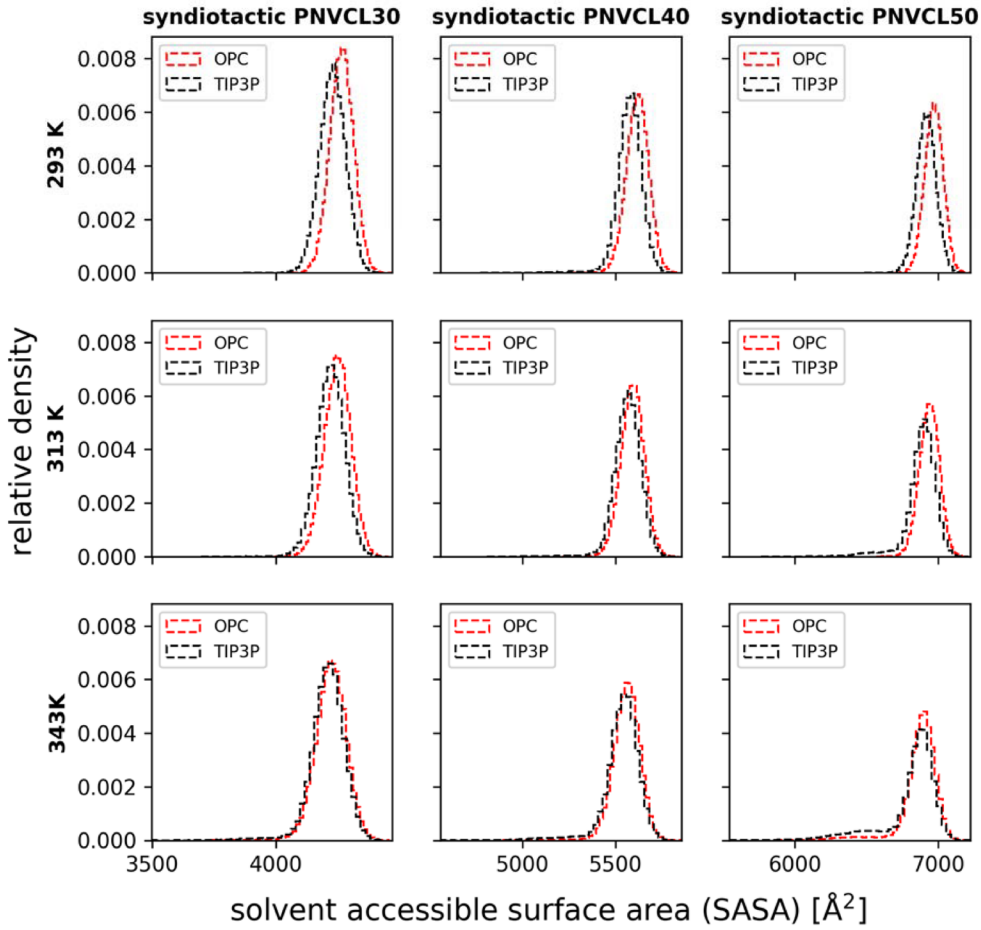

Figure S23. Influence of different water models on the solvent-accessible surface area (SASA) of syndiotactic PNVCL oligomers. The histograms depict the SASA observed in five independent 1 μs MD simulations for systems of PNVCL oligomers of varying length (30, 40, and 50 repeating units, from left to right) at different temperatures (293 K, 313K, and 343 K, from top to bottom) using the TIP3P water model (black) or the OPC water model (red).

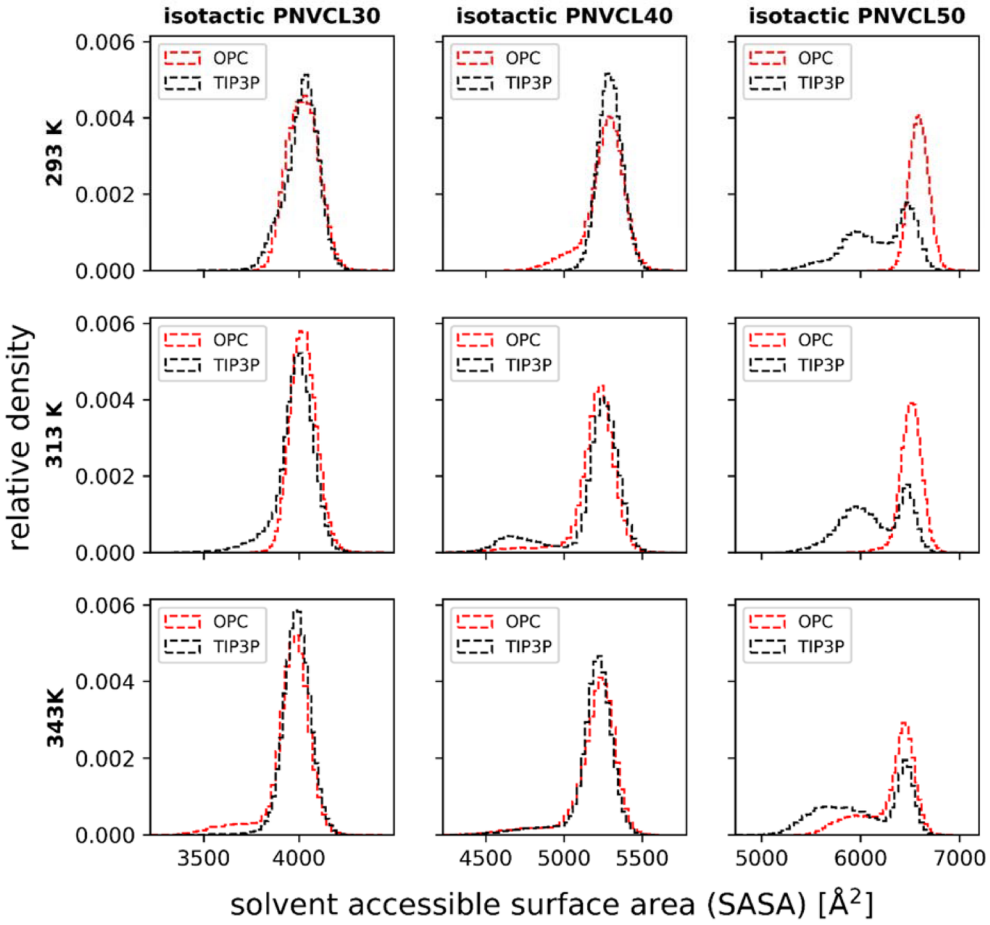

Figure S24. Influence of different water models on the solvent-accessible surface area (SASA) of isotactic PNVCL oligomers. The histograms depict the SASA observed in five independent 1 μs MD simulations for systems of PNVCL oligomers of varying length (30, 40, and 50 repeating units, from left to right) at different temperatures (293 K, 313K, and 343 K, from top to bottom) using the TIP3P water model (black) or the OPC water model (red).

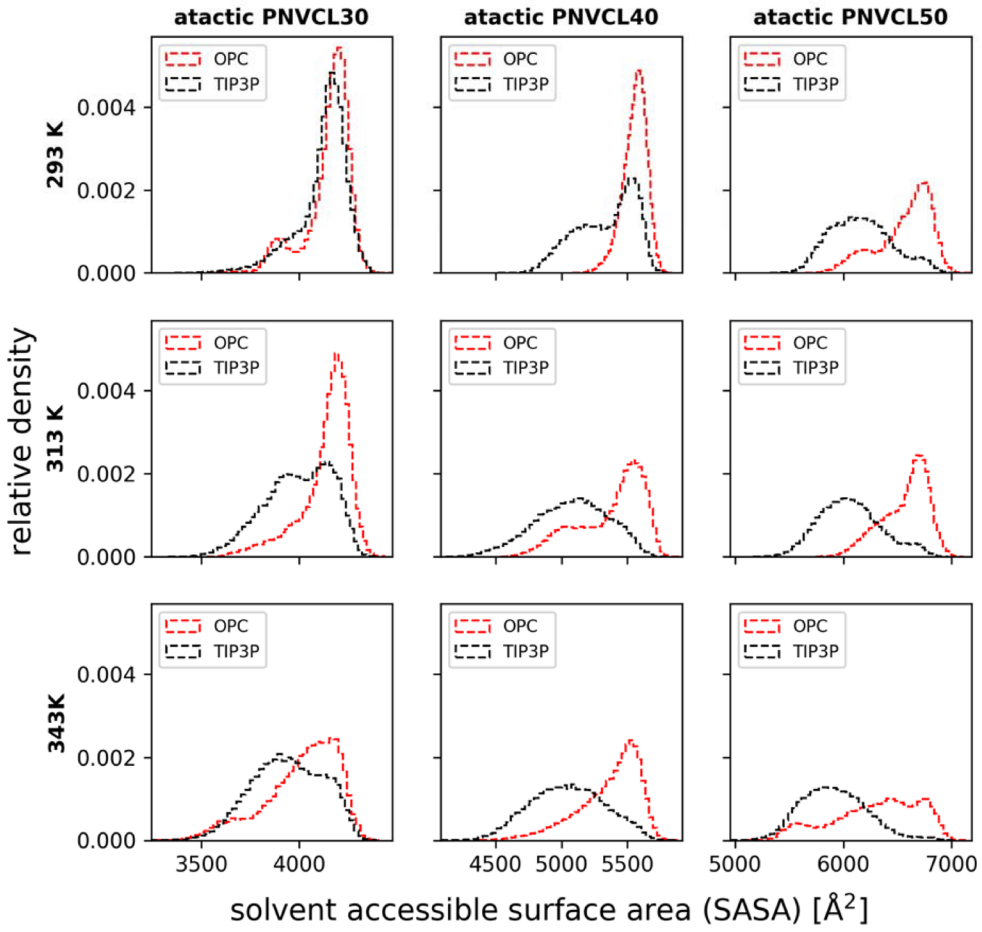

Figure S25. Influence of different water models on the solvent-accessible surface area (SASA) of atactic PNVCL oligomers. The histograms depict the SASA observed in five independent 1 μs MD simulations for systems of PNVCL oligomers of varying length (30, 40, and 50 repeating units, from left to right) at different temperatures (293 K, 313K, and 343 K, from top to bottom) using the TIP3P water model (black) or the OPC water model (red).

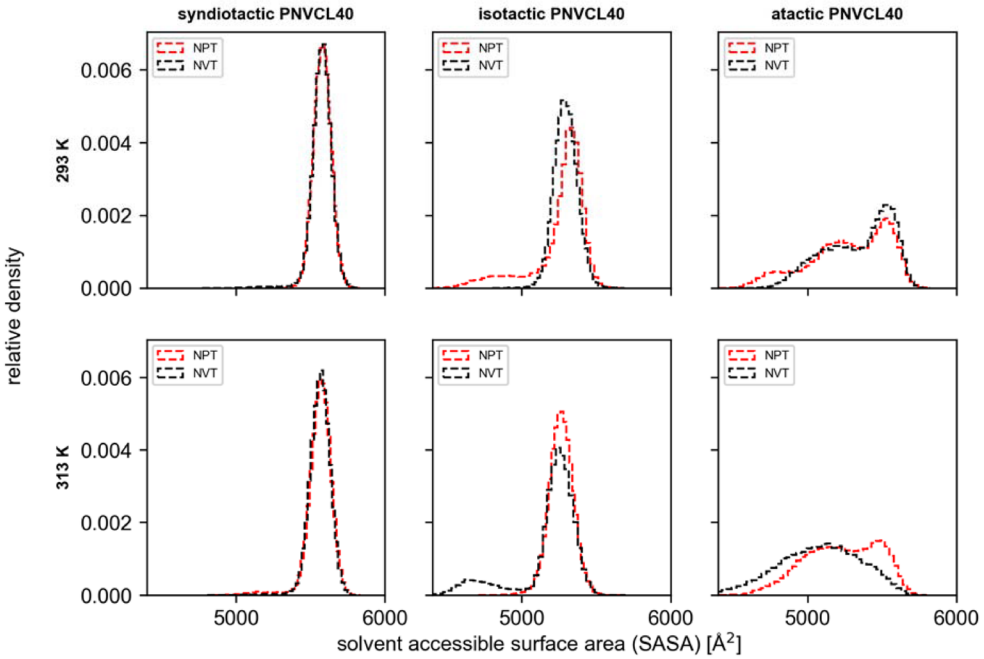

Figure S26. Influence of the MD ensemble (NVT / NPT) on the solvent-accessible surface area (SASA) of the iso-, syndio-, and atactic PNVCL 40mer. The histograms depict the SASA observed in five independent 1 µs MD simulations for each tacticity of PNVCL (from left to right) at different temperatures (293 K and 313K, from top to bottom) using the NVT (black) or NPT (red) ensemble.

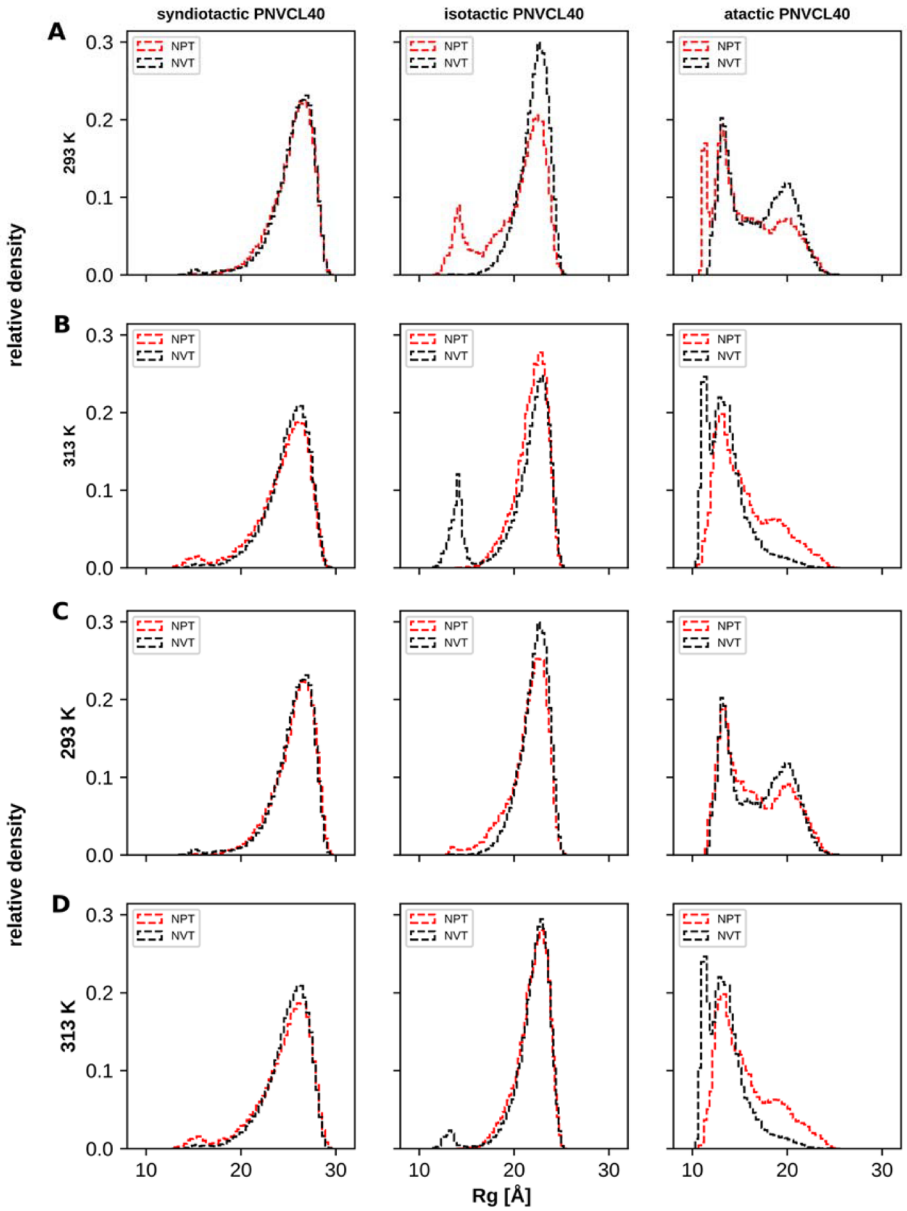

Figure S27. Influence of the MD ensemble (NVT / NPT) on the radius of gyration (R_g) of the iso-, syndio-, and atactic PNVCL 40mer. (**A, B**)The histograms depict the R_g observed in five independent 1 µs MD simulations for each tacticity of PNVCL (from left to right) at different temperatures (293 K (A) and 313K (B), from top to bottom) using the NVT (black) or NPT (red) ensemble. (**C, D**) Histograms are obtained by removing one deviating trajectory from the five trajectories of the three systems showing notable deviations in panel A and B, respectively (atactic PNVCL (293 K, NPT), isotactic PNVCL (293 K, NPT), isotactic PNVCL (313 K, NVT)).

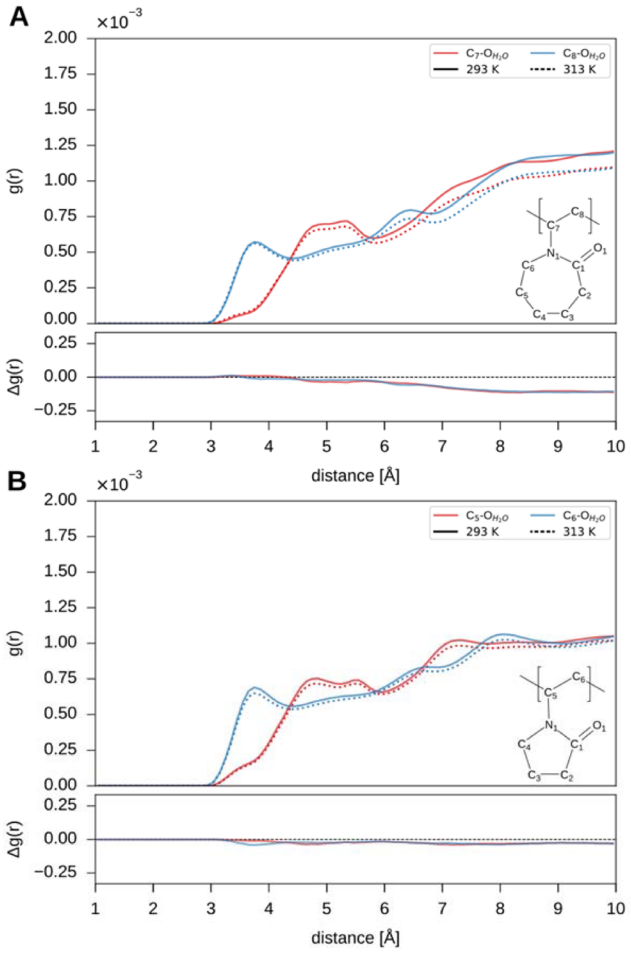

Figure S28. Radial distribution functions (RDFs) for the polymer backbone carbons atoms of PNVCL **(A)** and PVP **(B)** and the oxygen of the surrounding water molecules. Atom pairings are depicted in respective colors, and RDFs calculated from trajectories at 293 K, and 313 K are shown as solid and dotted lines, respectively. Differences in the RDFs, $\Delta g(r) = g(r)_{313} - g(r)_{293}$, are depicted in the plots below. Calculations were performed using CPPTRAJ[5].

Supplementary Tables

Table S1. Overview of performed simulations on poly(*N*-vinylcaprolactam) (PNVCL).

System				Temperature [a]	Length[b]	Replicas	Total [b]
Polymer	**Repeating units**	**Tacticity**	**MD ensemble/ water model**				
			NVT				
PNVCL	5	isotactic	TIP3P	293, 313, 343	1	5	15
PNVCL	5	syndiotactic	TIP3P	293, 313, 343	1	5	15
PNVCL	5	atactic	TIP3P	293, 313, 343	1	5	15
PNVCL	10	isotactic	TIP3P	293, 313, 343	1	5	15
PNVCL	10	syndiotactic	TIP3P	293, 313, 343	1	5	15
PNVCL	10	atactic	TIP3P	293, 313, 343	1	5	15
PNVCL	15	isotactic	TIP3P	293, 313, 343	1	5	15
PNVCL	15	syndiotactic	TIP3P	293, 313, 343	1	5	15
PNVCL	15	atactic	TIP3P	293, 313, 343	1	5	15
PNVCL	20	isotactic	TIP3P	293, 313, 343	1	5	15
PNVCL	20	syndiotactic	TIP3P	293, 313, 343	1	5	15
PNVCL	20	atactic	TIP3P	293, 313, 343	1	5	15
PNVCL	25	isotactic	TIP3P	293, 313, 343	1	5	15
PNVCL	25	syndiotactic	TIP3P	293, 313, 343	1	5	15
PNVCL	25	atactic	TIP3P	293, 313, 343	1	5	15
PNVCL	30	isotactic	TIP3P	293, 313, 343	1	5	15
PNVCL	30	syndiotactic	TIP3P	293, 313, 343	1	5	15
PNVCL	30	atactic	TIP3P	293, 313, 343	1	5	15
PNVCL	40	isotactic	TIP3P	293, 313, 343	1	5	15
PNVCL	40	syndiotactic	TIP3P	293, 313, 343	1	5	15
PNVCL	40	atactic	TIP3P	293, 313, 343	1	5	15
PNVCL	50	isotactic	TIP3P	293, 313, 343	1	5	15
PNVCL	50	syndiotactic	TIP3P	293, 313, 343	1	5	15
PNVCL	50	atactic	TIP3P	293, 313, 343	1	5	15
Sum							**360**
			NPT				
PNVCL	40	isotactic	TIP3P	293, 313	1	5	10
PNVCL	40	syndiotactic	TIP3P	293, 313	1	5	10
PNVCL	40	atactic	TIP3P	293, 313	1	5	10
Sum							**30**
			NVT				
PNVCL	30	isotactic	OPC	293, 313, 343	1	5	15
PNVCL	30	syndiotactic	OPC	293, 313, 343	1	5	15
PNVCL	30	atactic	OPC	293, 313, 343	1	5	15
PNVCL	40	isotactic	OPC	293, 313, 343	1	5	15
PNVCL	40	syndiotactic	OPC	293, 313, 343	1	5	15
PNVCL	40	atactic	OPC	293, 313, 343	1	5	15
PNVCL	50	isotactic	OPC	293, 313, 343	1	5	15
PNVCL	50	syndiotactic	OPC	293, 313, 343	1	5	15
PNVCL	50	atactic	OPC	293, 313, 343	1	5	15
Sum							**135**

Table S1 continued

			TIP3P				
PNVCL	50	isotactic	0.6 wt.-%	293, 313	1	5	10
PNVCL	50	syndiotactic	0.6 wt.-%	293, 313	1	5	10
PNVCL	50	atactic	0.6 wt.-%	293, 313	1	5	10
PNVCL	50	isotactic	0.8 wt.-%	293, 313	1	5	10
PNVCL	50	syndiotactic	0.8 wt.-%	293, 313	1	5	10
PNVCL	50	atactic	0.8 wt.-%	293, 313	1	5	10
Sum							**60**
Cumulative simulation time							**585**

[a] In [K].

[b] In [μs].

Table S2. Overview of performed simulations on poly(*N*-vinylpyrrolidone) (PVP):

System							
Polymer	**Repeating units**	**Tacticity**	**MD ensemble/ water model**	**Temperature[a]**	**Length[b]**	**Replicas**	**Total[b]**
			NVT				
PVP	30	isotactic	TIP3P	293, 313	0.5	5	5
PVP	30	syndiotactic	TIP3P	293, 313	0.5	5	5
PVP	30	atactic	TIP3P	293, 313	0.5	5·3	15
PVP	40	isotactic	TIP3P	293, 313	0.5	5	5
PVP	40	syndiotactic	TIP3P	293, 313	0.5	5	5
PVP	40	atactic	TIP3P	293, 313	0.5	5·3	15
PVP	50	isotactic	TIP3P	293, 313	0.5	5	5
PVP	50	syndiotactic	TIP3P	293, 313	0.5	5	5
PVP	50	atactic	TIP3P	293, 313	0.5	5·3	15
Cumulative simulation time							**75**

[a] In K.

[b] In μs.

Table S3. Number of atoms within each investigated system. Polymer (PNVCL/PVP) and simulation conditions (NVT/NPT and TIP3P/OPC) are provided for each section, number of repeating units and tacticity are given per row.

System		Number of atoms
PNVCL, NVT, TIP3P		
Repeating units	**Tacticity**	
5	isotactic	5073
5	atactic	4902
5	syndiotactic	4692
10	isotactic	10165
10	atactic	9400
10	syndiotactic	9559
15	isotactic	17369
15	atactic	16478
15	syndiotactic	17153
20	isotactic	26211
20	atactic	24459
20	syndiotactic	25215
25	isotactic	35779
25	atactic	33151
25	syndiotactic	33355
30	isotactic	46514
30	atactic	45164
30	syndiotactic	44609
40	isotactic	79159
40	atactic	78532
40	syndiotactic	77368
50	isotactic	123504
50	atactic	122310
50	syndiotactic	123150
PNVCL, NVT, OPC		
30	isotactic	61662
30	atactic	60254
30	syndiotactic	59478
40	isotactic	105548
40	atactic	104752
40	syndiotactic	103232
50	isotactic	164098
50	atactic	163098
50	syndiotactic	163670
PNVCL, NPT, TIP3P		
40	isotactic	79159
40	atactic	78532
40	syndiotactic	77368
PNVCL, NVT, TIP3P, 0.8 wt.-%		
50	isotactic	169311
50	atactic	167559
50	syndiotactic	168747
PNVCL, NVT, TIP3P, 0.6 wt.-%		
50	isotactic	227754
50	atactic	225354
50	syndiotactic	227061

Table S3 continued

System		Number of atoms
PVP, NVT, TIP3P		
Repeating units	Tacticity	
30	isotactic	53798
30	atactic	53804
30	atactic	51803
30	atactic	51782
30	syndiotactic	53696
40	isotactic	97348
40	atactic	97372
40	atactic	95350
40	atactic	97447
40	syndiotactic	97279
50	isotactic	154881
50	atactic	153132
50	atactic	152988
50	atactic	153057
50	syndiotactic	155220

Table S4. Residues containing cabon atoms with inverted chirality for atactic structures of PNVCL and PVP.

	Position in the chain																																																	
					5					10					15					20					25					30					35					40					45					50
PNVCL, NVT, TIP3P																																																		
5mer					x																																													
10mer	x	x		x	x		x	x	x	x																																								
15mer	x		x	x			x	x	x		x	x	x		x																																			
20mer		x		x				x					x	x	x	x		x	x																															
25mer	x	x		x			x		x			x		x		x	x	x	x			x	x		x																									
30mer		x					x		x	x	x			x		x	x	x	x		x	x		x	x	x	x	x	x																					
40mer								x		x				x	x	x	x				x	x	x		x	x	x		x	x			x	x				x	x											
50mer										x				x	x		x	x			x		x						x	x	x			x			x	x	x	x	x							x		
PNVCL, NPT, TIP3P																																																		
40mer								x		x				x	x	x	x				x	x	x		x	x	x		x	x			x	x				x	x											
PNVCL, NVT, OPC																																																		
30mer		x					x		x	x	x			x		x	x	x	x		x	x		x	x	x	x	x	x																					
40mer								x		x				x	x	x	x				x	x	x		x	x	x		x	x			x	x				x	x											
50mer										x				x	x		x	x			x		x						x	x	x			x			x	x	x	x	x							x		
PNVCL, NVT, TIP3P, different concentrations																																																		
50mer										x				x	x		x	x			x		x						x	x	x			x			x	x	x	x	x							x		
PVP, NVT, TIP3P																																																		
30mer				x	x		x	x		x	x	x	x	x				x	x	x	x			x			x	x	x																					
	x		x		x	x	x	x			x		x	x			x					x			x		x		x	x																				
		x	x	x	x	x			x		x	x	x	x			x	x		x	x		x	x					x	x																				
40mer		x	x			x			x		x	x	x		x	x		x	x	x					x	x		x	x	x	x	x		x			x													
		x	x			x	x	x		x					x				x			x	x			x		x	x					x		x	x	x		x										
	x	x			x	x		x			x				x			x	x		x	x	x		x		x			x	x	x	x		x	x	x	x	x											
50mer	x		x		x	x	x	x	x	x	x	x				x	x		x	x				x	x	x					x	x		x	x		x					x		x		x	x	x	x	x
	x	x						x		x		x	x				x		x	x			x			x			x			x	x	x					x	x	x			x		x	x			x
	x		x		x		x	x	x	x	x	x					x				x		x		x	x		x				x	x	x		x			x		x	x		x	x	x	x	x	x	x

Table S5. Partial charges and coordinates of the atoms of the PNVCL repeating unit. The repeating unit possesses two open valences/connect records (C9 and C10), its net charge is zero.

Atom number	Atom name[a]	X	Y	Z	Charge[b]
1	C10	3.540003	1.419779	0.000002	0.1586
2	N1	2.072742	1.385823	-0.113022	-0.1702
3	C1	1.361680	2.430967	0.394038	0.4927
4	C2	0.147772	2.431003	0.206963	-0.1076
5	C3	0.882646	1.277252	0.907811	0.0136
6	C4	0.873659	-0.037083	0.126603	-0.1299
7	C5	0.516471	-0.608169	-0.149407	0.0697
8	C6	1.454795	0.332093	-0.912610	-0.1441
9	H9	2.259787	-0.257933	-1.322608	0.0656
10	H10	0.934927	0.757022	-1.767444	0.0656
11	H7	0.993614	-0.902292	0.781933	0.0050
12	H8	0.402425	-1.514410	-0.740563	0.0050
13	H5	1.458537	-0.775905	0.666469	0.0292
14	H6	1.383829	0.119987	-0.823742	0.0292
15	H4	1.913757	1.579298	1.058816	0.0210
16	H3	0.460752	1.129275	1.898607	0.0210
17	H1	0.473614	3.375599	0.616797	0.0418
18	H2	0.392762	2.437013	-0.853078	0.0418
19	O1	1.880690	3.339947	0.991038	-0.6639
20	H19	3.751995	2.301651	0.578912	0.0885
21	C9	4.098076	0.210499	0.763167	0.0483
22	H17	5.182318	0.252471	0.698154	0.0096
23	H18	3.806962	-0.716729	0.274041	0.0096

[a] See Figure S6 for the structure.

[b] In e.

Table S6. Partial charges and coordinates of the atoms of the PVP repeating unit. The repeating unit possesses two open valences/connect records (C4 and C5); its net charge is zero.

Atom number	Atom name	X	Y	Z	Charge[a]
1	C4	3.540003	1.419779	0.000002	0.1324
2	N1	2.147718	1.340814	-0.422081	-0.1473
3	C2	1.262838	0.488983	0.154826	0.5274
4	C1	-0.049847	0.596013	-0.599976	-0.2009
5	C8	0.093183	1.888002	-1.406950	-0.0742
6	C3	1.612482	2.031987	-1.581003	-0.0750
7	H3	1.951550	1.570864	-2.506283	0.0560
8	H4	1.926608	3.068291	-1.597996	0.0560
9	H14	-0.428687	1.867039	-2.355686	0.0455
10	H15	-0.287779	2.726984	-0.83595	0.0455
11	H1	-0.884155	0.583035	0.08728	0.0767
12	H2	-0.135916	-0.278231	-1.24017	0.0767
13	O1	1.481789	-0.232962	1.08673	-0.6768
14	H5	3.613974	0.735868	0.83388	0.0888
15	C5	4.507986	0.953756	-1.09498	0.0573
16	H6	5.518135	1.052730	-0.70591	0.0059
17	H7	4.449030	1.624475	-1.94961	0.0059

[a] In e.

References

1. Scherer, M. K.; Trendelkamp-Schroer, B.; Paul, F.; Pérez-Hernández, G.; Hoffmann, M.; Plattner, N.; Wehmeyer, C.; Prinz, J.-H.; Noé, F., PyEMMA 2: A Software Package for Estimation, Validation, and Analysis of Markov Models. *J. Chem. Theory Comput.* **2015,** *11* (11), 5525-5542.
2. Frisch, M. J.; Trucks, G. W.; Schlegel, H. B.; Scuseria, G. E.; Robb, M. A.; Cheeseman, J. R.; Scalmani, G.; Barone, V.; Mennucci, B.; Petersson, G. A.; Nakatsuji, H.; Caricato, M.; Li, X.; Hratchian, H. P.; Izmaylov, A. F.; Bloino, J.; Zheng, G.; Sonnenberg, J. L.; Hada, M.; Ehara, M.; Toyota, K.; Fukuda, R.; Hasegawa, J.; Ishida, M.; Nakajima, T.; Honda, Y.; Kitao, O.; Nakai, H.; Vreven, T.; Montgomery, J. A., Jr.; Peralta, J. E.; Ogliaro, F.; Bearpark, M.; Heyd, J. J.; Brothers, E.; Kudin, K. N.; Staroverov, V. N.; Kobayashi, R.; Normand, J.; Raghavachari, K.; Rendell, A.; Burant, J. C.; Iyengar, S. S.; Tomasi, J.; Cossi, M.; Rega, N.; Millam, J. M.; Klene, M.; Knox, J. E.; Cross, J. B.; Bakken, V.; Adamo, C.; Jaramillo, J.; Gomperts, R.; Stratmann, R. E.; Yazyev, O.; Austin, A. J.; Cammi, R.; Pomelli, C.; Ochterski, J. W.; Martin, R. L.; Morokuma, K.; Zakrzewski, V. G.; Voth, G. A.; Salvador, P.; Dannenberg, J. J.; Dapprich, S.; Daniels, A. D.; Farkas, Ö.; Foresman, J. B.; Ortiz, J. V.; Cioslowski, J.; Fox, D. J. *Gaussian 09*, Revision A.02; Gaussian, Inc.: Wallingford CT, 2016.
3. Wang, J.; Wang, W.; Kollman, P. A.; Case, D. A., Automatic atom type and bond type perception in molecular mechanical calculations. *J. Mol. Graph. Model.* **2006,** *25* (2), 247-260.
4. Miller, B. R.; McGee, T. D.; Swails, J. M.; Homeyer, N.; Gohlke, H.; Roitberg, A. E., MMPBSA.py: An Efficient Program for End-State Free Energy Calculations. *J. Chem. Theory Comput.* **2012,** *8* (9), 3314-3321.
5. Roe, D. R.; Cheatham, T. E., PTRAJ and CPPTRAJ: Software for Processing and Analysis of Molecular Dynamics Trajectory Data. *J. Chem. Theory Comput.* **2013,** *9* (7), 3084-3095.

10. Publication III

PNVCL Microgels as Stimuli-Responsive Carrier for Okanin

Loading and Co-Solvent-Triggered Release of Okanin, a C_4 Plant Key Enzyme Inhibitor, into/from Functional Microgels

Jonas Dittrich[#], Fabian Kolodzy[#], Alexander Töpel, Andrij Pich, and Holger Gohlke

[#]these authors contributed equally.

DOI: 10.26434/chemrxiv-2022-sgbx9-v2 (ChemRxiv, 13.10.2022)

Loading and Co-Solvent-Triggered Release of Okanin, a C_4 Plant Key Enzyme Inhibitor, into/from Functional Microgels

Jonas Dittrich[a,b,†], Fabian Kolodzy[a,c,d,†], Alexander Töpel[a,c,d], Andrij Pich*[,a,c,d,e], Holger Gohlke*[,a,b,f]

[†]These authors contributed equally.

[a]Bioeconomy Science Center (BioSC), Forschungszentrum Jülich, 52425 Jülich, Germany

[b]Institute for Pharmaceutical and Medicinal Chemistry, Heinrich Heine University Düsseldorf, 40225 Düsseldorf, Germany

[c]DWI-Leibniz-Institute for Interactive Materials, RWTH Aachen University, 52056 Aachen, Germany

[d]Institute of Technical and Macromolecular Chemistry, RWTH Aachen University, 52074 Aachen, Germany

[e]Aachen Maastricht Institute for Biobased Materials, Maastricht University, Geleen, 6167 RD Netherlands

[f]John von Neumann Institute for Computing (NIC), Jülich Supercomputing Centre (JSC), and Institute of Bio- and Geosciences (IBG-4: Bioinformatics), Forschungszentrum Jülich GmbH, 52425 Jülich, Germany

Keywords: microgel carrier, all-atom molecular dynamics simulations, herbicide, free energy

Author ORCID:
Jonas Dittrich: 0000-0003-2377-2268
Fabian Kolodzy: 0000-0002-0311-0913
Alexander Töpel: 0000-0002-6801-2222
Andrij Pich: 0000-0003-1825-7798
Holger Gohlke: 0000-0001-8613-1447

*Corresponding Authors:

Andrij Pich
Address: Worringerweg 2, 52074 Aachen, Germany.
Phone: (+49) 241 80 23310
E-mail: pich@dwi.rwth-aachen.de

Holger Gohlke
Address: Universitätsstr. 1, 40225 Düsseldorf, Germany.
Phone: (+49) 211 81 13662; Fax: (+49) 211 81 13847
E-mail: gohlke@uni-duesseldorf.de

1 Abstract

The constantly growing world population leads to increasing demands for food, which challenges modern agriculture manifold. Pests, such as weeds, require the application of agrochemicals to increase crop yield. Due to the environmental impact of these potentially hazardous chemicals, the demand for more efficient formulations is increasing. Promising formulations consist of easily adaptable carriers from which controllable stimuli release the agrochemicals. Here, we investigated poly(*N*-vinylcaprolactam) (pVCL)-based microgels as a potential carrier for okanin, an inhibitor of the C_4 plant key enzyme phosphoenolpyruvate carboxylase, by combining experiments, molecular simulations, and free energy computations. Dynamic light scattering, scanning transmission electron and atomic force microscopy revealed that pVCL microgels collapse and rigidify upon the loading of okanin. The simulations identified loosely adsorbed okanin and tightly bound okanin mediating inter-chain crosslinks. With increasing okanin concentration, stacking interactions of okanin occur with adsorbed and bound okanin. These findings can explain the experimentally observed collapse and the rigidification of the microgels. Based on the atomistic insights, two poly(*N*-vinylcaprolactam-*co*-glycidyl methacrylate) microgels were synthesized, for which a doubled loading capacity of okanin was found. Finally, we investigated the triggered release of okanin using the addition of green solvents as a stimulus. This work establishes a basis for the further optimization of pVCL-based microgels as a carrier for the delivery of polyphenolic agrochemicals.

2 Introduction

Sustainable agriculture is of vital importance considering the growing world population. Crop productivity can be significantly increased by the use of fertilizers and pesticides.[1] However, wash off by rain, or spray drifts of the applied agrochemicals lead to a reduction of the applied amount of active ingredients.[2-3] Consecutively, the applied chemicals accumulate in the soil and groundwater, posing serious health risks for humans and animals. Therefore, reducing the environmental impact of hazardous chemicals is one of the most important challenges of modern sustainable agriculture. It can be addressed by either replacing chemicals with ecologically friendly alternatives or increasing the formulation's rain fastness and including either a long-term release or release-on-demand mechanism triggered by a specific stimulus.[4-5]

Different pathogens and pests are estimated to yield losses of up to 40%.[6] Without adequate protection, losses potentially rise to 80%.[7] Among all pests, weeds are possibly responsible for the highest loss.[7] Weeds are a major threat to global food production due to a rapid formation of resistance against commonly used herbicides. Hence, the constant development of novel herbicides is necessary. Chalcones are promising lead structures for the development of C_4 plant selective herbicides.[8-10] The natural polyphenolic compound okanin (2',3',4',3,4-Pentahydroxy-chalcone) was shown to be an efficient inhibitor of phosphoenolpyruvate carboxylase, a key enzyme for carbon fixation and biomass increase in the C_4 photosynthetic pathway of many of the world's most damaging weeds.[8, 11]

Microgels are crosslinked, macromolecular, porous colloids, usually showing high softness and deformability. In solution, many common microgels form stable dispersions and show a stimuli-responsive swelling.[12-13] The stimuli-responsiveness can be exploited for the controlled uptake and release of different substances by using triggers such as temperature[14-15], pH[16], and different solvents. A targeted release can be achieved by tailoring the responsiveness to these triggers. Recently, microgels have attracted attention as a versatile carrier and release system for metal ions[17], small molecules[14, 18-21], biomacromolecules[22-24], and even cells[25]. Many common monomers such as *N*-vinylcaprolactam (VCL) are suited for biological and medical applications due to the biocompatibility of the formed microgels.[26] Poly(*N*-vinylcaprolactam) (pVCL) is used for tissue engineering[27] and drug delivery[14, 18-19] as the lower critical solution temperature (LCST) is close to the human body temperature (~32 °C in water).[28] Polymer chains can be crosslinked either by forming new covalent bonds, e.g., with bifunctional monomers such as *N*,*N*'-methylenbis(acrylamide) (BIS), or by exploiting strong non-covalent interactions.[29-31] The latter is especially suited for the synthesis of degradable microgels, e.g., microgels crosslinked with the polyphenolic tannic acid, which degrade at basic conditions due to deprotonation of the

hydroxy groups.[30-31] Reactive co-monomers such as glycidyl methacrylate (GMA) can be utilized for post-polymerization modification via the addition of nucleophiles to the epoxy group.[32-33] pVCL-based microgels with a GMA-rich shell provide access to specific surface functionalization.[34] For the use of microgels in plant protection, the stimuli-responsiveness enables release as needed so agrochemicals can be retained over a longer period. This results in fewer applications per harvesting season and, thus, reduced operating costs, while simultaneously reducing the ecological footprint.[35-36] Furthermore, microgels can be modified to increase their adhesion to leaves and improve their rain-fastness. Anchor peptides, i.e., small peptides that bind to the wax layer of the plant leaves,[37] were successfully used to increase the rain-fastness of pesticide formulations. Microgels functionalized with anchor peptides were successfully used for the foliar fertilization of cucumber plants with Fe^{3+}-ions.[17]

pVCL interacts with polyphenolic moieties, as shown in the supramolecular crosslinking of pVCL with tannic acid by hydrogen bonds.[30] Thus, pVCL-based microgels should be promising candidates for binding okanin. However, a pH-triggered release of okanin from the carrier is unsuited as the resulting salt stress leads to a reduction in crop yield and quality.[38-39] Green solvents[40-41], which are environmentally compatible and authorized as additives in agricultural applications, provide a suitable alternative.

In this work, we combined experiments and molecular simulations to investigate the loading of okanin into pVCL-based microgels, elucidate the binding mode, and scrutinize the co-solvent-triggered release. First, we investigated the uptake of okanin into pure pVCL-based microgels under laboratory conditions using UV/Vis spectroscopy. Changes in the microgels' size upon okanin loading were traced via dynamic light scattering (DLS), and changes in the microgels' morphology were investigated using scanning transmission electron (STEM) and atomic force microscopy (AFM). Second, using all-atom molecular dynamics (MD) simulations of the uptake of okanin into the pVCL-based microgels, we obtained insights into the binding mode at the atomistic level. To improve the loading capacity of the microgel, we investigated the type of interaction between okanin and pVCL. Based on the simulation results, we incorporated glycidyl methacrylate (GMA) in both the core and shell of the pVCL microgels to increase the overall loading of okanin. Finally, we combined experimental and computational methods to analyze the co-solvent triggered release of okanin from microgels.

3 Materials and Methods

Materials. *N*-Vinylcaprolactam (VCL, TCI, > 98,0%) was distilled and recrystallized from *n*-hexane. Glycidyl methacrylate (GMA, Sigma-Aldrich, 97%) was distilled before use. 2,2'-Azobis(2-methylpropionamidine) dihydrochloride (AMPA, Sigma-Aldrich, 97%), *N*,*N*'-methylenbis(acrylamide) (BIS, Sigma-Aldrich, 99%), acetic acid (AcOH, Sigma-Aldrich, ≥ 99.0%), dimethyl sulfoxide (DMSO, Sigma-Aldrich, ≥ 99.0%), ethyl acetate (EtOAc, VWR Chemicals, 99.0%), and water (H_2O, Merck-Millipore, LC-MS-grade) were used without further purification.

UV/Vis spectroscopy. UV/Vis spectra were measured with a Jasco V-780 UV-Visible/NIR spectrophotometer equipped with the USE-753 cuvette holder in the range of 300 nm to 800 nm in steps of 0.5 nm and a scanning speed of 400 nm min^{-1}. Samples in an aqueous solution were measured in polystyrene cuvettes against ultra-pure water. Samples in DMSO were measured in Quartz SUPRASIL cuvettes from Hellma Analytics against DMSO. The optical path length of all cuvettes was 1.0 cm. To obtain maximum absorbance < 1.1, samples were diluted accordingly for all measurements.

Dynamic light scattering. Dynamic light scattering (DLS) was measured at 20 °C and 50 °C with a Zetasizer Nano ZS from Malvern, operating a laser at 632.8 nm with a power of 4 mW. The scattering angle was fixed to $\Phi = 173°$. Sample dispersions were prepared in ultra-pure water and measured in polystyrene cuvettes. The concentrations of the stock solutions of unloaded microgels are described in the Supplemental Materials and Methods. For unloaded microgels, 5 µL of the microgel stock solution were added to 1200 µL of ultra-pure water ($c_{DLS,\ sample}$ = ~50 µg mL^{-1}). For okanin-loaded microgels (c_{stock} = 1 mg mL^{-1}), 36 µL of the microgel stock solution were added to 1200 µL of ultra-pure water ($c_{DLS,\ sample}$ = ~30 µg mL^{-1}). A lower concentration for okanin-loaded microgels was chosen to account for the increased turbidity. Before each measurement, the temperature of the sample was equilibrated for 3 min. Measurements were repeated three times for each sample.

Raman spectroscopy. Raman spectra were measured on an RFS 100/s Raman spectrometer by Bruker with an Nd:YAG laser (λ = 1064 nm) with a spectral resolution of 4 cm^{-1}, a power of 200 mW, and 1000 scans in the range of 4000 cm^{-1} to 300 cm^{-1}. Samples were pressed into an aluminum pan before measurement. All spectra were baseline-corrected and normalized to the maximum if not stated otherwise.

Atomic force microscopy. Atomic force microscopy (AFM) was performed using a Veeco Instruments Nanoscope V microscope. An NCH POINTPROBE-Silicon SPM-sensor from NanoWorld, with a resonance frequency of 320 kHz, and a force constant of 42 N m^{-1} was used

as the cantilever. Images were recorded in tapping mode and analyzed with the software Gwyddion[42] (v. 2.51). Before use, silicon wafers were washed with toluene, dried with nitrogen, and activated with a Flecto10USB-MFC plasma etcher (Plasma Technology) with an air plasma at 0.2 mbar and a power of 100W for 180 s. The coating was achieved by spin coating 50 µL of the microgel dispersion (1.0 mg mL^{-1}) on the activated wafer at 2000 rpm for 60 s with a WS-650SZ-6NPP/LITE spin coater by Laurell.

Scanning transmission electron microscopy. Scanning transmission electron microscopy (STEM) measurements were performed on an Ultra-high Resolution Scanning Electron Microscope SU9000 (Hitachi-High Technologies America, Inc.) operating at a voltage of 30 kV. Therefore, 20 µL of a diluted microgel dispersion (0.1 g L^{-1}) were dropped on a TEM-grid (Carbon Film 200 Mesh Copper Grids, Electron Microscopy Sciences) and dried at room temperature overnight. All samples were sputtered with 2 nm carbon before the analysis. Images were analyzed with the software ImageJ[43].

Microgel synthesis and characterization. All pVCL-based microgels were synthesized by precipitation polymerization[32-34] with 10.538 mmol of monomers in 100 mL of ultra-pure water. The amount of VCL was 97.4 mol% (1428.6 mg, 10.264 mmol) for pure pVCL and 87.4 mol% (1282.0 mg, 9.210 mmol) for p(VCL-*co*-GMA). The amount of GMA in p(VCL-*co*-GMA) was 10.0 mol% (149.8 mg, 144 µL, 1.054 mmol, 10.0 mol%). 0.6 mol% AMPA (17.1 mg, 63 µmol) were used as the initiator and 2.0 mol% BIS (32.5 mg, 211 µmol) as the crosslinker. The composition of the microgels is summarized in Table S1.

The enrichment of GMA in the core (p(VCL/GMA_{core})) was achieved in a batch reaction according to Häntzschel et al. due to the higher reactivity of GMA compared to VCL.[32-33] A GMA-rich shell (p(VCL/GMA_{shell})) was obtained using a semi-batch approach with delayed addition of GMA as done in previous studies.[34] The GMA content of the lyophilized microgels was determined using Raman spectroscopy following an established procedure and was determined with 9.8 mol% and 10.7 mol% for p(VCL/GMA_{core}) and p(VCL/GMA_{shell}), respectively.[34] The Raman spectra are depicted in Figure S1. The microgels' morphology was investigated by AFM and STEM. The hydrodynamic radius (R_H) and the polydispersity index (PDI) as well as the volume phase transition temperature (VPTT) were determined by DLS. The temperature-dependent results for R_H as well as the results for the VPTT are depicted in Figure S2. More details on the microgel synthesis, the quantification of the GMA content by Raman spectroscopy, and the confirmation of the thermoresponsive properties are provided in the Supplemental Materials and Methods.

Loading of microgels with okanin. The okanin loading was investigated for pVCL, p(VCL/GMA_{shell}), and p(VCL/GMA_{core}). The workflow for the loading and purification process is depicted in Figure 1A. A microgel stock solution (13.69 mg mL^{-1}, 17.47 mg mL^{-1} and 13.42 mg mL^{-1} for pVCL, p(VCL/GMA_{core}), and p(VCL/GMA_{shell}), respectively) was used to prepare 2000 µL of a diluted microgel dispersion (1.0 mg mL^{-1}) in 2 mL centrifuge tubes. Okanin dissolved in DMSO was added to the microgel dispersions to obtain okanin concentrations of 0.014 mM, 0.05 mM, 0.1 mM, 0.5 mM, 1.0 mM, 1.3 mM, and 2.0 mM. DMSO was added so that the total volume of DMSO in each sample was 48 µL (2.4 vol.-%). For the microgels, these okanin concentrations correspond to a molar ratio n_{okanin}/n_{CU} of 0.002, 0.007, 0.014, 0.070, 0.139, 0.181, and 0.278, respectively, where n_{okanin} is the amount of okanin and n_{CU} is the number of the constitutional units (CU). The samples were mixed for 3 h. Quartz Crystal Microbalance with Dissipation monitoring (QCM-D, see Supplemental Material and Methods) experiments confirm the completion of the uptake within this time (Figure S3). Afterward, the dispersions were centrifuged for 5 min at 43 rcf (relative centrifugal force), and 1000 µL of the supernatant was taken for further purification. The microgel dispersion was centrifuged for 20 min at 6708 rcf, the supernatant was removed, and the microgel dispersion was re-dispersed in ultra-pure water. This step was repeated thrice. All loading experiments were done as triplicates. R_H and PDI of the loaded microgels were determined by DLS. Additionally, AFM and STEM were applied to determine the radius of the width (R_{AFM}, R_{STEM}) and the height (H_{AFM}) of the microgels.

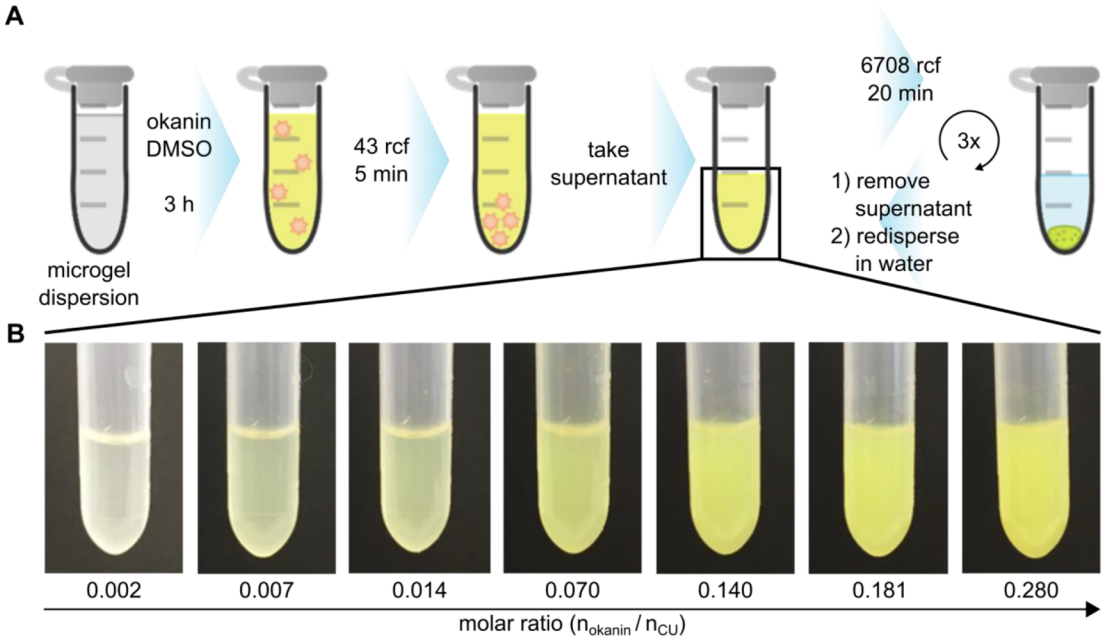

Figure 1: Experimental workflow and exemplary images for the loading of okanin into microgels. **A** Schematic workflow for the okanin loading and purification of the microgels. **B** Images of purified pVCL microgels loaded with varying amounts of okanin in relation to the number of constitutional units (n_{okanin}/n_{CU}). Schematics in this figure were created with Chemix (https://chemix.org).

Determination of the attenuation coefficient. Due to the low solubility, a stock solution of okanin could not be prepared in ultra-pure water. Thus, the attenuation coefficient was determined in a 2.4 vol.-% DMSO/water solution. For the first sample, an okanin stock solution in DMSO (c_{stock} = 1.332 mM) was prepared and 60 µL of the stock solution were added to 2500 µL of ultra-pure water such that the final okanin concentration was 31.22 µM. After measurement of the UV/Vis spectrum, 1280 µL of the solution were diluted in 1280 µL of a 2.4 vol.-% DMSO/water solution to obtain an okanin concentration of 15.61 µM. This dilution series was continued for concentrations of 7.81 µM, 3.92 µM, 1.94 µM, and 0.97 µM. The dilution series was prepared and measured in triplicates. The UV/Vis spectra are depicted in Figure S4. The average of the maximum absorbance at 377 nm for each point was calculated (Table S2) and plotted against the okanin concentration (Figure S5). The attenuation coefficient ε is equal to the slope of the linear fit ($\varepsilon_{377\,nm}$ = (3126 ± 14) · 10^1 L mol^{-1} cm^{-1}). Analogously, ε was determined in pure DMSO as the absorption maximum exhibits a bathochromic shift ($\varepsilon_{392\,nm}$ = (3279 ± 17) · 10^1 L mol^{-1} cm^{-1}), which is also observed for the binding of okanin to the microgels (Figure S6). The corresponding UV/Vis spectra are depicted in Figure S7 and the mean values for the maximal absorbance are listed in Table S3.

Measuring the loading of okanin into the microgel via UV/Vis. The loading of okanin into the microgels was determined by UV/Vis spectroscopy. 75 µL of the microgel stock solution (c_{stock} = 1 mg mL^{-1}) were added to 2500 µL of ultra-pure water (c_{sample} = ~30 µg mL^{-1}). As the turbidity of the solution depends on the initial okanin concentration (Figure 1B), the baseline correction could not be performed using the baseline of dispersed unloaded microgels. Instead, we performed a baseline correction that is independent of the swelling state of the microgel. A comparison of different baseline correction methods revealed that an exponential baseline correction is more suited than a linear baseline correction (Figure S8). The exponential baseline is defined as depicted in eq. 1:

$$A = a \cdot e^{b \cdot \lambda} \qquad \text{eq. 1}$$

where A is the absorbance at a certain wavelength, λ is the wavelength, and a and b are the fitting parameters. a and b were determined for each spectrum via a two-point method for λ_1 = 300 nm and λ_2 = 550 nm according to eq. 2 and eq. 3, respectively.

$$b = \frac{\ln\left(\frac{A_{\lambda_1}}{A_{\lambda_2}}\right)}{\lambda_1 - \lambda_2} \qquad \text{eq. 2}$$

$$a = \frac{A_{\lambda_2}}{e^{b \cdot \lambda_2}} \qquad \text{eq. 3}$$

The fitting parameters a and b as well as the maximal absorbance A_{max} before and after correction are listed in the Supporting Information (Table S3 for the calibration in DMSO and Table S4-6 for the loading of okanin into a pVCL, a p(VCL/GMA$_{core}$) and a p(VCL/GMA$_{shell}$) microgel, respectively). This correction was also applied to the calibration spectra (Figure S7) to obtain the corrected attenuation coefficient $\varepsilon_{392\,nm,corr.}$ = (3176 ± 17) · 10^1 L mol^{-1} cm^{-1} (Figure S5).

Co-solvent-triggered release. The co-solvent-triggered release was investigated for pVCL, p(VCL/GMA$_{shell}$), and p(VCL/GMA$_{core}$) loaded at an initial okanin concentration of 0.5 mM and 1.3 mM corresponding to a molar ratio of 0.070 and 0.181, respectively. The values of initial loading are shown in Table S7-9 for pVCL, p(VCL/GMA$_{shell}$), and p(VCL/GMA$_{core}$), respectively. 500 µL of the okanin-loaded microgel dispersion (1.0 mg mL^{-1}) were prepared in 1.5 mL centrifuge tubes. For water, DMSO, and AcOH, 50.0 µL (10.0 vol.-%) of the respective co-solvent were added. In the case of EtOAc, a mixture of 47.0 µL of EtOAc (9.4 vol.-%) and 3.0 µL of ultra-pure water was added due to the low solubility of EtOAc in water. The samples were mixed for 16 h. QCM-D experiments confirm the completion of the release within this time (Figure S3). Afterward, the dispersions were centrifuged for 20 min at 6708 rcf. 400 µL of the supernatant were

taken and diluted with 400 µL and 1200 µL of ultra-pure water for samples of microgels loaded at a molar ratio of 0.181 and 0.070, respectively, to determine the amount of released okanin by UV/Vis spectroscopy. All release experiments were performed in triplicates.

Computational approach. pVCL microgels often show a characteristic core-shell structure due to a gradient in crosslink density within the microgel resulting in a densely crosslinked core and less crosslinked shell.[44] To account for this core-shell structure of our microgel, we investigated the interaction of okanin with a syndiotactic linear pVCL 50mer ($M_w \approx 7{,}000$ g mol^{-1}), which represents the loosely crosslinked shell, as well as with a methyl-BIS-crosslinked cubic pVCL model with an inter-crosslink chain length of 20 repeating units ($M_w \approx 34{,}750$ g mol^{-1}), representing the densely crosslinked core (Figure 2).

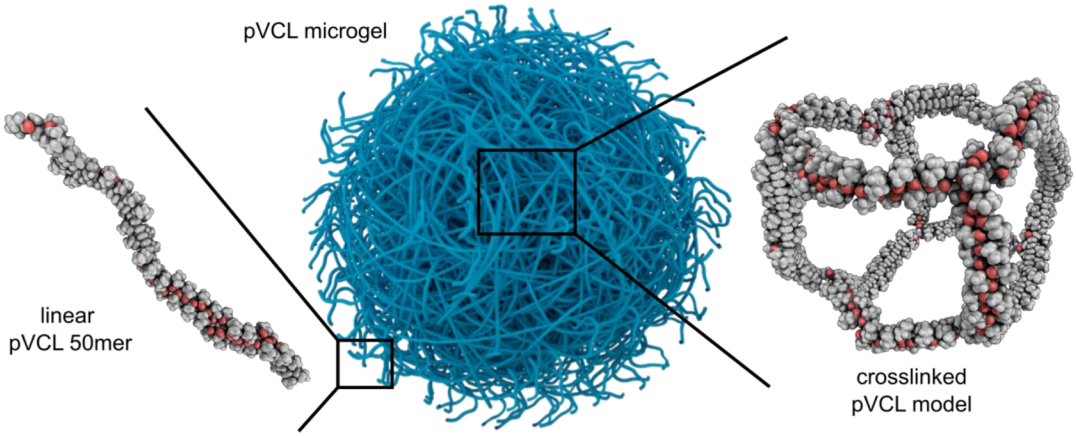

Figure 2: Decomposition of a microgel into atomistic models for the shell and core section. Simulations of linear oligomers mimic the loosely crosslinked shell of the microgel (left); the BIS-crosslinked cubic pVCL models mimic the highly crosslinked core (right).

We chose the representative models based on initial tests, in which we investigated the effect of the tacticity and crosslink density on the BIS-crosslinked polymers' thermo-responsiveness by simulating three different atactic as well as one syndiotactic and one isotactic polymer cube with an inter-crosslink chain length of 20 and 40 repeating units, respectively. For each tacticity, ten replicas were simulated for 500 ns at 293 K, 313 K, and 343 K in the TIP3P[45] water model, resulting in a cumulative simulation time of 150 µs (Table S10). In line with previous experiments[46], we found a dependency of the phase transition of the pVCL model on the polymer's tacticity. Atactic and isotactic pVCL models collapse irrespective of the temperature and inter-crosslink chain length (Figure S9 and Figure S10). Syndiotactic pVCL showed the expected thermo-responsiveness irrespective of the inter-crosslink chain length and was selected as a model representing the core section of a pVCL microgel. To evaluate the influence of the chosen water model, we performed simulations of a crosslinked pVCL model with an inter-crosslink chain

length of 20 in OPC[47] water (Table S11), resulting in a cumulative simulation time of 75 µs. In agreement with previous studies,[46] the collapse of the syndiotactic pVCL is well-defined using TIP3P water (Figure S9 and Figure S10), whereas the collapse is less pronounced in OPC water (Figure S11).

To elucidate the binding mode of the herbicide okanin with the pVCL microgel carrier at an atomistic level, we employed extensive all-atom MD simulations of systems comprising linear or crosslinked pVCL with varying concentrations of okanin. We examined the influence of the okanin concentration by increasing the number of okanin molecules, going from a simulation in pure water to a molar ratio n_{okanin}/n_{CU} of 0.04, 0.14, 0.28, 0.56 to 1.11 and 0.14, 0.56 to 1.11 for the crosslinked and the linear pVCL, respectively. An overview is provided in Table S12.

To further assess the impact of okanin at different concentrations on the polymers' conformation and thermo-responsiveness, we simulated ten replicas for 1 µs each at 293 K and 313 K for each okanin concentration, yielding a cumulative simulation time of 60 µs and 120 µs for the linear and the crosslinked pVCL, respectively.

Furthermore, we investigated the effect of ethyl acetate on the pVCL cube with an inter-crosslink chain length of 20 repeating units. Ethyl acetate is considered a preferred/recommended solvent[40-41] and can potentially be used to promote okanin release from the microgel. However, we note that it is not commonly used in agricultural applications and, thus, serves as an organic solvent reference and a benchmark in our study. We selected the crosslinked systems with a low (0.04) and high (0.28) initial n_{okanin}/n_{CU} and simulated each for 1 µs, yielding an additional cumulative simulation time of 80 µs for the okanin release.

Structure preparation. The generation of the parameters for the pVCL repeating unit was described in detail in our previous work.[46] For computing atomic charges, we followed the Restrained Electrostatic Potential (RESP) procedure.[48] The electrostatic potential (ESP) was calculated at the HF/6-31G* level using Gaussian09.[49] Afterwards, the ESP was fitted using the RESP charge fitting procedure implemented in antechamber.[50] We employed the same procedure for the tetra-methylated BIS moiety and okanin. The protonation state of okanin was determined using Epik[51] within Schrödinger's Maestro[52] program, revealing a predicted pK_a value of 7.3 for the hydroxy group at position 4' (Scheme 1), which we consider deprotonated in our simulations. For okanin, missing force field parameters were generated using the parmchk2 module of Amber20[53]. Oligomeric pVCL and the crosslinked pVCL structures were generated using the tleap module of Amber20. The library (lib) and parameter modification (frcmod) files used are available here: https://uni-duesseldorf.sciebo.de/s/iRpPo43wWEplpIb. Finally, the remaining open valence of the BIS moieties within the crosslinked pVCL model and the termini of the linear pVCL

oligomers were methyl-terminated. According to DLS measurements, the radius of the (swollen) microgel models is ~100-fold smaller than that of the experimental microgels.

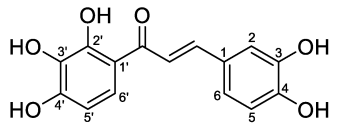

Okanin
2',3',4',3,4-Pentahydroxy-chalcone

Scheme 1: Chemical structure of okanin (2',3',4',3,4-Pentahydroxy-chalcone). Okanin has been identified as a selective inhibitor of phosphoenolpyruvate carboxylase, a key enzyme for carbon fixation in the C_4 photosynthetic pathway of damaging weeds.[8]

Molecular dynamics simulations and analysis. MD simulations were carried out with the Amber20 suite of programs[53-54] using the GPU-accelerated version of PMEMD[55-56] by following an established procedure.[46] We applied the GAFF2 force field[57] in all simulations. The structures were solvated in a cubic box of TIP3P[45] or OPC[47] water molecules. The systems comprising different tacticity and intra-crosslink chain lengths were solvated such that the distance between the boundary of the box and the closest solute atom was at least 12 Å. For the oligomeric and crosslinked pVCL systems with a variable amount of okanin, we employed PACKMOL[58] to randomly place okanin molecules within a box comprising ~102,900 water molecules, where the box is centered at the geometric center of the pVCL model. Periodic boundary conditions were applied using the particle mesh Ewald (PME) method[59] to treat long-range electrostatic interactions. Bond lengths involving bonds to hydrogen atoms were constrained by the SHAKE[60] algorithm. The time step for all MD simulations was 2 fs, and a direct-space non-bonded cutoff of 8 Å was applied.

Geometric analyses of the trajectories were performed with pytraj[61] and CPPTRAJ.[62] To investigate the properties of pVCL interacting with okanin, we determined key characteristics such as the radius of gyration (R_g) of the pVCL and the contacts of the okanin with the pVCL. We define a contact by a distance cutoff, i.e., as any heavy atom of the okanin within 6 Å of any atom of the pVCL. Furthermore, we consider okanin with at least five contacts "adsorbed" and with > 475 contacts "bound" (see next section).

Free energy calculations. Following an established procedure[46], we estimate the binding free energy for the adsorption/binding of okanin to the pVCL microgel using the molecular mechanics Poisson-Boltzmann surface area (MM-PBSA)[63-66] approach. Therefore, we estimate the changes in the effective energy ($\Delta E_{MM} + \Delta G_{solvation}$) and approximate the changes in configurational entropy of the solutes (ΔS_{config}) upon binding using normal mode analysis[67] (NMA) as implemented in MM-PBSA.py.[68] Thus, $\Delta G_{binding}$ is defined as depicted in eq. 4:

$$\Delta G_{binding} = \Delta E_{MM} + \Delta G_{solvation} - T\Delta S_{config} \quad \text{eq. 4}$$

E_{MM} is the sum of bonded and non-bonded molecular mechanics energies (eq. 5):

$$E_{MM} = \sum_{bonds} E_{bond} + \sum_{angles} E_{angle} + \sum_{torsions} E_{torsion} + \sum_{i \neq j}^{atoms} E_{vdW} + \sum_{i \neq j}^{atoms} E_{electrostatic} \quad \text{eq. 5}$$

G_{solv} denotes the solvation free energy (eq. 6):

$$G_{solv} = G_{pol} + G_{nonpol} \quad \text{eq. 6}$$

and changes in the configurational entropy ΔS_{config} are computed as the sum of the changes in translational, rotational, and vibrational entropy:

$$\Delta S_{config} = \Delta S_{trans} + \Delta S_{rot} + \Delta S_{vib} \quad \text{eq. 7}$$

G_{pol} is computed by solving the linear Poisson-Boltzmann equation[69-70] using a dielectric constant of 4 for the solute and 80 for water. G_{nonpol} is decomposed into a repulsive cavitation solvation free energy term G_{cavity} and an attractive dispersion solvation free energy term $G_{dispersion}$, which are calculated using a term linearly proportional to the molecular volume enclosed by the solvent-accessible surface area (SASA) and a surface-based integration method, respectively.[71] Finally, for the NMA, we assume that the polymer chains and the okanin molecules obey a rigid-rotor model, such that vibrational frequencies of normal modes can be calculated at local minima of the potential energy surface, and translational as well as rotational entropies can be calculated using standard statistical mechanical equations.[72] As done in previous works, for the NMA, we chose GB^{HCT} [73-74] as a water model, and each snapshot was minimized until the convergence criterion of a difference in minimized energies between two steps of < 0.001 kcal mol^{-1} is satisfied. We note that the ΔS_{trans} (eq. 7) depends on the solute concentration.[75] Chemical equilibria that do not conserve the number of molecules, such as binding reactions, are concentration-dependent.[76-77] Here, we obtain binding free energies for a standard state of 1 M termed $\Delta G^0_{\text{binding}}$. This results in a translational entropy for each component that is smaller by 6.4 cal mol^{-1} K^{-1} than the entropy value obtained for the standard state of an ideal gas (1 atm, 298.15 K). Finally, the temperature was set to 298 K for all MM-PBSA calculations, regardless of the simulation conditions.

In total, we calculated free energies for all okanin molecules in all seven trajectories of the linear oligomer (n_{okanin}/n_{CU} =0.14) where a coil-to-globule transition occurred (Figure S12), treating the okanin molecules as independent, following the "one-trajectory approach".[68] From the 490,000 frames in total (7 trajectories à 10,000 frames and 7 okanin molecules per system), we considered only frames where the okanin is at least adsorbed (> 5 contacts) (in total 281,065 frames) for the MM-PBSA analysis. We found a dependency of $\Delta G^0_{\text{binding}}$ on the number of contacts formed with the pVCL. For the linear regression, we find a root of 475 contacts. Thus, we consider okanin molecules with > 475 contacts "bound", as for these conformations, obtaining

a negative $\Delta G^0_{\text{binding}}$ is more probable. The distribution of obtained $\Delta G^0_{\text{binding}}$of bound okanin (> 475 contacts, 38,824 frames) is shown in Figure S13.

Determination of adsorbed/bound/stacked okanin species. Using contacts between the different moieties, i.e. contacts between okanin and i) the pVCL, ii) other okanin molecules, and iii) both of the aforementioned, it is possible to distinguish between different okanin species in our simulations. For okanin-polymer interactions, the determined threshold of at least 475 contacts for a potentially favorable interaction (see previous section) allows distinguishing *bound* okanin from loosely *adsorbed* okanin for low molar ratios of okanin and pVCL. For higher concentrations, however, we observe an increasing amount of stacked okanin molecules not only in aqueous solution but also onto already adsorbed or bound okanin. Thus, for higher okanin concentrations, the number of okanin molecules bound to the microgel cannot be determined solely from the contacts with the pVCL microgel but also has to include contacts with other okanin molecules. Choosing solely the same cutoff of 475 for the contacts to the microgel and other okanin molecules, however, overestimates the number of stacked okanin molecules within the microgel for higher molar ratios: To exclude okanin molecules that stack in solution, we thus require that at least 250 of the 475 contacts are formed with the pVCL for an okanin molecule to be considered *stacked within the microgel*. In an optimal stacking configuration, when both okanin molecules are parallel and the aromatic rings are placed atop each other, about ~250 contacts are computed for each of the involved okanin molecules. To account for possible deviations from the optimal configuration, we chose a cutoff of >200 contacts for the identification of okanin molecules involved in *stacking in solution*. Based on this classification scheme, we determined the amounts of bound and adsorbed okanin within the first layer on the microgel, okanin stacked within the microgel or in solution, and free okanin.

Quantification of okanin during release simulations in water and water/ethyl acetate. To elucidate the co-solvent-triggered release, we selected the last frames from the simulations of the crosslinked systems with an okanin/CU molar ratio of 0.04 and 0.28. All molecules within 6 Å of the pVCL microgel were kept, and all other molecules were discarded. Consecutively, the systems were re-solvated using either pure water or a saturated water/ethyl acetate solution. The resulting systems were neutralized again by adding Na^+ or Cl^- ions as needed. All okanin molecules with > 475 contacts at the first frame of the release simulations are regarded as “bound” and are traced through the 1 µs-long simulations. Every okanin molecule not at least adsorbed, i.e., shows >5 contacts, for 98.9% of the time is considered released. Therefore, the relative amount of okanin released corresponds to the number of released okanin molecules relative to the okanin molecules initially considered bound.

4 Results and Discussion

DLS, STEM, and AFM reveal that okanin triggers the collapse of the pVCL microgel and leads to a rigidification of the particle. As shown in previous works,[30-31] polyphenolic compounds form strong interactions with pVCL chains, e.g., tannic acid can be used for supramolecular crosslinking of pVCL. Therefore, pVCL-based microgels depict suitable candidates for use as carriers for the herbicide okanin. To determine the okanin loading capacity of the pVCL microgel, the initial molar ratio between okanin and the constitutional units of the microgel (n_{okanin}/n_{CU}) was varied, and the loading was determined via UV/Vis. A baseline correction of the UV/Vis spectra was performed to account for the absorbance caused by the turbidity of the microgel solution. The spectra of unloaded microgels cannot be used as a baseline since the turbidity increases with the molar ratio (Figure 1B). As the absorbance of the microgel dispersion decreases exponentially with the wavelength, we investigated using an exponential baseline instead of a linear one (Figure S8). We found that the exponential baseline correction (eq. 1-eq. 3) yields results that are more accurate. The UV/Vis spectra before and after baseline correction are depicted in Figure S6. The loading of the pVCL microgel in relation to the initial okanin concentration is depicted in Figure 3A. The loading increases linearly until a molar ratio of 0.18. Between molar ratios of 0.18 and 0.28, the amount of loaded okanin remains constant at ≈ 75 µg/mg. This observation correlates with the precipitation of okanin for molar ratios above a molar ratio of 0.18 indicating the saturation of the solution. The most efficient loading is achieved at a molar ratio of 0.18 as the loading is converged.

To elucidate the impact of the amount of loaded okanin on the swelling of the microgels, R_H was determined by DLS at 20 °C ($R_{H,\,20\,°C}$) and 50 °C ($R_{H,\,50\,°C}$) depending on the initial okanin concentration (Figure 3B). $R_{H,\,20\,°C}$ and $R_{H,\,50\,°C}$ both converge to a size of ≈ 160 nm at a molar ratio of 0.18. Independent of the temperature, fully loaded microgels are collapsed, while unloaded microgels show a temperature depending swelling (Figure S2). Therefore, the binding of okanin may lead to the loss of the microgel's thermo-responsiveness. Surprisingly, $R_{H,\,20\,°C}$ and $R_{H,\,50\,°C}$ do not continuously converge with increasing molar ratios. At a very low molar ratio (n_{okanin}/n_{CU} = 0.002), $R_{H,\,20\,°C}$ and $R_{H,\,50\,°C}$ both decrease. At higher molar ratios, $R_{H,\,20\,°C}$ increases again until reaching a molar ratio of 0.01 before the collapse of the microgels is triggered, whereas $R_{H,\,50\,°C}$ remains approximately constant (≈140-160 nm) with increasing molar ratio.

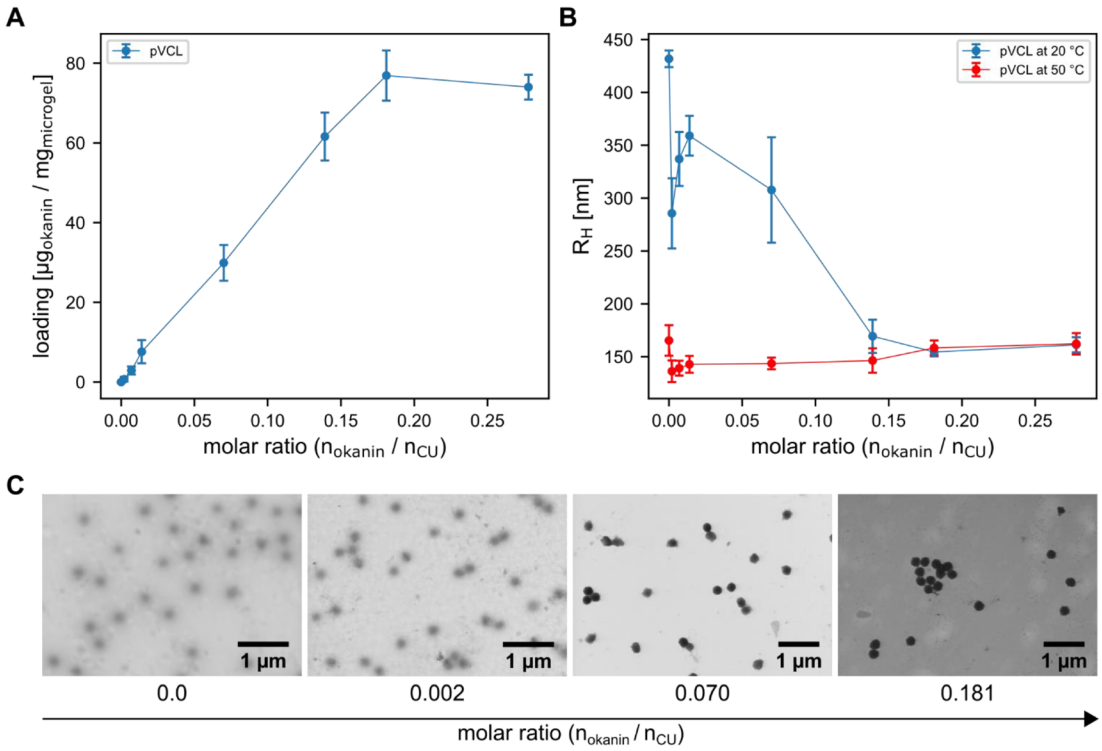

Figure 3: Influence of the loading of okanin on the hydrodynamic radius, the thermo-responsiveness, and the morphology of pVCL microgels. **A** Loading of okanin into pure pVCL microgels determined by UV/Vis for varying molar ratios n_{okanin}/n_{CU}. **B** R_H of pVCL microgels before and after loading with okanin as determined by DLS at 20 °C and 50 °C for varying n_{okanin}/n_{CU} ratios. **C** Exemplary STEM images of a pVCL microgel for varying n_{okanin}/n_{CU} ratios.

The morphology of the microgels for varying okanin concentrations during loading was investigated with STEM images (Figure 3C). A rigidification of the microgels upon loading is observed, in line with the collapse of the microgels. Two distinct morphologies are observed for a molar ratio of 0.070. This might be indicative of an inhomogeneous loading within the microgels (core/shell) with different impacts on the particles' size. While the loading of the core leads to neglectable changes in particle size, the collapse of the dangling ends can cause a substantial size decrease. Therefore, at a molar ratio of 0.070, some microgels might already be nearly saturated whereas others are not, potentially leading to the wide structural variety for this okanin/CU ratio. This observation also explains the high standard deviation observed in DLS for a molar ratio of 0.070 (Figure 3B). Surprisingly, the microgels shown in the STEM images already seem to be collapsed at a molar ratio of 0.070, which opposes the swelling determined by DLS (Figure 3B). The drying of the microgels during the preparation of STEM samples can explain this difference.

The removal of the solvent locally increases the okanin concentration and, thus, interactions between okanin and pVCL, that way enhancing the collapse.

To confirm the different effects on the size and morphology at low and high molar ratios observed by DLS, STEM and AFM images of the pVCL microgel with varying concentrations of okanin during the loading were recorded (Figure S14). Height profiles (H_{AFM}) and the radius (R_{AFM}) of the microgels were obtained (Table 1). Due to the stiffness of the loaded microgels, the cantilever moved the particles during the AFM, making it impossible to determine the particles' width with this method. Instead, the width of saturated microgels was determined from STEM images (Figure 3C). Histograms are shown in Figure S15. Due to the rigid structure of the saturated microgels, the radius of the particle (R_{STEM}) can be determined, which is usually not accessible for diffuse microgels using STEM, as they spread on the surface.

Table 1: Okanin loadings and dimensions of the pVCL microgel for varying molar ratios of okanin/CU determined by DLS, AFM, and STEM.

Molar ratio (n_{okanin}/n_{CU})	Okanin loading [$\mu g_{okanin}/mg_{microgel}$]	$R_{H,\,20\,°C}$ [nm]	$PDI_{20\,°C}$ [-]	$R_{H,\,50\,°C}$ [nm]	$PDI_{50\,°C}$ [-]	R_{STEM} [nm]	R_{AFM} [nm]	H_{AFM} [nm]
0.000	0	432 ± 8	0.159 ± 0.023	165 ± 14	0.162 ± 0.014	n.a.[1]	290 ± 36	96 ± 10
0.002	0.7 ± 0.6	286 ± 33	0.111 ± 0.044	136 ± 10	0.081 ± 0.019	n.a.[1]	277 ± 34	68 ± 6
0.070	29.9 ± 4.5	308 ± 50	0.215 ± 0.172	144 ± 5	0.050 ± 0.031	115 ± 13	n.a.[2]	138 ± 17
0.181	76.9 ± 6.3	154 ± 4	0.041 ± 0.031	158 ± 7	0.036 ± 0.019	117 ± 7	n.a.[2]	257 ± 15

[1]not available due to the diffuse morphology of the microgel.
[2]not available due to the rigid, spherical morphology of the microgel.

Compared to the untreated microgel with H_{AFM} and R_{AFM} of 96 nm and 290 nm, respectively, okanin loading at a molar ratio of 0.002 leads to a decrease in H_{AFM} and R_{AFM} to 68 nm and 277 nm, respectively. This observation agrees with the decrease of $R_{H,\,20\,°C}$ at 0.002 and indicates the collapse of the microgel's shell. At the molar ratio of 0.070, H_{AFM} increases again to 138 nm, which is in line with the observed increase in $R_{H,\,20\,°C}$. The deviation from 2 x R_{STEM} = 230 nm indicates that the microgels are still at least partly spread on the surface, in line with the previously described drying phenomenon. Finally, saturated microgels loaded at the high molar ratio of 0.181 show a height H_{AFM} of 257 ± 15 nm, which is in good agreement with 2 x R_{STEM} = 234 ± 14 nm, supporting the formation of a rigid sphere. The height increase is caused by the collapse and rigidification as the morphology continuously transitions from a spreading structure to a sharply defined spherical one.

Observed changes in the microgel's size and morphology might be caused by the formation of non-covalent okanin-mediated intra-chain crosslinks. The deviation between loading at low and high molar ratios might be caused by the structural inhomogeneity of the microgel, i.e., the loosely

crosslinked shell and the densely crosslinked core. While loading the core might lead to a slight decrease in the microgel's size, loading the shell and the accompanying collapse of the dangling chains might lead to the opposite effect. The strong decrease in size at very low molar ratios, however, might be explained by an increase in ionic strength, as it has been shown that ions and other osmolytes influence the phase transition of pVCL.[78-79] To validate our hypotheses and elucidate the interactions of okanin with the pVCL microgel at the atomistic scale, we performed molecular dynamics simulations.

Molecular dynamics simulations reveal a collapse of linear pVCL and compaction of crosslinked pVCL upon okanin loading. To elucidate the structural changes of the pVCL microgel upon okanin loading, we performed okanin loading simulations of linear and crosslinked pVCL representing the shell and the core of the microgel, respectively (Figure 2). For linear pVCL and a molar ratio (n_{okanin}/n_{CU}) of 0.14, we observed a coil-to-globule transition triggered by okanin (Figure S12, two and five out of ten trajectories for simulations at 293 K and 313 K, respectively). Interestingly, with higher amounts of okanin (molar ratio of 0.56 and 1.12), fewer coil-to-globule transitions are observed (Figure S12). In general, the collapse of linear pVCL leads to a decrease in particle size (Figure S12). For crosslinked pVCL, however, R_g and, thus, the size of the polymer increases slightly (Figure S16 to Figure S18) as the crosslinked pVCL forms porous structures (Figure S19) with an increasing amount of okanin.

Visual inspection of the okanin binding to the pVCL models revealed that the binding can be categorized into two types (Figure S20). The first type describes the frequent short-living adsorption of the okanin to only one polymer chain. The second type comprises molecules that are long-term bound to at least two chains, which may also be formed by a folded linear chain. To quantify the energetics of the two distinct binding types, we performed MM-PBSA calculations using trajectories of the linear pVCL, where a coil-to-globule transition occurred, as these trajectories comprise both types of interactions.

The collapse of linear pVCL and compaction of crosslinked pVCL is driven by minimizing the free energy of okanin binding. We performed MM-PBSA calculations on 490,000 frames from the simulation of a linear pVCL chain with a n_{okanin}/n_{CU} ratio of 0.14. We decided to use the results from the MM-PBSA analysis of okanin binding at a low n_{okanin}/n_{CU} ratio where stacking is not observed to focus on pure okanin microgel interactions. Considering MM-PBSA is an end-point method for estimating binding free energies, we only used frames where the okanin is at least adsorbed to the pVCL. The results of the MM-PBSA analysis for the adsorption and binding of okanin are depicted in Figure 4.

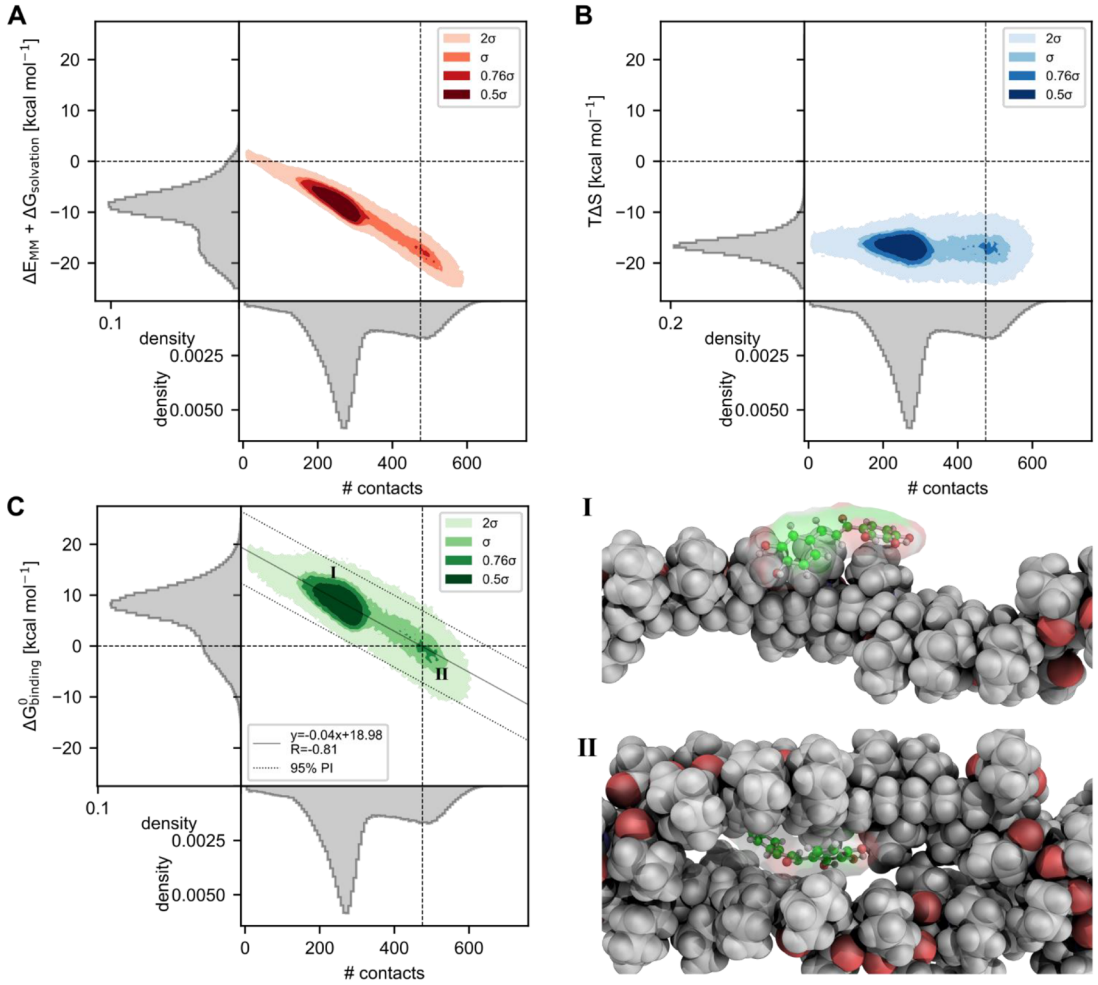

Figure 4: Two-dimensional histograms of the binding free energy of okanin to the linear pVCL 50mer and its components (changes in the gas phase energy and solvation free energy ($\Delta E_{MM} + \Delta G_{solvation}$, **A**) and changes in the configurational entropy of the solutes (TΔS, **B**)) in relation to the number of formed contacts. . The binding free energy ($\Delta G^0_{binding}$, **C**) of okanin to the pVCL polymer shows an inverse linear correlation (regression line shown solid, 95% prediction interval shown dotted, Pearson correlation coefficient and linear equation are depicted in the corresponding legend) with the number of formed contacts. Exemplary binding poses are shown for adsorbed okanin (**I**, < 475 contacts, $\Delta G^0_{binding} > 0$) and bound okanin (**II**, > 475 contacts, $\Delta G^0_{binding} < 0$). The MM-PBSA analysis was performed for trajectories of the linear pVCL 50mer, in which a collapse of the chain was observed; only frames where okanin formed contacts to pVCL were considered.

The MM-PBSA analysis reveals an inverse correlation of $\Delta E_{MM} + \Delta G_{solvation}$ for an increasing number of contacts (Figure 4A), i.e., the more contacts between the okanin and the pVCL, the more negative and, hence, favorable $\Delta E_{MM} + \Delta G_{solvation}$. Changes in the configurational entropy of the solutes (TΔS) upon the binding of okanin, however, are nearly independent of the number of formed contacts (Figure 4B). Therefore, the resulting change in binding free energy, $\Delta G^0_{binding}$, shows an inverse correlation with the number of formed contacts, too. A linear correlation reveals

that at ≈ 475 contacts, the unfavorable change in configurational entropy is outbalanced by the favorable change in $\Delta E_{MM} + \Delta G_{solvation}$. Note that for 38,824 frames where okanin has > 475 contacts with the pVCL, the $\Delta G^{0}_{binding}$ values are normally distributed with a mean value of -2.68 kcal mol^{-1} (Figure S13), indicating converged sampling of that property. The maximum number of contacts observed for the adsorption to a single pVCL chain is < 350 (Figure S21 and Figure S22). Thus, to achieve an energetically favorable binding pose, the okanin needs to be in contact with either at least two separate pVCL chains within a crosslinked pVCL microgel or within a collapsed linear chain. Within the crosslinked pVCL model, this promotes compaction as okanin forms interactions with two chains within the polymer network. For sections of the microgel containing dangling ends and a low crosslink density, comparable to the simulation using the linear pVCL oligomer, the binding of okanin leads to a substantial decrease in the particle size, as okanin promotes the coil-to-globule transition of single chains to achieve an energetically favorable binding mode.

The decomposition of ΔE_{MM} and $\Delta G_{solvation}$ yields further insights into the nature of interactions between the okanin and pVCL. ΔE_{MM} is decomposed into van der Waals (ΔE_{vdW}) and electrostatic energies (ΔE_{eel}) (eq. 5) as internal energies cancel due to the used one-trajectory approach. Upon okanin binding, both ΔE_{vdW} and ΔE_{eel} become increasingly favorable with an increasing number of formed contacts (Figure S23). Although both terms show favorable energies for the binding of okanin, ΔE_{vdW} contributes ~ 2.5 times more (~ -34.3 kcal mol^{-1} at 475 contacts, Figure S23A) than ΔE_{eel} (~ -13.3 kcal mol^{-1} at 475 contacts, Figure S23B). As expected, both ΔE_{vdW} and ΔE_{eel} contribute more favorably to the binding of okanin with an increasing number of contacts between okanin and the oligomer.

Changes in $G_{solvation}$ upon binding can be decomposed into changes in polar G_{pol} and nonpolar G_{nonpol} contributions (eq. 6), where G_{nonpol} can be further decomposed into a repulsive cavitation solvation free energy term G_{cavity}, and an attractive dispersion solvation free energy term $G_{dispersion}$. With an increasing number of contacts, ΔG_{pol} decreases linearly, i.e., okanin binding becomes more favorable with an increasing number of contacts (Figure S24A). The free energy needed for the endergonic processes of cavity formation (Figure S24B) and dispersion (Figure S24C), however, outweighs the aforementioned exergonic polar contribution, resulting in an overall unfavorable $\Delta G_{solvation}$.

To evaluate whether the binding is mainly dominated by polar or nonpolar interactions, we calculated the sum of the electrostatic terms, i.e., ΔE_{eel} and ΔG_{pol}, and the nonpolar ones, i.e., ΔE_{vdW} and ΔG_{nonpol}. The former sum is favorable with -38.9 kcal mol^{-1} at 475 contacts, whereas the latter is unfavorable with 22.6 kcal mol^{-1} at 475 contacts due to ΔG_{nonpol}. Hence, according to

the MM-PBSA analysis, polar interactions are the driving factor for okanin binding. Thus, we predict that the substitution or incorporation of moieties carrying additional (partially) charged moieties or hydrogen bond acceptors shall increase the okanin loading capacity of the microgel. This finding is well in line with using tannic acid as a supramolecular crosslinker for pVCL and other hydrogels, where hydrogen bonds were identified as the driving force for the physical crosslink.[30, 80]

MD simulations allow the quantification of different okanin species and interactions with respect to the okanin concentration in solution during loading. In our MD simulations, we identified increasing stacking interactions (Figure 5A-D, Figure S25) between the okanin molecules with increasing okanin concentrations. The stacking is observed for okanin in solution (Figure 5A, B, Figure S26) as well as for already adsorbed or bound okanin (Figure 5C, D, Figure S27 to Figure S29). Thus, a second okanin molecule might be either stacked onto an adsorbed okanin molecule (Figure 5C) or incorporated in the polymer-okanin-polymer configuration (Figure 5D) previously identified as bound okanin based on free energy calculations (Figure 4). The stacking of okanin inside the microgel might underlie the increased release of okanin from saturated microgels. The fraction of okanin found in a stacked configuration approximately linearly correlates with an increasing n_{okanin}/n_{CU} ratio (Figure 5E (blue line)). In preliminary tests, we aimed at determining the amount of bound okanin as those with > 475 contacts. However, with increasing n_{okanin}/n_{CU} ratio, this led to decreasing amounts of bound okanin (Figure 5E (green line) and Figure S27), although the number of adsorbed okanin molecules is less affected (Figure 5E (yellow line) and Figure S28). Including contacts to other okanin molecules (i.e., > 475 contacts formed with the polymer and other okanin molecules with at least 250 contacts to the polymer) allows distinguishing bound and/or stacked okanin in the microgel (Figure 5E (red line) and Figure S29) from adsorbed okanin or okanin stacked in solution in simulations with higher okanin concentrations. Additionally to the contact-based identification and quantification of stacked okanin, we monitored the increase in stacking interactions between the okanin molecules using radial distribution functions ($g(r)$) of the distances between the aromatic rings. $g(r)$ substantially increases around 4 Å for molar ratios above 0.28 (Figure S30), which supports the increased number of stacking interactions at high okanin concentrations.

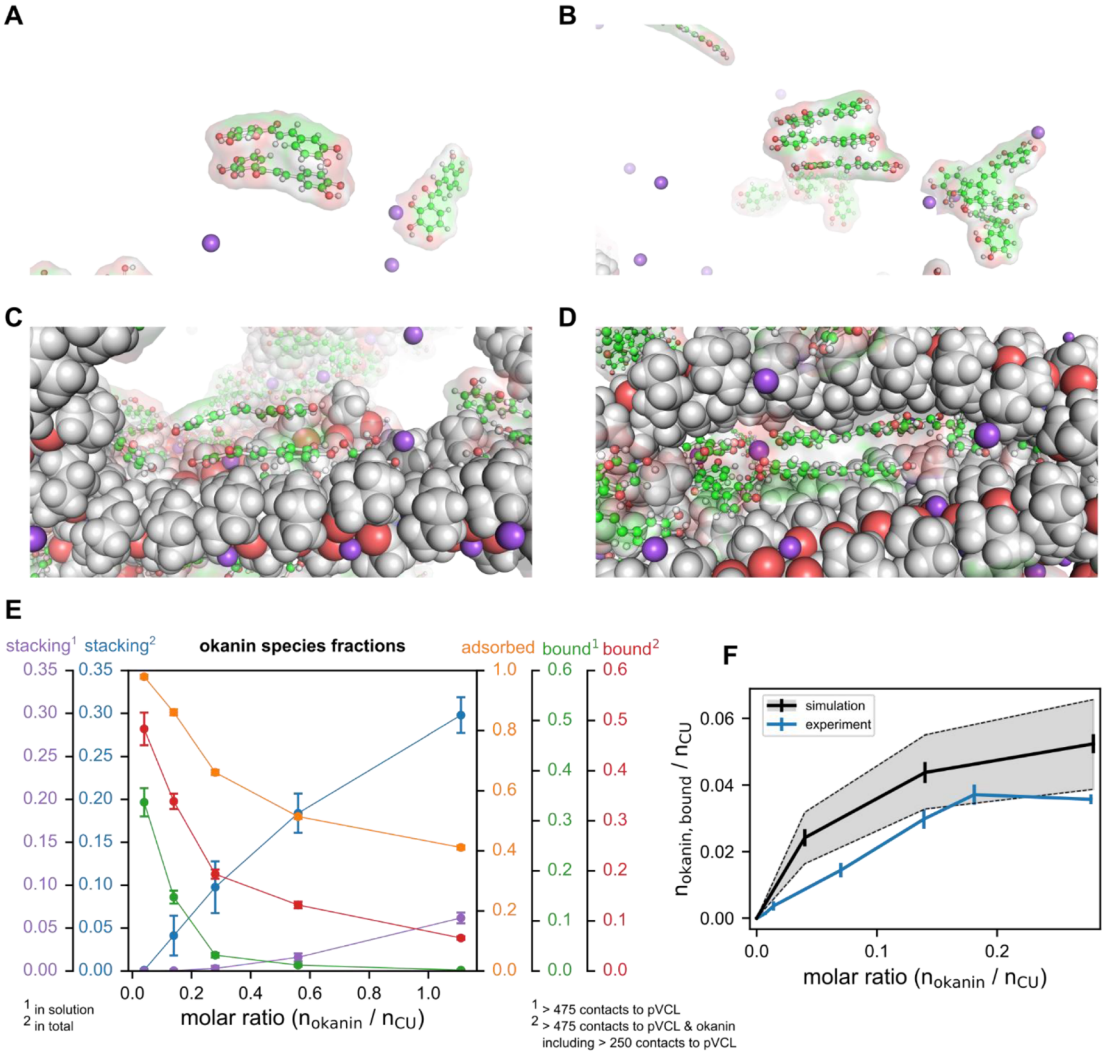

Figure 5: Quantification of different okanin species and interactions. Okanin stacks in solution (**A** two molecules, **B** three molecules), on adsorbed okanin (**C**), and within a bound state (**D**) at a high molar ratio (n_{okanin}/n_{CU} = 1.11). **E** Quantification of okanin species. Okanin species fractions are given in relation to the overall number of okanin molecules within the respective system. With increasing okanin concentration, the fraction of okanin molecules in a stacking configuration in solution increases linearly for molar ratios above 0.28 (purple), while the overall fraction including stacking to bound/adsorbed okanin (blue) increases linearly for all molar ratios. The fraction of adsorbed (yellow), bound (green), and stacked within the microgel (red) okanin decreases with increasing okanin concentration. **F** Comparison of experimentally determined bound okanin per constitutional unit ($n_{okanin,bound}/n_{CU}$) with okanin considered bound and/or stacked within the microgel (> 475 contacts to pVCL or > 475 contacts and at least 250 contacts formed with pVCL) in MD simulations. The grey shaded area depicts the uncertainty related to a change of the cutoff of ±25 contacts (i.e., 450 and 500 contacts for the upper and lower bound, respectively), which corresponds to a change of the computed binding free energy of approximately ±1 kcal mol^{-1}.

In conclusion, for an increasing n_{okanin}/n_{CU} ratio, okanin-okanin interactions become increasingly important for the behavior in solution for molar ratios above 0.28, however, stacking on already adsorbed or bound okanin is preferred at all simulated molar ratios (Figures S24-28). In solution, the increase in okanin-okanin stacking potentially leads to experimentally observed precipitation of the dispersed okanin. For low okanin concentrations, we found that okanin is primarily bound between two polymer chains as this binding mode is energetically favorably. For high concentrations, however, we observe stacking of okanin onto already adsorbed okanin, replacing one polymer chain in the polymer-okanin-polymer structure. Furthermore, we observe the incorporation of an additional okanin molecule in the polymer-okanin-polymer structure.

Considering these cases, the amount of bound and/or stacked okanin within the microgel (> 475 contacts to pVCL or > 475 contacts to pVCL and at least 250 contacts formed with the polymer) observed in simulations with increasing okanin concentration semi-quantitatively matches the experimentally determined loadings, particularly for n_{okanin}/n_{CU} ratios > 0.14 (Figure 5F). The slight overestimation of bound okanin in the simulations might be due to different length scales of the microgel particles with respect to the experiment, which may impact the access of okanin to the microgel or the egress in comparison to experimental loading/washing. Another reason might be the loss of okanin during the washing steps performed in the experimental loading process (Figure 1).

Incorporating GMA into pVCL microgels increases the overall loading capacity without changing the saturation concentration. To improve the loading capacity of pVCL-based microgels, we investigated the nature of the interactions between okanin and the pVCL microgel by MM-PBSA calculations. The calculations revealed that polar interactions are the driving factors for okanin binding to the microgel. Thus, we predicted that incorporating moieties carrying additional (partially) charged moieties or an increased number of hydrogen bond acceptors might benefit okanin loading.

To validate our hypothesis, we investigated the influence of GMA incorporation (10 mol%) on the loading capacity, as it contains more potential hydrogen bond acceptors.[32] To determine the influence of the localization of GMA, GMA was incorporated into the shell (p(VCL/GMA_{shell})) and the core (p(VCL/GMA_{core})). The amount of okanin-loaded into the p(VCL-*co*-GMA) microgels was determined analogously to pVCL using UV/Vis spectroscopy. The spectra are shown in Figure S31 and Figure S32 and the results are depicted in Figure 6A.

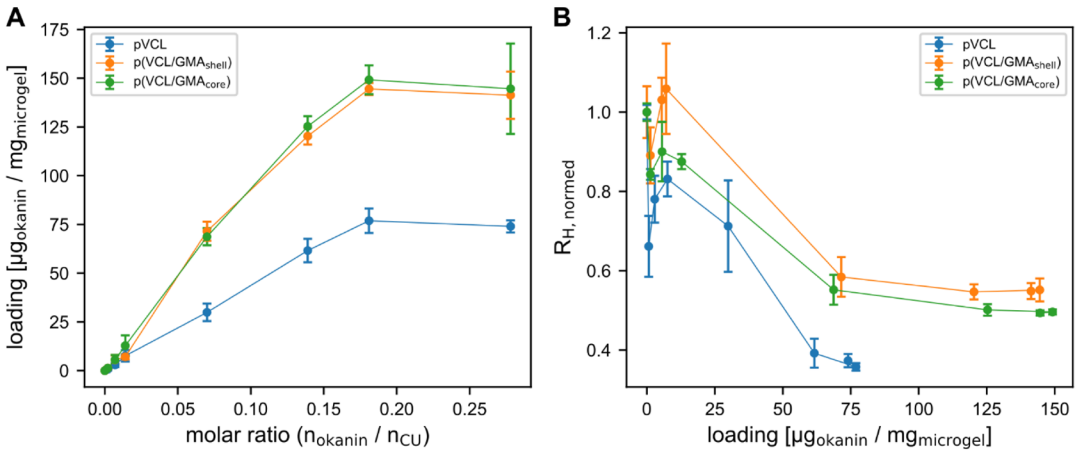

Figure 6: Determined okanin loading capacity of pVCL and p(VCL-*co*-GMA) microgels and effect on the microgel size. **A** Loading of okanin into pVCL and p(VCL-*co*-GMA) microgels determined by UV/Vis in dependency of the molar ratio n_{okanin}/n_{CU}. **B** $R_{H, normed}$ of pVCL and p(VCL-*co*-GMA) microgels determined by DLS at 20 °C.

The loading increases linearly for both p(VCL-*co*-GMA) microgels analogous to the pure pVCL microgel. Saturation of the microgels is achieved at a molar ratio of 0.18, independent of the microgel variant. The loading capacity of both p(VCL-*co*-GMA) microgels is ≈ 150 µg/mg and, thus, two-fold as large as the loading capacity of the pure pVCL microgel (≈ 75 µg/mg). A high amount of precipitate during the loading of okanin into p(VCL-*co*-GMA) at the highest okanin concentration led to larger errors in the amount of loaded okanin. For this reason, loading at even higher okanin concentrations is not accessible through experiment.

Surprisingly, the localization of the GMA within the microgel does not influence the loading of okanin as the loading profiles of p(VCL/GMA$_{shell}$) and p(VCL/GMA$_{core}$) are virtually identical (Figure 6A). We hypothesize that localization of the GMA-rich polymer segments in the microgel shell will enhance their accessibility and make okanin loading more efficient. $R_{H, 20\,°C}$ and $R_{H, 50\,°C}$ were determined for both p(VCL-*co*-GMA) microgels by DLS (Table S13). To determine if the collapse/compaction depends on the amount of bound okanin independent of the composition, $R_{H, 20\,°C}$ for all three microgel variants is plotted as a function of the loading and normalized to the size of the unloaded microgel, yielding the normalized hydrodynamic radius $R_{H, normed}$ (Table S13). The overall trend of $R_{H, normed}$ is similar for all three microgel variants (Figure 6B). The collapse of the GMA-containing microgels was also confirmed by AFM images (Figure S33 and Figure S34) and STEM images (Figure S35 to Figure S37). Analogous to the loading profile, the localization of the GMA within the microgels does not influence the changes in the microgel's size. Interestingly, the collapse of the microgel is triggered at loadings of 60 - 75 µg/mg, independent of the microgel composition. This is indicative of a critical amount of okanin

necessary to mediate non-covalent inter-chain crosslinks to trigger the collapse of the microgels. Moreover, further loading of okanin is observed even after the full collapse of the microgels. Thus, okanin molecules might bind onto the surface of the microgel at this point, or the collapse of the microgel might generate other sites within the microgel that are favorable for the binding of okanin.

Experiments and simulations show that the co-solvent-triggered release of okanin is more efficient than the release in pure water. For a controlled release of okanin, a suitable trigger is required to manipulate the interactions between okanin and its carrier. Green solvents depict promising candidates to shift the equilibrium between bound and unbound okanin by influencing the intermolecular interactions within the system. As release agents, we chose the green solvents EtOAc, DMSO, and AcOH. DMSO and AcOH are commonly used in agricultural formulations. The EtOAc was chosen as an organic solvent reference and as a benchmark. The co-solvent triggered release from pure pVCL microgels loaded at n_{okanin}/n_{CU} ratios of 0.07 and 0.18 were investigated by adding 9.4 vol.-% of EtOAc to the microgel dispersion. A reference was obtained by adding the same volume of water. The release of okanin in relation to the initial loading was determined via UV/Vis spectroscopy. Simultaneously, we investigated the co-solvent-induced release of okanin in MD simulations (see Quantification of okanin released during release simulations in water and water/ethyl acetate in the Materials and Methods). The comparison of both results is depicted in Figure 7A.

The relative release of pVCL loaded at a lower okanin is also lower than the release from microgels loaded at higher okanin concentration (Figure S38 to Figure S41 for simulation / Figure S42 and Figure S43 for experiments). For a low okanin loading, the release of okanin in water (2.7%) and EtOAc (10.7%) observed in experiments matches the observed release in MD simulations. For the pVCL microgel loaded at a high okanin concentration, 7.0% of the bound okanin molecules are released in water, whereas the release increases to 15.9% for EtOAc. The release observed in MD simulations also matches the experimental results for water and slightly overestimates the release in EtOAc. For the release in water, however, the overall number of released okanin molecules is lower and the desorption event is less likely. Thus, further sampling or increasing the system size might be necessary to further decrease the uncertainty in the estimated amount of released okanin.

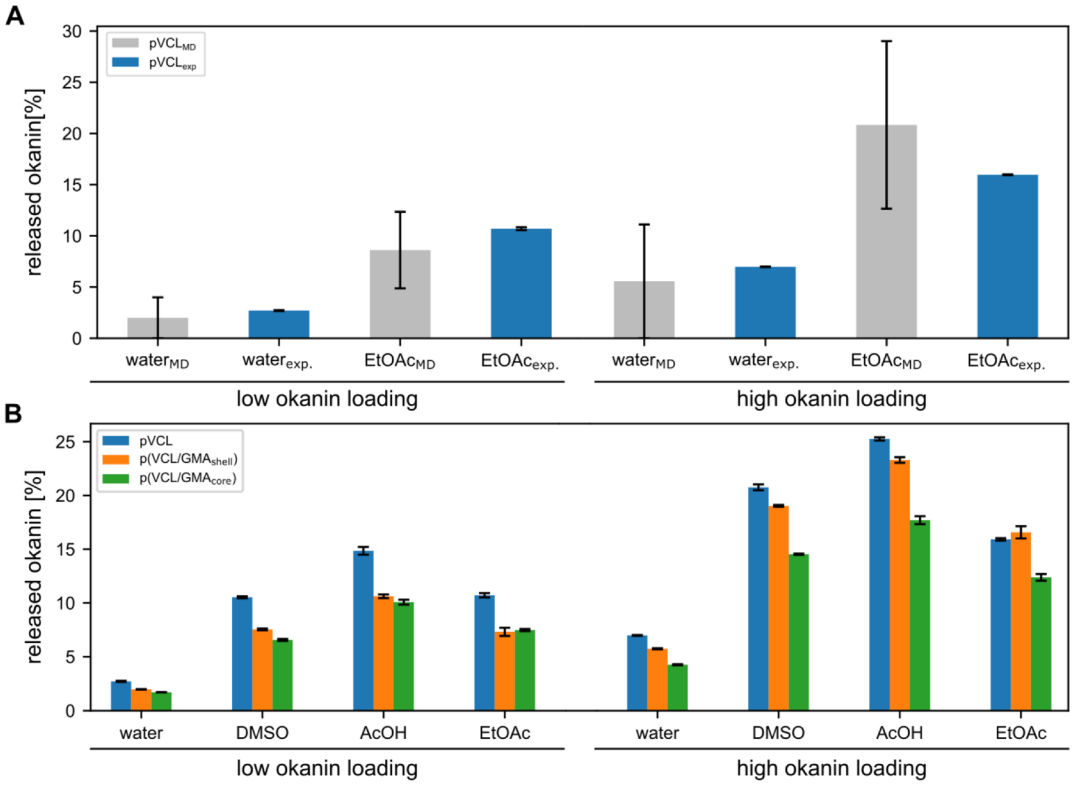

Figure 7: Co-solvent-triggered release of okanin in experiments and simulations. **A** Comparison of experimentally observed okanin release for EtOAc with release observed in MD simulations. The experimental values are compared to the release in MD simulations observed for microgels loaded at low okanin loadings (n_{okanin}/n_{CU} = 0.04 and n_{okanin}/n_{CU} = 0.07 for MD and experiment, respectively) and high okanin loading (n_{okanin}/n_{CU} = 0.28 and n_{okanin}/n_{CU} = 0.18 for MD and experiment, respectively). **B** Experimentally observed okanin release for different co-solvents (DMSO, AcOH, and EtOAc) for low (n_{okanin}/n_{CU} = 0.07) and high (n_{okanin}/n_{CU} = 0.18) okanin concentrations at loading. The initial loadings were 31.1 µg/mg and 73.0 µg/mg for pVCL, 65.7 µg/mg and 146.0 µg/mg for p(VCL/GMA$_{core}$) and 72.3 µg/mg and 144.2 µg/mg for p(VCL/GMA$_{shell}$).

Besides EtOAc, we investigated the effect of other common green solvents. We chose DMSO due to the high solubility of okanin and AcOH to probe the influence of a protic solvent. The results for the release from pVCL as well as p(VCL/GMA$_{shell}$) and p(VCL/GMA$_{core}$) are depicted in Figure 7B. Both solvents further increase the release compared to EtOAc, with the highest release observed for AcOH (25.3%). The observed trends for the different solvents are similar for all microgel variants, irrespective of the okanin concentration during loading. Although the relative release of okanin is decreased for the p(VCL-*co*-GMA) microgels, the absolute amount of okanin released is higher due to higher loading (Figure S43). The decreased relative release for the p(VCL-*co*-GMA) microgels compared to the pure pVCL microgel may be due to the okanin forming stronger interactions with the GMA moieties. Interestingly, the incorporation of GMA in

the core decreases the release stronger than in the shell, regardless of the amount of loaded okanin. This effect, however, is more pronounced for saturated microgels. Thus, we assume that the okanin is preferentially localized within the GMA-rich sections of the microgel. In the case of p(VCL/GMA_{shell}), the okanin is mainly bound to the shell from which a release is easier, whereas the release is hindered by diffusive traps in p(VCL/GMA_{core}), especially for (partially) collapsed microgels.

5 Conclusion

In this study, we investigated pVCL-based microgels as a potential carrier for okanin, an inhibitor of a C_4 plant key enzyme, in an integrated approach using experiments and simulations.

DLS, AFM, and TEM analysis revealed that upon loading of okanin, pVCL microgels collapse and rigidify. The loading profile, i.e., the amount of loaded okanin with respect to the okanin concentration during loading, was determined using UV/Vis spectroscopy. By performing molecular dynamics simulations of oligomeric and crosslinked pVCL in combination with free energy calculations, we identified two different binding modes of okanin. Besides the adsorption of okanin to the pVCL chains, we found energetically favorable binding modes in which okanin mediates inter-chain crosslinks. For high okanin concentrations, we furthermore find stacking interactions of okanin not only within the solution but also with already adsorbed or bound okanin. Considering these states, the amount of bound okanin observed in simulations is in line with the experimentally determined loading profile. These findings can explain the experimentally observed collapse of the microgels and the rigidification of the particles. Decomposition of the binding free energy revealed polar interactions as a driving factor for okanin binding. Based on these results, we synthesized two p(VCL-*co*-GMA) microgels, where the GMA is localized within either the shell or core sections of the microgel. Independent of the GMA localization, the overall loading capacity of the microgels for okanin is doubled. Finally, we investigated the triggered release of okanin from the microgels by the addition of green solvents.

Our findings show that p(VCL-*co*-GMA) microgels are promising potential carriers for the herbicide okanin. Next to the increased loading capacity of pVCL microgels that incorporate GMA, epoxy groups can be used for an easy surface modification of the microgel. If the epoxy groups are located within the shell of the microgel, they can be used to attach anchor peptides[37] to achieve an increased rain fastness of the carrier on the plant leaves. Finally, green solvents effectively triggered the (partial) release okanin, which provides a targeted way to release okanin on-demand. For the field application, this can potentially be achieved by a second spraying with an aqueous solution of a green solvent. Hence, this work establishes a basis for the further optimization of pVCL-based microgels for the delivery of herbicides with chemical properties such as okanin. In future works, the formulation efficiency in plant application has to be tested.

6 Acknowledgements

We gratefully acknowledge the computational support provided by the "Center for Information and Media Technology" (ZIM) at the Heinrich Heine University Düsseldorf and the computing time provided by the John von Neumann Institute for Computing (NIC) on the supercomputer JUWELS at Jülich Supercomputing Centre (JSC) (user IDs: HKF7, microgels). We greatly acknowledge Hannah Mathews and Nadja Wolter, who performed STEM measurements as well as Marta Santi, who prepared samples for AFM and conducted the AFM measurements.

ASSOCIATED CONTENT

Supporting Information. This material is available free of charge via the internet at https://uni-duesseldorf.sciebo.de/s/iRpPo43wWEplpIb.

AUTHOR INFORMATION

Corresponding Authors:

Andrij Pich
Address: Worringerweg 2, 52074 Aachen, Germany.
Phone: (+49) 241 80 23310
E-mail: pich@dwi.rwth-aachen.de

Holger Gohlke
Address: Universitätsstr. 1, 40225 Düsseldorf, Germany.
Phone: (+49) 211 81 13662; Fax: (+49) 211 81 13847
E-mail: gohlke@uni-duesseldorf.de

Author Contributions

J.D.† generated the atomistic models, performed the computational studies, analyzed results, and wrote the manuscript; F.K.† designed experiments, performed experimental studies, analyzed results, and wrote the manuscript; A.T. conceptualized experiments, analyzed results, and wrote the manuscript; A.P. conceived the study, supervised and managed the project, and wrote the manuscript; H.G. conceived the study, supervised and managed the project, and wrote the manuscript. All authors have approved the final version of the manuscript. †These authors contributed equally.

FUNDING SOURCES

This research is part of the scientific activities of the Bioeconomy Science Center, which were financially supported by the Ministry of Innovation, Science and Research of the German Federal State of North Rhine-Westphalia (MIWF) within the framework of the NRW Strategy Project BioSC (No. 313/323-400-00213) (funds to HG and AP within the FocusLab greenRelease). This work was performed in collaboration with the Center for Chemical Polymer Technology (CPT), which was supported by the EU (EUSMI, 731019) and the federal state of North Rhine-Westphalia (grant EFRE 300088302). We greatly acknowledge the Deutsche Forschungsgemeinschaft for financial support within the Collaborative Research Center SFB 985 “Functional Microgels and Microgel Systems”.

NOTES

The authors declare no competing financial interest.

7 References

1. Popp, J.; Pető, K.; Nagy, J., Pesticide productivity and food security. A review. *Agronomy for Sustainable Development* **2013,** *33* (1), 243-255.
2. Hunsche, M.; Alexeenko, A.; Damerow, L.; Noga, G., Rain-induced removal of copper from apple leaves: Influence of rain properties and tank-mix adjuvants on deposit characteristics at the micro scale. *Crop Protection* **2011,** *30* (4), 495-501.
3. Zhao, X.; Cui, H.; Wang, Y.; Sun, C.; Cui, B.; Zeng, Z., Development Strategies and Prospects of Nano-based Smart Pesticide Formulation. *Journal of Agricultural and Food Chemistry* **2018,** *66* (26), 6504-6512.
4. Roy, A.; Singh, S.; Bajpai, J.; Bajpai, A., Controlled pesticide release from biodegradable polymers. *Open Chemistry* **2014,** *12* (4), 453-469.
5. Athanassiou, C. G.; Kavallieratos, N. G.; Benelli, G.; Losic, D.; Usha Rani, P.; Desneux, N., Nanoparticles for pest control: current status and future perspectives. *Journal of Pest Science* **2018,** *91* (1), 1-15.
6. Savary, S.; Willocquet, L.; Pethybridge, S. J.; Esker, P.; McRoberts, N.; Nelson, A., The global burden of pathogens and pests on major food crops. *Nature Ecology & Evolution* **2019,** *3* (3), 430-439.
7. Oerke, E. C., Crop losses to pests. *The Journal of Agricultural Science* **2006,** *144* (1), 31-43.
8. Nguyen, G. T. T.; Erlenkamp, G.; Jäck, O.; Küberl, A.; Bott, M.; Fiorani, F.; Gohlke, H.; Groth, G., Chalcone-based Selective Inhibitors of a C4 Plant Key Enzyme as Novel Potential Herbicides. *Sci. Rep.* **2016,** *6* (1), 27333.
9. Chotsaeng, N.; Laosinwattana, C.; Charoenying, P., Herbicidal Activity of Flavokawains and Related trans-Chalcones against Amaranthus tricolor L. and Echinochloa crus-galli (L.) Beauv. *ACS Omega* **2019,** *4* (24), 20748-20755.
10. Liu, X.; Chen, Y.; Deng, Y.; Xiao, C.; Luan, S.; Huang, Q., Novel Galactosyl Moiety-Conjugated Furylchalcones Synthesized Facilely Display Significant Regulatory Effect on Plant Growth. *Journal of Agricultural and Food Chemistry* **2022,** *70* (6), 1766-1775.
11. Minges, A.; Janßen, D.; Offermann, S.; Groth, G., Efficient In Vivo Screening Method for the Identification of C4 Photosynthesis Inhibitors Based on Cell Suspensions of the Single-Cell C4 Plant Bienertia sinuspersici. *Frontiers in Plant Science* **2019,** *10*.
12. Plamper, F. A.; Richtering, W., Functional Microgels and Microgel Systems. *Acc. Chem. Res.* **2017,** *50* (2), 131-140.
13. Karg, M.; Pich, A.; Hellweg, T.; Hoare, T.; Lyon, L. A.; Crassous, J. J.; Suzuki, D.; Gumerov, R. A.; Schneider, S.; Potemkin, I. I.; Richtering, W., Nanogels and Microgels: From Model Colloids to Applications, Recent Developments, and Future Trends. *Langmuir* **2019,** *35* (19), 6231-6255.
14. Dirksen, M.; Dargel, C.; Meier, L.; Brändel, T.; Hellweg, T., Smart microgels as drug delivery vehicles for the natural drug aescin: uptake, release and interactions. *Colloid and Polymer Science* **2020,** *298* (6), 505-518.
15. Vihola, H.; Laukkanen, A.; Hirvonen, J.; Tenhu, H., Binding and release of drugs into and from thermosensitive poly(N-vinyl caprolactam) nanoparticles. *European Journal of Pharmaceutical Sciences* **2002,** *16* (1), 69-74.
16. Hoare, T.; Pelton, R., Impact of Microgel Morphology on Functionalized Microgel−Drug Interactions. *Langmuir* **2008,** *24* (3), 1005-1012.

17. Meurer, R. A.; Kemper, S.; Knopp, S.; Eichert, T.; Jakob, F.; Goldbach, H. E.; Schwaneberg, U.; Pich, A., Biofunctional Microgel-Based Fertilizers for Controlled Foliar Delivery of Nutrients to Plants. *Angew. Chem. Int. Ed.* **2017,** *56* (26), 7380-7386.

18. Wang, Y.; Nie, J.; Chang, B.; Sun, Y.; Yang, W., Poly(vinylcaprolactam)-Based Biodegradable Multiresponsive Microgels for Drug Delivery. *Biomacromolecules* **2013,** *14* (9), 3034-3046.

19. Li, X.; Li, H.; Zhang, C.; Pich, A.; Xing, L.; Shi, X., Intelligent nanogels with self-adaptive responsiveness for improved tumor drug delivery and augmented chemotherapy. *Bioactive Materials* **2021,** *6* (10), 3473-3484.

20. Li, X.; Sun, H.; Li, H.; Hu, C.; Luo, Y.; Shi, X.; Pich, A., Multi-Responsive Biodegradable Cationic Nanogels for Highly Efficient Treatment of Tumors. *Advanced Functional Materials* **2021,** *31* (26), 2100227.

21. Belthle, T.; Demco, D. E.; Pich, A., Nanostructuring the Interior of Stimuli-Responsive Microgels by N-Vinylimidazoles Quaternized with Hydrophobic Alkyl Chains. *Macromolecules* **2022,** *55* (3), 844-861.

22. Blackburn, W. H.; Dickerson, E. B.; Smith, M. H.; McDonald, J. F.; Lyon, L. A., Peptide-Functionalized Nanogels for Targeted siRNA Delivery. *Bioconjugate Chemistry* **2009,** *20* (5), 960-968.

23. Malmsten, M.; Bysell, H.; Hansson, P., Biomacromolecules in microgels — Opportunities and challenges for drug delivery. *Current Opinion in Colloid & Interface Science* **2010,** *15* (6), 435-444.

24. Li, F.; Wang, C.; Guo, W., Multifunctional Poly-N-Isopropylacrylamide/DNAzyme Microgels as Highly Efficient and Recyclable Catalysts for Biosensing. *Advanced Functional Materials* **2018,** *28* (10), 1705876.

25. Steinhilber, D.; Rossow, T.; Wedepohl, S.; Paulus, F.; Seiffert, S.; Haag, R., A Microgel Construction Kit for Bioorthogonal Encapsulation and pH-Controlled Release of Living Cells. *Angewandte Chemie International Edition* **2013,** *52* (51), 13538-13543.

26. Vihola, H.; Laukkanen, A.; Valtola, L.; Tenhu, H.; Hirvonen, J., Cytotoxicity of thermosensitive polymers poly(N-isopropylacrylamide), poly(N-vinylcaprolactam) and amphiphilically modified poly(N-vinylcaprolactam). *Biomaterials* **2005,** *26* (16), 3055-3064.

27. Du, Y.; Lo, E.; Ali, S.; Khademhosseini, A., Directed assembly of cell-laden microgels for fabrication of 3D tissue constructs. *Proceedings of the National Academy of Sciences* **2008,** *105* (28), 9522-9527.

28. Ramos, J.; Imaz, A.; Forcada, J., Temperature-sensitive nanogels: poly(N-vinylcaprolactam) versus poly(N-isopropylacrylamide). *Polym. Chem.* **2012,** *3* (4), 852-856.

29. Schroeder, R.; Richtering, W.; Potemkin, I. I.; Pich, A., Stimuli-Responsive Zwitterionic Microgels with Covalent and Ionic Cross-Links. *Macromolecules* **2018,** *51* (17), 6707-6716.

30. López, C. M.; Pich, A., Supramolecular Stimuli-Responsive Microgels Crosslinked by Tannic Acid. *Macromolecular Rapid Communications* **2018,** *39* (6), 1700808.

31. Jung, S. H.; Bulut, S.; Busca Guerzoni, L. P. B.; Günther, D.; Braun, S.; De Laporte, L.; Pich, A., Fabrication of pH-degradable supramacromolecular microgels with tunable size and shape via droplet-based microfluidics. *Journal of Colloid and Interface Science* **2022,** *617*, 409-421.

32. Häntzschel, N.; Zhang, F.; Eckert, F.; Pich, A.; Winnik, M. A., Poly(N-vinylcaprolactam-co-glycidyl methacrylate) Aqueous Microgels Labeled with Fluorescent LaF3:Eu Nanoparticles. *Langmuir* **2007,** *23* (21), 10793-10800.

33. Häntzschel, N.; Hund, R.-D.; Hund, H.; Schrinner, M.; Lück, C.; Pich, A., Hybrid Microgels with Antibacterial Properties. *Macromol. Biosci.* **2009,** *9* (5), 444-449.
34. Gau, E.; Mate, D. M.; Zou, Z.; Oppermann, A.; Töpel, A.; Jakob, F.; Wöll, D.; Schwaneberg, U.; Pich, A., Sortase-Mediated Surface Functionalization of Stimuli-Responsive Microgels. *Biomacromolecules* **2017,** *18* (9), 2789-2798.
35. Singh, A.; Dhiman, N.; Kar, A. K.; Singh, D.; Purohit, M. P.; Ghosh, D.; Patnaik, S., Advances in controlled release pesticide formulations: Prospects to safer integrated pest management and sustainable agriculture. *Journal of Hazardous Materials* **2020,** *385*, 121525.
36. Trenkel, M. E., Slow- and Controlled-release and Stabilized Fertilizers: An Option for Enhancing Nutrient Use Efficiency in Agriculture. International Fertilizer Industry Association: 2010.
37. Dittrich, J.; Brethauer, C.; Goncharenko, L.; Bührmann, J.; Zeisler-Diehl, V.; Pariyar, S.; Jakob, F.; Kurkina, T.; Schreiber, L.; Schwaneberg, U.; Gohlke, H., Rational Design Yields Molecular Insights on Leaf-Binding of Anchor Peptides. *ACS Appl. Mater. Interfaces* **2022**.
38. Shahid, M. A.; Sarkhosh, A.; Khan, N.; Balal, R. M.; Ali, S.; Rossi, L.; Gómez, C.; Mattson, N.; Nasim, W.; Garcia-Sanchez, F., Insights into the Physiological and Biochemical Impacts of Salt Stress on Plant Growth and Development. *Agronomy* **2020,** *10* (7), 938.
39. Flowers, T. J.; Garcia, A.; Koyama, M.; Yeo, A. R., Breeding for salt tolerance in crop plants — the role of molecular biology. *Acta Physiologiae Plantarum* **1997,** *19* (4), 427-433.
40. Prat, D.; Wells, A.; Hayler, J.; Sneddon, H.; McElroy, C. R.; Abou-Shehada, S.; Dunn, P. J., CHEM21 selection guide of classical- and less classical-solvents. *Green Chem.* **2016,** *18* (1), 288-296.
41. Alfonsi, K.; Colberg, J.; Dunn, P. J.; Fevig, T.; Jennings, S.; Johnson, T. A.; Kleine, H. P.; Knight, C.; Nagy, M. A.; Perry, D. A.; Stefaniak, M., Green chemistry tools to influence a medicinal chemistry and research chemistry based organisation. *Green Chem.* **2008,** *10* (1), 31-36.
42. Nečas, D.; Klapetek, P., Gwyddion: an open-source software for SPM data analysis. *Open Physics* **2012,** *10* (1), 181-188.
43. Rasband, W., ImageJ: Image processing and analysis in Java. *Astrophysics Source Code Library* **2012**, ascl: 1206.013.
44. Balaceanu, A.; Verkh, Y.; Kehren, D.; Tillmann, W.; Pich, A., Thermoresponsive Core-Shell Microgels. Synthesis and Characterisation. *Z. Phys. Chem.* **2014,** *228* (2-3), 253-267.
45. Jorgensen, W. L.; Chandrasekhar, J.; Madura, J. D.; Impey, R. W.; Klein, M. L., Comparison of simple potential functions for simulating liquid water. *J. Chem. Phys.* **1983,** *79* (2), 926-935.
46. Dittrich, J.; Kather, M.; Holzberger, A.; Pich, A.; Gohlke, H., Cumulative Submillisecond All-Atom Simulations of the Temperature-Induced Coil-to-Globule Transition of Poly(N-vinylcaprolactam) in Aqueous Solution. *Macromolecules* **2020,** *53* (22), 9793-9810.
47. Izadi, S.; Anandakrishnan, R.; Onufriev, A. V., Building Water Models: A Different Approach. *J. Phys. Chem. Lett.* **2014,** *5* (21), 3863-3871.
48. Bayly, C. I.; Cieplak, P.; Cornell, W.; Kollman, P. A., A well-behaved electrostatic potential based method using charge restraints for deriving atomic charges: the RESP model. *J. Phys. Chem.* **1993,** *97* (40), 10269-10280.

49. Frisch, M. J.; Trucks, G. W.; Schlegel, H. B.; Scuseria, G. E.; Robb, M. A.; Cheeseman, J. R.; Scalmani, G.; Barone, V.; Mennucci, B.; Petersson, G. A.; Nakatsuji, H.; Caricato, M.; Li, X.; Hratchian, H. P.; Izmaylov, A. F.; Bloino, J.; Zheng, G.; Sonnenberg, J. L.; Hada, M.; Ehara, M.; Toyota, K.; Fukuda, R.; Hasegawa, J.; Ishida, M.; Nakajima, T.; Honda, Y.; Kitao, O.; Nakai, H.; Vreven, T.; Montgomery, J. A., Jr.; Peralta, J. E.; Ogliaro, F.; Bearpark, M.; Heyd, J. J.; Brothers, E.; Kudin, K. N.; Staroverov, V. N.; Kobayashi, R.; Normand, J.; Raghavachari, K.; Rendell, A.; Burant, J. C.; Iyengar, S. S.; Tomasi, J.; Cossi, M.; Rega, N.; Millam, J. M.; Klene, M.; Knox, J. E.; Cross, J. B.; Bakken, V.; Adamo, C.; Jaramillo, J.; Gomperts, R.; Stratmann, R. E.; Yazyev, O.; Austin, A. J.; Cammi, R.; Pomelli, C.; Ochterski, J. W.; Martin, R. L.; Morokuma, K.; Zakrzewski, V. G.; Voth, G. A.; Salvador, P.; Dannenberg, J. J.; Dapprich, S.; Daniels, A. D.; Farkas, Ö.; Foresman, J. B.; Ortiz, J. V.; Cioslowski, J.; Fox, D. J. *Gaussian 09*, Revision A.02; Gaussian, Inc.: Wallingford CT, 2016.
50. Wang, J.; Wang, W.; Kollman, P. A.; Case, D. A., Automatic atom type and bond type perception in molecular mechanical calculations. *J. Mol. Graph. Model.* **2006,** *25* (2), 247-260.
51. Shelley, J. C.; Cholleti, A.; Frye, L. L.; Greenwood, J. R.; Timlin, M. R.; Uchimaya, M., Epik: a software program for pK(a) prediction and protonation state generation for drug-like molecules. *J. Comput. Aided Mol. Des.* **2007,** *21* (12), 681-91.
52. Schrödinger *Maestro*, Schrödinger: New York, NY, 2019.
53. Case, D. A.; Ben-Shalom, I. Y.; Brozell, S. R.; Cerutti, D. S.; Cheatham III, T. E.; Cruzeiro, V. W. D.; Darden, T. A.; Duke, R. E.; Ghoreishi, D.; Gilson, M. K.; Gohlke, H.; Goetz, A. W.; Greene, D.; Harris, R.; Homeyer, N.; Izadi, S.; Kovalenko, A.; Kurtzman, T.; Lee, T. S.; LeGrand, S.; Li, P.; Lin, C.; Liu, J.; Luchko, T.; Luo, R.; Mermelstein, D. J.; Merz, K. M.; Miao, Y.; Monard, G.; Nguyen, C.; Nguyen, H.; Omelyan, I.; Onufriev, A.; Pan, F.; Qi, R.; Roe, D. R.; Roitberg, A.; Sagui, C.; Schott-Verdugo, S.; Shen, J.; Simmerling, C. L.; Smith, J.; Salomon-Ferrer, R.; Swails, J.; Walker, R. C.; Wang, J.; Wei, H.; Wolf, R. M.; Wu, X.; Xiao, L.; York , D. M.; Kollman, P. A. *AMBER*, University of California: San Francisco, 2021.
54. Case, D. A.; Cheatham III, T. E.; Darden, T.; Gohlke, H.; Luo, R.; Merz Jr., K. M.; Onufriev, A.; Simmerling, C.; Wang, B.; Woods, R. J., The Amber biomolecular simulation programs. *J. Comput. Chem.* **2005,** *26* (16), 1668-1688.
55. Salomon-Ferrer, R.; Götz, A. W.; Poole, D.; Le Grand, S.; Walker, R. C., Routine Microsecond Molecular Dynamics Simulations with AMBER on GPUs. 2. Explicit Solvent Particle Mesh Ewald. *J. Chem. Theory Comput.* **2013,** *9* (9), 3878-3888.
56. Le Grand, S.; Götz, A. W.; Walker, R. C., SPFP: Speed without compromise—A mixed precision model for GPU accelerated molecular dynamics simulations. *Comput. Phys. Commun.* **2013,** *184* (2), 374-380.
57. Wang, J.; Wolf, R. M.; Caldwell, J. W.; Kollman, P. A.; Case, D. A., Development and testing of a general amber force field. *J. Comput. Chem.* **2004,** *25* (9), 1157-1174.
58. Martínez, L.; Andrade, R.; Birgin, E. G.; Martínez, J. M., PACKMOL: A package for building initial configurations for molecular dynamics simulations. *J. Comput. Chem.* **2009,** *30* (13), 2157-2164.
59. Darden, T.; York, D.; Pedersen, L., Particle mesh Ewald: An N·log(N) method for Ewald sums in large systems. *J. Chem. Phys.* **1993,** *98* (12), 10089-10092.

60. Ryckaert, J.-P.; Ciccotti, G.; Berendsen, H. J. C., Numerical integration of the cartesian equations of motion of a system with constraints: molecular dynamics of n-alkanes. *J. Comput. Phys.* **1977,** *23* (3), 327-341.
61. Nguyen, H.; Roe, D. R.; Swails, J.; Case, D. A. PYTRAJ: Interactive data analysis for molecular dynamics simulations. , 2016.
62. Roe, D. R.; Cheatham, T. E., PTRAJ and CPPTRAJ: Software for Processing and Analysis of Molecular Dynamics Trajectory Data. *J. Chem. Theory Comput.* **2013,** *9* (7), 3084-3095.
63. Srinivasan, J.; Cheatham, T. E.; Cieplak, P.; Kollman, P. A.; Case, D. A., Continuum Solvent Studies of the Stability of DNA, RNA, and Phosphoramidate−DNA Helices. *J. Am. Chem. Soc.* **1998,** *120* (37), 9401-9409.
64. Kollman, P. A.; Massova, I.; Reyes, C.; Kuhn, B.; Huo, S.; Chong, L.; Lee, M.; Lee, T.; Duan, Y.; Wang, W.; Donini, O.; Cieplak, P.; Srinivasan, J.; Case, D. A.; Cheatham, T. E., Calculating Structures and Free Energies of Complex Molecules: Combining Molecular Mechanics and Continuum Models. *Acc. Chem. Res.* **2000,** *33* (12), 889-897.
65. Massova, I.; Kollman, P. A., Combined molecular mechanical and continuum solvent approach (MM-PBSA/GBSA) to predict ligand binding. *Perspect. Drug Discov. Des.* **2000,** *18* (1), 113-135.
66. Homeyer, N.; Gohlke, H., Free Energy Calculations by the Molecular Mechanics Poisson−Boltzmann Surface Area Method. *Mol. Inform.* **2012,** *31* (2), 114-122.
67. Case, D. A., Normal mode analysis of protein dynamics. *Curr. Opin. Struct. Biol.* **1994,** *4* (2), 285-290.
68. Miller, B. R.; McGee, T. D.; Swails, J. M.; Homeyer, N.; Gohlke, H.; Roitberg, A. E., MMPBSA.py: An Efficient Program for End-State Free Energy Calculations. *J. Chem. Theory Comput.* **2012,** *8* (9), 3314-3321.
69. Honig, B.; Nicholls, A., Classical electrostatics in biology and chemistry. *Science* **1995,** *268* (5214), 1144-1149.
70. Gilson, M. K.; Sharp, K. A.; Honig, B. H., Calculating the electrostatic potential of molecules in solution: Method and error assessment. *J. Comput. Chem.* **1988,** *9* (4), 327-335.
71. Tan, C.; Tan, Y.-H.; Luo, R., Implicit Nonpolar Solvent Models. *J. Phys. Chem. B* **2007,** *111* (42), 12263-12274.
72. McQuarrie, D. A., *Statistical Mechanics*. 2nd ed.; University Science Books: 2000.
73. Hawkins, G. D.; Cramer, C. J.; Truhlar, D. G., Pairwise solute descreening of solute charges from a dielectric medium. *Chem. Phys. Lett.* **1995,** *246* (1), 122-129.
74. Hawkins, G. D.; Cramer, C. J.; Truhlar, D. G., Parametrized Models of Aqueous Free Energies of Solvation Based on Pairwise Descreening of Solute Atomic Charges from a Dielectric Medium. *J. Phys. Chem.* **1996,** *100* (51), 19824-19839.
75. Janin, J., For Guldberg and Waage, with love and cratic entropy. *Proteins: Structure, Function, and Bioinformatics* **1996,** *24* (4), i-ii.
76. Gilson, M. K.; Given, J. A.; Bush, B. L.; McCammon, J. A., The statistical-thermodynamic basis for computation of binding affinities: a critical review. *Biophys. J.* **1997,** *72* (3), 1047-1069.
77. Luo, H.; Sharp, K., On the calculation of absolute macromolecular binding free energies. *PNAS* **2002,** *99* (16), 10399-10404.

78. Narang, P.; de Oliveira, T. E.; Venkatesu, P.; Netz, P. A., The role of osmolytes in the temperature-triggered conformational transition of poly(N-vinylcaprolactam): an experimental and computational study. *Phys. Chem. Chem. Phys.* **2020,** *22* (9), 5301-5313.

79. Umapathi, R.; Venkatesu, P., Assessing the efficiency of imidazolium-based ionic liquids on the phase behavior of a synthetic biomedical thermoresponsive polymer. *J. Colloid Interface Sci.* **2018,** *511*, 174-183.

80. Fan, H.; Wang, L.; Feng, X.; Bu, Y.; Wu, D.; Jin, Z., Supramolecular Hydrogel Formation Based on Tannic Acid. *Macromolecules* **2017,** *50* (2), 666-676.

8 TOC Figure

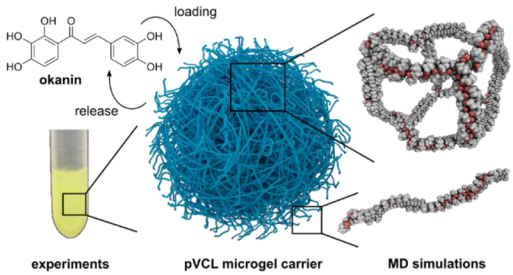

For Table of Contents only.

SUPPORTING INFORMATION

Loading and Co-Solvent-Triggered Release of Okanin, a C_4 Plant Key Enzyme Inhibitor, into/from Functional Microgels

Jonas Dittrich[a,b,†], Fabian Kolodzy[a,c,d,†], Alexander Töpel[a,c,d], Andrij Pich*[,a,c,d,e], Holger Gohlke*[,a,b,f]

[†]These authors contributed equally.

[a]Bioeconomy Science Center (BioSC), Forschungszentrum Jülich, 52425 Jülich, Germany

[b]Institute for Pharmaceutical and Medicinal Chemistry, Heinrich Heine University Düsseldorf, 40225 Düsseldorf, Germany

[c]DWI-Leibniz-Institute for Interactive Materials, RWTH Aachen University, 52056 Aachen, Germany

[d]Institute of Technical and Macromolecular Chemistry, RWTH Aachen University, 52074 Aachen, Germany

[e]Aachen Maastricht Institute for Biobased Materials, Maastricht University, Geleen, 6167 RD Netherlands

[f]John von Neumann Institute for Computing (NIC), Jülich Supercomputing Centre (JSC), and Institute of Bio- and Geosciences (IBG-4: Bioinformatics), Forschungszentrum Jülich GmbH, 52425 Jülich, Germany

Keywords: microgel carrier, all-atom molecular dynamics simulations, herbicide, free energy

Author ORCID:
Jonas Dittrich: 0000-0003-2377-2268
Fabian Kolodzy: 0000-0002-0311-0913
Alexander Töpel: 0000-0002-6801-2222
Andrij Pich: 0000-0003-1825-7798
Holger Gohlke: 0000-0001-8613-1447

*Corresponding Authors:

Andrij Pich
Address: Worringerweg 2, 52074 Aachen, Germany.
Phone: (+49) 241 80 23310
E-mail: pich@dwi.rwth-aachen.de

Holger Gohlke
Address: Universitätsstr. 1, 40225 Düsseldorf, Germany.
Phone: (+49) 211 81 13662; Fax: (+49) 211 81 13847
E-mail: gohlke@uni-duesseldorf.de

Table of Contents

Supplemental Materials and Methods 9

Supplemental Tables 13

Table S1: Mass, molar amounts, and theoretical compositions of the pVCL-based microgels. 13

Table S2: Dependency of the maximal absorbance A_{max}(377 nm) on the okanin concentration c(okanin) determined in an aqueous solution of 2.4 vol.-% DMSO. 13

Table S3: Dependency of the maximal absorbance A_{max}(392 nm) on the okanin concentration c(okanin) determined in pure DMSO. UV/Vis spectra were corrected by an exponential baseline described by the fitting parameters a and b to obtain a corrected absorbance $A_{max,cor.}$(392 nm). 14

Table S4: Dependency of the loading of okanin into pVCL microgels calculated from UV/Vis spectroscopy on the molar ratio of okanin to the number of constitutional units n_{okanin}/n_{CU} used in the loading process. UV/Vis spectra were corrected by an exponential baseline described by the fitting parameters a and b to obtain an corrected absorbance $A_{max,cor.}$(392 nm). 15

Table S5: Dependency of the loading of okanin into p(VCL/GMA_{core}) microgels calculated from UV/Vis spectroscopy on the molar ratio of okanin to the number of constitutional units n_{okanin}/n_{CU} used in the loading process. UV/Vis spectra were corrected by an exponential baseline described by the fitting parameters a and b to obtain a corrected absorbance $A_{max,cor.}$(392 nm). 16

Table S6: Dependency of the loading of okanin into p(VCL/GMA_{shell}) microgels calculated from UV/Vis spectroscopy on the molar ratio of okanin to the number of constitutional units n_{okanin}/n_{CU} used in the loading process. UV/Vis spectra were corrected by an exponential baseline described by the fitting parameters a and b to obtain a corrected absorbance $A_{max,cor.}$(392 nm). 17

Table S7: Dependency of the concentration of okanin in the supernatant $c_{supernatant}$(okanin) and the relative okanin amount released from a pVCL microgel on the initial loading. The dilution was 1:1 for 0.070 and 1:3 for 0.181. Triplicates were performed and all obtained maximal absorbances and the mean value are provided. 18

Table S8: Dependency of the concentration of okanin in the supernatant $c_{supernatant}$(okanin) and the relative okanin amount released from a p(VCL/GMA_{core}) microgel on

the initial loading. The dilution was 1:1 for 0.070 and 1:3 for 0.181. Triplicates were performed and all obtained maximal absorbances and the mean value are provided. 19

Table S9: Dependency of the concentration of okanin in the supernatant $c_{supernatant}$(okanin) and the relative okanin amount released from a pVCL microgel on the initial loading. The dilution was 1:1 for 0.070 and 1:3 for 0.181. Triplicates were performed and all obtained maximal absorbances and the mean value are provided. 20

Table S10: Overview of performed simulations for testing optimal simulation conditions for the crosslinked pVCL model in TIP3P water. 21

Table S11: Overview of performed simulations for testing optimal simulation conditions for the crosslinked pVCL model in OPC water. 22

Table S12: Overview of performed simulations for probing interactions between okanin and linear/crosslinked pVCL. 23

Table S13: Dependency of the hydrodynamic radius and the polydispersity index at 20 °C and 50 °C of okanin-loaded microgels determined by DLS on the molar ratio of okanin to the number of constitutional units n_{okanin}/n_{CU} used in the loading process. To compare the different microgels, the hydrodynamic radii were normed by using the hydrodynamic radius of the unloaded microgel ($R_H(n_{okanin}/n_{CU} = 0)$) as reference. 24

Supplemental Figures **26**

Figure S1: Raman spectra of pVCL-based microgels (A pVCL, B p(VCL/GMA_{shell}) and C p(VCL/GMA_{core})). D Excerpt of the Raman spectra from the spectra normalized to the peak of the carbonyl stretching vibration of VCL (1636 cm^{-1}). The peak at 1726 cm^{-1} correlates to the carbonyl stretching vibration of GMA. The GMA content was determined as 10.7 mol% for p(VCL/GMA_{shell}) and 9.8 mol% for p(VCL/GMA_{core}). 26

Figure S2: Determination of the VPTT for pVCL-based microgels by temperature-dependent DLS measurements. A logistic fit was applied to trends of R_H to determine the VPTT from the turning point (A pVCL (29 °C), B p(VCL/GMA_{core}) (29 °C), and C p(VCL/GMA_{shell}) (28 °C)). 27

Figure S3: Real-time frequency changes $\Delta f_5/5$ and dissipation ΔD_5 by QCM-D at 25 °C A for the adsorption and desorption of/from a clean SiO_2-sensor and B for the

uptake and release into/from p(VCL/GMA$_{shell}$) microgels bound to a SiO_2-sensor. The sensor is equilibrated in an aqueous solution of 2.4 vol% DMSO. The uptake was initiated by switching the solvent to an aqueous solution (2.4 vol% DMSO) with 0.4 mM okanin, and the release was initiated by switching to ultrapure water. The decrease in $\Delta f_5/5$ is indicative of an increase in the mass bound to the sensor. The microgels are too large for a quantitative analysis, so the curves only give access to the qualitative uptake and release kinetics. 28

Figure S4: UV/Vis spectra of a dilution series of okanin in 2.4 vol% DMSO/water to determine the attenuation coefficient. The measurements were repeated thrice (M1, M2 and M3). 29

Figure S5: UV/Vis spectra of a dilution series of okanin in 2.4 vol% DMSO/water to determine the attenuation coefficient. The measurements were repeated thrice (M1, M2 and M3). 30

Figure S6: UV/Vis spectra of a pVCL microgel loaded with different molar ratios of okanin to repeating units (n_{okanin}/n_{CU}) before and after exponential baseline correction. The measurements were repeated thrice (M1, M2, and M3). 31

Figure S7: UV/Vis spectra of a dilution series of okanin in 2.4 vol% DMSO/water to determine the attenuation coefficient. The measurements were repeated thrice (M1, M2, and M3). 32

Figure S8: Empirical comparison between linear and exponential baseline correction in UV/Vis spectroscopy. A UV/Vis spectra of a p(VCL/GMA$_{shell}$) microgel (0.03 mg/mL) at 20 °C and 50 °C. B UV/Vis spectra of okanin in DMSO for different concentrations (dashed: exponential baseline, dotted: linear baseline). C The UV/Vis spectrum for the microgel at 20 °C and the spectra of okanin were added to mimic the spectrum of a swollen microgel loaded with three different loading degrees of okanin (dashed: exponential baseline, dotted: linear baseline). D The UV/Vis spectrum for the microgel at 50 °C and the spectra of okanin were added to mimic the spectrum of a collapsed microgel loaded with three different loading degrees of okanin (dashed: exponential baseline, dotted: linear baseline). E A linear baseline correction is applied to all spectra. F An exponential baseline correction is applied to all spectra. 33

Figure S9: Radius of gyration (R_g) of the crosslinked pVCL model with inter-crosslink chain lengths of 20 repeating units in combination with TIP3P water[5] at 293 K,

313 K, and 343 K. Geometric analysis was performed with cpptraj[6]. Only the syndiotactic crosslinked pVCL model shows the experimentally observed thermo-responsiveness, i.e., a swollen conformation (high R_g) at low temperatures (293 K) and a collapsed conformation (low R_g) at higher temperatures (313 K). 34

Figure S10: Radius of gyration (R_g) of the crosslinked pVCL model with inter-crosslink chain lengths of 40 repeating units in combination with TIP3P water[5] at 293 K, 313 K, and 343 K. Geometric analysis was performed with cpptraj[6]. Only the syndiotactic crosslinked pVCL model shows the experimentally observed thermo-responsiveness, i.e., a swollen conformation (high R_g) at low temperatures (293 K) and a collapsed conformation (low R_g) at higher temperatures (313 K). 35

Figure S11: Radius of gyration (R_g) of the crosslinked pVCL model with inter-crosslink chain lengths of 20 repeating units in combination with OPC water[7] at 293 K, 313 K, and 343 K. Geometric analysis was performed with cpptraj[6] 36

Figure S12: Radius of gyration (R_g) of the syndiotactic pVCL 50mer for different okanin concentrations (n_{okanin}/n_{VCL} = 0.14, 0.56, and 1.11, respectively) at 293 K and 313 K. Geometric analysis was performed with cpptraj[6]. 37

Figure S13: Distribution of binding free energies obtained from MM-PBSA computations for all okanin molecules considered bound (> 475 contacts). Parameters of the Gaussian fit (dotted line) are indicated in the legend. 38

Figure S14: Exemplary AFM images, height profiles and histograms of a pVCL microgel for varying n_{okanin}/n_{CU} ratios. The collapse of the microgels upon binding of okanin leads to a rigidification of the microgel. As a result, the microgel's height increases..... 39

Figure S15: Histograms of R_{STEM} of a pVCL microgel for varying n_{okanin}/n_{CU} ratios. Due to the diffuse morphology of the unloaded microgels, the results for a molar ratio of 0.000 and 0.002 are expected to be biased. The collapse of the microgels upon binding of okanin leads to a rigidification of the microgel so that D_{STEM} can be determined. 40

Figure S16: Radius of gyration (R_g) of the crosslinked pVCL model for different okanin concentrations (n_{okanin}/n_{VCL} = 0, 0.04, and 0.14, respectively) at 293 K and 313 K. Geometric analysis was performed with cpptraj[6] 41

Figure S17: Radius of gyration (R_g) of the crosslinked pVCL model for different okanin concentrations (n_{okanin}/n_{VCL} = 0.28, 0.56, and 1.11, respectively) at 293 K and 313 K. Geometric analysis was performed with cpptraj[6] 42

Figure S18: Distribution of radius of gyration (R_g) for simulations of the crosslinked pVCL model for different okanin concentrations (Figure S16 and Figure S17) depicted as histogram (left) and as cumulative relative frequency (right). 43

Figure S19: Porous MG structures obtained after 1 µs simulation of the crosslinked pVCL with okanin (n_{okanin}/n_{CU} = 0.28) at 293 K exemplarily shown for four different replicas. 44

Figure S20: Binding of okanin to the crosslinked pVCL. The okanin is either in solution (A), loosely adsorbed to the surface of the pVCL (B, two molecules), or bound within the polymer between at least two pVCL chains (C). 45

Figure S21: Number of contacts for each of the seven okanin molecules (n_{okanin}/n_{VCL} = 0.14) within each of the ten simulations of the linear pVCL at 293 K. Only trajectories with a coil-to-globule transition of the oligomer comprises okanin with more than 350 contacts (dashed line) to the pVCL. 46

Figure S22: Number of contacts for each of the seven okanin molecules (n_{okanin}/n_{VCL} = 0.14) within each of the ten simulations of the linear pVCL at 313 K. Only trajectories with a coil-to-globule transition of the oligomer comprises okanin with more than 350 contacts (dashed line) to the pVCL. 47

Figure S23: Two-dimensional histograms of the changes in the decomposed molecular mechanics energies (ΔE_{MM}) of okanin binding to the linear pVCL 50mer in relation to the number of formed contacts. The changes in the intermolecular energies shown here comprise changes in the van der Waals (A, ΔE_{vdW}) and electrostatic energies (B, ΔE_{eel}). Calculations were performed using MMPBSA.py[8]. 48

Figure S24: Two-dimensional histograms of the changes in the decomposed solvation free energy ($\Delta G_{solvation}$) of okanin to the linear pVCL 50mer in relation to the number of formed contacts. The solvation free energy is decomposed into the polar part (A, ΔG_{pol}), a repulsive cavitation solvation free energy term (B, G_{cavity}), and an attractive dispersion solvation free energy term (C, $G_{dispersion}$). Calculations were performed using MMPBSA.py[8]. 49

Figure S25: Fraction of stacking okanin ($n_{okanin,stacking,total}/n_{okanin,total}$) in dependence of the molar ratio of okanin and the constitutional units (0.04 - 1.11, colored according

to the legend) over the simulation time of 1000 ns. The standard deviation is shown as a translucent area, the dashed lines indicate the mean for the last 400 ns of the simulations. 50

Figure S26: Fraction of stacking okanin in solutiom ($n_{okanin,stacking,solv}/n_{okanin,total}$) in dependence of the molar ratio of okanin and the constitutional units (0.04 - 1.11, colored according to the legend) over the simulation time of 1000 ns. The standard deviation is shown as a translucent area, the dashed lines indicate the mean for the last 400 ns of the simulations. 51

Figure S27: Relation of bound (> 475 contacts to the gel) okanin molecules ($n_{okanin,bound}$) to the number of constitutional units (n_{CU}) in dependence of the molar ratio of okanin and the constitutional units (0.04 - 1.11, colored according to the legend) over the simulation time of 1000 ns. The standard deviation is shown as a translucent area, the dashed lines indicate the mean for the last 400 ns of the simulations. 52

Figure S28: Relation of adsorbed (> 5 contacts to the gel) okanin molecules ($n_{okanin,adsorbed}$) to the number of constitutional units (n_{CU}) in dependence of the molar ratio of okanin and the constitutional units (0.04 - 1.11, colored according to the legend) over the simulation time of 1000 ns. The standard deviation is shown as a translucent area, the dashed lines indicate the mean for the last 400 ns of the simulations. 53

Figure S29: Relation of bound and stacked (> 475 contacts to the gel and > 250 contacts to the gel) okanin molecules ($n_{okanin,bound}$) to the number of constitutional units (n_{CU}) in dependence of the molar ratio of okanin and the constitutional units (0.04 - 1.11, colored according to the legend) over the simulation time of 1000 ns. The standard deviation is shown as a translucent area, the dashed lines indicate the mean for the last 400 ns of the simulations. 54

Figure S30: Radial distribution functions ($g(r)$) for the two aromatic rings (R1, R2) of okanin for different okanin concentrations. For okanin / pVCL ratios above 0.28, an increase in $g(r)$ around 4 Å is indicative of increased stacking interactions of okanin. 55

Figure S31: UV/Vis spectra of a p(VCL/GMA_{core}) microgel loaded with different molar ratios of okanin to repeating units (n_{okanin}/n_{CU}) before and after exponential baseline-correction. The measurements were repeated thrice (M1, M2 and M3). 56

Figure S32: UV/Vis spectra of a p(VCL/GMA_{shell}) microgel loaded with different molar ratios of okanin to repeating units (n_{okanin}/n_{CU}) before and after exponential baseline-correction. The measurements were repeated thrice (M1, M2 and M3). 57

Figure S33: Exemplary AFM images, height profiles and histograms of a p(VCL/GMA_{core}) microgel A without okanin loading and B loaded at a molar ratio of 0.181. The collapse of the microgels upon binding of okanin leads to a rigidification of the microgel. As a result, the microgel's height increases. 58

Figure S34: Exemplary AFM images, height profiles and histograms of a p(VCL/GMA_{shell}) microgel A without okanin loading and B loaded at a molar ratio of 0.181. The collapse of the microgels upon binding of okanin leads to a rigidification of the microgel. As a result, the microgel's height increases. 58

Figure S35: STEM images of a p(VCL/GMA_{shell}) microgel A without okanin (R_{STEM} = 203 ± 18 nm) and B loaded with n_{okanin}/n_{CU} = 0.18 (R_{STEM} = 126 ± 7 nm). High-resolution images of the loaded microgel C before purification and D after purification. 59

Figure S36: STEM images of a p(VCL/GMA_{core}) microgel A without okanin (R_{STEM} = 125 ± 15 nm) and B loaded with n_{okanin}/n_{CU} = 0.18 (R_{STEM} = 109 ± 11 nm). C High-resolution images of the loaded microgel after purification. 60

Figure S37: STEM images of a pVCL microgel A without okanin (R_{STEM} = 170 ± 22 nm) and B loaded with n_{okanin}/n_{CU} = 0.18 (R_{STEM} = 117 ± 7 nm). C High-resolution images of the loaded microgel after purification. 61

Figure S38: Contacts of okanin molecules during the release simulation (n_{okanin}/n_{VCL} = 0.04 during okanin loading simulation) in water at 293 K. Only okanin molecules with more than 475 contacts at the first frame are tracked for release. Every okanin molecule not at least adsorbed, i.e., shows >5 contacts, for 98.9% of the time, is considered released. 62

Figure S39: Contacts of okanin molecules during the release simulation (n_{okanin}/n_{VCL} = 0.04 during okanin loading simulation) in a saturated water ethylacetat (EtOAc) solution at 293 K. Only okanin molecules with more than 475 contacts at the first frame are tracked for release. Every okanin molecule not at least adsorbed, i.e., shows >5 contacts, for 98.9% of the time, is considered released. 63

Figure S40: Contacts of okanin molecules during the release simulation (n_{okanin}/n_{VCL} = 1.14 during okanin loading simulation) in water at 293 K. Only okanin molecules with more than 475 contacts at the first frame are tracked for release. Every okanin molecule not at least adsorbed, i.e., shows >5 contacts, for 98.9% of the time, is considered released. 64

Figure S41: Contacts of okanin molecules during the release simulation (n_{okanin}/n_{VCL} = 1.14 during okanin loading simulation) in a saturated water ethylacetat (EtOAc) solution at 293 K. Only okanin molecules with more than 475 contacts at the first frame are tracked for release. Every okanin molecule not at least adsorbed, i.e., shows >5 contacts, for 98.9% of the time, is considered released..... 65

Figure S42: Concentration of okanin in the supernatant after co-solvent-triggered release from pVCL-based microgels (1.0 mg/mL) for different co-solvents (10 %(*m*/*m*) DMSO, 10 %(*m*/*m*) AcOH, and 9.4 %(*m*/*m*) EtOAc) for low (n_{okanin}/n_{CU} = 0.07) and high (n_{okanin}/n_{CU} = 0.18) okanin concentrations at loading. The initial loadings were 31.1 µg/mg and 73.0 µg/mg for pVCL, 65.7 µg/mg and 146.0 µg/mg for p(VCL/GMA_{core}) and 72.3 µg/mg and 144.2 µg/mg for p(VCL/GMA_{shell}). 66

Figure S43: UV/Vis spectra of the supernatant after the release of okanin from pVCL-based microgels (A pVCL, B p(VCL/GMA_{core}), and C p(VCL/GMA_{shell})). The microgels were previously loaded at a molar ratio n_{okanin}/n_{CU} of 0.070 (low loading) and 0.181 (high loading). The initial loadings were 31.1 µg/mg and 73.0 µg/mg for pVCL, 65.7 µg/mg and 146.0 µg/mg for p(VCL/GMA_{core}) and 72.3 µg/mg and 144.2 µg/mg for p(VCL/GMA_{shell}). The measurements were repeated thrice (M1: line, M2: dashed, and M3: dotted). The dilution were 1:1 and 1:3 for low and high loadings, respectively. 67

Supplemental References **68**

1 Supplemental Materials and Methods

Synthesis of pVCL microgels. Pure pVCL microgels were synthesized by free radical precipitation polymerization. The masses and molar amounts of the used compounds are shown in Table S1. The monomer VCL and the crosslinker BIS were dissolved in 98 mL of water. The solution was heated to 70 °C and degassed for 30 min at 400 rpm. The polymerization was started by the addition of AMPA dissolved in 2 mL of water. The solution was stirred at 70 °C for 30 min at 400 rpm. Then, the mixture was cooled to room temperature and transferred into a dialysis tube (regenerated cellulose, MWCO: 12 kDa). The microgels were dialyzed against de-ionized water for 7 d, with the repetitive exchange of the dialysis water, to remove oligomers. Finally, the microgels were freeze-dried. The product was obtained with a yield of 89.9 % and a stock solution was prepared (13.69 mg mL^{-1}).

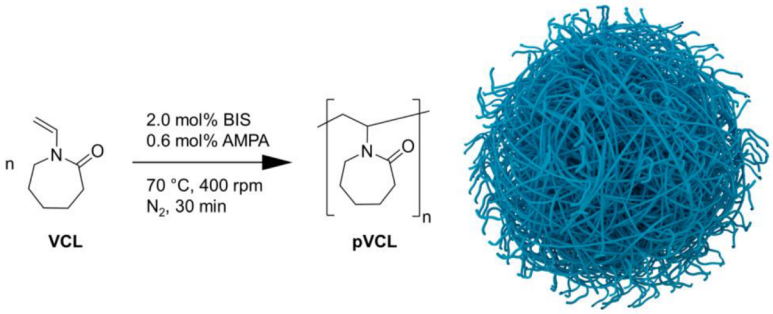

Synthesis of p(VCL/GMA$_{core}$) microgels. p(VCL/GMA$_{core}$) microgels were synthesized by free radical precipitation polymerization in a batch approach.[1-2] The masses, volumes, and molar amounts of the used compounds are shown in Table S1. The monomers VCL and GMA as well as the crosslinker BIS were dissolved in 98 mL of water. The solution was heated to 70 °C and degassed for 30 min at 400 rpm. The polymerization was started by the addition of AMPA dissolved in 2 mL of water. The solution was stirred at 70 °C for 30 min at 400 rpm. Then, the mixture was cooled to room temperature and transferred into a dialysis tube (regenerated cellulose, MWCO: 12 kDa). The microgels were dialyzed against de-ionized water for 7 d, with the repetitive exchange of the dialysis water to remove oligomers. Finally, the microgels were freeze-dried. The product was obtained with a yield of 90.1 % and a stock solution was prepared (17.47 mg mL^{-1}). A GMA content 9.8 mol% was determined via Raman spectroscopy.

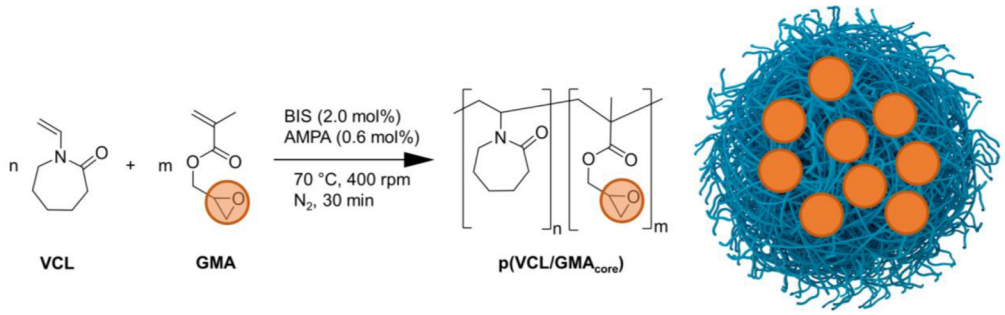

Synthesis of p(VCL/GMA$_{shell}$) microgels. p(VCL/GMA$_{shell}$) microgels were synthesized by free radical precipitation polymerization in a semi-batch approach.[3] The masses, volumes, and molar amounts of the used compounds are shown in Table S1. The monomer VCL and the crosslinker BIS were dissolved in 98 mL of water. The solution was heated to 70 °C and degassed for 30 min at 400 rpm. The polymerization was started by the addition of AMPA dissolved in 2 mL of water. After 3 min, GMA is added in one shot to the reaction mixture. The solution was stirred at 70 °C for 30 min at 400 rpm. Then, the mixture was cooled to room temperature and transferred into a dialysis tube (regenerated cellulose, MWCO: 12 kDa). The microgels were dialyzed against de-ionized water for 7 d, with the repetitive exchange of the dialysis water to remove oligomers. Finally, the microgels were freeze-dried. The product was obtained with a yield of 86.2 % and a stock solution was prepared (13.42 mg mL^{-1}). A GMA content 10.7 mol% was determined via Raman spectroscopy.

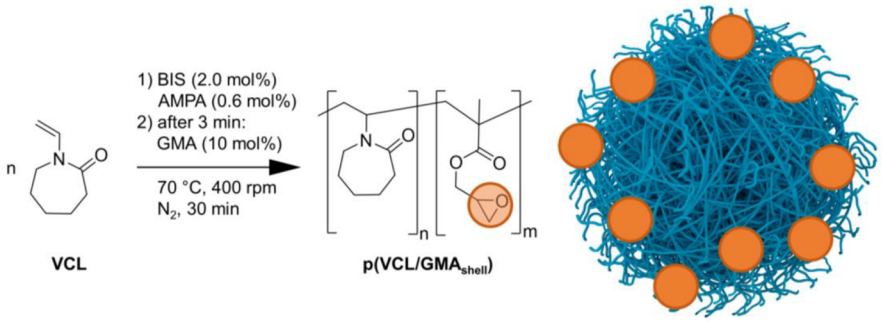

Quantification of the GMA content in microgels via Raman spectroscopy. The GMA content in p(VCL/GMA$_{core}$) and p(VCL/GMA$_{shell}$) microgels was determined by Raman spectroscopy from the GMA carbonyl stretching vibration (1726 cm^{-1}) and the VCL carbonyl stretching vibration (1636 cm^{-1}). The Raman calibration function (eq. 1) determined by Gau et al.[3] is used for the calculation:

$$\text{GMA [mol\%]} = 0.94294 \cdot \frac{I(1726\ \text{cm}^{-1})}{I(1636\ \text{cm}^{-1})} - 0.00123 \qquad \text{eq. 1}$$

The Raman spectra of the pVCL-based microgel are shown in Figure S1A-C. The excerpt of the carbonyl stretching vibration normalized to the carbonyl stretching vibration of VCL is presented in Figure S1B for all three microgels.

Investigation of the thermoresponsive properties of the microgels by temperature-dependent dynamic light scattering. Before each measurement series, the temperature of the sample was set to 15 °C and equilibrated for 10 min. R_H and the *PDI* are determined from 15 °C to 50 °C using heating steps of 1 °C. To confirm the reversibility, R_H and the *PDI* are also determined from 50 °C to 15 °C using cooling steps of 3 °C. After each change of the temperature, the sample was equilibrated for 3 min. A logistic fit was applied to determine the VPTT from the turning point. The temperature trends are depicted in Figure S2.

Quartz Crystal Microbalance with Dissipation monitoring (QCM-D). QCM-D was measured at 25 °C on SiO_2-coated quartz crystal sensors (QSX 303, Biolin Scientific AB) with a Qsense Explorer flow module with integrated temperature control by Biolin Scientific AB. Solvents were pumped using a multichannel peristaltic pump (IPC ISMATEC) with Teflon tubing and operating at a fixed flow rate of 50 µL min^{-1}. The simultaneous measurements of the frequency *f* and the energy dissipation *D* were performed for the fundamental resonance frequency ($n = 1$, *i.e.*, $f = 5$ MHz) and the six overtones ($n = 3$, 5, 7, 9, 11, and 13 corresponding to $f = 15$, 25, 35, 45, 55, and 65 Mhz, respectively). The resolution in *f* and *D* is $\pm 1 \cdot 10^{-2}$ Hz and $\pm 1 \cdot 10^{-8}$, respectively.

SiO_2-sensors were oxidized by radiation with air plasma for 300 s, silanized in 5 mL EtOH with 1 vol% TPTMS, rinsed with 9 mL EtOH and dried under nitrogen flow. 50 µL of p(VCL/GMA_{shell}) microgel stock solution was spincoated at 2000 rpm (800 rpm/s as initial acceleration) for 1 min to bind the microgels to the sensor surface. Each measurement started with the equilibration of the sensor in an aqueous solution of 2.4 vol% DMSO for 1 h. Then, an aqueous solution of 2.4 vol% DMSO and 0.4 mM okanin was added to measure the uptake kinetics of okanin to the microgels. After 1 h, the solvent was exchanged to ultrapure water to measure the release kinetics. As the microgels' size exceeds the Sauerbrey limit, uptake and release cannot be quantified. The real-time changes of the frequency $\Delta f_5/5$ and the dissipation ΔD_5 are shown in Figure S3 for the microgel-covered sensors and a clean sensor as a reference.

Empirical comparison between linear and exponential baseline correction in UV/Vis spectroscopy. As the binding of okanin induces the collapse of the microgels, UV/Vis spectra of a microgel are measured below and above the VPTT of VCL (~32 °C)[4] as a reference for the swollen and the collapsed state. The UV/Vis spectra of the microgel at the sample concentration (30 µg/mL) at 20 °C and 50 °C are shown in Figure S8A (microgel spectra). Spectra of pure

okanin (okanin spectra) were measured at three different concentrations (Figure S8B). To mimic the UV/Vis spectra of microgels loaded with different okanin amounts, the okanin spectra are each added to the spectrum of the microgel at 20 °C (Figure S8C) and 50 °C (Figure S8D). Thereby, six new spectra are obtained corresponding to microgels in different swelling states and loaded with different amounts of okanin (microgel-okanin spectra).

As the turbidity caused by the microgels biases the quantification of okanin within the microgels, a baseline correction is applied. To obtain accurate results, this correction must fully subtract the absorbance caused by light-scattering of the microgels independent of the swelling degree and amount of okanin. Therefore, an application of the baseline correction to the okanin spectra and the microgel-okanin spectra must result in identical maxima for the same okanin concentration. In Figure S8**E**, a linear baseline correction is applied. The spectra with the same okanin concentration deviate from another indicating that this method is not suited to obtain accurate results. In Figure S8**F**, the baseline correction is repeated with an exponential baseline. The deviation of the spectra with the same okanin concentration is reduced and the maxima for the spectra with the same okanin concentration are virtually identical. For this reason, an exponential baseline correction is used for the quantification of okanin loading into microgels.

2 Supplemental Tables

Table S1: Mass, molar amounts, and theoretical compositions of the pVCL-based microgels.

	pVCL				p(VCL-*co*-GMA)			
	m [mg]	*V* [µL]	*n* [mmol]	n/n_{total} [mol%]	*m* [mg]	*V* [µL]	*n* [mmol]	n/n_{total} [mol%]
VCL	1428.6	-	10.264	97.4	1282.0	-	9.210	87.4
GMA	-	-	-	-	149.8	144	1.054	10.0
BIS	32.5	-	0.211	2.0	32.5	-	0.211	2.0
AMPA	17.1	-	0.063	0.6	17.1	-	0.063	0.6
Σ	1478.2	-	10.538	100.0	1481.4	-	10.538	100.0

Table S2: Dependency of the maximal absorbance A_{max}(377 nm) on the okanin concentration *c*(okanin) determined in an aqueous solution of 2.4 vol.-% DMSO.

***c*(okanin)**		A_{max}**(377 nm) [a.u.]**			
[µM]	[mg/L]	M1	M2	M3	Mean
32.22	9.00	0.9769	0.9691	0.9727	0.9729 ± 0.0032
15.61	4.50	0.4811	0.4730	0.4770	0.4770 ± 0.0034
7.81	2.25	0.2367	0.2341	0.2292	0.2333 ± 0.0032
3.92	1.13	0.1156	0.1121	0.1099	0.1125 ± 0.0024
1.94	0.56	0.0561	0.0538	0.0528	0.0542 ± 0.0014
0.97	0.28	0.0252	0.0258	0.0235	0.0248 ± 0.0010

Table S3: Dependency of the maximal absorbance A_{max}(392 nm) on the okanin concentration c(okanin) determined in pure DMSO. UV/Vis spectra were corrected by an exponential baseline described by the fitting parameters a and b to obtain a corrected absorbance $A_{max,cor.}$(392 nm).

c(okanin)			**a**	**$b \cdot 10^2$**	**A_{max}(392 nm)**	**$A_{max,cor.}$(392 nm)**
[µM]	[mg/L]		[a.u.]	[a.u.]	[a.u.]	[a.u.]
31.22	9.00	M1	15.044	-1.525	1.0356	0.9981
		M2	108.564	-2.196	0.9941	0.9754
		M3	45.869	-1.900	1.0069	0.9813
		Mean	-	-	1.0122 ± 0.0174	0.9849 ± 0.0097
15.61	4.50	M1	12.248	-1.675	0.5245	0.5085
		M2	29.236	-1.983	0.5123	0.5006
		M3	13.588	-1.724	0.5052	0.4915
		Mean	-	-	0.5140 ± 0.0080	0.5002 ± 0.0070
7.81	2.25	M1	3.087	-1.434	0.2660	0.2558
		M2	5.026	-1.632	0.2483	0.2416
		M3	0.808	-1.003	0.2501	0.2361
		Mean	-	-	0.2548 ± 0.0080	0.2445 ± 0.0083
3.92	1.13	M1	0.996	-1.286	0.1332	0.1278
		M2	1.030	-1.357	0.1186	0.1157
		M3	0.766	-1.252	0.1224	0.1175
		Mean	-	-	0.1247 ± 0.0062	0.1203 ± 0.0054
1.94	0.56	M1	0.264	-1.058	0.0673	0.0642
		M2	0.187	-0.995	0.0575	0.0554
		M3	0.160	-0.921	0.0610	0.0578
		Mean	-	-	0.0620 ± 0.0041	0.0591 ± 0.0038
0.97	0.28	M1	0.113	-0.957	0.0334	0.0324
		M2	0.012	-0.295	0.0268	0.0256
		M3	0.069	-0.827	0.0301	0.0302
		Mean	-	-	0.0301 ± 0.0028	0.0294 ± 0.0029

Table S4: Dependency of the loading of okanin into pVCL microgels calculated from UV/Vis spectroscopy on the molar ratio of okanin to the number of constitutional units n_{okanin}/n_{CU} used in the loading process. UV/Vis spectra were corrected by an exponential baseline described by the fitting parameters *a* and *b* to obtain an corrected absorbance $A_{max,cor.}$(392 nm).

n_{okanin}/n_{CU}	*c*(okanin)		*a*	$b \cdot 10^2$	A_{max}(392 nm)	$A_{max,cor.}$(392 nm)	Loading
[-]	[mM]		[a.u.]	[a.u.]	[a.u.]	[a.u.]	[µg/mg]
0.002	0.014	M1	1.537	-1.528	n.a.[1]	0.0010	0.3
		M2	3.379	-1.746	n.a.[1]	0.0049	1.5
		M3	0.592	-1.322	n.a.[1]	0.0012	0.4
		Mean	-	-	n.a.[1]	0.0024 ± 0.0018	0.7 ± 0.6
0.007	0.05	M1	2.071	-1.468	0.0052	0.0050	1.6
		M2	1.880	-1.563	0.0094	0.0125	3.9
		M3	2.129	-1.489	0.0089	0.0104	3.2
		Mean	-	-	0.0078 ± 0.0019	0.0093 ± 0.0032	2.9 ± 1.0
0.014	0.1	M1	1.970	-1.372	0.0155	0.0115	3.6
		M2	3.300	-1.559	0.0342	0.0329	10.2
		M3	1.609	-1.285	0.0345	0.0290	9.0
		Mean	-	-	0.0281 ± 0.0089	0.0244 ± 0.0093	7.6 ± 2.9
0.070	0.5	M1	4.144	-1.526	0.0841	0.0785	24.5
		M2	1.927	-1.074	0.1398	0.1140	35.5
		M3	2.469	-1.234	0.1116	0.0950	29.6
		Mean	-	-	0.1118 ± 0.0227	0.0958 ± 0.0145	29.9 ± 4.5
0.139	1.0	M1	2.388	-0.959	0.2693	0.2159	67.3
		M2	2.080	-0.992	0.2118	0.1712	53.3
		M3	2.262	-0.973	0.2542	0.2064	64.3
		Mean	-	-	0.2451 ± 0.0243	0.1978 ± 0.019´3	61.6 ± 6.0
0.181	1.3	M1	2.646	-0.945	0.3395	0.2744	85.5
		M2	2.456	-1.016	0.2718	0.2267	70.6
		M3	2.872	-1.043	0.2879	0.2391	74.5
		Mean	-	-	0.2997 ± 0.0289	0.2467 ± 0.0203	76.9 ± 6.3
0.278	2.0	M1	2.366	-0.928	0.3048	0.2432	75.8
		M2	2.511	-1.006	0.2706	0.2235	69.6
		M3	2.562	-1.007	0.2937	0.2456	76.5
		Mean	-	-	0.2897 ± 0.0143	0.2374 ± 0.0099	74.0 ± 3.1

[1]not available because no local maximum was observed due to the absorbance of the microgel

Table S5: Dependency of the loading of okanin into p(VCL/GMA$_{core}$) microgels calculated from UV/Vis spectroscopy on the molar ratio of okanin to the number of constitutional units n_{okanin}/n_{CU} used in the loading process. UV/Vis spectra were corrected by an exponential baseline described by the fitting parameters *a* and *b* to obtain a corrected absorbance $A_{max,cor.}$(392 nm).

n_{okanin}/n_{CU}	*c*(okanin)		*a*	$b \cdot 10^2$	A_{max}(392 nm)	$A_{max,cor.}$(392 nm)	Loading
[-]	[mM]		[a.u.]	[a.u.]	[a.u.]	[a.u.]	[µg/mg]
0.002	0.014	M1	1.500	-1.176	0.0114	0.0019	0.6
		M2	1.686	-1.252	0.0189	0.0051	1.6
		M3	1.966	-1.282	0.0146	0.0056	1.7
		Mean	-	-	0.0150 ± 0.0031	0.0042 ± 0.0016	1.3 ± 0.5
0.007	0.05	M1	1.722	-1.104	0.0577	0.0073	2.3
		M2	1.632	-1.146	0.0506	0.0215	6.7
		M3	1.794	-1.134	0.0546	0.0254	7,9
		Mean	-	-	0.0543 ± 0.029	0.0181 ± 0.0078	5.6 ± 2.4
0.014	0.1	M1	1.817	-1.111	0.0598	0.0174	5.4
		M2	2.313	-1.132	0.0818	0.0556	17.3
		M3	2.379	-1.159	0.0737	0.0502	15.6
		Mean	-	-	0.0718 ± 0.0091	0.0411 ± 0.0169	12.8 ± 5.3
0.070	0.5	M1	2.532	-0.866	0.2827	0.2007	62.5
		M2	2.928	-0.959	0.2982	0.2302	71.7
		M3	3.017	-0.965	0.2985	0.2306	71.9
		Mean	-	-	0.2931 ± 0.0074	0.2205 ± 0.0140	68.7 ± 4.4
0.139	1.0	M1	3.565	-0.892	0.5401	0.4251	132.5
		M2	3.536	-0.949	0.4711	0.3854	120.1
		M3	3.715	-0.953	0.4864	0.3962	123.5
		Mean	-	-	0.4992 ± 0.0296	0.4022 ± 0.0167	125.3 ± 5.2
0.181	1.3	M1	4.078	-0.892	0.6367	0.5112	159.3
		M2	3.808	-0.930	0.5713	0.4689	146.1
		M3	4.183	-0.972	0.5513	0.4558	142.1
		Mean	-	-	0.5865 ± 0.0365	0.4787 ± 0.0236	149.2 ± 7.4
0.278	2.0	M1	4.332	-0.896	0.7013	0.5690	177.3
		M2	3.747	-0.948	0.5001	0.4064	126.6
		M3	3.849	-0.956	0.5111	0.4171	130.0
		Mean	-	-	0.5708 ± 0.0923	0.4642 ± 0.0743	144.6 ± 23.2

Table S6: Dependency of the loading of okanin into p(VCL/GMA$_{shell}$) microgels calculated from UV/Vis spectroscopy on the molar ratio of okanin to the number of constitutional units n_{okanin}/n_{CU} used in the loading process. UV/Vis spectra were corrected by an exponential baseline described by the fitting parameters *a* and *b* to obtain a corrected absorbance $A_{max,cor.}$(392 nm).

n_{okanin}/n_{CU}	*c*(okanin)		*a*	*b* • 10^2	A_{max}(392 nm)	$A_{max,cor.}$(392 nm)	Loading
[-]	[mM]		[a.u.]	[a.u.]	[a.u.]	[a.u.]	[µg/mg]
0.002	0.014	M1	1.959	-1.024	0.0315	0.0020	0.6
		M2	1.562	-0.980	0.0372	0.0055	1.7
		M3	1.614	-0.961	0.0436	0.0053	1.7
		Mean	-	-	0.0374 ± 0.0049	0.0043 ± 0.0016	1.3 ± 0.5
0.007	0.05	M1	2.026	-1.011	0.0401	0.0070	2.2
		M2	1.765	-0.969	0.0646	0.0232	7.2
		M3	1.876	-0.981	0.0635	0.0228	7.1
		Mean	-	-	0.0561 ± 0.0113	0.0177 ± 0.0075	5.5 ± 2.4
0.014	0.1	M1	2.279	-0.984	0.0617	0.0173	5.4
		M2	1.178	-1.074	0.0386	0.0237	7.4
		M3	1.366	-1.036	0.0493	0.0276	8.6
		Mean	-	-	0.0499 ± 0.0094	0.0229 ± 0.0042	7.1 ± 1.3
0.070	0.5	M1	2.589	-0.740	0.3466	0.2070	64.5
		M2	2.666	-0.776	0.3646	0.2419	75.4
		M3	2.679	-0.785	0.3596	0.2393	74.6
		Mean	-	-	0.3569 ± 0.0076	0.2294 ± 0.0159	71.5 ± 4.9
0.139	1.0	M1	2.980	-0.712	0.5824	0.4013	125.1
		M2	2.866	-0.773	0.5265	0.3888	121.2
		M3	2.800	-0.775	0.5034	0.3677	114.6
		Mean	-	-	0.5374 ± 0.0332	0.3859 ± 0.0139	120.3 ± 4.3
0.181	1.3	M1	3.210	-0.742	0.6454	0.4701	146.5
		M2	3.048	-0.758	0.6307	0.4717	147.0
		M3	3.055	-0.775	0.6004	0.4497	140.1
		Mean	-	-	0.6255 ± 0.0187	0.4638 ± 0.0100	144.5 ± 3.1
0.278	2.0	M1	3.431	-0.752	0.6852	0.5053	157.5
		M2	3.011	-0.761	0.5967	0.4423	137.8
		M3	2.928	-0.761	0.5622	0.4123	128.5
		Mean	-	-	0.6147 ± 0.0518	0.4533 ± 0.0388	141.3 ± 12.1

Table S7: Dependency of the concentration of okanin in the supernatant $c_{supernatant}$(okanin) and the relative okanin amount released from a pVCL microgel on the initial loading. The dilution was 1:1 for 0.070 and 1:3 for 0.181. Triplicates were performed and all obtained maximal absorbances and the mean value are provided.

n_{okanin}/n_{CU}	Okanin loading	Solvent		A_{max}(377 nm)	$c_{supernatant}$(okanin)	Released okanin
[-]	[$\mu g_{okanin}/mg_{microgel}$]			[a.u.]	[µM]	[%(*m*/*m*)]
0.070	31.1	Water	M1	0.0469	0.86	2.78
			M2	0.0452	0.83	2.68
			M3	0.0448	0.83	2.65
			mean	0.0456 ± 0.0009	0.84 ± 0.02	2.70 ± 0.05
		DMSO	M1	0.1787	3.30	10.59
			M2	0.1756	3.24	10.40
			M3	0.1788	3.30	10.60
			mean	0.1777 ± 0.0015	3.28 ± 0.03	10.53 ± 0.09
		AcOH	M1	0.2564	4.73	15.19
			M2	0.2534	4.67	15.01
			M3	0.2424	4.47	14.36
			mean	0.2507 ± 0.0060	4.62 ± 0.11	14.85 ± 0.36
		EtOAc	M1	0.1783	3.29	10.56
			M2	0.1783	3.29	10.56
			M3	0.1854	3.42	10.99
			mean	0.1807 ± 0.0034	3.33 ± 0.06	10.71 ± 0.20
0.181	73.0	Water	M1	0.1371	5.06	6.93
			M2	0.1391	5.13	7.02
			M3	0.1385	5.11	7.00
			mean	0.1382 ± 0.0008	5.10 ± 0.03	6.98 ± 0.04
		DMSO	M1	0.4105	15.14	20.95
			M2	0.4148	15.30	20.95
			M3	0.4034	18.60	25.47
			mean	0.4096 ± 0.0047	15.11 ± 0.17	20.76 ± 0.27
		AcOH	M1	0.4922	18.16	25.12
			M2	0.5041	18.60	25.47
			M3	0.4986	18.39	25.19
			mean	0.4983 ± 0.0049	18.38 ± 0.18	25.26 ± 0.15
		EtOAc	M1	0.3124	11.52	15.94
			M2	0.3176	11.72	16.04
			M3	0.3122	11.52	15.77
			mean	0.3141 ± 0.0025	11.59 ± 0.09	15.92 ± 0.11

Table S8: Dependency of the concentration of okanin in the supernatant $c_{supernatant}$(okanin) and the relative okanin amount released from a p(VCL/GMA_{core}) microgel on the initial loading. The dilution was 1:1 for 0.070 and 1:3 for 0.181. Triplicates were performed and all obtained maximal absorbances and the mean value are provided.

n_{okanin}/n_{CU}	Okanin loading	Solvent		A_{max}(377 nm)	$c_{supernatant}$(okanin)	Released okanin
[-]	[$\mu g_{okanin}/mg_{microgel}$]			[a.u.]	[µM]	[%(*m*/*m*)]
0.070	65.7	Water	M1	0.0607	1.12	1.70
			M2	0.0599	1.11	1.68
			M3	0.0596	1.10	1.67
			mean	0.0601 ± 0.0005	1.11 ± 0.01	1.69 ± 0.01
		DMSO	M1	0.2316	4.27	6.50
			M2	0.2312	4.26	6.49
			M3	0.2381	4.39	6.68
			mean	0.2336 ± 0.0032	4.31 ± 0.06	6.56 ± 0.09
		AcOH	M1	0.3540	6.53	9.93
			M2	0.3705	6.83	10.40
			M3	0.3519	6.49	9.87
			mean	0.3588 ± 0.0083	6.62 ± 0.15	10.07 ± 0.23
		EtOAc	M1	0.2659	4.90	7.46
			M2	0.2709	5.00	7.60
			M3	0.2625	4.84	7.37
			mean	0.2664 ± 0.0035	4.91 ± 0.06	7.48 ± 0.10
0.181	146.0	Water	M1	0.1663	6.13	4.20
			M2	0.1676	6.18	4.24
			M3	0.1710	6.31	4.32
			mean	0.1683 ± 0.0020	6.21 ± 0.07	4.25 ± 0.05
		DMSO	M1	0.5740	21.17	14.50
			M2	0.5724	21.11	14.46
			M3	0.5784	21.34	14.61
			mean	0.5749 ± 0.0025	21.21 ± 0.09	14.53 ± 0.06
		AcOH	M1	0.6798	25.08	17.18
			M2	0.7122	26.27	18.00
			M3	0.7099	26.19	17.94
			mean	0.7006 ± 0.0147	25.85 ± 0.54	17.70 ± 0.37
		EtOAc	M1	0.5072	18.71	12.82
			M2	0.4821	17.79	12.18
			M3	0.4805	17.72	12.14
			mean	0.4899 ± 0.0122	18.07 ± 0.45	12.38 ± 0.31

Table S9: Dependency of the concentration of okanin in the supernatant $c_{supernatant}$(okanin) and the relative okanin amount released from a pVCL microgel on the initial loading. The dilution was 1:1 for 0.070 and 1:3 for 0.181. Triplicates were performed and all obtained maximal absorbances and the mean value are provided.

n_{okanin}/n_{CU}	Okanin loading	Solvent		A_{max}(377 nm)	$c_{supernatant}$(okanin)	Released okanin
[-]	[$\mu g_{okanin}/mg_{microgel}$]			[a.u.]	[µg/mL]	[%(*m*/*m*)]
0.070	72.3	Water	M1	0.0766	1.41	1.96
			M2	0.0778	1.43	1.98
			M3	0.0759	1.40	1.94
			mean	0.0768 ± 0.0008	1.42 ± 0.01	1.96 ± 0.02
		DMSO	M1	0.2976	5.49	7.59
			M2	0.2976	5.49	7.59
			M3	0.2909	5.37	7.42
			mean	0.2954 ± 0.0032	5.45 ± 0.06	7.54 ± 0.08
		AcOH	M1	0.4071	7.51	10.39
			M2	0.4184	7.72	10.67
			M3	0.4226	7.79	10.78
			mean	0.4160 ± 0.0065	7.67 ± 0.12	10.62 ± 0.17
		EtOAc	M1	0.2653	4.89	6.77
			M2	0.2991	5.52	7.63
			M3	0.2946	5.43	7.52
			mean	0.2863 ± 0.0150	5.28 ± 0.28	7.31 ± 0.38
0.181	144.2	Water	M1	0.2257	8.33	5.77
			M2	0.2248	8.29	5.75
			M3	0.2210	8.15	5.65
			mean	0.2238 ± 0.0020	8.26 ± 0.07	5.73 ± 0.05
		DMSO	M1	0.7412	27.34	18.96
			M2	0.7483	27.60	19.14
			M3	0.7420	27.37	18.98
			mean	0.7438 ± 0.0032	27.44 ± 0.12	19.03 ± 0.08
		AcOH	M1	0.9228	34.04	23.61
			M2	0.8980	33.13	22.97
			M3	0.9114	33.62	23.32
			mean	0.9107 ± 0.0101	33.60 ± 0.37	23.30 ± 0.26
		EtOAc	M1	0.6566	24.22	16.80
			M2	0.6172	22.77	15.79
			M3	0.6693	24.69	17.12
			mean	0.6477 ± 0.0222	23.89 ± 0.82	16.57 ± 0.57

Table S10: Overview of performed simulations for testing optimal simulation conditions for the crosslinked pVCL model in TIP3P water.

system	tacticity	T [K]	replica	time [ns]	# water molecules [TIP3P]	# VCL moieties
pVCL cube, 20	atactic	293	30	500	52499 / 51565 / 52031	240
pVCL cube, 20	atactic	313	30	500	52499 / 51565 / 52031	240
pVCL cube, 20	atactic	343	30	500	52499 / 51565 / 52031	240
pVCL cube, 20	isotactic	293	10	500	51494	240
pVCL cube, 20	isotactic	313	10	500	51494	240
pVCL cube, 20	isotactic	343	10	500	51494	240
pVCL cube, 20	syndiotactic	293	10	500	51449	240
pVCL cube, 20	syndiotactic	313	10	500	51449	240
pVCL cube, 20	syndiotactic	343	10	500	51449	240
pVCL cube, 40	atactic	293	30	500	172669 / 168768 / 169597	480
pVCL cube, 40	atactic	313	30	500	172669 / 168768 / 169597	480
pVCL cube, 40	atactic	343	30	500	172669 / 168768 / 169597	480
pVCL cube, 40	isotactic	293	10	500	165415	480
pVCL cube, 40	isotactic	313	10	500	165415	480
pVCL cube, 40	isotactic	343	10	500	165415	480
pVCL cube, 40	syndiotactic	293	10	500	163923	480
pVCL cube, 40	syndiotactic	313	10	500	163923	480
pVCL cube, 40	syndiotactic	343	10	500	163923	480

Table S11: Overview of performed simulations for testing optimal simulation conditions for the crosslinked pVCL model in OPC water.

system	tacticity	T [K]	replica	time [ns]	# water molecules [OPC]	# VCL moieties
pVCL cube, 20	atactic	293	30	500	52489 / 51554 / 52025	240
pVCL cube, 20	atactic	313	30	500	52489 / 51554 / 52025	240
pVCL cube, 20	atactic	343	30	500	52489 / 51554 / 52025	240
pVCL cube, 20	isotactic	293	10	500	51486	240
pVCL cube, 20	isotactic	313	10	500	51486	240
pVCL cube, 20	isotactic	343	10	500	51486	240
pVCL cube, 20	syndiotactic	293	10	500	51440	240
pVCL cube, 20	syndiotactic	313	10	500	51440	240
pVCL cube, 20	syndiotactic	343	10	500	51440	240

Table S12: Overview of performed simulations for probing interactions between okanin and linear/crosslinked pVCL.

system	tacticity	T [K]	replica	time [ns]	# water molecules	# VCL moieties	# okanin molecules
linear pVCL 50mer	syndiotactic	293	10	1000	102898	50	7
linear pVCL 50mer	syndiotactic	313	10	1000	102898	50	7
linear pVCL 50mer	syndiotactic	293	10	1000	102898	50	28
linear pVCL 50mer	syndiotactic	313	10	1000	102898	50	28
linear pVCL 50mer	syndiotactic	293	10	1000	102898	50	56
linear pVCL 50mer	syndiotactic	313	10	1000	102898	50	56
pVCL cube, 20	syndiotactic	293	10	1000	102898	240	-
pVCL cube, 20	syndiotactic	313	10	1000	102898	240	-
pVCL cube, 20	syndiotactic	293	10	1000	102898	240	12
pVCL cube, 20	syndiotactic	313	10	1000	102898	240	12
pVCL cube, 20	syndiotactic	293	10	1000	102898	240	31
pVCL cube, 20	syndiotactic	313	10	1000	102898	240	31
pVCL cube, 20	syndiotactic	293	10	1000	102898	240	65
pVCL cube, 20	syndiotactic	313	10	1000	102898	240	65
pVCL cube, 20	syndiotactic	293	10	1000	102898	240	130
pVCL cube, 20	syndiotactic	313	10	1000	102898	240	130
pVCL cube, 20	syndiotactic	293	10	1000	102898	240	260
pVCL cube, 20	syndiotactic	313	10	1000	102898	240	260

Table S13: Dependency of the hydrodynamic radius and the polydispersity index at 20 °C and 50 °C of okanin-loaded microgels determined by DLS on the molar ratio of okanin to the number of constitutional units n_{okanin}/n_{CU} used in the loading process. To compare the different microgels, the hydrodynamic radii were normed by using the hydrodynamic radius of the unloaded microgel ($R_H(n_{okanin}/n_{CU} = 0)$) as reference.

Microgel	n_{okanin}/n_{CU}	c(okanin)	$R_{H,\,20\,°C}$	$R_{H,normed,\,20\,°C}$	$PDI_{20\,°C}$	$R_{H,\,50\,°C}$	$R_{H,normed,\,50\,°C}$	$PDI_{50\,°C}$
	[-]	[mM]	[nm]	[nm]	[-]	[nm]	[nm]	[-]
pVCL	0	0	432 ± 8	1.000 ± 0.018	0.159 ± 0.023	165 ± 14	1.000 ± 0.088	0.162 ± 0.014
	0.002	0.014	286 ± 33	0.661 ± 0.077	0.111 ± 0.044	136 ± 10	0.824 ± 0.062	0.081 ± 0.019
	0.007	0.05	337 ± 26	0.780 ± 0.059	0.132 ± 0.073	139 ± 7	0.842 ± 0.043	0.081 ± 0.085
	0.014	0.1	359 ± 19	0.831 ± 0.043	0.167 ± 0.063	143 ± 8	0.864 ± 0.048	0.069 ± 0.037
	0.070	0.5	308 ± 50	0.712 ± 0.115	0.215 ± 0.172	144 ± 5	0.868 ± 0.033	0.050 ± 0.031
	0.139	1.0	169 ± 16	0.392 ± 0.036	0.058 ± 0.039	146 ± 12	0.885 ± 0.070	0.091 ± 0.093
	0.181	1.3	154 ± 4	0.358 ± 0.010	0.041 ± 0.031	158 ± 7	0.958 ± 0.042	0.036 ± 0.019
	0.278	2.0	161 ± 7	0.373 ± 0.017	0.084 ± 0.048	162 ± 10	0.982 ± 0.061	0.106 ± 0.062
p(VCL/GMA$_{core}$)	0	0	263 ± 6	1.000 ± 0.022	0.046 ± 0.025	119 ± 4	1.000 ± 0.037	0.017 ± 0.008
	0.002	0.014	222 ± 4	0.843 ± 0.014	0.080 ± 0.044	141 ± 28	1.184 ± 0.232	0.184 ± 0.104
	0.007	0.05	237 ± 20	0.900 ± 0.075	0.058 ± 0.037	113 ± 5	0.948 ± 0.042	0.038 ± 0.036
	0.014	0.1	230 ± 5	0.875 ± 0.019	0.053 ± 0.029	112 ± 4	0.942 ± 0.034	0.012 ± 0.007
	0.070	0.5	145 ± 10	0.552 ± 0.038	0.067 ± 0.054	126 ± 5	1.062 ± 0.041	0.056 ± 0.044
	0.139	1.0	132 ± 4	0.501 ± 0.014	0.038 ± 0.028	134 ± 7	1.125 ± 0.062	0.032 ± 0.023
	0.181	1.3	130 ± 2	0.496 ± 0.007	0.029 ± 0.022	133 ± 6	1.119 ± 0.053	0.020 ± 0.013
	0.278	2.0	130 ± 2	0.494 ± 0.007	0.017 ± 0.012	133 ± 6	1.114 ± 0.051	0.023 ± 0.011

Table S13 continued

Microgel	n_{okanin}/n_{CU}	c(okanin)	$R_{H,\ 20\ °C}$	$R_{H,normed,\ 20\ °C}$	$PDI_{20\ °C}$	$R_{H,\ 50\ °C}$	$R_{H,normed,\ 50\ °C}$	$PDI_{50\ °C}$
	[-]	[mM]	[nm]	[nm]	[-]	[nm]	[nm]	[-]
p(VCL/GMA$_{shell}$)	0	0	366 ± 24	1.000 ± 0.065	0.281 ± 0.022	170 ± 9	1.000 ± 0.053	0.149 ± 0.008
	0.002	0.014	326 ± 26	0.891 ± 0.071	0.243 ± 0.019	157 ± 9	0.920 ± 0.052	0.167 ± 0.139
	0.007	0.05	378 ± 20	1.031 ± 0.056	0.229 ± 0.044	162 ± 6	0.949 ± 0.038	0.053 ± 0.018
	0.014	0.1	388 ± 42	1.059 ± 0.114	0.254 ± 0.076	163 ± 7	0.959 ± 0.038	0.068 ± 0.023
	0.070	0.5	214 ± 18	0.584 ± 0.050	0.278 ± 0.092	171 ± 25	1.003 ± 0.149	0.281 ± 0.195
	0.139	1.0	200 ± 7	0.547 ± 0.019	0.161 ± 0.060	187 ± 16	1.099 ± 0.096	0.207 ± 0.055
	0.181	1.3	202 ± 11	0.552 ± 0.029	0.155 ± 0.030	183 ± 11	1.074 ± 0.062	0.131 ± 0.084
	0.278	2.0	201 ± 7	0.549 ± 0.020	0.141 ± 0.019	187 ± 14	1.095 ± 0.080	0.160 ± 0.064

3 Supplemental Figures

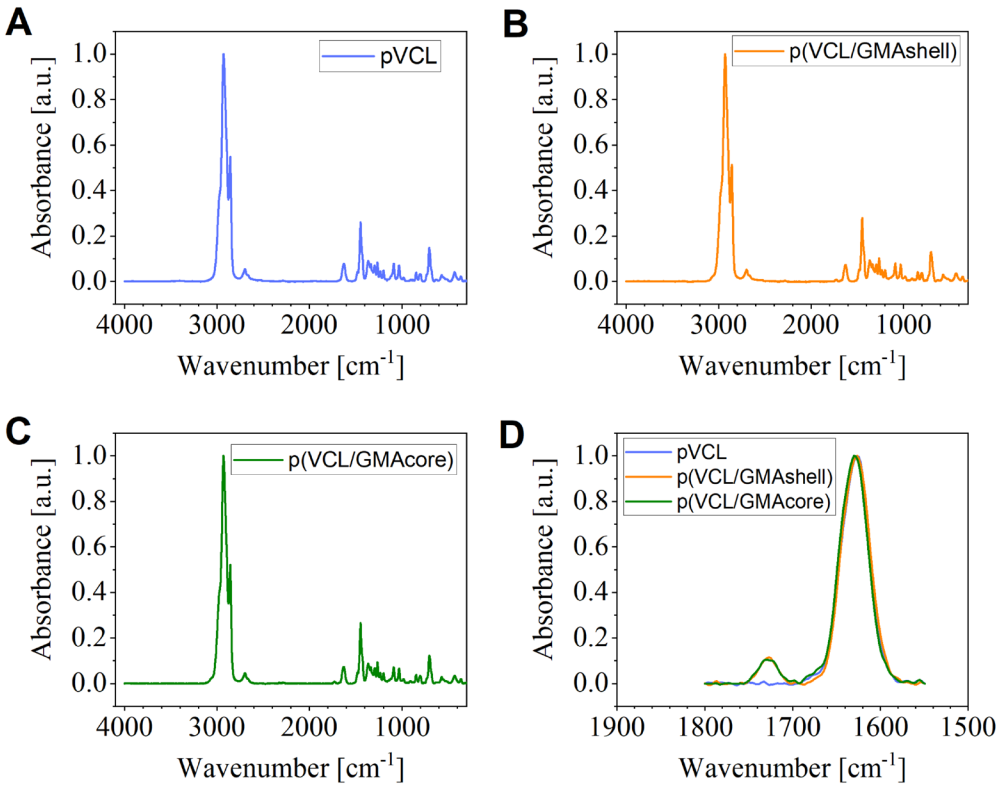

Figure S1: Raman spectra of pVCL-based microgels (**A** pVCL, **B** p(VCL/GMA$_{shell}$) and **C** p(VCL/GMA$_{core}$)). **D** Excerpt of the Raman spectra from the spectra normalized to the peak of the carbonyl stretching vibration of VCL (1636 cm^{-1}). The peak at 1726 cm^{-1} correlates to the carbonyl stretching vibration of GMA. The GMA content was determined as 10.7 mol% for p(VCL/GMA$_{shell}$) and 9.8 mol% for p(VCL/GMA$_{core}$).

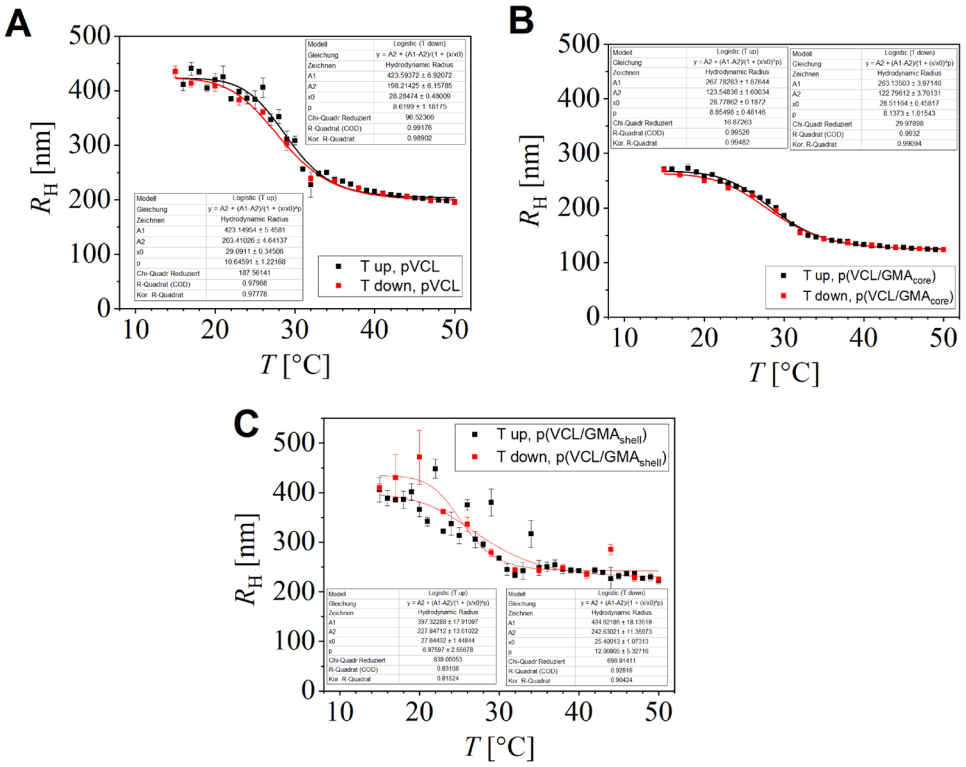

Figure S2: Determination of the VPTT for pVCL-based microgels by temperature-dependent DLS measurements. A logistic fit was applied to trends of R_H to determine the VPTT from the turning point (**A** pVCL (29 °C), **B** p(VCL/GMA$_{core}$) (29 °C), and **C** p(VCL/GMA$_{shell}$) (28 °C)).

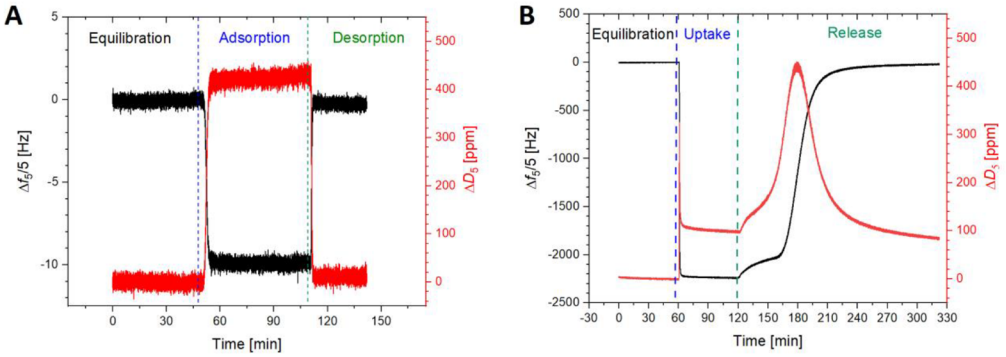

Figure S3: Real-time frequency changes $\Delta f_5/5$ and dissipation ΔD_5 by QCM-D at 25 °C **A** for the adsorption and desorption of/from a clean SiO_2-sensor and **B** for the uptake and release into/from p(VCL/GMA_{shell}) microgels bound to a SiO_2-sensor. The sensor is equilibrated in an aqueous solution of 2.4 vol% DMSO. The uptake was initiated by switching the solvent to an aqueous solution (2.4 vol% DMSO) with 0.4 mM okanin, and the release was initiated by switching to ultrapure water. The decrease in $\Delta f_5/5$ is indicative of an increase in the mass bound to the sensor. The microgels are too large for a quantitative analysis, so the curves only give access to the qualitative uptake and release kinetics.

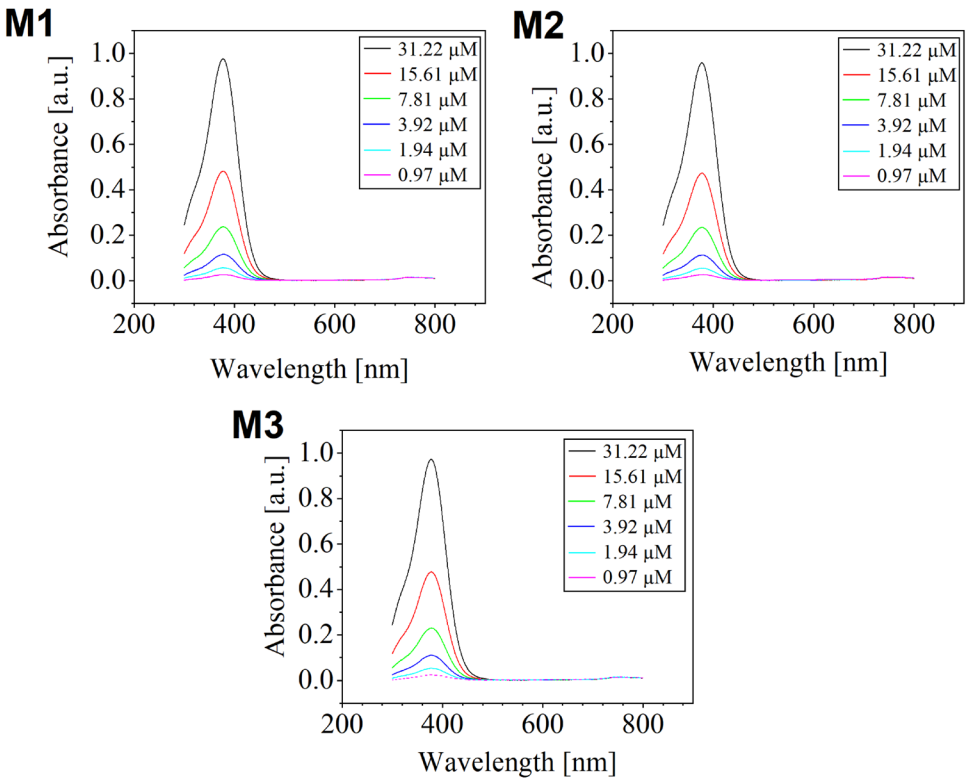

Figure S4: UV/Vis spectra of a dilution series of okanin in 2.4 vol% DMSO/water to determine the attenuation coefficient. The measurements were repeated thrice (M1, M2 and M3).

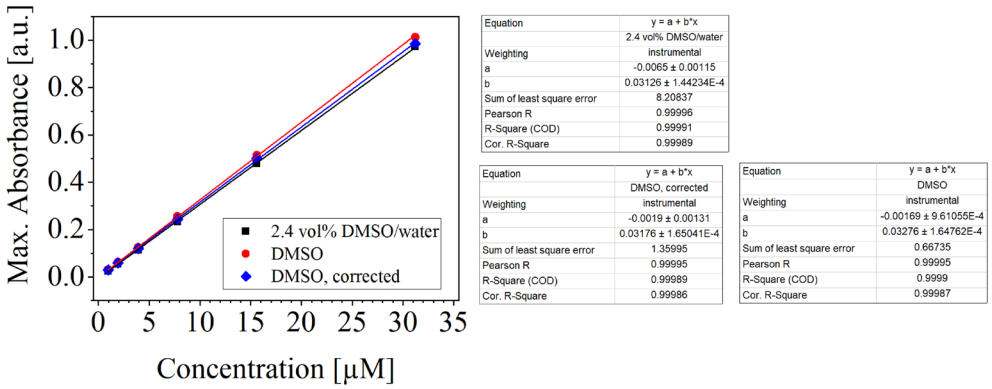

Equation	y = a + b*x
	2.4 vol% DMSO/water
Weighting	instrumental
a	-0.0065 ± 0.00115
b	0.03126 ± 1.44234E-4
Sum of least square error	8.20837
Pearson R	0.99996
R-Square (COD)	0.99991
Cor. R-Square	0.99989

Equation	y = a + b*x
	DMSO, corrected
Weighting	instrumental
a	-0.0019 ± 0.00131
b	0.03176 ± 1.65041E-4
Sum of least square error	1.35995
Pearson R	0.99995
R-Square (COD)	0.99989
Cor. R-Square	0.99986

Equation	y = a + b*x
	DMSO
Weighting	instrumental
a	-0.00169 ± 9.61055E-4
b	0.03276 ± 1.64762E-4
Sum of least square error	0.66735
Pearson R	0.99995
R-Square (COD)	0.9999
Cor. R-Square	0.99987

Figure S5: UV/Vis spectra of a dilution series of okanin in 2.4 vol% DMSO/water to determine the attenuation coefficient. The measurements were repeated thrice (M1, M2 and M3).

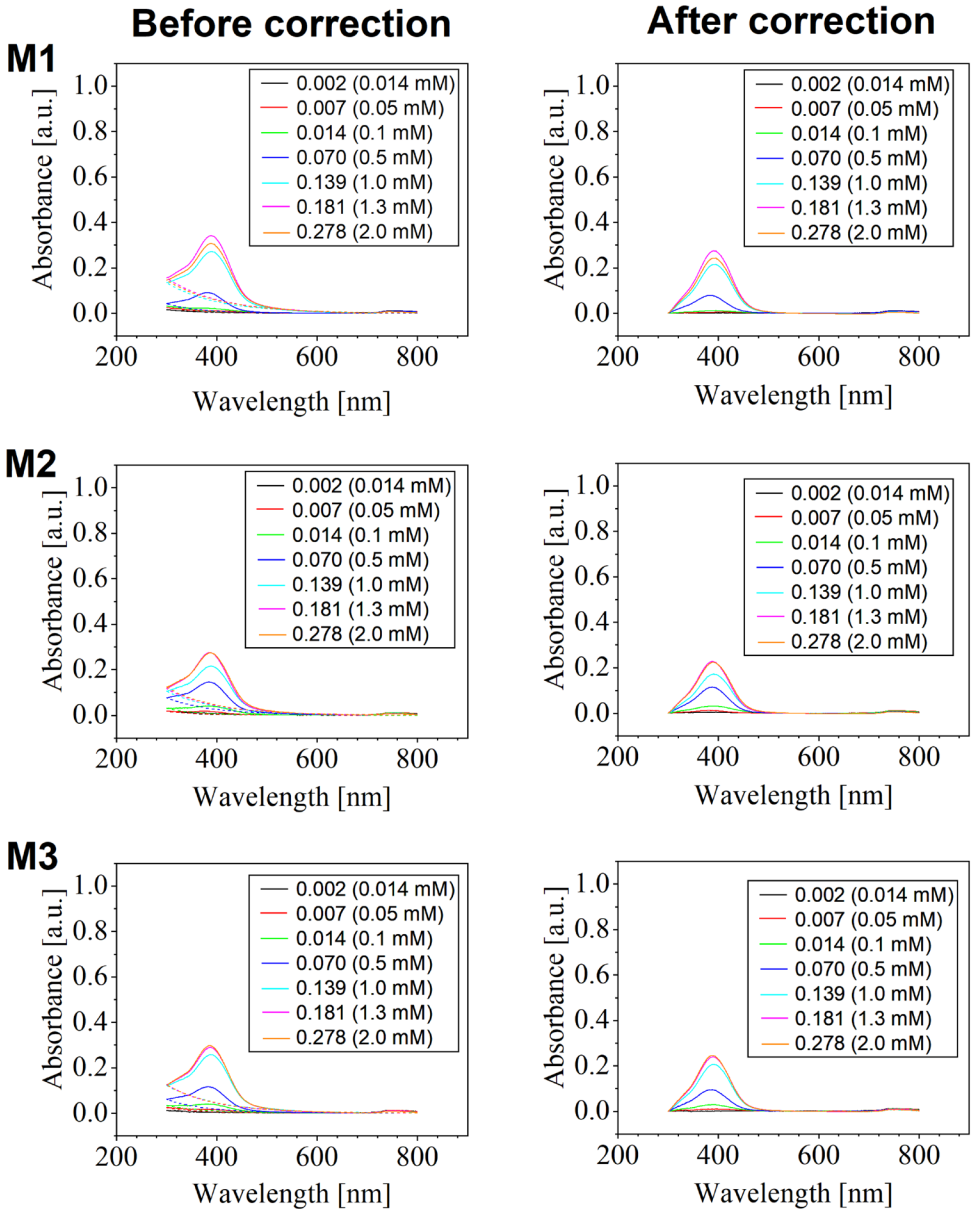

Figure S6: UV/Vis spectra of a pVCL microgel loaded with different molar ratios of okanin to repeating units (n_{okanin}/n_{CU}) before and after exponential baseline correction. The measurements were repeated thrice (M1, M2, and M3).

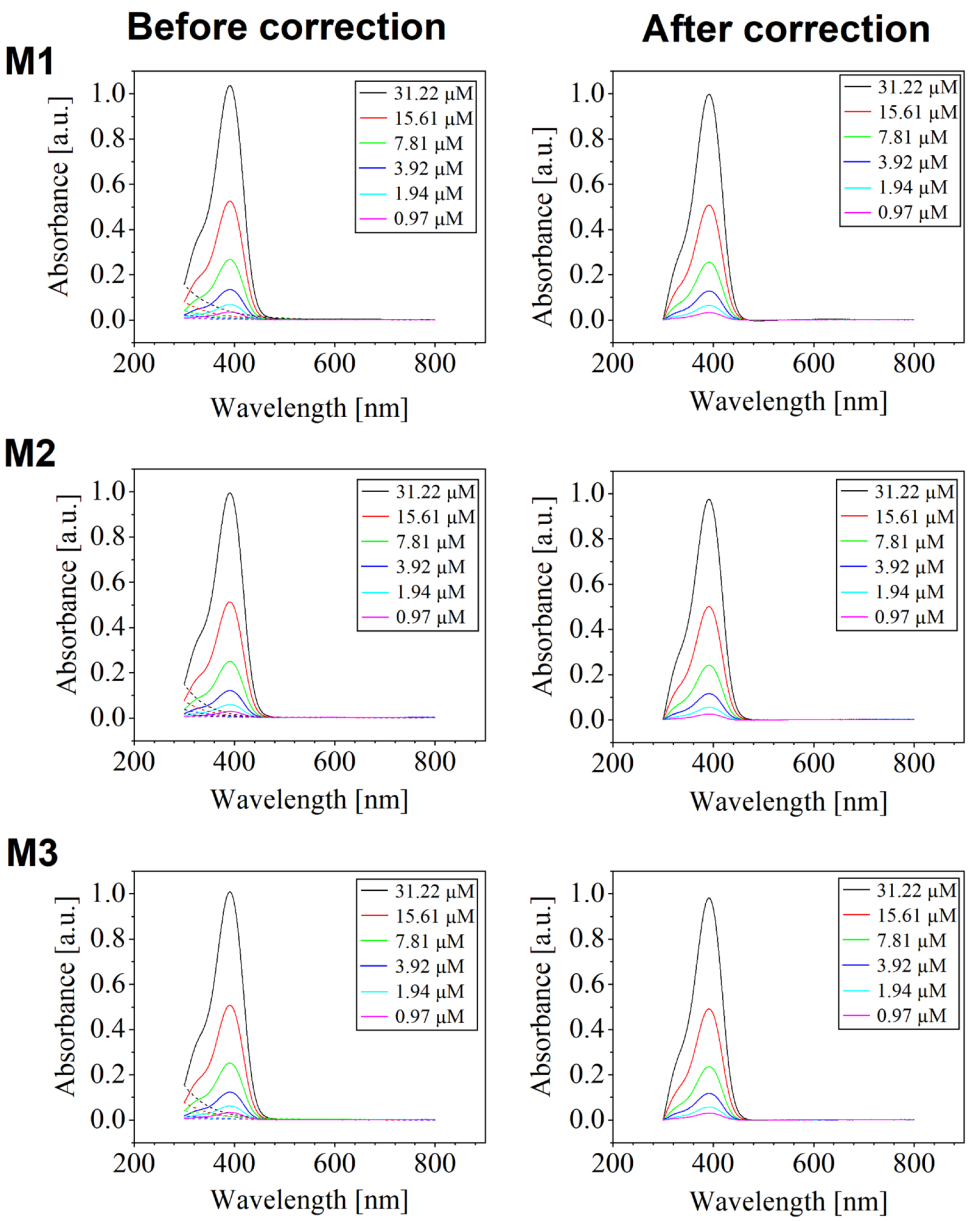

Figure S7: UV/Vis spectra of a dilution series of okanin in 2.4 vol% DMSO/water to determine the attenuation coefficient. The measurements were repeated thrice (M1, M2, and M3).

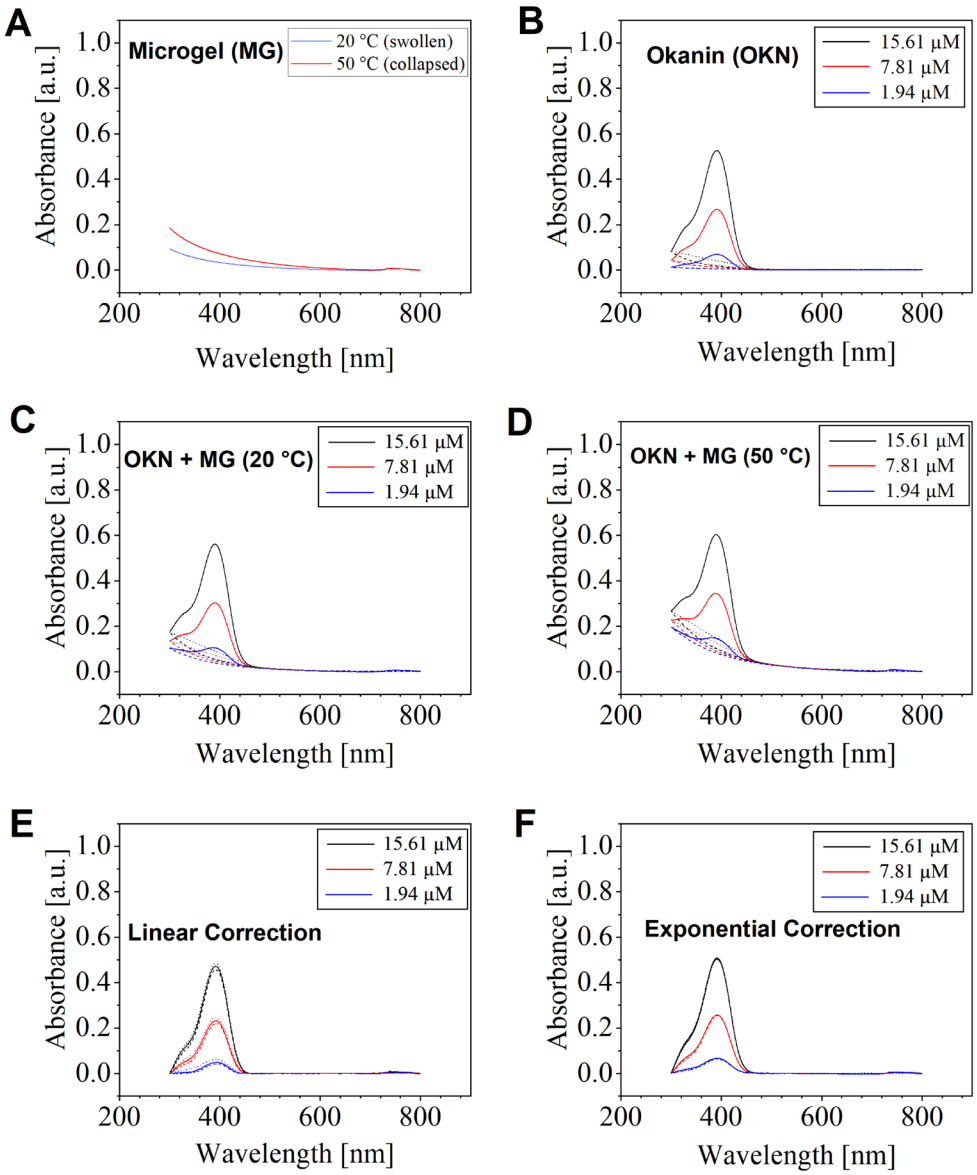

Figure S8: Empirical comparison between linear and exponential baseline correction in UV/Vis spectroscopy. **A** UV/Vis spectra of a p(VCL/GMA$_{shell}$) microgel (0.03 mg/mL) at 20 °C and 50 °C. **B** UV/Vis spectra of okanin in DMSO for different concentrations (dashed: exponential baseline, dotted: linear baseline). **C** The UV/Vis spectrum for the microgel at 20 °C and the spectra of okanin were added to mimic the spectrum of a swollen microgel loaded with three different loading degrees of okanin (dashed: exponential baseline, dotted: linear baseline). **D** The UV/Vis spectrum for the microgel at 50 °C and the spectra of okanin were added to mimic the spectrum of a collapsed microgel loaded with three different loading degrees of okanin (dashed: exponential baseline, dotted: linear baseline). **E** A linear baseline correction is applied to all spectra. **F** An exponential baseline correction is applied to all spectra.

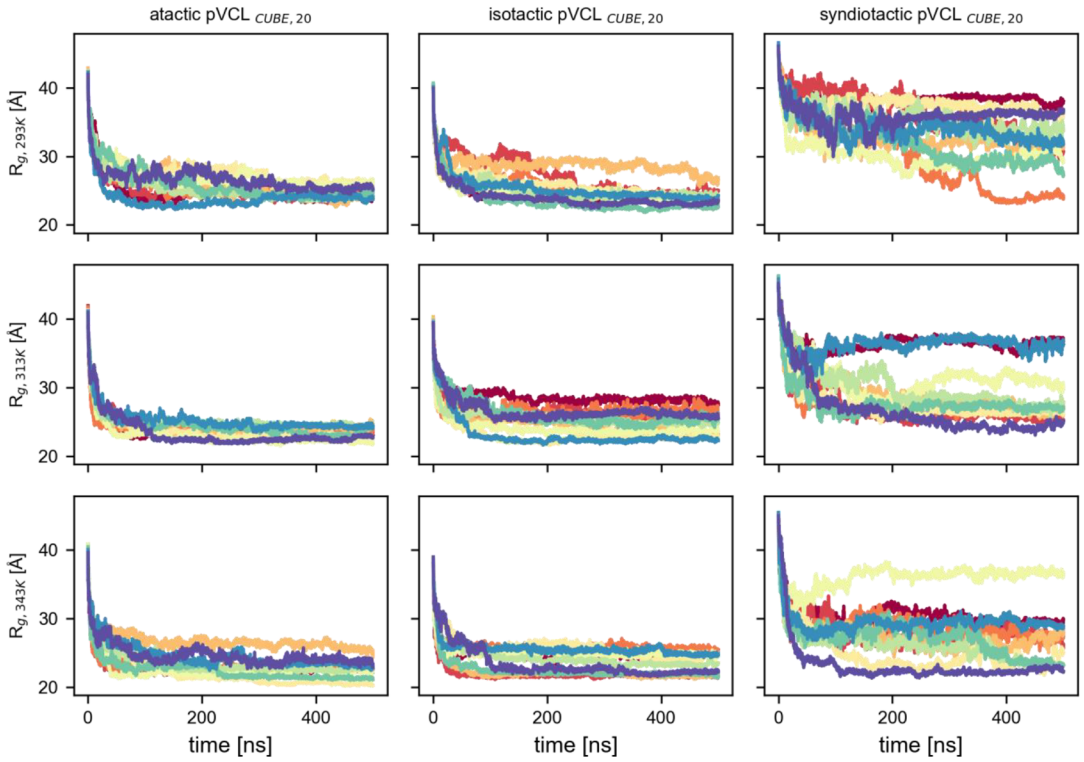

Figure S9: Radius of gyration (R_g) of the crosslinked pVCL model with inter-crosslink chain lengths of 20 repeating units in combination with TIP3P water[5] at 293 K, 313 K, and 343 K. Geometric analysis was performed with cpptraj[6]. Only the syndiotactic crosslinked pVCL model shows the experimentally observed thermo-responsiveness, i.e., a swollen conformation (high R_g) at low temperatures (293 K) and a collapsed conformation (low R_g) at higher temperatures (313 K).

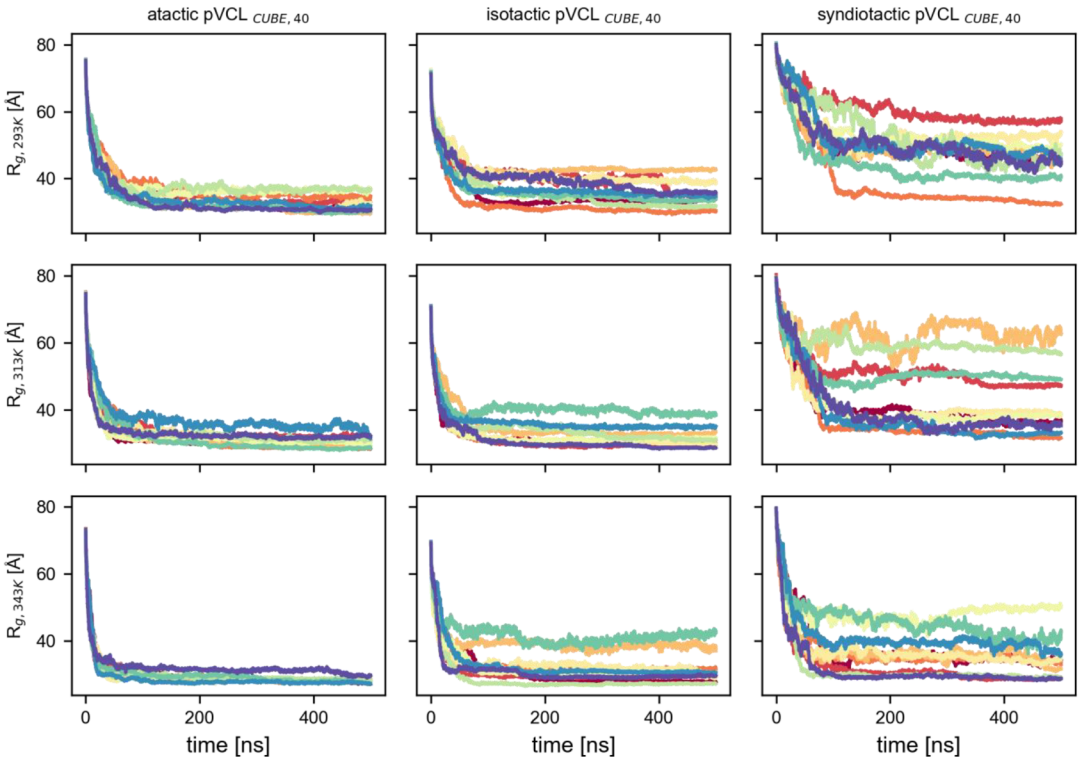

Figure S10: Radius of gyration (R_g) of the crosslinked pVCL model with inter-crosslink chain lengths of 40 repeating units in combination with TIP3P water[5] at 293 K, 313 K, and 343 K. Geometric analysis was performed with cpptraj[6]. Only the syndiotactic crosslinked pVCL model shows the experimentally observed thermo-responsiveness, i.e., a swollen conformation (high R_g) at low temperatures (293 K) and a collapsed conformation (low R_g) at higher temperatures (313 K).

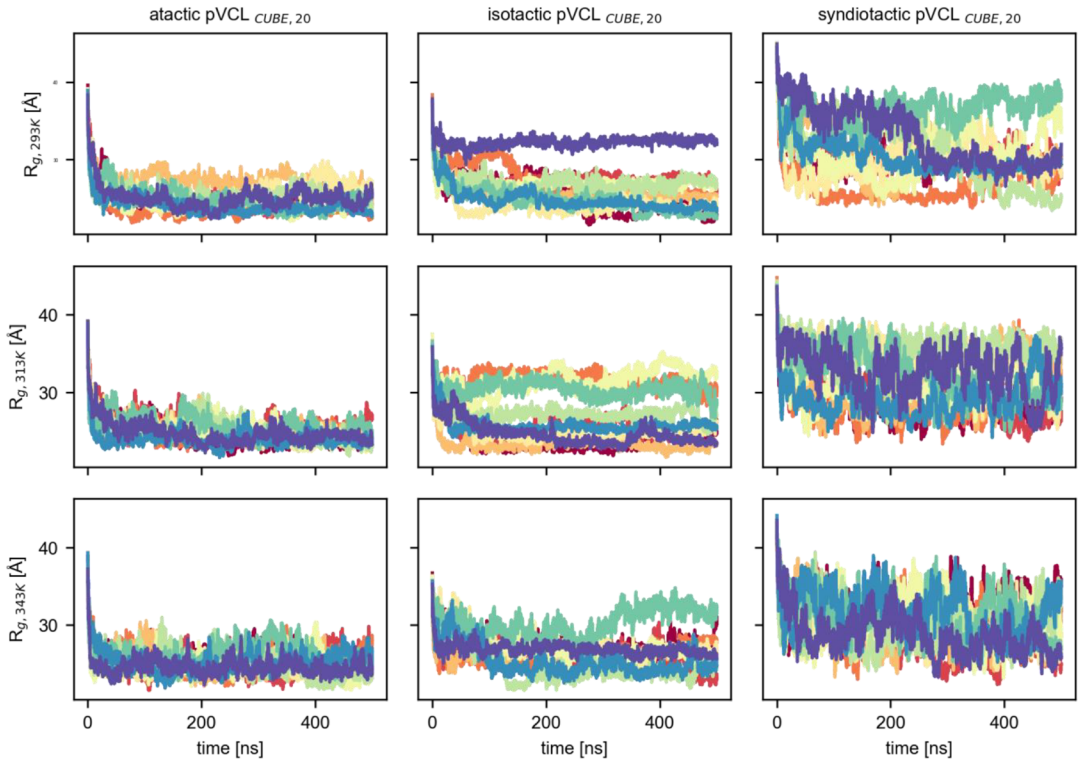

Figure S11: Radius of gyration (R_g) of the crosslinked pVCL model with inter-crosslink chain lengths of 20 repeating units in combination with OPC water[7] at 293 K, 313 K, and 343 K. Geometric analysis was performed with cpptraj[6]

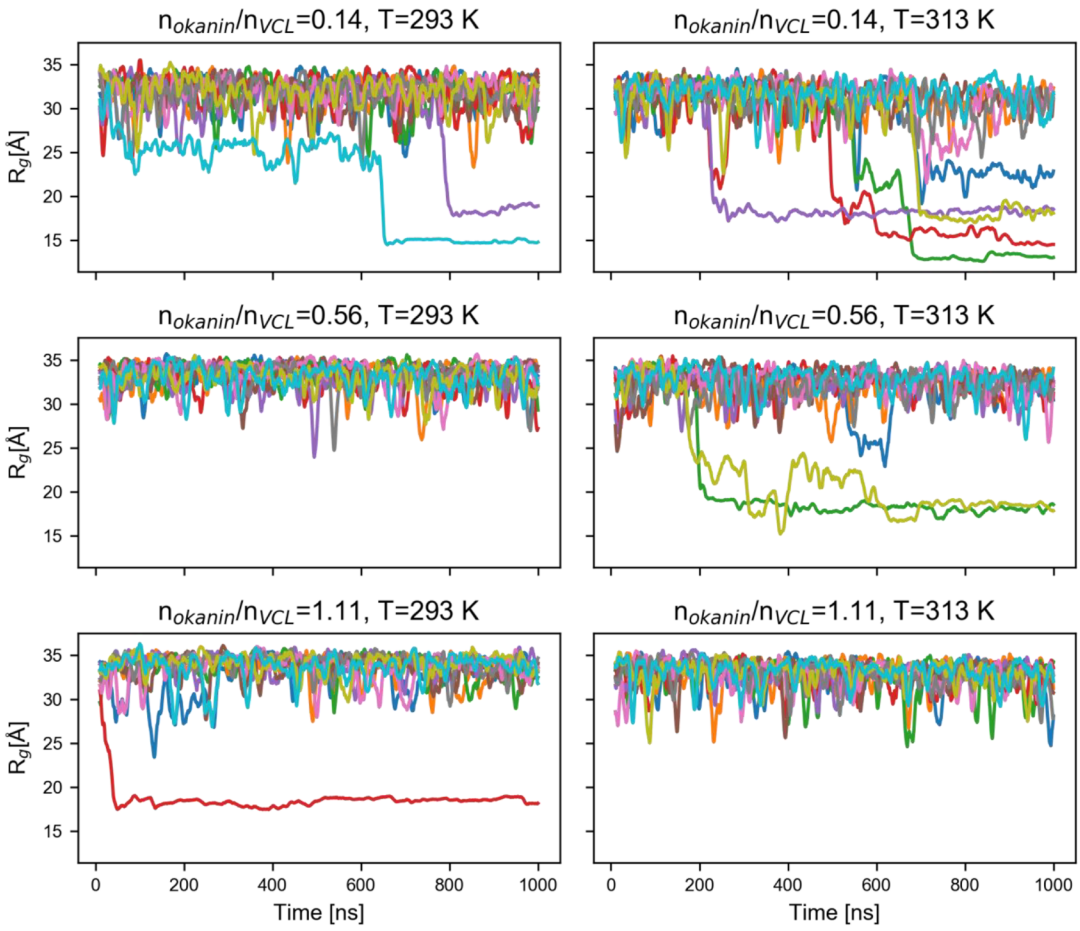

Figure S12: Radius of gyration (R_g) of the syndiotactic pVCL 50mer for different okanin concentrations (n_{okanin}/n_{VCL} = 0.14, 0.56, and 1.11, respectively) at 293 K and 313 K. Geometric analysis was performed with cpptraj[6].

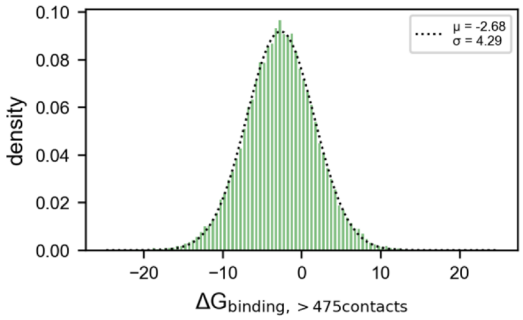

Figure S13: Distribution of binding free energies obtained from MM-PBSA computations for all okanin molecules considered bound (> 475 contacts). Parameters of the Gaussian fit (dotted line) are indicated in the legend.

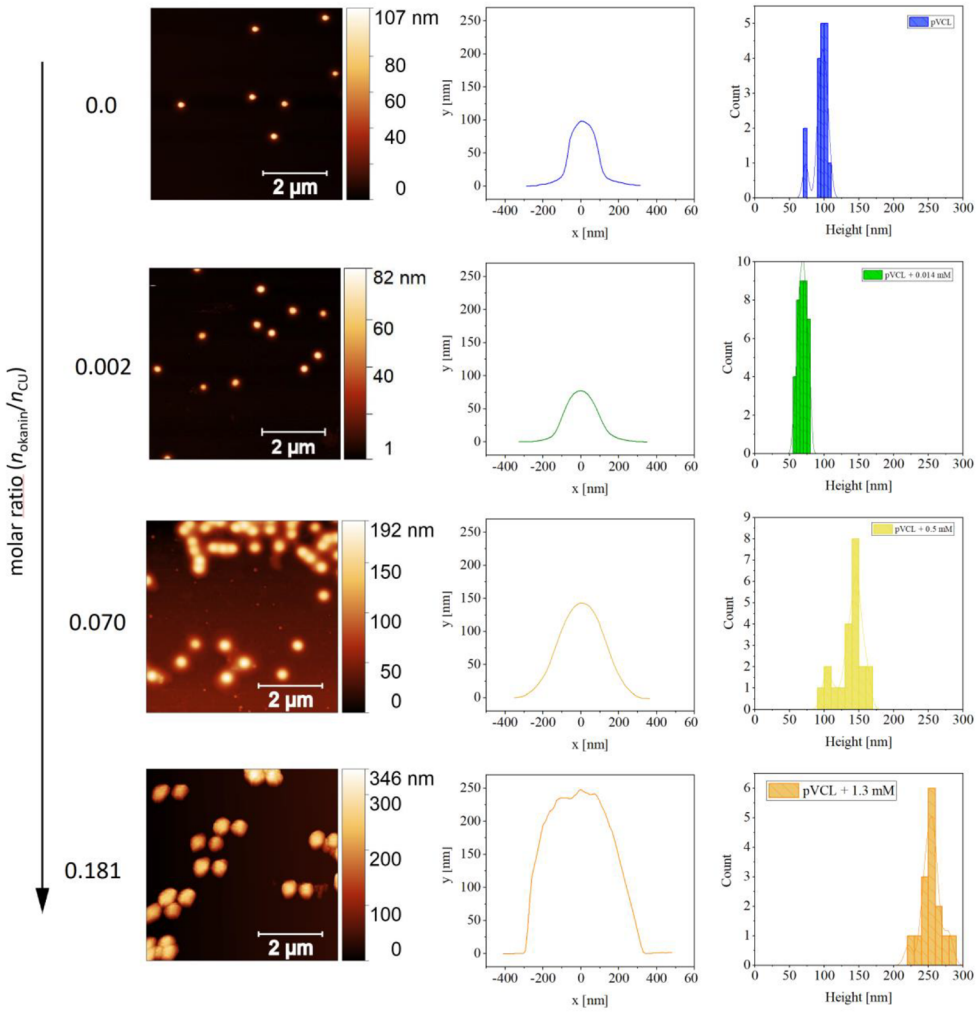

Figure S14: Exemplary AFM images, height profiles and histograms of a pVCL microgel for varying n_{okanin}/n_{CU} ratios. The collapse of the microgels upon binding of okanin leads to a rigidification of the microgel. As a result, the microgel's height increases.

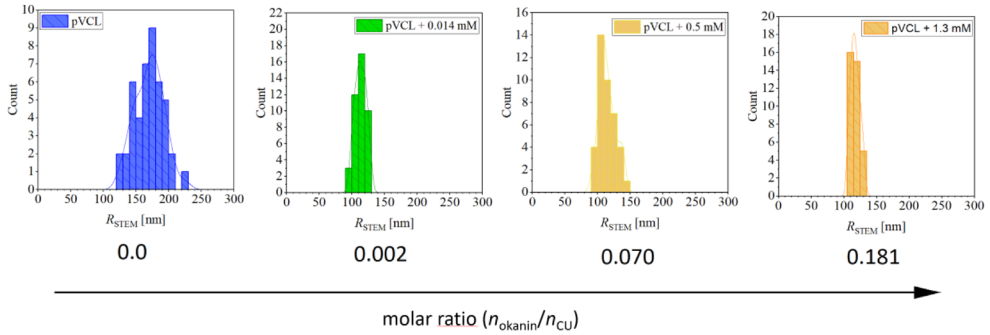

Figure S15: Histograms of R_{STEM} of a pVCL microgel for varying n_{okanin}/n_{CU} ratios. Due to the diffuse morphology of the unloaded microgels, the results for a molar ratio of 0.000 and 0.002 are expected to be biased. The collapse of the microgels upon binding of okanin leads to a rigidification of the microgel so that D_{STEM} can be determined.

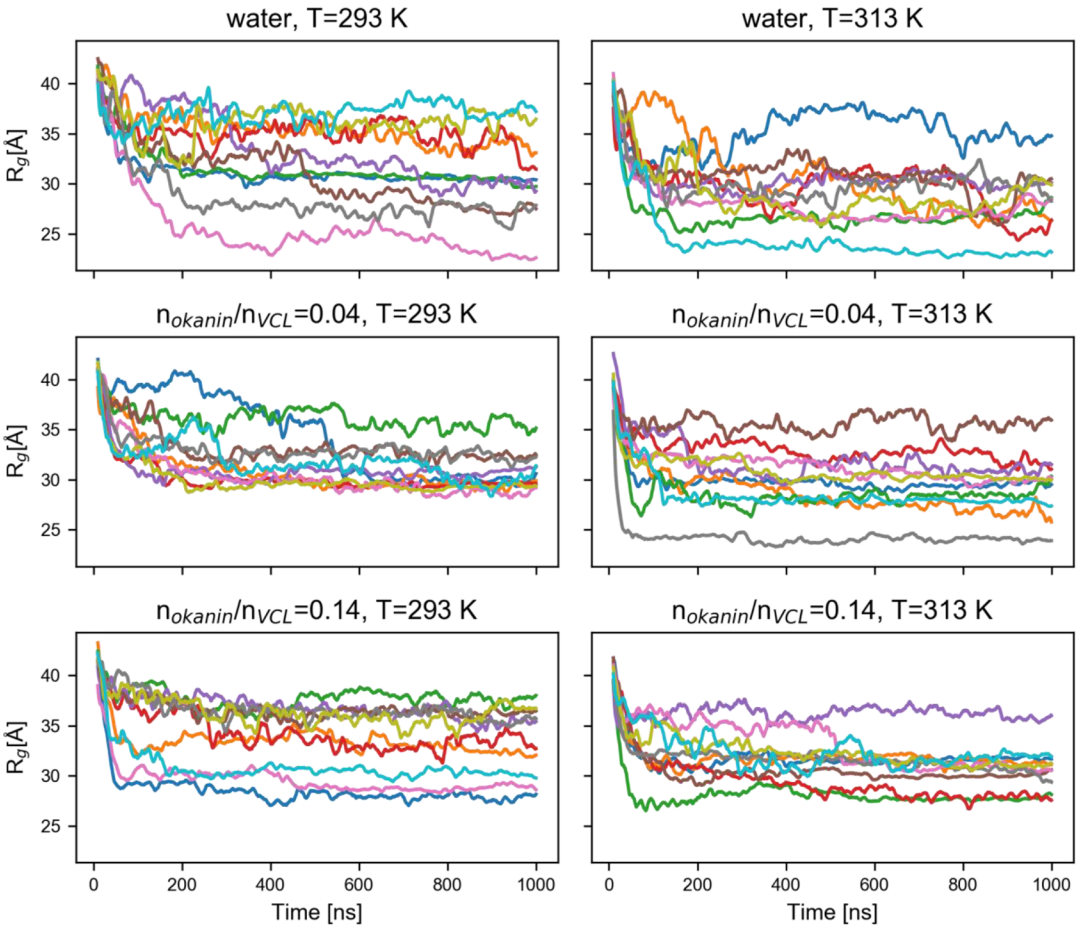

Figure S16: Radius of gyration (R_g) of the crosslinked pVCL model for different okanin concentrations (n_{okanin}/n_{VCL} = 0, 0.04, and 0.14, respectively) at 293 K and 313 K. Geometric analysis was performed with cpptraj[6]

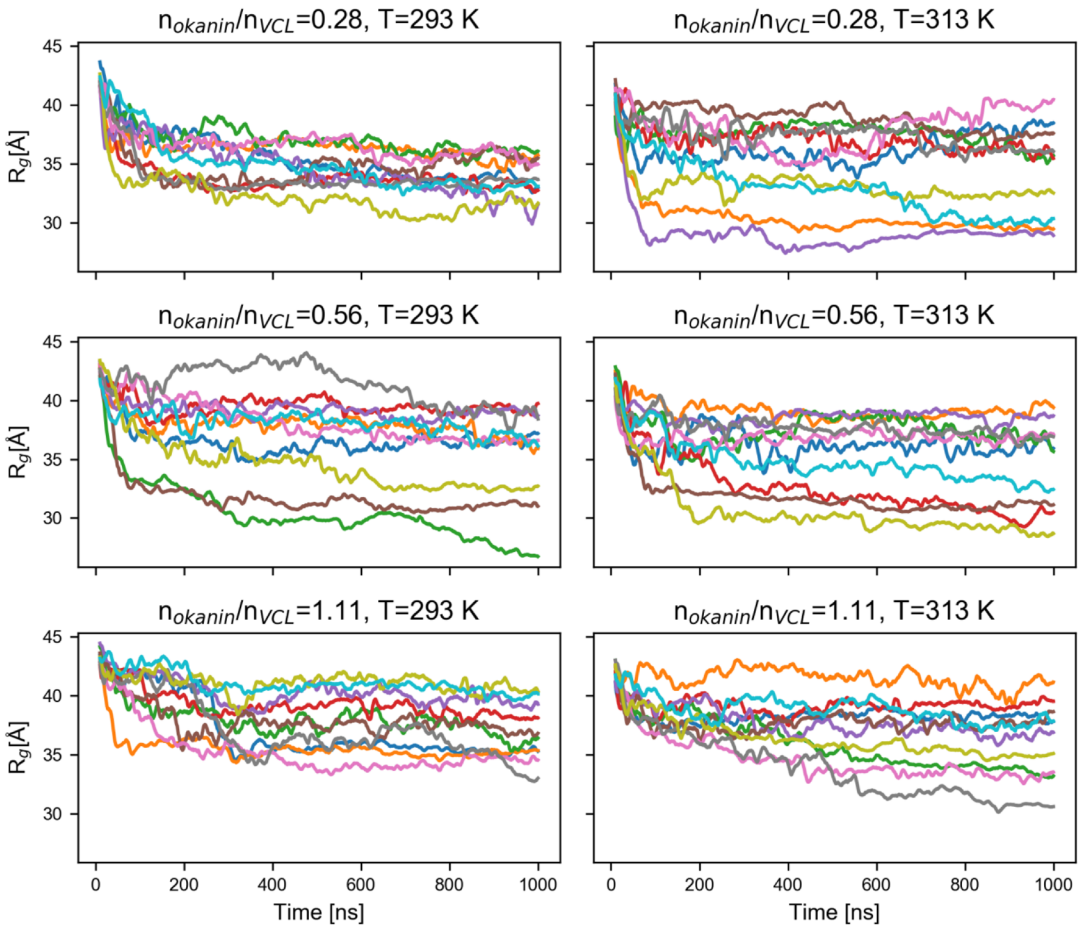

Figure S17: Radius of gyration (R_g) of the crosslinked pVCL model for different okanin concentrations (n_{okanin}/n_{VCL} = 0.28, 0.56, and 1.11, respectively) at 293 K and 313 K. Geometric analysis was performed with cpptraj[6]

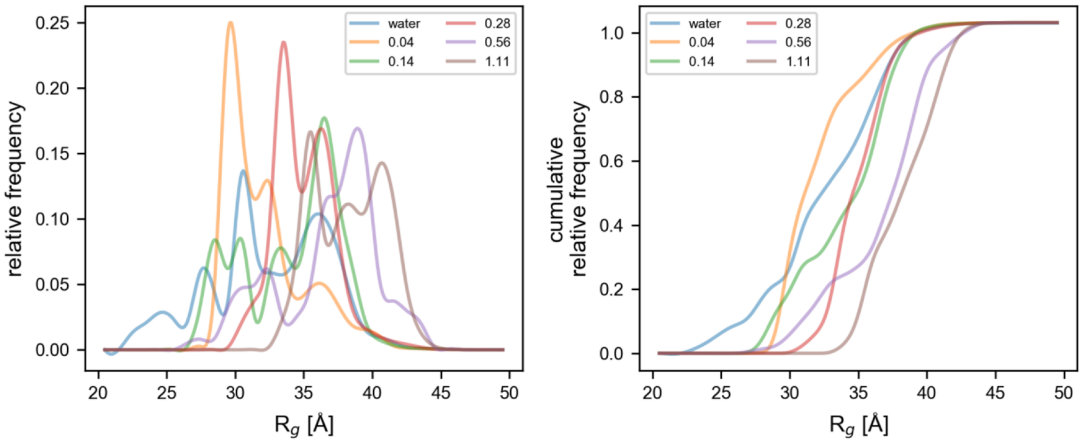

Figure S18: Distribution of radius of gyration (R_g) for simulations of the crosslinked pVCL model for different okanin concentrations (Figure S16 and Figure S17) depicted as histogram (left) and as cumulative relative frequency (right).

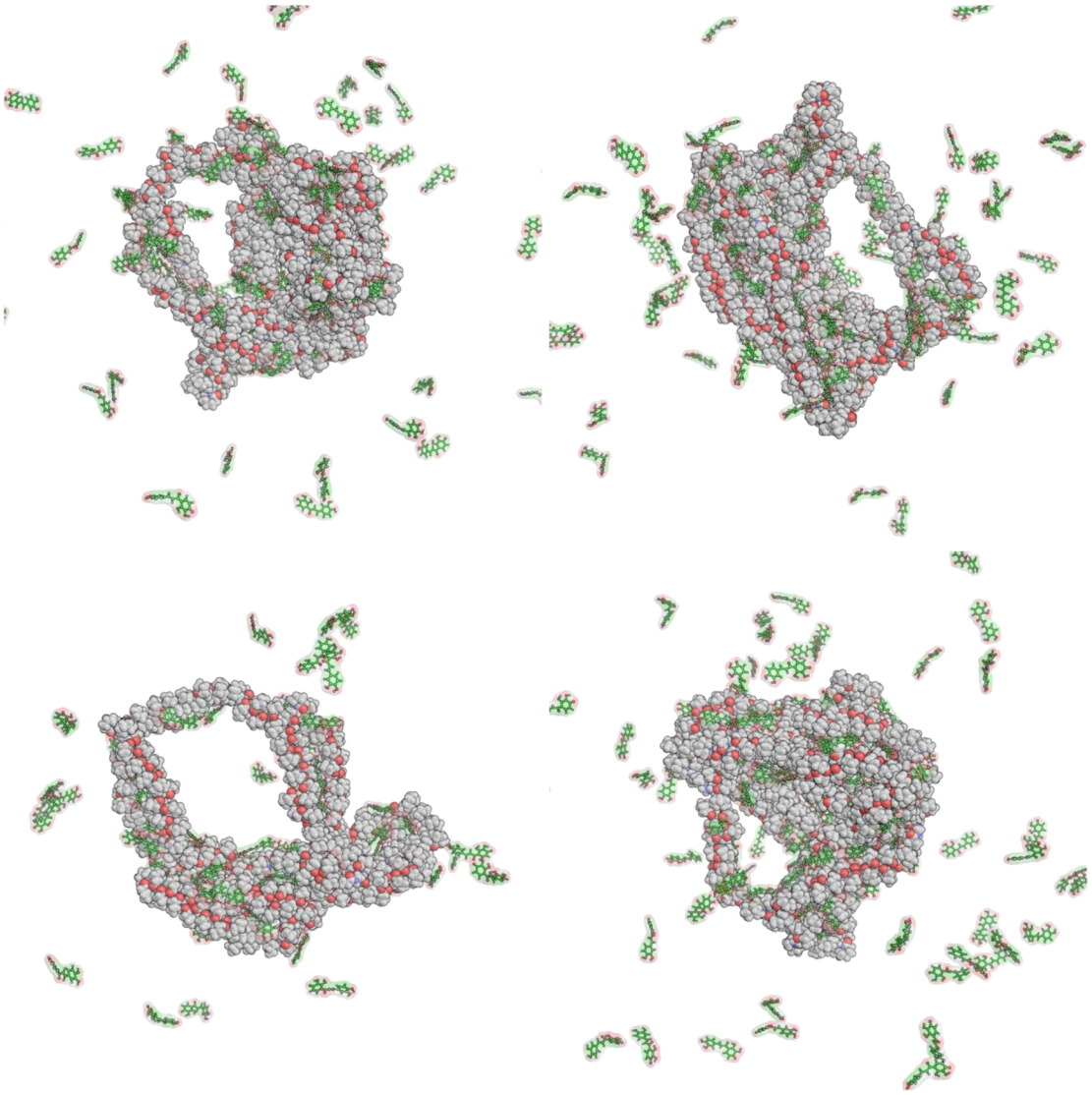

Figure S19: Porous MG structures obtained after 1 µs simulation of the crosslinked pVCL with okanin (n_{okanin}/n_{CU} = 0.28) at 293 K exemplarily shown for four different replicas.

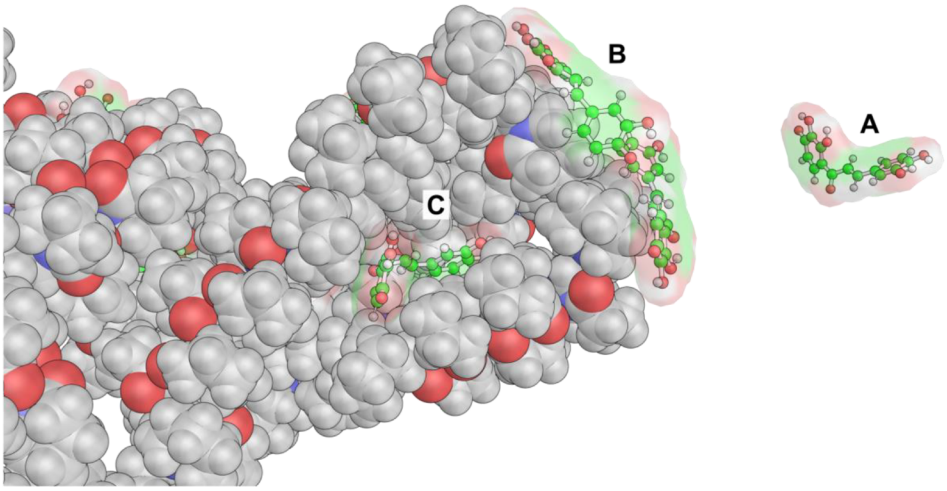

Figure S20: Binding of okanin to the crosslinked pVCL. The okanin is either in solution (**A**), loosely adsorbed to the surface of the pVCL (**B**, two molecules), or bound within the polymer between at least two pVCL chains (**C**).

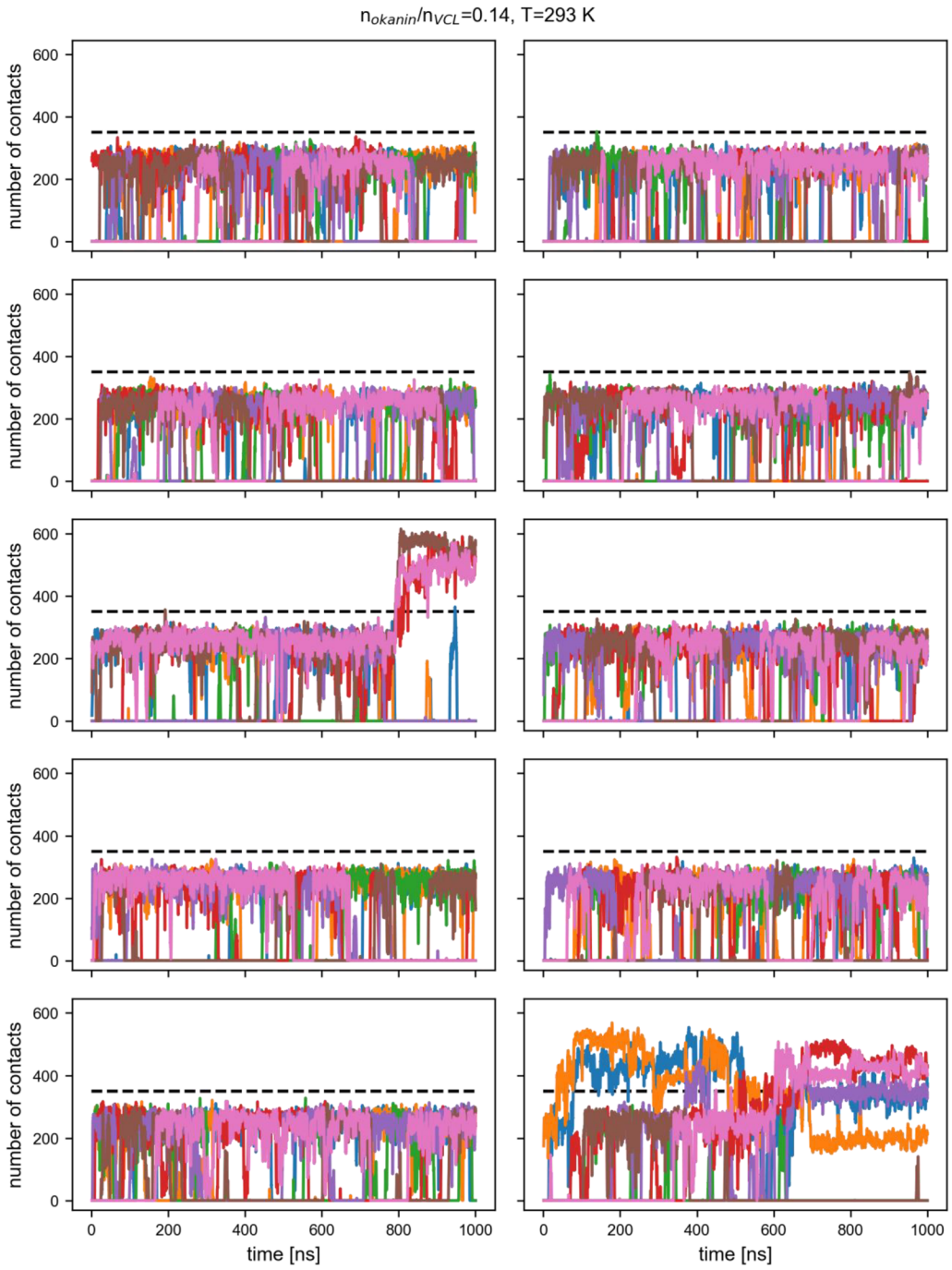

Figure S21: Number of contacts for each of the seven okanin molecules (n_{okanin}/n_{VCL} = 0.14) within each of the ten simulations of the linear pVCL at 293 K. Only trajectories with a coil-to-globule transition of the oligomer comprises okanin with more than 350 contacts (dashed line) to the pVCL.

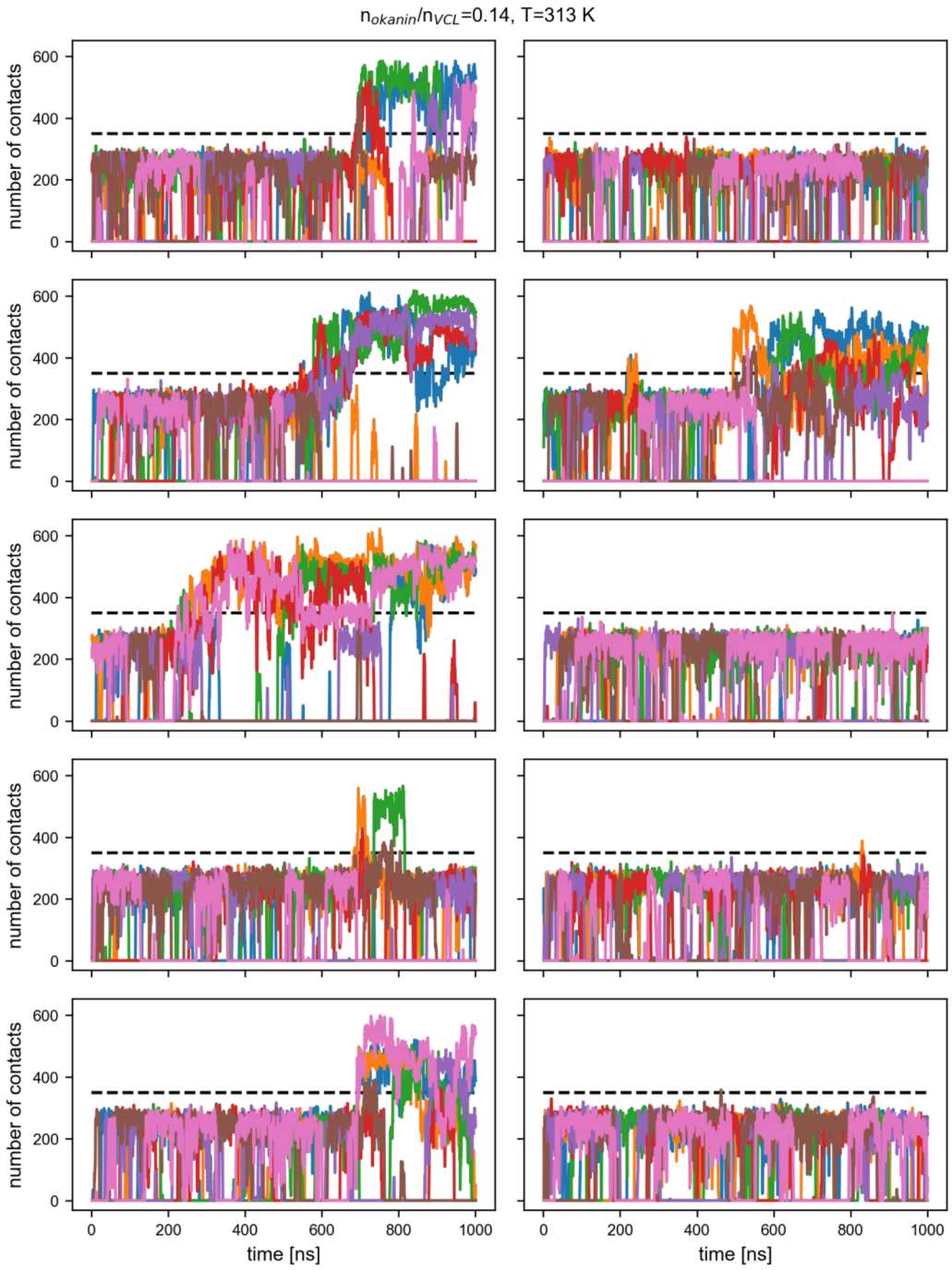

Figure S22: Number of contacts for each of the seven okanin molecules (n_{okanin}/n_{VCL} = 0.14) within each of the ten simulations of the linear pVCL at 313 K. Only trajectories with a coil-to-globule transition of the oligomer comprises okanin with more than 350 contacts (dashed line) to the pVCL.

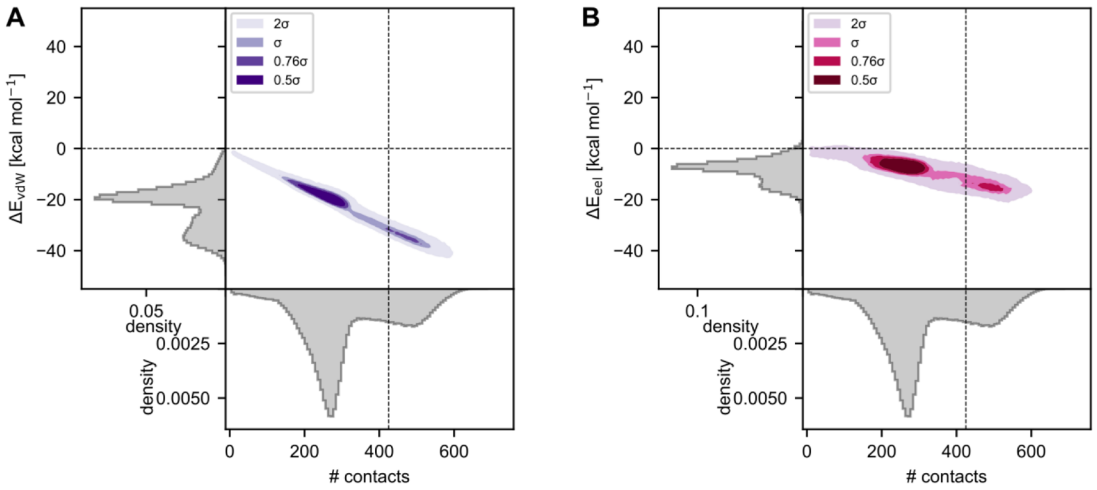

Figure S23: Two-dimensional histograms of the changes in the decomposed molecular mechanics energies (ΔE_{MM}) of okanin binding to the linear pVCL 50mer in relation to the number of formed contacts. The changes in the intermolecular energies shown here comprise changes in the van der Waals (**A**, ΔE_{vdW}) and electrostatic energies (**B**, ΔE_{eel}). Calculations were performed using MMPBSA.py[8].

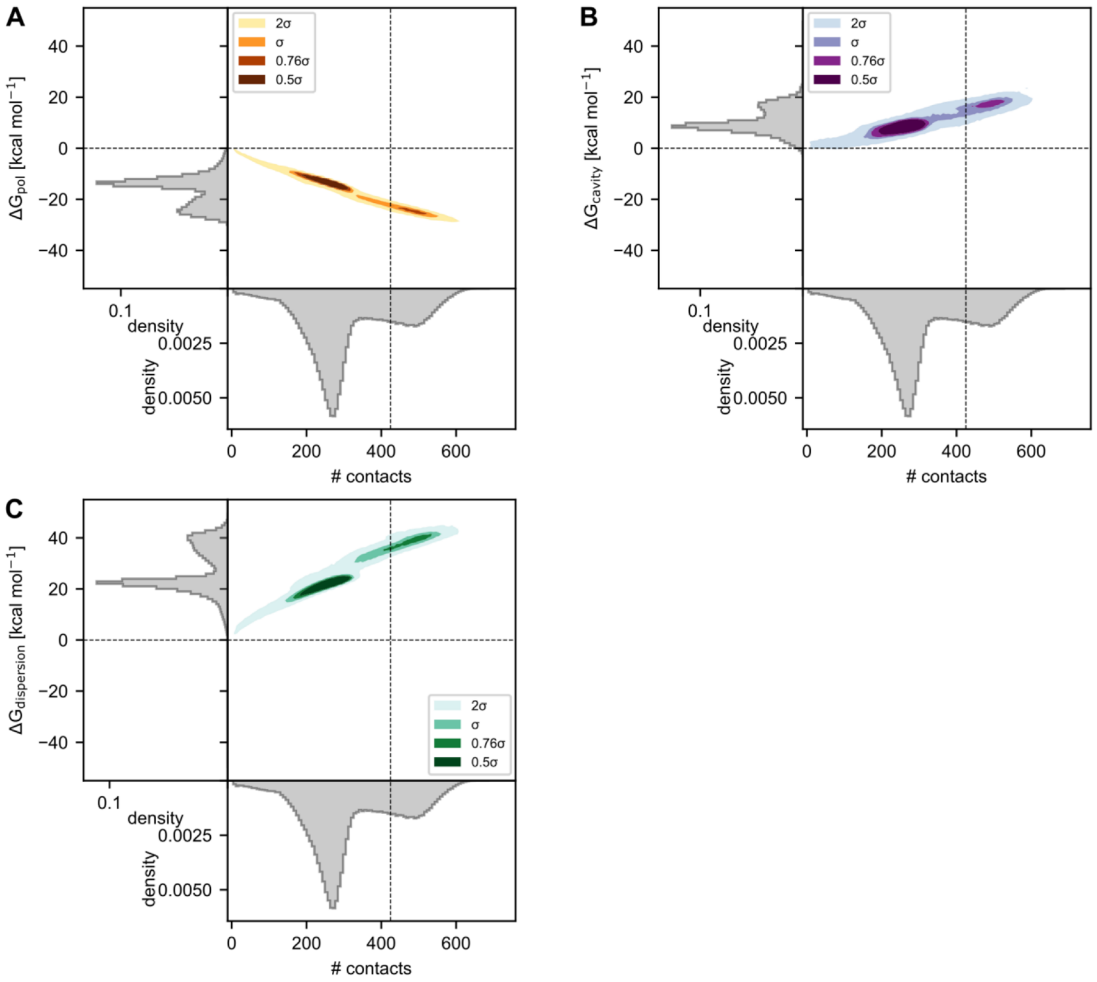

Figure S24: Two-dimensional histograms of the changes in the decomposed solvation free energy ($\Delta G_{solvation}$) of okanin to the linear pVCL 50mer in relation to the number of formed contacts. The solvation free energy is decomposed into the polar part (**A**, ΔG_{pol}), a repulsive cavitation solvation free energy term (**B**, G_{cavity}), and an attractive dispersion solvation free energy term (**C**, $G_{dispersion}$). Calculations were performed using MMPBSA.py[8].

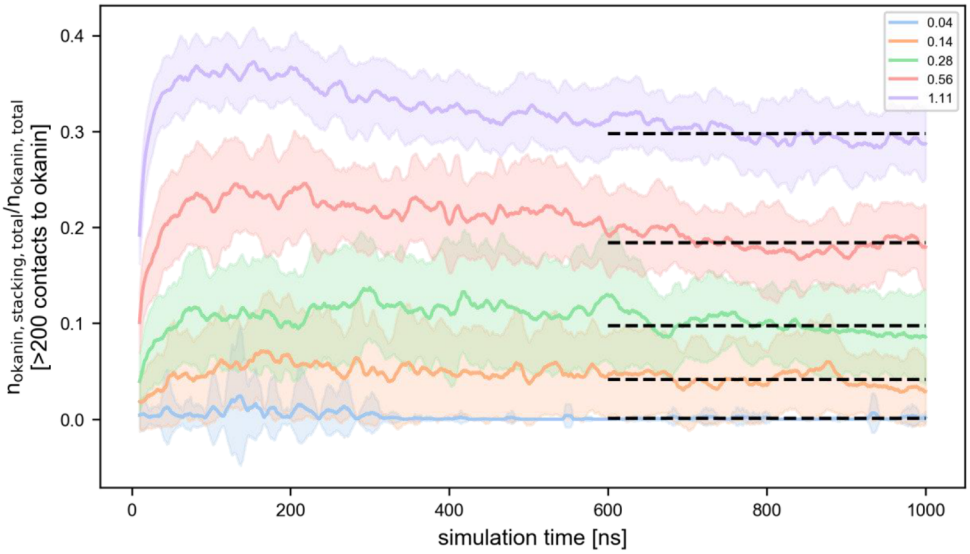

Figure S25: Fraction of stacking okanin ($n_{okanin,stacking,total}/n_{okanin,total}$) in dependence of the molar ratio of okanin and the constitutional units (0.04 - 1.11, colored according to the legend) over the simulation time of 1000 ns. The standard deviation is shown as a translucent area, the dashed lines indicate the mean for the last 400 ns of the simulations.

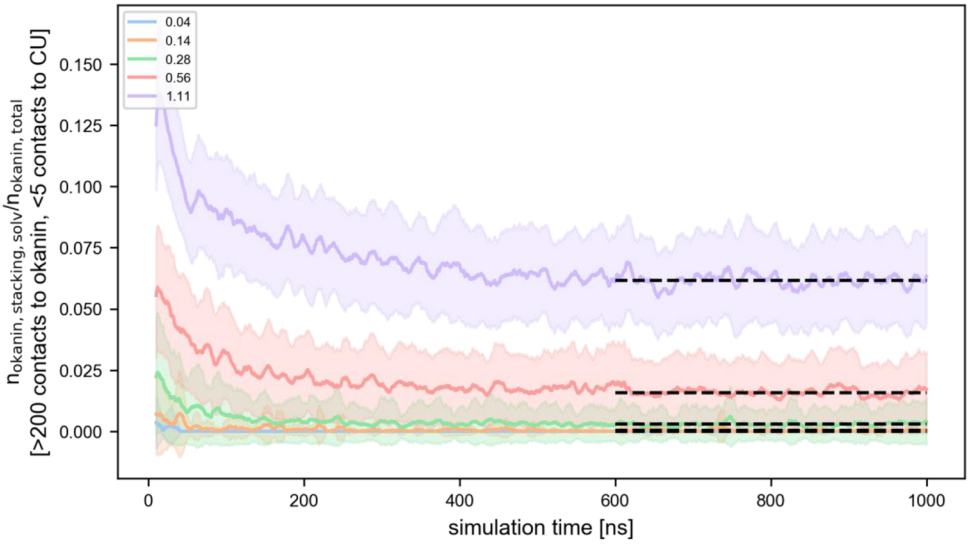

Figure S26: Fraction of stacking okanin in solutiom ($n_{okanin,stacking,solv}/n_{okanin,total}$) in dependence of the molar ratio of okanin and the constitutional units (0.04 - 1.11, colored according to the legend) over the simulation time of 1000 ns. The standard deviation is shown as a translucent area, the dashed lines indicate the mean for the last 400 ns of the simulations.

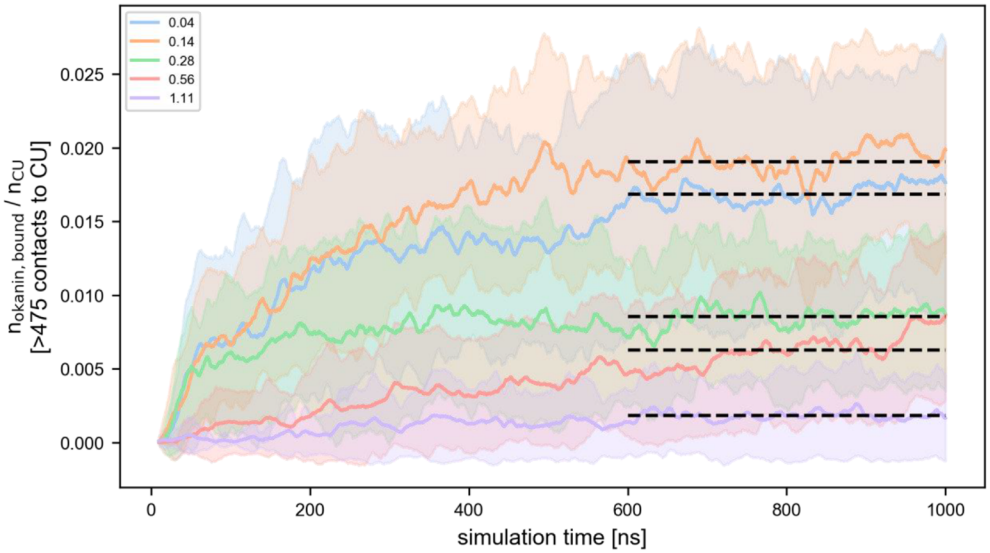

Figure S27: Relation of bound (> 475 contacts to the gel) okanin molecules ($n_{okanin,bound}$) to the number of constitutional units (n_{CU}) in dependence of the molar ratio of okanin and the constitutional units (0.04 - 1.11, colored according to the legend) over the simulation time of 1000 ns. The standard deviation is shown as a translucent area, the dashed lines indicate the mean for the last 400 ns of the simulations.

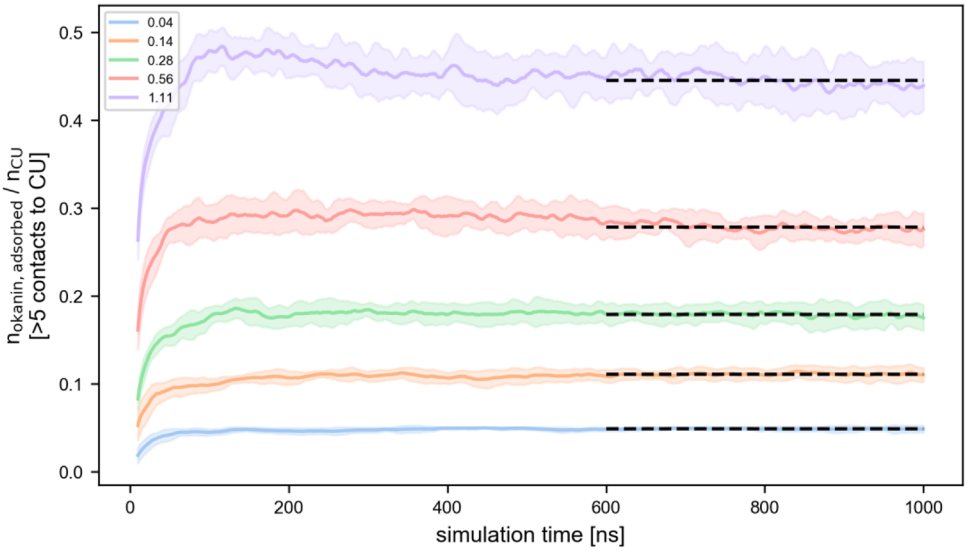

Figure S28: Relation of adsorbed (> 5 contacts to the gel) okanin molecules ($n_{okanin,adsorbed}$) to the number of constitutional units (n_{CU}) in dependence of the molar ratio of okanin and the constitutional units (0.04 - 1.11, colored according to the legend) over the simulation time of 1000 ns. The standard deviation is shown as a translucent area, the dashed lines indicate the mean for the last 400 ns of the simulations.

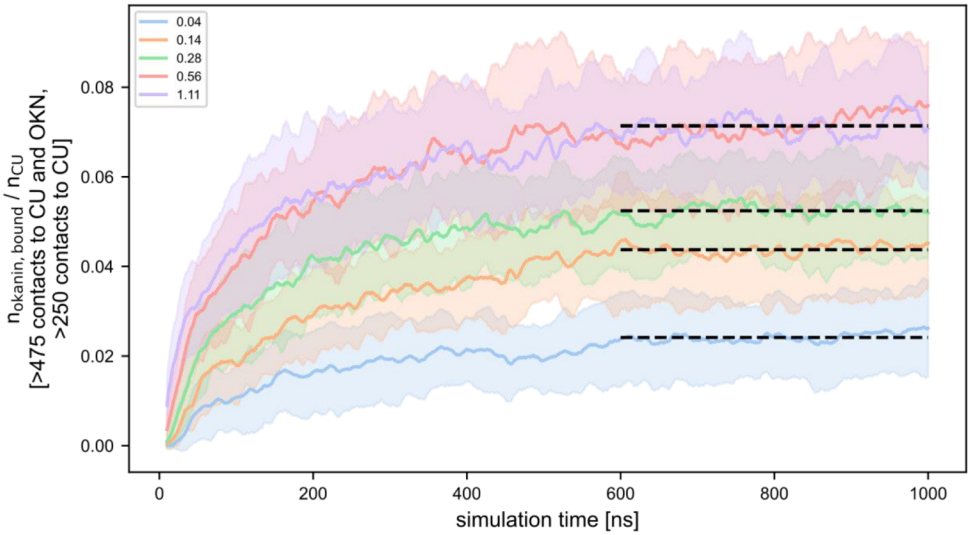

Figure S29: Relation of bound and stacked (> 475 contacts to the gel and > 250 contacts to the gel) okanin molecules ($n_{okanin,bound}$) to the number of constitutional units (n_{CU}) in dependence of the molar ratio of okanin and the constitutional units (0.04 - 1.11, colored according to the legend) over the simulation time of 1000 ns. The standard deviation is shown as a translucent area, the dashed lines indicate the mean for the last 400 ns of the simulations.

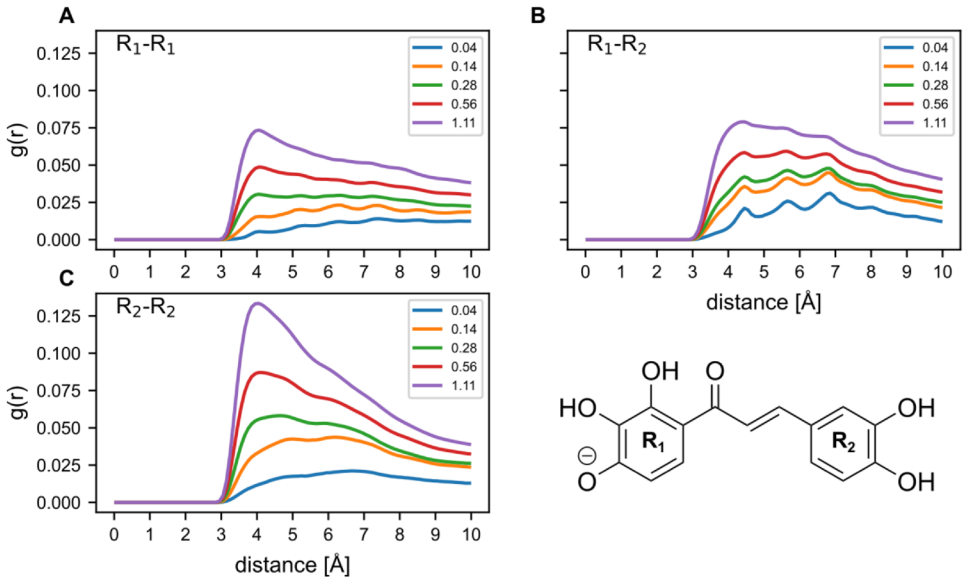

Figure S30: Radial distribution functions ($g(r)$) for the two aromatic rings (R1, R2) of okanin for different okanin concentrations. For okanin / pVCL ratios above 0.28, an increase in $g(r)$ around 4 Å is indicative of increased stacking interactions of okanin.

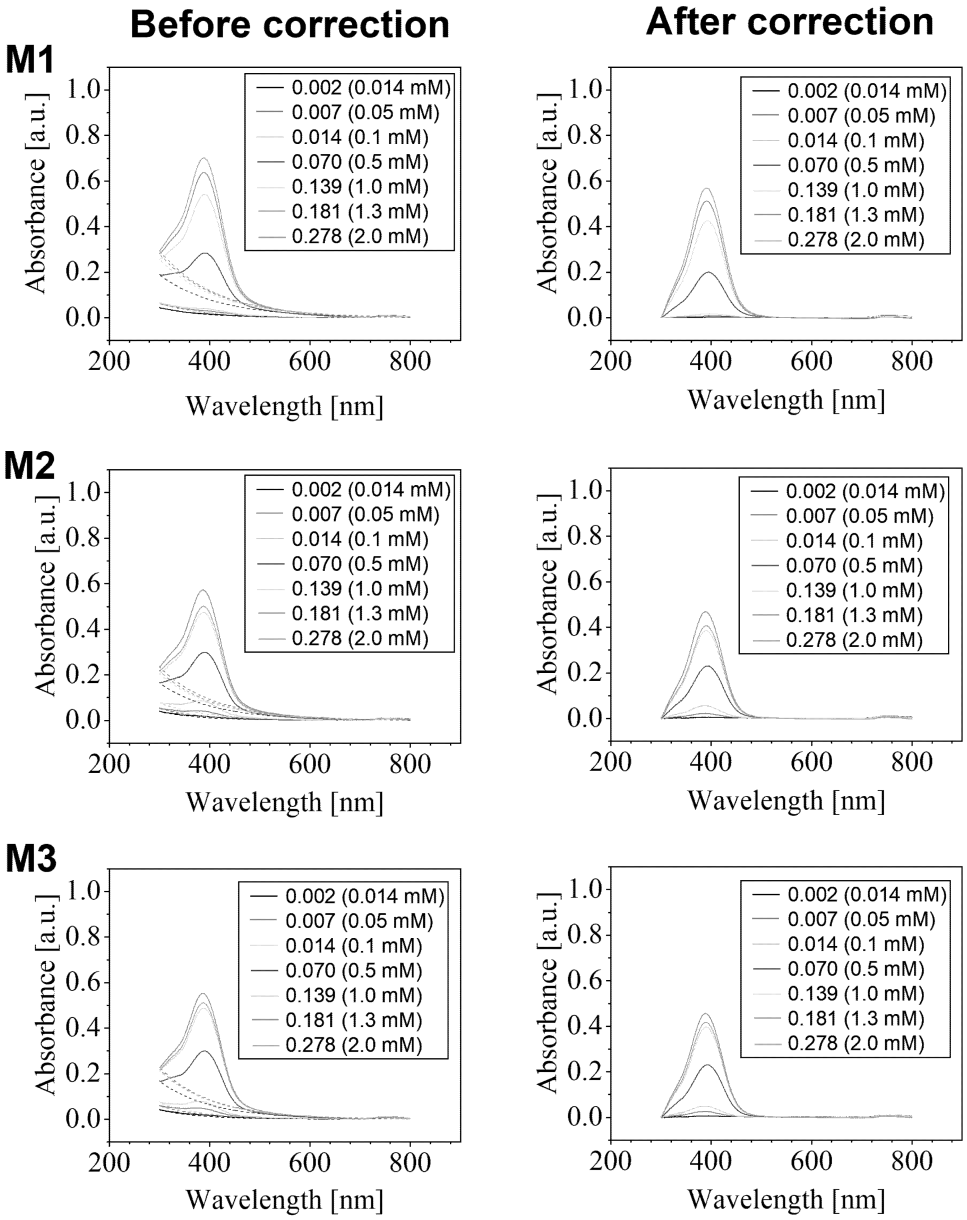

Figure S31: UV/Vis spectra of a p(VCL/GMA$_{core}$) microgel loaded with different molar ratios of okanin to repeating units (n_{okanin}/n_{CU}) before and after exponential baseline-correction. The measurements were repeated thrice (M1, M2 and M3).

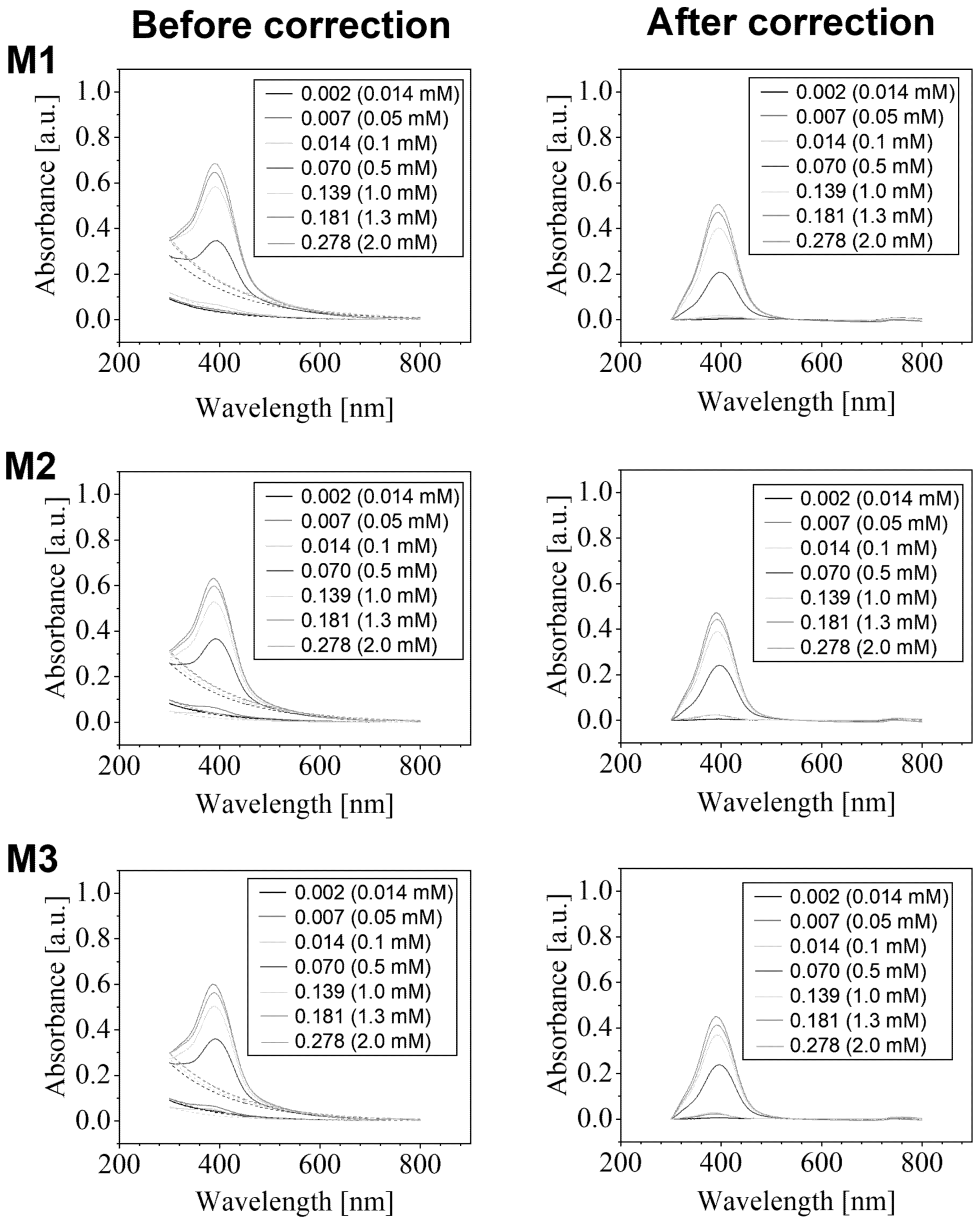

Figure S32: UV/Vis spectra of a p(VCL/GMA$_{shell}$) microgel loaded with different molar ratios of okanin to repeating units (n_{okanin}/n_{CU}) before and after exponential baseline-correction. The measurements were repeated thrice (M1, M2 and M3).

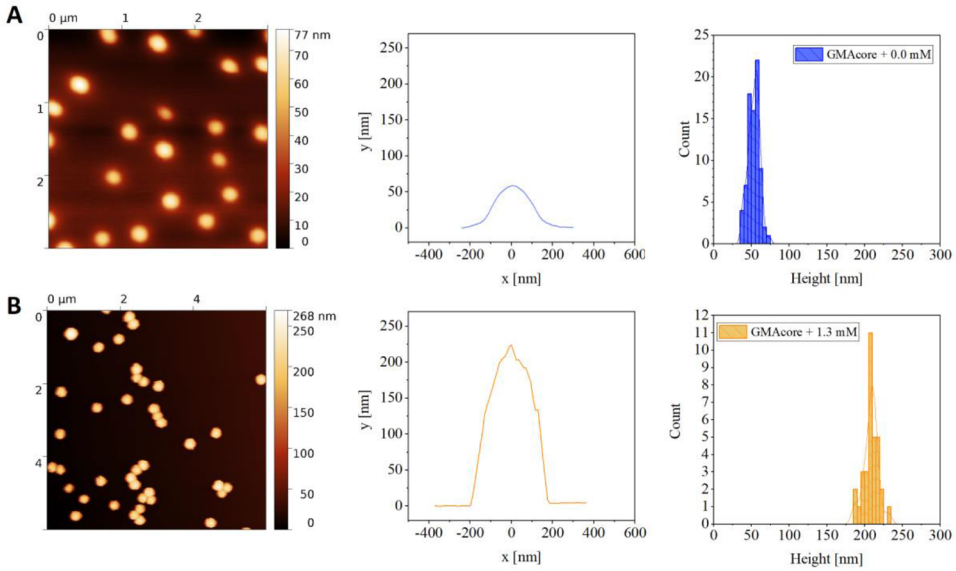

Figure S33: Exemplary AFM images, height profiles and histograms of a p(VCL/GMA$_{core}$) microgel **A** without okanin loading and **B** loaded at a molar ratio of 0.181. The collapse of the microgels upon binding of okanin leads to a rigidification of the microgel. As a result, the microgel's height increases.

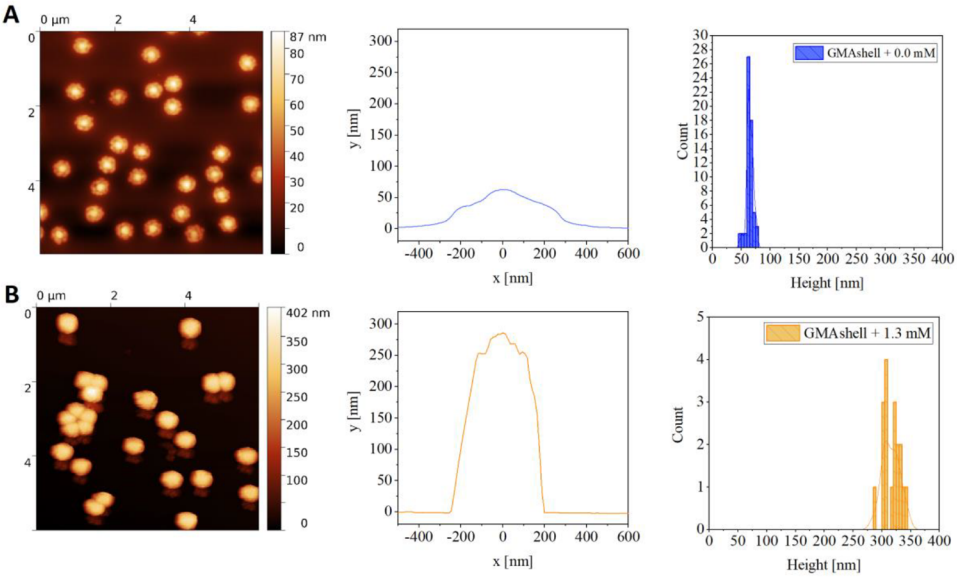

Figure S34: Exemplary AFM images, height profiles and histograms of a p(VCL/GMA$_{shell}$) microgel **A** without okanin loading and **B** loaded at a molar ratio of 0.181. The collapse of the microgels upon binding of okanin leads to a rigidification of the microgel. As a result, the microgel's height increases.

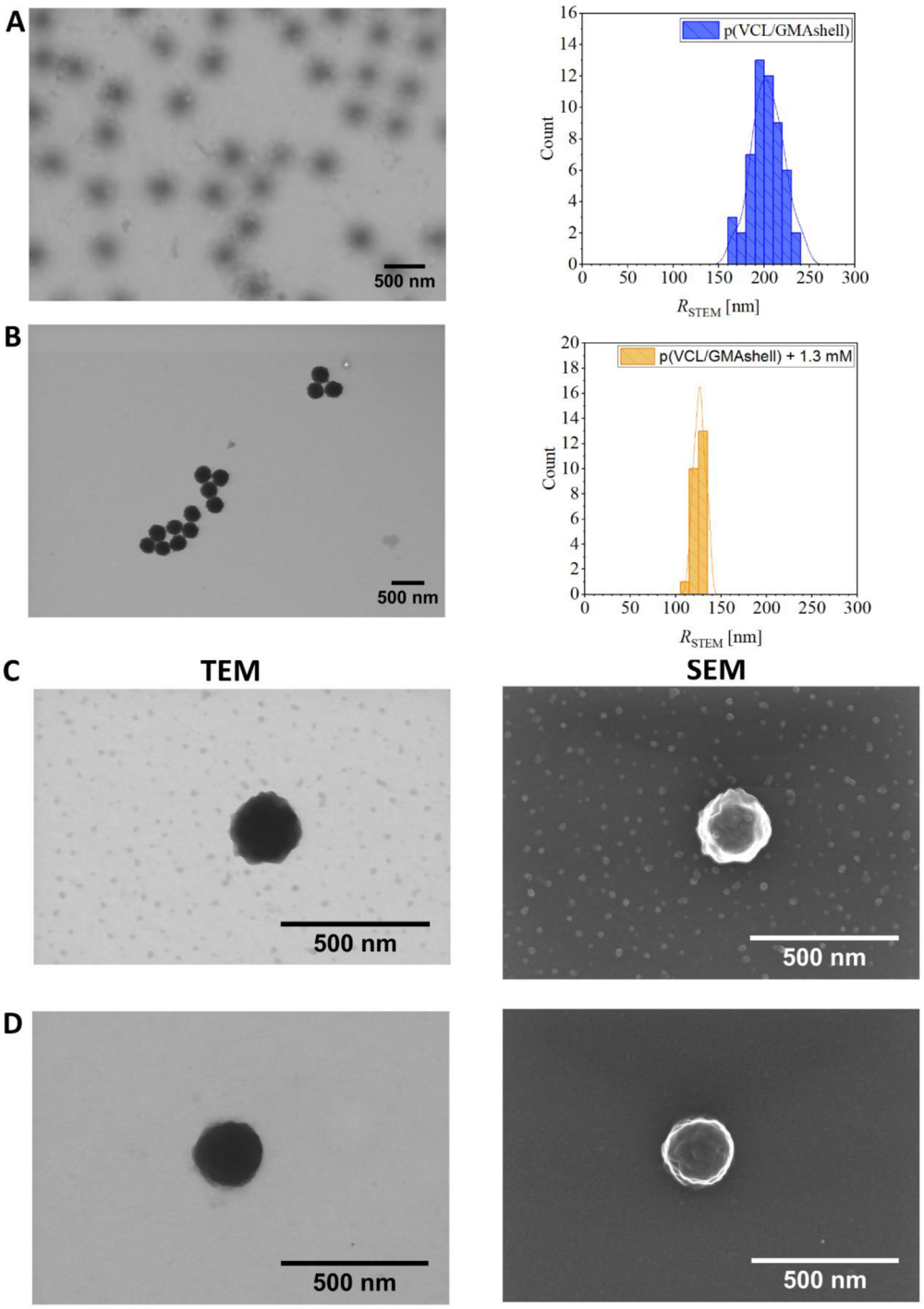

Figure S35: STEM images of a p(VCL/GMA$_{shell}$) microgel **A** without okanin (R_{STEM} = 203 ± 18 nm) and **B** loaded with n_{okanin}/n_{CU} = 0.18 (R_{STEM} = 126 ± 7 nm). High-resolution images of the loaded microgel **C** before purification and **D** after purification.

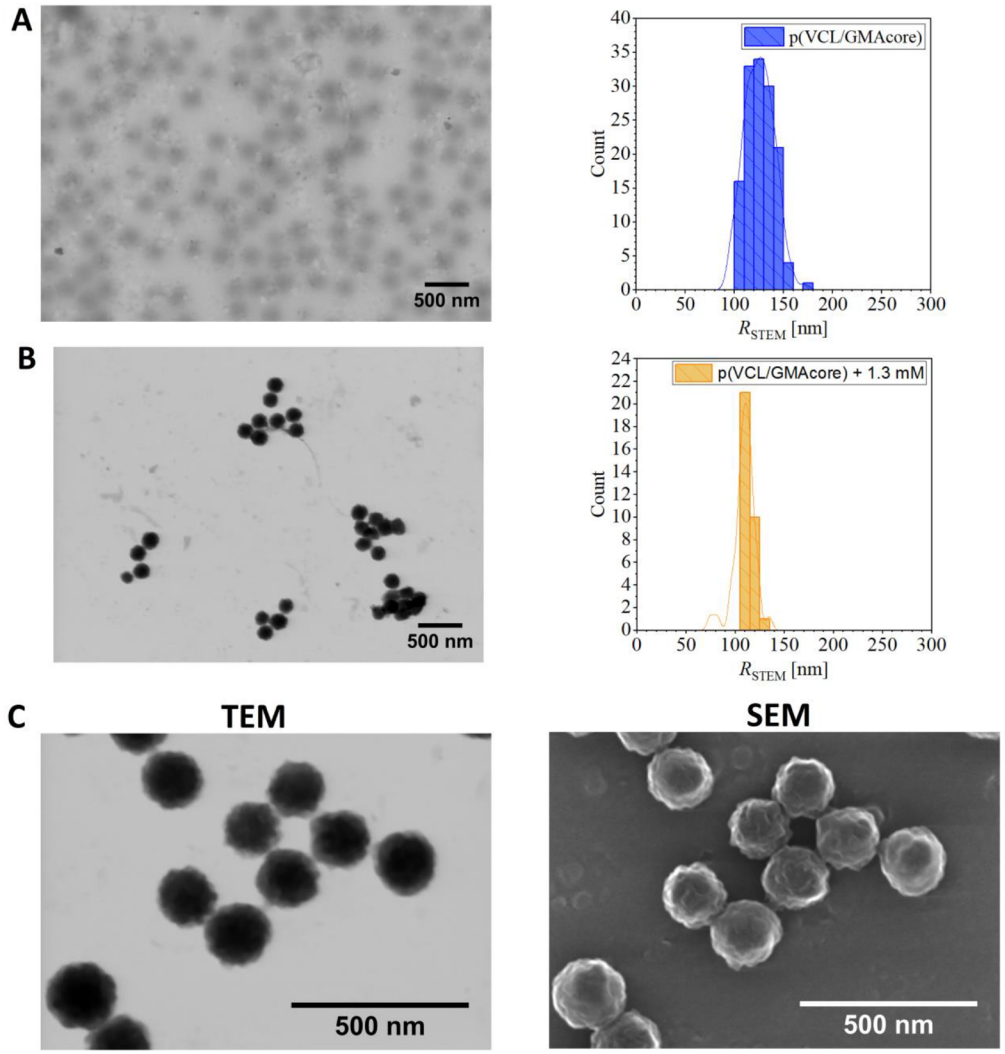

Figure S36: STEM images of a p(VCL/GMA_{core}) microgel **A** without okanin (R_{STEM} = 125 ± 15 nm) and **B** loaded with n_{okanin}/n_{CU} = 0.18 (R_{STEM} = 109 ± 11 nm). **C** High-resolution images of the loaded microgel after purification.

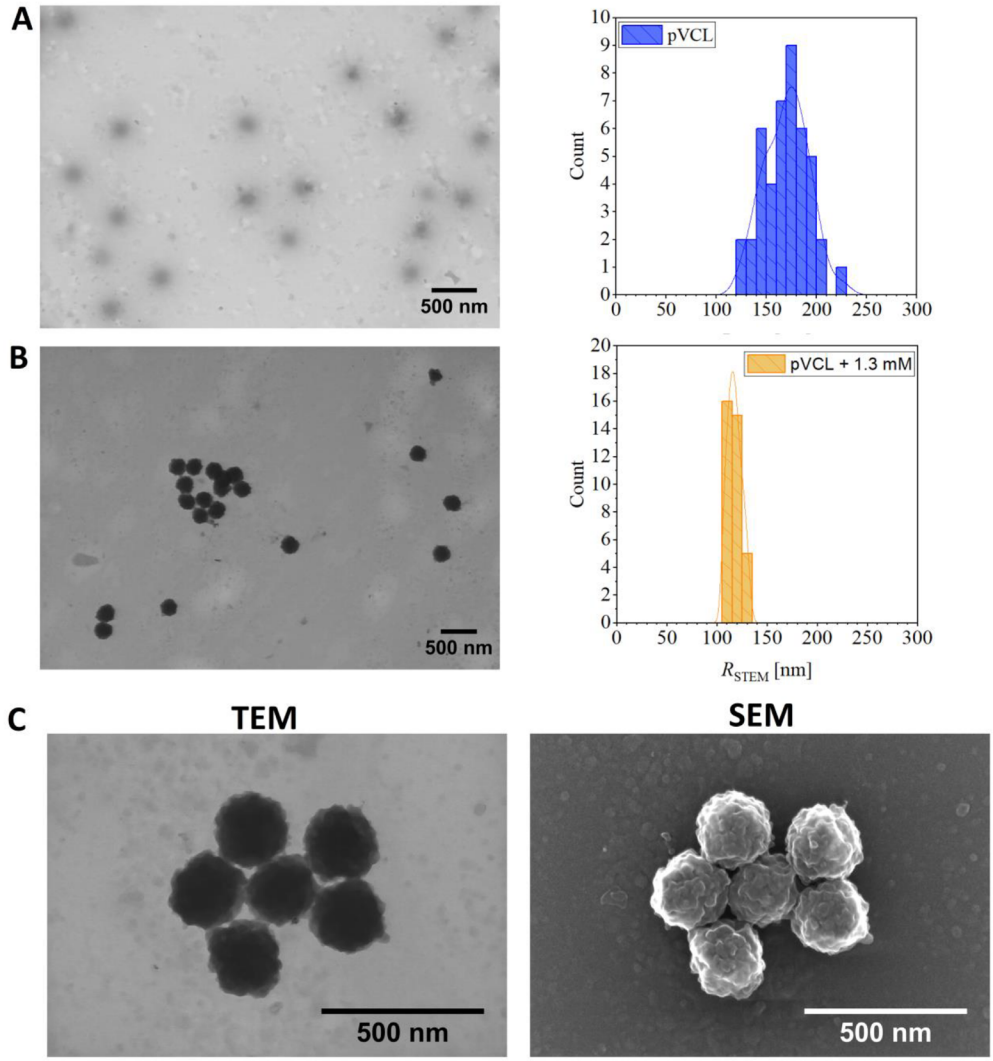

Figure S37: STEM images of a pVCL microgel **A** without okanin (R_{STEM} = 170 ± 22 nm) and **B** loaded with n_{okanin}/n_{CU} = 0.18 (R_{STEM} = 117 ± 7 nm). **C** High-resolution images of the loaded microgel after purification.

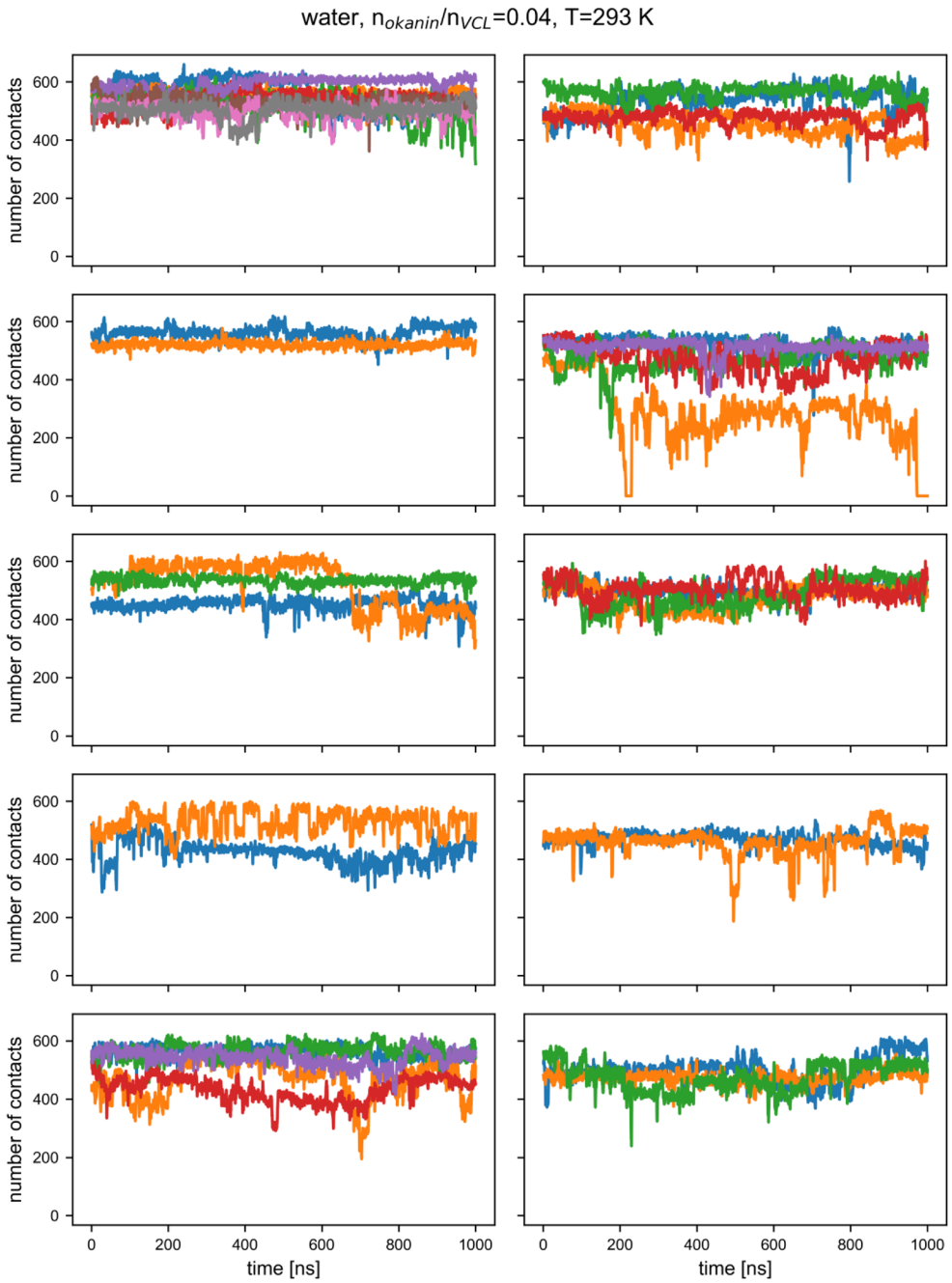

Figure S38: Contacts of okanin molecules during the release simulation (n_{okanin}/n_{VCL} = 0.04 during okanin loading simulation) in water at 293 K. Only okanin molecules with more than 475 contacts at the first frame are tracked for release. Every okanin molecule not at least adsorbed, i.e., shows >5 contacts, for 98.9% of the time, is considered released.

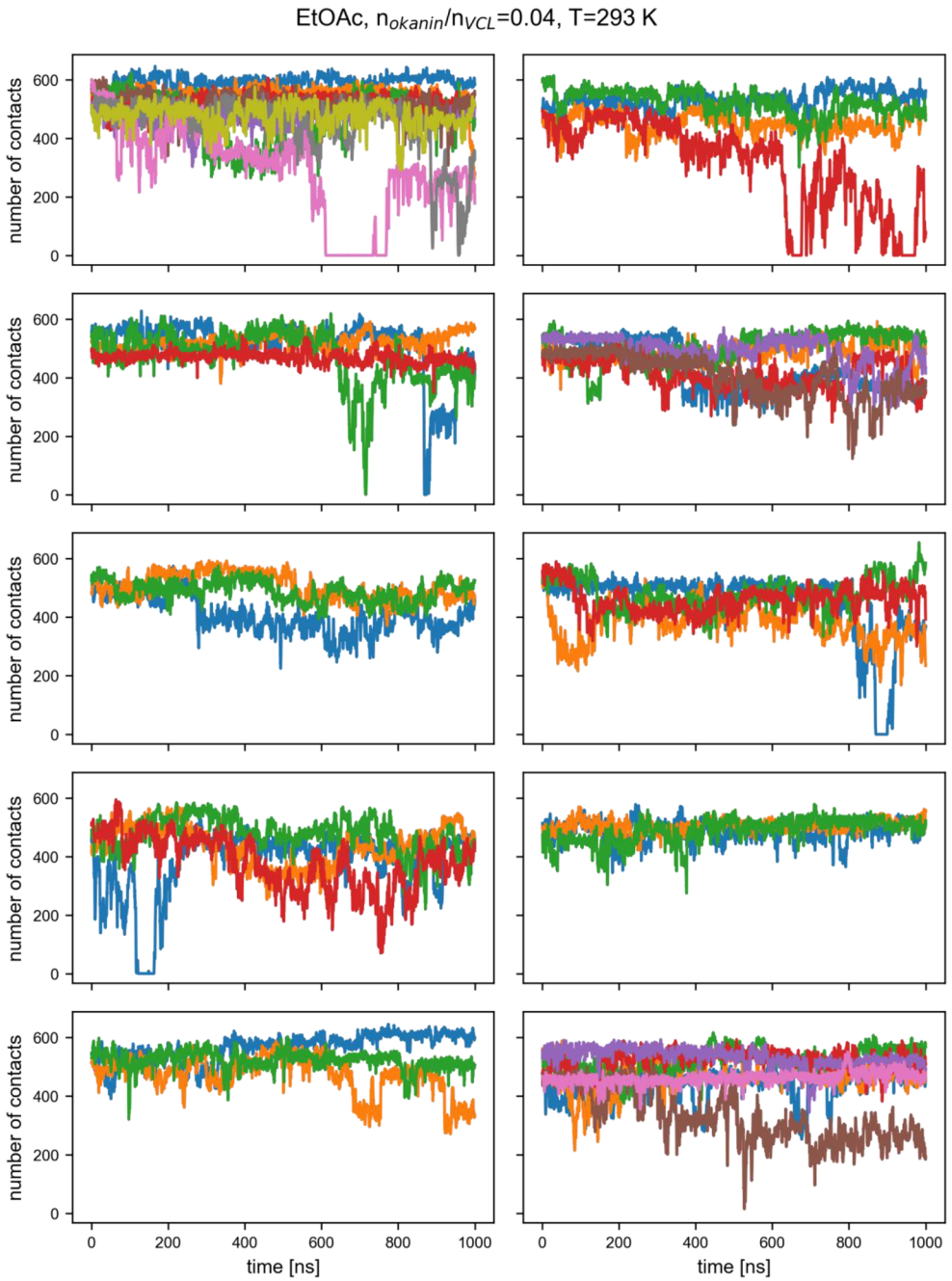

Figure S39: Contacts of okanin molecules during the release simulation (n_{okanin}/n_{VCL} = 0.04 during okanin loading simulation) in a saturated water ethylacetat (EtOAc) solution at 293 K. Only okanin molecules with more than 475 contacts at the first frame are tracked for release. Every okanin molecule not at least adsorbed, i.e., shows >5 contacts, for 98.9% of the time, is considered released.

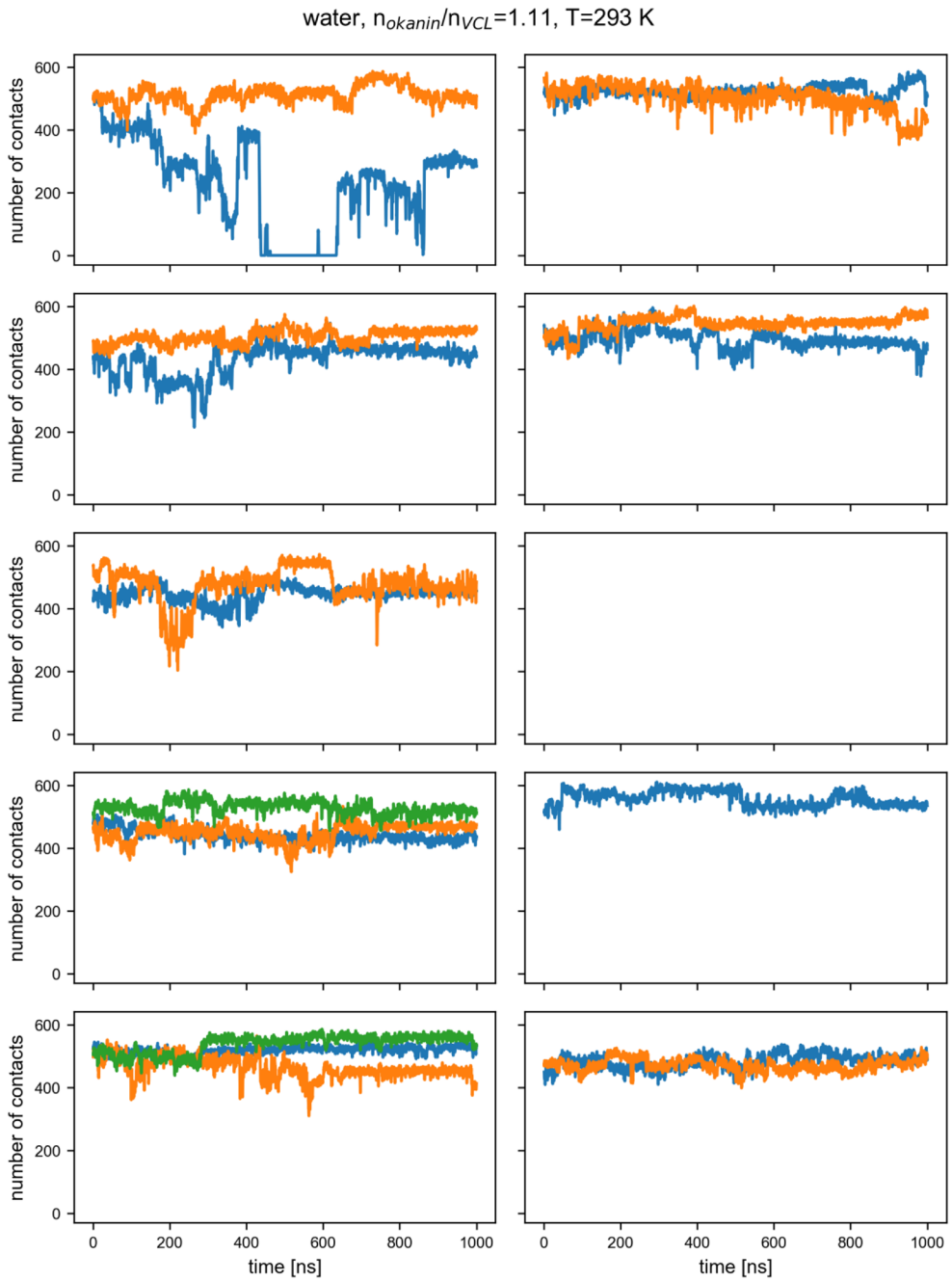

Figure S40: Contacts of okanin molecules during the release simulation (n_{okanin}/n_{VCL} = 1.14 during okanin loading simulation) in water at 293 K. Only okanin molecules with more than 475 contacts at the first frame are tracked for release. Every okanin molecule not at least adsorbed, i.e., shows >5 contacts, for 98.9% of the time, is considered released.

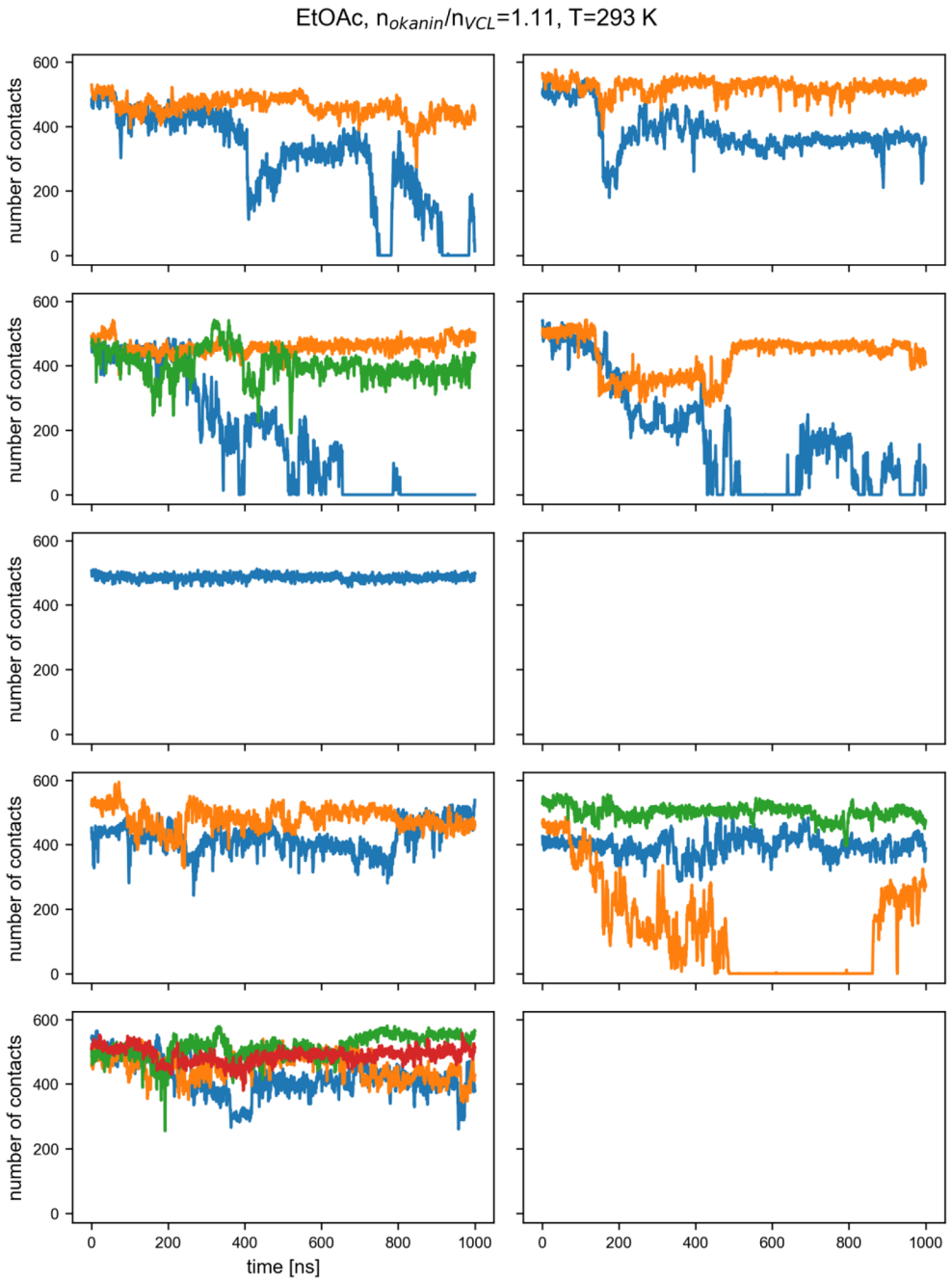

Figure S41: Contacts of okanin molecules during the release simulation (n_{okanin}/n_{VCL} = 1.14 during okanin loading simulation) in a saturated water ethylacetat (EtOAc) solution at 293 K. Only okanin molecules with more than 475 contacts at the first frame are tracked for release. Every okanin molecule not at least adsorbed, i.e., shows >5 contacts, for 98.9% of the time, is considered released.

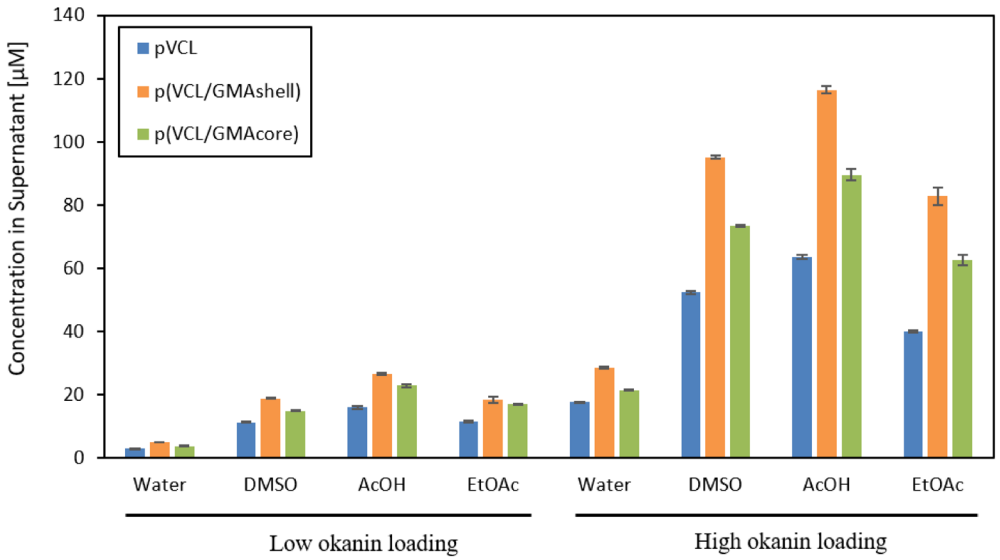

Figure S42: Concentration of okanin in the supernatant after co-solvent-triggered release from pVCL-based microgels (1.0 mg/mL) for different co-solvents (10 %(*m*/*m*) DMSO, 10 %(*m*/*m*) AcOH, and 9.4 %(*m*/*m*) EtOAc) for low (n_{okanin}/n_{CU} = 0.07) and high (n_{okanin}/n_{CU} = 0.18) okanin concentrations at loading. The initial loadings were 31.1 µg/mg and 73.0 µg/mg for pVCL, 65.7 µg/mg and 146.0 µg/mg for p(VCL/GMA_{core}) and 72.3 µg/mg and 144.2 µg/mg for p(VCL/GMA_{shell}).

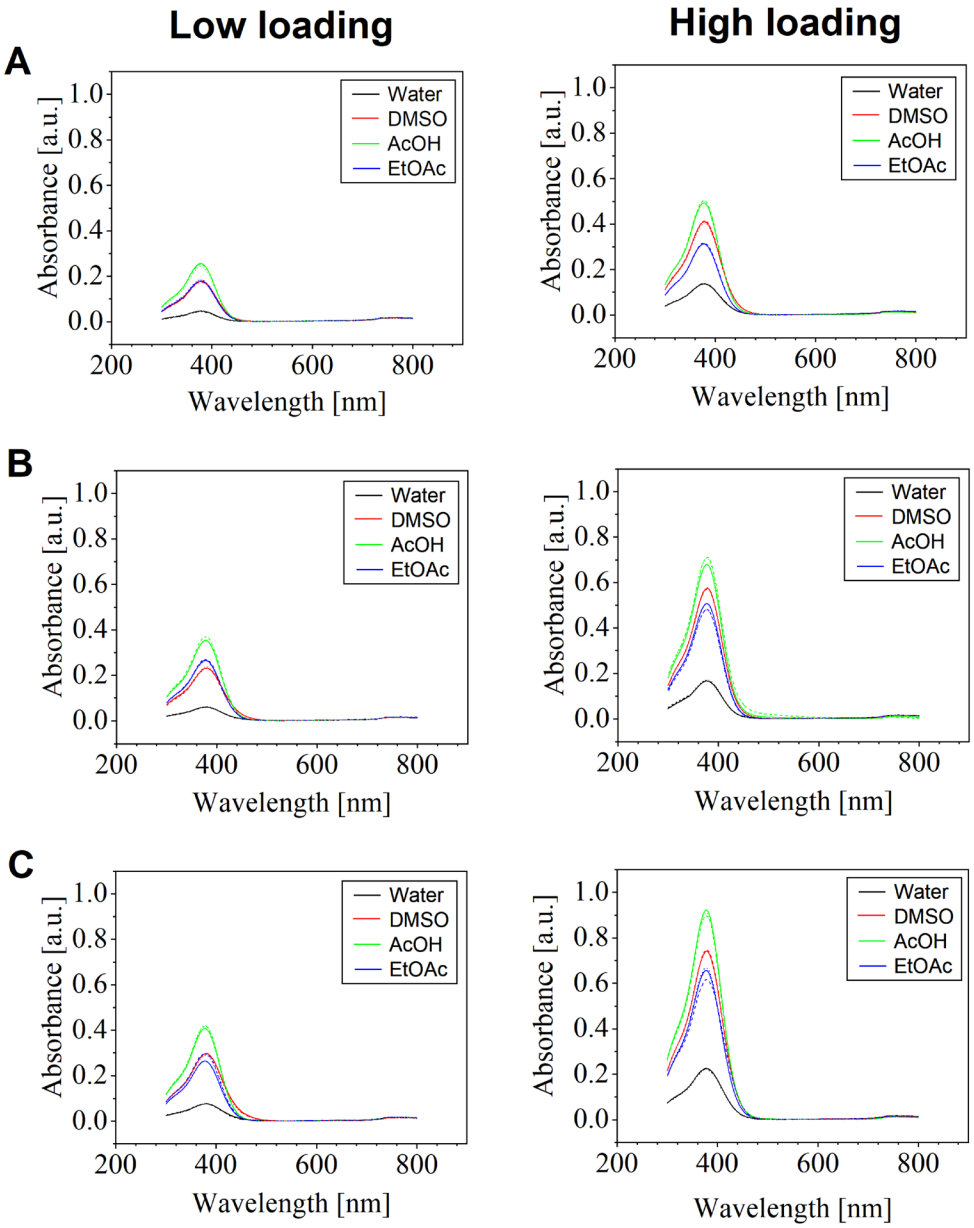

Figure S43: UV/Vis spectra of the supernatant after the release of okanin from pVCL-based microgels (**A** pVCL, **B** p(VCL/GMA$_{core}$), and **C** p(VCL/GMA$_{shell}$)). The microgels were previously loaded at a molar ratio n_{okanin}/n_{CU} of 0.070 (low loading) and 0.181 (high loading). The initial loadings were 31.1 µg/mg and 73.0 µg/mg for pVCL, 65.7 µg/mg and 146.0 µg/mg for p(VCL/GMA$_{core}$) and 72.3 µg/mg and 144.2 µg/mg for p(VCL/GMA$_{shell}$). The measurements were repeated thrice (M1: line, M2: dashed, and M3: dotted). The dilution were 1:1 and 1:3 for low and high loadings, respectively.

4 Supplemental References

1. Häntzschel, N.; Zhang, F.; Eckert, F.; Pich, A.; Winnik, M. A., Poly(N-vinylcaprolactam-co-glycidyl methacrylate) Aqueous Microgels Labeled with Fluorescent LaF3:Eu Nanoparticles. *Langmuir* **2007,** *23* (21), 10793-10800.
2. Häntzschel, N.; Hund, R.-D.; Hund, H.; Schrinner, M.; Lück, C.; Pich, A., Hybrid Microgels with Antibacterial Properties. *Macromol. Biosci.* **2009,** *9* (5), 444-449.
3. Gau, E.; Mate, D. M.; Zou, Z.; Oppermann, A.; Töpel, A.; Jakob, F.; Wöll, D.; Schwaneberg, U.; Pich, A., Sortase-Mediated Surface Functionalization of Stimuli-Responsive Microgels. *Biomacromolecules* **2017,** *18* (9), 2789-2798.
4. Balaceanu, A.; Verkh, Y.; Demco, D. E.; Möller, M.; Pich, A., Correlated Morphological Changes in the Volume Temperature Transition of Core–Shell Microgels. *Macromolecules* **2013,** *46* (12), 4882-4891.
5. Jorgensen, W. L.; Chandrasekhar, J.; Madura, J. D.; Impey, R. W.; Klein, M. L., Comparison of simple potential functions for simulating liquid water. *J. Chem. Phys.* **1983,** *79* (2), 926-935.
6. Roe, D. R.; Cheatham, T. E., PTRAJ and CPPTRAJ: Software for Processing and Analysis of Molecular Dynamics Trajectory Data. *J. Chem. Theory Comput.* **2013,** *9* (7), 3084-3095.
7. Izadi, S.; Anandakrishnan, R.; Onufriev, A. V., Building Water Models: A Different Approach. *J. Phys. Chem. Lett.* **2014,** *5* (21), 3863-3871.
8. Miller, B. R.; McGee, T. D.; Swails, J. M.; Homeyer, N.; Gohlke, H.; Roitberg, A. E., MMPBSA.py: An Efficient Program for End-State Free Energy Calculations. *J. Chem. Theory Comput.* **2012,** *8* (9), 3314-3321.

11. Curriculum Vitae

Personal information

Name	Jonas Dittrich
Place of Birth	Duisburg, Germany
Date of Birth	10. August 1992

Education

2018-2023 Doctoral Studies
Heinrich Heine University Düsseldorf (HHU)
Institute for Pharmaceutical and Medicinal Chemistry
Project: "GreenRelease for Plant Health"

2016-2018 Master Studies, Hochschule Niederrhein (HSNR), Krefeld
M.Sc., Applied Chemistry, Organic Chemistry

2012-2016 Integrated Bachelor Degree Program
Henkel AG & Co. KGaA, Düsseldorf
Hochschule Niederrhein (HSNR), Krefeld
B.Sc., Chemistry and Biotechnology, Organic Chemistry

2003-2012 Gymnasium Rheinkamp Europaschule Moers
allgemeine Hochschulreife / A-levels

Experience

2018-2023 Research Associate, HHU
Computational Chemistry and Organic Chemistry

Teaching Assistant, HHU
Teaching and supervising pharmacy students within the Organic Chemistry practical course

2016-2017 Research Associate, HSNR, Polymer Chemistry

2012-2016 Henkel AG & Co. KGaA, Adhesive Technologies
Research and Development, Silicones and Sealants

2015 Leibniz Institute for Catalysis, Rostock, Metalorganic Chemistry

2014-2016 Tutor for Physical Chemistry, HSNR

Skills

Computational & Programming Skills

Molecular modeling and related software

Molecular dynamics and free energy estimations

Python scientific programming and machine learning

Generation of publication-quality figures and graphics

LINUX in HPC environments

Languages

German	Mother tongue
English	Fluent, Business and Scientific English

Advanced Training

Interdisciplinary Graduate and Research Academy (iGRAD), HHU Düsseldorf:

I Good Scientific Practice for Doctoral Researchers

II Optimizing Writing Strategies for Publishing Research in English

III Leadership Skills

IV Gentechnische Arbeiten in gentechnischen Anlagen

Publications

Peer-reviewed articles

Dittrich, J.[#], Brethauer, C.[#], Goncharenko, L., Bührmann, J., Zeisler-Diehl, V., Pariyar, S., Jakob, F., Kurkina, T., Schreiber, L., Schwaneberg, U., Gohlke, H.
"Rational design yields molecular insights on leaf binding of the anchor peptide Macaque Histatin"
ACS Applied Materials & Interfaces, **2022**, 14, 28412-28426.

Dittrich, J., Kather, M., Holzberger, A., Pich, A., Gohlke, H.
"Cumulative Submillisecond All-Atom Simulations of the Temperature-Induced Coil-to-Globule Transition of Poly(N-vinylcaprolactam) in Aqueous Solution"
Macromolecules, **2020**, 53, 9793−9810.

Dittrich, J., Schmidt, D., Pfleger, C., Gohlke, H.,
"Converging a knowledge-based scoring function: DrugScore^{2018}"
J. Chem. Inf. Model. **2019**, 59, 509-521.

Ramp, P., Pfleger, C., Dittrich, J., Mack, C., Gohlke, H., Bott, M.
"Physiological, Biochemical, and Structural Bioinformatic Analysis of the Multiple Inositol Dehydrogenases from Corynebacterium glutamicum"
Microbiol. Spectr. **2022**, 10, 5, e0195022.

Preprint

Dittrich, J.[#], Kolodzy, F.[#], Töpel, A., Pich, A., Gohlke, H.
"Loading and Co-Solvent-Triggered Release of Okanin, a C_4 Plant Key Enzyme Inhibitor, into/from Functional Microgels"
DOI: 10.26434/chemrxiv-2022-sgbx9-v2 (ChemRxiv, 13.10.2022)

Perez-Garcia, P., Chow, J., Costanzi, E., Gurschke, M.F., Dittrich, J., Dierkes, R.F., Applegate, V., Feuerriegel, G., Tete, P., Danso, D., Schumacher, J., Pfleger, C., Gohlke, H., Smits, S.H.J., Schmitz, R.A., Streit, W.R.
"The first archaeal PET-degrading enzyme belongs to the feruloyl esterase family"
DOI: 10.1101/2022.10.14.512230 (BioRxiv, 2022)

[#]these authors contributed equally.

Poster Presentations

Jonas Dittrich, Christopher Pfleger, Holger Gohlke
"Deorphanizing the Uncharted Esterome Space"
NIC-Symposium 2022, Jülich, Germany, September 29th-30th, 2022.

Jonas Dittrich, Shyam Pariyar, Felix Jakob, Ulrich Schwaneberg, Andrij Pich, Holger Gohlke
"Supporting a novel plant protection technology by molecular dynamics simulations"
SciMeetings, ACS Fall 2020 Virtual Meeting, USA, August 17, 2020
DOI: 10.1021/scimeetings.0c06684

Jonas Dittrich, Holger Gohlke
"Investigating the thermo-responsiveness of poly(N-vinylcaprolactam) oligomers and microgels using all-atom molecular dynamics simulations"
NIC-Symposium 2020, Jülich, Germany, February 27th-28th, 2020.

Liudmyla Goncharenko, Alexander Töpel, Tim Sassmann, Xu Wenjing, Jonas Dittrich, Raphael Soeur, Larissa Hussmann, Patrick Schwinges, Caspar Langenbach, Michael Wustmans, Shyam Pariyar, Janina Zierul, Alexander Hofmann, Henning Lenz, Fabio Fiorani, Andrij Pich, Uwe Conrath, Stefanie Bröring, Georg Noga, Claudia Knief, Georg Groth, Holger Gohlke, Ulrich Schurr, Ulrich Schwaneberg, Felix Jakob,
"*GreenRelease: Technology advancement*" ["best poster" award],
4th International BioSC Symposium, Cologne, Germany, November 12th-13th, 2019.

Jonas Dittrich, Felix Jakob, Ulrich Schwaneberg, Andrij Pich, Holger Gohlke,
"All-atom molecular simulations on formation and characteristics of microgels",
3rd International BioSC Symposium, Bonn, Germany, November 18th -19th, 2018.

Jonas Dittrich, Denis Schmidt, Christopher Pfleger, Holger Gohlke,
"Converging a knowledge-based scoring function: DrugScore^{2017}",
32nd Molecular Modeling Workshop, Erlangen, Germany, March 12th-14th, 2018.

12. Bibliography

(1) United Nations, Department of Economic and Social Affairs, Population Division (2019). Probabilistic Population Projections Rev. 1 based on the World Population Prospects 2019 Rev. 1. http://population.un.org/wpp/ (accessed 16.07.2021).

(2) Hunter, M. C.; Smith, R. G.; Schipanski, M. E.; Atwood, L. W.; Mortensen, D. A., Agriculture in 2050: Recalibrating Targets for Sustainable Intensification. *Bioscience* **2017,** *67* (4), 386-391.

(3) Hasegawa, T.; Havlík, P.; Frank, S.; Palazzo, A.; Valin, H., Tackling food consumption inequality to fight hunger without pressuring the environment. *Nat. Sustain.* **2019,** *2* (9), 826-833.

(4) McKenzie, F. C.; Williams, J., Sustainable food production: constraints, challenges and choices by 2050. *Food Secur.* **2015,** *7* (2), 221-233.

(5) Döös, B. R., Population growth and loss of arable land. *Glob. Environ. Change* **2002,** *12* (4), 303-311.

(6) Oerke, E. C., Crop losses to pests. *J. Agric. Sci.* **2006,** *144* (1), 31-43.

(7) Pimentel, D.; Acquay, H.; Biltonen, M.; Rice, P.; Silva, M.; Nelson, J.; Lipner, V.; Giordano, S.; Horowitz, A.; D'Amore, M., Environmental and Economic Costs of Pesticide Use. *Bioscience* **1992,** *42* (10), 750-760.

(8) Busi, R.; Goggin, D. E.; Heap, I. M.; Horak, M. J.; Jugulam, M.; Masters, R. A.; Napier, R. M.; Riar, D. S.; Satchivi, N. M.; Torra, J.; Westra, P.; Wright, T. R., Weed resistance to synthetic auxin herbicides. *Pest Manage. Sci.* **2018,** *74* (10), 2265-2276.

(9) Petroski, R. J.; Stanley, D. W., Natural Compounds for Pest and Weed Control. *J. Agric. Food Chem.* **2009,** *57* (18), 8171-8179.

(10) Nguyen, G. T. T.; Erlenkamp, G.; Jäck, O.; Küberl, A.; Bott, M.; Fiorani, F.; Gohlke, H.; Groth, G., Chalcone-based Selective Inhibitors of a C4 Plant Key Enzyme as Novel Potential Herbicides. *Sci. Rep.* **2016,** *6* (1), 27333.

(11) Flamini, G., Chapter 13 - Natural Herbicides as a Safer and More Environmentally Friendly Approach to Weed Control: A Review of the Literature Since 2000. In *Stud. Nat. Prod. Chem.*, Atta ur, R., Ed. Elsevier: 2012; Vol. 38, pp 353-396.

(12) Dayan, F. E.; Cantrell, C. L.; Duke, S. O., Natural products in crop protection. *Biorg. Med. Chem.* **2009,** *17* (12), 4022-4034.

(13) Hedin, P. A., Use of Natural Products in Pest Control. In *Naturally Occurring Pest Bioregulators*, American Chemical Society: 1991; Vol. 449, pp 1-11.

(14) López, Ó.; Fernández-Bolaños, J. G.; Gil, M. V., New trends in pest control: the search for greener insecticides. *Green Chem.* **2005,** *7* (6), 431-442.

(15) Srivastav, A. L., Chapter 6 - Chemical fertilizers and pesticides: role in groundwater contamination. In *Agrochemicals Detection, Treatment and Remediation*, Prasad, M. N. V., Ed. Butterworth-Heinemann: 2020; pp 143-159.

(16) Arias-Estévez, M.; López-Periago, E.; Martínez-Carballo, E.; Simal-Gándara, J.; Mejuto, J.-C.; García-Río, L., The mobility and degradation of pesticides in soils and the pollution of groundwater resources. *Agric. Ecosyst. Environ.* **2008,** *123* (4), 247-260.

(17) Hallberg, G. R., The Impacts of Agricultural Chemicals on Ground Water Quality. *GeoJournal* **1987,** *15* (3), 283-295.

(18) Schweizer, E. E., New Technological Developments to Reduce Groundwater Contamination by Herbicides. *Weed Technol.* **1988,** *2* (2), 223-227.

(19) Singh, H.; Sharma, A.; Bhardwaj, S. K.; Arya, S. K.; Bhardwaj, N.; Khatri, M., Recent advances in the applications of nano-agrochemicals for sustainable agricultural development. *Environmental Science: Processes & Impacts* **2021,** *23* (2), 213-239.

(20) Prasad, R.; Bhattacharyya, A.; Nguyen, Q. D., Nanotechnology in Sustainable Agriculture: Recent Developments, Challenges, and Perspectives. *Front. Microbiol.* **2017,** *8* (1014).

(21) Zulfiqar, F.; Navarro, M.; Ashraf, M.; Akram, N. A.; Munné-Bosch, S., Nanofertilizer use for sustainable agriculture: Advantages and limitations. *Plant Sci.* **2019,** *289*, 110270.

(22) Raliya, R.; Saharan, V.; Dimkpa, C.; Biswas, P., Nanofertilizer for Precision and Sustainable Agriculture: Current State and Future Perspectives. *J. Agric. Food Chem.* **2018,** *66* (26), 6487-6503.

(23) Kavetsou, E.; Koutsoukos, S.; Daferera, D.; Polissiou, M. G.; Karagiannis, D.; Perdikis, D. C.; Detsi, A., Encapsulation of Mentha pulegium Essential Oil in Yeast Cell Microcarriers: An Approach to Environmentally Friendly Pesticides. *J. Agric. Food Chem.* **2019,** *67* (17), 4746-4753.

(24) Meurer, R. A.; Kemper, S.; Knopp, S.; Eichert, T.; Jakob, F.; Goldbach, H. E.; Schwaneberg, U.; Pich, A., Biofunctional Microgel-Based Fertilizers for Controlled Foliar Delivery of Nutrients to Plants. *Angew. Chem. Int. Ed.* **2017,** *56* (26), 7380-7386.

(25) Pich, A.; Richtering, W., Microgels by Precipitation Polymerization: Synthesis, Characterization, and Functionalization. In *Chemical Design of Responsive Microgels*, Pich, A.; Richtering, W., Eds. Springer Berlin Heidelberg: Berlin, Heidelberg, 2011; pp 1-37.

(26) Büscher, N.; Sayoga, G. V.; Rübsam, K.; Jakob, F.; Schwaneberg, U.; Kara, S.; Liese, A., Biocatalyst Immobilization by Anchor Peptides on an Additively Manufacturable Material. *Org. Process Res. Dev.* **2019,** *23* (9), 1852-1859.

(27) Grimm, A. R.; Sauer, D. F.; Mirzaei Garakani, T.; Rübsam, K.; Polen, T.; Davari, M. D.; Jakob, F.; Schiffels, J.; Okuda, J.; Schwaneberg, U., Anchor Peptide-Mediated Surface Immobilization of a Grubbs-Hoveyda-Type Catalyst for Ring-Opening Metathesis Polymerization. *Bioconj. Chem.* **2019,** *30* (3), 714-720.

(28) Rübsam, K.; Weber, L.; Jakob, F.; Schwaneberg, U., Directed evolution of polypropylene and polystyrene binding peptides. *Biotechnol. Bioeng.* **2018,** *115* (2), 321-330.

(29) Rübsam, K.; Stomps, B.; Böker, A.; Jakob, F.; Schwaneberg, U., Anchor peptides: A green and versatile method for polypropylene functionalization. *Polymer* **2017,** *116*, 124-132.

(30) Gau, E.; Mate, D. M.; Zou, Z.; Oppermann, A.; Töpel, A.; Jakob, F.; Wöll, D.; Schwaneberg, U.; Pich, A., Sortase-Mediated Surface Functionalization of Stimuli-Responsive Microgels. *Biomacromolecules* **2017,** *18* (9), 2789-2798.

(31) Prabaharan, M.; Grailer, J. J.; Steeber, D. A.; Gong, S., Stimuli-Responsive Chitosan-graft-Poly(N-vinylcaprolactam) as a Promising Material for Controlled Hydrophobic Drug Delivery. *Macromol. Biosci.* **2008,** *8* (9), 843-851.

(32) Liu, J.; Detrembleur, C.; Hurtgen, M.; Debuigne, A.; De Pauw-Gillet, M.-C.; Mornet, S.; Duguet, E.; Jérôme, C., Reversibly crosslinked thermo- and redox-responsive nanogels for controlled drug release. *Polym. Chem.* **2014,** *5* (1), 77-88.

(33) Halligan, S. C.; Dalton, M. B.; Murray, K. A.; Dong, Y.; Wang, W.; Lyons, J. G.; Geever, L. M., Synthesis, characterisation and phase transition behaviour of temperature-responsive physically crosslinked poly (N-vinylcaprolactam) based polymers for biomedical applications. *Materials Science and Engineering: C* **2017,** *79*, 130-139.

(34) Liu, L.; Bai, S.; Yang, H.; Li, S.; Quan, J.; Zhu, L.; Nie, H., Controlled release from thermo-sensitive PNVCL-co-MAA electrospun nanofibers: The effects of hydrophilicity/hydrophobicity of a drug. *Materials Science and Engineering: C* **2016,** *67*, 581-589.

(35) Cortez-Lemus, N. A.; Licea-Claverie, A., Poly(N-vinylcaprolactam), a comprehensive review on a thermoresponsive polymer becoming popular. *Prog. Polym. Sci.* **2016,** *53*, 1-51.

(36) Gandhi, A.; Paul, A.; Sen, S. O.; Sen, K. K., Studies on thermoresponsive polymers: Phase behaviour, drug delivery and biomedical applications. *Asian Journal of Pharmaceutical Sciences* **2015,** *10* (2), 99-107.

(37) Kocak, G.; Tuncer, C.; Bütün, V., pH-Responsive polymers. *Polym. Chem.* **2017,** *8* (1), 144-176.

(38) Dai, S.; Ravi, P.; Tam, K. C., pH-Responsive polymers: synthesis, properties and applications. *Soft Matter* **2008,** *4* (3), 435-449.

(39) Rübsam, K.; Davari, M. D.; Jakob, F.; Schwaneberg, U., KnowVolution of the polymer-binding peptide LCI for improved polypropylene binding. *Polymers* **2018,** *10* (4), 423.

(40) Sanghvi, A. B.; Miller, K. P. H.; Belcher, A. M.; Schmidt, C. E., Biomaterials functionalization using a novel peptide that selectively binds to a conducting polymer. *Nature Materials* **2005,** *4* (6), 496-502.

(41) Ejima, H.; Matsuno, H.; Serizawa, T., Biological Identification of Peptides that Specifically Bind to Poly(phenylene vinylene) Surfaces: Recognition of the Branched or Linear Structure of the Conjugated Polymer. *Langmuir* **2010,** *26* (22), 17278-17285.

(42) Bolivar, J. M.; Gascon, V.; Marquez-Alvarez, C.; Blanco, R. M.; Nidetzky, B., Oriented Coimmobilization of Oxidase and Catalase on Tailor-Made Ordered Mesoporous Silica. *Langmuir* **2017,** *33* (20), 5065-5076.

(43) Care, A.; Bergquist, P. L.; Sunna, A., Solid-binding peptides: smart tools for nanobiotechnology. *Trends Biotechnol.* **2015,** *33* (5), 259-268.

(44) Liu, Z.; Ma, S.; Duan, S.; Xuliang, D.; Sun, Y.; Zhang, X.; Xu, X.; Guan, B.; Wang, C.; Hu, M.; Qi, X.; Zhang, X.; Gao, P., Modification of Titanium Substrates with Chimeric Peptides Comprising Antimicrobial and Titanium-Binding Motifs Connected by Linkers To Inhibit Biofilm Formation. *ACS Appl. Mater. Interfaces* **2016,** *8* (8), 5124-5136.

(45) Zernia, S.; Ott, F.; Bellmann-Sickert, K.; Frank, R.; Klenner, M.; Jahnke, H.-G.; Prager, A.; Abel, B.; Robitzki, A.; Beck-Sickinger, A. G., Peptide-Mediated Specific Immobilization of Catalytically Active Cytochrome P450 BM3 Variant. *Bioconj. Chem.* **2016,** *27* (4), 1090-1097.

(46) Iijima, K.; Nagahama, H.; Takada, A.; Sawada, T.; Serizawa, T.; Hashizume, M., Surface functionalization of polymer substrates with hydroxyapatite using polymer-binding peptides. *Journal of Materials Chemistry B* **2016,** *4* (21), 3651-3659.

(47) Gong, W.; Wang, J.; Chen, Z.; Xia, B.; Lu, G., Solution Structure of LCI, a Novel Antimicrobial Peptide from Bacillus subtilis. *Biochemistry* **2011,** *50* (18), 3621-3627.

(48) Epand, R. M.; Vogel, H. J., Diversity of antimicrobial peptides and their mechanisms of action. *Biochim. Biophys. Acta* **1999,** *1462* (1), 11-28.

(49) Cardoso, M. H.; Oshiro, K. G. N.; Rezende, S. B.; Cândido, E. S.; Franco, O. L., Chapter Ten - The Structure/Function Relationship in Antimicrobial Peptides: What Can we Obtain From Structural Data? In *Adv. Protein Chem. Struct. Biol.*, Donev, R., Ed. Academic Press: 2018; Vol. 112, pp 359-384.

(50) Serizawa, T.; Sawada, T.; Matsuno, H., Highly Specific Affinities of Short Peptides against Synthetic Polymers. *Langmuir* **2007,** *23* (22), 11127-11133.

(51) Serizawa, T.; Sawada, T.; Matsuno, H.; Matsubara, T.; Sato, T., A Peptide Motif Recognizing a Polymer Stereoregularity. *J. Am. Chem. Soc.* **2005,** *127* (40), 13780-13781.

(52) Mulnaes, D.; Porta, N.; Clemens, R.; Apanasenko, I.; Reiners, J.; Gremer, L.; Neudecker, P.; Smits, S. H. J.; Gohlke, H., TopModel: Template-Based Protein Structure Prediction at Low Sequence Identity Using Top-Down Consensus and Deep Neural Networks. *J. Chem. Theory Comput.* **2020,** *16* (3), 1953-1967.

(53) Kristiansen, P. E.; Fimland, G.; Mantzilas, D.; Nissen-Meyer, J., Structure and Mode of Action of the Membrane-permeabilizing Antimicrobial Peptide Pheromone Plantaricin A*. *J. Biol. Chem.* **2005,** *280* (24), 22945-22950.

(54) Sato, T.; Kawasaki, T.; Mine, S.; Matsumura, H., Functional Role of the C-Terminal Amphipathic Helix 8 of Olfactory Receptors and Other G Protein-Coupled Receptors. *Int. J. Mol. Sci.* **2016,** *17* (11), 1930.

(55) Zhang, B.; Sun, B.; Li, X.; Yu, Y.; Tian, Y.; Xu, X.; Jin, Z., Synthesis of pH- and ionic strength-responsive microgels and their interactions with lysozyme. *Int. J. Biol. Macromol.* **2015,** *79*, 392-397.

(56) Dadsetan, M.; Taylor, K. E.; Yong, C.; Bajzer, Ž.; Lu, L.; Yaszemski, M. J., Controlled release of doxorubicin from pH-responsive microgels. *Acta Biomater.* **2013,** *9* (3), 5438-5446.

(57) Narang, P.; de Oliveira, T. E.; Venkatesu, P.; Netz, P. A., The role of osmolytes in the temperature-triggered conformational transition of poly(N-vinylcaprolactam): an experimental and computational study. *Phys. Chem. Chem. Phys.* **2020,** *22* (9), 5301-5313.

(58) Bergman, M. J.; Pedersen, J. S.; Schurtenberger, P.; Boon, N., Controlling the morphology of microgels by ionic stimuli. *Soft Matter* **2020,** *16* (11), 2786-2794.

(59) Bradley, M.; Vincent, B.; Burnett, G., Uptake and release of surfactants from polyampholyte microgel particles. *Colloid. Polym. Sci.* **2009,** *287* (3), 345-350.

(60) Aseyev, V.; Hietala, S.; Laukkanen, A.; Nuopponen, M.; Confortini, O.; Du Prez, F. E.; Tenhu, H., Mesoglobules of thermoresponsive polymers in dilute aqueous solutions above the LCST. *Polymer* **2005,** *46* (18), 7118-7131.

(61) Madhusudana Rao, K.; Mallikarjuna, B.; Krishna Rao, K. S. V.; Siraj, S.; Chowdoji Rao, K.; Subha, M. C. S., Novel thermo/pH sensitive nanogels composed from poly(N-vinylcaprolactam) for controlled release of an anticancer drug. *Colloids Surf. B. Biointerfaces* **2013,** *102*, 891-897.

(62) Shao, L.; Hu, M.; Chen, L.; Xu, L.; Bi, Y., RAFT polymerization of N-vinylcaprolactam and effects of the end group on the thermal response of poly(N-vinylcaprolactam). *React. Funct. Polym.* **2012,** *72* (6), 407-413.

(63) Bertrand, O.; Gohy, J.-F., Photo-responsive polymers: synthesis and applications. *Polym. Chem.* **2017,** *8* (1), 52-73.

(64) Moniruzzaman, M.; Sabey, C. J.; Fernando, G. F., Photoresponsive polymers: An investigation of their photoinduced temperature changes during photoviscosity measurements. *Polymer* **2007,** *48* (1), 255-263.

(65) Sun, S.; Liang, S.; Xu, W.-C.; Xu, G.; Wu, S., Photoresponsive polymers with multi-azobenzene groups. *Polym. Chem.* **2019,** *10* (32), 4389-4401.

(66) Demirel, G. B.; von Klitzing, R., A New Multiresponsive Drug Delivery System using Smart Nanogels. *Chemphyschem* **2013,** *14* (12), 2833-2840.

(67) Wang, Y.; Nie, J.; Chang, B.; Sun, Y.; Yang, W., Poly(vinylcaprolactam)-Based Biodegradable Multiresponsive Microgels for Drug Delivery. *Biomacromolecules* **2013,** *14* (9), 3034-3046.

(68) Maji, S.; Zhang, Z.; Voorhaar, L.; Pieters, S.; Stubbe, B.; Van Vlierberghe, S.; Dubruel, P.; De Geest, B. G.; Hoogenboom, R., Thermoresponsive polymer coated gold nanoparticles: from MADIX/RAFT copolymerization of N-vinylpyrrolidone and N-

vinylcaprolactam to salt and temperature induced nanoparticle aggregation. *RSC Adv.* **2015,** *5* (53), 42388-42398.

(69) Thorne, J. B.; Vine, G. J.; Snowden, M. J., Microgel applications and commercial considerations. *Colloid. Polym. Sci.* **2011,** *289* (5), 625.

(70) Klinger, D.; Landfester, K., Stimuli-responsive microgels for the loading and release of functional compounds: Fundamental concepts and applications. *Polymer* **2012,** *53* (23), 5209-5231.

(71) Wei, M.; Gao, Y.; Li, X.; Serpe, M. J., Stimuli-responsive polymers and their applications. *Polym. Chem.* **2017,** *8* (1), 127-143.

(72) Indulekha, S.; Arunkumar, P.; Bahadur, D.; Srivastava, R., Thermoresponsive polymeric gel as an on-demand transdermal drug delivery system for pain management. *Mater. Sci. Eng., C* **2016,** *62*, 113-122.

(73) Li, X.; Zhong, H.; Li, X.; Jia, F.; Cheng, Z.; Zhang, L.; Yin, J.; An, L.; Guo, L., Synthesis of attapulgite/N-isopropylacrylamide and its use in drug release. *Mater. Sci. Eng., C* **2014,** *45*, 170-175.

(74) Ward, M. A.; Georgiou, T. K., Thermoresponsive Polymers for Biomedical Applications. *Polymers* **2011,** *3* (3), 1215.

(75) Peteu, S. F.; Oancea, F.; Sicuia, O. A.; Constantinescu, F.; Dinu, S., Responsive Polymers for Crop Protection. *Polymers* **2010,** *2* (3), 229-251.

(76) Pergushov, D. V.; Sigolaeva, L. V.; Balabushevich, N. G.; Sharifullin, T. Z.; Noyong, M.; Richtering, W., Loading of doxorubicin into surface-attached stimuli-responsive microgels and its subsequent release under different conditions. *Polymer* **2021,** *213*, 123227.

(77) Saha, P.; Santi, M.; Emondts, M.; Roth, H.; Rahimi, K.; Großkurth, J.; Ganguly, R.; Wessling, M.; Singha, N. K.; Pich, A., Stimuli-Responsive Zwitterionic Core–Shell Microgels for Antifouling Surface Coatings. *ACS Appl. Mater. Interfaces* **2020,** *12* (52), 58223-58238.

(78) Wang, X.; Wu, C., Light-Scattering Study of Coil-to-Globule Transition of a Poly(N-isopropylacrylamide) Chain in Deuterated Water. *Macromolecules* **1999,** *32* (13), 4299-4301.

(79) Walter, J.; Ermatchkov, V.; Vrabec, J.; Hasse, H., Molecular dynamics and experimental study of conformation change of poly(N-isopropylacrylamide) hydrogels in water. *Fluid Phase Equilib.* **2010,** *296* (2), 164-172.

(80) Tavagnacco, L.; Zaccarelli, E.; Chiessi, E., On the molecular origin of the cooperative coil-to-globule transition of poly(N-isopropylacrylamide) in water. *Phys. Chem. Chem. Phys.* **2018,** *20* (15), 9997-10010.

(81) Graziano, G., On the temperature-induced coil to globule transition of poly-N-isopropylacrylamide in dilute aqueous solutions. *Int. J. Biol. Macromol.* **2000,** *27* (1), 89-97.

(82) Ramos, J.; Imaz, A.; Forcada, J., Temperature-sensitive nanogels: poly(N-vinylcaprolactam) versus poly(N-isopropylacrylamide). *Polym. Chem.* **2012,** *3* (4), 852-856.

(83) Vihola, H.; Laukkanen, A.; Valtola, L.; Tenhu, H.; Hirvonen, J., Cytotoxicity of thermosensitive polymers poly(N-isopropylacrylamide), poly(N-vinylcaprolactam) and amphiphilically modified poly(N-vinylcaprolactam). *Biomaterials* **2005,** *26* (16), 3055-3064.

(84) Chee, C. K.; Rimmer, S.; Soutar, I.; Swanson, L., Fluorescence investigations of the conformational behaviour of Poly(N-vinylcaprolactam). *React. Funct. Polym.* **2006,** *66* (1), 1-11.

(85) Dušek, K.; Dušková-Smrčková, M., Volume Phase Transition in Gels: Its Discovery and Development. *Gels* **2020,** *6* (3), 22.

(86) Koochaki, A.; Moghbeli, M. R.; Javan Nikkhah, S., Coil-to-globule transition of thermo-responsive γ-substituted poly (ε-caprolactone) in water: A molecular dynamics simulation study. *Curr. Appl. Phys.* **2018,** *18* (11), 1313-1319.

(87) Wu, C.; Wang, X., Globule-to-Coil Transition of a Single Homopolymer Chain in Solution. *Phys. Rev. Lett.* **1998,** *80* (18), 4092-4094.

(88) Zhelavskyi, O. S.; Kyrychenko, A., Atomistic molecular dynamics simulations of the LCST conformational transition in poly(N-vinylcaprolactam) in water. *J. Mol. Graph. Model.* **2019,** *90*, 51-58.

(89) Zhang, C.; Peng, H.; Puttick, S.; Reid, J.; Bernardi, S.; Searles, D. J.; Whittaker, A. K., Conformation of Hydrophobically Modified Thermoresponsive Poly(OEGMA-co-TFEA) across the LCST Revealed by NMR and Molecular Dynamics Studies. *Macromolecules* **2015,** *48* (10), 3310-3317.

(90) Alaghemandi, M.; Spohr, E., Molecular Dynamics Investigation of the Thermo-Responsive Polymer Poly(N-isopropylacrylamide). *Macromol. Theory Simul.* **2012,** *21* (2), 106-112.

(91) de Oliveira, T. E.; Marques, C. M.; Netz, P. A., Molecular dynamics study of the LCST transition in aqueous poly(N-n-propylacrylamide). *Phys. Chem. Chem. Phys.* **2018,** *20* (15), 10100-10107.

(92) Hachisu, S., Strategies for discovering resistance-breaking, safe and sustainable commercial herbicides with novel modes of action and chemotypes. *Pest Manage. Sci.* **2021,** *77* (7), 3042-3048.

(93) Holt, J. S.; Lebaron, H. M., Significance and Distribution of Herbicide Resistance. *Weed Technol.* **1990,** *4* (1), 141-149.

(94) Yuan, J. S.; Tranel, P. J.; Stewart, C. N., Non-target-site herbicide resistance: a family business. *Trends Plant Sci.* **2007,** *12* (1), 6-13.

(95) Baylis, A. D., Why glyphosate is a global herbicide: strengths, weaknesses and prospects. *Pest Manage. Sci.* **2000,** *56* (4), 299-308.

(96) Duke, S. O.; Powles, S. B., Glyphosate: a once-in-a-century herbicide. *Pest Manage. Sci.* **2008,** *64* (4), 319-325.

(97) Myers, J. P.; Antoniou, M. N.; Blumberg, B.; Carroll, L.; Colborn, T.; Everett, L. G.; Hansen, M.; Landrigan, P. J.; Lanphear, B. P.; Mesnage, R.; Vandenberg, L. N.; vom Saal, F. S.; Welshons, W. V.; Benbrook, C. M., Concerns over use of glyphosate-based herbicides and risks associated with exposures: a consensus statement. *Environ. Health* **2016,** *15* (1), 19.

(98) Van Bruggen, A. H. C.; He, M. M.; Shin, K.; Mai, V.; Jeong, K. C.; Finckh, M. R.; Morris, J. G., Environmental and health effects of the herbicide glyphosate. *Sci. Total Environ.* **2018,** *616-617*, 255-268.

(99) Annett, R.; Habibi, H. R.; Hontela, A., Impact of glyphosate and glyphosate-based herbicides on the freshwater environment. *J. Appl. Toxicol.* **2014,** *34* (5), 458-479.

(100) Guyton, K. Z.; Loomis, D.; Grosse, Y.; El Ghissassi, F.; Benbrahim-Tallaa, L.; Guha, N.; Scoccianti, C.; Mattock, H.; Straif, K., Carcinogenicity of tetrachlorvinphos, parathion, malathion, diazinon, and glyphosate. *The Lancet Oncology* **2015,** *16* (5), 490-491.

(101) Kogevinas, M., Probable carcinogenicity of glyphosate. *BMJ* **2019,** *365*, l1613.

(102) Benbrook, C. M., How did the US EPA and IARC reach diametrically opposed conclusions on the genotoxicity of glyphosate-based herbicides? *Environmental Sciences Europe* **2019,** *31* (1), 2.

(103) Vencill, W. K.; Nichols, R. L.; Webster, T. M.; Soteres, J. K.; Mallory-Smith, C.; Burgos, N. R.; Johnson, W. G.; McClelland, M. R., Herbicide Resistance: Toward an Understanding of Resistance Development and the Impact of Herbicide-Resistant Crops. *Weed Sci.* **2012,** *60* (SP1), 2-30.

(104) Ranson, S. L.; Thomas, M., Crassulacean Acid Metabolism. *Annual Review of Plant Physiology* **1960,** *11* (1), 81-110.

(105) Bassham, J. A.; Benson, A. A.; Calvin, M., The path of carbon in photosynthesis VIII. The role of malic acid. *J. Biol. Chem.* **1950,** *185* (2), 781-787.

(106) Slack, C. R.; Hatch, M. D., Comparative studies on the activity of carboxylases and other enzymes in relation to the new pathway of photosynthetic carbon dioxide fixation in tropical grasses. *The Biochemical journal* **1967,** *103* (3), 660-665.

(107) Yamori, W.; Hikosaka, K.; Way, D. A., Temperature response of photosynthesis in C3, C4, and CAM plants: temperature acclimation and temperature adaptation. *Photosynth. Res.* **2014,** *119* (1), 101-117.

(108) Colin, L. D. J.; Furbank, R. T.; Hatch, M. D., Inorganic Carbon Diffusion between C_4 Mesophyll and Bundle Sheath Cells: Direct Bundle Sheath CO_2 Assimilation in Intact Leaves in the Presence of an Inhibitor of the C_4 Pathway. *Plant Physiol.* **1989,** *91* (4), 1356-1363.

(109) Furbank, R. T.; Hatch, M. D., Mechanism of C4 Photosynthesis: The Size and Composition of the Inorganic Carbon Pool in Bundle Sheath Cells. *Plant Physiol.* **1987,** *85* (4), 958-964.

(110) Herrera, A., Crassulacean acid metabolism and fitness under water deficit stress: if not for carbon gain, what is facultative CAM good for? *Ann. Bot.* **2008,** *103* (4), 645-653.

(111) Díaz-Tielas, C.; Sotelo, T.; Graña, E.; Reigosa, M. J.; Sánchez-Moreiras, A. M., Phytotoxic Potential of Trans-chalcone on Crop Plants and Model Species. *J. Plant Growth Regul.* **2014,** *33* (2), 181-194.

(112) Paulus, J. K.; Schlieper, D.; Groth, G., Greater efficiency of photosynthetic carbon fixation due to single amino-acid substitution. *Nat. Commun.* **2013,** *4* (1), 1518.

(113) Waterhouse, A.; Bertoni, M.; Bienert, S.; Studer, G.; Tauriello, G.; Gumienny, R.; Heer, F. T.; de Beer, T. A P.; Rempfer, C.; Bordoli, L.; Lepore, R.; Schwede, T., SWISS-MODEL: homology modelling of protein structures and complexes. *Nucleic Acids Res.* **2018,** *46* (W1), W296-W303.

(114) Leebens-Mack, J. H.; Barker, M. S.; Carpenter, E. J.; Deyholos, M. K.; Gitzendanner, M. A.; Graham, S. W.; Grosse, I.; Li, Z.; Melkonian, M.; Mirarab, S.; Porsch, M.; Quint, M.; Rensing, S. A.; Soltis, D. E.; Soltis, P. S.; Stevenson, D. W.; Ullrich, K. K.; Wickett, N. J.; DeGironimo, L.; Edger, P. P.; Jordon-Thaden, I. E.; Joya, S.; Liu, T.; Melkonian, B.; Miles, N. W.; Pokorny, L.; Quigley, C.; Thomas, P.; Villarreal, J. C.; Augustin, M. M.; Barrett, M. D.; Baucom, R. S.; Beerling, D. J.; Benstein, R. M.; Biffin, E.; Brockington, S. F.; Burge, D. O.; Burris, J. N.; Burris, K. P.; Burtet-Sarramegna, V.; Caicedo, A. L.; Cannon, S. B.; Çebi, Z.; Chang, Y.; Chater, C.; Cheeseman, J. M.; Chen, T.; Clarke, N. D.; Clayton, H.; Covshoff, S.; Crandall-Stotler, B. J.; Cross, H.; dePamphilis, C. W.; Der, J. P.; Determann, R.; Dickson, R. C.; Di Stilio, V. S.; Ellis, S.; Fast, E.; Feja, N.; Field, K. J.; Filatov, D. A.; Finnegan, P. M.; Floyd, S. K.; Fogliani, B.; García, N.; Gâteblé, G.; Godden, G. T.; Goh, F.; Greiner, S.; Harkess, A.; Heaney, J. M.; Helliwell, K. E.; Heyduk, K.; Hibberd, J. M.; Hodel, R. G. J.; Hollingsworth, P. M.; Johnson, M. T. J.; Jost, R.; Joyce, B.; Kapralov, M. V.; Kazamia, E.; Kellogg, E. A.; Koch, M. A.; Von Konrat, M.; Könyves, K.; Kutchan, T. M.; Lam, V.; Larsson, A.; Leitch, A. R.; Lentz, R.; Li, F.-W.; Lowe, A. J.; Ludwig, M.; Manos, P. S.; Mavrodiev, E.; McCormick, M. K.; McKain, M.; McLellan, T.; McNeal, J. R.; Miller, R. E.; Nelson, M. N.; Peng, Y.; Ralph, P.; Real, D.; Riggins, C. W.; Ruhsam, M.; Sage, R. F.; Sakai, A. K.; Scascitella, M.; Schilling, E. E.; Schlösser, E.-M.; Sederoff, H.; Servick, S.; Sessa, E. B.; Shaw, A. J.; Shaw, S. W.; Sigel, E. M.; Skema, C.; Smith, A. G.; Smithson, A.; Stewart, C. N.; Stinchcombe, J. R.; Szövényi, P.; Tate, J. A.; Tiebel, H.; Trapnell, D.; Villegente, M.; Wang, C.-N.; Weller, S. G.; Wenzel, M.; Weststrand, S.; Westwood, J. H.; Whigham, D. F.; Wu, S.; Wulff, A. S.; Yang, Y.; Zhu, D.; Zhuang, C.; Zuidof, J.; Chase, M. W.; Pires, J. C.; Rothfels, C. J.; Yu, J.; Chen, C.; Chen, L.; Cheng, S.; Li, J.; Li, R.; Li, X.; Lu, H.; Ou, Y.; Sun, X.; Tan, X.; Tang, J.; Tian, Z.; Wang, F.; Wang, J.; Wei, X.; Xu, X.; Yan, Z.; Yang, F.; Zhong, X.; Zhou, F.; Zhu, Y.; Zhang, Y.; Ayyampalayam, S.; Barkman, T. J.; Nguyen, N.-p.; Matasci, N.; Nelson, D. R.; Sayyari, E.; Wafula, E. K.; Walls, R. L.; Warnow, T.; An, H.; Arrigo, N.; Baniaga, A. E.; Galuska, S.; Jorgensen, S. A.; Kidder, T. I.; Kong, H.; Lu-Irving, P.; Marx, H. E.; Qi, X.; Reardon, C. R.; Sutherland, B. L.; Tiley, G. P.; Welles, S. R.; Yu, R.; Zhan, S.; Gramzow, L.; Theißen, G.; Wong, G. K.-S.; One Thousand Plant Transcriptomes, I., One thousand plant transcriptomes and the phylogenomics of green plants. *Nature* **2019,** *574* (7780), 679-685.

(115) van Gunsteren, W. F.; Berendsen, H. J. C., Computer Simulation of Molecular Dynamics: Methodology, Applications, and Perspectives in Chemistry. *Angewandte Chemie International Edition in English* **1990,** *29* (9), 992-1023.

(116) Karplus, M.; McCammon, J. A., Molecular dynamics simulations of biomolecules. *Nat. Struct. Biol.* **2002,** *9* (9), 646-652.

(117) Berendsen, H., *Simulating the physical world*. Cambridge University Press Cambridge: 2007.

(118) Brunette, E. S.; Flemmer, R. C.; Flemmer, C. L. In *A review of artificial intelligence*, 2009 4th International Conference on Autonomous Robots and Agents, 10-12 Feb. 2009; 2009; pp 385-392.

(119) Goh, G. B.; Hodas, N. O.; Vishnu, A., Deep learning for computational chemistry. *J. Comput. Chem.* **2017,** *38* (16), 1291-1307.

(120) Jumper, J.; Evans, R.; Pritzel, A.; Green, T.; Figurnov, M.; Ronneberger, O.; Tunyasuvunakool, K.; Bates, R.; Žídek, A.; Potapenko, A.; Bridgland, A.; Meyer, C.; Kohl, S. A. A.; Ballard, A. J.; Cowie, A.; Romera-Paredes, B.; Nikolov, S.; Jain, R.; Adler, J.; Back, T.; Petersen, S.; Reiman, D.; Clancy, E.; Zielinski, M.; Steinegger, M.; Pacholska, M.; Berghammer, T.; Bodenstein, S.; Silver, D.; Vinyals, O.; Senior, A. W.; Kavukcuoglu, K.; Kohli, P.; Hassabis, D., Highly accurate protein structure prediction with AlphaFold. *Nature* **2021,** *596* (7873), 583-589.

(121) Baek, M.; DiMaio, F.; Anishchenko, I.; Dauparas, J.; Ovchinnikov, S.; Lee, G. R.; Wang, J.; Cong, Q.; Kinch, L. N.; Schaeffer, R. D.; Millán, C.; Park, H.; Adams, C.; Glassman, C. R.; DeGiovanni, A.; Pereira, J. H.; Rodrigues, A. V.; van Dijk, A. A.; Ebrecht, A. C.; Opperman, D. J.; Sagmeister, T.; Buhlheller, C.; Pavkov-Keller, T.; Rathinaswamy, M. K.; Dalwadi, U.; Yip, C. K.; Burke, J. E.; Garcia, K. C.; Grishin, N. V.; Adams, P. D.; Read, R. J.; Baker, D., Accurate prediction of protein structures and interactions using a three-track neural network. *Science* **2021**, eabj8754.

(122) Alder, B. J.; Wainwright, T. E., Phase transition for a hard sphere system. *J. Chem. Phys.* **1957,** *27* (5), 1208-1209.

(123) Sherrill, C. D.; Manolopoulos, D. E.; Martínez, T. J.; Michaelides, A., Electronic structure software. *J. Chem. Phys.* **2020,** *153* (7), 070401.

(124) BrooksIII, C. L.; Case, D. A.; Plimpton, S.; Roux, B.; Spoel, D. v. d.; Tajkhorshid, E., Classical molecular dynamics. *J. Chem. Phys.* **2021,** *154* (10), 100401.

(125) Case, D. A.; Ben-Shalom, I. Y.; Brozell, S. R.; Cerutti, D. S.; Cheatham III, T. E.; Cruzeiro, V. W. D.; Darden, T. A.; Duke, R. E.; Ghoreishi, D.; Gilson, M. K.; Gohlke, H.; Goetz, A. W.; Greene, D.; Harris, R.; Homeyer, N.; Izadi, S.; Kovalenko, A.; Kurtzman, T.; Lee, T. S.; LeGrand, S.; Li, P.; Lin, C.; Liu, J.; Luchko, T.; Luo, R.; Mermelstein, D. J.; Merz, K. M.; Miao, Y.; Monard, G.; Nguyen, C.; Nguyen, H.; Omelyan, I.; Onufriev, A.; Pan, F.; Qi, R.; Roe, D. R.; Roitberg, A.; Sagui, C.; Schott-Verdugo, S.; Shen, J.; Simmerling, C. L.; Smith, J.; Salomon-Ferrer, R.; Swails, J.; Walker, R. C.; Wang, J.; Wei, H.; Wolf, R. M.; Wu, X.; Xiao, L.; York , D. M.; Kollman, P. A. AMBER, University of California: San Francisco, 2021.

(126) Case, D. A.; Cheatham III, T. E.; Darden, T.; Gohlke, H.; Luo, R.; Merz Jr., K. M.; Onufriev, A.; Simmerling, C.; Wang, B.; Woods, R. J., The Amber biomolecular simulation programs. *J. Comput. Chem.* **2005,** *26* (16), 1668-1688.

(127) Brooks, B. R.; Brooks III, C. L.; Mackerell Jr., A. D.; Nilsson, L.; Petrella, R. J.; Roux, B.; Won, Y.; Archontis, G.; Bartels, C.; Boresch, S.; Caflisch, A.; Caves, L.; Cui, Q.; Dinner, A. R.; Feig, M.; Fischer, S.; Gao, J.; Hodoscek, M.; Im, W.; Kuczera, K.; Lazaridis, T.; Ma, J.; Ovchinnikov, V.; Paci, E.; Pastor, R. W.; Post, C. B.; Pu, J. Z.; Schaefer, M.; Tidor, B.; Venable, R. M.; Woodcock, H. L.; Wu, X.; Yang, W.; York, D. M.; Karplus, M., CHARMM: The biomolecular simulation program. *J. Comput. Chem.* **2009,** *30* (10), 1545-1614.

(128) Brooks, B. R.; Bruccoleri, R. E.; Olafson, B. D.; States, D. J.; Swaminathan, S.; Karplus, M., CHARMM: A program for macromolecular energy, minimization, and dynamics calculations. *J. Comput. Chem.* **1983,** *4* (2), 187-217.

(129) Van Der Spoel, D.; Lindahl, E.; Hess, B.; Groenhof, G.; Mark, A. E.; Berendsen, H. J. C., GROMACS: Fast, flexible, and free. *J. Comput. Chem.* **2005,** *26* (16), 1701-1718.

(130) Berendsen, H. J. C.; van der Spoel, D.; van Drunen, R., GROMACS: A message-passing parallel molecular dynamics implementation. *Comput. Phys. Commun.* **1995,** *91* (1), 43-56.

(131) Salomon-Ferrer, R.; Götz, A. W.; Poole, D.; Le Grand, S.; Walker, R. C., Routine Microsecond Molecular Dynamics Simulations with AMBER on GPUs. 2. Explicit Solvent Particle Mesh Ewald. *J. Chem. Theory Comput.* **2013,** *9* (9), 3878-3888.

(132) Götz, A. W.; Williamson, M. J.; Xu, D.; Poole, D.; Le Grand, S.; Walker, R. C., Routine Microsecond Molecular Dynamics Simulations with AMBER on GPUs. 1. Generalized Born. *J. Chem. Theory Comput.* **2012,** *8* (5), 1542-1555.

(133) Izadi, S.; Anandakrishnan, R.; Onufriev, A. V., Building Water Models: A Different Approach. *J. Phys. Chem. Lett.* **2014,** *5* (21), 3863-3871.

(134) Jorgensen, W. L.; Chandrasekhar, J.; Madura, J. D.; Impey, R. W.; Klein, M. L., Comparison of simple potential functions for simulating liquid water. *J. Chem. Phys.* **1983,** *79* (2), 926-935.

(135) Song, D.; Luo, R.; Chen, H.-F., The IDP-Specific Force Field ff14IDPSFF Improves the Conformer Sampling of Intrinsically Disordered Proteins. *J. Chem. Inf. Model.* **2017,** *57* (5), 1166-1178.

(136) Maier, J. A.; Martinez, C.; Kasavajhala, K.; Wickstrom, L.; Hauser, K. E.; Simmerling, C., ff14SB: Improving the Accuracy of Protein Side Chain and Backbone Parameters from ff99SB. *J. Chem. Theory Comput.* **2015,** *11* (8), 3696-3713.

(137) Tian, C.; Kasavajhala, K.; Belfon, K. A. A.; Raguette, L.; Huang, H.; Migues, A. N.; Bickel, J.; Wang, Y.; Pincay, J.; Wu, Q.; Simmerling, C., ff19SB: Amino-Acid-Specific Protein Backbone Parameters Trained against Quantum Mechanics Energy Surfaces in Solution. *J. Chem. Theory Comput.* **2020,** *16* (1), 528-552.

(138) Galindo-Murillo, R.; Robertson, J. C.; Zgarbová, M.; Šponer, J.; Otyepka, M.; Jurečka, P.; Cheatham, T. E., Assessing the Current State of Amber Force Field Modifications for DNA. *J. Chem. Theory Comput.* **2016,** *12* (8), 4114-4127.

(139) Zgarbová, M.; Otyepka, M.; Šponer, J.; Mládek, A.; Banáš, P.; Cheatham, T. E.; Jurečka, P., Refinement of the Cornell et al. Nucleic Acids Force Field Based on Reference Quantum Chemical Calculations of Glycosidic Torsion Profiles. *J. Chem. Theory Comput.* **2011,** *7* (9), 2886-2902.

(140) Kirschner, K. N.; Yongye, A. B.; Tschampel, S. M.; González-Outeiriño, J.; Daniels, C. R.; Foley, B. L.; Woods, R. J., GLYCAM06: A generalizable biomolecular force field. Carbohydrates. *J. Comput. Chem.* **2008,** *29* (4), 622-655.

(141) Dickson, C. J.; Madej, B. D.; Skjevik, Å. A.; Betz, R. M.; Teigen, K.; Gould, I. R.; Walker, R. C., Lipid14: The Amber Lipid Force Field. *J. Chem. Theory Comput.* **2014,** *10* (2), 865-879.

(142) Wang, J.; Wolf, R. M.; Caldwell, J. W.; Kollman, P. A.; Case, D. A., Development and testing of a general amber force field. *J. Comput. Chem.* **2004,** *25* (9), 1157-1174.

(143) Berman, H., The Protein Data Bank: a historical perspective. *Acta Cryst. A* **2008,** *64* (1), 88-95.

(144) Berman, H. M.; Westbrook, J.; Feng, Z.; Gilliland, G.; Bhat, T. N.; Weissig, H.; Shindyalov, I. N.; Bourne, P. E., The Protein Data Bank. *Nucleic Acids Res.* **2000,** *28* (1), 235-242.

(145) Yee, A. A.; Savchenko, A.; Ignachenko, A.; Lukin, J.; Xu, X.; Skarina, T.; Evdokimova, E.; Liu, C. S.; Semesi, A.; Guido, V.; Edwards, A. M.; Arrowsmith, C. H., NMR and X-ray Crystallography, Complementary Tools in Structural Proteomics of Small Proteins. *J. Am. Chem. Soc.* **2005,** *127* (47), 16512-16517.

(146) Snyder, D. A.; Chen, Y.; Denissova, N. G.; Acton, T.; Aramini, J. M.; Ciano, M.; Karlin, R.; Liu, J.; Manor, P.; Rajan, P. A.; Rossi, P.; Swapna, G. V. T.; Xiao, R.; Rost, B.; Hunt, J.; Montelione, G. T., Comparisons of NMR Spectral Quality and Success in Crystallization Demonstrate that NMR and X-ray Crystallography Are Complementary Methods for Small Protein Structure Determination. *J. Am. Chem. Soc.* **2005,** *127* (47), 16505-16511.

(147) Consortium, T. U., UniProt: the universal protein knowledgebase in 2021. *Nucleic Acids Res.* **2020,** *49* (D1), D480-D489.

(148) Consortium, T. U., UniProt: a hub for protein information. *Nucleic Acids Res.* **2014,** *43* (D1), D204-D212.

(149) Lindorff-Larsen, K.; Piana, S.; Dror, R. O.; Shaw, D. E., How Fast-Folding Proteins Fold. *Science* **2011,** *334* (6055), 517-520.

(150) Nguyen, H.; Maier, J.; Huang, H.; Perrone, V.; Simmerling, C., Folding Simulations for Proteins with Diverse Topologies Are Accessible in Days with a Physics-Based Force Field and Implicit Solvent. *J. Am. Chem. Soc.* **2014,** *136* (40), 13959-13962.

(151) Geng, H.; Chen, F.; Ye, J.; Jiang, F., Applications of Molecular Dynamics Simulation in Structure Prediction of Peptides and Proteins. *Comput. Struct. Biotechnol. J.* **2019,** *17*, 1162-1170.

(152) Levitt, M.; Warshel, A., Computer simulation of protein folding. *Nature* **1975,** *253* (5494), 694-698.

(153) Jiang, F.; Wu, Y.-D., Folding of Fourteen Small Proteins with a Residue-Specific Force Field and Replica-Exchange Molecular Dynamics. *J. Am. Chem. Soc.* **2014,** *136* (27), 9536-9539.

(154) Dünweg, B.; Kremer, K., Molecular dynamics simulation of a polymer chain in solution. *J. Chem. Phys.* **1993,** *99* (9), 6983-6997.

(155) Fixman, M., Simulation of polymer dynamics. I. General theory. *J. Chem. Phys.* **1978,** *69* (4), 1527-1537.

(156) Wu, Z.; Milano, G.; Müller-Plathe, F., Combination of Hybrid Particle-Field Molecular Dynamics and Slip-Springs for the Efficient Simulation of Coarse-Grained Polymer Models: Static and Dynamic Properties of Polystyrene Melts. *J. Chem. Theory Comput.* **2021,** *17* (1), 474-487.

(157) Kong, X.; Rudnicki, P. E.; Choudhury, S.; Bao, Z.; Qin, J., Dendrite Suppression by a Polymer Coating: A Coarse-Grained Molecular Study. *Adv. Funct. Mater.* **2020,** *30* (15), 1910138.

(158) Müller-Plathe, F., Coarse-Graining in Polymer Simulation: From the Atomistic to the Mesoscopic Scale and Back. *Chemphyschem* **2002,** *3* (9), 754-769.

(159) Salerno, K. M.; Agrawal, A.; Perahia, D.; Grest, G. S., Resolving Dynamic Properties of Polymers through Coarse-Grained Computational Studies. *Phys. Rev. Lett.* **2016,** *116* (5), 058302.

(160) Kremer, K.; Müller-Plathe, F., Multiscale simulation in polymer science. *Mol. Simul.* **2002,** *28* (8-9), 729-750.

(161) Chu, Y.; Sun, L.; Yang, X.; Wang, J.; Huang, W., Multiscale simulation and theoretical prediction for the elastic properties of unidirectional fiber-reinforced polymer containing random void defects. *Polym. Compos.* **2021,** *42* (6), 2958-2972.

(162) Mochizuki, K., Reduction of water-mediated repulsion drives poly(N-vinylcaprolactam) collapse upon heating. *Phys. Chem. Chem. Phys.* **2020,** *22* (3), 1053-1060.

(163) Shudo, Y.; Izumi, A.; Hagita, K.; Nakao, T.; Shibayama, M., Structure-mechanical property relationships in crosslinked phenolic resin investigated by molecular dynamics simulation. *Polymer* **2017,** *116*, 506-514.

(164) Shen, J.; Lin, X.; Liu, J.; Li, X., Effects of Cross-Link Density and Distribution on Static and Dynamic Properties of Chemically Cross-Linked Polymers. *Macromolecules* **2019,** *52* (1), 121-134.

(165) Danilov, D.; Sedghamiz, E.; Fliegl, H.; Frisch, H.; Barner-Kowollik, C.; Wenzel, W., Tacticity dependence of single chain polymer folding. *Polym. Chem.* **2020,** *11* (20), 3439-3445.

(166) Hu, W., Chain folding in polymer melt crystallization studied by dynamic Monte Carlo simulations. *J. Chem. Phys.* **2001,** *115* (9), 4395-4401.

(167) Mukherji, D.; Wagner, M.; Watson, M. D.; Winzen, S.; de Oliveira, T. E.; Marques, C. M.; Kremer, K., Relating side chain organization of PNIPAm with its conformation in aqueous methanol. *Soft Matter* **2016,** *12* (38), 7995-8003.

(168) Haq, M. A.; Su, Y.; Wang, D., Mechanical properties of PNIPAM based hydrogels: A review. *Materials Science and Engineering: C* **2017,** *70*, 842-855.

(169) Plunkett, K. N.; Zhu, X.; Moore, J. S.; Leckband, D. E., PNIPAM Chain Collapse Depends on the Molecular Weight and Grafting Density. *Langmuir* **2006,** *22* (9), 4259-4266.

(170) García, E. J.; Hasse, H., Studying equilibria of polymers in solution by direct molecular dynamics simulations: poly(N-isopropylacrylamide) in water as a test case. *Eur. Phys. J. Spec. Top.* **2019,** *227* (14), 1547-1558.

(171) Dalgicdir, C.; Rodríguez-Ropero, F.; van der Vegt, N. F. A., Computational Calorimetry of PNIPAM Cononsolvency in Water/Methanol Mixtures. *J. Phys. Chem. B* **2017,** *121* (32), 7741-7748.

(172) Du, H.; Qian, X., Molecular dynamics simulations of PNIPAM-co-PEGMA copolymer hydrophilic to hydrophobic transition in NaCl solution. *J. Polym. Sci., Part B: Polym. Phys.* **2011,** *49* (15), 1112-1122.

(173) Oliveira, T. E. d.; Mukherji, D.; Kremer, K.; Netz, P. A., Effects of stereochemistry and copolymerization on the LCST of PNIPAm. *J. Chem. Phys.* **2017,** *146* (3), 034904.

(174) Sun, X.; Qian, X., Atomistic Molecular Dynamics Simulations of the Lower Critical Solution Temperature Transition of Poly(N-vinylcaprolactam) in Aqueous Solutions. *J. Phys. Chem. B* **2019,** *123* (23), 4986-4995.

(175) Camara, M.; Liao, H.; Xu, J.; Zhang, J.; Swai, R., Molecular dynamics study of the intercalation and conformational transition of poly (N-vinyl caprolactam), a thermosensitive polymer in hydrated Na-montmorillonite. *Polymer* **2019,** *179*, 121718.

(176) Condon, J. E.; Martin, T. B.; Jayaraman, A., Effect of conjugation on phase transitions in thermoresponsive polymers: an atomistic and coarse-grained simulation study. *Soft Matter* **2017,** *13* (16), 2907-2918.

(177) Dubovik, A. S.; Makhaeva, E. E.; Grinberg, V. Y.; Khokhlov, A. R., Energetics of Cooperative Transitions of N-Vinylcaprolactam Polymers in Aqueous Solutions. *Macromol. Chem. Phys.* **2005,** *206* (9), 915-928.

(178) Edelman, G. M.; Gally, J. A., Degeneracy and complexity in biological systems. *PNAS* **2001,** *98* (24), 13763-13768.

(179) Malinowski, R., Understanding of Leaf Development—the Science of Complexity. *Plants* **2013,** *2* (3), 396-415.

(180) Toussaint, O.; Schneider, E. D., The thermodynamics and evolution of complexity in biological systems. *Comp. Biochem. Physiol., A: Mol. Integr. Physiol.* **1998,** *120* (1), 3-9.

(181) Hsu, C. F.; Wei, S.-Y.; Huang, H.-P.; Hsu, L.; Chi, S.; Peng, C.-K., Entropy of Entropy: Measurement of Dynamical Complexity for Biological Systems. *Entropy* **2017,** *19* (10), 550.

(182) Shannon, C. E., A mathematical theory of communication. *Bell Syst. Tech. J.* **1948,** *27* (3), 379-423.

(183) Walpole, J.; Papin, J. A.; Peirce, S. M., Multiscale Computational Models of Complex Biological Systems. *Annu. Rev. Biomed. Eng.* **2013,** *15* (1), 137-154.

(184) Thompson, J. M. T.; Kohl, P.; Noble, D.; Winslow, R. L.; Hunter, P. J., Computational modelling of biological systems: tools and visions. *Philos. Trans. A Math. Phys. Eng. Sci.* **2000,** *358* (1766), 579-610.

(185) Brodland, G. W., How computational models can help unlock biological systems. *Semin. Cell Dev. Biol.* **2015,** *47-48*, 62-73.

(186) Karr, Jonathan R.; Sanghvi, Jayodita C.; Macklin, Derek N.; Gutschow, Miriam V.; Jacobs, Jared M.; Bolival, B.; Assad-Garcia, N.; Glass, John I.; Covert, Markus W., A Whole-Cell Computational Model Predicts Phenotype from Genotype. *Cell* **2012,** *150* (2), 389-401.

(187) Aminpour, M.; Montemagno, C.; Tuszynski, J. A., An Overview of Molecular Modeling for Drug Discovery with Specific Illustrative Examples of Applications. *Molecules* **2019,** *24* (9), 1693.

(188) Jorgensen, W. L., The Many Roles of Computation in Drug Discovery. *Science* **2004,** *303* (5665), 1813-1818.

(189) Curtarolo, S.; Hart, G. L. W.; Nardelli, M. B.; Mingo, N.; Sanvito, S.; Levy, O., The high-throughput highway to computational materials design. *Nature Materials* **2013,** *12* (3), 191-201.

(190) Oganov, A. R.; Pickard, C. J.; Zhu, Q.; Needs, R. J., Structure prediction drives materials discovery. *Nature Reviews Materials* **2019,** *4* (5), 331-348.

(191) Urban, A.; Seo, D.-H.; Ceder, G., Computational understanding of Li-ion batteries. *npj Computational Materials* **2016,** *2* (1), 16002.

(192) Sticklen, M. B., Plant genetic engineering for biofuel production: towards affordable cellulosic ethanol. *Nature Reviews Genetics* **2008,** *9* (6), 433-443.

(193) Bakan, B.; Marion, D., Assembly of the cutin polyester: from cells to extracellular cell walls. *Plants* **2017,** *6* (4), 57.

(194) Fich, E. A.; Segerson, N. A.; Rose, J. K. C., The Plant Polyester Cutin: Biosynthesis, Structure, and Biological Roles. *Annu. Rev. Plant Biol.* **2016,** *67* (1), 207-233.

(195) Kolattukudy, P. E., Biopolyester Membranes of Plants: Cutin and Suberin. *Science* **1980,** *208* (4447), 990-1000.

(196) Gagic, V.; Kleijn, D.; Báldi, A.; Boros, G.; Jørgensen, H. B.; Elek, Z.; Garratt, M. P. D.; de Groot, G. A.; Hedlund, K.; Kovács-Hostyánszki, A.; Marini, L.; Martin, E.; Pevere, I.;

Potts, S. G.; Redlich, S.; Senapathi, D.; Steffan-Dewenter, I.; Świtek, S.; Smith, H. G.; Takács, V.; Tryjanowski, P.; van der Putten, W. H.; van Gils, S.; Bommarco, R., Combined effects of agrochemicals and ecosystem services on crop yield across Europe. *Ecol. Lett.* **2017,** *20* (11), 1427-1436.

(197) Gomes, T. C. F.; Skaf, M. S., Cellulose-Builder: A toolkit for building crystalline structures of cellulose. *J. Comput. Chem.* **2012,** *33* (14), 1338-1346.

(198) Martínez, L.; Andrade, R.; Birgin, E. G.; Martínez, J. M., PACKMOL: A package for building initial configurations for molecular dynamics simulations. *J. Comput. Chem.* **2009,** *30* (13), 2157-2164.

(199) Kabsch, W.; Sander, C., Dictionary of protein secondary structure: Pattern recognition of hydrogen-bonded and geometrical features. *Biopolymers* **1983,** *22* (12), 2577-2637.

(200) Jarzynski, C., Nonequilibrium equality for free energy differences. *Phys. Rev. Lett.* **1997,** *78* (14), 2690.

(201) Zhang, Q.; Weber, C.; Schubert, U. S.; Hoogenboom, R., Thermoresponsive polymers with lower critical solution temperature: from fundamental aspects and measuring techniques to recommended turbidimetry conditions. *Mater. Horiz.* **2017,** *4* (2), 109-116.

(202) Tager, A. A.; Safronov, A. P.; Sharina, S. V.; Galayev, I. Y., Thermodynamics of aqueous solutions of polyvinylcaprolactam. *Polym. Sci. USSR* **1990,** *32* (3), 469-474.

(203) Meeussen, F.; Nies, E.; Berghmans, H.; Verbrugghe, S.; Goethals, E.; Du Prez, F., Phase behaviour of poly(N-vinyl caprolactam) in water. *Polymer* **2000,** *41* (24), 8597-8602.

(204) Maeda, Y.; Nakamura, T.; Ikeda, I., Hydration and Phase Behavior of Poly(N-vinylcaprolactam) and Poly(N-vinylpyrrolidone) in Water. *Macromolecules* **2002,** *35* (1), 217-222.

(205) Mikheeva, L. M.; Grinberg, N. V.; Mashkevich, A. Y.; Grinberg, V. Y.; Thanh, L. T. M.; Makhaeva, E. E.; Khokhlov, A. R., Microcalorimetric Study of Thermal Cooperative Transitions in Poly(N-vinylcaprolactam) Hydrogels. *Macromolecules* **1997,** *30* (9), 2693-2699.

(206) Kollman, P. A.; Massova, I.; Reyes, C.; Kuhn, B.; Huo, S.; Chong, L.; Lee, M.; Lee, T.; Duan, Y.; Wang, W.; Donini, O.; Cieplak, P.; Srinivasan, J.; Case, D. A.; Cheatham, T. E., Calculating Structures and Free Energies of Complex Molecules: Combining Molecular Mechanics and Continuum Models. *Acc. Chem. Res.* **2000,** *33* (12), 889-897.

(207) Gohlke, H.; Case, D. A., Converging free energy estimates: MM-PB(GB)SA studies on the protein–protein complex Ras–Raf. *J. Comput. Chem.* **2004,** *25* (2), 238-250.

(208) Chotsaeng, N.; Laosinwattana, C.; Charoenying, P., Herbicidal Activity of Flavokawains and Related trans-Chalcones against Amaranthus tricolor L. and Echinochloa crus-galli (L.) Beauv. *ACS Omega* **2019,** *4* (24), 20748-20755.

(209) Cakmak, I., Enrichment of cereal grains with zinc: Agronomic or genetic biofortification? *Plant Soil* **2008,** *302* (1), 1-17.

(210) Singh, A.; Dhiman, N.; Kar, A. K.; Singh, D.; Purohit, M. P.; Ghosh, D.; Patnaik, S., Advances in controlled release pesticide formulations: Prospects to safer integrated pest management and sustainable agriculture. *Journal of Hazardous Materials* **2020,** *385*, 121525.

(211) Trenkel, M. E., *Slow- and Controlled-release and Stabilized Fertilizers: An Option for Enhancing Nutrient Use Efficiency in Agriculture*. International Fertilizer Industry Association: 2010.

(212) Prat, D.; Wells, A.; Hayler, J.; Sneddon, H.; McElroy, C. R.; Abou-Shehada, S.; Dunn, P. J., CHEM21 selection guide of classical- and less classical-solvents. *Green Chem.* **2016,** *18* (1), 288-296.

(213) Alfonsi, K.; Colberg, J.; Dunn, P. J.; Fevig, T.; Jennings, S.; Johnson, T. A.; Kleine, H. P.; Knight, C.; Nagy, M. A.; Perry, D. A.; Stefaniak, M., Green chemistry tools to influence a medicinal chemistry and research chemistry based organisation. *Green Chem.* **2008,** *10* (1), 31-36.